Beiträge zur numerischen Homogenisierung mikroheterogener Materialien mittels Zwei-Skalen Finite Elemente Methoden

DISSERTATION

zur Erlangung des Grades eines Doktors
der Ingenieurwissenschaften

vorgelegt von
M.Sc. Andreas Fischer

eingereicht bei der Naturwissenschaftlich-Technischen Fakultät
der Universität Siegen

Siegen 2024

Betreuer

Prof. Dr.-Ing. habil. Bernhard Eidel
Technische Universität Bergakademie Freiberg

Gutachter

Prof. Dr.-Ing. habil. Chuanzeng Zhang
Universität Siegen
Prof. Dr.-Ing. habil. Kerstin Weinberg
Universität Siegen

Tag der mündlichen Prüfung
06.11.2025

Danksagung

An dieser Stelle möchte ich mich bei einigen Personen bedanken, die mich auf dem Weg zu dieser Arbeit begleitet und unterstützt haben.

Der größte Dank gebührt Professor Eidel. Es dürfte im Wintersemester 2014/15 zu Beginn meines Master-Studiums gewesen sein, als Sie mir das erste Zwei-Skalen FEM-Paper überreicht haben. Aus einem „Schauen Sie sich das mal an“ wurde eine HiWi-Tätigkeit, eine Masterarbeit, eine Beschäftigung als wissenschaftlicher Mitarbeiter und schließlich entstanden in den vergangenen 10 Jahren die dieser kumulativen Promotion zugrundeliegenden Veröffentlichungen. Ohne Ihre Führung und Ideen, welche Aspekte der Zwei-Skalen FEM wir noch unter die Lupe nehmen könnten, wäre diese Arbeit nicht entstanden. Ich bedanke mich für die allzeit gute Zusammenarbeit und die Geduld, die Sie mit mir in den letzten 10 Jahren haben mussten. Ein kleiner Vergleich, um zu verdeutlichen, wie lange 10 Jahre sind: Der FC Schalke 04 hat seit der Saison 2014/15 eine Vizemeisterschaft gefeiert, je zweimal Champions und Europa League gespielt, ist zweimal ab- und einmal wieder aufgestiegen und hat 15 Trainer (zum Teil mehrfach) verschlissen. Ich bin mir zwar sicher, dass ein erneuter Aufstieg unmittelbar bevorsteht, hoffe aber trotzdem, dass wir nach diesen 10 Jahren besser dastehen als der beste Fussballverein des Ruhrgebietes.

Bedanken möchte ich mich auch bei Professor Zhang und Professor Weinberg für die Übernahme der Rolle der Gutachter sowie Professor Kraemer und Professor Plato für die Bereitschaft zur Mitarbeit in der Promotionskommission.

Ein großer Dank gebührt Ajinkya Gote, der als Kollege in der Heisenberg-Gruppe (mehr oder weniger freiwillig) auch immer wieder in den Kontakt mit den Zwei-Skalen Finite Elemente Methoden gekommen ist. Deine Unterstützung beim „Number Crunching“ war eine große Hilfe im Laufe der Jahre.

Nicht zu vergessen auch Fabian Gücker und Pratik Pradhan, die als studentische Hilfskräfte die von mir geschriebenen Matlab-Funktionen und Skripte in einen Highspeed-C++-Code mit ordentlicher Parallelisierung überführt und somit die Berechnung vieler Overkill-Lösungen erst ermöglicht haben.

Schlussendlich möchte ich mich bei meiner Familie und meinen Freunden bedanken, die mich in den letzten Jahren nie mit den Fragen „Was macht deine Doktorarbeit?“ und „Wann reichst du die Arbeit endlich ein?“ genervt haben. Ich danke euch für eure Empathie, auch wenn ich mir sicher bin, dass der ein oder andere nicht mehr mit dem Abschluss des Promotionsverfahrens gerechnet hat - nehmt das!

Veröffentlichungen

a) Begutachtete Veröffentlichungen:

i) Eidel, B., Fischer, A. (2018): The Heterogeneous Multiscale Finite Element Method for the Homogenization of Linear Elastic Solids and a Comparison with the FE^2 Method, Computer Methods in Applied Mechanics and Engineering, Vol. 329, pp. 332-368.

ii) Fischer, A., Eidel, B. (2019): Convergence and error analysis of FE-HMM/FE^2 for energetically consistent micro-coupling conditions in linear elastic solids, European Journal of Mechanis - A/Solids, Vol. 77.

iii) Fischer, A., Eidel, B. (2020): Error analysis for quadtree-type mesh-coarsening algorithms adapted to pixelized heterogeneous microstructures, Computational Mechanics, Vol. 65, pp. 1467-1491.

iv) Eidel, B., Fischer, A., Gote, A. (2020): From image data towards microstructure information – accuracy analysis at the digital core of materials, ZAMM-Journal of Applied Mathematics and Mechanics, Vol. 101(6).

v) Gote, A., Fischer, A., Zhang C., Eidel, B. (2022): Computational Homogenization of Concrete in the Cyber Size-Resolution-Discretization (SRD) Parameter Space. Finite Elements in Analysis and Design, Vol. 198.

b) Weitere Veröffentlichungen:

vi) Eidel, B., Fischer, A. (2016): The Heterogeneous Multiscale Finite Element Method FE-HMM for the Homogenization of Linear Elastic Solids, Proceedings of Applied Mathematics and Mechanics(PAMM), Vol.16, Issue-1, pp.521-522.

vii) Eidel, B., Fischer, A., Gote, A. (2018): A nonlinear FE-HMM formulation along with a novel algorithmic structure for finite deformation elasticity. Proceedings of Applied Mathematics and Mechanics (PAMM), Vol.18, Issue 1, pp.1-2.

viii) Eidel, B., Fischer, A., Gote, A. (2019): A nonlinear finite element heterogeneous multiscale method for the homogenization of hyperelastic solids and a novel staggered two-scale solution algorithm, zur Begutachtung eingereicht.

Die unter a) aufgeführten, begutachteten Veröffentlichungen bilden den Inhalt dieser kumulativen Promotionsschrift. Zusätzlich wurde auch die unter b) Punkt viii) aufgeführte und zur Begutachtung eingereichte Veröffentlichung aus dem Bereich nichtlinearer Zwei-Skalen Finite Elemente Methoden aufgenommen, da sie bemerkenswerte Ergebnisse zur Lösung von verschachtelten nichtlinearen Gleichungssystemen enthält.

Zusammenfassung

Die numerische Homogenisierung umfasst Verfahren zur Lösung von Problemen mit mehreren Skalen. Das Ziel ist hierbei das zugrundeliegende Problem auf einer Makroskala unter Berücksichtigung des Einflusses einer heterogenen Mikroskala zu lösen. Numerische Homogenisierungsverfahren liefern somit ein besseres Verständnis des makroskopischen Problems bei gleichzeitiger Reduktion des numerischen Aufwandes gegenüber Analysen mit einer vollständigen Analyse der Mikroskala.

Die Heterogene Multiskalen Finite Elemente Methode ist eines dieser numerischen Homogenisierungsverfahren und liefert durch eine vollständige a priori Fehleranalyse einen neuen und gleichzeitig bedeutenden Beitrag zur numerischen Homogenisierung mittels Zwei-Skalen Finite Elemente Methoden.

In dieser Arbeit und den ihr zugrunde liegenden Veröffentlichungen wurde die Implementierung der Heterogenen Multiskalen Finite Elemente Methode für vektorwertige Probleme aus dem Bereich Elastizität beschrieben und zahlreiche weitere Aspekte untersucht. Dazu gehören

i) Bestätigung der a priori Konvergenzaussagen für lineare Elastizität anhand zahlreicher Beispiele unterschiedlicher Regularität mit unterschiedlichen Kopplungsbedingungen der beiden Skalen und linearen sowie quadratischen Ansatzfunktionen.

ii) Vergleich der Heterogenen Multiskalen Finite Elemente Methode mit der FE^2-Methode. Obwohl beide Methoden auf unterschiedlichen Ansätzen beruhen, konnte anhand zahlreicher Beispiele die quantitative Übereinstimmung der Ergebnisse gezeigt werden, sodass die a priori Konvergenzaussagen auch auf die FE^2-Methode übertragen werden können.

iii) Während sich üblicherweise in der Literatur die Fehleranalysen mit dem Fehler auf der Makroskala beschäftigen, erfolgte in dieser Arbeit zusätzlich eine Untersuchung der Fehler auf der Mikroskala. Hierfür wurde zwischen dem Diskretisierungsfehler und einem Auflösungsfehler, der die Auflösung der Mikroskala berücksichtigt, unterschieden.

iv) Eine Untersuchung der Fehlerschätzung auf der heterogenen Mikroskala lieferte einen angepassten Fehlerschätzer-Algorithmus mit dem sich die Qualität der Fehlerschätzung auf der Mikroskala deutlich verbessern lässt.

v) Unterschiedliche adaptive und uniforme Netzvergröberungsalgorithmen, die als Preprocessor zur Reduktion der Freiheitsgrade der Mikroskala eingesetzt werden können, wurden anhand ihrer Auswirkungen auf den Diskretisierungs- und den Auflösungsfehler untersucht.

vi) Um den hohen numerischen Aufwand nicht-linearer Zwei-Skalen Probleme, der sich durch die wiederholte Lösung von verschachtelten Makro- und Mikrogleichungssystemen ergibt, zu reduzieren, wurde ein neuer Lösungsalgorithmus eingeführt, der die Berechnungen deutlich beschleunigen kann.

Abstract

Numerical homogenization includes methods for solving multiscale problems. The goal here is to solve the underlying problem on a macroscale, taking into account the influence of a heterogeneous microscale. Numerical homogenization methods thus provide a better understanding of the macroscopic problem while at the same time reducing the numerical effort compared to a complete analysis of the microscale.

The Finite Element Heterogeneous Multiscale Method is one of these numerical homogenization methods and, through a complete a priori error analysis, provides a new and at the same time significant contribution to numerical homogenization by two-scale finite element methods.

In this work and the publications on which it is based, the implementation of the Finite Element Heterogeneous Multiscale Method for vector-valued problems in the field of elasticity was described and numerous other aspects were examined. These include

i) Confirmation of the a priori convergence statements for linear elasticity using numerous examples with different regularity with different coupling conditions of the two scales and linear and quadratic shape functions.

ii) Comparison of the Finite Element Heterogeneous Multiscale Method with the FE^2 method. Although both methods are based on different approaches, the quantitative agreement of the results was shown using numerous examples, so that the a priori convergence statements can also be transferred to the FE^2 method.

iii) While error analyzes in the literature usually deal with errors on the macroscale, this work also examined errors on the microscale. For this purpose, a distinction was made between the discretization error and a resolution error that takes the resolution of the microscale into account.

iv) An investigation of the error estimation on the heterogeneous microscale provided an adapted error estimator algorithm with which the quality of the error estimation on the microscale can be significantly improved.

v) Different adaptive and uniform mesh coarsening algorithms that can be used as a preprocessor to reduce the microscale degrees of freedom were examined based on their effects on the discretization and resolution errors.

vi) In order to reduce the high numerical effort of non-linear two-scale problems, which results from the repeated solution of nested macro and micro equation systems, a new solution algorithm was introduced that can significantly speed up the calculations.

Inhaltsverzeichnis

1 Einleitung **1**

2 Zwei-Skalen Finite Elemente Methoden **3**

2.1 Das Modellproblem für lineare Elastizität 4

2.2 Numerische Homogenisierung 5

2.3 Zwei-Skalen FE-Verfahren 6

2.3.1 Heterogene Multiskalen Finite Elemente Methode 6

2.3.2 FE^2-Methode 8

2.3.3 Finite Zellen Methode 9

2.4 Weitere Verfahren 11

2.5 Mikro-Makro-Kopplung und repräsentatives Volumenelement 11

3 Fehlerkonvergenz und Verfeinerungsstrategien **16**

3.1 Fehlerzerlegung 17

3.1.1 Fehler auf der Mikroskala 17

3.1.2 Fehler auf der Makroskala 17

3.2 A priori Konvergenzaussagen 18

3.3 Optimale Netzverfeinerungsstrategie 19

3.4 Fehlerschätzung bei heterogenen Mikrostrukturen 22

4 Vernetzung **25**

4.1 Uniforme Netzvergröberung 25

4.2 Adaptive Netzvergröberung 26

5 Nichtlineare FE-HMM **28**

5.1 Standard Lösungs-Algorithmus 28

5.2 Alternierender Lösungs-Algorithmus 29

6 Zusammenfassung **31**

7 Literatur **33**

8 Anlagen **38**

8.1 Veröffentlichung: The heterogeneous multiscale finite element method for the homogenization of linear elastic solids and a comparison with the FE^2 method 38

8.2 Veröffentlichung: Convergence and error analysis of FE-HMM/FE^2 for energetically consistent micro-coupling conditions in linear elastic solids 76

8.3 Veröffentlichung: Error analysis for quadtree-type mesh coarsening algorithms adapted to pixelized heterogeneous microstructures 98

8.4 Veröffentlichung: From image data towards microstructure information – Accuracy analysis at the digital core of materials 124

8.5 Veröffentlichung: Computational homogenization of concrete in the cyber Size-Resolution-Discretization (SRD) parameter space 150

8.6 Veröffentlichung: A nonlinear finite element heterogeneous multiscale method for the homogenization of hyperelastic solids and a novel staggered two-scale solution algorithm 165

1 Einleitung

Viele Materialien weisen eine heterogene Mikrostruktur mit lokal unterschiedlichen mechanischen Eigenschaften auf. In der Materialwissenschaft werden durch die gezielte Kombination von Materialien mit unterschiedlichen mechanischen Eigenschaften Verbundmaterialien erzeugt, die für den jeweiligen Anwendungsfall optimierte mechanische Eigenschaften aufweisen. Faserverstärkte Kunststoffe zeichnen sich beispielsweise durch eine Kombination des geringen Gewichtes des Kunststoffes mit den guten mechanischen Eigenschaften der verwendeten Fasern - üblicherweise Glas- oder Kohlenstofffasern - aus. Hierdurch lassen sich Bauteile herstellen, die gleichzeitig extrem leicht sind aber trotzdem hohen Beanspruchungen standhalten können. Anwendung finden solche Bauteile beispielsweise in der Automobil- oder Luftfahrtindustrie, da hier Gewichtseinsparungen einhergehen mit einer Reduktion der Betriebskosten.

Durch immer leistungsfähigere Computer und Rechencluster gewinnt der Einsatz von numerischen Berechnungen in Industrie und Forschung immer mehr an Bedeutung. Bereits im frühen Entwicklungsstadium können durch numerische Simulationen Erkenntnisse für die Produktentwicklung gewonnen werden ohne aufwändige Versuche durchführen zu müssen. Das Vorhandensein leistungsfähiger, kommerzieller Software-Tools im Bereich des Computer-Aided Engineering (CAE) führt dazu, dass numerische Simulationen heute zum Standard-Werkzeug in der Ingenieurwissenschaft geworden sind.

Die Finite Elemente Methode (FEM) ist ein in vielen Bereichen der Ingenieurwissenschaft eingesetztes Verfahren zur numerischen Bestimmung einer Näherungslösung von Differentialgleichungen. Die Qualität der Näherungslösung steigt hierbei mit der Anzahl der Finiten Elemente (FE), die zur Diskretisierung des betrachteten Körpers verwendet werden. Im Gegenzug bedeutet eine feiner werdende Diskretisierung allerdings auch mehr Freiheitsgrade und damit einen höheren numerischen Aufwand. Trotz der hohen Leistungsfähigkeit moderner Computer und Rechencluster gibt es weiterhin Grenzen bei der Durchführung numerischer Berechnungen. Die Anzahl der Freiheitsgrade der zu lösenden Berechnungsaufgaben können nicht beliebig groß werden, der numerischen Aufwand und die benötigte Berechnungs-Genauigkeit müssen stets abgewogen werden.

Die heterogene Mikrostruktur von Materialien hat einen wesentlichen Einfluss auf das makroskopische Verhalten der Bauteile oder Strukturen - angefangen beim Deformationsverhalten bis hin zum Versagen von Strukturen unter mechanischer Beanspruchung. Um zuverlässige Berechnungsergebnisse zu erhalten ist es erforderlich in der Modellierung die Mikroheterogenität der Werkstoffe zu berücksichtigen. Da die Mikrostruktur jedoch im Vergleich zu den makroskopischen Abmessungen eines Bauteils auf einer deutlich kleineren Skala aufgelöst werden muss, ergibt sich zwangsläufig eine sehr hohe Anzahl an Freiheitsgraden bei der Berücksichtigung der vollständigen, fein aufgelösten Mikrostruktur.

Sollen in einer Finite Elemente Analyse mit Elementen der Kantenlänge H heterogene Verbundmaterialien und insbesondere der Einfluss der Mikrostruktur mit der charakteristischen Länge ϵ auf das makroskopische Materialverhalten analysiert werden, so müssen die zugehörigen Finiten Elemente so fein gewählt werden, dass diese die Mikrostruktur tatsächlich erfassen können - es muss also gelten $H \leq \epsilon$.

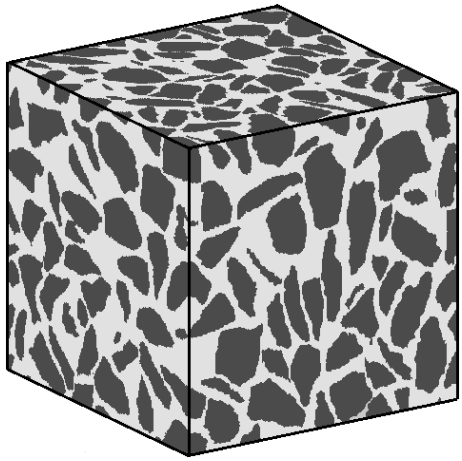


Abbildung 1: Heterogene Mikrostruktur einer Betonprobe, analysiert in Gote et al. [26].

Als Beispiel dient die in Abb. 1 dargestellte Mikrostruktur einer Betonprobe, die von Huang et al. [33] mittels Computer-Tomografie aufgenommen wurde und aus grobkörnigen Zuschlagsstoffen in einer Zementmatrix sowie Lufteinschlüssen besteht. Die Aufnahme der kubischen Probe besteht aus $371 \times 371 \times 371$ Voxeln, die Kantenlänge des Kubus beträgt $37,1\,\mathrm{mm}$. Werden die einzelnen Voxel als Input-Daten für eine FE-Analyse verwendet, wobei jeder Voxel einem 8-Knoten Element entspricht und jeder Knoten 3 Freiheitsgrade hat, ergibt sich bereits eine Randwertproblem mit über 150 Mio. Freiheitsgraden. Üblicherweise weisen Bauteile aus Beton deutlich größere Abmessungen auf, nimmt man beispielsweise eine Betondecke mit den Maßen $4\,\mathrm{m} \times 5\,\mathrm{m} \times 0,16\,\mathrm{m}$, so ergeben sich bei einer entsprechend feinen Diskretisierung bereits fast 10 Billionen Freiheitsgrade.

Numerische Homogenisierungsverfahren mittels Zwei-Skalen Finite Elemente Methoden bieten einen leistungsfähigen Ansatz für die Lösung mikroheterogener Randwertprobleme, da sie die Genauigkeit der Modellierung mit effizienten Berechnungen verbinden. Hierfür wird das zu lösende Modellproblem auf zwei Skalen aufgeteilt - eine Makro-Skala, die das makroskopische Bauteilverhalten abbildet und eine Mikro-Skala, die die heterogene Mikrostruktur erfasst. Beide Skalen sind miteinander gekoppelt und interagieren miteinander. Neben den Verschiebungen auf dem Makrolevel, die Aufschluss über das Deformationsverhalten des Bauteils oder der Struktur geben, können auch Verschiebungen auf dem Mikrolevel berechnet werden. Mit Hilfe dieser Mikroverschiebungen können Phänomene wie Schädigung, Plastizität oder Rissausbreitung innerhalb der Mikrostruktur erfasst und deren Auswirkungen auf das makroskopische Deformationsverhalten analysiert werden.

Die im Rahmen dieser Arbeit entstandenen Veröffentlichungen liefern Beiträge zu bisher nicht behandelten Aspekten der numerischen Homogenisierung mittels Zwei-Skalen Finite Elemente Verfahren.

2 Zwei-Skalen Finite Elemente Methoden

Grundsätzlich basieren Zwei-Skalen Finite Elemente Methoden auf einer Verschachtelung von FE-Analysen auf dem Mikro- und Makrolevel und werten die reale Mikrostruktur nur auf repräsentativen Volumenelementen (RVE) bzw. Mikrogebieten an ausgewählten Stützstellen aus.

Die Grundlage zahlreicher Lösungsansätzen zur Bestimmung der effektiven Materialeigenschaften mittels Zwei-Skalen FE-Verfahren - wie beispielsweise der FE^2-Methode - ist die Hill-Mandel Bedingung [29, 30], die die Gleichheit der Energiedichte auf dem Makro- und dem Mikrolevel fordert. Formuliert für einen Punkt auf dem Makrolevel mit einem zugehörigen Mikrogebiet mit dem Volumen V lautet die Bedingung

$$\bar{\boldsymbol{\sigma}} : \dot{\bar{\boldsymbol{\varepsilon}}} = \frac{1}{V} \int_V \boldsymbol{\sigma} : \dot{\boldsymbol{\varepsilon}} \, dV \tag{1}$$

mit den makroskopischen Spannungen und Verzerrungen $\bar{\boldsymbol{\sigma}}$ und $\bar{\boldsymbol{\varepsilon}}$ sowie den mikroskopischen Spannungen und Verzerrungen $\boldsymbol{\sigma}$ und $\boldsymbol{\varepsilon}$. Die Spannungen auf dem Makrolevel $\bar{\boldsymbol{\sigma}}$ lassen sich hierbei als Volumenmittel der Mikrospannungen $\boldsymbol{\sigma}$ berechnen

$$\bar{\boldsymbol{\sigma}} = \frac{1}{V} \int_V \boldsymbol{\sigma} \, dV \, . \tag{2}$$

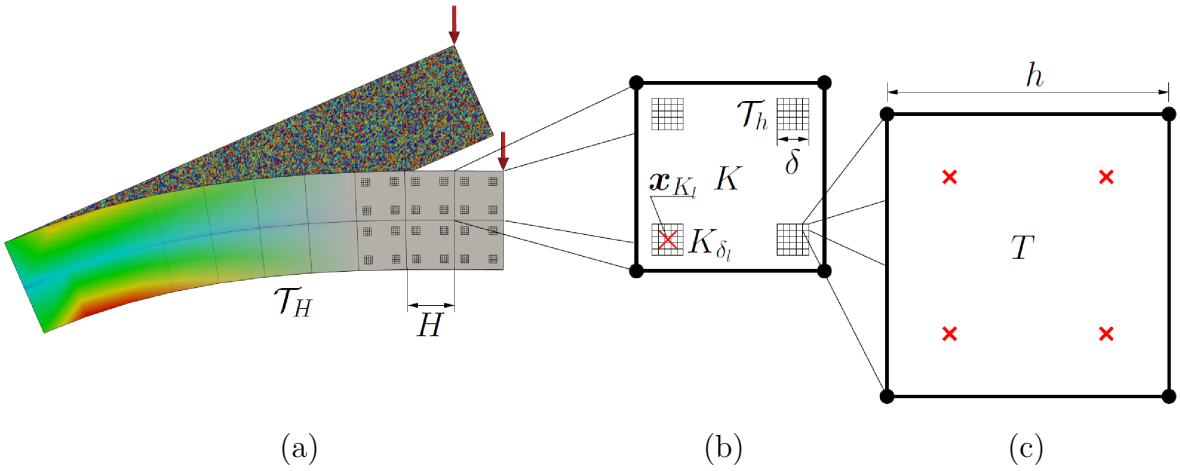


Abbildung 2: Schema von Zwei-Skalen Finite Elemente Methoden: (a) Makroskopisches Randwertproblem mit Makrodiskretisierung, (b) Ein Makroelement mit Mikrogebieten an den Quadraturstellen, (c) Mikroelement mit Standard Quadraturstellen, aus Eidel und Fischer [21].

Das Schema einer Zwei-Skalen Finite Elemente Methode ist in Abb. 2 dargestellt. Abgebildet sind (a) das diskretisierte makroskopische Randwertproblem mit Elementen der Größe H, (b) ein Element $K \in \mathcal{T}_H$ auf dem Makrolevel, in dessen 2×2 Quadratur-Stützstellen $\boldsymbol{x}_{K_l}$ Mikro-FE-Netze der Kantenlänge δ aufgebaut werden, und (c) ein Element $T \in \mathcal{T}_h$ auf dem Mikrolevel mit der Kantenlänge h und 2×2 Quadratur-Stützstellen.

Das makroskopische Randwertproblem wird hierbei mit vergleichsweise groben Elementen, deren Kantenlänge H deutlich größer ist als die charakteristische Länge der Mikroheterogenität ϵ, diskretisiert. In den Stützstellen der numerischen Quadratur werden

Mikrogebiete, deren Größe δ größer oder gleich der charakteristischen Länge der Mikroheterogenität ϵ sein sollte, aufgebaut. Diese Mikrogebiete werden wiederum mit Mikroelementen der Kantenlänge h diskretisiert, durch die Diskretisierung der Mikrogebiete mit Elementen der Größe $h \leq \epsilon$ erfassen die Mikroelemente die Mikroheterogenität.

Es findet ein Informationsaustausch zwischen den beiden Skalen statt. Während die makroskopischen Verschiebungen vom Makro- auf das Mikrolevel übertragen werden, werden die Informationen über die Materialeigenschaften und die Spannungen vom Mikro- auf das Makrolevel übergeben.

Der numerische Aufwand solcher Zwei-Skalen FE-Verfahren ist zwar deutlich geringer als der Aufwand von Ein-Skalen FE-Verfahren mit sehr feiner Diskretisierung mit Elementen $H \leq \epsilon$, sollte allerdings nicht unterschätzt werden. Der Balken aus Abb. 2 ist mit 10×2 Makroelementen diskretisiert, jedes Makroelement weist vier Stützstellen für die numerische Integration auf. In jeder dieser Stützstellen wird wiederum ein Mikronetz mit 5×5 Elementen aufgespannt. Das gesamte Randwertproblem besteht folglich aus 20 Makroelementen mit insgesamt 80 Mikrogebieten, jedes wiederum mit 25 Mikroelementen diskretisiert. Trotz der recht groben Diskretisierungen auf Mikro- und Makrolevel ergeben sich hier in Summe bereits 2000 Elemente auf dem Mikrolevel. In der Praxis werden auf Makro- und Mikroebene deutlich feinere Vernetzungen verwendet, sodass die Anzahl der gesamten Freiheitsgrade eines solchen Randwertproblems schnell in den Bereich einiger Millionen vorstößt.

2.1 Das Modellproblem für lineare Elastizität

Ein Körper $\mathcal{B}$ bildet einen begrenzten Unterraum von $\mathbb{R}^d$, $d = 2, 3$. Seine Ränder $\partial\mathcal{B} = \partial\mathcal{B}_D \cup \partial\mathcal{B}_N$ werden gebildet durch $\partial\mathcal{B}_D$, einem Rand mit Dirichlet-Randbedingungen, und $\partial\mathcal{B}_N$, einem Rand mit Neumann-Randbedingungen.

Der Körper weist eine mikroheterogene Struktur auf, wird durch Volumenkräfte $\boldsymbol{f}$ und Oberflächenkräfte $\boldsymbol{g}$ belastet und befindet sich im statischen Gleichgewicht.

Gesucht werden die Verschiebung $\boldsymbol{u}^\epsilon = (u_1^\epsilon, \ldots, u_d^\epsilon)$ des Körpers, die gegeben sind durch die Lösung des Gleichungssystems

$$\left.\begin{aligned} -\frac{\partial}{\partial x_j}\left(\mathbb{A}^\epsilon_{ijlm}\frac{\partial u_l^\epsilon}{\partial x_m}\right) &= f_i \quad \text{in} \quad \mathcal{B} \\ u_i^\epsilon &= \bar{u}_i \quad \text{auf} \quad \partial\mathcal{B}_D \\ \mathbb{A}^\epsilon_{ijlm}\frac{\partial u_l^\epsilon}{\partial x_m}\, n_j &= g_i \quad \text{auf} \quad \partial\mathcal{B}_N \end{aligned}\right\} \tag{3}$$

Es wird ein linear elastisches Stoffgesetz angenommen $\sigma_{ij}^\epsilon = \mathbb{A}^\epsilon_{ijlm}\varepsilon^\epsilon_{lm}$, wobei $\mathbb{A}^\epsilon_{ijlm}$ der heterogene Elastizitätstensor ist.

In $(3)_2$ beschreibt $\bar{u}_i$ die vorgegebenen Verschiebungen auf dem Dirichlet Rand, in $(3)_3$ beschreibt $n_j = (n_1, \ldots, n_d)$ den Einheitsnormalenvektor auf dem Rand $\partial\mathcal{B}_N$. Der Superskript ϵ beschreibt hier und im Folgenden die Abhängigkeit der jeweiligen Größe von der heterogenen Mikrostruktur.

Durch Multiplikation mit geeigneten Testfunktionen $\boldsymbol{v}$ lässt sich die starke Form des Modellproblems in die schwach Form überführen:

Gesucht werden die Verschiebungen $\boldsymbol{u}^\epsilon$, so dass

$$B^\epsilon(\boldsymbol{u}^\epsilon, \boldsymbol{v}) \overset{\text{def}}{=} \int_{\mathcal{B}} \mathbb{A}^\epsilon(\boldsymbol{x})\, \boldsymbol{\varepsilon}(\boldsymbol{u}^\epsilon) : \boldsymbol{\varepsilon}(\boldsymbol{v})\, dV = \int_{\mathcal{B}} \boldsymbol{f} \cdot \boldsymbol{v}\, dV + \int_{\partial\mathcal{B}_N} \boldsymbol{g} \cdot \boldsymbol{v}\, dA \tag{4}$$

für alle $\boldsymbol{v} \in \mathcal{V}$ erfüllt ist. $\mathcal{V}$ ist hierbei der Raum der zulässigen Verschiebungen, die die homogenen Randbedingungen erfüllen

$$\mathcal{V} = \{\boldsymbol{v}; \boldsymbol{v} \in H^1(\mathcal{B})^d, \boldsymbol{v}|_{\partial\mathcal{B}_D} = \boldsymbol{0}\}\,. \tag{5}$$

2.2 Numerische Homogenisierung

Die Berechnung der effektiven, makroskopischen Materialeigenschaften einer heterogenen Mikrostruktur ist eine Aufgabe, die mittels numerischer Homogenisierungsverfahren gelöst werden kann. Altmann et al. [9] präsentierten einen ausführlichen Überblick über das Thema numerische Homogenisierung, deren Entstehung sowie zahlreiche Verfahren zur numerischen Homogenisierung mit unterschiedlichen Ansätzen.

Grundsätzlich ist es das Ziel der numerischen Homogenisierung die Eigenschaften einer heterogenen Mikrostruktur von einer Mikro-Skala auf eine Makro-Skala zu übertragen. Für das in Gleichung (3) präsentierte Modellproblem für lineare Elastizität bedeutet das, dass der Einfluss des mikroheterogenen Elastizitätstensors auf der Mikro-Skala analysiert und eine effektiver, makroskopischer Elastizitätstensor ermittelt wird.

Die Vorteile der numerischen Homogenisierung liegen hierbei auf der Hand. Zum einen ist hier Reduktion des numerischen Berechnungsaufwandes, die manche Probleme überhaupt erst für eine numerische Untersuchung zugänglich macht, zu nennen. Zum anderen liefert die Homogenisierung ein besseres Verständnis des makroskopischen Verhaltens, das maßgeblich durch die Mikrostruktur beeinflusst wird - bis hin zum Versagen der Makrostruktur aufgrund von Phänomenen wie zum Beispiel Rissausbreitung auf der Mikroebene.

Erste Ansätze zur Bestimmung der makroskopischen Materialeigenschaften von mikroheterogenen Materialien präsentierten Voigt [57] und Reuss [51] bereits in den Jahren 1910 bzw. 1929. Voigt verwendet hierbei den arithmetischen Mittelwert der Mikrostruktur mit dem Volumen V, gleichbedeutend mit einem uniformen Verzerrungszustand der Mikrostruktur

$$\mathbb{A}^{\text{Voigt}} = \frac{1}{|V|} \int_V \mathbb{A}^\epsilon dV\,, \tag{6}$$

Reuss hingegen verwendet den harmonischen Mittelwert, gleichbedeutend mit einem uniformen Spannungszustand der Mikrostruktur

$$\mathbb{A}^{\text{Reuss}} = \frac{1}{|V|} \left(\int_V (\mathbb{A}^\epsilon)^{-1}\, dV \right)^{-1}\,. \tag{7}$$

Diese beiden Ansätze stellten sich später als eine obere und untere Schranke bei der Berechnung der makroskopischen Materialeigenschaften mikroheterogener Strukturen heraus.

Datenbasierte FE-Berechnungen [40, 41] umgehen die Notwendigkeit einer Material-Modellierung indem sie experimentell gewonnene Materialdaten als Grundlage verwenden. Eidel [20] beschreibt den Einsatz von neuronalen Netzen zur effizienten Bestimmung des makroskopischen Elastizitätstensors, wobei keine expliziten numerischen Berechnungen erforderlich sind und der numerische Aufwand somit auf ein Minimum reduziert wird.

Das Modellproblem aus Gleichung (3) lässt sich durch die Verwendung des homogenisierten Elastizitätstensors in das homogenisierte Modellproblem überführen. Dieses lautet in der starken Form:

Gesucht werden die homogenisierten Verschiebung $\boldsymbol{u}^0 = (u_1^0, \dots, u_d^0)$ des Körpers, die gegeben sind durch die Lösung des Gleichungssystems

$$\left.\begin{aligned} -\frac{\partial}{\partial x_j}\left(\mathbb{A}^0_{ijlm}\frac{\partial u_l^0}{\partial x_m}\right) &= f_i \qquad \text{in} \quad \mathcal{B} \\ u_i^0 &= \bar{u}_i \qquad \text{auf} \quad \partial\mathcal{B}_D \\ \mathbb{A}^0_{ijlm}\frac{\partial u_l^0}{\partial x_m}\, n_j &= g_i \qquad \text{auf} \quad \partial\mathcal{B}_N \end{aligned}\right\} \tag{8}$$

Analog zu dem ursprünglichen Modellproblem lässt sich auch das homogenisierte Modellproblem durch Multiplikation mit geeigneten Testfunktionen $\boldsymbol{v}$ in eine schwache Form überführen

$$B^0(\boldsymbol{u}^0, \boldsymbol{v}) = \int_{\mathcal{B}} \mathbb{A}^0\, \boldsymbol{\varepsilon}(\boldsymbol{u}^0) : \boldsymbol{\varepsilon}(\boldsymbol{v})\, dV = \int_{\mathcal{B}} \boldsymbol{f}\cdot\boldsymbol{v}\, dV + \int_{\partial\mathcal{B}_N} \boldsymbol{g}\cdot\boldsymbol{v}\, dA \qquad \forall\, \boldsymbol{v} \in \mathcal{V}\,. \tag{9}$$

Hierbei beschreibt $\mathbb{A}^0$ den homogenisierten Elastizitätstensor, der Superskript 0 beschreibt hier und im Folgenden eine Abhängigkeit der jeweiligen Größe von der homogenisierten Mikrostruktur. Die Lösung des in Gleichung (8) beschriebenen homogenisierten Modellproblems kann mit Hilfe einer Standard Finite Elemente Methode berechnet werden, der homogenisierte Elastizitätstensor ist jedoch bei heterogenen Mikrostrukturen nicht bekannt und muss folglich mit Hilfe numerischer Homogenisierungsverfahren bestimmt werden.

2.3 Zwei-Skalen FE-Verfahren

An dieser Stelle werden ausgewählte Zwei-Skalen Finite Elemente Verfahren vorgestellt.

2.3.1 Heterogene Multiskalen Finite Elemente Methode E und Engquist [17] haben 2003 die Heterogene Multiskalen Methode (engl. *Heterogeneous Multiscale Method*, HMM) beschrieben, Abdulle und Schwab [6] diesen Ansatz 2005 aufgegriffen und erstmals eine Beschreibung der Heterogenen Multiskalen Finite Elemente Methode (engl. *Finite Element Heterogeneous Multiscale Method*, FE-HMM) veröffentlicht.

Die Basis der FE-HMM liegt in der mathematischen Homogenisierung durch asymptotische Expansion [8, 11, 13, 53]. Eine Zusammenfassung der Homogenisierung durch asymptotische Expansion ist auch im Anhang der ersten dieser kumulativen Dissertationsschrift zugrunde liegenden Veröffentlichung [21] zu finden.

Der Ausgangspunkt der FE-HMM liegt in einer Modifizierung der Bilinearform $B^0(\boldsymbol{u}^0, \boldsymbol{v})$ aus Gleichung (9). Die diskrete Form dieser Bilinearform ergibt sich durch das Einsetzen der diskreten Verschiebungen $\boldsymbol{u}^H$ und der diskreten Testfunktionen $\boldsymbol{v}^H$ und lautet

$$B^0(\boldsymbol{u}^H, \boldsymbol{v}^H) = \sum_{K \in \mathcal{T}_H} \sum_{l=1}^{N_{qp}} \omega_{K_l} \cdot \left[\mathbb{A}^0(\boldsymbol{x}_{K_l}) \, \boldsymbol{\varepsilon}(\boldsymbol{u}^H(\boldsymbol{x}_{K_l})) : \boldsymbol{\varepsilon}(\boldsymbol{v}^H(\boldsymbol{x}_{K_l})) \right] . \tag{10}$$

Diskrete Größen auf dem Makrolevel werden hier und im Folgenden durch den Superskript H beschrieben, Größen auf dem Mikrolevel durch den Superskript h.

Da der homogenisierte Elastizitätstensor $\mathbb{A}^0$ an den Stützstellen $\boldsymbol{x}_{K_l}$ nicht bekannt ist, wird die virtuelle Arbeit in der diskreten Bilinearform durch eine weitere Bilinearform ersetzt

$$B^0(\boldsymbol{u}^H, \boldsymbol{v}^H) \approx \sum_{K \in \mathcal{T}_H} \sum_{l=1}^{N_{qp}} \omega_{K_l} \cdot \left[\frac{1}{|K_l|} \int_{K_l} \mathbb{A}^\epsilon(\boldsymbol{x}) \, \boldsymbol{\varepsilon}(\boldsymbol{u}^h_{K_l}) : \boldsymbol{\varepsilon}(\boldsymbol{v}^h_{K_l}) \, dV \right] = B^H(\boldsymbol{u}^H, \boldsymbol{v}^H) \tag{11}$$

mit den diskreten Mikroverschiebungen $\boldsymbol{u}^h_{K_l}$ auf dem Mikrogebiet l des Makroelementes K. Physikalisch betrachtet wird also die Energiedichte auf dem Makrolevel mit der Energiedichte auf dem Mikrolevel approximiert, das Vorgehen entspricht also der Hill-Mandel-Bedingung aus Gleichung (1).

Aus mathematischer Sicht führt das Ersetzen der Bilinearform aus Gleichung (10) zu einer modifizierten Bilinearform, welche wiederum eine vollständige diskrete a priori Fehleranalyse erlaubt und somit ein zentraler Bestandteil der FE-HMM ist. Erst durch diese diskrete Fehleranalyse lassen sich Rückschlüsse auf die Konvergenz von Fehlern in Abhängigkeit der Mikro- und Makrodiskretisierung ziehen und erlauben die Bestimmung einer optimalen Netzverfeinerungsstrategie. Die Anwendung dieser Verfeinerungsstrategien sorgt wiederum dafür, dass der numerische Aufwand durch die Netzverfeinerungen nicht unnötig stark ansteigt und keine Berechnungsressourcen verschwendet werden. Die Vorstellung der Konvergenzaussagen für die FE-HMM erfolgt in Abschnitt 3.2, die Ableitung der optimalen Verfeinerungsstrategie für unterschiedliche Normen erfolgt in Abschnitt 3.3.

Das Mikroproblem der FE-HMM ähnelt dem Zellen-Problem der asymptotischen Expansion. Formuliert für ein Mikrogebiet K_l lautet es:

Gesucht werden die Verschiebungen $\boldsymbol{u}^h_{K_l}$, so dass sowohl die Bedingungen für die Kopplung der beiden Skalen

$$\left(\boldsymbol{u}^h_{K_l} - \boldsymbol{u}^H_{lin,K_l} \right) \in \mathcal{S}^q(K_l, \mathcal{T}_h) \tag{12}$$

als auch die Mikro-Bilinearform

$$B_{K_l}(\boldsymbol{u}^h_{K_l}, \boldsymbol{w}^h_{K_l}) := \int_{K_l} \boldsymbol{\sigma}^\epsilon(\boldsymbol{u}^h_{K_l}) : \boldsymbol{\varepsilon}(\boldsymbol{w}^h_{K_l}) \, dV = 0 \quad \forall \, \boldsymbol{w}^h_{K_l} \in \mathcal{S}^q(K_l, \mathcal{T}_h) \tag{13}$$

in dem Mikro FE-Raum

$$\mathcal{S}^q(K_l, \mathcal{T}_h) = \left\{ \boldsymbol{w}^h \in \mathcal{W}(K_l); \boldsymbol{w}^h \in (\mathcal{P}^q(T))^d, T \in \mathcal{T}_h \right\} \tag{14}$$

erfüllt sind. $\mathcal{P}^q$ beschreibt hierbei den Raum der Polynome auf dem Element T.

Die Berechnung der Steifigkeit der Makroelemente erfolgt durch das Einsetzen der Ansatzfunktionen der Finiten Elemente in die modifizierte Bilinearform aus Gleichung (11). Ersetzt man hier die Verschiebungen $\boldsymbol{u}^H$ und die Testfunktionen $\boldsymbol{v}^H$ durch die Ansatzfunktionen $\boldsymbol{N}_I^H, \boldsymbol{N}_J^H$ ergibt sich die Steifigkeit der Makroelemente zu

$$\boldsymbol{k}_{IJ}^{mac} = B^H(\boldsymbol{N}_I^H, \boldsymbol{N}_J^H) = \sum_{l=1}^{N_{qp}} \frac{\omega_{K_l}}{|K_l|} \left(\boldsymbol{d}_{K_l}^{h(I)} \right)^T \boldsymbol{K}_{K_l}^{mic} \boldsymbol{d}_{K_l}^{h(J)}, \tag{15}$$

wobei $\boldsymbol{d}_{K_l}^h$ die Verschiebungen der Knoten auf dem Mikrogebiet und $\boldsymbol{K}_{K_l}^{mic}$ die Mikrosteifigkeitsmatrix beschreiben. Durch Assemblieren der einzelnen Einträge $\boldsymbol{k}_{IJ}^{mac}$ ergibt sich die resultierende makroskopische Elementsteifigkeitsmatrix des Makroelementes K

$$\boldsymbol{k}_K^{mac} = \sum_{l=1}^{N_{qp}} \frac{\omega_{K_l}}{|K_l|} \boldsymbol{T}_{K_l}^T \boldsymbol{K}_{K_l}^{mic} \boldsymbol{T}_{K_l} \tag{16}$$

mit der Transformationsmatrix

$$\boldsymbol{T}_{K_l} = \left[\left[\left[\boldsymbol{d}^{h(I,x_i)} \right]_{i=1,\dots,d} \right]_{I=1,\dots,N_{node}} \right] . \tag{17}$$

Hierbei sind $\boldsymbol{d}^{h(I,x_i)}$ die dimensionslosen Verschiebungen des Mikroproblems, das durch die makroskopische Ansatzfunktion N_I^H in x_i-Richtung getrieben wird. Die Verschiebungen auf dem Mikrolevel ergeben sich aus der Lösung des Mikrogleichungssystems

$$\boldsymbol{K}_{K_l}^{mic} \boldsymbol{d}^{h(I,x_i)} = \boldsymbol{0} \,, \tag{18}$$

das unter Berücksichtigung der Mikro-Makro-Kopplungsbedingungen gelöst werden muss.

2.3.2 FE^2-Methode Bereits 1990 präsentierten Guedes und Kikuchi [28] einen Ansatz zur numerischen Homogenisierung und damit die erste Formulierung der FE^2-Methode (engl. *FE^2 Method*, FE^2) für den Fall linearer Elastizität. Die FE^2-Methode hat im Laufe der Jahre Anwendung in vielen physikalischen und ingenieurwissenschaftlichen Bereichen gefunden. Hierzu gehört unter anderem die Anwendung auf Probleme mit gekoppelten Feldern, wie zum Beispiel elektro-mechanische [54], thermo-mechanische [59] oder magneto-mechanische [35] Probleme.

Eine ausführliche Vorstellung der FE^2-Methode präsentierte Schröder [55]. Der homogenisierte Elastizitätstensor $\mathbb{A}^0$ kann in jedem Quadraturpunkt auf dem Makrolevel berechnet mittels

$$\mathbb{A}^0 = \mathbb{A}^{\text{Voigt}} - \frac{1}{|K_l|} \boldsymbol{L}^T (\boldsymbol{K}_{K_l}^{mic})^{-1} \boldsymbol{L} \tag{19}$$

mit dem arithmetisch gemittelten Elastizitätstensor $\mathbb{A}^{\text{Voigt}}$ aus Gleichung (6) sowie der Matrix $\boldsymbol{L}$, die sich durch Assemblieren der elementweise berechneten $\boldsymbol{l}_e$

$$\boldsymbol{l}_e = \int_T \boldsymbol{B}^T \mathbb{A}^\epsilon \, dV \tag{20}$$

ergibt. Die Matrix $\boldsymbol{B}$ wiederum enthält die partiellen Ableitungen der FE-Ansatzfunktionen. Miehe und Koch [44] beschreiben wie für unterschiedliche Mikro-Makro-Kopplungsbedingungen der homogenisierte Elastizitätstensor $\mathbb{A}^0$ und die makroskopischen Spannungen berechnet werden können. Mit Hilfe des homogenisierten Elastizitätstensors kann im Anschluss das homogenisierte Modellproblem aus Gleichung (8) gelöst werden.

FE-HMM und FE^2 weisen, obwohl sie mit der asymptotischen Expansion und der Hill-Mandel Bedingung unterschiedliche Ansätze verfolgen, einige Parallelen auf. In Eidel und Fischer [21] wird gezeigt, dass für periodische Kopplungsbedingungen auch die asymptotische Expansion die Hill-Mandel Bedingung erfüllt. Die Gleichheit der Energiedichte auf Mikro- und Makrolevel wird in der FE-HMM durch die modifizierte Bilinearform aus Gleichung (11) erzwungen.

Im Gegensatz zu FE^2-Verfahren erfordert die FE-HMM allerdings keine explizite Berechnung des homogenisierten Elastizitätstensors, sondern nutzt eine Transformation der Mikrosteifigkeiten auf das Makrolevel. Wie auch im Rahmen der FE-HMM der homogenisierte Elastizitätstensor berechnet werden kann, präsentierte Abdulle [2] erstmals.

Der detaillierte Vergleich der FE-HMM und der FE^2-Methode ist in der ersten dieser kumulativen Promotionsschrift zugrunde liegenden Veröffentlichung [21] in Abschnitt 4.2 zu finden, in dieser Veröffentlichung wurden FE-HMM und FE^2-Methode anhand einiger numerischer Beispiele auch quantitativ verglichen. Die Ergebnisse zeigen hierbei, trotz ihrer unterschiedlichen Ansätze, eine Übereinstimmung der Ergebnisse der beiden Methoden. Durch die quantitative Übereinstimmung von FE-HMM und FE^2-Methode sind folglich die Aussagen zur Mikro- und Makrokonvergenz sowie zu den optimalen Netzverfeinerungsstrategien auch für die FE^2-Methode gültig. Trotz zahlreicher Veröffentlichungen im Zusammenhang mit der FE^2-Methode, existieren keine vergleichbaren diskreten a priori Fehleranalysen aus denen sich diese Verfeinerungsstrategien für die FE^2-Methode ableiten lassen. Die Übertragbarkeit der Ergebnisse der FE-HMM auf die FE^2-Methode liefert somit einen neuen, wichtigen Beitrag zur FE^2-Methode.

2.3.3 Finite Zellen Methode Die Finite Zellen Methode (engl. *Finite Cell Method*, FCM) wurde erstmals von Parvizian et al. [49] präsentiert und nutzt eine Erweiterung des physikalischen Gebiets des betrachteten Körpers. Diese wird so gewählt, dass ein möglichst simples physikalisches Gebiet dabei entsteht, das wiederum durch möglichst simple Elemente diskretisiert werden kann. Die Anwendung der FCM zur numerischen Homogenisierung heterogener Materialien wurde erstmals durch Düster et al. [16] beschrieben.

Abbildung 3 zeigt eine heterogene Mikrostruktur mit Poren und Einschlüssen, das physikalische Gebiet $\mathcal{B}$ wird ausgedehnt auf das erweiterte Gesamtgebiet $\mathcal{B}_e$, das wiederum gleichmäßig, ohne Berücksichtigung der Grenzen des ursprünglichen physikalischen Gebiets und ohne Berücksichtigung der Poren und Einschlüsse, diskretisiert wird.

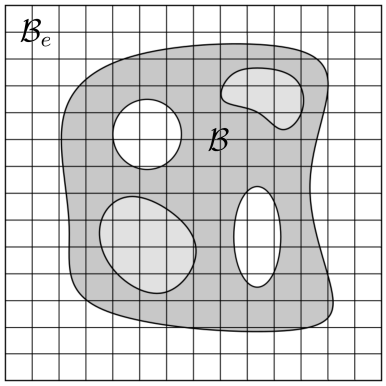


Abbildung 3: Heterogene Mikrostruktur mit Poren und Einschlüssen.

Der Elastizitätstensor wird dabei definiert als

$$\mathbb{A}_e^\epsilon = \begin{cases} \mathbb{A}^\epsilon & \forall \boldsymbol{x} \in \mathcal{B} \\ \alpha \mathbb{A}_m & \forall \boldsymbol{x} \in \mathcal{B}_e \setminus \mathcal{B} \end{cases} \tag{21}$$

mit dem Elastizitätstensor der Matrix $\mathbb{A}_m$ sowie einem Skalierungsfaktor α. Wird der Skalierungsfaktor als 0 gewählt, tragen Elemente, die außerhalb des ursprünglichen physikalischen Gebiets liegen, nicht mehr zur Steifigkeit bei. Um Probleme bei der Lösung des zugehörigen Gleichungssystems zu vermeiden, sollte α auf einen sehr kleinen Wert, aber ungleich 0 gesetzt werden.

Zwangsläufig entstehen durch diese Vernetzung Zellen im Bereich der Ränder des ursprünglichen physikalischen Gebiets sowie in Bereichen mit unterschiedlichen Materialeigenschaften oder Poren, die durch diesen Rand oder die Material-Heterogenität geschnitten werden. Für diese Zellen wird die numerische Integration angepasst, beispielsweise indem die Anzahl der Integrationspunkte erhöht wird oder die entsprechenden Zellen bei der numerischen Integration in feiner aufgelöste Sub-Zellen aufgeteilt werden. Diese Verfeinerungen der numerischen Integration werden wiederholt ausgeführt, bis die Auswirkungen der weiteren Verfeinerung auf das Gesamtergebnis unterhalb einer Toleranz liegt.

Der Vorteil der Finite Zellen Methode gegenüber der FE-HMM und FE^2-Verfahren ist die einfache Vernetzung des erweiterten physikalischen Gebiets, bei der die Ränder des ursprünglichen physikalischen Gebiets und Phasengrenzen nicht berücksichtigt werden. Bei den zuvor betrachteten Zwei-Skalen FE-Verfahren kann durch komplexe physikalische Formen oder durch eine starke Material-Heterogenität ein hoher Vernetzungsaufwand auf Makro- und Mikroebene entstehen.

Im Gegenzug ergibt sich allerdings ein erhöhter numerischer Aufwand durch die Notwendigkeit der angepassten numerischen Integration. Der Anstieg des numerischen Aufwandes beschränkt sich bei der Finite Zellen Methode jedoch auf die numerische Integration, da dem Gleichungssystem keine zusätzlichen Freiheitsgrade hinzugefügt werden. Durch die geringere Zahl an Freiheitsgraden auf dem Mikrogebiet leidet allerdings zwangsläufig auch die Qualität der berechneten Mikro-Verschiebungen.

2.4 Weitere Verfahren

Es existieren zahlreiche weitere Methoden, die zur numerischen Homogenisierung und zur Lösung von multiskalen Problemen geeignet sind. Hierzu gehören unter anderem der von Gravenkamp und Duczek [27] beschriebene Skalierte Rand Finite Elemente Methode (engl. *Scaled Boundary Finite Element Method*, SBFEM) / Spektrale Zellen Methode (engl. *Spectral Cell Method*, SCM) basierte Ansatz, die von Moulinec und Suquet [46] beschriebene numerische Homogenisierung basierend auf der schnellen Fourier Transformation (engl. *Fast Fourier Transformation*, FFT) oder die von Hou und Wu [32] beschriebene Multiskalen Finite Elemente Methode (engl. *Multiscale Finite Element Method*, MsFEM). Letztere wurde von Ming und Yue [45] mit der HMM, die die Grundlage für die FE-HMM bildet, verglichen und bildet die Grundlage für die von Efendiev et al. [19] beschriebene Verallgemeinerte Multiskalen Finite Elemente Methode (engl. *Generalized Multiscale Finite Element Method*, GMsFEM). Da diese Verfahren grundlegend andere Ansätze verfolgen als die im Abschnitt 2.3 präsentierten Zwei-Skalen FE-Verfahren, werden sie hier nicht im Detail vorgestellt.

2.5 Mikro-Makro-Kopplung und repräsentatives Volumenelement

Für die Berechnung von Verschiebungen auf dem Mikrolevel, die durch das makroskopische Verschiebungsfeld getrieben werden, muss eine Kopplung der Mikro- und Makroebene erfolgen. Die bisher veröffentlichten a priori Fehleranalysen beschränken sich üblicherweise auf periodische Kopplungsbedingungen [1, 2, 6]. Abdulle und Nonnenmacher [7] beschreiben die Implementierung von periodischen und Dirichlet-Kopplungsbedingungen für skalarwertige Randwertprobleme.

Für Anwendungen im Bereich Elastizität werden üblicherweise die folgenden Kopplungsbedingungen verwendet:

i) Dirichlet- oder lineare Verschiebungs-Kopplungsbedingungen

ii) Periodische Kopplungsbedingungen

iii) Neumann- oder uniforme Spannungs-Kopplungsbedingungen

Die Beschreibung der Implementierung von uniformen Spannungs-Kopplungsbedingungen im Rahmen der FE-HMM wurde erstmalig in der zweiten dieser kumulativen Promotionsschrift zugrundeliegenden Veröffentlichung [24] beschrieben. Außerdem erfolgte in dieser Veröffentlichung eine detaillierte Untersuchung der Fehlerkonvergenz der einzelnen Randbedingungen für unterschiedliche Randwertprobleme aus dem Bereich linearer Elastizität. Die einzelnen Kopplungsbedingungen sowie die Implementierung in einer Zwei-Skalen FEM wird im Folgenden präsentiert.

Dirichlet-Kopplungsbedingungen Bei der Dirichlet-Kopplung handelt es sich um die simpelste Methode der Kopplung, die Verschiebungen $\mathbf{u}^h$ auf den Rändern des Mikrogebiets entsprechen den Verschiebungen $\mathbf{u}^H$, die sich aus dem Verschiebungszustand des Makroelements ergeben

$$\mathbf{u}^h = \mathbf{u}^H \text{ auf } \delta K_l \,. \tag{22}$$

Entsprechend können einzelne Freiheitsgrade direkt aus dem Mikro-Gleichungssystem heraus entfernt werden, das resultierende Gleichungssystem besitzt keine Starrkörper-Freiheitsgrade und kann ohne weitere Randbedingungen gelöst werden.

Periodische Kopplungsbedingungen Bei periodischer Kopplung müssen die Fluktuationen der Verschiebungen, also die Differenz aus den tatsächlichen Verschiebungen auf dem Mikrogebiet $\mathbf{u}^h$ und den Verschiebungen des Makroelements $\mathbf{u}^H$, auf gegenüberliegenden Rändern übereinstimmen

$$\mathbf{u}^h - \mathbf{u}^H|^+ = \mathbf{u}^h - \mathbf{u}^H|^- \text{ auf } \delta K_l \,. \tag{23}$$

Die Superskripte $^+$ und $^-$ bezeichnen hierbei die gegenüberliegenden Ränder.

Gleichzeitig müssen die gegenüberliegenden Ränder anti-periodische Oberflächenspannungen aufweisen

$$\mathbf{t}|^+ = -\mathbf{t}|^- \text{ auf } \delta K_l \,. \tag{24}$$

Die Oberflächenspannungen auf den Rändern des Mikrogebiets werden berechnet aus den zugehörigen Spannungen und dem Normalenvektor auf dem jeweiligen Rand

$$\mathbf{t} = \boldsymbol{\sigma}_{K_l} \boldsymbol{n}(\boldsymbol{x}) \text{ auf } \delta K_l \,. \tag{25}$$

Im Gegensatz zur Dirichlet-Kopplung entfernen periodische Kopplungsbedingungen nicht alle Starrkörper-Freiheitsgrade aus dem Mikro-Gleichungssystem, nur die rotatorischen Freiheitsgrade werden durch die Randbedingungen aus dem Gleichungssystem entfernt. Um zusätzlich die translatorischen Freiheitsgrade zu entfernen, müssen weitere Bedingungen formuliert werden. Abdulle und Nonnenmacher [7] beschreiben beispielsweise eine zusätzliche Bedingung für das Integral der Fluktuationen auf dem Mikrogebiet, alternativ kann aber auch, wie in der zweiten dieser kumulativen Promotionsschrift zugrundeliegenden Veröffentlichung [24] beschrieben, ein Knoten auf dem Mikrogebiet mit einer zusätzlichen Dirichlet-Kopplung versehen werden. Eine naheliegende Lösung wäre die starre Kopplung eines Knotens in der Mitte des Mikrogebiets an die zugehörige makroskopische Quadratur-Stützstelle.

Neumann-Kopplungsbedingungen Neumann-Kopplungsbedingungen setzen konstante Oberflächenspannungen auf den Rändern voraus

$$\mathbf{t} = const \,. \tag{26}$$

Analog zu periodischen Kopplungsbedingungen entfernen auch Neumann-Kopplungsbedingungen nicht alle Starrkörper-Freiheitsgrade aus dem zugehörigen Mikro-Gleichungssystem, neben den translatorischen werden auch die rotatorischen Freiheitsgrade nicht aus dem Gleichungssystem entfernt. Entsprechend sind zusätzliche Gleichungen nötig, um auch diese Freiheitsgrade aus dem Mikro-Gleichungssystem zu entfernen. Ein Ansatz hierfür bietet der von Javili et al. [36] beschriebene Semi-Dirichlet-Ansatz. Hierbei werden Dirichlet-Randbedingungen aufgebracht, die so gewählt werden, dass keine zusätzlichen Kräfte für deren Realisierung nötig sind und die Kopplung somit keinen Einfluss auf das zugehörige Spannungs- und Verschiebungsfeld hat.

Aufbringen der Kopplungsbedingungen Das Aufbringen der Kopplungsbedingungen kann beispielsweise wie von Abdulle und Nonnenmacher [7] beschrieben mit Hilfe von Lagrange Multiplikatoren erfolgen. Das Gleichungssystem auf dem Mikrolevel aus Gleichung (18) wird um die Lagrange Multiplikatoren $\boldsymbol{\lambda}$ erweitert und lautet

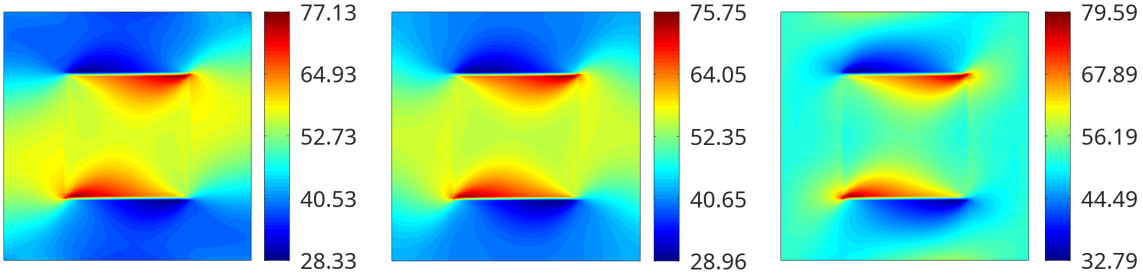
$$\begin{bmatrix} \boldsymbol{K}_{K_l}^{mic} & \boldsymbol{G}^T \\ \boldsymbol{G} & \boldsymbol{0} \end{bmatrix} \begin{bmatrix} \boldsymbol{d}^h \\ \boldsymbol{\lambda} \end{bmatrix} = \begin{bmatrix} \boldsymbol{0} \\ \boldsymbol{G}\boldsymbol{d}^H \end{bmatrix} . \tag{27}$$

Hierbei beschreibt $\boldsymbol{G}$ eine Matrix, die die Erfüllung der Kopplungsbedingungen sicherstellt und entsprechend von der Wahl der Kopplungsbedingungen abhängt. Eine weitere Möglichkeit die Randbedingungen aufzubringen ist die statische Kondensation, die in der zweiten dieser kumulativen Promotionsschrift zugrundeliegenden Veröffentlichung [24] ebenfalls beschrieben wird. Vorteil hierbei ist, dass keine zusätzliche Kopplungs-Matrix $\boldsymbol{G}$ aufgestellt und keine zusätzlichen Lagrange-Multiplikatoren $\boldsymbol{\lambda}$ berechnet werden müssen.

Die unterschiedlichen Kopplungsbedingungen haben einen Einfluss auf die resultierenden Steifigkeiten. Saeb et al. [52] beschreiben die oben genannten Randbedingungen sowie die Annahmen von Voigt aus Gleichung (6) und Reuss aus Gleichung (7), die eine obere und untere Schranke der möglichen Steifigkeiten bilden. Während die Voigt-Schranke die größtmögliche Steifigkeit liefert, beschreibt die Reuss-Schranke die geringstmögliche Steifigkeit.

Die Hierarchie der Steifigkeiten ergibt sich zu:

$$\mathbb{A}^{\text{Reuss}} \leq \mathbb{A}^{\text{Neumann}} \leq \mathbb{A}^{\text{Periodisch}} \leq \mathbb{A}^{\text{Dirichlet}} \leq \mathbb{A}^{\text{Voigt}} \tag{28}$$

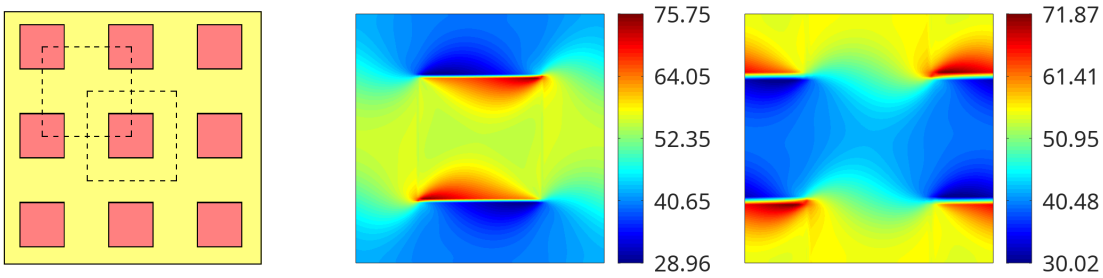


(a) Dirichlet **(b)** Periodisch **(c)** Neumann

Abbildung 4: Vergleichsspannung nach von Mises für ein Matrixeinschlussproblem mit unterschiedlichen Kopplungsbedingungen.

Abbildung 4 zeigt den Verlauf der Vergleichsspannung nach von Mises für ein Matrixeinschlussproblem mit den unterschiedlichen Kopplungsbedingungen. Da sich hier die Heterogenität auf das Innere des Mikrogebiets beschränkt, hat sie nur geringe Auswirkungen auf die Ränder der Mikrostruktur. Die Ränder weisen bei periodischer Kopplung nur geringfügige Fluktuationen auf, sodass Dirichlet- und periodische Kopplungsbedingungen hier zu einer guten qualitativen Übereinstimmung führen. Im Gegensatz dazu zeigt die Spannungsverteilung, die sich bei der Verwendung von Neumann-Kopplungsbedingungen ergibt, gerade in den Randbereichen größere Abweichungen.

Wahl des RVEs Neben der Wahl der Mikro-Makro-Kopplungsbedingung hat auch die Wahl des repräsentativen Volumen- (3D) bzw. Flächenelements (2D) einen Einfluss auf die Ergebnisse der numerischen Homogenisierung, Wang et al. [58] zeigen dies am Beispiel der Rissausbreitung in Beton. Schröder [55] präsentierte Spannungsverläufe bei unterschiedlicher Wahl des repräsentativen Volumenelements unter unterschiedlichen Kopplungsbedingungen.



(a) Struktur **(b)** RVE1 **(c)** RVE2

Abbildung 5: (a) Heterogene Struktur mit unterschiedlichen RVEs sowie Vergleichsspannung nach von Mises für (b) das RVE mit Matrixeinschluss in der Mitte und (c) das RVE mit Matrixeinschlüssen in den Ecken bei periodischer Kopplung.

Abbildung 5(a) zeigt eine heterogene Struktur mit regelmäßig angeordneten Einschlüssen in einer Matrix. Zwei mögliche RVEs sind in die Mikrostruktur eingezeichnet, einmal befindet sich der Einschluss in der Mitte des RVEs, einmal in den Ecken. Die zugehörigen Vergleichsspannungen nach von Mises bei periodischer Kopplung sind in Abb. 5(b) für den Fall des Einschlusses in der Mitte des RVEs und (c) für den Fall des Einschlusses in den Ecken des RVEs abgebildet.

		$\mathbb{A}_{11} = \mathbb{A}_{22}$	$\mathbb{A}_{12}$	$\mathbb{A}_{33}$
	$\mathbb{A}^{\text{Voigt}}$	68162.39	24252.14	21955.13
Mitte	$\mathbb{A}^{\text{Dirichlet}}$	63546.79	24311.35	19132.45
Ecke	$\mathbb{A}^{\text{Dirichlet}}$	65021.20	24085.56	20486.85
	$\mathbb{A}^{\text{Periodic}}$	63460.78	24351.27	18612.13
Mitte	$\mathbb{A}^{\text{Neumann}}$	62573.87	25210.58	18479.56
Ecke	$\mathbb{A}^{\text{Neumann}}$	62015.83	24915.23	18491.90
	$\mathbb{A}^{\text{Reuss}}$	61554.88	25025.20	18264.84

Tabelle 1: Numerische Ergebnisse der Einträge des homogenisierten Elastizitätstensors für das Matrixeinschlussproblem.

Tabelle 1 zeigt die Einträge der berechneten homogenisierten Elastizitätstensoren für unterschiedliche Kopplungsbedingungen und die in Abbildung 5(a) präsentierten RVEs sowie die Einträge der Elastizitätstensoren nach Voigt und Reuss. Es zeigt sich bei Dirichlet und Neumann-Kopplung eine Abhängigkeit von der Wahl des RVEs, während die Ergebnisse bei periodischer Kopplung sowie den Berechnungen nach Voigt und Reuss unabhängig von der Wahl des RVEs sind. Die Hierarchie der Steifigkeiten gemäß Gleichung (28) ist erfüllt.

Für reale Mikrostrukturen, bei denen die Mikroheterogenität nicht regelmäßig verteilt ist, kann die Wahl des RVEs eine Herausforderung darstellen. Bogunia et al. [12] beschreiben die stochastische Modellierung von Schäumen, Kanit et al. [38] beschäftigen sich mit der Bestimmung der Größe des RVEs, Schröder et al. [56] präsentieren ein Verfahren zur Approximation heterogener Mikrostrukturen, bei dem die reale Mikrostruktur durch ein statistisch ähnliches RVE (engl. *statistically similar RVE*, SSRVE) mit deutlich geringerer Komplexität ersetzt wird.

3 Fehlerkonvergenz und Verfeinerungsstrategien

Die ersten Fehleranalysen im Zusammenhang mit der Heterogenen Multiskalen Methode erfolgten durch E et al. [18], die den Fehler zwischen der Lösung der HMM und der exakten Lösung unterteilen in einen Standard-Fehler aufgrund der numerischen Lösung auf dem Makrolevel und einem zweiten Anteil, der sich aus dem Fehler bei der Abschätzung der Steifigkeitsmatrix ergibt. Abdulle [1] hat den Ansatz von E et al. aufgegriffen und lieferte eine erste a priori Fehleranalyse für den vollständig diskreten Fall, in Abdulle [2] folgte eine Analyse für Elastizitäts-Probleme. Zuvor haben bereits Matache und Schwab [43] eine Fehleranalyse für Zwei-Skalen Finite Elemente Methoden präsentiert und dabei einen Saturationseffekt bei der Fehlerkonvergenz beschrieben, wenn nur auf einer Skala eine Netzverfeinerung durchgeführt wird.

Neben der a priori Fehleranalyse ist auch die a posteriori Fehlerschätzung Gegenstand zahlreicher Veröffentlichungen. Die erste a posteriori Fehlerschätzung für numerische Multiskalen-Verfahren präsentierte Ohlberger [48], der dafür eine Umformulierung der Heterogenen Multiskalen Methode nutzte und erstmals die Konvergenz in Abhängigkeit der Mikro- und Makrodiskretisierung untersuchte. Abdulle und Nonnenmacher [4] beschrieben die a posteriori Fehlerschätzung im Kontext der FE-HMM und unterteilten den Gesamtfehler dabei erstmals in einen Makrofehler, einen Modellierungsfehler und einen Mikrofehler. Ebenso beschrieben Abdulle und Nonnenmacher [5] die a posteriori Fehlerschätzung auf dem Makrolevel und adaptive Netzverfeinerung auf dem Mikro- und Makrolevel.

Eine erste mathematische Analyse der Finite Zellen Methode und ihrer Konvergenzeigenschaften wurde von Dauge et al. [14] präsentiert. Di Stolfo [15] hat im Kontext der Finite Zellen Methode eine Fehlerschätzung und die daraus resultierende Netzverfeinerungsstrategie präsentiert, wobei zwischen einem Diskretisierungs- und einem Quadraturfehler unterschieden wird.

Zusammenfassend lässt sich sagen, dass sich zahlreiche Veröffentlichungen im Zusammenhang mit Zwei-Skalen FE-Verfahren mit den Themen a priori und a posteriori Fehlerschätzung sowie adaptiver Netzverfeinerung beschäftigen, der Fokus wird hierbei allerdings jeweils auf das Makrolevel gelegt. Neben dem Fehler in den makroskopischen Größen können jedoch auch die Fehler auf den Mikrogebieten untersucht werden.

Was die Veröffentlichungen bisher schuldig geblieben sind:

i) Eine Analyse der Fehler auf spezifischen Mikrogebieten

ii) Eine Analyse unterschiedlicher Kopplungsbedingungen

iii) Eine Analyse der Auswirkungen der Verwendung adaptiver FE-Netze auf dem Mikrolevel

iv) Die Fragestellung wie Fehlerschätzung am Interface zweier unterschiedlicher Phasen erfolgen kann

v) Eine Analyse des Modellierungs- bzw. Auflösungsfehlers

3.1 Fehlerzerlegung

3.1.1 Fehler auf der Mikroskala Der Mikrofehler e^{ϵ}_{mic} auf dem Mikrogebiet K_l lässt sich aufteilen in einen Diskretisierungsfehler $e^{\epsilon\ h}_{mic}$ und einen Auflösungsfehler $e^{\epsilon\ \square}_{mic}$, der durch die Auflösung der Mikrostruktur getrieben wird. Es gilt

$$\begin{aligned} e^{\epsilon}_{mic} &= \|\boldsymbol{u}^{h_\square,h} - \boldsymbol{u}^{0,0}\|_{K_l} && (29)\\ &= \|\boldsymbol{u}^{h_\square,h} - \boldsymbol{u}^{h_\square,0} + \boldsymbol{u}^{h_\square,0} - \boldsymbol{u}^{0,0}\|_{K_l} && (30)\\ &\leq \underbrace{\|\boldsymbol{u}^{h_\square,h} - \boldsymbol{u}^{h_\square,0}\|_{K_l}}_{e^{\epsilon\ h}_{mic}} + \underbrace{\|\boldsymbol{u}^{h_\square,0} - \boldsymbol{u}^{0,0}\|_{K_l}}_{e^{\epsilon\ \square}_{mic}} && (31) \end{aligned}$$

mit den berechneten Mikroverschiebungen $\boldsymbol{u}^{h_\square,h}$ für eine Auflösung $h_\square$ und eine Diskretisierung h, den Mikroverschiebungen $\boldsymbol{u}^{h_\square,0}$ für eine Auflösung $h_\square$ und eine Diskretisierung $h \to 0$ und den exakten Mikroverschiebungen $\boldsymbol{u}^{0,0}$.



(a) 1024^2px **(b)** 32^2px **(c)** 1^2px

Abbildung 6: Modellierung einer Mikrostruktur mittels (a) 1024^2, (b) 32^2 und (c) 1^2 Elementen, aus Eidel et al. [23].

Abbildung 6 zeigt eine Mikrostruktur mit unterschiedlichen Auflösungen, der zugehörige Auflösungsfehler $e^{\epsilon\ \square}_{mic}$ auf dem Mikrogebiet nimmt mit abnehmender Auflösung von (a) nach (c) zu.

3.1.2 Fehler auf der Makroskala Der Gesamtfehler der FE-HMM-Lösung lässt sich in einen Makrofehler, einen Modellierungsfehler und einen auf das Makrolevel propagierten Mikrofehler unterteilen. Letzterer kann analog zu Gleichung (31) aufgeteilt werden

$$\|\boldsymbol{u}^0 - \boldsymbol{u}^H\| \leq \underbrace{\|\boldsymbol{u}^0 - \boldsymbol{u}^{0,H}\|}_{e_{mac}} + \underbrace{\|\boldsymbol{u}^{0,H} - \widetilde{\boldsymbol{u}}^H\|}_{e_{mod}} + \underbrace{\underbrace{\|\widetilde{\boldsymbol{u}}^H - \boldsymbol{u}^{\square,H}\|}_{e^H_{mic}} + \underbrace{\|\boldsymbol{u}^{\square,H} - \boldsymbol{u}^H\|}_{e^{\square}_{mic}}}_{e_{mic}} . \qquad (32)$$

Hierbei ist $\boldsymbol{u}^H$ die FE-HMM-Lösung, $\boldsymbol{u}^0$ die exakte Lösung des homogenisierten Modellproblems aus (8), $\boldsymbol{u}^{0,H}$ die Lösung einer Ein-Skalen FEM mit exaktem $\mathbb{A}^0$ und $\widetilde{\boldsymbol{u}}^H$ die Lösung der FE-HMM mit exakten Mikrofunktionen in $\mathcal{W}$ aus Gleichung (14).

Makrofehler Der Makrofehler entspricht dem Diskretisierungsfehler, der aus Ein-Skalen FE-Verfahren bekannt ist, und beschreibt den Einfluss der Makrodiskretisierung auf die makroskopischen Verschiebungen. Grundsätzlich gilt hierbei, dass der Diskretisierungsfehler mit feiner werdender Diskretisierung abnimmt. Der Makrofehler lässt sich berechnen als die Differenz der exakten Lösung des homogenisierten Modellproblems $\boldsymbol{u}^0$ und einer mittels Ein-Skalen FEM mit exaktem homogenisierten Elastizitätstensor $\mathbb{A}^0$ bestimmten Lösung $\boldsymbol{u}^{0,H}$.

Mikrofehler Die Besonderheit des Mikrofehlers liegt darin, dass es sich in e_{mic} um einen Fehler auf dem Mikrogebiet handelt, der in den Makrogrößen gemessen wird.

In der FE-HMM werden die Steifigkeiten der Makroelemente nach Gleichung (16) durch eine direkte Transformation der Steifigkeiten der zugehörigen Mikrogebiete mittels zuvor berechneter Transformationsmatrizen berechnet. Sowohl die Diskretisierung des Mikrogebiets als auch die Qualität der Auflösung der heterogenen Mikrostruktur beeinflussen die Mikrosteifigkeitsmatrix und auch die Einträge in den Transformationsmatrizen und damit zwangsläufig auch die Makrosteifigkeiten. Hierdurch kann von einem auf das Makrolevel propagierten Mikrofehler gesprochen werden.

Modellierungsfehler Der Modellierungsfehler beschreibt schließlich den Einfluss der Kopplung der beiden Skalen. Es gilt

$$e_{mod} = \begin{cases} 0 & \text{für periodische Kopplung mit } \delta/\epsilon \in \mathbb{N} \\ C\dfrac{\epsilon}{\delta} & \text{für Dirichlet Kopplung mit } \delta > \epsilon \end{cases} \tag{33}$$

unter der Bedingung, dass der Elastizitätstensor $\mathbb{A}^\epsilon$ periodisch ist auf dem zugehörigen Mikrogebiet [37].

3.2 A priori Konvergenzaussagen

In den dieser kumulativen Promotionsschrift zugrundeliegenden Veröffentlichungen [21, 23, 24, 25] werden die einzelnen Fehler in der L^2-, der H^1- und der Energie-Norm betrachtet. Diese Normen sind definiert als

$$L^2\text{-Norm:} \quad ||\boldsymbol{u}||_{L^2(\mathcal{B})} := \sqrt{\int_{\mathcal{B}} \boldsymbol{u} : \boldsymbol{u}\, dV}\,, \tag{34}$$

$$H^1\text{-Norm:} \quad ||\boldsymbol{u}||_{H^1(\mathcal{B})} := \sqrt{\left(\sum_{i,j=1}^{d} \int_{\mathcal{B}} \left(\frac{\partial u_i}{\partial x_j}\right)^2 dV + \sum_{i=1}^{d} \int_{\mathcal{B}} (u_i)^2\, dV\right)}\,, \tag{35}$$

$$\text{Energie-Norm:} \quad ||\,\boldsymbol{u}\,||_{A(\mathcal{B})} := \sqrt{\int_{\mathcal{B}} \mathbb{A}\,\boldsymbol{\varepsilon}(\boldsymbol{u}) : \boldsymbol{\varepsilon}(\boldsymbol{u})\, dV}\,. \tag{36}$$

Für Probleme mit ausreichender Regularität gelten laut Abdulle [3] die folgenden a priori Konvergenzaussagen für die makroskopische Lösung $\boldsymbol{u}^H$ in den drei zuvor definierten Normen

$$||\boldsymbol{u}^0 - \boldsymbol{u}^H||_{L^2(\mathcal{B})} \leq C\left(H^{p+1} + \left(\frac{h}{\epsilon}\right)^{2q}\right) + e_{mod} + e_{mic}^{\square}, \tag{37}$$

$$||\boldsymbol{u}^0 - \boldsymbol{u}^H||_{H^1(\mathcal{B})} \leq C\left(H^{p} + \left(\frac{h}{\epsilon}\right)^{2q}\right) + e_{mod} + e_{mic}^{\square}, \tag{38}$$

$$||\boldsymbol{u}^0 - \boldsymbol{u}^H||_{A(\mathcal{B})} \leq C\left(H^{p} + \left(\frac{h}{\epsilon}\right)^{2q}\right) + e_{mod} + e_{mic}^{\square}, \tag{39}$$

wobei p und q den Grad der Ansatzfunktionen auf dem Makro- und Mikrolevel beschreiben.

Die Fehlerkonvergenz in Abhängigkeit von der Makrodiskretisierung H entspricht hierbei der Fehlerkonvergenz von Ein-Skalen FE-Verfahren. Der Fehler der Verschiebungen konvergiert mit der Ordnung $p+1$, die Spannungen und Verzerrungen konvergieren mit der Ordnung p.

Demgegenüber zeigt die Abhängigkeit von der Mikrodiskretisierung ein ungewöhnliches Konvergenzverhalten, da sowohl die Verschiebungen als auch die Spannungen und Verzerrungen auf dem Makrogebiet mit der Ordnung $2q$ konvergieren.

Die Übereinstimmung der Konvergenzordnung der Verschiebungen mit der Konvergenzordnung der Spannungen und Verzerrungen ist auch für Ein-Skalen FE-Verfahren ein bekanntes Phänomen und wird als Superkonvergenz beschrieben [10]. In diesem Fall kann jedoch nicht von einem vergleichbaren Phänomen gesprochen werden, da es sich lediglich um den auf das Makrolevel propagierten Mikrodiskretisierungsfehler handelt. Betrachtet man den Mikrodiskretisierungsfehler auf dem Mikrolevel konvergiert dieser mit der Ordnung $q+1$ in der L^2-Norm und mit der Ordnung q in der H^1- und der Energie-Norm

$$||\boldsymbol{u}^{0,0} - \boldsymbol{u}^{h_\square,h}||_{L^2(K_l)} \leq C\left(\frac{h}{\epsilon}\right)^{q+1} + e_{mic}^{\epsilon\,\square}, \tag{40}$$

$$||\boldsymbol{u}^{0,0} - \boldsymbol{u}^{h_\square,h}||_{H^1(K_l)} \leq C\left(\frac{h}{\epsilon}\right)^{q} + e_{mic}^{\epsilon\,\square}, \tag{41}$$

$$||\boldsymbol{u}^{0,0} - \boldsymbol{u}^{h_\square,h}||_{A(K_l)} \leq C\left(\frac{h}{\epsilon}\right)^{q} + e_{mic}^{\epsilon\,\square}. \tag{42}$$

3.3 Optimale Netzverfeinerungsstrategie

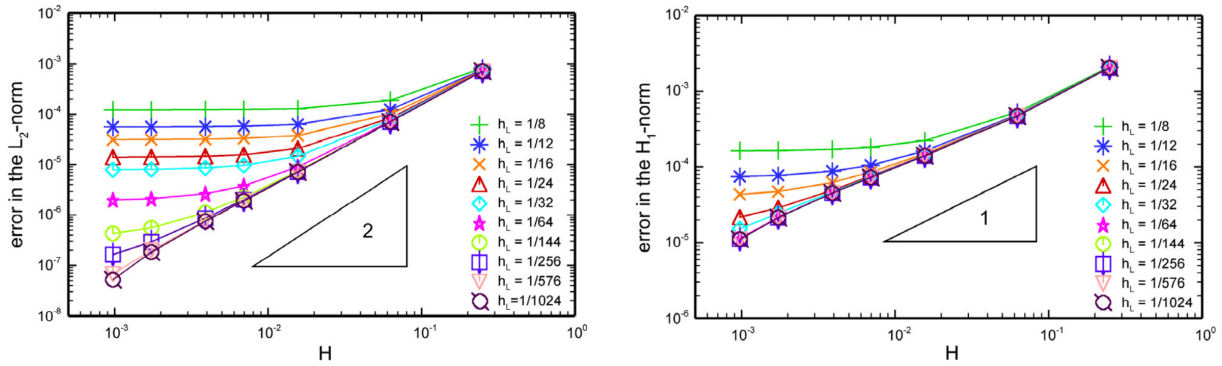
Die ungewöhnliche Konvergenz des auf das Makrolevel übertragenen Mikrodiskretisierungsfehlers von $2q$ in allen betrachteten Normen führt dazu, dass die Verfeinerungsstrategie für eine optimale Konvergenz der Makrolösung $\boldsymbol{u}^H$ nur in Ausnahmefällen der trivialen Lösung einer gleichmäßigen Netzverfeinerung auf Mikro- und Makroebene entspricht.

Vielmehr ist die optimale Netzverfeinerungsstrategie abhängig von der betrachteten Norm und dem Grad der Makro- und Mikroansatzfunktionen.

L^2-Norm	H^1-/Energie-Norm
$N_{mic} = (N_{mac})^{(p+1)/2q}$	$N_{mic} = (N_{mac})^{p/2q}$

Tabelle 2: Optimale Verfeinerungsstrategien: N_{mic} beschreibt die Anzahl der Knoten pro Raumrichtung auf dem Mikrolevel, N_{mac} die Anzahl der Knoten pro Raumrichtung auf dem Makrolevel.

Die optimalen Verfeinerungsstrategien für die drei Normen sind in Tab. 2 gegeben. Für lineare Ansatzfunktionen auf beiden Skalen $p = q = 1$ ergibt sich beispielsweise für eine optimale Konvergenz in der L^2-Norm $N_{mic} = N_{mac}$, Mikro- und Makrodiskretisierung müssen also proportional zueinander verfeinert werden. Im Gegensatz dazu ist $N_{mic} = (N_{mac})^{1/2}$, also eine unterproportionale Verfeinerung der Mikrodiskretisierung ausreichend, um eine optimale Konvergenz in der H^1- und der Energie-Norm zu erzielen. Hier würde eine uniforme Netzverfeinerung auf Makro- und Mikrolevel zu unnötig feinen Mikrodiskretisierungen führen und letztendlich einen unnötigen numerischen (Mehr-)Aufwand bedeuten.



(a) L^2-Norm **(b)** H^1-Norm

Abbildung 7: Untersuchung der optimalen Verfeinerungsstrategie, berechnete Fehler in der (a) L^2-Norm und (b) H^1-Norm, aus Eidel und Fischer [21].

Abbildung 7 zeigt die Ergebnisse von Fehlerberechnungen in der L^2-Norm und der H^1-Norm für zahlreiche Mikro- und Makrodiskretisierungen.

Das zugrundeliegende Makro-RWP besteht aus einer quadratischen Platte der Seitenlänge $l = 1\,\mathrm{m}$ und Dicke $t = 0.1\,\mathrm{m}$. Die Platte ist auf einer Seite fest gelagert, die gegenüberliegende Seite wird durch eine Linienlast von $q_0 = 1\,[\mathrm{N/mm^2}]$ belastet. Der mikroheterogene Elastizitätstensor wird beschrieben durch

$$\mathbb{A}^\epsilon = \begin{bmatrix} A^\epsilon_{11} & 35 & 0 \\ 35 & A^\epsilon_{22} & 0 \\ 0 & 0 & 50 \end{bmatrix} \frac{\mathrm{N}}{\mathrm{m}^2} \quad \text{mit} \quad \begin{aligned} A^\epsilon_{11} &= [500/(5 + 3.5 \cdot \sin(2\pi x_1/\epsilon))]\,, \\ A^\epsilon_{22} &= [500/(5 + 3.5 \cdot \cos(2\pi x_1/\epsilon))]\,. \end{aligned} \tag{43}$$

Die Berechnungen erfolgten jeweils mit linearen Ansatzfunktionen auf dem Mikro- und Makrolevel ($p = q = 1$). Es ergeben sich die oben beschriebenen optimalen Verfeinerungsstrategien einer proportionalen Netzverfeinerung für die optimale Konvergenz der

Makrolösung in der L^2-Norm und einer unterproportionalen Netzverfeinerung auf dem Mikrolevel für die optimale Konvergenz der Makrolösung in der H^1-Norm.

Entlang der einzelnen Linien wird die Mikrodiskretisierung (hier mit $\mathrm{h_L}$ bezeichnet) konstant gehalten und der Gesamtfehler für unterschiedliche Makrodiskretisierungen berechnet. Einige dieser Linien zweigen früher oder später von der Geraden mit der optimalen Konvergenz (Ordnung 2 in der L^2-Norm, Ordnung 1 in der H^1-Norm) ab und bilden im Extremfall horizontale Linien. An diesen Stellen nimmt der Gesamtfehler trotz feiner werdender Makrodiskretisierung nur noch geringfügig ab, der Mikrodiskretisierungsfehler ist hier die dominierende Größe. Eine weitere Verfeinerung des Makronetzes zahlt sich nicht mehr aus, sie erhöht den numerischen Aufwand, kann den Gesamtfehler aber nur noch geringfügig beeinflussen.

Im Gegensatz dazu weisen die Berechnungen mit den gröbsten Makrodiskretisierungen trotz stark unterschiedlicher Mikrodiskretisierungen einen nahezu identischen Gesamtfehler auf. In diesem Fall ist der Makrodiskretisierungsfehler die dominierende Größe und die Verwendung feinerer Mikrodiskretisierungen zahlt sich nicht aus.

Abbildung 7(a) zeigt für den Fehler in der L^2-Norm, dass, sobald die Mikrodiskretisierung nicht mehr proportional zur Makrodiskretisierung verfeinert wird, der Mikrofehler an Dominanz gegenüber dem Makrofehler gewinnt und somit die Konvergenz von der optimal möglichen Konvergenzordnung von 2 abweicht. Im Extremfall einer sehr groben Mikrodiskretisierung, beispielsweise mit $\mathrm{h_L} = 1/8$, tritt nach 3 Verfeinerungsschritten der Makrodiskretisierung H keine sichtbare Reduktion des Gesamtfehlers auf. Für die feinste Makrodiskretisierung zweigen alle Kurven mit einer Mikrodiskretisierung $\mathrm{h_L} > 1/1024$ von der optimalen Konvergenzgerade ab. Die proportionale Netzverfeinerung auf Mikro- und Makrolevel muss für eine optimale Konvergenz streng eingehalten werden.

Demgegenüber zeigt Abb. 7(b) den Fehler in der H^1-Norm. Hier findet das Abzweigen von der optimalen Konvergenzordnung erst deutlich später statt, eine proportionale Verfeinerung des Mikro- und Makronetzes ist also nicht notwendig. Betrachtet man die zugehörigen Fehler der feinsten Makrodiskretisierungen, so zeigt sich, dass kein sichtbarer Unterschied zwischen dem Ergebnis mit $\mathrm{h_L} = 1/64$ und dem Ergebnis mit $\mathrm{h_L} = 1/1024$ existiert. An dieser Stelle dominiert also der Makrodiskretisierungsfehler und ein feineres Mikronetz zeigt keine positiven Auswirkungen auf die Konvergenz des Gesamtfehlers. Hier ist die unterproportionale Verfeinerung des Mikronetzes ausreichend, um eine optimale Konvergenz zu erreichen. Durch die gröbere Mikrodiskretisierung können im Gegenzug zahlreiche Freiheitsgrade auf den einzelnen Mikrogebieten eingespart werden, hier liegt zwischen den Berechnungen mit $\mathrm{h_L} = 1/64$ und mit $\mathrm{h_L} = 1/1024$, die keinen nennenswerten Unterschied im Gesamtfehler aufweisen, der Faktor 16 pro Raumrichtung.

Nur wenn die Netzverfeinerung auf Mikro- und Makrolevel der optimalen Verfeinerungsstrategie folgt, kann vermieden werden das - früher oder später - Mikro- oder Makrofehler dominieren und gleichzeitig durch eine übermäßige Netzverfeinerung auf einer der beiden Skalen ein unnötig hoher numerischer Aufwand betrieben wird und somit Berechnungsressourcen verschwendet werden.

3.4 Fehlerschätzung bei heterogenen Mikrostrukturen

Voraussetzung für die Durchführung von Konvergenzuntersuchungen ist die möglichst exakte Bestimmung des Diskretisierungsfehlers. Grundsätzlich kann dieser mit Hilfe einer Referenz-Lösung, die mit der exakten Lösung möglichst genau übereinstimmt, berechnet werden. Eine gute Übereinstimmung mit der exakten Lösung kann hierbei jedoch nur durch sehr feine Diskretisierungen auf Makro- und Mikrolevel erreicht werden, was gleichbedeutend mit einem extrem hohen numerischen Aufwand bei der Berechnung der Referenz-Lösung ist.

Um diesen hohen numerischen Aufwand der Berechnung einer Referenz-Lösung zu vermeiden, kann der Diskretisierungsfehler von FE-Verfahren alternativ durch geeignete Verfahren geschätzt werden. Ein Beispiels für ein solches Verfahren bietet der von Zienkiewicz und Zhu [60, 61] beschriebene Fehlerschätzer.

Der Fehlerschätzer von Zienkiewicz und Zhu beruht auf der Existenz superkonvergenter Punkte im Inneren des Elements, laut Barlow [10] befinden sich diese bei rechtwinkligen Vier-Knoten-Elementen beispielsweise in der Mitte des Elements. Mit Hilfe des von Zienkiewicz und Zhu beschriebenen Verfahrens (engl. *Superconvergent Patch Recovery*, SPR) werden die superkonvergenten Spannungen und Verzerrungen aus dem Inneren der Elemente auf die Elementknoten übertragen.

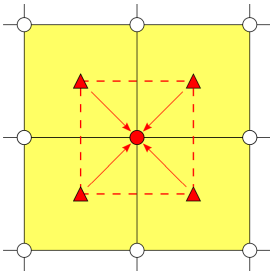


Abbildung 8: Patch zur Berechnung superkonvergenter Knotenspannungen und -verzerrungen, aus Fischer und Eidel [24].

Abbildung 8 veranschaulicht das Vorgehen der SPR um die Spannungen und Verzerrungen des zentralen, rot markierten Elementknotens zu berechnen. Hierfür wird ein Patch verwendet, der alle an den Knoten angrenzenden Elemente umfasst. In den superkonvergenten Punkten in der Mitte dieser Elemente werden die Spannungen und Verzerrungen ausgewertet. Anschließend wird ein bi-lineares Polynom durch diese Punkte gelegt mit dessen Hilfe schlussendlich die Spannungen und Verzerrungen des zentralen Knoten des Patches ausgewertet werden können.

Das daraus resultierende superkonvergente Spannungs- $\boldsymbol{\sigma}^\star$ und Verzerrungsfeld $\boldsymbol{\varepsilon}^\star$ wird mit den Spannungen $\boldsymbol{\sigma}^H$ und Verzerrungen $\boldsymbol{\varepsilon}^H$ aus den Standard-Stützstellen der einzelnen Elemente verglichen um den Diskretisierungsfehler abzuschätzen

$$\begin{aligned} \|\bar{e}\|_{A(\mathcal{B})} &= \sqrt{\int_{\mathcal{B}} (\boldsymbol{\sigma}^\star - \boldsymbol{\sigma}^H) \colon (\boldsymbol{\varepsilon}^\star - \boldsymbol{\varepsilon}^H)\, dV} \\ &\approx \left[\sum_{K \in \mathcal{T}_H} \left(\sum_{l=1}^{N_{qp}} \omega_{K_l} (\boldsymbol{\sigma}^\star - \boldsymbol{\sigma}^H)(\boldsymbol{x}^H_{K_l}) \colon (\boldsymbol{\varepsilon}^\star - \boldsymbol{\varepsilon}^H)(\boldsymbol{x}^H_{K_l})\, det\boldsymbol{J} \right) \right]^{1/2} . \end{aligned} \tag{44}$$

Die Qualität der Fehlerschätzung wird mit dem Effektivitätsindex θ gemessen, der als das Verhältnis des geschätzten Fehlers $\bar{e}$ zu dem tatsächlichen Fehler e definiert ist. Exemplarisch ausgedrückt durch den Effektivitätsindex der geschätzten Spannungen ergibt sich

$$\theta = \frac{\|\bar{e}\|}{\|e\|} = \frac{\|\boldsymbol{\sigma}^\star - \boldsymbol{\sigma}^H\|}{\|\boldsymbol{\sigma}^0 - \boldsymbol{\sigma}^H\|} = \frac{\|\boldsymbol{\sigma}^\star - \boldsymbol{\sigma}^0 + \boldsymbol{\sigma}^0 - \boldsymbol{\sigma}^H\|}{\|\boldsymbol{\sigma}^0 - \boldsymbol{\sigma}^H\|}\,, \tag{45}$$

wobei $\boldsymbol{\sigma}^0$ die exakte Lösung beschreibt. Eine Fallunterscheidung liefert schließlich die obere und untere Grenze des Effektivitätsindex

$$1 - \frac{\|\boldsymbol{\sigma}^\star - \boldsymbol{\sigma}^0\|}{\|\boldsymbol{\sigma}^0 - \boldsymbol{\sigma}^H\|} \leq \theta \leq 1 + \frac{\|\boldsymbol{\sigma}^\star - \boldsymbol{\sigma}^0\|}{\|\boldsymbol{\sigma}^0 - \boldsymbol{\sigma}^H\|}\,. \tag{46}$$

Da der Fehler der superkonvergenten Spannungen $\boldsymbol{\sigma}^\star$ in einer höheren Ordnung konvergiert als der Fehler der Standard-Spannungen $\boldsymbol{\sigma}^H$ konvergieren beide Grenzen gegen 1.

Um die Schätzung des Diskretisierungsfehlers auf heterogene Strukturen anwenden zu können, muss die von Zienkiewicz und Zhu beschriebene SPR geringfügig angepasst werden, da die Phasen der einzelnen Elemente keine Berücksichtigung finden. Hierdurch können einzelne Patches aus Elementen unterschiedlicher Phasen bestehen.

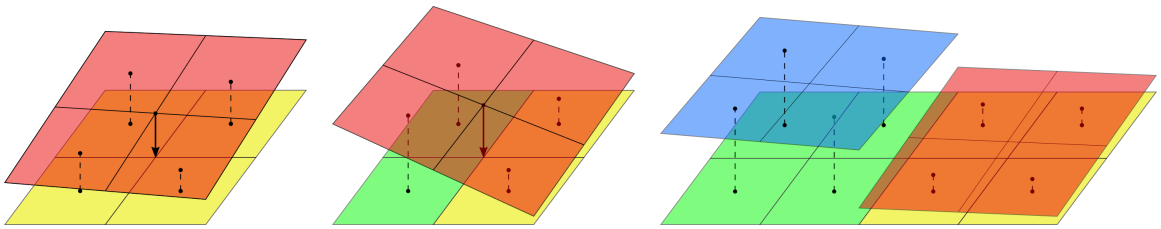


Abbildung 9: Bestimmung der Knotenspannung für (a) homogene und (b) heterogene Patches mittels SPR und (c) mittels Duplex-Spannungen, aus Fischer und Eidel [25].

Abbildung 9(a) veranschaulicht das Prinzip der SPR. Die Spannungen des zentralen Knoten des Patches werden bestimmt indem ein Polynom durch die Spannungen und Verzerrungen in den superkonvergenten Punkten in der Elementmitte gelegt wird.

Einen Patch mit Elementen unterschiedlicher Phasen ist in Abb. 9(b) zu sehen. In diesem Fall treffen an der Phasengrenze eine sehr steife (grün) und eine sehr weiche (gelb) Phase aufeinander. Dem Elementknoten zwischen diesen beiden Phasen wird durch die SPR zwangsläufig eine aus der hohen Spannung der steifen Phase und der niedrigen Spannung der weichen Phase gemittelte Spannung zugewiesen. Der Spannungsverlauf an der Phasengrenze wird also geglättet, in der Realität treten dort jedoch Spannungssprünge auf. Diese Glättung der Spannungen an den Phasengrenzen stellt eine Verfälschung des Spannungsverlaufs dar und verschlechtert die Qualität der Fehlerschätzung.

In Fischer und Eidel [25] wurde diese Tatsache untersucht und für Knoten, die sich an Phasengrenzen befinden, eine Duplex-Spannung eingeführt. Die Knoten erhalten eine zu den Elementen der steiferen Phase zugehörige Spannung und eine zu den Elementen der weicheren Phase zugehörige Spannung. Auf diese Weise kann der diskrete Spannungssprung an der Phasengrenze berücksichtigt werden, was zu einer Verbesserung der Qualität der Fehlerschätzung führt. Der Spannungsverlauf mit den Duplex-Spannungen an einer Phasengrenze ist in Abb. 9(c) dargestellt.

4 Vernetzung

Durch moderne Techniken können hochauflösende Aufnahmen von heterogenen Mikrostrukturen erzeugt werden. Verfahren wie die Fokussierte Ionenstrahl-Tomographie (engl. *Focused Ion Beam*, FIB) [31] oder Röntgenverfahren (engl. *X-Ray*) [39] können hierbei Auflösungen im Bereich weniger μm realisieren, die idealerweise als Input für Finite Elemente Berechnungen verwendet werden können [50, 42].

Zwangsläufig stellt sich die Frage nach der benötigten Auflösung, wenn die generierten Aufnahmen als Input für FE-Analysen verwendet werden sollen. Die in Abb. 1 dargestellte Betonprobe besteht aus $371 \times 371 \times 371$ Voxeln bei einer Kantenlänge von $37,1\,\mathrm{mm}$, was einer Auflösung von $100\,\mu\mathrm{m}$ je Raumrichtung entspricht. Mit den oben genannten Verfahren sind auch deutlich feinere Auflösungen möglich, allerdings weist das FE-Netz so bereits über 150 Mio. Freiheitsgrade auf. Um den numerischen Aufwand auf ein vertretbares Maß zu reduzieren, müssen die Größe der Probe und die Auflösung in einem gesunden Verhältnis zueinanderstehen. Den Einfluss der Auflösung auf Simulationsergebnisse untersuchten beispielsweise Hutzenlaub et al. [34] für poröse Materialien oder Nguyen et al. [47] für die Rissausbreitung in heterogenen Materialien.

Es ist naheliegend, die pixel- (2D) bzw. voxelbasierten (3D) Informationen über die Mikrostruktur direkt als Input für die Simulation zu verwenden, da man sich hierdurch eine aufwändige Vernetzung der Struktur spart. Des Weiteren sind pixel- und voxelbasierte Vernetzungen der optimale Ausgangspunkt für Quadtree- bzw. Octreebasierte Netzvergröberungen, die als Preprocessor zur Reduktion des numerischen Aufwandes eingesetzt werden können.

4.1 Uniforme Netzvergröberung

Bei uniformen Netzvergröberungen wird das FE-Netz gleichmäßig, auch über die Phasengrenzen hinweg, vergröbert. Die Auflösung der Mikrostruktur wird hierdurch herabgesetzt, was wiederum zu einem Anstieg des Auflösungsfehlers $e^{\epsilon\,\square}_{mich}$ führt. Bei der uniformen Netzvergröberung können beispielsweise jeweils 2×2 Elemente der ursprünglichen Diskretisierung zu einem neuen, vergröberten Element zusammengefasst werden. Hierbei müssen Regeln definiert werden, wie an Phasengrenzen verfahren werden soll, da hier Elemente mit unterschiedlichen Phasen zusammengefasst werden müssen.

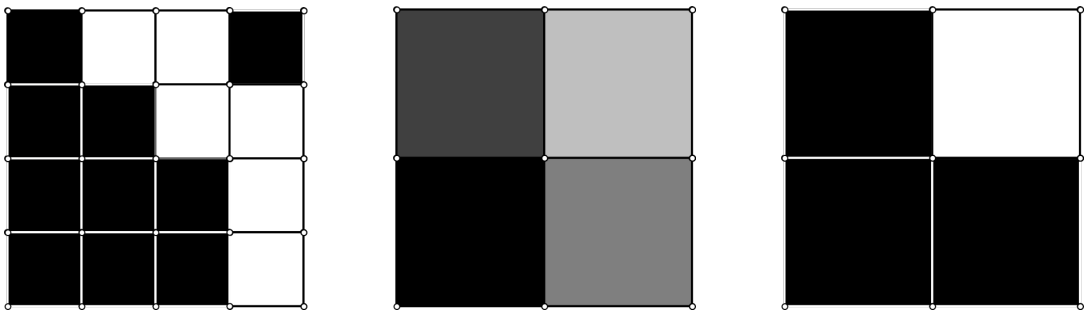


Abbildung 10: Uniforme Netzvergröberung einer (a) heterogenen Struktur mit 4×4 Elementen mittels (b) Phasenmittelung und (c) Beibehalten der ursprünglichen Phasen, aus Eidel et al. [23].

Die uniforme Vergröberung der in Abb. 10(a) dargestellten 4×4 Elemente umfassenden heterogenen Mikrostruktur wird mit zwei unterschiedlichen Regeln für die Phasengrenzen vergröbert. Abbildung 10(b) zeigt eine Mittelung der Phasen, neben den ursprünglichen Phasen in schwarz und weiß, entstehen an den Phasengrenzen gemittelte graue Phasen. In der Berechnung werden die zugehörigen Elementsteifigkeiten durch eine Mittelung der Steifigkeiten der ursprünglichen Phasen berücksichtigt, ausgedrückt mit den beiden Volumenanteilen und E-Moduli der Phasen ergibt sich

$$\mathrm{E}_{res} = \mathrm{Volfrac}_{P1} \cdot \mathrm{E}_{P1} + \mathrm{Volfrac}_{P2} \cdot \mathrm{E}_{P2}\,. \tag{47}$$

Demgegenüber werden in Abb. 10(c) die ursprünglichen Phasen beibehalten, die Phase des vergröberten Elements entspricht hierbei der in dem ursprünglichen 2×2 Elemente umfassenden Patch häufiger auftretenden Phase. Bei einer Gleichverteilung der Phasen, wie in dem rechten unteren Patch der Struktur aus Abb. 10(a), werden weitere Regeln zur Phasenbestimmung definiert. Die resultierende Phase wird hier beispielsweise so gewählt, dass die Volumenanteile der gesamten vergröberten Struktur möglichst genau mit den Volumenanteilen der ursprünglichen Struktur übereinstimmen.

Während bei der Einführung der gemittelten Phasen das arithmetische Mittel der Steifigkeiten konstant bleibt, werden bei der Beibehaltung der ursprünglichen Phasen die Phasenanteile der einzelnen Phasen und somit die gemittelten Steifigkeiten verändert. Im Gegenzug bleibt hier der diskrete Steifigkeitssprung an der Phasengrenze erhalten und wird nicht durch gemittelte Phasen geglättet.

4.2 Adaptive Netzvergröberung

Adaptive Netzverfeinerungen und -vergröberungen werden in FE-Verfahren üblicherweise verwendet, um den Diskretisierungsfehler möglichst gering zu halten ohne jedoch durchgehend eine sehr feine Diskretisierung verwenden zu müssen. Hierbei wird im Anschluss an eine Berechnung der Diskretisierungsfehler geschätzt und anschließend Elemente mit hohen Diskretisierungsfehlern verfeinert. Im Gegenzug können Elemente mit geringen Diskretisierungsfehlern vergröbert werden, um den numerischen Aufwand zu reduzieren. Diese adaptive Netzanpassung wird ausgeführt bis der maximale elementweise Diskretisierungsfehler unterhalb eines vorher definierten Grenzwertes liegt.

Um den numerischen Aufwand bereits vor dem erstmaligen Ausführen einer Berechnung und einer anschließenden Fehlerschätzung durch adaptive Netzvergröberungen reduzieren zu können, müssen Annahmen bezüglich der zu erwartenden Diskretisierungsfehler gemacht werden. Bei heterogenen Mikrostrukturen ist zu erwarten, dass die maximalen Diskretisierungsfehler an den Phasengrenzen auftreten werden, sodass es sinnvoll ist, dort eine feinere Diskretisierung als im Inneren der jeweiligen Phasen zu verwenden. Die ursprüngliche, feine Diskretisierung der Mikrostruktur wird an den Phasengrenzen folglich beibehalten und lediglich die Elemente im Inneren einer Phase vergröbert. Auf diese Weise wird die heterogene Mikrostruktur selbst nicht verändert, der Modellierungsfehler bleibt unverändert.

Mittels uniformer Netzvergröberung kann die Mikrostruktur praktisch bis auf ein einzelnes Element vergröbert werden, was der Berechnung der makroskopischen Materialeigenschaften nach Voigt aus Gleichung (6) entspricht. Demgegenüber sind der adaptiven Netzvergröberung Grenzen gesetzt, da nach einigen Vergröberungsschritten die maximale

Vergröberung im Inneren der Phasen erreicht wird und keine weiteren Vergröberungs-Schritte möglich sind.

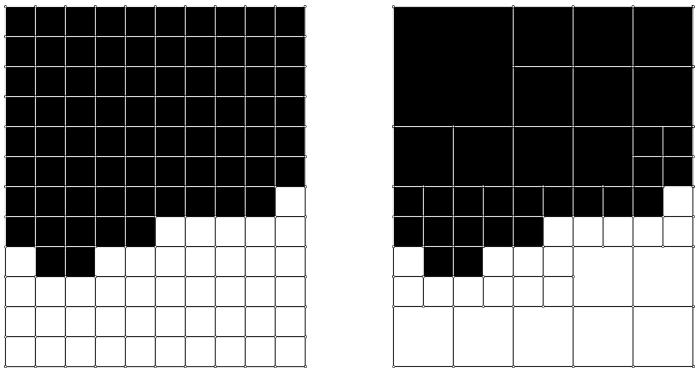


Abbildung 11: (a) Heterogenen Struktur mit zwei Phasen, (b) adaptiv vergröbertes Netz nach zwei Schritten, aus Eidel et al. [23].

Abbildung 11(a) zeigt eine heterogene Mikrostruktur mit zwei unterschiedlichen Phasen. In Abb. 11(b) ist das Ergebnis nach zwei Vergröberungsschritten zu sehen, die Anzahl der Elemente konnte von 120 Elementen der ursprünglichen Mikrostruktur auf 54 Elemente reduziert werden.

Am effektivsten ist eine adaptive Netzvergröberung, wenn die einzelnen Phasen der heterogenen Mikrostruktur möglichst große, zusammenhängende Gebiete bilden und die Gesamtlänge der Phasengrenzen möglichst gering ist. Ein optimales Beispiel für eine solche Mikrostruktur bildet der in der dritten dieser kumulativen Promotionsschrift zugrundeliegenden Veröffentlichung [25] in Abschnitt 4.3 betrachtete kreisförmige Einschluss in einer quadratischen Matrix. Nach drei adaptiven Vergröberungsschritten wurde die Zahl der Freiheitsgrade um mehr als 97% reduziert, der zugehörige Diskretisierungsfehler steigt hierbei, abhängig von der Mikro-Makro-Kopplungsbedingung, um lediglich 18-27% in den betrachteten Normen.

Die Auswirkungen der adaptiven Netzvergröberung in Form der Reduktion der Freiheitsgrade und dem zugehörigen Anstieg des Diskretisierungsfehlers sind anhand zahlreicher Beispiele [25] untersucht worden. In der vierten dieser kumulativen Promotionsschrift zugrundeliegenden Veröffentlichung [23] wird zusätzlich der Modellierungs- oder auch Auflösungsfehler, der durch die uniforme Netzvergröberung entsteht, untersucht.

Es ist offensichtlich, dass beide Netzvergröberungsalgorithmen ihre Vorteile haben. Während der uniformen Netzvergröberung keine Grenzen gesetzt sind und nahezu beliebige Vergröberungen möglich sind, verspricht die adaptive Netzvergröberung einen vergleichsweise geringen Anstieg des Diskretisierungsfehlers und keinen Anstieg des Auflösungsfehlers.

5 Nichtlineare FE-HMM

Bei nichtlinearen FE-Berechnungen - beispielsweise auf Grund nichtlinearer Stoffgesetze oder Berücksichtigung von Effekten wie Plastizität oder Schädigung - können die zugehörigen Gleichungssysteme auf beiden Skalen mit dem Newton-Verfahren gelöst werden. Hierfür sind in der Regel mehrere Iterationen nötig, wodurch der numerische Aufwand deutlich höher ist im Vergleich zu linearen FE-Berechnungen. In jedem Makro- und Mikro-Iterationsschritt muss die zugehörige Steifigkeitsmatrix neu berechnet und das Gleichungssystem gelöst werden.

5.1 Standard Lösungs-Algorithmus

Der übliche Ansatz zur Lösung von nichtlinearen Berechnungsaufgaben mittels Zwei-Skalen FE-Verfahren besteht aus einer Verschachtelung der Makro- und Mikroiterationen.

Algorithmus 1: Standard

```
while Makro-Residuum < Makro-Toleranz do
    Makro-Iteration;
    while Mikro-Residuum < Mikro-Toleranz
     do
        Mikro-Iteration;
    end
end
```

Algorithmus 1 veranschaulicht die Verschachtelung der Newton-Iterationen auf Makro- und Mikroebene. Solange das Makro-Residuum eine definierte Makro-Toleranz nicht unterschreitet, wird ein Makro-Iterationsschritt ausgeführt. In einem solchen Iterationsschritt wird für jedes Mikrogebiet das zugehörige, ebenfalls nichtlineare Gleichungssystem gelöst. Die Mikro-Iterationsschritte werden solange ausgeführt, bis das Mikro-Residuum der einzelnen Mikrogebiete unterhalb einer Mikro-Toleranz liegt. Erst, wenn das Mikro-Residuum aller Mikrogebiete unterhalb der definierten Toleranz liegt, kann die zugehörige Makro-Steifigkeitsmatrix aufgestellt werden und der Makro-Iterationsschritt wird ausgeführt.

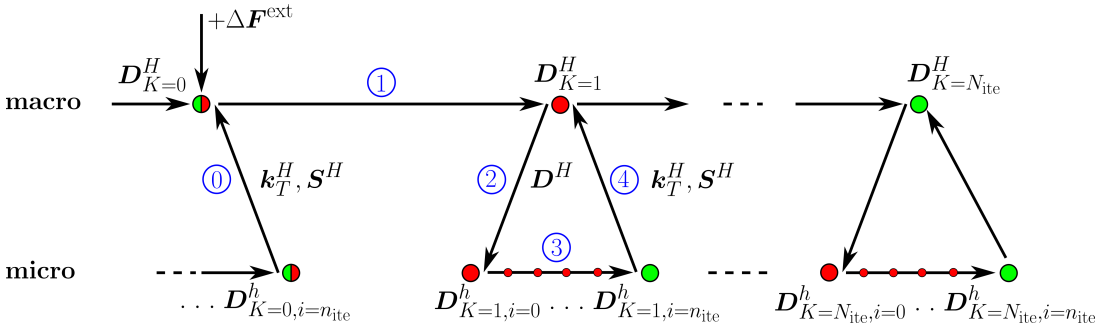


Abbildung 12: Ablauf und Datenaustausch des verschachtelten Newton-Verfahrens.

Der Ablauf der Makro- und Mikro-Iterationsschritte und der Datenaustausch zwischen den beiden Skalen wird in Abb. 12 dargestellt. Hierbei beschreibt $\boldsymbol{D}^H$ die Makroverschiebungen, $\boldsymbol{D}^h$ die Mikroverschiebungen, $\boldsymbol{k}^H_T$ die tangentiale Steifigkeitsmatrix des Makro-

elements und $\boldsymbol{S}^H$ die makroskopischen Spannungen. Der Index K bezeichnet den jeweiligen Makro-Iterationsschritt, der Index i den Mikro-Iterationsschritt. Rot gefüllte Kreise sind gleichbedeutend mit Nicht-Gleichgewichts-Zuständen, grün gefüllte Kreise mit Gleichgewichts-Zuständen.

Der Ablauf der Makro- und Mikroiterationen ist in Abb. 12 in einzelne Schritte unterteilt worden.

Schritt	Aktion
⓪	Da die Mikro- und Makroverschiebungen zu Beginn der Iterationen noch gleich null sind, sind in diesem Schritt keine Iteration auf dem Mikrogebiet nötig und die tangentiale Steifigkeitsmatrix $\boldsymbol{k}_T^H$ und Spannung $\boldsymbol{S}^H$ können in diesem Schritt sofort an das Makrolevel übergeben werden
①	Mit Hilfe der zuvor elementweise berechneten tangentialen Steifigkeitsmatrizen wird das Makro-Gleichungssystem aufgebaut und gelöst und so die neuen makroskopischen Knotenverschiebungen $\boldsymbol{D}_{K=1}^H$ bestimmt.
②	Die neuen makroskopischen Knotenverschiebungen werden anschließend auf das Mikrogebiet übertragen.
③	Es folgen die Iterationsschritte des Mikro-Newton-Verfahrens zur Berechnung der Knotenverschiebungen auf dem Mikrolevel $\boldsymbol{D}_{K=1}^h$, die enden sobald der Gleichgewichts-Zustand auf dem Mikrolevel erreicht wird.
④	Nach Abschluss der Mikro-Iterationen werden die tangentiale Steifigkeitsmatrix $\boldsymbol{k}_T^H$ und die aus den Knotenverschiebungen $\boldsymbol{D}_{K=1,i=n_{ite}}^h$ berechnete Spannung $\boldsymbol{S}^H$ auf das Makrolevel übertragen.
...	Die Schritte ① bis ④ werden anschließend so lange durchgeführt, bis ein makroskopischer Gleichgewichtszustand erreicht wird.

Tabelle 3: Ablauf der Mikro- und Makroiterationsschritte beim Standard Lösungs-Algorithmus.

5.2 Alternierender Lösungs-Algorithmus

Der hohe Aufwand der verschachtelten Newton-Iterationen kann durch eine geringfügige Modifikation des Lösungs-Algorithmus reduziert werden. Solange der makroskopische Gleichgewichtszustand noch nicht erreicht ist, ist es nicht unbedingt erforderlich das Mikrogleichungssystem bis hin zu seinem Gleichgewichtszustand zu lösen. In Schritt ③ des in Abb. 12 dargestellten Schemas wird also lediglich ein Mikro-Iterationsschritt ausgeführt.

Algorithmus 2: Alternierend

```
while Makro-Residuum < Makro-Toleranz
 do
    Makro-Iteration;
    Mikro-Iteration;
end
```

Algorithmus 2 zeigt den daraus resultierende Ablauf der Berechnungen, bei dem sich

Makro- und Mikroiterationen abwechseln, wodurch von einem alternierenden Lösungs-Algorithmus gesprochen werden kann.

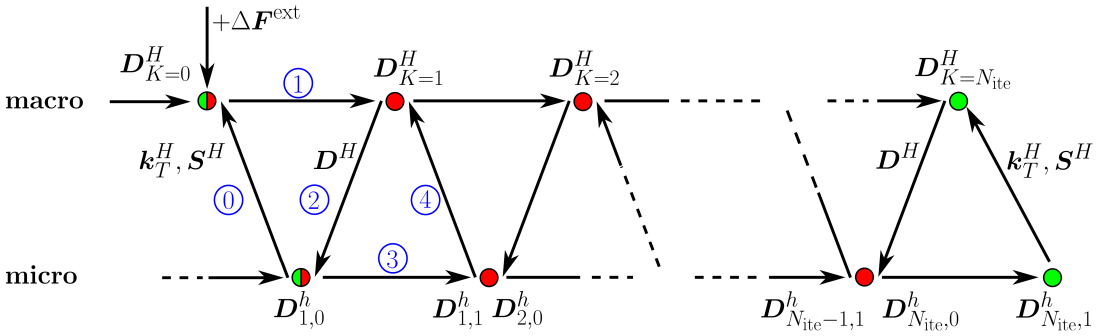


Abbildung 13: Ablauf und Datenaustausch des alternierenden Newton-Verfahrens.

Schritt	Aktion
⓪ - ②	Analog zu Standard Lösungs-Algorithmus aus Tab. 3.
③	Auf Mikroebene wird lediglich ein Iterationsschritt des Mikro-Newton-Verfahrens zur Berechnung der Knotenverschiebungen $\boldsymbol{D}^h_{1,1}$ ausgeführt. Damit beschreibt der Endzustand der Mikroiteration im Allgemeinen keinen Gleichgewichtszustand mehr.
④	Analog zu Standard Lösungs-Algorithmus aus Tab. 3.
⋯	Die Schritte ① bis ④ werden anschließend so lange durchgeführt, bis auf Mikro- und Makroebene ein Gleichgewichtszustand erreicht wird.

Tabelle 4: Ablauf der Mikro- und Makroiterationsschritte beim alternierenden Lösungs-Algorithmus.

Bei diesem Vorgehen konvergieren das Mikro- und Makro-Gleichungssystem parallel zueinander. Es ist offensichtlich, dass in Schritt ③, der üblicherweise mit dem größten numerischen Aufwand verbunden ist, durch die Einsparung einiger Iterationsschritte numerischer Aufwand eingespart werden kann. Im Gegenzug leidet jedoch die Qualität der zugehörigen tangentialen Steifigkeitsmatrix und der gemittelten makroskopischen Spannungen, die in Schritt ④ an das Makrolevel übergeben werden. Die schlechtere Qualität dieser Größen - resultierend aus der Tatsache, dass sie nicht aus Gleichgewichtszuständen gewonnen wurden - hat zur Folge, dass die Konvergenz des Newton-Verfahrens beeinträchtigt wird, wodurch der alternierende Lösungs-Algorithmus gegenüber dem Standard Lösungs-Algorithmus im Allgemeinen zusätzliche Makro-Iterationsschritte erfordert. Nichtsdestotrotz kann der alternierende Lösungs-Algorithmus eine wertvolle Zeitersparnis liefern, wenn die Reduktion der Berechnungszeit in Schritt ③ so groß ist, dass sie eine Zunahme der Anzahl der Makroiterationen rechtfertigt.

In [22] wird die Effizienz des alternierenden Lösungs-Algorithmus anhand einiger Beispiele untersucht. Der Speedup-Faktor liegt hier üblicherweise im Bereich 1.5-1.8, in einzelnen Fällen wird sogar ein Speedup-Faktor größer 2 erreicht, was eine deutliche Reduktion der Berechnungszeit bedeutet.

6 Zusammenfassung

Zusammenfassend lassen sich die folgenden Ergebnisse der dieser Arbeit zugrundeliegenden Veröffentlichungen festhalten.

In der Veröffentlichung *The heterogeneous multiscale finite element method for the homogenization of linear elastic solids and a comparison with the FE^2 method* wurde eine vollständige Formulierung der FE-HMM für lineare Elastizität präsentiert. Durch einen ausführlichen konzeptionellen Vergleich der FE-HMM mit der FE^2-Methode wurden Gemeinsamkeiten und Unterschiede zwischen den beiden Methoden aufgezeigt. Ein quantitativer Vergleich der beiden Methoden anhand einiger Mikro- und Makrorandwertprobleme lieferte schlussendlich eine Übereinstimmung der Berechnungsergebnisse. Diese quantitative Übereinstimmung erlaubt die Übertragung der Konvergenzaussagen, die durch eine vollständige diskrete a priori Fehleranalyse im Rahmen der FE-HMM hergeleitet wurden, auf die FE^2-Methode und liefert somit einen neuen, wichtigen Beitrag zur FE^2-Methode. Anhand der präsentierten Beispiele konnte außerdem gezeigt werden, dass die a priori Konvergenzaussagen gültig sind und die Ableitung der optimalen Netzverfeinerungsstrategie ermöglichen. Schlussendlich hat die Veröffentlichung auch einen Beitrag geleistet, die vorwiegend in mathematischen Veröffentlichungen behandelte FE-HMM mit der in zahlreichen Zweigen der Ingenieurwissenschaft eingesetzten FE^2 zusammenzubringen.

In der Veröffentlichung *Convergence and error analysis of FE-HMM/FE^2 for energetically consistent micro-coupling conditions in linear elastic solids* wurde erstmals die Konvergenz des Mikrofehlers auf dem Makrolevel unter Verwendung unterschiedlicher Kopplungsbedingungen und Ansatzfunktionen untersucht. Die Implementierung von Neumann-Randbedingungen zur Kopplung der Mikro- und Makroskala im Rahmen der FE-HMM wurde ebenfalls erstmals in dieser Veröffentlichung beschrieben. Anhand diverser numerischer Beispiele mit Mikro- und Makrorandwertproblemen unterschiedlicher Regularität wurde deren Auswirkung auf die Fehlerkonvergenz untersucht. Außerdem wurde der Modellierungsfehler bei Dirichlet-Kopplung bei unterschiedlichen Verhältnissen der Größe der Mikrogebiete δ zur charakteristischen Länge der Mikroheterogenität ϵ untersucht und so die a priori Aussagen eines Anstiegs des Modellierungsfehlers bei steigendem ϵ/δ-Verhältnis bestätigt.

Die Veröffentlichung *Error analysis for quadtree-type mesh coarsening algorithms adapted to pixelized heterogeneous microstructures* untersucht adaptive Vergröberungsalgorithmen, die als Preprocessor zur Reduktion der Größe des Mikrorandwertproblems eingesetzt werden können. Es wurde gezeigt, dass der Gradient der Elementgröße an Phasengrenzen nicht zu stark gewählt werden sollte, um einen unnötig starken Anstieg des Diskretisierungsfehlers in diesem Bereich zu vermeiden. Um die Fehlerschätzung für heterogene Strukturen anwendbar zu machen, wurde der Algorithmus der SPR angepasst und eine Duplex-Spannung für Knoten an Phasenübergängen eingeführt. Anhand einiger numerischer Beispiele konnte der Nutzen der Netzvergröberung validiert werden. Gerade in den ersten Vergröberungsschritten steht eine starke Reduktion der Anzahl der Freiheitsgrade einem lediglich geringfügigen Anstieg des Diskretisierungsfehlers gegenüber. Zudem wurde anhand der Konvergenzuntersuchung eines kreisförmigen Einschlusses in einer Matrix gezeigt, dass eine Quadtree-basierte Vernetzung des kreisförmigen Einschlusses keine Nachteile gegenüber einer annähernd glatten Vernetzung bietet. Schlussendlich bieten direkt aus Pixel-Informationen abgeleitete Netze also eine optimale Grundlage für die

Verwendung auf der Mikro-Skala eines Zwei-Skalen FE-Verfahrens. Durch die präsentierten Netzvergröberungsalgorithmen kann der numerische Aufwand hierbei ohne einen übermäßigen Anstieg des Diskretisierungsfehlers reduziert werden.

In der Veröffentlichung *From image data towards microstructure information – Accuracy analysis at the digital core of materials* wurde die Auswirkung der Auflösung der Mikrostruktur auf die Berechnungsergebnisse untersucht. Zwei unterschiedliche Algorithmen zur Vergröberung der Auflösung wurden präsentiert - zum einen ein Algorithmus bei dem die ursprünglichen Material-Phasen beibehalten werden, zum anderen ein Algorithmus bei dem durch die Vereinigung von Pixeln unterschiedlicher Phasen auch neue Misch-Phasen entstehen können. Durch die Entstehung von Pixeln mit Misch-Phasen wird der Steifigkeitssprung an Phasengrenzen geglättet, was dazu führt, dass auch die Spannungsverläufe in diesen Bereichen verfälscht werden. Bei der Vergröberung unter Beibehaltung der ursprünglichen Phasen wird dagegen das Verhältnis der unterschiedlichen Phasen verändert. Es hat sich gezeigt, dass der Einfluss der Auflösung der Mikrostruktur deutlich größeren Einfluss auf der Mikro-Skala als auf der Makro-Skala hat. Wenn also nur das makroskopische Verhalten der Struktur von Interesse ist, so ist eine relativ grobe Auflösung der Mikrostruktur ausreichend, um zuverlässige Vorhersagen zu treffen. Erst wenn mikroskopische Größen im Fokus stehen - wenn beispielsweise Plastizität oder Schädigung in der Mikrostruktur berücksichtigt werden sollen, dann muss die Mikrostruktur auch ausreichend fein aufgelöst werden.

Die Veröffentlichung *Computational homogenization of concrete in the cyber Size-Resolution-Discretization (SRD) parameter space* beschäftigt sich mit einer realen 3D-Materialprobe und Möglichkeiten zur Reduktion des numerischen Berechnungsaufwandes. Hierfür wird der SRD-Parameterraum eingeführt (S - Size, R - Resolution, D - Discretization) und der Einfluss der einzelnen Parameter auf die Berechnungsergebnisse untersucht. Des Weiteren wurde untersucht inwiefern Ergebnisse eine 2D-Analyse auf eine 3D-Analyse übertragbar sind.

In der zur Begutachtung eingereichten Veröffentlichung *A nonlinear finite element heterogeneous multiscale method for the homogenization of hyperelastic solids and a novel staggered two-scale solution algorithm* wurde eine vollständige Formulierung der FE-HMM für geometrische Nichtlinearität und Hyperelastizität präsentiert. Die a priori Aussagen zur Konvergenz der Fehler für den vollständig linearen Fall wurden im Rahmen der nichtlinearen FE-HMM untersucht und konnten für ausreichend reguläre Randwertprobleme bestätigt werden. Für die effiziente Lösung der nichtlinearen, verschachtelten Gleichungssysteme auf Mikro- und Makroebene wurde ein neuer Lösungsalgorithmus vorgestellt und anhand einiger numerischer Beispiele der Vorteil gegenüber dem Standard-Lösungsalgorithmus untersucht. Hierbei konnte eine signifikante Reduktion der Berechnungsdauer durch die Verwendung des neuen Lösungsalgorithmus von bis zu Faktor 2.6 festgestellt werden.

7 Literatur

[1] A. Abdulle. On a-priori error analysis of fully discrete heterogeneous multiscale fem. *SIAM Multiscale Model. Simul.*, 4(2):447–459, 2005.

[2] A. Abdulle. Analysis of a heterogeneous multiscale fem for problems in elasticity. *Math. Models Methods Appl. Sci.*, 16(4):615–635, 2006.

[3] A. Abdulle. The Finite Element Heterogeneous Multiscale Method: A computational strategy for multiscale PDEs. *GAKUTO Int. Ser. Math. Sci. Appl.*, 31:133–181, 2009.

[4] A. Abdulle and A. Nonnenmacher. A posteriori error analysis of the heterogeneous multiscale method for homogenization problems. *C. R. Acad. Sci. Paris*, Ser. I 347:1081–1086, 2009.

[5] A. Abdulle and A. Nonnenmacher. Adaptive finite element heterogeneous multiscale method for homogenization problems. *Comput. Methods Appl. Mech. Engrg.*, 200:2710–2726, 2011.

[6] A. Abdulle and C. Schwab. Heterogeneous multiscale fem for diffusion problems on rough surfaces. *Multiscale Model. Simul.*, 3(1):195–220, 2005.

[7] A. M. Abdulle and A. Nonnenmacher. A short and versatile finite element multiscale code for homogenization problems. *Comput. Methods Appl. Mech. Engrg.*, 198:2839–2859, 2009.

[8] G. Allaire. Homogenization and two-scale convergence. *SIAM J. Math. Anal.*, 23(6):1482–1518, 1992.

[9] R. Altmann, P. Henning, and D. Peterseim. Numerical homogenization beyond scale separation. *Acta Numer.*, 30:1–86, 2021.

[10] J. Barlow. Optimal stress locations in finite element models. *Int. J. Numer. Methods Eng.*, 10(2):243–251, 1976.

[11] A. Bensoussan, J. L. Lions, and G. Papanicolau. Asymptotic analysis for periodic structures. *North-Holland, Amsterdam*, 1976.

[12] L. Bogunia, S. Buchen, and K. Weinberg. Microstructure characterization and stochastic modeling of open-cell foam based on μct-image analysis. *GAMM-Mitteilungen*, 45:e202200018, 2022.

[13] D. Cioranescu and P. Donato. An introduction to homogenization. *Oxford University Press, New York*, 1999.

[14] M. Dauge, A. Düster, and E. Rank. Theoretical and numerical investigation of the finite cell method. *J. Sci. Comput.*, 65(3):1039–1064, 2015.

[15] P. Di Stolfo, A. Rademacher, and A. Schröder. Dual weighted residual error estimation for the finite cell method. *J. Numerical Math.*, 27(2):101–122, 2019.

[16] A. Düster, H.-G. Sehlhorst, and E. Rank. Numerical homogenization of heterogeneous and cellular materials utilizing the finite cell method. *Comput. Mech.*, 50(4):413–431, 2012.

[17] W. E and B. Enquist. The heterogeneous multiscale methods. *Commun. Math. Sci.*, 1:87–132, 2003.

[18] W. E, P. Ming, and P. Zhang. Analysis of the heterogeneous multiscale method for elliptic homogenization problems. *J. Amer. Math. Soc.*, 18:121–156, 2005.

[19] Y. Efendiev, J. Galvis, and T. Y. Hou. Generalized multiscale finite element methods (GMsFEM). *J. Comput. Phys.*, 251:116–135, 2013.

[20] B. Eidel. Deep CNNs as universal predictors of elasticity tensors in homogenization. *Comput. Methods Appl. Mech. Engrg.*, 403(A), 2023.

[21] B. Eidel and A. Fischer. The heterogeneous multiscale finite element method for the homogenization of linear elastic solids and a comparison with the FE^2 method. *Comput. Methods Appl. Mech. Engrg.*, 329:332–368, 2018.

[22] B. Eidel, A. Fischer, and A. Gote. A nonlinear finite element heterogeneous multiscale method for the homogenization of hyperelastic solids and a novel staggered two-scale solution algorithm. *https://arxiv.org/abs/1908.08292*, zur Begutachtung eingereicht, 2019.

[23] B. Eidel, A. Fischer, and A. Gote. From image data towards microstructure information – accuracy analysis at the digital core of materials. *ZAMM-Z Angew. Math. Me.*, 2020.

[24] A. Fischer and B. Eidel. Convergence and error analysis of FE-HMM/FE^2 for energetically consistent micro-coupling conditions in linear elastic solids. *Eur. J. Mech. A/Solids*, 77, 2019.

[25] A. Fischer and B. Eidel. Error analysis for quadtree-type mesh coarsening algorithms adapted to pixelized heterogeneous microstructures. *Comput. Mech.*, 16(04):615, 2020.

[26] A. Gote, A. Fischer, C. Zhang, and B. Eidel. Computational homogenization of concrete in the cyber Size-Resolution-Discretization (SRD) parameter space. *Finite Elem. Anal. Des.*, 198, 2022.

[27] H. Gravenkamp and S. Duczek. Automatic image-based analyses using a coupled quadtree-SBFEM/SCM approach. *Comput. Mech.*, 60(4):559–584, 2017.

[28] J. M. Guedes and N. Kikuchi. Preprocessing and postprocessing for materials based on the homogenization method with adaptive finite element methods. *Comput. Methods Appl. Mech. Engrg.*, 83(2):143–198, 1990.

[29] R. Hill. Elastic properties of reinforced solids: Some theoretical principles. *J. Mech. Phys. Solids*, 11(5):357–372, 1963.

[30] R. Hill. On constitutive macro-variables for heterogeneous solids at finite strain. *Proc. R. Soc. A: Math. Phys. Eng. Sci.*, 326(1565):131–147, 1972.

[31] L. Holzer and M. Cantoni. Review of FIB-tomography In: Utke I, Moshkalev S, Russell P (eds) Nanofabrication using focused ion and electron beams, Oxford series on nanomanufacturing. *Oxford University Press, Oxford*, 559201222:410–435, 2011.

[32] T. Y. Hou and X. Wu. A multiscale finite element method for elliptic problems in composite materials and porous media. *J. Comput. Phys.*, 134:169–189, 1997.

[33] Y. Huang, Z. Yang, W. Ren, G. Liu, and C. Zhang. 3D meso-scale fracture modelling and validation of concrete based on in-situ X-ray Computed Tomography images using damage plasticity model. *Int. J. Solids Struct.*, 67-68:340–352, 2015.

[34] T. Hutzenlaub, J. Becker, R. Zengerle, and S. Thiele. How coarsening the 3D reconstruction of a porous material influences diffusivity and conductivity values. *ECS Electrochem. Lett.*, 2(2):F14–F17, 2013.

[35] A. Javili, G. Chatzigeorgiou, and P. Steinmann. Computational homogenization in magneto-mechanics. *Int. J. Solids Struct.*, 50:4197–4216, 2013.

[36] A. Javili, S. Saeb, and P. Steinmann. Aspects of implementing constant traction boundary conditions in computational homogenization via semi-dirichlet boundary conditions. *Comput. Mech.*, 59:21–35, 2017.

[37] O. Jecker and A. Abdulle. Numerical experiments for multiscale problems in linear elasticity. *In: Karasözen, B., Manguoğlu, M., Tezer-Sezgin, M., Göktepe, S., Uğur, Ö., (eds.), Numerical Mathematics and Advanced Applications ENUMATH 2015*, volume 112 of Lecture Notes in Computational Science and Engineering:pp. 123–131. Springer International Publishing, Cham, 2016.

[38] T. Kanit, S. Forest, I. Galliet, V. Mounoury, and D. Jeulin. Determination of the size of the representative volume element for random composites: statistical and numerical approach. *Int. J. Solids Struct.*, 40:3647–3679, 2003.

[39] R. Ketcham and W. Carlson. Acquisition, optimization and interpretation of X-ray computed tomographic imagery: applications to the geosciences. *Comput. Geosci.*, 27:381–400, 2001.

[40] T. Kirchdoerfer and M. Ortiz. Data-driven computational mechanics. *Comput. Methods Appl. Mech. Engrg.*, 304:81–101, 2016.

[41] T. Korzeniowski and K. Weinberg. Data-driven finite element computation of open-cell foam structures. *Comput. Methods Appl. Mech. Engrg.*, 400:115487, 2022.

[42] G. Legrain, P. Cartraud, I. Perreard, and N. Moës. An X-FEM and level set computational approach for image-based modelling: application to homogenization. *Int. J. Numer. Methods Eng.*, 86(7):915–934, 2011.

[43] A. Matache and C. Schwab. Two-scale fem for homogenization problems. *Math. Model. Anal.*, 36(4):537–572, 2002.

[44] C. Miehe and A. Koch. Computational micro-to-macro transitions of discretized microstructures undergoing small strains. *Arch. Appl. Mech.*, 71:300–317, 2002.

[45] P. Ming and X.-H. Yue. Numerical methods for multiscale elliptic problems. *J. Comput. Phys.*, 214:421–445, 2006.

[46] H. Moulinec and P. Suquet. A numerical method for computing the overall response of nonlinear composites with complex microstructure. *Comput. Methods Appl. Mechan. Eng.*, 157(1-2):69–94, 1998.

[47] T. Nguyen, J. Yvonnet, Q.-Z. Zhu, M. Bornert, and C. Chateau. A phase field method to simulate crack nucleation and propagation in strongly heterogeneous materials from direct imaging of their microstructure. *Eng. Fract. Mech.*, 139:18–39, 2015.

[48] M. Ohlberger. A posteriori error estimates for the heterogeneous multiscale finite element method for elliptic homogenization problems. *Multiscale Model. Simul.*, 4(1):88–114, 2005.

[49] J. Parvizian, A. Düster, and E. Rank. Finite cell method. *Comput. Mech.*, 41(1):121–133, 2007.

[50] W. Ren, Z. Yang, R. Sharma, C. Zhang, and P. J. Withers. Two-dimensional X-ray CT image based meso-scale fracture modelling of concrete. *Eng. Fract. Mech.*, 133:24–39, 2015.

[51] A. Reuss. Berechnung der fließgrenze von mischkristallen auf grund der plastizitätsbedingung für einkristalle. *Z. Angew. Math. Mech.*, 9(1):49–58, 1929.

[52] S. Saeb, P. Steinmann, and A. Javili. Aspects of computational homogenization at finite deformations: A unifying review from Reuss' to Voigt's bound. *Appl. Mech. Rev.*, 68 (050801), 2016.

[53] E. Sanchez-Palencia. Non-homogenous media and vibration theory. *In: Lecture Notes in Physics*, 127:Springer, Berlin, 1980.

[54] J. Schröder. Derivation of the localization and homogenization conditions for electro-mechanically coupled problems. *Comput. Mater. Sci.*, 46(3):595–599, 2009.

[55] J. Schröder. A numerical two-scale homogenization scheme: the FE^2-method. *in: J. Schröder, K. Hackl (Eds.), Plasticity and Beyond, in: CISM International Centre for Mechanical Sciences*, pages 1–64, 2014.

[56] J. Schröder, D. Balzani, and D. Brands. Approximation of random microstructures by periodic statistically similar representative volume elements based on lineal-path functions. *Arch. Appl. Mech.*, 81(7):975–997, 2011.

[57] W. Voigt. Lehrbuch der Kristallphysik. *Teubner*, 1910.

[58] X. Wang, Z. Yang, J. Yates, A. Jivkov, and C. Zhang. Monte carlo simulations of mesoscale fracture modelling of concrete with random aggregates and pores. *Constr. Build. Mater.*, 75:35–45, 2015.

[59] I. Özdemir, W. A. M. Brekelmans, and M. G. D. Geers. FE^2 computational homogenization for the thermo-mechanical analysis of heterogeneous solids. *Comput. Methods Appl. Mech. Engrg.*, 198:602–613, 2008.

[60] O. C. Zienkiewicz and J. Z. Zhu. The Superconvergent Patch Recovery and a posteriori error estimates. Part 1: The recovery technique. *Internat. J. Numer. Methods Engrg.*, 33(7):1331–1364, 1992.

[61] O. C. Zienkiewicz and J. Z. Zhu. The Superconvergent Patch Recovery and a posteriori error estimates. Part 2: Error estimates and adaptivity. *Internat. J. Numer. Methods Engrg.*, 33(7):1365–1382, 1992.

8 Anlagen

8.1 Veröffentlichung: The heterogeneous multiscale finite element method for the homogenization of linear elastic solids and a comparison with the FE^2 method

Die erste Veröffentlichung von Prof. Bernhard Eidel und Andreas Fischer mit dem Titel **The heterogeneous multiscale finite element method for the homogenization of linear elastic solids and a comparison with the FE^2 method** erschien 2018 in *Computer Methods in Applied Mechanics and Engineering*. Im Folgenden wird der Anteil des Doktoranden an der Veröffentlichung dokumentiert.

Die Weiterentwicklung des Matlab-Codes, um ihn auch für vektorwertigen Randwertprobleme der linearen Elastizität anwendbar zu machen, lag vollständig in der Hand des Doktoranden. Neben der grundsätzlichen Weiterentwicklung des bestehenden Codes wurden auch zusätzliche Features implementiert. Dazu zählen beispielsweise sämtliche Postprocessing-Tools oder auch die Funktionen zur Berechnung des homogenisierten Elastizitätstensors. Zusätzlich wurden für den Vergleich der FE-HMM mit der FE^2-Methode unterschiedliche Varianten der FE^2-Methode ebenfalls in einem Matlab-Code implementiert.

An der Veröffentlichung selbst wurde der Doktorand an verschiedenen Stellen federführend tätig. Die Einleitung im ersten Kapitel erfolgte weitestgehend durch Prof. Eidel, lediglich die Formulierung der Ziele der Veröffentlichung wurde von beiden Autoren parallel erarbeitet. Im zweiten Abschnitt folgt ein detaillierter Aufschrieb der FE-HMM für lineare Elastizität, auch hier hat sich Prof. Eidel schwerpunktmäßig betätigt, der Einfluss des Doktoranden zeigt sich aber auch hier an einigen Stellen. Einige Details dieses theoretischen Aufschriebs wurden jedoch auch erst durch die Implementierung in den Matlab-Code deutlich. Als Beispiele sind die Darstellung der Mikroprobleme, die zur Transformation der Mikrosteifigkeiten auf das Makrolevel gelöst werden müssen, als Einheitsverschiebungszustände oder auch die Einheitsverzerrungszustände zur Berechnung des homogenisierten Elastizitätstenors zu nennen.

Die Vorstellung der Konvergenzaussagen zu Beginn von Kapitel 3 wurde von Prof. Eidel übernommen, die Einführung in die SPR geht auf der Doktoranden zurück. Der Schwerpunkt des vierten Kapitels in dem zunächst die FE^2-Methode vorgestellt und anschließend der Vergleich mit der FE-HMM durchgeführt wird, stammt erneut federführend von Prof. Eidel.

Der Schwerpunkt der Arbeit des Doktoranden an dem Aufschrieb der Veröffentlichung liegt in Kapitel 5 in dem zahlreiche numerische Beispiels präsentiert werden. Die Implementierung der Mikro- und Makrorandwertprobleme in den Matlab-Code lag dabei genauso in den Händen des Doktoranden wie die Durchführung und Auswertung der Berechnungen. Auch die grafische Darstellung der Ergebnisse in Form von Spannungs- und Verzerrungsplots sowie der Diagramme zur Konvergenz der Diskretisierungsfehler lag in der Hand des Doktoranden, genauso wie die Diskussion der Ergebnisse.

Die abschließende Zusammenfassung der wesentlichen Ergebnisse in Kapitel 6 erfolgte schließlich durch beide Autoren gemeinsam.

Available online at www.sciencedirect.com
ScienceDirect
Comput. Methods Appl. Mech. Engrg. 329 (2018) 332–368
Computer methods in applied mechanics and engineering
www.elsevier.com/locate/cma

The heterogeneous multiscale finite element method for the homogenization of linear elastic solids and a comparison with the FE^2 method

Bernhard Eidel*, Andreas Fischer

Heisenberg-Group, Institute of Mechanics, Department Mechanical Engineering, University Siegen, 57068 Siegen, Paul-Bonatz-Str. 9-11, Germany

Received 27 January 2017; received in revised form 27 August 2017; accepted 3 October 2017
Available online 19 October 2017

Highlights

- Aspects of FE-HMM implementation for the vector-valued field problem of linear elasticity.
- Explanation of FE-HMM by direct links to asymptotic homogenization.
- Unified conceptual and numerical comparison of FE-HMM with FE^2.
- Assessment and verification of a priori error estimates and of superconvergence.
- Assessment of optimal uniform micro-/macromesh refinement strategies.

Abstract

The Heterogeneous Multiscale Finite Element Method (FE-HMM) is a two-scale FEM based on asymptotic homogenization for solving multiscale partial differential equations. It was introduced in [W. E, B. Engquist, Commun. Math. Sci. 1 (2003) 87–132]. The objective of the present work is an FE-HMM formulation for the homogenization of linear elastic solids in a geometrical linear frame, and doing so, of a vector-valued field problem. A key ingredient of FE-HMM is that macrostiffness is estimated by stiffness sampling on heterogeneous microdomains in terms of a modified quadrature formula, which implies an equivalence of energy densities of the microscale with the macroscale. Beyond this coincidence with the Hill–Mandel condition, which is the cornerstone of the FE^2 method, we elaborate a conceptual comparison with the latter method. After developing an algorithmic framework we (i) assess the existing a priori convergence estimates for the micro- and macro-errors in various norms, (ii) verify optimal strategies in uniform micro–macromesh refinements based on the estimates, (iii) analyze superconvergence properties of FE-HMM, and (iv) compare FE-HMM with FE^2 by numerical results.
© 2017 Elsevier B.V. All rights reserved.

Keywords: Heterogeneous multiscale method; Finite element method; Homogenization; Macro-to-micro modeling; Estimates; Superconvergence

* Corresponding author.
E-mail address: bernhard.eidel@uni-siegen.de (B. Eidel).

https://doi.org/10.1016/j.cma.2017.10.001
0045-7825/© 2017 Elsevier B.V. All rights reserved.

1. Introduction

Almost all matter is heterogeneous in its structural composition and so are the mechanical properties of solids heterogeneous. As a consequence, deformation and failure of solids and structures at large can be critically influenced by the heterogeneity at small scales, typically referred to as microscales. Homogenization theories provide a framework for the macroscopic modeling of microheterogeneous matter via averaging. Spatial homogenization problems are typically described by partial differential equations (PDEs). For their solution on arbitrary domains and for complex boundary conditions numerical methods must be used. Which among many numerical homogenization methods is best suited for particular problems is still a controversial issue and therefore a most active field of research. Little discussion is about the existing benefits and future promises of numerical homogenization; first, homogenization can reduce the computational costs or can give at all access to problems, which are prohibitive in full microresolution. Second, averaging out small-scale fluctuations of a homogenized solid can provide a better understanding of processes at large. Third, and complementary to the second aspect, the explicit sampling of properties and analysis of processes on representative microdomains allow for predictions on critical phenomena like the initiation of failure of structures at large. Hence, in two-scale numerical schemes you can achieve the one, the description of processes at macroscopic scales without abandoning the other, the added value of small-scale processes, and finally, analyze their interactions.

The Heterogeneous Multiscale Finite Element Method, FE-HMM, is a numerical homogenization method for problems described by PDEs with fast oscillations in the components of the stiffness tensor, the conductivity tensor, or alike. Mathematical homogenization based on asymptotic expansion provides a sound theoretical basis for FE-HMM. It is guiding to a considerable extent the particular formulation of the numerical method in order to preserve theoretical characteristics.

The physical problems treated so far in FE-HMM for spatial[1] two-scale problems are diffusion on rough surfaces, [4], stationary and instationary heat conduction, [5], Darcy-flow, [6], and transport problems, [7]. In conclusion, existing FE-HMM implementations and simulations so far have been restricted to scalar-valued field problems.

The progress of FE-HMM and the underlying Heterogeneous Multiscale Method (HMM) since the seminal papers of E, Engquist and coworkers, [1,8], is described in the overview papers [3] and [9]. The focus in [6] is the fully discrete analysis of multiscale PDEs covering elliptic, parabolic and advection diffusion problems. For elliptic problems, a comparison of the FE-HMM with the multiscale finite element method (MsFEM) as introduced in [10,11] is presented in [12].

Abdulle presents in [13] the mathematical analysis of FE-HMM for the elliptic case of linear elasticity. The focus is on the fully discrete convergence analysis taking into account the discretization errors at both micro and macrolevels. Simulation results are not considered in that reference. Abdulle [13] points out, that no convergence estimates of the overall numerical process taking into account the microscopic and the macroscopic discretization parameters have been given for micro–macro methods, even not for the linear case. Many of the cited micro–macro methods can be classified as FE^2 methods, which are equally two-level finite element methods for numerical homogenization. The FE^2 method has its origins in solid mechanics, [14–20], and has found considerable interest in academia and industry; as a versatile method FE^2 has been used in non-linear problems of elasticity and inelasticity. For recent, comprehensive overviews of the FE^2 method we refer to [21,22] and [23]. In order to account for size-dependency observed in materials science, Kouznetsova et al. [24,25] have introduced a second-order homogenization into FE^2. Beyond solid mechanics, FE^2 has continuously reached out for various physical branches including multifield problems with a coupling of mechanics with thermo-/electro-/magneto-fields, [26–29] to name but a few.

The theoretical cornerstone of the FE^2 method is the macro homogeneity condition or Hill–Mandel condition, [30,31]. This condition postulates the equality of macroscopic stress power with corresponding stress power on the microscale. Similarly, FE-HMM is a methodology based on a two-scale energy equivalence since its very first, most general conception in the HMM framework [1]. Remarkably, the two methods have not yet been compared in more detail, and to the best of our knowledge, convergence properties for FE^2 covering both the microscale and the macroscale error have neither been derived nor have been measured in numerical tests. This is remarkable, since already one decade has past since the work of Abdulle [13] in which the author points out this gap.

[1] The most general Heterogeneous Multiscale Method (HMM) introduced in [1] also covers problems living on multiple time scales, see [2,3].

In view of the addressed issues and open gaps, the present work has the following main aims:

(i) We derive an FE-HMM formulation for linear elasticity in a geometrical linear frame and address aspects of its implementation. We point to the method's roots in asymptotic homogenization, which are summarized in the Appendix for ready reference. Next, we continue with the FE-HMM characteristics of nonstandard numerical quadrature on the macroscale, which then leads to a detailed algorithmic framework. Therein, the novel aspect is the FE-HMM implementation for a vector-valued field problem putting the method into the context of solid mechanics. The setting of linear elasticity considerably eases a thorough comparison with related methods like FE^2, see point (ii) below. In its extension to the vector-valued case of field problems for elliptic PDEs the present work stands on the shoulders of the FE-HMM framework for scalar-valued cases proposed in [4] and [5,32]. Moreover, the present work considerably takes profit from Abdulle's analysis in [13] and aims to complement that reference.

(ii) We elaborate a conceptual, algorithmic and numerical comparison of FE-HMM with the FE^2 method. The comparison will comprise conceptual aspects like the link of the underlying mathematical theory of asymptotic homogenization in FE-HMM with the physical postulate of energy density equivalence in FE^2. It covers the macro–micro kinematical coupling concept and, vice-versa, the micro-to-macro data transfer in terms of stiffness and stress.

(iii) We assess the existing a priori error estimates in various norms (L^2-, H^1-, energy-norm) and for the coefficients of the homogenized elasticity tensor. We anticipate that the error analysis including a priori estimates are – for our understanding – the strongest result and most valuable contribution of FE-HMM to the field of numerical homogenization, and the weakest spot of FE^2 to go without them. While the existence of error estimates in FE-HMM is remarkable, the content of the estimates is even more exciting, since they seem at a first glance to be at odds with familiar estimates from standard finite element methods. Here, we will analyze the inherent property of FE-HMM to exhibit superconvergence properties for the micro-FEM part in that the error in the L^2-norm and in the H^1-norm exhibit the same convergence order. Superconvergence in standard finite element methods, – if present at all – refers to the non-standard property of stress and strain to converge pointwise in the same order as displacements as the primary variables. Superconvergence in standard FEM according to Barlow [33] requires several premises in that it is restricted to particular element shapes and, additionally, is restricted to particular element sites. For the microscale FEM part of FE-HMM in contrast, superconvergence does not require any premises. An additional benefit of error estimates in FE-HMM is that they allow for optimal uniform macro-/micromesh-refinement strategies—how to refine the micromesh for uniform macromesh refinement, if the full convergence order shall be achieved but for minimal computational costs?

2. The heterogeneous multiscale finite element method

2.1. Model problem of linear elasticity

We consider a body $\mathcal{B}$, a bounded subset of $\mathbb{R}^d$, $d = 2, 3$, with boundary $\partial\mathcal{B} = \partial\mathcal{B}_D \cup \partial\mathcal{B}_N$ where the Dirichlet boundary $\partial\mathcal{B}_D$ and the Neumann boundary $\partial\mathcal{B}_N$ are disjoint sets. The closure of the body $\mathcal{B}$ is denoted by $\overline{\mathcal{B}}$. The body, which exhibits an inhomogeneous microstructure, is subject to body forces $\boldsymbol{f}$ and surface tractions $\bar{\boldsymbol{t}}$ and in static equilibrium.

2.1.1. The microproblem

The displacement $\boldsymbol{u}^\epsilon = (u_1^\epsilon, \dots, u_d^\epsilon)$ of the body is given by the solution of the system

$$\left.\begin{aligned} -\frac{\partial}{\partial x_j}\left(\mathbb{A}^\epsilon_{ijlm}\frac{\partial u_l^\epsilon}{\partial x_m}\right) &= f_i \quad \text{in} \quad \mathcal{B} \\ u_i^\epsilon &= \bar{u}_i \quad \text{on} \quad \partial\mathcal{B}_D \\ \left(\mathbb{A}^\epsilon_{ijlm}\frac{\partial u_l^\epsilon}{\partial x_m}\right) n_j &= \bar{t}_i \quad \text{on} \quad \partial\mathcal{B}_N \end{aligned}\right\}. \tag{1}$$

The constitutive law is assumed to be linear elastic where $\mathbb{A}^\epsilon_{ijlm}$ is the fourth order elasticity tensor. Superscript ϵ throughout indicates the dependency of suchlike marked quantities on the heterogeneity of the elastic material. Note that the body forces $\boldsymbol{f}$ and the traction vectors $\bar{\boldsymbol{t}}$ are assumed not to depend on ϵ. In $(1)_3$, $\boldsymbol{n} = (n_1, \dots, n_d)$ is the unit outward normal to $\partial\mathcal{B}$.

For $\mathbb{A}^\epsilon_{ijlm}$ the following symmetries hold $\mathbb{A}^\epsilon_{ijlm} = \mathbb{A}^\epsilon_{jilm} = \mathbb{A}^\epsilon_{lmij}$ for any $i, j, l, m = 1, \dots, d$. For the deformation kinematics geometrical linearity is assumed to hold with the linearized strain tensor $\boldsymbol{\varepsilon}$

$$\varepsilon_{ij}(\boldsymbol{u}^\epsilon) = \frac{1}{2}\left(\frac{\partial u^\epsilon_i}{\partial x_j} + \frac{\partial u^\epsilon_j}{\partial x_i}\right). \tag{2}$$

It can be written in compact format by means of the linear differential operator $\boldsymbol{L}$

$$\boldsymbol{\varepsilon}(\boldsymbol{u}^\epsilon) = \boldsymbol{L}\,\boldsymbol{u}^\epsilon. \tag{3}$$

For a finite element formulation the strong form (1) is transformed into a variational or weak form. Multiplying the strong form by a test function $\boldsymbol{v} \in \mathcal{V}$, using the Green formula yields the following variational formulation:

Find $\boldsymbol{u}^\epsilon$ such that

$$\underbrace{\int_{\mathcal{B}} \mathbb{A}^\epsilon(\boldsymbol{x})\,\boldsymbol{\varepsilon}(\boldsymbol{u}^\epsilon) : \boldsymbol{\varepsilon}(\boldsymbol{v})\,dV}_{\stackrel{\text{def}}{=} B_\epsilon(\boldsymbol{u}^\epsilon, \boldsymbol{v})} = \underbrace{\int_{\mathcal{B}} \boldsymbol{f}\cdot\boldsymbol{v}\,dV + \int_{\partial\mathcal{B}_N} \bar{\boldsymbol{t}}\cdot\boldsymbol{v}\,dA}_{\stackrel{\text{def}}{=} F(\boldsymbol{v})} \tag{4}$$

which has to hold for all $\boldsymbol{v} \in \mathcal{V}$, where $\mathcal{V}$ is the space of admissible displacements, i.e. virtual displacements that fulfill homogeneous Dirichlet boundary conditions

$$\mathcal{V} = \{\boldsymbol{v};\, \boldsymbol{v} \in H^1(\mathcal{B})^d,\, \boldsymbol{v}|_{\partial\mathcal{B}_D} = \boldsymbol{0}\}. \tag{5}$$

The existence and uniqueness of the solution of problem (4) can be shown by use of the first Korn inequality and the Lax–Milgram theorem, [34,35].

The direct numerical solution of (4) by a standard finite element formulation is prohibitive for small ϵ, since a proper account of the microheterogeneity of characteristic length ϵ requires an even finer finite element resolution with typical element size h, hence $h \ll \epsilon$. This is the main reason for numerical homogenization based on sampling in small regions of confined size instead of an accurate account of microstructure's heterogeneity everywhere.

The theoretical basis of FE-HMM is mathematical homogenization by asymptotic expansion, [36–39]. To put things into perspective and for ready reference we provide the main results of asymptotic homogenization for linearized elasticity in Appendix A.1. These contents are used at various places in the present paper to explain, how FE-HMM is constructed along the lines of asymptotic homogenization.

2.1.2. The macroproblem

The strong form of the macroscopic/homogenized boundary value problem (BVP) reads

$$\left.\begin{aligned} -\frac{\partial}{\partial x_j}\left(\mathbb{A}^0_{ijlm}\frac{\partial u^0_l}{\partial x_m}\right) &= \langle f_i\rangle && \text{in} \quad \mathcal{B} \\ u^0_i &= \langle \bar{u}_i\rangle_\Gamma && \text{on} \quad \partial\mathcal{B}_D \\ \left(\mathbb{A}^0_{ijlm}\frac{\partial u^0_l}{\partial x_m}\right) n_j &= \langle \bar{t}_i\rangle_\Gamma && \text{on} \quad \partial\mathcal{B}_N \end{aligned}\right\} \tag{6}$$

for a derivation see Appendix A.1. The macroscopic displacement is denoted by u^0_i and $\mathbb{A}^0$ is the homogenized elasticity tensor. The term in brackets in $(6)_{1,3}$ is the macroscopic stress obtained by a volume average over the microdomain, hence it equals $\langle\boldsymbol{\sigma}^0\rangle$, see Appendix A.1.

The values for the Dirichlet as well as Neumann boundary conditions in $(6)_{2,3}$ are obtained by surface averages according to (A.32) of corresponding boundary conditions in $(1)_{2,3}$. Similarly, $\langle f_i\rangle$ is the volume average of body forces in $(1)_1$.

The solution of the homogenized problem is obtained from the variational form

$$B_0(\boldsymbol{u}^0, \boldsymbol{v}) = \int_{\mathcal{B}} \mathbb{A}^0\,\boldsymbol{\varepsilon}(\boldsymbol{u}^0) : \boldsymbol{\varepsilon}(\boldsymbol{v})\,dV = \int_{\mathcal{B}} \boldsymbol{f}\cdot\boldsymbol{v}\,dV + \int_{\partial\mathcal{B}_N} \bar{\boldsymbol{t}}\cdot\boldsymbol{v}\,dA \qquad \forall\,\boldsymbol{v} \in \mathcal{V}, \tag{7}$$

which follows from multiplying the strong form (6) by test functions $\boldsymbol{v}$ along with the application of Green's formula. For notational convenience we skip in (7) and in the rest of the paper the averaging symbols $\langle\bullet\rangle$, $\langle\bullet\rangle_\Gamma$ for $\boldsymbol{f}$, $\bar{\boldsymbol{u}}$ and $\bar{\boldsymbol{t}}$ but keep in mind that these quantities follow from volume and surface averages, respectively.

There is an alternative route to derive (7); the asymptotic stress expansion (A.5) is plugged into he variational form (4). The resultant weak form expressions are arranged according to their orders $\mathcal{O}(\epsilon^n)$, $n = 1, -1, -2$. Each of them is multiplied by ϵ^n with corresponding n along with the limit of $\epsilon \to 0^+$. Doing so the above macroscale variational form can be identified. Hence, it is the same process as carried out for the identification of the macroscopic balance of linear momentum in Appendix A.1.

Next we consider the piecewise linear continuous FEM in macro- and microspace, respectively. The domain $\mathcal{B}$ is a convex polygonal domain in order to avoid regularity issues.

We define a macro finite element space as

$$\mathcal{S}^p_{\partial\mathcal{B}_D}(\mathcal{B}, \mathcal{T}_H) = \left\{ \boldsymbol{u}^H \in H^1(\mathcal{B})^d ; \boldsymbol{u}^H|_{\partial\mathcal{B}_D} = \bar{\boldsymbol{u}} ; \boldsymbol{u}^H|_K \in \mathcal{P}^p(K)^d, \ \forall\, K \in \mathcal{T}_H \right\}, \tag{8}$$

where $\mathcal{P}^p$ is the space of (in the present work: linear, $p = 1$) polynomials on the element K, $\mathcal{T}_H$ the (quasi-uniform) triangulation of $\mathcal{B} \subset \mathbb{R}^d$. Index/superscript H denotes the characteristic element size, with $H \gg \epsilon$ for efficiency. The space $\mathcal{S}^p_{\partial\mathcal{B}_D}$ is a subspace of $\mathcal{V}$ defined in (5).

For the solution of (1) in the macrodomain we use the two-scale FEM framework of the FE-HMM as originally proposed in [1] and analyzed for elliptic PDEs in [40], and, with the focus on linear elasticity, in [13].

The macrosolution of the FE-HMM is given by the following variational form:

Find $\boldsymbol{u}^H \in \mathcal{S}_{\mathcal{B}_D}(\mathcal{B}, \mathcal{T}_H)$ such that

$$B_H(\boldsymbol{u}^H, \boldsymbol{v}^H) = \int_{\mathcal{B}} \boldsymbol{f} \cdot \boldsymbol{v}^H \, dV + \int_{\partial\mathcal{B}_N} \bar{\boldsymbol{t}} \cdot \boldsymbol{v}^H \, dA \qquad \forall \boldsymbol{v}^H \in \mathcal{S}_{\partial\mathcal{B}_D}(\mathcal{B}, \mathcal{T}_H), \tag{9}$$

which reads as a standard finite element formulation.

2.2. The modified macro bilinear form of FE-HMM

If the homogenized constitutive tensor $\mathbb{A}^0(\boldsymbol{x})$ is explicitly known, the bilinear form $B_H(\boldsymbol{u}^H, \boldsymbol{v}^H)$ can be calculated using standard numerical quadrature according to (10), where $\boldsymbol{x}_{K_l}$ and ω_{K_l} are the quadrature points and quadrature weights, respectively

$$B_H(\boldsymbol{u}^H, \boldsymbol{v}^H) = \sum_{K \in \mathcal{T}_H} \sum_{l=1}^{N_{qp}} \omega_{K_l} \cdot \left[\mathbb{A}^0(\boldsymbol{x}_{K_l}) \, \boldsymbol{\varepsilon}(\boldsymbol{u}^H(\boldsymbol{x}_{K_l})) : \boldsymbol{\varepsilon}(\boldsymbol{v}^H(\boldsymbol{x}_{K_l})) \right] \tag{10}$$

$$\approx \sum_{K \in \mathcal{T}_H} \sum_{l=1}^{N_{qp}} \omega_{K_l} \cdot \left[\frac{1}{|K_\delta|} \int_{K_\delta} \mathbb{A}^\epsilon(\boldsymbol{x}) \, \boldsymbol{\varepsilon}(\boldsymbol{u}^h_{K_\delta}) : \boldsymbol{\varepsilon}(\boldsymbol{v}^h_{K_\delta}) \, dV \right]. \tag{11}$$

Since $\mathbb{A}^0(\boldsymbol{x})$ is typically not known for heterogeneous materials, the ansatz of FE-HMM is to approximate the virtual work expression at point $\boldsymbol{x}_{K_l}$ in the semidiscrete form (10) by another bilinear form using the known microheterogeneous elasticity tensor $\mathbb{A}^\epsilon$, see (11). According to this approximation, the solution $\boldsymbol{u}^h_{K_\delta}$ is obtained on microsampling domains $K_\delta = \boldsymbol{x}_{K_l} + \delta\,[-1/2, +1/2]^d$, $\delta \geq \epsilon$, which are each centered at the quadrature points $\boldsymbol{x}_{K_l}$ of K, $l = 1, \ldots, N_{qp}$. For a visualization see Fig. 1. These microsampling domains with volume $|K_\delta|$ provide the additive contribution to the stiffness matrix of the macro finite element.

Remark 1. From a physical point of view, the approximation of (10) by (11) indicates that the FE-HMM is a numerical homogenization scheme that is based on the equality of the macroenergy density with the microenergy density.

From a mathematical point of view, the replacement of the pointwise integrand value by another bilinear form indicates that FE-HMM is a modified numerical quadrature formula. Since it is this setting that enables the fully discrete a priori error analysis, it is a key FE-HMM ingredient. The inserted product of test functions leads to a priori estimates of the convergence order of the micro error, which seem to be at odds with familiar results for FEM; for details see Section 3 along with its references to original work.

On Notation The microdomains attached to the macro quadrature points l in the macroelement K are distinguishable by index l. In order to avoid too heavy notation we will use K_δ instead of K_{δ_l} in the rest of the paper.

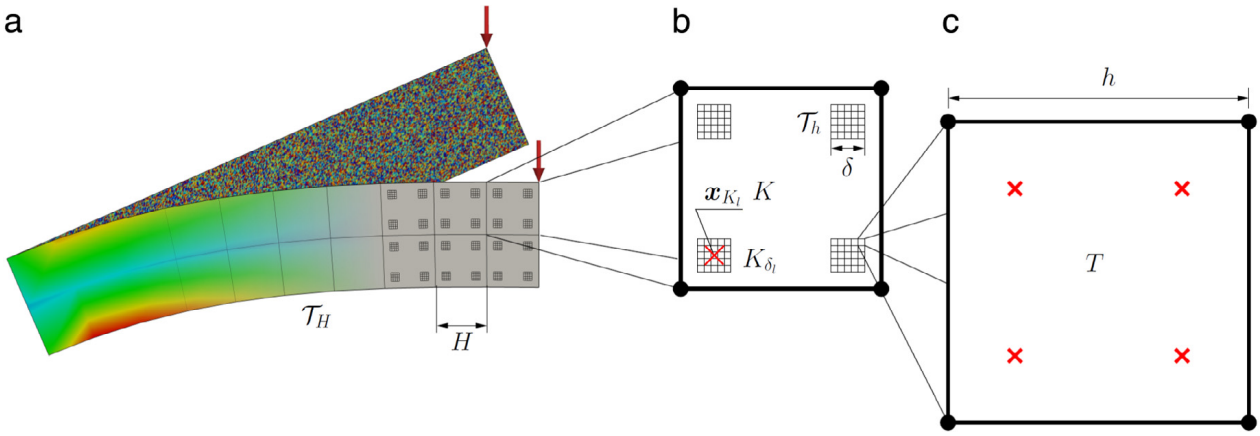


Fig. 1. Two-scale finite element method: (a) Macroscopic BVP with macrodiscretization, (b) one macro finite element with microdomains centered at the quadrature points, (c) micro finite element with standard quadrature points.

2.3. *Variational formulation of the microproblem*

It can be shown that the FE-HMM microproblem resembles the discrete version of the cell problem of asymptotic expansion, if it is formulated for each microdomain K_δ in K with $l = 1, \ldots, N_{qp}$, $K \in \mathcal{T}_H$ like this:
Find $\boldsymbol{u}^h_{K_\delta}$ such that the conditions for macro–micro coupling and for the micro bilinear form (12) are fulfilled:

$$\left.\begin{aligned} \left(\boldsymbol{u}^h_{K_\delta} - \boldsymbol{u}^H_{lin,K_\delta}\right) &\in \mathcal{S}^q(K_\delta, \mathcal{T}_h) \\ B_{K_\delta}(\boldsymbol{u}^h_{K_\delta}, \boldsymbol{w}^h_{K_\delta}) &:= \int_{K_\delta} \mathbb{A}^\epsilon(\boldsymbol{x})\, \boldsymbol{\varepsilon}(\boldsymbol{u}^h_{K_\delta}) : \boldsymbol{\varepsilon}(\boldsymbol{w}^h_{K_\delta})\, dV = 0 \\ &\forall\, \boldsymbol{w}^h_{K_\delta} \in \mathcal{S}^q(K_\delta, \mathcal{T}_h)\,, \end{aligned}\right\} \tag{12}$$

where the micro finite element space $\mathcal{S}^q(K_\delta, \mathcal{T}_h)$ is defined by

$$\mathcal{S}^q(K_\delta, \mathcal{T}_h) = \{\boldsymbol{w}^h \in \mathcal{W}(K_\delta);\, \boldsymbol{w}^h \in (\mathcal{P}^q(T))^d,\ T \in \mathcal{T}_h\}\,. \tag{13}$$

In (13) $\mathcal{T}_h$ is a quasi-uniform discretization of the sampling domain K_δ with mesh size $h \ll \varepsilon$ resolving the finescale, $\mathcal{W}(K_\delta)$ denotes the coupling condition or boundary conditions used for computing the microfunctions, and $\mathcal{P}^q$ is the space of polynomials on the element T. In the present work we restrict to linear shape functions, hence $q = 1$ and consider periodic boundary conditions (PBCs), see (A.27).

The linearization of $\boldsymbol{u}^H$ in $(12)_1$ is carried out at the quadrature point $\boldsymbol{x}_{K_l}$

$$\boldsymbol{u}^H_{lin,K_\delta} = \boldsymbol{u}^H(\boldsymbol{x}_{K_l}) + (\boldsymbol{x} - \boldsymbol{x}_{K_l}) \cdot \nabla \boldsymbol{u}^H(\boldsymbol{x}_{K_l})\,. \tag{14}$$

Remark 2. Note that (12) resembles for PBC the discrete version of the cell problem of asymptotic homogenization, (A.26), if $\boldsymbol{u}^h_{K_\delta} - \boldsymbol{u}^H_{lin,K_\delta} = \boldsymbol{\chi}^h_{K_\delta}$ and if $\boldsymbol{u}^H$ follows the linearization of (14). Then, replacing $\boldsymbol{u}^h_{K_\delta}$, $(12)_2$ reads as

$$\int_{K_\delta} \mathbb{A}^\epsilon(\boldsymbol{x})\, \boldsymbol{\varepsilon}(\boldsymbol{\chi}^h_{K_\delta} + \boldsymbol{u}^H_{lin,K_\delta}) : \boldsymbol{\varepsilon}(\boldsymbol{w}^h_{K_\delta})\, dV = 0 \qquad \forall\, \boldsymbol{w}^h_{K_\delta} \in \mathcal{S}^q(K_\delta, \mathcal{T}_h)\,. \tag{15}$$

The linearized $\boldsymbol{u}^H_{K_\delta}$ is the FE-HMM counterpart of the quantity $\boldsymbol{I}^{lm}$ in asymptotic homogenization; they both induce a homogeneous deformation in the microdomain/unit cell and (15) coincides with (A.26). Furthermore, we hint already here at the coincidence of FE-HMM with the FE^2 method with respect to the above superposition of a homogeneous deformation with periodic fluctuations, which is frequently referred to as strain-driven, first order computational homogenization.

2.4. Bases for spaces

For the solution of (12) a basis $\{N_I^H\}_{I=1}^{M_{mac}}$ for the macro finite element space $\mathcal{S}_0^1(\mathcal{B}, \mathcal{T}_H)$ is employed in order to represent the macrosolution $\boldsymbol{u}^H$ of (9). Similarly, a basis $\{N_i^h\}_{i=1}^{M_{mic}}$ of the micro finite element space $\mathcal{S}_0^1(K_\delta, \mathcal{T}_h)$, (13), is introduced in order to represent the solution $\boldsymbol{u}^h$ of a microproblem. In (16), M_{mac} denotes the number of nodes of the macrodomain, and M_{mic} in (17) denotes the number of nodes of each microdomain. Hence, the macro- and the microsolution follow the representation

$$\boldsymbol{u}^H = \sum_{I=1}^{M_{mac}} N_I^H \, \boldsymbol{d}_I^H \,, \qquad \boldsymbol{d}_I^H = \{d_{I,x_1}^H, d_{I,x_2}^H, d_{I,x_3}^H\}^T \,, \tag{16}$$

$$\boldsymbol{u}^h = \sum_{i=1}^{M_{mic}} N_i^h \, \boldsymbol{d}_i^h \,, \qquad \boldsymbol{d}_i^h = \{d_{i,x_1}^h, d_{i,x_2}^h, d_{i,x_3}^h\}^T \,, \tag{17}$$

where $\boldsymbol{d}_I^H$ is the displacement vector of macronode I, and $\boldsymbol{d}_i^h$ is the displacement vector for micronode i.

The node-based shape functions $\{N_{I/i}^{H/h}\}$ exhibit the standard properties (i) partition of unity: $\sum_{j\in\mathcal{N}} N_j(\boldsymbol{X}_i) \equiv 1 \quad \forall \boldsymbol{X}_i \in \mathcal{B}/K_l$ and (ii) compact support $N_j(\boldsymbol{X}_{j'}) = \delta_{jj'} \quad \forall\, j, j' \in \mathcal{N}$, where $\mathcal{N}$ is the set of finite element nodes.

2.5. Macrostiffness calculation

According to (11), FE-HMM can be seen as a bottom-up multiscale method in that the required information for estimating stiffness on the macrolevel is obtained from microsampling domains $K_\delta, l = 1, \ldots, N_{qp}$.

The macro bilinear form $B_H^e(\boldsymbol{u}^H, \boldsymbol{v}^H)$ is the virtual work of internal forces in a macro finite element e. The corresponding bilinear form in terms of the shape functions $B_H^e(\boldsymbol{N}_I^H, \boldsymbol{N}_J^H)$ extracts the stiffness matrix contribution $\boldsymbol{k}_{IJ}^{e,mac}$ for macronodes I, J, a $d \times d$ matrix. Consequently, we replace in (10) the displacements $\boldsymbol{u}^H, \boldsymbol{v}^H$ by macro shape function matrices $\boldsymbol{N}_I^H, \boldsymbol{N}_J^H$ and obtain[2]

$$\boldsymbol{k}_{IJ}^{e,mac} = B_H^e(\boldsymbol{N}_I^H, \boldsymbol{N}_J^H) = \sum_{l=1}^{N_{qp}} \frac{\omega_{K_l}}{|K_\delta|} \int_{K_\delta} (\boldsymbol{L}\boldsymbol{u}_{K_\delta}^{h(I)})^T \, \mathbb{A}^\epsilon(\boldsymbol{x}) \, \boldsymbol{L}\boldsymbol{u}_{K_\delta}^{h(J)} \, dV \,. \tag{18}$$

In (18) $\boldsymbol{u}_{K_\delta}^{h(I)}$ is the counterpart of $\boldsymbol{u}_{K_\delta}^h$ in (12). It is the dimensionless solution of the microproblem on K_δ, which is driven by the shape function N_I^H at macronode I. In the following, we add $x_i, i = 1, \ldots, d$ to account for the vector-valued field problem of dimension d. Consequently, $\boldsymbol{u}_{K_\delta}^{h(I,x_i)}$ is the microsolution driven by a macroelement unit-displacement state $\boldsymbol{u}_{lin,K_\delta}^{H(I,x_i)}$ at node I in x_i-direction.

For stiffness calculation, problem (12) is to be reformulated as follows: Find $\boldsymbol{u}_{K_\delta}^{h(I,x_i)}$ on each K_δ such that the conditions for the kinematical coupling and for the micro bilinear form are fulfilled

$$\left.\begin{aligned} \left(\boldsymbol{u}_{K_\delta}^{h(I,x_i)} - \boldsymbol{u}_{lin,K_\delta}^{H(I,x_i)}\right) &\in \mathcal{S}^q(K_\delta, \mathcal{T}_h) \\ B_{K_\delta}(\boldsymbol{u}_{K_\delta}^{h(I,x_i)}, \boldsymbol{w}_{K_\delta}^{h(I,x_i)}) &:= \int_{K_\delta} (\boldsymbol{L}\boldsymbol{u}_{K_\delta}^{h(I,x_i)})^T \, \mathbb{A}^\epsilon(\boldsymbol{x}) \, \boldsymbol{L}\boldsymbol{w}_{K_\delta}^{h(I,x_i)} dV = 0 \\ &\forall \boldsymbol{w}_{K_\delta}^{h(I,x_i)} \in \mathcal{S}_{per}^q(K_\delta, \mathcal{T}_h) \end{aligned}\right\} . \tag{19}$$

In order to realize the coupling of the macrodisplacement field $\boldsymbol{u}_{lin,K_\delta}^{H(I,x_i)}$ with the yet unknown microdisplacement field $\boldsymbol{u}_{K_\delta}^{h(I,x_i)}$, the two fields are expanded into the same basis $\{N_i^h\}_{i=1}^{M_{mic}}$ of $\mathcal{S}^1(K_\delta, \mathcal{T}_h)$,

$$\boldsymbol{u}_{lin,K_\delta}^{H(I,x_i)} = \sum_{m=1}^{M_{mic}} N_{m,K_\delta}^h \boldsymbol{d}_m^{H(I,x_i)} \,, \quad \boldsymbol{d}_m^{H(I,x_i)} = \left(d_{m,x_1}^{H(I,x_i)}, d_{m,x_2}^{H(I,x_i)}, d_{m,x_3}^{H(I,x_i)}\right)^T \,, \tag{20}$$

$$\boldsymbol{u}_{K_\delta}^{h(I,x_i)} = \sum_{m=1}^{M_{mic}} N_{m,K_\delta}^h \boldsymbol{d}_m^{h(I,x_i)} \,, \quad \boldsymbol{d}_m^{h(I,x_i)} = \left(d_{m,x_1}^{h(I,x_i)}, d_{m,x_2}^{h(I,x_i)}, d_{m,x_3}^{h(I,x_i)}\right)^T \,. \tag{21}$$

[2] Note that matrix $\boldsymbol{N}_I^H$ is a $d \times d$ diagonal matrix with elements N_I^H; hence for $d = 3$ it holds $\boldsymbol{N}_I^H = \mathrm{diag}(N_I^H, N_I^H, N_I^H)$. Similarly, matrix $\boldsymbol{u}^{h(I)}$ in (18) is a $d \times d$ diagonal matrix $\mathrm{diag}(u_x, u_y, u_z)$.

The solution of the microproblems for the minimizers $\boldsymbol{d}^{h(I,x_i)}$ is presented in Section 2.6. We continue with the calculation of the macroelement stiffness matrix in (18) and obtain

$$\begin{aligned}\boldsymbol{k}_{IJ}^{e,mac} &= B_H^e\left[\boldsymbol{N}_I^H, \boldsymbol{N}_J^H\right]\\ &= \sum_{l=1}^{N_{qp}} \frac{\omega_{K_l}}{|K_\delta|}\left(\boldsymbol{d}^{h(I,x_i)}\right)^T \sum_{T\in\mathcal{T}_h}\left(\sum_{m=1}^{n_{node}}\sum_{n=1}^{n_{node}} \int_T \boldsymbol{B}_m^{e,T}\,\mathbb{A}^\epsilon\,\boldsymbol{B}_n^e\,dV\boldsymbol{d}_n^{h(J,x_i)}\right)\\ &= \sum_{l=1}^{N_{qp}} \frac{\omega_{K_l}}{|K_\delta|}\left(\boldsymbol{d}^{h(I)}\right)^T \boldsymbol{K}_{K_\delta}^{mic}\,\boldsymbol{d}^{h(J)}\,,\end{aligned} \tag{22}$$

where $\boldsymbol{d}^{h(I)} = \left(\boldsymbol{d}^{h(I,x_1)}|\boldsymbol{d}^{h(I,x_2)}|\boldsymbol{d}^{h(I,x_3)}\right)$ for $d = 3$. The assembly of $\boldsymbol{k}_{IJ}^{e,mac}$ yielding $\boldsymbol{k}^{e,mac}$ implies the arrangement of $\boldsymbol{d}^{h(I)}$ in different columns for $I = 1,\ldots,N_{node}$, which yields the transformation matrix $\boldsymbol{T}_{K_\delta}$. Doing so we obtain

$$\boldsymbol{k}_K^{e,mac} = \sum_{l=1}^{N_{qp}} \frac{\omega_{K_l}}{|K_\delta|}\,\boldsymbol{T}_{K_\delta}^T\,\boldsymbol{K}_{K_\delta}^{mic}\,\boldsymbol{T}_{K_\delta} \tag{23}$$

$$\text{with}\quad \boldsymbol{T}_{K_\delta} = \left[\left[\left[\boldsymbol{d}^{h(I,x_i)}\right]_{i=1,\ldots,d}\right]_{I=1,\ldots,N_{node}}\right]. \tag{24}$$

Eqs. (23) and (24) give insight into important characteristics of $\boldsymbol{T}_{K_l}$. First, the matrix dimensions

$$\begin{aligned}\boldsymbol{k}_K^{e,mac} &\in \mathbb{R}^{(N_{node}\cdot d)\times(N_{node}\cdot d)}\\ \boldsymbol{T}_{K_\delta} &\in \mathbb{R}^{(M_{mic}\cdot d)\times(N_{node}\cdot d)}\\ \boldsymbol{K}_{K_\delta}^{mic} &\in \mathbb{R}^{(M_{mic}\cdot d)\times(M_{mic}\cdot d)}\end{aligned} \tag{25}$$

reveal that $\boldsymbol{T}_{K_\delta}$ "compresses"[3] the total microstiffness matrix $\boldsymbol{K}_{K_\delta}^{mic}$ to the dimensions of the macroelement stiffness matrix $\boldsymbol{k}_K^{e,mac}$. For that reason $\boldsymbol{T}_{K_\delta}$ is a micro–macrostiffness transfer operator along with a model reduction/coarse-graining. Second, the transformation matrix $\boldsymbol{T}_{K_\delta}$ is built up by the column vectors $\boldsymbol{d}^{h(I,x_i)}$, $x_i\,|\,i = 1,\ldots,d$, $I = 1,\ldots,N_{node}$.

The macroelement shape functions each represent a unit displacement state for each macronode I in each direction of space $x_i\,|\,i = 1,\ldots,d$. They drive the microproblem in terms of the corresponding nodal values $\boldsymbol{d}_m^{H(I,x_i)}, m = 1,\ldots,M_{mic}$ via (20) in each microdomain to evaluate the macroelement stiffness $\boldsymbol{k}_{IJ}^{e,mac}$. Each unit displacement state in x_i-direction induces in $\boldsymbol{d}^{H(I,x_i)}$ nonzero components only in x_i, for example $\boldsymbol{d}^{H(I,x_i)}|_{i=2} = \left[0, d_{1,x_2}^{H(I,x_2)}, 0,\ldots,0, d_{M_{mic},x_2}^{H(I,x_2)}, 0\right]^T$.

Fig. 2 (left) visualizes a unit displacement state, the corresponding uniform deformation of microdomains and (right) the microsolution obtained for the additional constraint of PBC.[4]

2.6. Solution of the microproblems

While the element stiffness matrix of a macro finite element is computed by the modified quadrature formula expanding the collocation points to sampling domains, the element stiffness matrix $\boldsymbol{k}_{mn}^{e,mic}$ of a micro finite element is computed by standard Gauss–Legendre quadrature in the ξ-, η-, ζ-parameter space on the unit cube (of side length 2)

$$\boldsymbol{k}_{mn}^{e,mic} \approx \sum_{k=1}^{n_{gp}} \omega_k\,\boldsymbol{B}_m^{e\,T}(\xi_k,\eta_k,\zeta_k)\,\mathbb{A}^\epsilon\,\boldsymbol{B}_n^e(\xi_k,\eta_k,\zeta_k)\;\det\boldsymbol{J}(\xi_k,\eta_k,\zeta_k)\,, \tag{26}$$

where $\boldsymbol{B}_m^e = \boldsymbol{L}\,\boldsymbol{N}_m$ and where $\boldsymbol{J}(\xi_k,\eta_k,\zeta_k)$ is the Jacobian for an isoparametric finite element formulation.

[3] Following the terminology of HMM, $\boldsymbol{T}_{K_\delta}$ can be called a stiffness compression operator, see [1], Sec.2.1.

[4] The problem deals with a stiff inclusion in a softer matrix, analyzed in detail in Section 5.1.

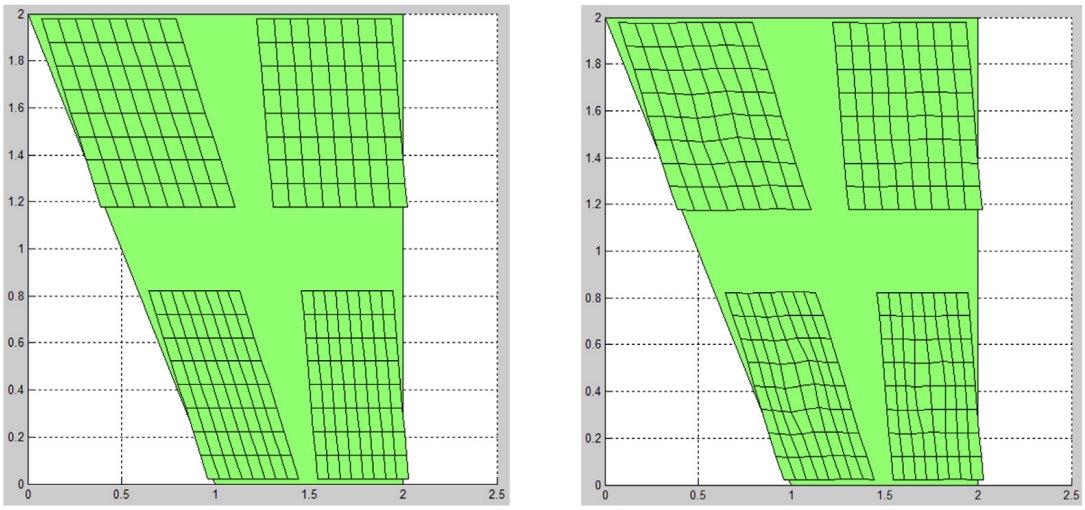


Fig. 2. Macro-to-micro and periodic kinematical coupling: (left) exemplary unit displacement state at a macronode I in an x_i-direction mediated by a macro shape function N_I and the corresponding linearized displacements $u_{lin,K_\delta}^{H(I,x_i)}$ on the microdomains which is a homogeneous deformation state; (right) the microdomains after energy minimization subject to the additional constraint of PBC result in the microsolutions $u_{lin,K_\delta}^{h(I,x_i)}$.

The assembly of the element microstiffness matrices on the sampling domain K_δ yields the total microstiffness matrix

$$\boldsymbol{K}_{K_\delta}^{mic} = \mathop{\mathbf{A}}_{e=1}^{num_{ele}} \boldsymbol{k}_{K_\delta}^{e,mic} \tag{27}$$

required for the solution of a microproblem.

The problem (19) can be rewritten as a minimization problem

$$\int_{K_\delta} (\boldsymbol{L}\boldsymbol{u}_{K_\delta}^{h(I,x_i)})^T \mathbb{A}^\epsilon \boldsymbol{L}\boldsymbol{u}_{K_\delta}^{h(I,x_i)} \, dV \quad \rightarrow \quad \min \tag{28}$$

over all functions $\boldsymbol{u}_{K_\delta}^{h(I,x_i)} \in \mathcal{S}^1(K_\delta, \mathcal{T}_h)$ satisfying $\boldsymbol{u}_{K_\delta}^{h(I,x_i)} - \boldsymbol{u}_{K_\delta}^{H(I,x_i)} \in \mathcal{S}^1_{per}(K_\delta, \mathcal{T}_h)$.

For the solution of the microproblem (28), we choose the method of Lagrange multipliers and thus arrive at a saddlepoint problem, see for example [41]. It is convenient for our purposes to express the strain energy by the microdomain stiffness matrix and the microdisplacement vector.

Doing so, the problem reads: Minimize for each node on a macro finite element $I = 1, \ldots, N_{node}$ and for each direction of space $x_i \,|\, i = 1, \ldots, d$ the functional

$$\mathcal{L}(\boldsymbol{d}^{h(I,x_i)}, \boldsymbol{\lambda}^{(I,x_i)}) = \frac{1}{2}\left(\boldsymbol{d}^{h(I,x_i)}\right)^T \boldsymbol{K}_{K_\delta}^{mic} \boldsymbol{d}^{h(I,x_i)} + \boldsymbol{\lambda}^{(I,x_i)\,T} \boldsymbol{G} \left(\boldsymbol{d}^{h(I,x_i)} - \overline{\boldsymbol{d}}^{H(I,x_i)}\right), \tag{29}$$

where $\boldsymbol{G}$ contains the kinematical coupling conditions and reads for $d = 3$

$$\boldsymbol{G} = \begin{bmatrix} b_1 & 0 & 0 & \ldots\ldots & b_{M_{mic}} & 0 & 0 \\ 0 & b_1 & 0 & \ldots\ldots & 0 & b_{M_{mic}} & 0 \\ 0 & 0 & b_1 & \ldots\ldots & 0 & 0 & b_{M_{mic}} \\ & & & \overline{\boldsymbol{G}} & & & \end{bmatrix}. \tag{30}$$

In $\boldsymbol{G}$, the first d rows contain the normalization condition for the fluctuations, the macro–micro coupling condition, to which the first d Lagrange multipliers are associated; for details see (33)–(36). The submatrix $\overline{\boldsymbol{G}}$ contains the L non-redundant periodic coupling conditions for adjacent nodes at opposite edges/faces in 2d/3d on the microdomain boundary with the associated $L \cdot d$ Lagrange multipliers. The vector of Lagrange multipliers $\boldsymbol{\lambda}^{(I,x_i)} \in \mathbb{R}^{(1+L)\cdot d}$ reads for $d = 3$

$$\boldsymbol{\lambda}^{(I,x_i)} = \{\lambda_{0,x_1}^{(I,x_i)}, \lambda_{0,x_2}^{(I,x_i)}, \lambda_{0,x_3}^{(I,x_i)}, \lambda_{1,x_1}^{(I,x_i)}, \lambda_{1,x_2}^{(I,x_i)}, \lambda_{1,x_3}^{(I,x_i)}, \ldots, \lambda_{L,x_1}^{(I,x_i)}, \lambda_{L,x_2}^{(I,x_i)}, \lambda_{L,x_3}^{(I,x_i)}\}^T. \tag{31}$$

The first variations of $\mathcal{L}$ with respect to its variables give the stationarity condition

$$\begin{bmatrix} \boldsymbol{K}^{mic}_{K_\delta} & \boldsymbol{G}^T \\ \boldsymbol{G} & \boldsymbol{0} \end{bmatrix} \begin{bmatrix} \boldsymbol{d}^{h(I,x_i)} \\ \boldsymbol{\lambda}^{(I,x_i)} \end{bmatrix} = \begin{bmatrix} \boldsymbol{0} \\ \boldsymbol{G}\,\boldsymbol{d}^{H(I,x_i)} \end{bmatrix} \text{ for } I = 1,\dots,N_{node},\ i = 1,\dots,d\,. \tag{32}$$

This set of linear equations is to be solved for $\boldsymbol{d}^{h(I,x_i)}$ and $\boldsymbol{\lambda}^{(I,x_i)}$. Since the coefficient matrix in (32) is constant for all macro unit displacement states (I, x_i), the solution vectors as well as the right-hand sides for $I = 1,\dots,N_{node}$ and $x_i, i = 1,\dots,d$ are augmented to full matrices, hence, $\boldsymbol{d}^{h(I,x_i)} \to \boldsymbol{T}$, $\boldsymbol{\lambda}^{(I,x_i)} \to \boldsymbol{\Lambda}$, $\boldsymbol{d}^{H(I,x_i)} \to \boldsymbol{d}^H$.

The coefficients $b_i, i = 1,\dots,M_{mic}$ in (30) follow from the kinematical macro–micro coupling condition, $(19)_1$, which can be written as

$$\int_{K_\delta} \left(\boldsymbol{u}^{h(I,x_i)}_{K_\delta} - \boldsymbol{u}^{H(I,x_i)}_{lin,K_\delta} \right) dV = \boldsymbol{c}\,. \tag{33}$$

Since (33) is the discrete counterpart of the normalization condition (A.21) for the periodic fluctuations, the particular choice of the constant is inconsequential for the microsolution. Here we choose $\boldsymbol{c} = \boldsymbol{0}$.

With (21), it holds

$$\int_{K_\delta} \boldsymbol{u}^{h(I,x_i)}\,dV = \sum_{T\in\mathcal{T}_h} \sum_{m=1}^{M_{mic}} \boldsymbol{d}^{h(I,x_i)}_m \underbrace{\int_T \boldsymbol{N}^h_m\,dV}_{=:b_m} = \sum_{T\in\mathcal{T}_h} \boldsymbol{d}^{h(I,x_i)} \cdot \boldsymbol{b} \tag{34}$$

$$\int_{K_\delta} \boldsymbol{u}^{H(I,x_i)}_{lin}\,dV = \sum_{T\in\mathcal{T}_h} \sum_{m=1}^{M_{mic}} \boldsymbol{d}^{H(I,x_i)}_m \int_T \boldsymbol{N}^h_m\,dV = \sum_{T\in\mathcal{T}_h} \boldsymbol{d}^{H(I,x_i)} \cdot \boldsymbol{b} \tag{35}$$

$$\begin{aligned} \text{where}\quad b_m &= \int_T \boldsymbol{N}^h_m\,dV = \frac{1}{n_{node}}\,|T| \\ &= \frac{1}{4}\,|T| \quad \text{for } d = 2, \text{ quadrilaterals and } q = 1\,, \\ &= \frac{1}{8}\,|T| \quad \text{for } d = 3, \text{ hexahedra and } q = 1\,. \end{aligned} \tag{36}$$

Using the method of Lagrange multipliers, the PBC are not strongly imposed on the FE space but rather weakly enforced. In [4] it is found that despite of this weak coupling of scales, the error estimates of [40] still hold, where in the latter reference, the PBC are strongly imposed on the FE space.

2.7. The homogenized elasticity tensor and its efficient computation

The direct stiffness sampling on microdomains circumvents the necessity to calculate the homogenized elasticity tensor $\mathbb{A}^0$ and therefore the necessity of an explicit macroscopic constitutive model. Notwithstanding, calculating $\mathbb{A}^0$ in terms of its numerical approximation $\mathbb{A}^{0,h}$ offers a second route to numerical homogenization. In its derivation we follow [13] and propose an efficient way of its computation.

A reference simplex $\hat{K}$ with its local vectorial basis $\hat{N}^H_{0,j} = (1-\xi_1-\dots-\xi_d)\otimes e_j$, $\hat{N}^H_{i,j} = \xi_i \otimes e_j$, $i, j = 1,\dots,d$ is considered. With $\hat{u}^h_{i,j}$ being the solution to (2.3) such that $\hat{u}^h_{i,j} - \hat{N}^H_{i,j} \in \mathcal{S}_{\text{per}}(K_\delta, \mathcal{T}_h)$ we can compute the numerical homogenized elasticity tensor as follows

$$\begin{aligned} \frac{1}{|K_\delta|}\int_{K_\delta} \mathbb{A}^\epsilon(x)\boldsymbol{\varepsilon}(\hat{u}^h_{i,j}) : \boldsymbol{\varepsilon}(\hat{u}^h_{l,m})\,d\boldsymbol{\xi} &= \frac{1}{|Y|}\int_Y \mathbb{A}^{0,h}\boldsymbol{\varepsilon}(\hat{N}^H_{i,j}) : \boldsymbol{\varepsilon}(\hat{N}^H_{l,m})\,d\boldsymbol{y} \\ &= \mathbb{A}^{0,h}\boldsymbol{\varepsilon}(\hat{N}^H_{i,j}) : \boldsymbol{\varepsilon}(\hat{N}^H_{l,m})\,. \end{aligned} \tag{37}$$

With

$$\boldsymbol{\varepsilon}(\hat{N}^H_{i,j}) = 1/2(e_i \otimes e_j + e_j \otimes e_i), \qquad i, j = 1,\dots,d\,, \tag{38}$$

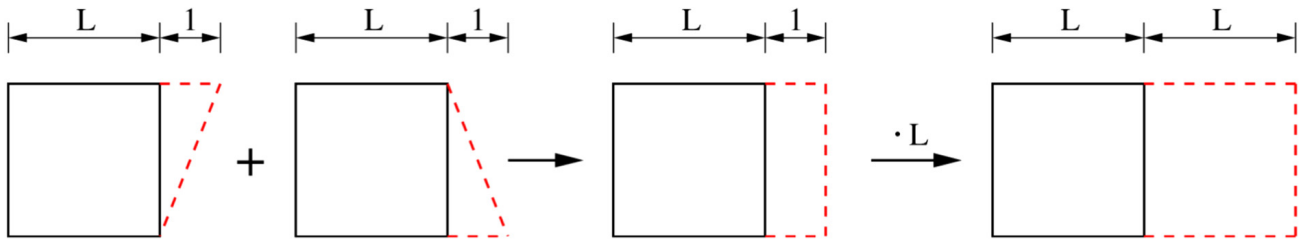


Fig. 3. Superposition of two unit displacement states and the making of a unit strain state.

(37) yields the coefficients of the homogenized elasticity tensor

$$\mathbb{A}^{0,h}_{ijlm} = \frac{1}{|K_\delta|}\int_{K_\delta} \mathbb{A}^{\epsilon}(x)\boldsymbol{\varepsilon}(\hat{u}^h_{i,j}) : \boldsymbol{\varepsilon}(\hat{u}^h_{l,m})\, d\boldsymbol{x}, \qquad i,j,l,m = 1,\dots,d\,. \tag{39}$$

The error introduced by approximating $\mathbb{A}^0_{ijlm}$ by $\mathbb{A}^{0,h}_{ijlm}$ follows $|\mathbb{A}^{0,h}_{ijlm} - \mathbb{A}^0_{ijlm}| \leq C(h/\epsilon)^{2q}$, see [6], Sec. 3.2.2.

The homogenized elasticity tensor is calculated by inserting selected macro shape functions of a reference element in the variational formulation of the microproblem, which leads to a macroscopic unit strain state as shown in (38). By doing so the homogenized elasticity tensor can be calculated coefficient wise by evaluating the corresponding strains on the microdomain.

The homogenized elasticity tensor $\mathbb{A}^{0,h}$ can be calculated alongside the FE-HMM calculation most efficiently from the already available results for the calculation of the macroelement stiffness matrix. For that purpose the microdisplacements are used, which follow from the unit displacement states of a macroelement.

While the notation above is limited to simplex reference elements, the application of a unit strain state can be easily expanded to other elements. The unit displacement states have to be combined and multiplied by a corresponding factor, such that they yield the corresponding unit strain states on the macrodomain.
Fig. 3 exemplarily visualizes this procedure for a quadrilateral. Two unit displacement states of the nodes on the right macroelement side are superimposed. The resultant constant strain state is multiplied with the element length and results in a unitary strain state.

Remark 3. The described computation of the homogenized elasticity tensor is only valid for linear elasticity. For nonlinear elasticity, the microstrains have to be calculated from the microdisplacements, which result from the macro unit strain state.

2.8. The macrosolution

The global macroquantities, the stiffness matrix $\boldsymbol{K}^{mac}$, the force vector $\boldsymbol{F}$ and the displacement vector $\boldsymbol{D}$ follow from a standard assembly of the corresponding macroelement matrices/vectors

$$\boldsymbol{K}^{mac} = \mathop{\mathbf{A}}_{e=1}^{num_{ele}} \boldsymbol{k}^{e,mac}\,, \qquad \boldsymbol{F} = \mathop{\mathbf{A}}_{e=1}^{num_{ele}} \boldsymbol{f}^{e}\,, \qquad \boldsymbol{D} = \mathop{\mathbf{A}}_{e=1}^{num_{ele}} \boldsymbol{d}^{e,H}\,. \tag{40}$$

Prescribed displacements $\boldsymbol{D} = \boldsymbol{D}_d$ on Dirichlet boundaries $\partial\mathcal{B}_D$ are eliminated by static condensation

$$\begin{bmatrix} \boldsymbol{K}_{11} & \boldsymbol{K}_{12} \\ \boldsymbol{K}_{21} & \boldsymbol{K}_{22} \end{bmatrix} \begin{bmatrix} \boldsymbol{D} \\ \boldsymbol{D}_d \end{bmatrix} = \begin{bmatrix} \boldsymbol{F}_I \\ \boldsymbol{F}_d \end{bmatrix}. \tag{41}$$

The first set of equations in (41) gives the desired macrosolution $\boldsymbol{K}_{11}\boldsymbol{D} = \boldsymbol{F}_I - \boldsymbol{K}_{12}\boldsymbol{D}_d$.

2.9. Postprocessing

After the solution of the macroproblem, the microproblem can be finally solved. Now, the microproblems in a macro finite element are driven by the true, linearized macrodisplacements, $\boldsymbol{u}^H_{lin,K}$, which results in the microsolution

vector $\boldsymbol{u}^h$. The postprocessing is carried out in the following steps

$$\boldsymbol{u}^h = \sum_i^{M_{mic}} N_i^h \boldsymbol{d}_i^h \,, \tag{42}$$

$$\boldsymbol{u}^{Hh}(\boldsymbol{x}) = \boldsymbol{u}^H(\boldsymbol{x}_{K_l}) + \boldsymbol{u}^h \qquad \text{for } \boldsymbol{x} \in K \in \mathcal{T}_H \,, \tag{43}$$

$$\varepsilon_{ij}(\boldsymbol{u}^H) = \frac{1}{2}\left(\frac{\partial u_i^H}{\partial x_j} + \frac{\partial u_j^H}{\partial x_i}\right) , \tag{44}$$

$$\varepsilon_{ij}(\boldsymbol{u}^{Hh}) = \frac{1}{2}\left(\frac{\partial u_i^{Hh}}{\partial x_j} + \frac{\partial u_j^{Hh}}{\partial x_i}\right) , \tag{45}$$

$$\boldsymbol{\sigma}(\boldsymbol{u}^{Hh}) = \mathbb{A}^\epsilon\, \boldsymbol{\varepsilon}(\boldsymbol{u}^{Hh}) = \mathbb{A}^\epsilon\, \boldsymbol{\varepsilon}(\boldsymbol{u}^h) \,, \tag{46}$$

$$\boldsymbol{\sigma}(\boldsymbol{u}^H) = \frac{1}{|K_\epsilon|}\int_{K_\epsilon} \boldsymbol{\sigma}(\boldsymbol{u}^h)\, dV \tag{47}$$

$$= \mathbb{A}^{0,h}\, \boldsymbol{\varepsilon}(\boldsymbol{u}^H) \,. \tag{48}$$

The true resultant microdisplacements are obtained by the superposition of the macrosolution at the center of the microdomain $\boldsymbol{x}_{K_l}$ with the microsolution according to (43). From the macrosolution $\boldsymbol{u}^H$ we obtain the macrostrains $\boldsymbol{\varepsilon}(\boldsymbol{u}^H)$, (44), and from the resultant microsolution $\boldsymbol{u}^{Hh}$ the microstrains $\boldsymbol{\varepsilon}(\boldsymbol{u}^{Hh})$, (45).

Next, microstresses $\boldsymbol{\sigma}(\boldsymbol{u}^{Hh})$, (46), and the macrostresses $\boldsymbol{\sigma}(\boldsymbol{u}^H)$, (47), are calculated.

The second equality in (46) is due to (43). The equality of macrostress according to (47) with (48) follows from the fact that macrostress is defined as the volume average of microstress in asymptotic homogenization, and that the homogenized elasticity tensor is identified in this averaging process, see Appendix A.1.

2.10. Algorithm

For convenience, we summarize the FE-HMM algorithm for the geometrically linear, linear elastic case in Table 1. Step 1 can be understood as a stiffness preprocessor using already the microsolver. Step 2 is referred to as the macrosolver, step 3 uses again the microsolver for the postprocessing.

3. Convergence and a priori error estimates

For the fully discrete case [13] provides convergence results. In the periodic case, the macrosolution $\boldsymbol{u}^H$ approximates the homogenized solution $\boldsymbol{u}^0$, see Theorem 4.1 in [13]. Since $\boldsymbol{u}^0$ does not capture the small scale oscillations of $\boldsymbol{u}^\epsilon$, its numerical approximation $\boldsymbol{u}^H$ equally cannot. But similar to the first order correction according to (A.38) and the corresponding enriched approximation (A.39), the reconstructed microsolution $\boldsymbol{u}^{Hh}$ according to (43) approximates the true fine scale solution $\boldsymbol{u}^\epsilon$ in the H^1-norm, see Theorem 4.2. in [13].

3.1. A priori estimates

In view of reliable solution data for engineering decisions, a key property of numerical methods is the existence of error estimates with guaranteed bounds.

FE-HMM exhibits a priori as well as a posteriori estimates for various types of partial differential equations. For elliptic PDEs we refer to [40] and [42], for the (elliptic) case of linear elasticity in a geometrical linear setting to [13]. A posteriori error indicators along with adaptive mesh refinement have been presented in [43] and [44].

We restrict to a priori estimates for the elliptic problem of linear elastic solids in a geometrical linear frame provided in [13]. In Section 5 we assess these estimates for uniform discretizations.

The total error of the FE-HMM-method can be decomposed into three parts

$$\|\boldsymbol{u}^0 - \boldsymbol{u}^H\| \le \underbrace{\|\boldsymbol{u}^0 - \boldsymbol{u}^{0,H}\|}_{e_{mac}} + \underbrace{\|\boldsymbol{u}^{0,H} - \widetilde{\boldsymbol{u}}^H\|}_{e_{mod}} + \underbrace{\|\widetilde{\boldsymbol{u}}^H - \boldsymbol{u}^H\|}_{e_{mic}} , \tag{49}$$

where e_{mac}, e_{mod}, e_{mic} are the macro error, the modeling error, and the micro error.

Table 1
Algorithm for FE-HMM in linear elasticity.

1. **Macrostiffness calculation by stiffness sampling on microdomains**
   For all macro finite elements $K \in \mathcal{T}_H$:
   (a) For each microdomain K_δ, $l = 1, \dots, N_{qp}$:
   Compute $\boldsymbol{K}_{K_\delta}^{mic}$ (27) from $\boldsymbol{k}_{ij}^{e,mic}$ (26).
   (b) For all macronodes I of element K, $I = 1, \dots, N_{node}$:
   For all directions x_i, $i = 1, \dots, d$:
   On each microdomain K_δ, $l = 1, \dots, N_{qp}$:
   – Calculate $\boldsymbol{u}_{lin,K_\delta}^{H(I,x_i)}$ and $\boldsymbol{d}^{H(I,x_i)}$.
   – Solve for $\boldsymbol{d}^{h(I,x_i)}$, (32), and assemble it in $\boldsymbol{T}_{K_l}$, (24).
   (c) Compute $\boldsymbol{k}^{e,mac}$ from $\boldsymbol{T}_{K_\delta}$, $l = 1, \dots, N_{qp}$, and $\boldsymbol{K}_{K_\delta}^{mic}$, (23).
   (Option: Calculate $\mathbb{A}^{0,h}$, (39)).

2. **Macroproblem**
   (a) By assembly obtain $\boldsymbol{K}^{mac}$, $\boldsymbol{F}$, and $\boldsymbol{D}$, (40).
   (b) Solve for $\boldsymbol{D}$, (41), obtain $\boldsymbol{u}^H$.

3. **Postprocessing on microdomains and on the macrodomain**
   For all macro finite elements $K \in \mathcal{T}_H$:
   (a) For each microdomain K_δ, $l = 1, \dots, N_{qp}$:
   i. From $\boldsymbol{u}^H$ calculate $\boldsymbol{d}_{lin}^H$.
   ii. Solve for $\boldsymbol{d}^h$, (32).
   iii. Calculate $\boldsymbol{u}^{Hh}$, (43), and $\boldsymbol{\varepsilon}(\boldsymbol{u}^{Hh})$, (45).
   iv. Compute $\boldsymbol{\sigma}(\boldsymbol{u}^h)$, (46).
   (b) Calculate $\boldsymbol{\sigma}(\boldsymbol{u}^H)$ by averaging microstresses, (47).
   (or, optionally, via $\mathbb{A}^{0,h}$, (48)).

Here, $\boldsymbol{u}^0$ is the solution of the homogenized equation, (6), $\boldsymbol{u}^H$ is the FE-HMM solution, $\boldsymbol{u}^{0,H}$ is the standard FEM solution of problem (7), therefore obtained through exact $\mathbb{A}^0$; and $\widetilde{\boldsymbol{u}}^H$ is the FE-HMM solution obtained through exact microfunctions (in $W(K_\delta)$).

For sufficiently regular problems, the following a priori estimates hold in the L^2-norm, the H^1-norm and the energy-norm:

$$\|\boldsymbol{u}^0 - \boldsymbol{u}^H\|_{L^2(\mathcal{B})} \leq C \left(H^{p+1} + \left(\frac{h}{\epsilon}\right)^{2q} \right) + e_{mod} \,. \tag{50}$$

$$\|\boldsymbol{u}^0 - \boldsymbol{u}^H\|_{H^1(\mathcal{B})} \leq C \left(H^{p} + \left(\frac{h}{\epsilon}\right)^{2q} \right) + e_{mod} \,, \tag{51}$$

$$\|\boldsymbol{u}^0 - \boldsymbol{u}^H\|_{A(\mathcal{B})} \leq C \left(H^{p} + \left(\frac{h}{\epsilon}\right)^{2q} \right) + e_{mod} \,. \tag{52}$$

Remark 4. (i) Abdulle [6] underlines that for the fully discrete analysis of FE-HMM the setting of the modified quadrature formula according to (11) is essential. The reason is that the error analysis crucially relies on conditions (ellipticity condition and approximation condition, first studied by Ciarlet and Raviart, see [45]) which ensure that a FEM with numerical quadrature converges with the same rate to the exact solution than the same FEM with exact integration.
(ii) Eqs. (50) and (51) provide relations of the macro error and the micro error. They enable strategies to achieve the optimal convergence order for minimal computational costs in micro–macro uniform discretizations. Details will be discussed in Section 5 dealing with numerical examples.

3.2. Superconvergence

The convergence order of $2q$ of the FE-HMM micro error according to (50) is already in the L^2-norm at odds with familiar results of standard FEM. The fact however, that the micro error in the H^1-norm scales in the same order

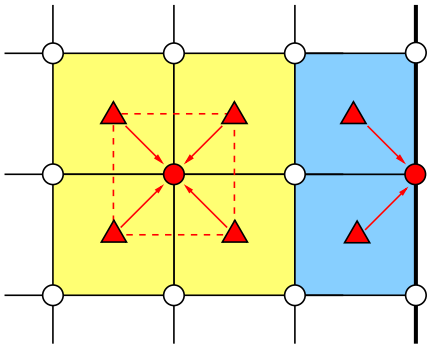


Fig. 4. Recovery of nodal stresses from stresses of surrounding superconvergent points (marked by a △) here, for $p = 1$ in the element center of rectangular quadrilaterals for both a node in the bulk and a node at the surface.

as in the L^2-norm is even more unusual, since it indicates the same order of a derivative as the primary quantity. This phenomenon is called *superconvergence*. We contrast this type of standard FE-HMM superconvergence with the (non-standard) superconvergence in single-scale FEM. For the latter Barlow [33] has shown that superconvergence exists only at particular sites of finite elements of rectangular shape and, moreover, that the number and locus of these points depend on the polynomial order of the shape functions. Zienkiewicz and Zhu presented in [46,47] a procedure for the transfer of the superconvergence property from superconvergent, inner element points to element nodes referred to as "superconvergent patch recovery" (SPR). Based on these superconvergent nodal values the same authors constructed a refinement indicator for adaptive remeshing.

Here, we analyze superconvergence for the numerical homogenization by FE-HMM.

3.2.1. Macro FEM and micro FEM

The macro error of FE-HMM in the L^2-norm (here: of displacements) scales in the order $\mathcal{O}(H^{p+1})$. The corresponding macro error in the H^1-norm and in the energy norm (hence of strain and stress) scales in the order $\mathcal{O}(H^p)$, one order below the displacements.

Following the analysis of [33], for $p = 1$, superconvergence of strain and stress – hence order $p + 1 = 2$ – can be expected in the element center of macro finite elements, if they exhibit rectangular shapes, which implies that the error in the H^1-norm and in the energy norm exhibit the same convergence order as the error in the L^2-norm.

Since the micro errors of FE-HMM in the H^1-norm and in the energy norm exhibit the same convergence order as the error in the L^2-norm, $\mathcal{O}((h/\varepsilon)^{2q})$, superconvergence is standard for the micropart of FE-HMM, which therefore is not restricted to rectangular element shapes and not to Barlow's nominally superconvergent points.

3.2.2. The superconvergent patch recovery for the macro FEM

In order to verify superconvergence of the macro FEM in the FE-HMM context, the rationale of the SPR according to [46] is applied; strain and stress are calculated at superconvergent element sites, for $p = 1$ in the center of an element. Next, these values are transferred by a least-square procedure to the finite element node in the direct neighborhood. Elements having such a node in common are referred to as the patch in the superconvergent recovery procedure. For a visualization see Fig. 4.

Stresses on the patch are prescribed component-wise by

$$\sigma_p^\star = \boldsymbol{P}\boldsymbol{a} \tag{53}$$

with

$$\boldsymbol{P} = [1,\ x,\ y,\ xy] \quad \text{and} \quad \boldsymbol{a} = [a_1,\ a_2,\ a_3,\ a_4]\ . \tag{54}$$

Vector $\boldsymbol{P}$ contains polynomial terms of the ansatz functions, here for $d = 2$ and the case of linear quadrilaterals. For the determination of the unknown vector $\boldsymbol{a}$ the function

$$F(\boldsymbol{a}) = \sum_{i=1}^{n} (\sigma_h(x_i,\ y_i) - \sigma_p^\star(x_i,\ y_i))^2$$

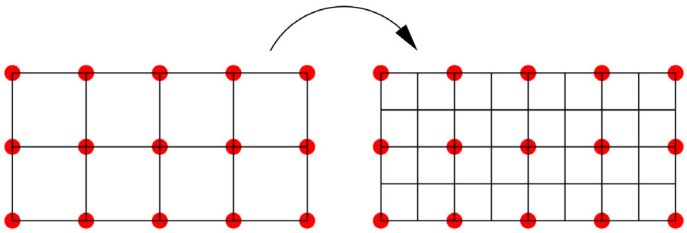


Fig. 5. Exemplary hierarchical refinement of a finite element mesh preserving the initial nodal points.

Table 2
Algorithm for assessing superconvergence.

1. Computation of the solution of a BVP for various meshes, which must be hierarchical to ensure a proper comparison of stress and strain at identical nodes, for an example see Fig. 5.
2. Evaluation of stresses and strains in the superconvergent points and recovery of nodal values by means of the superconvergent patch recovery procedure.
3. Selection of the solution obtained on the finest mesh as the "overkill"-solution.
4. Pointwise calculation of the convergence order of the nodal error in the energy-norm.

$$= \sum_{i=1}^{n} (\sigma_h(x_i,\ y_i) - \boldsymbol{P}(x_i,\ y_i)\mathbf{a})^2 \tag{55}$$

has to be minimized. Therein, $(x_i,\ y_i)$ are the coordinates of the superconvergent points, n is the number of superconvergent points of the total patch and $\sigma_h(x_i,\ y_i)$ are the stresses in these superconvergent points. Minimization of $F(\boldsymbol{a})$ implies that $\boldsymbol{a}$ fulfills the condition

$$\sum_{i=1}^{n} \boldsymbol{P}^T(x_i,\ y_i)\,\boldsymbol{P}(x_i,\ y_i)\,\boldsymbol{a} \ = \ \sum_{i=1}^{n} \boldsymbol{P}^T(x_i,\ y_i)\,\sigma_h(x_i,\ y_i)\,, \tag{56}$$

which can be solved for $\boldsymbol{a}$

$$\boldsymbol{a} \ = \ \boldsymbol{A}^{-1}\,\boldsymbol{b} \tag{57}$$

with

$$\boldsymbol{A} \ = \ \sum_{i=1}^{n} \boldsymbol{P}^T(x_i,\ y_i)\,\boldsymbol{P}(x_i,\ y_i) \quad \text{and} \quad \boldsymbol{b} \ = \ \sum_{i=1}^{n} \boldsymbol{P}^T(x_i,\ y_i)\,\sigma_h(x_i,\ y_i)\,. \tag{58}$$

Stresses in the central node of the patch can be recovered by inserting its nodal coordinates $(x_N,\ y_N)$ into the $\boldsymbol{P}$-Vector in (53). Summarizing, the numerical assessment of the superconvergence property of stresses and strains can be calculated as described in Table 2

4. Conceptual comparison of FE-HMM with the FE^2 method

The aim of the present section is a conceptual comparison of the FE-HMM with the FE^2 method, which reveals similarities, but also differences in some noticeable aspects.

4.1. The FE^2-method

To put things into perspective we briefly reiterate the building blocks of the FE^2 method.

The basic idea of computational homogenization in the FE^2 method is to solve at each integration point of the macroproblem the associated microproblem. For the case of the first-order strain-driven computational

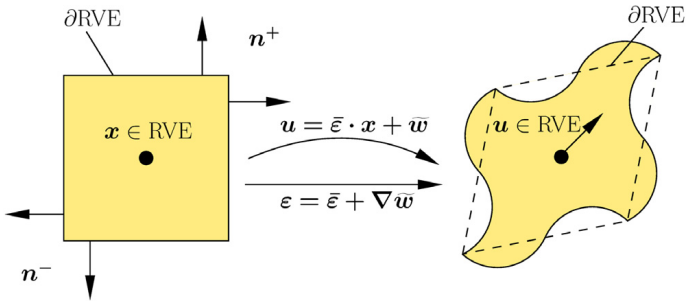


Fig. 6. Periodic boundary conditions (PBC) on the boundary of the microsampling domain ∂RVE.

homogenization the macroproblem provides input to the problem at the microscale in terms of macroscopic deformation and, vice-versa, the microproblem provides stiffness information in terms of the macroscopic tangent and stress. The latter is obtained from averaging microstresses, which implies that a constitutive law does not exist on the macroscale.

The theoretical cornerstone of the FE^2 method is the Hill–Mandel condition, which postulates that the stress power on the macrolevel must be equal to the average microscopic stress power in a so-called Representative Volume Element, RVE

$$\overline{\boldsymbol{\sigma}} : \dot{\overline{\boldsymbol{\varepsilon}}} = \frac{1}{V} \int_{\mathrm{RVE}} \boldsymbol{\sigma} : \dot{\boldsymbol{\varepsilon}} \, dV \qquad \longleftrightarrow \qquad \frac{1}{V} \int_{\mathrm{RVE}} \boldsymbol{\sigma} : \dot{\boldsymbol{\varepsilon}} \, dV - \overline{\boldsymbol{\sigma}} : \dot{\overline{\boldsymbol{\varepsilon}}} = 0 \,, \tag{59}$$

where macrostress $\overline{\boldsymbol{\sigma}}$ is calculated as the volumetric mean of microstresses $\boldsymbol{\sigma}$ according to

$$\overline{\boldsymbol{\sigma}} = \frac{1}{V} \int_{\mathrm{RVE}} \boldsymbol{\sigma} \, dV \,. \tag{60}$$

Boundary conditions for the RVE, which are consistent to the Hill–Mandel postulate, are the constraint condition $\dot{\boldsymbol{\varepsilon}} := \dot{\overline{\boldsymbol{\varepsilon}}}$ on the whole RVE (Voigt condition), the constraint condition of constant stress $\boldsymbol{\sigma} = \overline{\boldsymbol{\sigma}}$ on the whole RVE (Reuss condition). Moreover, linear Dirichlet and linear Neumann conditions each fulfill the condition as well. Finally, PBC are consistent with the postulate. They are visualized in Fig. 6. Macrostrain $\overline{\boldsymbol{\varepsilon}}$ yields a homogeneous deformation on the RVE, which is superimposed by periodic fluctuations $\widetilde{\boldsymbol{w}}$.

For a proper definition of PBC, the boundary of the RVE is divided into pairwise periodic parts $\partial\mathrm{RVE}^+$ and $\partial\mathrm{RVE}^-$ with a corresponding sign convention for position vectors $\boldsymbol{x}^+$ and $\boldsymbol{x}^-$ and normal vectors $\boldsymbol{n}^+ = -\boldsymbol{n}^-$. For pairwise periodicity of the displacements, i.e. $\widetilde{\boldsymbol{w}}^+ = \widetilde{\boldsymbol{w}}^- = \widetilde{\boldsymbol{w}}$ along with

$$\int_{\mathrm{RVE}} \widetilde{\boldsymbol{\sigma}} : \dot{\widetilde{\boldsymbol{\varepsilon}}} \, dV = \int_{\partial\mathrm{RVE}} \widetilde{\boldsymbol{t}} \cdot \dot{\widetilde{\boldsymbol{w}}} \, dA = \int_{\partial\mathrm{RVE}} (\boldsymbol{t} - \overline{\boldsymbol{\sigma}}\boldsymbol{n}) \cdot (\dot{\boldsymbol{u}} - \dot{\overline{\boldsymbol{\varepsilon}}}\boldsymbol{x}) \, dA = 0 \,, \tag{61}$$

yields

$$\int_{\partial\mathrm{RVE}} \widetilde{\boldsymbol{t}} \cdot \dot{\widetilde{\boldsymbol{w}}} \, dA = \int_{\partial\mathrm{RVE}^+} \widetilde{\boldsymbol{t}}^+ \cdot \dot{\widetilde{\boldsymbol{w}}} \, dA + \int_{\partial\mathrm{RVE}^-} \widetilde{\boldsymbol{t}}^- \cdot \dot{\widetilde{\boldsymbol{w}}} \, dA = \int_{\partial\mathrm{RVE}^-} (\widetilde{\boldsymbol{t}}^+ + \widetilde{\boldsymbol{t}}^-) \cdot \dot{\widetilde{\boldsymbol{w}}} \, dA = 0 \,, \tag{62}$$

which implies the additional condition $\widetilde{\boldsymbol{t}}^+ = -\widetilde{\boldsymbol{t}}^-$. Thus, the PBC satisfying the macrohomogeneity condition can be given as

$$\widetilde{\boldsymbol{w}}^+ = \widetilde{\boldsymbol{w}}^- \qquad \text{and} \qquad \widetilde{\boldsymbol{t}}^+ = -\widetilde{\boldsymbol{t}}^- \qquad \text{on} \quad \partial\mathrm{RVE} \,. \tag{63}$$

The homogenized elasticity tensor $\overline{\mathbb{A}}$ is calculated for each macro quadrature point. If static condensation is applied, $\overline{\mathbb{A}}$ can be calculated according to

$$\frac{d\,\overline{\boldsymbol{\sigma}}}{d\,\overline{\boldsymbol{\varepsilon}}} =: \overline{\mathbb{A}} = \mathbb{A}^{\mathrm{Voigt}} - \frac{1}{|K_l|} \overline{\boldsymbol{L}}^T (\boldsymbol{K}^{mic}_{K_l})^{-1} \overline{\boldsymbol{L}} \,, \tag{64}$$

with

$$\mathbb{A}^{\mathrm{Voigt}} = \langle \mathbb{A} \rangle = \frac{1}{|K_l|} \sum_{T \in \mathcal{T}_h} \int_T \mathbb{A}^{\varepsilon} \, dV \,, \qquad \overline{\boldsymbol{L}} = \mathop{\mathbf{A}}_{e=1}^{num_{ele}} \overline{\boldsymbol{l}}_e \,, \quad \overline{\boldsymbol{l}}_e = \int_T \boldsymbol{B}^T \mathbb{A}^{\varepsilon} \, dV \,. \tag{65}$$

The corresponding system of linear equations which has to be solved to obtain $\overline{\mathbb{A}}$ is

$$\boldsymbol{K}^{\mathrm{mic}}_{K_l}\,\boldsymbol{X} = \overline{\boldsymbol{L}}\,. \tag{66}$$

The number of right hand sides follows from the dimension of $\overline{\boldsymbol{L}}$, hence depends on $\boldsymbol{B}$ according to $(65)_{2,3}$. The number is 3 for $d = 2$, and 6 for $d = 3$.

4.2. Comparison

4.2.1. Homogeneity condition. Energy equivalence

While the FE^2-method is built on the Hill–Mandel condition (59), FE-HMM is built on asymptotic expansion. It is a straightforward exercise to show that for PBC, asymptotic homogenization theory fulfills the Hill–Mandel condition. With the strain influence function already introduced in (A.23) a direct calculation of microstrain from macrostrain is obtained

$$\varepsilon_{ij} = E^{kl}_{ij}(\boldsymbol{y})\,\overline{\varepsilon}_{kl}(\boldsymbol{x}) = \left(\mathbb{I}_{ijkl} + \frac{\partial \chi^{kl}_i}{\partial y_j}\right)\overline{\varepsilon}_{kl}\,. \tag{67}$$

With (67) we obtain

$$\begin{aligned}\frac{1}{V}\int_V \sigma_{ij}\,\varepsilon_{ij}\,dV &= \frac{1}{V}\int_V \sigma_{ij}\left(\mathbb{I}_{ijkl} + \frac{\partial \chi^{kl}_i}{\partial y_j}\right)dV\,\overline{\varepsilon}_{kl}\\ &= \underbrace{\frac{1}{V}\int_V \sigma_{ij}\,dV}_{=\overline{\sigma}_{ij}}\,\overline{\varepsilon}_{ij} + \frac{1}{V}\underbrace{\int_V \sigma_{ij}\frac{\partial \chi^{kl}_i}{\partial y_j}\,dV}_{=0}\,\overline{\varepsilon}_{kl}\\ &= \overline{\sigma}_{ij}\,\overline{\varepsilon}_{ij}\,.\end{aligned} \tag{68}$$

For the evaluation of the second integral in (68) we have used integration by parts

$$\int_V \sigma_{ij}\frac{\partial \chi^{kl}_i}{\partial y_j}\,dV\,\overline{\varepsilon}_{kl} = \int_{\partial V}\chi^{kl}_i\sigma_{ij}n_j\,d\gamma\,\overline{\varepsilon}_{kl} - \int_V \chi^{kl}_i\frac{\partial \sigma_{ij}}{\partial y_j}\,dV\,\overline{\varepsilon}_{kl} = 0 \tag{69}$$

with $\boldsymbol{n}$ being the unit normal to the boundary. Here we exploited periodicity, namely that χ^{kl}_i is equal on the opposite site of the unit cell, whereas surface tractions $t_i = \sigma_{ij}n_j$ are equal and of opposite sign on opposite sites of the unit cell. The second integral in (69) vanishes, since it holds $\partial\sigma_{ij}/\partial y_j = 0$ for equilibrium.

Equivalence of energy densities in FE-HMM is enforced in the frame of a modified quadrature rule for the calculation of the macrostiffness matrix by stiffness sampling on microdomains, see (11). Already in its very first, most general proposal, the Heterogeneous Multiscale Method (HMM) for variational problems was built on energy equivalence in terms of a fine-scale to coarse-scale stiffness transfer, see Sec. 2.2 in [1]. For that reason we can call the FE-HMM energy equivalence "E-macrohomogeneity condition" for the initials of energy and the authors.

4.2.2. Kinematics of coupling conditions

Both FE-HMM and FE^2 attach the microdomains to the macrodomain at the quadrature points of macro finite elements as visualized in Fig. 1. The explicit kinematical coupling follow for FE^2 from the energy equivalence condition (59), and for FE-HMM from the cell problem of asymptotic homogenization. Periodic boundary conditions meet these requirements such that the macro–micro kinematical coupling effectively coincides for FE^2 and FE-HMM; in FE^2 strain at the macro quadrature point $\overline{\boldsymbol{\varepsilon}}$ induces a homogeneous deformation in the attached RVE with the corresponding displacement field $\boldsymbol{u} = \overline{\boldsymbol{\varepsilon}}\cdot\boldsymbol{X}$. In FE-HMM the homogeneous deformation in the microdomain is induced by the linearized macrodisplacement field $\boldsymbol{u}^H_{lin}$, which is superimposed by periodic fluctuations following from constrained energy minimization in the RVE and microdomain, respectively. In the above nomenclature, the periodic fluctuations are referred to as $\widetilde{\boldsymbol{w}}$ in FE^2, in FE-HMM as the difference $\boldsymbol{u}^h - \boldsymbol{u}^H_{lin}$, and in asymptotic homogenization as $\boldsymbol{\chi}^{lm}$.

The enforcement of coupling conditions have been realized in the FE^2 method either by static condensation/elimination, [15], by the method of Lagrange multipliers, [48], or by the Penalty method, [49]. In FE-HMM, the coupling was realized by Lagrange multipliers in [4,5,50]. For a discussion of the role of different types of boundary conditions on the RVE we refer to [51,52].

4.2.3. Micro-to-macro coupling/bottom-up data transfer

In strain-driven two-level finite element frameworks, the microscale must pass over stress and stiffness information to the macroscale. For the particular case of linear elasticity, the deformation-dependent tangential material stiffness boils down to the constant elasticity tensor.

Stiffness transfer in FE^2 is carried out by the effective fourth-order constitutive tensor $\overline{\mathbb{A}}$, although its computation may differ. It can be carried out by numerical perturbation as proposed in [19], by Lagrange multiplier techniques, [48], or by static condensation, [15]. The effective constitutive tensor is passed over to the corresponding macro quadrature point, where it enters the macroelement stiffness matrix.

For FE-HMM in practice, the bottom-up stiffness transfer can be carried out by two different means, either by (i) a direct stiffness matrix transfer mediated by micro-to-macro transformation matrices or by (ii) the homogenized constitutive (here: elasticity) tensor, where the latter coincides with the FE^2 method. We anticipate that the two variants of stiffness transfer show quantitative agreement, see Section 5. Notwithstanding, it is only the first approach of the stiffness matrix transfer which enables due to its underlying modified quadrature formula the derivation of unified a priori estimates and therefore is a key, indispensable FE-HMM ingredient, see Section 4.2.5.

4.2.4. Data-driven versus model-driven method

Closely related to the bottom-up data transfer is the discrimination between data- and model-driven methods. Within the FE^2 method, a macroscopic constitutive model is not defined since not required. Instead, the macroscale is fed by homogenized microdata in terms of stress and stiffness, see Section 4.2.3. In this respect FE^2 is a data-driven method, in view of the absent macro constitutive equations it can even be called an "equation-free" method.

Similarly, the sole constitutive input for FE-HMM is $\mathbb{A}^\epsilon$, which lives on the microscale. It is passed over to the macroscale via the transformed microstiffness matrix, and macrostresses are calculated by averaging microstresses. Of course, the macroscale solver is a finite element method but the physical model is not declared.

4.2.5. A priori error estimates

FE-HMM is endowed with a priori estimates for the macro error and the micro error in the L^1-, H^2- and the energy-norm as well as with estimates for the coefficients of the homogenized elasticity tensor, see Section 3.1.

While the a priori estimates of the macro error in FE-HMM directly follow from the approximation condition for standard FEM, [45], the a priori estimate for the micro error and its propagation to the macroscale crucially relies on the FE-HMM setting as a modified quadrature rule and on the method's roots in asymptotic homogenization, see [13,53]. FE^2 lacks these roots and, as a consequence, no unified a priori estimate covering both the macro and the micro error exists. Moreover, there are, to the best of our knowledge, even no numerical convergence tests available for FE^2.

Unified a priori estimates allow in FE-HMM for micro–macro uniform refinement strategies, which are optimal in that the full convergence order can be achieved for a minimum of computational costs. This is a considerable benefit of FE-HMM compared with FE^2. In numerical tests related to scalar-valued field problems it was shown that the a priori estimates are quite sharp, [5,6]. For the present case of linear elasticity, the a priori estimates and derived optimal micro–macro uniform refinement strategies will be assessed in Section 5.

4.2.6. Numerical costs

The method of Lagrange multipliers for stiffness calculation in FE-HMM requires to solve the microproblem for $N_{node} \times d$ right hand sides. Since the microstiffness matrix is independent of the unit displacement states, it is a linear set of equations with $N_{node} \times d$ different right hand sides thus reducing the computational complexity. In FE^2 using the static condensation method, the number of right hand sides in the microproblem is 3 for $d = 2$, and 6 for $d = 3$, hence cheaper than the FE-HMM approach using Lagrange multipliers. Of course, the solution of the microproblems in FE^2 by the method of Lagrange multipliers is equally more expensive than static condensation, see [48]. Moreover, if static condensation is used in FE-HMM, the numerical costs are the same as in FE^2. If FE-HMM takes the route using the homogenized elasticity tensor $\mathbb{A}^{0,h}$, the numerical effort is exactly the same as in FE^2.

In either case, linear problems, here for both geometrical linearity and material linearity, are solved not only by FE-HMM but also by FE^2 in one single step, no iterations are required, see [13], Sec. 1; for that reason the algorithm in Table 1 similarly applies to the FE^2 method.

Beyond parallelization several approaches can reduce the computational complexity of two-level FEM. Methods based on Fast-Fourier Transforms (FFT) as introduced in [54] use a direct, point-wise discretization of the Lippmann–Schwinger equation, with improvements in [15] and [55]. In an effort to reduce the computation time by a modified modeling [56] introduce into FE^2 the rationale of a statistically similar representative volume element (SSRVE) in order to replace the true microstructure in its full geometrical complexity by a surrogate, which resembles the original one by geometrical features as analyzed by different geometrical similarity measures.

4.2.7. Limitations

The classical FE^2 method has proven to be equally suitable for linear and non-linear problems. It has been applied to non-linear elasticity, to various inelastic constitutive models, and to multifield problems with a coupling of mechanics with thermo-/electro-/magneto-fields. The versatility of FE^2 is its big plus; the extension of FE-HMM to finite deformation non-linear elasticity is a non-trivial task, most notably to provide the mathematical analysis in terms of estimates for that case.

In the frame of first-order computational homogenization methods FE^2 and FE-HMM exhibit inherent limitations. Inhomogeneous deformation modes such as bending cannot be properly represented on the microscale. As a consequence, the microscale is not appropriate to capture geometrical size effects in material behavior. This issue was overcome by second order computational homogenization as introduced into FE^2 in [24,25]. For a thorough discussion of the limitations and future challenges we refer to [57]. Alternative to the second-order homogenization to capture the size effect, one can introduce surface/interface energies into homogenization which are more intuitive and can be physically motivated as described in [58] and [59].

4.2.8. Relation to other methods

There is a remarkable connection of FE^2 and FE-HMM to the fully nonlocal, cluster-based Quasicontinuum Method (CQC), which was introduced in [60]. In CQC, nanosampling domains in the shape of spherical clusters are used to approximate the sum over all lattice sites of a crystal by a weighted sub-sum. For a modification to an energy-based approach of this concept endowing the method with a variational structure see [61,62]. The nanosampling domains of CQC are strongly coupled to the displacement field of the finite elements. Additionally, the clusters are coupled by the nonlocal interactions of the atoms in the sampling domain with other atoms within the cutoff-radius. The concept of scale-separation is a necessary theoretical requirement in FE^2 and FE-HMM. Quite in contrast, CQC as an atomistic–continuum coupling method aims at a seamless transition between the scales. For CQC, the sole constitutive input originates from the fine scale (potential of atomic interactions), and consequently, no explicit coarse-scale constitutive model exists. It is remarkable that in this particular characteristics, CQC is close to FE^2 and FE-HMM, but is in contrast to other atomistic–continuum coupling methods, which equally require a coarse-scale/macro model, [63].

In conclusion, innovative quadrature formula (FE-HMM) and summation rules (CQC), see [64], have been advancing multiscale modeling to a considerable extent.

5. Numerical examples

This section assesses the numerical performance of the FE-HMM method. The results and corresponding errors are measured in the following norms

$$L^2\text{-norm:} \quad \|\boldsymbol{u}\|_{L^2(\Omega)} := \sqrt{\int_\Omega \boldsymbol{u} : \boldsymbol{u}\, dV}\,, \tag{70}$$

$$H^1\text{-norm:} \quad \|\boldsymbol{u}\|_{H^1(\Omega)} := \sqrt{\left(\sum_{i,j=1}^{d} \int_\Omega \left(\frac{\partial u_i}{\partial x_j}\right)^2 dV + \sum_{i=1}^{d} \int_\Omega (u_i)^2\, dV\right)}\,, \tag{71}$$

$$\text{energy-norm:} \quad \|\,\boldsymbol{u}\,\|_{A(\Omega)} := \sqrt{\int_\Omega \mathbb{A}\,\boldsymbol{\varepsilon}(\boldsymbol{u}) : \boldsymbol{\varepsilon}(\boldsymbol{u})\, dV} = \sqrt{\boldsymbol{d}^T\, \boldsymbol{K}\, \boldsymbol{d}}\,, \tag{72}$$

$$\text{maximum-norm:} \quad \|\,\boldsymbol{u}\,\|_\infty := \sup_{\boldsymbol{x}\in\Omega} |\boldsymbol{u}|\,. \tag{73}$$

Four benchmark problems subject to plane strain conditions will be analyzed,

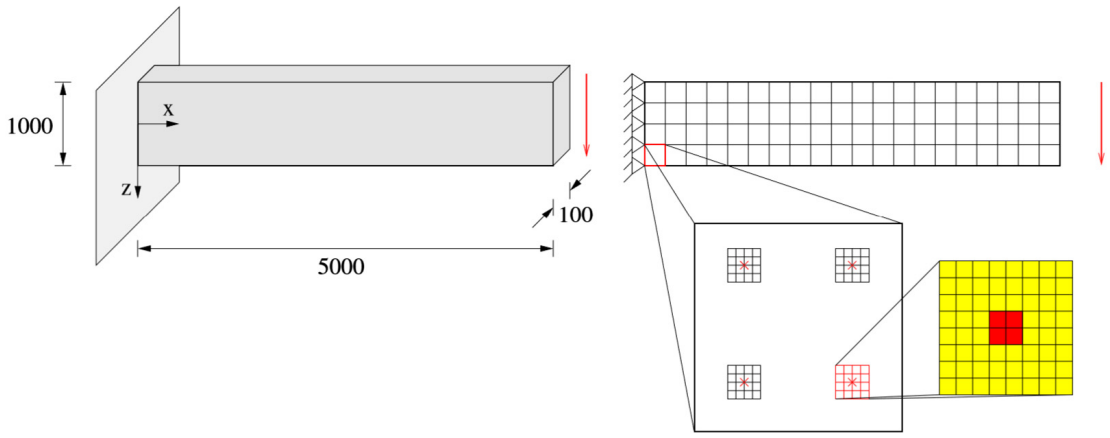


Fig. 7. Matrix–inclusion material for beam bending. Geometry, boundary conditions, loading and finite element discretizations.

(i) a matrix–inclusion problem,
(ii) a microstructure with an analytical solution for homogenization,
(iii) a non-uniformly periodic microstructure,
(iv) a uniformly periodic tessellation inspired by M.C. Escher.

Key aspects are

(A) the convergence order of the simulation results, where the errors are calculated by means of an accurate reference solution ("overkill"-solution) on very fine meshes. Doing so, the a priori estimates will be assessed.
(B) Based on the unified error estimates covering the macro error and the micro error, tests will be carried out on how full convergence orders can be achieved for minimal costs in uniform micro–macromesh refinements.
(C) Superconvergence employing the superconvergent patch recovery will be tested.
(D) Simulation results of FE-HMM are compared with those of FE^2, thus complementing the conceptual comparison of Section 4.2.
(E) Finally, the reconstruction of the microsolution from the macrosolution shall demonstrate the capability of postprocessing small scale features, which can be used to investigate local phenomena like stress concentrations, which eventually may initiate inelastic deformations and failure mechanisms.

To improve the readability but still properly document the present simulation results, we provide the numerical convergence data in tabular form as a supplement and restrict here to the more telling convergence diagrams.

The elasticity tensor will be given in standard Voigt notation. Moreover, we replace the x_i, $i = 1, \ldots, d$ coordinate system by a x-, y-, z-coordinate system.

5.1. Matrix–inclusion problem for beam-bending

In the first numerical example we consider the microstructure of a stiff inclusion in a soft matrix, hence a problem with uniformly periodic coefficients, $\delta = \epsilon$, such that periodic boundary conditions are applied to the microdomains. The Young's moduli of the inclusion $E_i = 100\,000$ N/mm^2 and the matrix phase $E_m = 40\,000$ N/mm^2 exhibit the contrast of $E_i/E_m = 2.5$, for the Poisson's ratio it holds $\nu = 0.2$. The volume ratio of the inclusion phase is $V_i/V_{tot} = 1/16$.

The beam as displayed in Fig. 7 exhibits length $l_1 = 5000$ mm, height $l_2 = 1000$ mm, and thickness $t = 100$ mm. The external line load is $q_0 = 1$ N/mm^2. The side length of the square microcell is $\epsilon = 5$ mm, hence $\epsilon/l_1 = 5/5000 \ll 1$ and $\epsilon/l_2 = 5/1000 \ll 1$.

5.1.1. Macro- and microconvergence

The simulation results are obtained along with a reference solution with 3200×640 macroelements and 32×32 microelements. The results turn out to be invariant with respect to a variation of ϵ. Fig. 8 (left) shows the total error

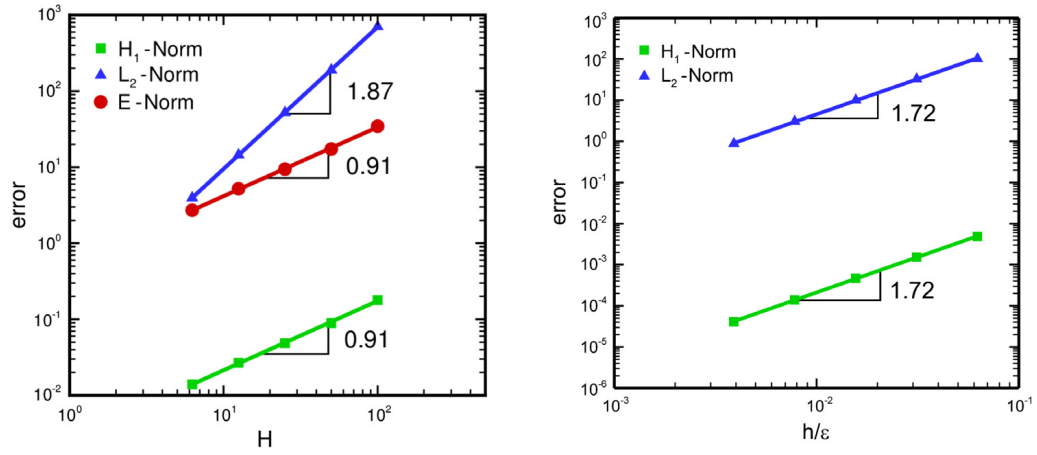


Fig. 8. Matrix–inclusion problem for beam bending. (Left:) Macro- and (right:) microconvergence.

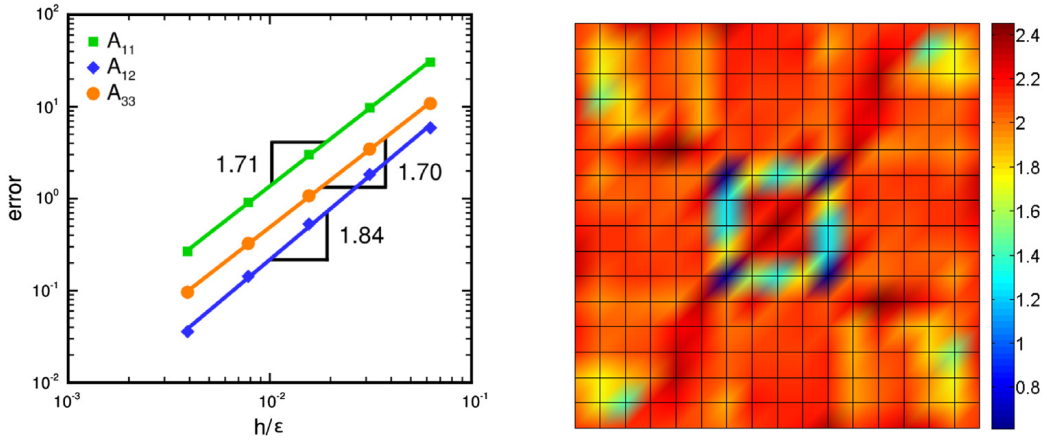


Fig. 9. Matrix–inclusion problem for beam bending. (Left) convergence of $\mathbb{A}^{0,h}$ components, (right) local convergence order of the error in the energy-norm on the microdomain at [4980.3 mm, 105.3 mm].

as a function of the macrodiscretization while keeping the microdiscretization fixed; the mean convergence orders in the L^2-norm of almost 2, and in the H^1- and in the energy-norm of almost 1 confirm the a priori estimates of Section 3.1.

Similarly, the convergence of the micro error in the right diagram of Fig. 8 is in reasonable agreement with the theoretical predictions. The deviation (1.72 versus 2) is due to the magnitude of the stiffness jump at the inclusion–matrix interface, which lowers the regularity of the microproblem. This assertion is underpinned by the local convergence distribution of the error in the energy-norm as shown in the right of Fig. 9; at the matrix–inclusion interphase, most notably at the corners, the convergence order is considerably reduced. The reference solution for micro error calculation is obtained using 200 × 40 macroelements and 2048 × 2048 microelements.

5.1.2. Homogenized elasticity tensor

Next, we assess the convergence estimate for the components of the approximate homogenized elasticity tensor $\mathbb{A}^{0,h}$ where the reference solution $\mathbb{A}^0$ is obtained on a microdomain discretized by 2048 × 2048 elements. The convergence as a function of h/ϵ is shown in the left diagram of Fig. 9. The mean slope varies between 1.70 for coefficient $\mathbb{A}_{33}$ and 1.84 for coefficient $\mathbb{A}_{12}$ and well agrees with the convergence of the micro errors in the L^2-norm and the H^1-norm. The deviation from the theoretical order 2 is caused by the aforementioned reduced regularity of the microproblem for its material stiffness contrast.

Table 3
Matrix–inclusion problem for beam bending. Comparison of the standard FE-HMM with the FE-HMM($\mathbb{A}^{0,h}$)/FE^2 solution.

	Microelements Macroelements	64×64 50×10	100×20	200×40	400×80
FE-HMM	$\|\boldsymbol{u}\|_\infty$	11.8018	11.8498	11.8630	11.8667
	$\|\boldsymbol{u}\|_A$	1080.36	1082.50	1083.07	1083.22
FE$^2 \mathrel{\widehat{=}}$	$\|\boldsymbol{u}\|_\infty$	11.8018	11.8498	11.8630	11.8667
FE-HMM($\mathbb{A}^{0,h}$)	Deviation	$4.09 \cdot 10^{-11}$	$-6.72 \cdot 10^{-13}$	$4.68 \cdot 10^{-13}$	$3.58 \cdot 10^{-11}$
	$\|\boldsymbol{u}\|_A$	1080.36	1082.50	1083.07	1083.22
	Deviation	$2.18 \cdot 10^{-11}$	$-3.38 \cdot 10^{-11}$	$2.35 \cdot 10^{-10}$	$1.96 \cdot 10^{-11}$

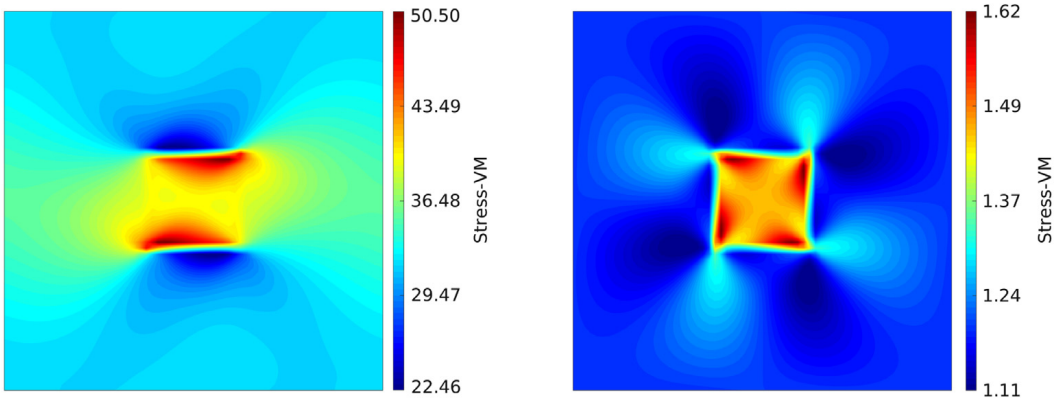


Fig. 10. Matrix–inclusion problem for beam bending. Von-Mises stress distribution (left) on the microdomain at $x = 21.1$, $y = 21.1$ (mm) and (right) on the microdomain at $x = 4978.9$, $y = 978.9$ (mm).

5.1.3. Comparison of FE-HMM with FE^2

In practice, the use of $\mathbb{A}^{0,h}$ in the FE-HMM simulation is an alternative route to the standard FE-HMM solution method. The difference between the solutions is quantitatively analyzed in Table 3; the normed percental deviation is throughout less than 5×10^{-10} and independent of the macrodiscretization.

Since the FE^2 method draws in the homogenization process on the fourth order constitutive tensor, here $\mathbb{A}^{0,h}$, it coincides with the FE-HMM byproduct of the homogenized elasticity tensor. The simulation results for FE-HMM along with the micro–macrostiffness matrix transfer show quantitative agreement with the FE^2, which underpin the identity of the methods by numerical means as well.

5.1.4. Postprocessing on selected microdomains

Fig. 10 displays the von-Mises stress distributions on two different microdomains, in the lower left and in the upper right of the beam. The stiff inclusion attracts stress, while the stress in the soft matrix is considerably smaller. Right at the interface of the inclusion with the matrix, a stress jump can be observed; the fact that the stiffer inclusion carries over large stresses shielding the softer matrix in terms of the matrix' strong local reduction of stress is referred to as stress-shielding.

Refined information is obtained by the contour plots of relevant stress components and strain components for the two points considered in the lower left of the beam, Fig. 11, and for the upper right of the beam, Fig. 12.

Remark 5. The H^1-norm depends on the chosen physical unit of the primary quantity; the smaller the (length) unit, the larger the weight of the primary quantity compared to the derivative. In the limiting case the H^1-norm equals the L^2-norm, and the macro error in the H^1-norm will show the same order as in the L^2-norm—in contrast to the estimates. In order to avoid this falsifying effect, we use in the first example of Section 5.1 the length unit of kilometer instead of millimeter for evaluating the H^1-norm.

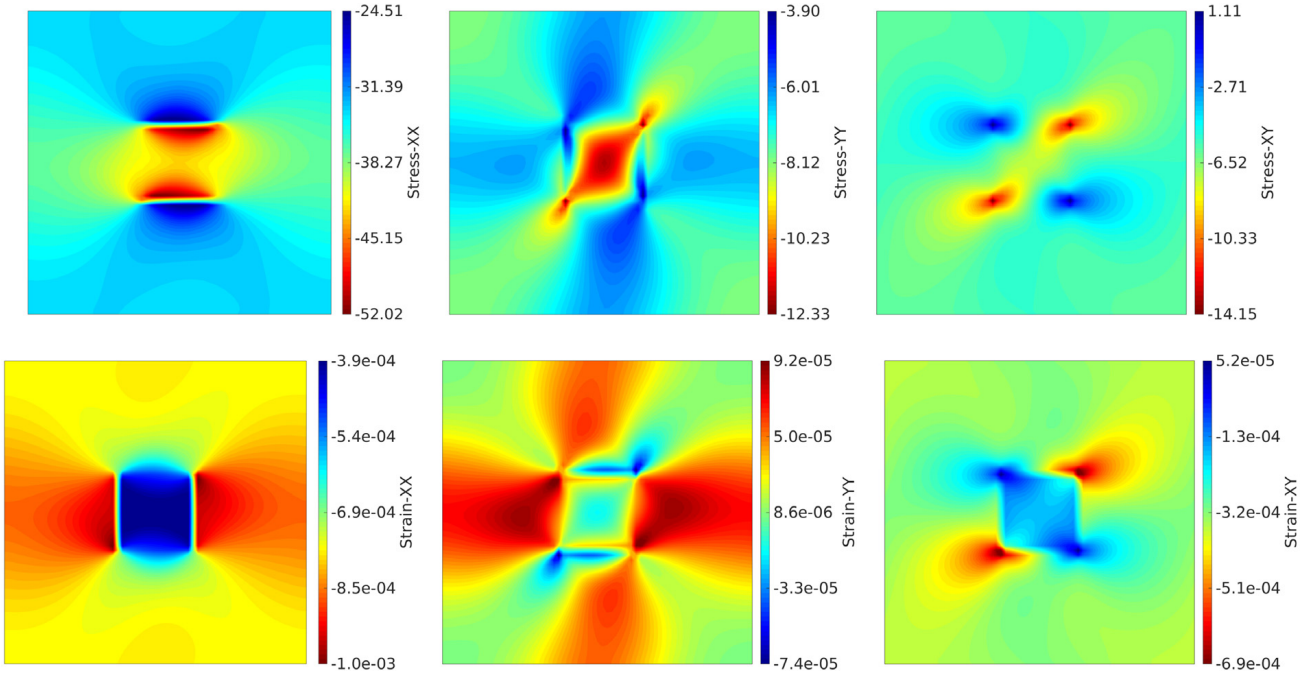


Fig. 11. Matrix–inclusion problem for beam bending. On the microdomain for the macro Gauss point at [21.1 mm, 21.1 mm] (first row) stress σ_{xx}, σ_{yy} and τ_{xy} in [N/mm^2] and (bottom row) strain ε_{xx}, ε_{yy} and γ_{xy} are displayed.

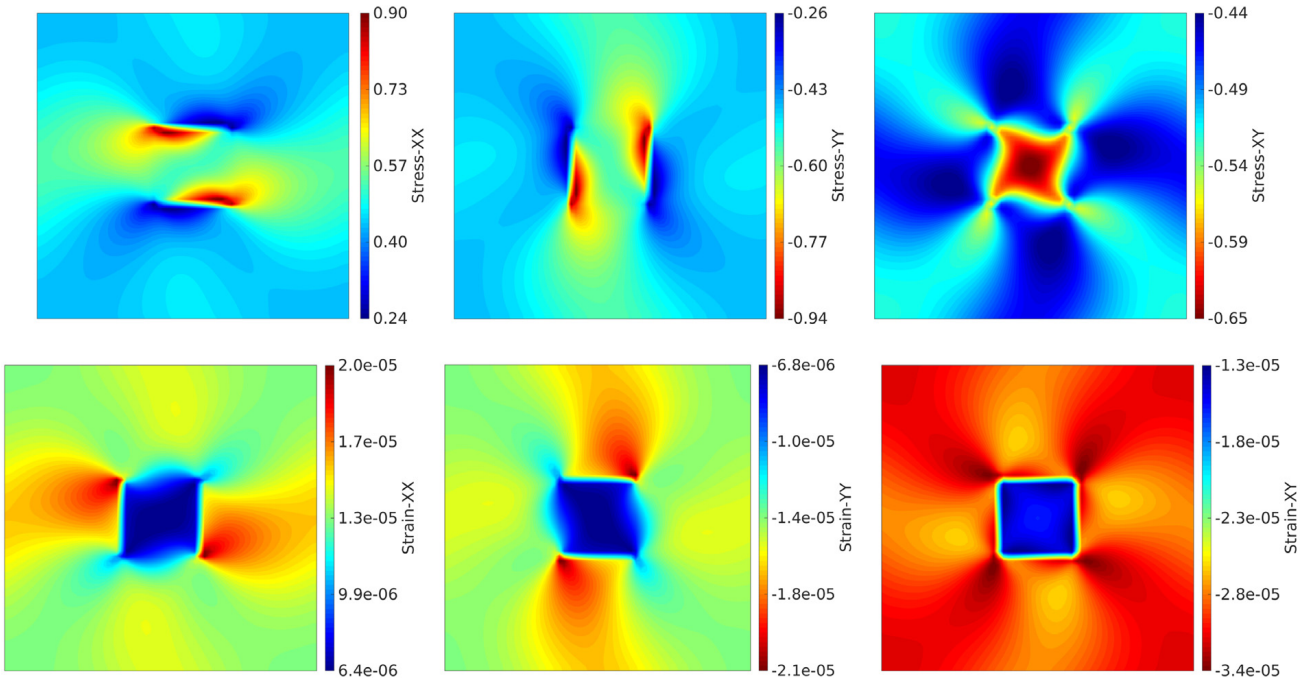


Fig. 12. Matrix–inclusion problem for beam bending. On the microdomain for the macro Gauss point at [4978.9 mm, 978.9 mm] (first row) stress σ_{xx}, σ_{yy} and τ_{xy} in [N/mm^2] and (bottom row) strain ε_{xx}, ε_{yy} and γ_{xy} are displayed.

5.2. Assessment of superconvergence in the FE-HMM

Since the present example is uniformly periodic, the homogenized elasticity tensor is constant everywhere including the superconvergent element center.

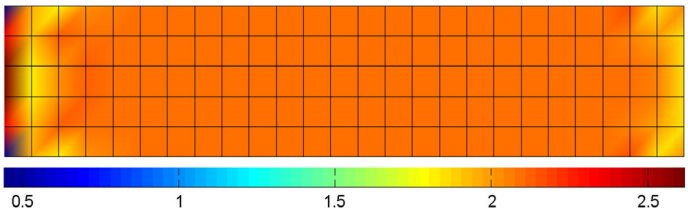


Fig. 13. Superconvergence test. Convergence order of the local error in the energy-norm for the macrodomain in FE-HMM.

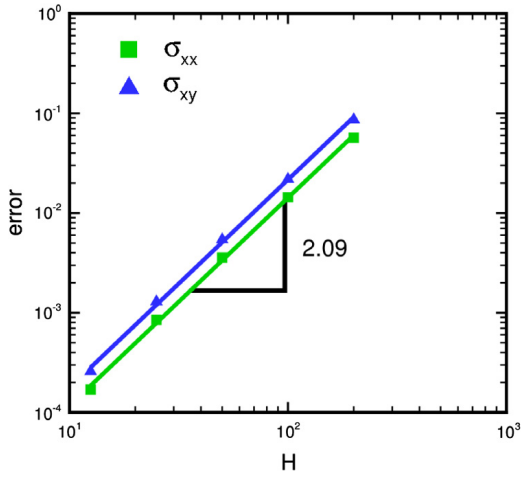


Fig. 14. Superconvergence test. Convergence of the error in stress components σ_{xx} and σ_{xy} for the nodes at [2400 mm, 400 mm].

Table 4
Superconvergence test. Convergence of the global macro error in the energy-norm, $\epsilon = 5$ mm.

Macroelements Microelements	25 × 5 32 × 32	50 × 10	100 × 20	200 × 40	400 × 80	Order
$\|\mathbf{u}^0 - \mathbf{u}^H\|_A$	4.6020	2.3821	1.3401	0.7034	0.2751	0.9888

5.2.1. Superconvergence for the macro FEM

The error in the energy-norm is computed at mesh nodes of the coarsest discretization, here using a 25 × 5 mesh. Then, a hierarchical, uniform mesh refinement is carried out making 4 elements out of one of the coarsest mesh. The reference solution is obtained for 800 × 160 elements. The microdomain constantly exhibits a discretization of 32 × 32 elements, with $\epsilon = 5$ mm.

Fig. 13 displays the local convergence order of the error in the energy-norm as a contour plot in the macrodomain. Obviously, superconvergence shows up in the macro error of FE-HMM in terms of order two (instead of one according to the error estimates of standard FE-HMM) almost everywhere. A reduced order is observed at the sites of load application and reaction forces; the variations beyond and below order 2 are most pronounced at the clamped end.

Fig. 14 displays the convergence of the error of the stress components σ_{xx} and σ_{xy} as a function of the macroelement size. Component σ_{yy} was discarded for its virtually vanishing magnitude. The convergence order of 2.09 demonstrates superconvergence of stresses at that particular node.

The integral error in the energy-norm is shown in Table 4. Superconvergence is not obtained. Instead we see the standard convergence order of one. The reason for the lost superconvergence is that for the integral error all nodes of the macrodomain are considered. The nodes at the re-entrant corners of the clamped edge exhibit only orders in the range of 0.5, see Fig. 13, which spoils the overall convergence order.

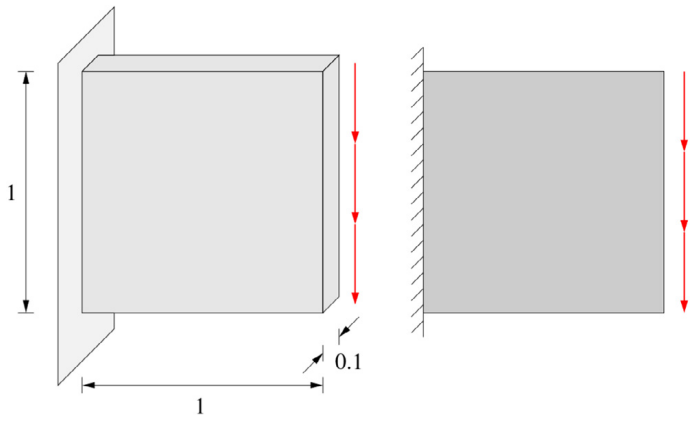


Fig. 15. Square plate for the homogenization of a microstructure endowed with an analytical solution.

5.3. Problem with an analytical solution of the homogenized tensor

The BVP of the present example is a square plate of sidelength $l = 1$ m and thickness $t = 0.1$ m, which is clamped at one edge and loaded by a constant line load of $q_0 = 1$ [N/mm^2] at the opposite edge, see Fig. 15.

The microheterogeneous elasticity tensor is uniformly periodic

$$\mathbb{A}^\epsilon(\boldsymbol{x}) = \begin{bmatrix} A^\epsilon_{11} & 35 & 0 \\ 35 & A^\epsilon_{22} & 0 \\ 0 & 0 & 50 \end{bmatrix} \frac{\mathrm{N}}{\mathrm{m}^2} \qquad \text{with} \quad \begin{aligned} A^\epsilon_{11} &= [500/(5 + 3.5 \cdot \sin(2\pi x_1/\epsilon))] \\ A^\epsilon_{22} &= [500/(5 + 3.5 \cdot \cos(2\pi x_1/\epsilon))] \end{aligned}$$

with components in [N/m^2]. It was used in [5] for heat conduction in a slightly different format.

In contrast to the matrix–inclusion problem, the microheterogeneous tensor exhibits an analytical solution, such that FE-HMM can here be assessed by an exact solution without drawing to an overkill solution.

According to [39] and [43] the exact homogenized tensor $\mathbb{A}^0$ and the exact volumetric mean $\langle \mathbb{A}^\epsilon \rangle$ is given by

$$\mathbb{A}^0 \approx \begin{bmatrix} 100 & 35 & 0 \\ 35 & 140 & 0 \\ 0 & 0 & 50 \end{bmatrix} \frac{\mathrm{N}}{\mathrm{m}^2}, \qquad \langle \mathbb{A}^\epsilon \rangle = \begin{bmatrix} 140 & 35 & 0 \\ 35 & 140 & 0 \\ 0 & 0 & 50 \end{bmatrix} \frac{\mathrm{N}}{\mathrm{m}^2}. \tag{74}$$

The comparison of A^0 with $\langle \mathbb{A}^\epsilon \rangle$ shows that the volumetric mean cannot account for the induced anisotropy due to the laminate character of the microstructure; component $\langle \mathbb{A}^\epsilon_{11} \rangle$ considerably deviates from the exact solution.

5.3.1. Macro- and microconvergence

The simulation results for the macroconvergence are obtained based on a reference solution using 2560 × 2560 macroelements and 32 × 32 microelements. The results are invariant with respect to ϵ.

Fig. 16 (left) displays the total error as a function of the macrodiscretization for a constant microdiscretization. The observed convergence order in the L^2-norm of 1.62 instead of 2, and in the H^1-norm as well as the energy-norm of almost 0.84 instead of 1 are in reasonable agreement with the a priori estimates. The deviation from the theoretical order can be traced back to notch effects at the clamped end.

The convergence of the micro error in the diagram of Fig. 16 (center) for various h/ϵ keeping H fixed confirms the theoretical predictions in quantitative agreement. The reference microsolution is obtained using 50 × 50 macroelements and 2048 × 2048 microelements.

5.3.2. Homogenized elasticity tensor

The obtained results by FE-HMM can capture the exact values of the above elasticity tensors in good agreement. A microdiscretization using 160 × 160 elements yields

$$\mathbb{A}^{0,h} = \begin{bmatrix} 100.0037 & 35 & 0 \\ 35 & 140.0280 & 0 \\ 0 & 0 & 50 \end{bmatrix} \frac{\mathrm{N}}{\mathrm{m}^2}, \qquad \langle \mathbb{A}^\epsilon \rangle^h = \begin{bmatrix} 140.0280 & 35 & 0 \\ 35 & 140.0280 & 0 \\ 0 & 0 & 50 \end{bmatrix} \frac{\mathrm{N}}{\mathrm{m}^2}.$$

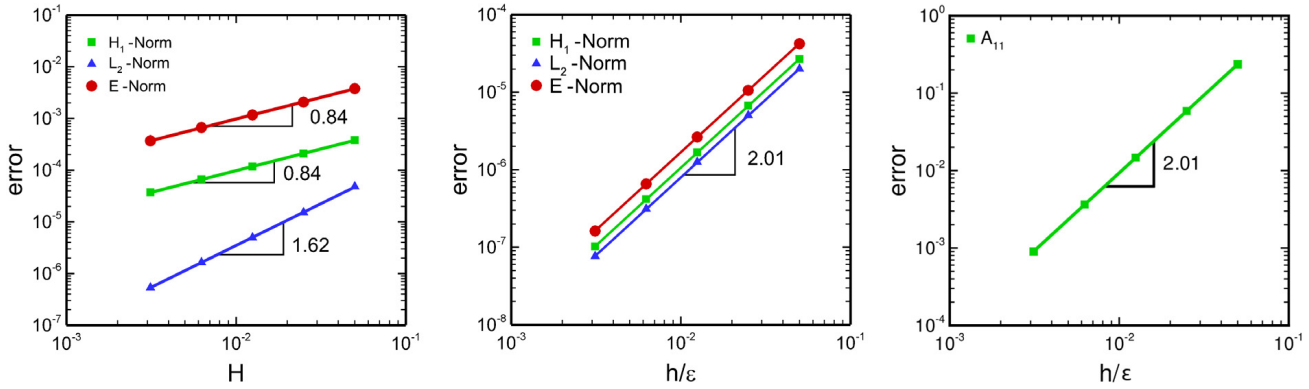


Fig. 16. Microstructure with an analytical solution of homogenization. (left) macroconvergence, microconvergence of (center) the solution, and (right) of component $\mathbb{A}^{0,h}_{11}$ of the homogenized tensor.

The convergence of the components of the approximate homogenized elasticity tensor $\mathbb{A}^{0,h}$ is displayed in the right diagram of Fig. 16. The slope indicates order 2 in agreement with the theory, $|\mathbb{A}^{0,h} - \mathbb{A}^0| \leq C(h/\epsilon)^2$. The reference solution $\mathbb{A}^0$ is obtained on a microdomain with a discretization of 2560 × 2560 elements. Note that component $\mathbb{A}^{0,h}_{22}$ does not change in the leading 9 digits for meshes finer than 40 × 40 elements, the reason, why the diagram in Fig. 16 is restricted to component $\mathbb{A}^{0,h}_{11}$.

5.3.3. *Comparison of FE-HMM with FE²*

Table 5 shows, that FE-HMM and FE² exhibit virtually the same results.

Table 5
Microstructure with an analytical solution of homogenization. Convergence of the standard FE-HMM solution in comparison to the FE-HMM($\mathbb{A}^{0,h}$)/FE² solution and the percentaged deviation from standard FE-HMM.

	Microelements	20 × 20			
	Macroelements	20 × 20	40 × 40	80 × 80	160 × 160
FE-HMM	$\|\boldsymbol{u}\|_\infty$ in 10^{-3}	77.7902	78.3328	78.5746	78.6865
	$\|\boldsymbol{u}\|_A$ in 10^{-3}	81.6746	81.7999	81.8388	81.8510
FE² ≙	$\|\boldsymbol{u}\|_\infty$ in 10^{-3}	77.7902	78.3328	78.5746	78.6865
FE-HMM($\mathbb{A}^{0,h}$)	Deviation	$2.82 \cdot 10^{-13}$	$1.50 \cdot 10^{-13}$	$2.20 \cdot 10^{-13}$	$1.64 \cdot 10^{-11}$
	$\|\boldsymbol{u}\|_A$ in 10^{-3}	81.6746	81.7999	81.8388	81.8510
	Deviation	$1.38 \cdot 10^{-13}$	$1.16 \cdot 10^{-13}$	$1.26 \cdot 10^{-12}$	$8.78 \cdot 10^{-12}$

5.3.4. *Optimal refinement strategies*

The a priori error estimates ($\delta/\epsilon \in \mathbb{N}$ along with periodic coupling) enable an optimal uniform refinement strategy for uniform macro- (H) and micro- (h) meshes, see [6]. For $p = q = 1$ i.e. bilinear shape functions for the macro- as well as on the micro-FE, we obtain

$$\|\boldsymbol{u}^0 - \boldsymbol{u}^H\|_{L^2(\Omega)} \leq C\left(H^2 + \left(\frac{h}{\epsilon}\right)^2\right), \quad \|\boldsymbol{u}^0 - \boldsymbol{u}^H\|_{H^1(\Omega)} \leq C\left(H + \left(\frac{h}{\epsilon}\right)^2\right).$$

We denote by L the number of microelements in each direction of space of the microdomain. Similarly, M is the number of macroelements per direction. Consequently, the microelement size is $h = \epsilon/L$ and it holds $h_L := h/\epsilon = 1/L$ for the micromesh, and $H_M = 1/M$ for the macromesh.

Denoting by N_{mac} the number of macro DOF and by N_{mic} the number of micro DOF, the above rates of convergence show that the following choices are the best uniform refinement strategies that is full order achieved for minimal computational costs.

$$\begin{array}{lll} L^2\text{-norm:} & N_{mic} = N_{mac} & \Longleftrightarrow \quad h_L = H_M \\ H^1\text{-norm:} & N_{mic} = \sqrt{N_{mac}} & \Longleftrightarrow \quad h_L = \sqrt{H_M} \end{array}$$

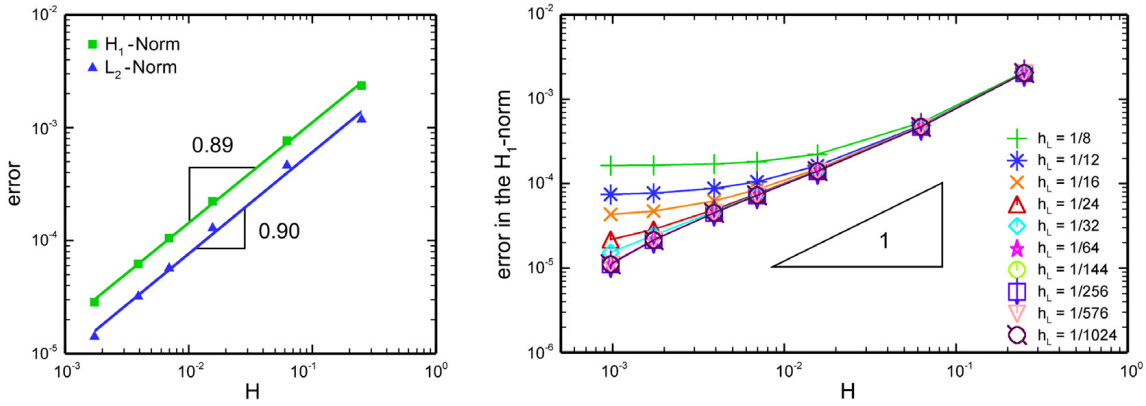


Fig. 17. Optimal and suboptimal refinement strategies for the H^1-error.

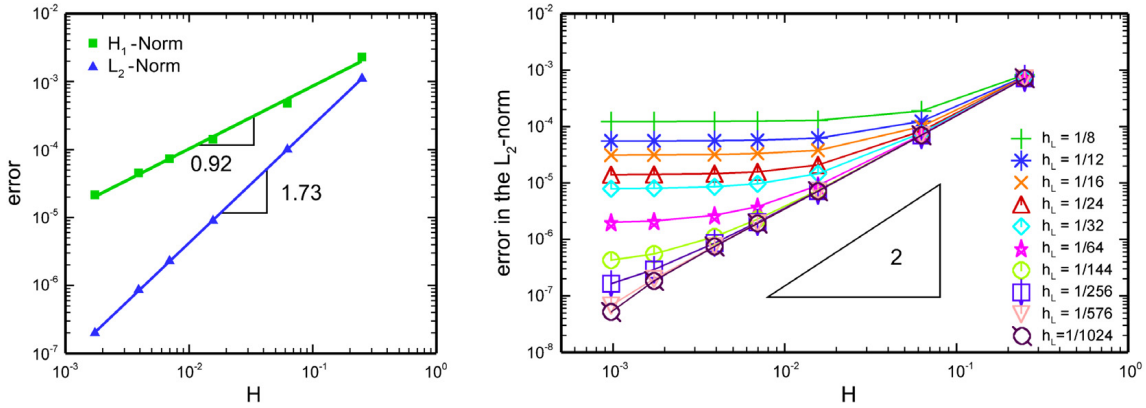


Fig. 18. Optimal and suboptimal refinement strategies for the L^2-error.

We compute the solutions of the problem for uniform macromesh refinement $H_M = 1/8, 1/12, 1/16, \ldots, 1/1024$. In the diagrams of Fig. 17 (right) and Fig. 18 (right) the micromesh is kept fixed for each of the distinct solid lines and is successively refined from one line to the other. Optimal refinements clearly follow the ratio $h_L = H_M$ for the error in the L^2-norm, Fig. 18, and $h_L = \sqrt{H_L}$ for the error in the H^1-norm, Fig. 17. The results demonstrate the sharpness of the a priori bounds. Similar results for piecewise bilinear FE are reported in [6].

5.4. *Non-uniformly periodic tensor*

The present example serves the purpose to analyze FE-HMM for a non-uniformly periodic microstructure, which is given by a Young's modulus of

$$E^{\epsilon} = \frac{1.5 + \sin(2\pi x_1/\epsilon)}{1.5 + \sin(2\pi x_2/\epsilon)} + \frac{1.5 + \sin(2\pi x_2/\epsilon)}{1.5 + \sin(2\pi x_1/\epsilon)} + \sin(4x_1x_2) + 1 \quad [\mathrm{N/m^2}]$$

as displayed for $\epsilon = 0.005$ m in Fig. 19 on the domain $[0, 1]\,\mathrm{m} \times [0, 1]\,\mathrm{m}$, see [5]. The coordinate system is centered in the domain, axes align with the boundaries.

The macro BVP is almost the same as in the previous example of Section 5.3. Only the line load at the free edge is adopted to $q_0 = 0.01$ N/m, since the Young's modulus is significantly smaller than in the previous example.

5.4.1. *Macro- and microconvergence*

The convergence of the macro error for a fixed microdiscretization is displayed in the left diagram of Fig. 20. The corresponding reference solution is obtained by 2560 × 2560 macroelements and 40 × 40 microelements. The

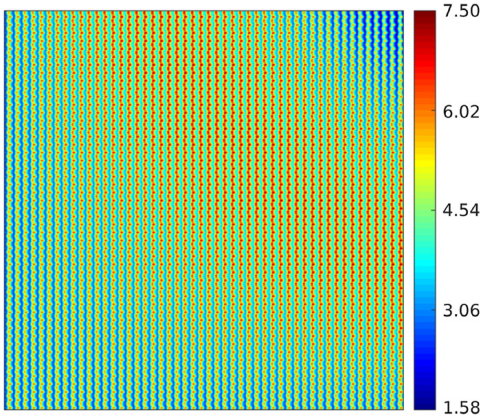


Fig. 19. Young's modulus distribution for a non-uniformly periodic elasticity tensor for $\epsilon = 0.005\,\mathrm{m}$ on a domain $[0, 1]\,\mathrm{m} \times [0, 1]\,\mathrm{m}$.

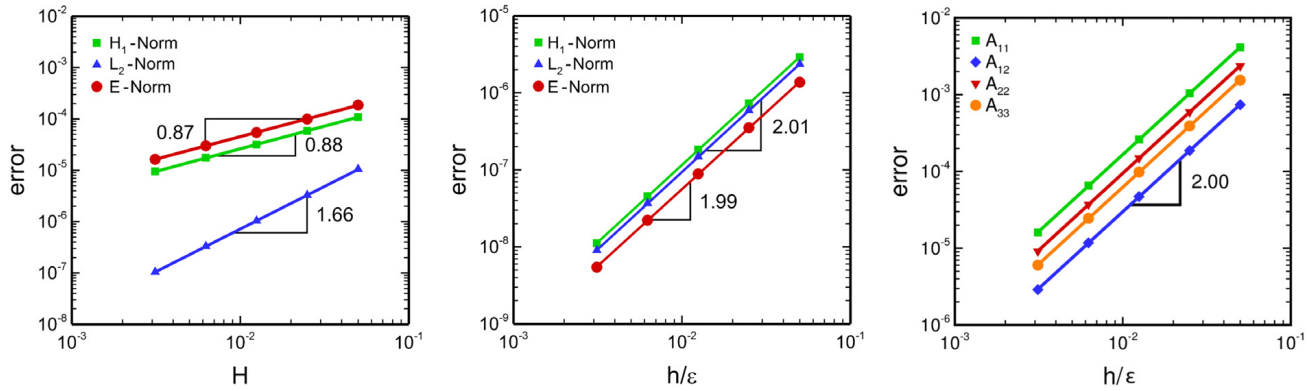


Fig. 20. Non-uniformly periodic tensor; (left) macroconvergence, microconvergence of (center) the solution, and (right) the components of the homogenized tensor $\mathbb{A}^{0,h}$.

convergence order is below the theoretical order in the L^2-norm (1.66 instead of 2), and in the H^1- as well as in the energy-norm (0.88 instead of 1), which is due to the reduced regularity of the macro BVP, compare the results with those in Section 5.3.

The convergence of the micro error for a fixed macrodiscretization is displayed in the center diagram of Fig. 20. Full order of convergence is obtained for the micro error in the L^2-norm and in the H^1-norm, respectively. The reference solution for micro error calculation is obtained by 40×40 macroelements and 2048×2048 microelements.

5.4.2. Homogenized elasticity tensor

Next, we assess the convergence estimate for the components of the approximate homogenized elasticity tensor $\mathbb{A}^{0,h}$. The convergence as a function of the microdiscretization is shown in the right diagram of Fig. 20. The slope indicates order 2 for all components of the elasticity tensor in the plane strain case in perfect agreement with the theory, [6].

5.4.3. Comparison of the FE-HMM variants, and with the FE^2 method

The deviation of the FE-HMM solution based on micro–macrostiffness transfer in comparison with the second version using the homogenized elasticity tensor is throughout less than $4 \cdot 10^{-11}$ and thus in the range of machine precision, see Table 6. Since the latter FE-HMM version coincides with FE^2, the coincidence of FE-HMM and FE^2 is underpinned again by numerical means in the present non-uniformly periodic setting.

Table 6
Non-uniformly periodic tensor. Convergence of the standard FE-HMM solution in comparison to the FE^2 solution along with the percentaged deviation.

	microelements macroelements	20×20 20×20	40×40	80×80	160×160
FE-HMM	$\|\boldsymbol{u}\|_\infty$ in 10^{-3}	20.0246	20.1980	20.2810	20.3214
	$\|\boldsymbol{u}\|_A$ in 10^{-3}	4.15603	4.16176	4.16353	4.16408
$FE^2 \mathrel{\widehat{=}}$ FE-HMM($\mathbb{A}^{0,h}$)	$\|\boldsymbol{u}\|_\infty$ in 10^{-3}	20.0246	20.1980	20.2810	20.3214
	Deviation	$3.79 \cdot 10^{-11}$	$4.47 \cdot 10^{-14}$	$1.41 \cdot 10^{-14}$	$-1.29 \cdot 10^{-13}$
	$\|\boldsymbol{u}\|_A$ in 10^{-3}	4.15603	4.16176	4.16353	4.16408
	Deviation	$2.73 \cdot 10^{-14}$	$2.81 \cdot 10^{-14}$	$-8.33 \cdot 10^{-16}$	$-2.70 \cdot 10^{-13}$

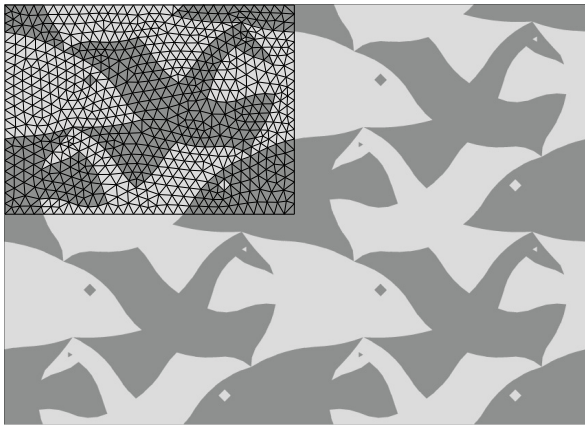


Fig. 21. Escher's periodic Bird and Fish tessellation: (left) the original, (right) RVE and its discretization using triangular elements with $q = 1$.

5.5. Escher's bird and fish tessellation

While Lord Kelvin was concerned with the problem, how to pack equal-sized objects together to fill space with minimal surface area, the graphic artist M.C. Escher (1898–1972) was devoted to the question, how to fill the plane by tessellations[5] with most intriguing beauty.

While from 1887 until 1993 the tetrakaidecahedron was continuously but erroneously believed[6] to be the right answer of Kelvin to his minimization problem, the answer to Escher's question is simple in that it is clearly non-unique at any time, as beauty is in the eye of the beholder.[7]

It is a well-known mathematical result that of all the regular polygons, only the triangle, square, and hexagon can be used for a tessellation. Escher combined them applying reflections, glide reflections, translations, and rotations to augment his playground for creating a larger variety of tessellations.

From Escher's oeuvre in the field which he called "regular divisions of the plane" we devote our analysis to the "Bird/Fish (1941 B)" tessellation, an artistic artifact that is uniformly periodic and consists of two phases, Fig. 21. Here we choose $\delta = \varepsilon = 28.5$ mm. The macroscopic BVP is the same as in Section 5.1, and the Poisson's ratio and Young's moduli exhibit the same values, thus showing a contrast of the bright face to the dark face of $E_b/E_d = 2.5$.

5.5.1. Macro and microconvergence

Fig. 22 shows in its left diagram the convergence of the normed error for macroscopic mesh refinement for a reference solution of 4 096 000 DOFs (3200×640 macroelements) and with 1462 DOFs on each microdomain. Similarly, Fig. 22 shows in its right diagram the convergence of the normed errors for microscopic mesh refinement

[5] Tessellations are arrangements of closed shapes that completely cover the plane without overlapping and without leaving gaps.

[6] The so-called Weaire–Phelan structure was shown in 1993 to solve the Kelvin problem with even smaller surface area.

[7] *"At moments of great enthusiasm it seems to me that no one in the world has ever made something this beautiful and important"*—M.C. Escher.

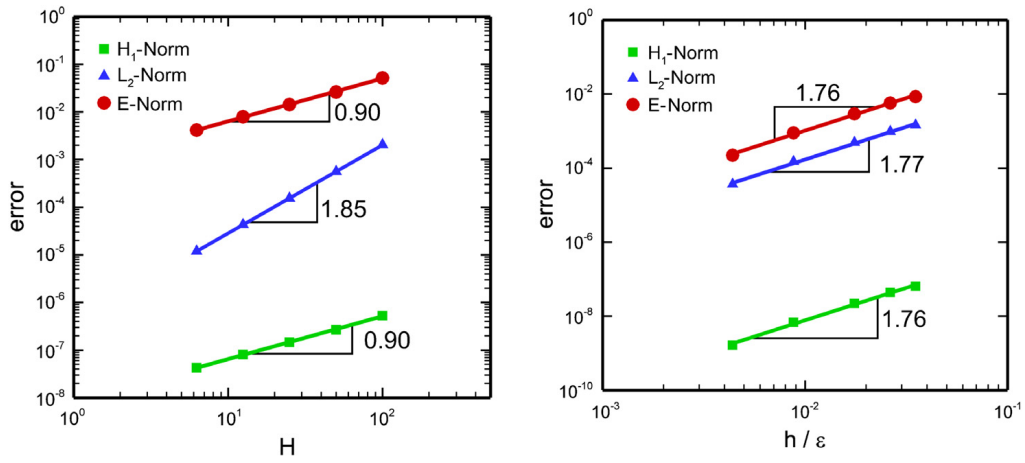


Fig. 22. Escher's periodic Bird/Fish tessellation. (Left:) Macroconvergence, (right:) microconvergence.

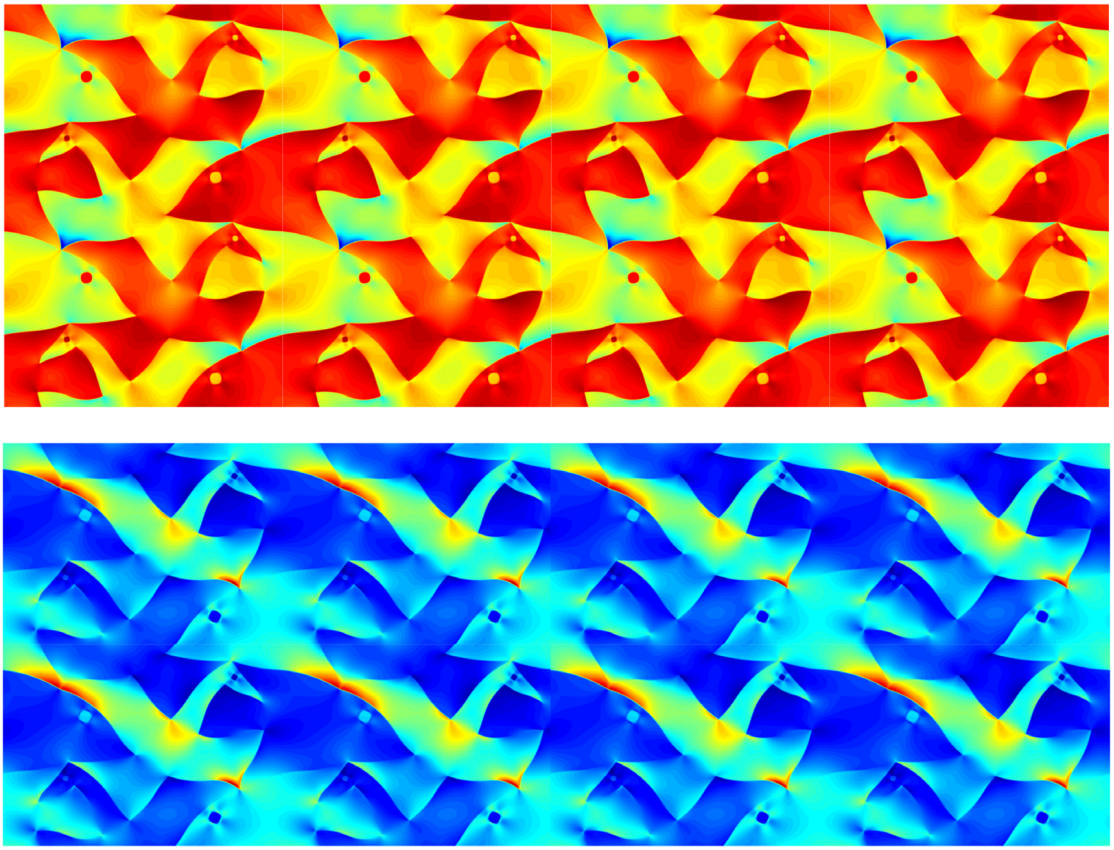


Fig. 23. Escher's periodic Bird and Fish tessellation. Contour plot of (top:) shear strain γ_{xy} and of (bottom) von-Mises stress at the macro-quadrature point ($x = 4978.9$ mm, $y = 978.9$ mm).

for a reference solution of 16 000 DOFs on the macrodomain (200 × 40 macroelements) and 312 506 DOFs on each microdomain.

The convergence rates for $p = q = 1$ reasonably agree with the theoretical values. The deviations are in the reduced regularity of the problem sets on the two scales.

At the end, we abstain from homogenizing (the elasticities of) bird and fish and discover the microscale simulation results displayed in Fig. 23.

6. Summary

The novel contributions and main results shall be summarized.

1. Based on the seminal contributions of E, Engquist and Abdulle we have presented an FE-HMM formulation for linear elasticity in a geometrical linear frame. For this case of a vector-valued field problem we have generalized the FE-HMM micro-to-macrostiffness transfer by deriving corresponding transformation matrices which follow from macroelement unit displacement states and result in energy minimizers. By virtue of the present setting in solid mechanics, a clear mechanical interpretation of FE-HMM as an energy-based homogenization scheme is facilitated. Moreover, this setting opens the door to a conceptual and numerical comparison with other two-scale finite element homogenization concepts.
2. A conceptual comparison of the FE-HMM with the FE^2 method was presented; they both have in common the equivalence of micro-with macroenergy densities; it was shown that for periodic boundary conditions the macro-homogeneity condition of Hill–Mandel as the theoretical cornerstone of FE^2 can be derived from asymptotic homogenization as the theoretical foundation of FE-HMM, which is the deepest common root of the two methods. FE^2 in its micro-to-macrostiffness transfer draws on the homogenized fourth order constitutive tensor while keeping the macroscopic bilinear form unaltered. FE-HMM however crucially relies on a modified quadrature formula in the macroscopic bilinear form, which results in a micro-to-macrostiffness matrix transfer, a setting which enables the a priori error analysis. For that reason the stiffness matrix transfer is a key ingredient of FE-HMM. The homogenized elasticity tensor –coinciding with the one of FE^2 – must be seen as a byproduct. The existence of a priori estimates is the particular strength and key novel contribution of FE-HMM to the field of numerical homogenization in general, and in particular to two-scale finite element methods like FE^2. Here, FE-HMM and its protagonists, W. E, B. Engquist, A. Abdulle and coworkers have brought mathematical rigor into the fully discrete analysis of two-scale finite element methods for homogenization. For FE^2 methods, in spite of their considerable progress in a multitude of applications, a thorough mathematical analysis is missing.
3. In representative benchmark problems FE-HMM has been assessed for periodic boundary conditions imposed on the microdomains. Here we checked in various norms the a priori error estimates as given in [40] for the general case of elliptic PDEs and for linear elasticity in [13]. For sufficient regularity of the BVP, the estimates have been verified for both the macro error and the micro error and for the coefficients of the homogenized elasticity tensor.

   Remarkably, superconvergence holds for the micro error in FE-HMM in that stress and strain (and equally the error in the energy-norm and in the H^1-norm) converges in the same order as displacements (and equally the error in the L^2-norm). In contrast to the notion of superconvergence in standard, single-scale finite element methods, which holds only at particular points for particular element shapes, the verified estimates for the micro error are generally valid. We have demonstrated by the application of the Superconvergent Patch Recovery (SPR) technique, that for the macro error in FE-HMM standard superconvergence holds at the so-called Barlow points.

   Moreover, the existing predictions for FE-HMM concerning the optimal uniform micro–macro refinement strategies on how to obtain full order for minimal computational costs are corroborated by the numerical results in the present work.
4. Furthermore, the simulations have shown quantitative agreement of the two FE-HMM variants with FE^2. Of course, for the coincidence of the two methods in practice, FE-HMM findings equally apply for the FE^2 method with respect to (i) the micro and macroconvergence orders including superconvergence and with respect to (ii) the derived optimal uniform micro–macromesh refinement strategies.

In conclusion, the present work shall contribute to bridge the still existing gap between the mathematics of multiscale modeling with FE-HMM as an excellent example, and, on the other hand, the engineering community, in which the popular FE^2 method has been growing into different branches of solid mechanics by virtue of its versatility. Here, FE-HMM as a non-standard discretization method, which is endowed with a fully-fledged mathematical structure at least for the linear case, advances numerical homogenization more than by an ϵ towards reliability as a key ingredient of scientific computations.

Acknowledgment

The first author acknowledges support by the Deutsche Forschungsgemeinschaft (DFG) within the Heisenberg program (grant no. EI 453/2-1). Simulations were performed with computing resources granted by RWTH Aachen University under project ID prep0005.

Appendix. Mathematical basis of FE-HMM

A.1. Asymptotic homogenization

This part presents the derivation and main results of asymptotic homogenization for linearized elasticity. It is a main reference point to underpin the mathematical basis of FE-HMM. For mathematical homogenization by asymptotic expansion we refer to [36–39].

In the two-scale mathematical homogenization theory, various fields are assumed to depend on two coordinates, $\boldsymbol{x}$ as the coarse- or macroscale position vector, and $\boldsymbol{y}$ as the fine- or microscale position vector. These two vectors are related by $\boldsymbol{y} = \boldsymbol{x}/\epsilon$ with $0 < \epsilon \ll 1$.

The unit cell domain Y is typically chosen a rectangular domain, in which the microstructure is assumed to be locally periodic (Y-periodic). Even if the microstructure is not periodic, the response functions $\boldsymbol{r}^\epsilon$ are in either case assumed to be locally periodic.

In addition to the symmetries introduced in Section 2.1.1 we assume for $\mathbb{A}^\epsilon_{ijlm}$

$$\mathbb{A}^\epsilon_{ijlm}(\boldsymbol{x}) = \mathbb{A}_{ijlm}\left(\frac{\boldsymbol{x}}{\epsilon}\right) = \mathbb{A}_{ijlm}(\boldsymbol{y}) \text{ is } Y\text{-periodic for any } i, j, l, m = 1, \dots, d. \tag{A.1}$$

The derivative of a response function $\boldsymbol{r}^\epsilon(\boldsymbol{x})$ with respect to the macroscale variable x_i can be calculated by the chain rule according to

$$\frac{d}{dx_i} = \frac{\partial}{\partial x_i} + \frac{1}{\epsilon}\frac{\partial}{\partial y_i}\,. \tag{A.2}$$

For the case of linear elasticity we consider the yet unknown response functions $\boldsymbol{u}^\epsilon$, $\varepsilon^\epsilon_{ij}$, σ^ϵ_{ij} and their expansions into series

$$u^\epsilon_i(\boldsymbol{x},\boldsymbol{y}) = u^0_i(\boldsymbol{x}) + \epsilon\, u^1_i(\boldsymbol{x},\boldsymbol{y}) + \epsilon^2\, u^2_i(\boldsymbol{x},\boldsymbol{y}) + \mathcal{O}(\epsilon^3) \tag{A.3}$$

$$\varepsilon^\epsilon_{ij}(\boldsymbol{x},\boldsymbol{y}) = \frac{1}{\epsilon}\,\varepsilon^{-1}_{ij}(\boldsymbol{x},\boldsymbol{y}) + \varepsilon^0_{ij}(\boldsymbol{x},\boldsymbol{y}) + \epsilon\,\varepsilon^1_{ij}(\boldsymbol{x},\boldsymbol{y}) + \mathcal{O}(\epsilon^2) \tag{A.4}$$

$$\sigma^\epsilon_{ij}(\boldsymbol{x},\boldsymbol{y}) = \frac{1}{\epsilon}\,\sigma^{-1}_{ij}(\boldsymbol{x},\boldsymbol{y}) + \sigma^0_{ij}(\boldsymbol{x},\boldsymbol{y}) + \epsilon\,\sigma^1_{ij}(\boldsymbol{x},\boldsymbol{y}) + \mathcal{O}(\epsilon^2)\,. \tag{A.5}$$

The strain expansion (A.4) is obtained by inserting the expansion for $u^\epsilon_i(\boldsymbol{x})$ into (2) with an account of (A.2) and with the following nomenclature for the strain components of various "orders"

$$\varepsilon^{-1}_{ij} = u^0_{(ij)y}\,, \qquad \varepsilon^s_{ij} = u^s_{(ij)x} + u^{s+1}_{(ij)y} \quad \text{for } s = 0, 1, \dots \tag{A.6}$$

where the abbreviation $u^k_{(ij)y} = 1/2(\partial u^k_i/\partial y_j + \partial u^k_j/\partial y_i)$ (and analogously for $u^k_{(ij)x}$) is employed. For each scale an elasticity relation is assumed to hold

$$\sigma^s_{ij}(\boldsymbol{x},\boldsymbol{y}) = \mathbb{A}^\epsilon_{ijkl}(\boldsymbol{x})\,\varepsilon^s_{kl}(\boldsymbol{x},\boldsymbol{y}) \quad \text{for } s = -1, 0, 1, \dots\,. \tag{A.7}$$

Inserting (A.5) into the balance of linear momentum $(1)_1$ yields

$$\frac{1}{\epsilon^2}\frac{\partial \sigma^{-1}_{ij}}{\partial y_j} + \frac{1}{\epsilon}\left(\frac{\partial \sigma^{-1}_{ij}}{\partial x_j} + \frac{\partial \sigma^0_{ij}}{\partial y_j}\right) + \left(\frac{\partial \sigma^0_{ij}}{\partial x_j} + \frac{\partial \sigma^1_{ij}}{\partial y_j} + f_i\right) + \mathcal{O}(\epsilon) = 0\,, \tag{A.8}$$

from which, according to the order, different balance equations follow (by multiplying (A.8) by ϵ^n and considering the limit $\epsilon \to 0^+$, each for $n = 2, 1, 0$)

$$\mathcal{O}\left(\epsilon^{-2}\right): \quad \frac{\partial \sigma^{-1}_{ij}}{\partial y_j} = 0 \tag{A.9}$$

$$\mathcal{O}\left(\epsilon^{-1}\right): \quad \frac{\partial \sigma_{ij}^{-1}}{\partial x_j} + \frac{\partial \sigma_{ij}^{0}}{\partial y_j} = 0 \tag{A.10}$$

$$\mathcal{O}(1): \quad \frac{\partial \sigma_{ij}^{0}}{\partial x_j} + \frac{\partial \sigma_{ij}^{1}}{\partial y_j} + f_i = 0\,. \tag{A.11}$$

For the Dirichlet and Neumann boundary conditions $(1)_{2,3}$ we obtain by (A.3) and (A.5)

$$u_i^0 + \epsilon\, u_i^1 + \epsilon^2\, u_i^2 + \mathcal{O}(\epsilon^3) = \bar{u}_i \qquad \text{on} \quad \partial\mathcal{B}_D \tag{A.12}$$

$$\left[\frac{1}{\epsilon}\,\sigma_{ij}^{-1} + \sigma_{ij}^{0} + \epsilon\,\sigma_{ij}^{1} + \mathcal{O}(\epsilon^2)\right] n_j = \bar{t}_i \qquad \text{on} \quad \partial\mathcal{B}_N\,. \tag{A.13}$$

The boundary conditions for various orders of ϵ are identified from (A.12) and (A.13) according to

$$\left.\begin{array}{l} \mathcal{O}(1): \quad u_i^0 = \bar{u}_i \\ \mathcal{O}\left(\epsilon^n\right): \quad u_i^n = 0\,,\, n \in \mathbb{N} \end{array}\right\} \quad \text{on} \quad \partial\mathcal{B}_D\,, \tag{A.14}$$

$$\left.\begin{array}{l} \mathcal{O}(1): \quad \sigma_{ij}^0 n_j = \bar{t}_i \\ \mathcal{O}\left(\epsilon^n\right): \quad \sigma_{ij}^n = 0\,,\, n = -1, 1, 2, \ldots \end{array}\right\} \quad \text{on} \quad \partial\mathcal{B}_N\,. \tag{A.15}$$

It can be shown, that $\partial u_i^0/\partial y_j = 0$, which implies $\boldsymbol{u}^0 = \boldsymbol{u}(\boldsymbol{x})$ as already anticipated in (A.3), and moreover, that $\sigma_{ij}^{-1} = 0$. Thus, the first term in the expansion of $\boldsymbol{u}^\epsilon$, i.e. $\boldsymbol{u}^0$, is the coarse-scale/macroscale displacement field, and according to $(A.14)_1$ and $(A.15)_1$ the Dirichlet as well as Neumann boundary conditions (A.12), (A.13) refer to the macroproblem.

For $\sigma_{ij}^{-1} = 0$ it follows from the $\mathcal{O}\left(\epsilon^{-1}\right)$ equilibrium, (A.10), that

$$\frac{\partial \sigma_{ij}^{0}}{\partial y_j} = 0\,, \tag{A.16}$$

which yields along with the kinematical relations $(A.6)_2$ and the elastic constitutive law (A.7) for $s = 0$

$$\frac{\partial}{\partial y_j}\Big[\mathbb{A}_{ijkh}^{\epsilon} \underbrace{\left(u_{(kh)x}^0 + u_{(kh)y}^1\right)}_{\varepsilon_{kh}^0}\Big] = 0\,. \tag{A.17}$$

A separation of variables $\boldsymbol{x}$ and $\boldsymbol{y}$ in (A.17) is achieved by the ansatz

$$u_k^1(\boldsymbol{x}, \boldsymbol{y}) = \chi_k^{lm}(\boldsymbol{y})\, u_{(lm)x}^0\,, \tag{A.18}$$

where $\chi_k^{lm}(\boldsymbol{y})$ is the so-called first-order displacement influence function, which is locally periodic (Y-periodic) and symmetric $\chi_k^{lm}(\boldsymbol{y}) = \chi_k^{ml}(\boldsymbol{y})$. Inserting (A.18) into (A.17) along with the identity $u_{(kh)x}^0 = \mathbb{I}_{khlm} u_{(lm)x}^0$ where $\mathbb{I}_{khlm} = 1/2\,(\delta_{kl}\delta_{hm} + \delta_{km}\delta_{hl})$ results in

$$\frac{\partial}{\partial y_j}\left[\mathbb{A}_{ijkh}^{\epsilon}\left(\mathbb{I}_{khlm} + \frac{\partial \chi_k^{lm}(\boldsymbol{y})}{\partial y_h}\right)\right] u_{(kh)x}^0 = 0\,, \tag{A.19}$$

which must hold for arbitrary macrostrain $u_{(kh)x}^0$ leading to the cell problem, which reads:

Find for any $l, m \in \{1, \ldots, d\}$ the functions $\chi_k^{lm}(\boldsymbol{y})$ as the solutions of the system

$$\left.\begin{array}{l} -\dfrac{\partial}{\partial y_j}\left(\mathbb{A}_{ijkh}^{\epsilon}\dfrac{\partial \chi_k^{lm}(\boldsymbol{y})}{\partial y_h}\right) = \dfrac{\partial \mathbb{A}_{ijlm}^{\epsilon}}{\partial y_j} \qquad \text{in } Y,\ i = 1, \ldots, d\,, \\ \chi_k^{lm} \text{ is } Y\text{-periodic}\,. \end{array}\right\} \tag{A.20}$$

Since the field χ_k^{lm} enters the cell problem by $\nabla_y \boldsymbol{\chi}^{lm}$, it is determined up to a constant vector. For definiteness, however, uniqueness can be achieved by imposing the normalization condition

$$\int_Y \chi_k^{lm}(\boldsymbol{y})\, d\boldsymbol{y} = 0\,. \tag{A.21}$$

It can be shown, that if (A.21) holds, the microstrain can be calculated from macrostrain by means of an elastic strain influence function $E^{mn}_{kl}(\boldsymbol{y})$

$$\varepsilon^0_{kl} = E^{mn}_{kl}(\boldsymbol{y})\, \boldsymbol{u}^0_{(mn)x}(\boldsymbol{x}) := \varepsilon_{kl}(\boldsymbol{x}, \boldsymbol{y}) \tag{A.22}$$

with

$$E^{mn}_{kl}(\boldsymbol{y}) = \mathbb{I}_{klmn} + \frac{\partial \chi^{mn}_k(\boldsymbol{y})}{\partial y_l} \tag{A.23}$$

thereby realizing a separation of variables similar to (A.18).

With an eye towards the representation of the microproblem in the discrete case of FE-HMM we prefer to rewrite the cell problem (A.20) as

$$\frac{\partial}{\partial y_j}\left(\mathbb{A}^{\epsilon}_{ijkh}\, \varepsilon_{kh}(\boldsymbol{\chi}^{lm} + \boldsymbol{I}^{lm})\right) = 0\,. \tag{A.24}$$

In (A.24) $\boldsymbol{I}^{lm}$ is a vector-valued function given by

$$I^{lm}_k(y) = y_m \delta_{kl}, \quad \delta_{kl} \text{ is the Kronecker symbol.} \tag{A.25}$$

The weak form of the cell problem in the format of (A.24) reads

$$\int_Y \mathbb{A}^{\epsilon}_{ijkh}(\boldsymbol{y})\, \varepsilon_{kh}(\boldsymbol{\chi}^{lm} + \boldsymbol{I}^{lm}) : \varepsilon_{ij}(\boldsymbol{w})\, d\boldsymbol{y} = 0\,, \qquad \boldsymbol{w} \in \mathcal{W}_{per}(Y)\,, \tag{A.26}$$

where $\mathcal{W}_{per}$ is given by

$$\mathcal{W}_{per}(Y) = \left\{ \boldsymbol{w};\, \boldsymbol{w} \in H^1_{per}(Y)^d\,;\ \int_Y w_i\, d\boldsymbol{y} = 0\,,\ i = 1, \ldots, d \right\}. \tag{A.27}$$

Averaging the microscale elasticity law, i.e. (A.7) for $s = 0$, $\sigma^0_{ij} = \mathbb{A}^{\epsilon}_{ijkh}\left(u^0_{(kh)x} + u^1_{(kh)y}\right)$ with an account of (A.18) leads to

$$\langle \sigma^0_{ij} \rangle = \mathbb{A}^0_{ijkh}\, \varepsilon^0_{kh} \tag{A.28}$$

where $\langle \sigma^0_{ij} \rangle = 1/|Y| \int_Y \sigma^0_{ij}(\boldsymbol{x}, \boldsymbol{y})\, d\boldsymbol{y}$ and where the homogenized tensor $\mathbb{A}^0(\boldsymbol{x}) = (\mathbb{A}^0_{ijkl})$ is identified as

$$\mathbb{A}^0_{ijlm} = \frac{1}{|Y|}\int_Y \mathbb{A}^{\epsilon}_{ijlm}(\boldsymbol{y}) + \mathbb{A}^{\epsilon}_{ijkh}(\boldsymbol{y}) \frac{\partial \chi^{lm}_k(\boldsymbol{y})}{\partial y_h}\, d\boldsymbol{y}\,, \tag{A.29}$$

which equally verifies the above symmetries of elasticity.

Integration the second term in (A.11) over the unit cell domain yields

$$\frac{1}{|Y|}\int_Y \frac{\partial \sigma^1_{ij}}{\partial y_j} d\boldsymbol{y} = \frac{1}{|Y|}\int_{\partial \mathcal{B}} \sigma^1_{ij}\, n_j\, dA = 0\,. \tag{A.30}$$

With (A.30), the boundary conditions $(A.14)_1$ and $(A.15)_1$, integration of the $\mathcal{O}(1)$ balance equation (A.11) over the unit cell results in the macroscopic BVP

$$\left.\begin{aligned} -\frac{\partial}{\partial x_j}\left(\langle \sigma^0_{ij} \rangle\right) &= \langle f_i \rangle && \text{in} \quad \mathcal{B} \\ u^0_i &= \langle \bar{u}_i \rangle_{\Gamma} && \text{on} \quad \partial\mathcal{B}_D \\ \langle \sigma^0_{ij} \rangle\, n_j &= \langle \bar{t}_i \rangle_{\Gamma} && \text{on} \quad \partial\mathcal{B}_N \end{aligned}\right\}. \tag{A.31}$$

In $(A.31)_1$ $\langle f_i \rangle$ is defined as the volume average of f_i, $\langle \boldsymbol{f}(\boldsymbol{x}) \rangle = 1/|Y| \int_Y \boldsymbol{f}(\boldsymbol{x}, \boldsymbol{y})\, d\boldsymbol{y}$. In $(A.31)_{2,3}$ $\langle \bullet \rangle_{\Gamma}$ defines a surface average according to

$$\langle \bar{u}_i \rangle_{\Gamma} := \frac{1}{|\Gamma_D|}\int_{\Gamma_D} \bar{u}_i\, dA\,, \qquad \langle \bar{t}_i \rangle_{\Gamma} := \frac{1}{|\Gamma_N|}\int_{\Gamma_N} \bar{t}_i\, dA\,, \tag{A.32}$$

where Γ is that particular surface area ($\Gamma \in \partial\mathcal{B}$) to which the averaging is applied. Hence, $\langle \bullet \rangle_{\Gamma}$ is the surface counterpart to the volume average $\langle \sigma^0_{ij} \rangle$.

Remarks. Three remarks are in order. First, that $\boldsymbol{I}^{lm}$ is to be understood as a displacement vector which induces by its definition a unitary strain $\boldsymbol{\varepsilon}(\boldsymbol{I}^{lm})$ with components $\varepsilon_{ij}^{lm} = 1/2(\partial I_i^{lm}/\partial y_j + \partial I_j^{lm}/\partial y_i)$. The corresponding strain vectors in Voigt notation read

$$\begin{array}{lll} \boldsymbol{\varepsilon}^{11} = (1,0,0,0,0,0)^T & \boldsymbol{\varepsilon}^{22} = (0,1,0,0,0,0)^T & \boldsymbol{\varepsilon}^{33} = (0,0,1,0,0,0)^T \\ \boldsymbol{\varepsilon}^{12} = (0,0,0,1,0,0)^T & \boldsymbol{\varepsilon}^{13} = (0,0,0,0,1,0)^T & \boldsymbol{\varepsilon}^{23} = (0,0,0,0,0,1)^T \end{array}$$

where $\boldsymbol{\varepsilon}^{lm} = (\varepsilon_{11}^{lm}, \varepsilon_{22}^{lm}, \varepsilon_{33}^{lm}, 2\varepsilon_{12}^{lm}, 2\varepsilon_{13}^{lm}, 2\varepsilon_{23}^{lm})^T$, [65]. In analogy to the homogenization of a second order PDE for a scalar-valued field problem, [13], $(\boldsymbol{\varepsilon}^{lm})_{l,m=1}^{d}$ is the canonical basis of the symmetric, six-dimensional strain space.

Second, introducing with $\boldsymbol{U}^{lm} := \boldsymbol{\chi}^{lm} + \boldsymbol{I}^{lm}$ the superposition of the Y-periodic fluctuations with the (prescribed) displacement field that induces a unitary, homogeneous strain on the cell, it follows for (A.29)

$$\mathbb{A}_{ijlm}^0 = \frac{1}{|Y|}\int_Y \mathbb{A}_{ijlm}^{\epsilon} + \mathbb{A}_{ijkh}^{\epsilon}\frac{\partial \chi_k^{lm}}{\partial y_h}\,d\boldsymbol{y} \tag{A.33}$$

$$= \frac{1}{|Y|}\int_Y \mathbb{A}_{ijlm}^{\epsilon} + \mathbb{A}_{ijkh}^{\epsilon}\,\varepsilon_{kh}(\boldsymbol{\chi}^{lm})\,d\boldsymbol{y} \tag{A.34}$$

$$= \frac{1}{|Y|}\int_Y \mathbb{A}_{ijlm}^{\epsilon} + \mathbb{A}_{ijkh}^{\epsilon}\,\varepsilon_{kh}(\boldsymbol{U}^{lm} - \boldsymbol{I}^{lm})\,d\boldsymbol{y} \tag{A.35}$$

$$= \frac{1}{|Y|}\int_Y \mathbb{A}_{ijkh}^{\epsilon}\,\varepsilon_{kh}(\boldsymbol{U}^{lm})\,d\boldsymbol{y} = \frac{1}{|Y|}\int_Y \sigma_{ij}^0(\boldsymbol{U}^{lm})\,d\boldsymbol{y}\,. \tag{A.36}$$

Hence, component $\mathbb{A}_{ijlm}^0$ of the homogenized elasticity tensor equals the averaged microstress for the solution $\boldsymbol{U}^{lm}$ of the cell problem.

Third, a note on notation. As indicated by its three indices χ_k^{lm} is a third order tensor; in (A.19) for example, the partial derivative of χ_k^{lm} with respect to y_h yields a fourth order tensor, which is in dimensional consistency with the fourth order unity tensor in (A.19). In (A.24) however, $\boldsymbol{\chi}^{lm}$ as well as $\boldsymbol{I}^{lm}$ are to be understood as vector-valued functions, where the superscripts lm are frozen, and only one index is active. Then the calculation of strain from a displacement field as e.g. in (A.24) is a reasonable operation. Hence, the change in notation shall reflect this characteristics.

A.2. General convergence

From homogenization theory the following convergence results and estimates are known.

1. The microdisplacements $\boldsymbol{u}^{\epsilon}$, solution of (1), converge for $\epsilon \to 0$ – usually in a weak sense –to $\boldsymbol{u}^0$, the solution of the homogenized problem (7), see [39], Sec.10. For the corresponding strong error estimate it holds

$$\|\boldsymbol{u}^{\epsilon} - \boldsymbol{u}^0\|_{L^2(\mathcal{B})} \leq C\epsilon\,. \tag{A.37}$$

2. Due to the oscillations of the fine scale solution, strong error estimates in the H^1-norm can usually not be obtained since the gradients of the oscillations are in general not $\mathcal{O}(\epsilon)$ quantities. The homogenized solution requires a correction through information of the fine scale. This can be done defining the corrector given by

$$\boldsymbol{u}^1(\boldsymbol{x}, \boldsymbol{x}/\epsilon) = \sum_{j=1}^{d} \omega^l(\boldsymbol{x}, \boldsymbol{x}/\epsilon)\frac{\partial \boldsymbol{u}^0(x)}{\partial x_j}\,, \tag{A.38}$$

where ω^l is a $d \times d$ matrix given by $\omega^l = (\omega_{km}^l)_{1\leq k,m\leq d} = \left(\chi_k^{lm}\right)_{1\leq k,m\leq d}$, and where $\boldsymbol{\chi}^{lm}(\boldsymbol{x}, \boldsymbol{x}/\epsilon)$ is the solution of the cell problem. With this correction an error estimate in the H^1-norm can be obtained

$$\|\boldsymbol{u}^{\epsilon} - (\boldsymbol{u}^0 + \epsilon\,\boldsymbol{u}^1(\boldsymbol{x}, \boldsymbol{x}/\epsilon))\|_{H^1(\mathcal{B})} \leq C\sqrt{\epsilon}\,, \tag{A.39}$$

where a boundary layer term yields a $\sqrt{\epsilon}$ instead of a ε convergence rate, for a thorough analysis see [39], Sec. 4.1.

Appendix B. Supplementary Material

Supplementary material related to this article can be found online at http://dx.doi.org/10.1016/j.cma.2017.10.001.

References

[1] W. E, B. Engquist, The heterogeneous multi-scale methods, Commun. Math. Sci. 1 (2003) 87–132.
[2] X. Li, W. E, Multiscale modeling of the dynamics of solids at finite temperature, J. Mech. Phys. Solids 53 (2005) 1650–1685.
[3] W. E, B. Engquist, X. Li, W. Ren, E. Vanden-Eijnden, Heterogeneous multiscale methods: A review, Commun. Comput. Phys. 2 (2007) 367–450.
[4] A. Abdulle, C. Schwab, Heterogeneous multiscale FEM for diffusion problems on rough surfaces, Multiscale Model. Simul. 3 (1) (2005) 195–220.
[5] A. Abdulle, A. Nonnenmacher, A short and versatile finite element multiscale code for homogenization problems, Comput. Methods Appl. Mech. Engrg. 198 (2009) 2839–2859.
[6] A. Abdulle, The finite element heterogeneous multiscale method: a computational strategy for multiscale PDEs, GAKUTO Internat. Ser. Math. Sci. Appl. 31 (2009) 133–181.
[7] A. Abdulle, S. Attinger, in: I. Lirkov, S. Margenov, J. Waśasniewski (Eds.), Numerical Methods for Transport Problems in Microdevices, in: Lecture Notes in Computer Science, vol. 3743, Springer-Verlag, Berlin Heidelberg, 2006, pp. 67–75.
[8] W. E, B. Engquist, Z. Huang, Heterogeneous multiscale method: A general methodology for multiscale modeling, Phys. Rev. B: Condens. Matter 67 (2003) 092101.
[9] A. Abdulle, W. E, B. Engquist, E. Vanden-Eijnden, The heterogeneous multiscale method, Acta Numer. 466 (2012) 1–87.
[10] T. Hou, X. Wu, A multiscale finite element method for elliptic problems in composite materials and porous media, J. Comput. Phys. 134 (1997) 169–189.
[11] T. Hou, X. Wu, Z. Cai, Convergence of a multiscale finite element method for elliptic problems with rapidly oscillating coefficients, Math. Comp. 68 (1999) 913–943.
[12] P. Ming, X. Yue, Numerical methods for multiscale elliptic problems, J. Comput. Phys. 214 (2006) 421–445.
[13] A. Abdulle, Analysis of the heterogeneous multiscale FEM for problems in elasticity, Math. Models Methods Appl. Sci. 16 (4) (2006) 615–635.
[14] J.M. Guedes, N. Kikuchi, Preprocessing and postprocessing for materials based on the homogenization method with adaptive finite element methods, Comput. Methods Appl. Mech. Engrg. 83 (1990) 143–198.
[15] J.C. Michel, H. Moulinec, P. Suquet, Effective properties of composite materials with periodic microstructure: a computational approach, Comput. Methods Appl. Mech. Engrg. 172 (1999) 109–143.
[16] C. Miehe, J. Schröder, J. Schotte, Computational homogenization analysis in finite plasticity Simulation of texture development in polycrystalline materials, Comput. Methods Appl. Mech. Engrg. 171 (1999) 387–418.
[17] C. Miehe, J. Schotte, J. Schröder, Computational homogenization analysis in finite plasticity Simulation of texture development in polycrystalline materials, Comput. Mater. Sci. 16 (1–4) (1999) 372–382.
[18] J. Fish, Q. Yu, K. Shek, Computational damage mechanics for composite materials based on mathematical homogenization, Internat. J. Numer. Methods Engrg. 45 (1999) 1657–1679.
[19] F. Feyel, J.L. Chaboche, FE2 multiscale approach for modelling the elastoviscoplastic behaviour of long fibre SiC/Ti composite materials, Comput. Methods Appl. Mech. Engrg. 183 (2000) 309–330.
[20] D. Perić, E.A. de Souza Neto, R.A. Feijóo, M. Partovi, A.J. Carneiro Molina, On micro-to-macro transitions for multi-scale analysis of non-linear heterogeneous materials: unified variational basis and finite element implementation, Internat. J. Numer. Methods Engrg. 87 (2010) 149–170.
[21] M.G.D. Geers, V.G. Kouznetsova, W.A.M. Brekelmans, Computational homogenization, in: R. Pippan, P. Gumbsch (Eds.), Multiscale Modelling of Plasticity and Fracture by Means of Dislocation Mechanics, in: CISM International Centre for Mechanical Sciences, 2010, pp. 327–394.
[22] J. Schröder, A numerical two-scale homogenization scheme: the FE^2-method, in: J. Schröder, K. Hackl (Eds.), Plasticity and Beyond, in: CISM International Centre for Mechanical Sciences, 2014, pp. 1–64.
[23] S. Saeb, P. Steinmann, A. Javili, Aspects of computational homogenization at finite deformations: a unifying review from Reuss' to Voigt's bound, Appl. Mech. Rev. 68 (2016) 050801.
[24] V. Kouznetsova, W.A.M. Brekelmans, F.P.T. Baaijens, An approach to micro-macro modeling of heterogeneous materials, Comput. Mech. 27 (2002) 37–48.
[25] V. Kouznetsova, M.G.D. Geers, W.A.M. Brekelmans, Multi-scale constitutive modelling of heterogeneous materials with a gradient-enhanced computational homogenization scheme, Internat. J. Numer. Methods Engrg. 54 (2002) 1235–1260.
[26] I. Özdemir, W.A.M. Brekelmans, M.G.D. Geers, FE^2 computational homogenization for the thermo-mechanical analysis of heterogeneous solids, Comput. Methods Appl. Mech. Engrg. 198 (2008) 602–613.
[27] J. Schröder, Derivation of the localization and homogenization conditions for electro-mechanically coupled problems, Comput. Mater. Sci. 46 (3) (2009) 595–599.
[28] A. Javili, G. Chatzigeorgiou, P. Steinmann, Computational homogenization in magneto-mechanics, Internat. J. Numer. Methods Engrg. 50 (25.26) (2013) 4197–4216.
[29] M.-A. Keip, P. Steinmann, J. Schröder, Two-scale computational homogenization of electro-elasticity at finite strains, Comput. Methods Appl. Mech. Engrg. 278 (2014) 62–79.

[30] R. Hill, Elastic properties of reinforced solids: some theoretical principles, J. Mech. Phys. Solids 11 (1963) 357–372.
[31] R. Hill, On constitutive macro-variables for heterogeneous solids at finite strain, Proc. R. Soc. Lond. Ser. A 326 (1972) 131–147.
[32] A. Nonnenmacher, Adaptive Finite Element Methods for Multiscale Partial Differential Equations, (Ph.D. Thesis), École Polytechnique Fédérale de Lausanne, 2011 No 5097.
[33] J. Barlow, Optimal stress locations in finite element models, Internat. J. Numer. Methods Engrg. 10 (1976) 243–251.
[34] T.J.R. Hughes, The Finite Element Method: Linear Static and Dynamic Finite Element Analysis, Dover Publications, Mineola, New York, 2000.
[35] D. Braess, Finite Elements, Cambridge University Press, Cambridge UK, 1997.
[36] A. Bensoussan, J.L. Lions, G. Papanicolau, Asymptotic Analysis for Periodic Structures, North-Holland, Amsterdam, 1976.
[37] E. Sanchez-Palencia, Non-Homogeneous Media and Vibration Theory, in: Lecture Notes in Physics, vol. 127, Springer, Berlin, 1980.
[38] G. Allaire, Homogenization and two-scale convergence, SIAM J. Math. Anal. 23 (1992) 1482–1518.
[39] D. Cioranescu, P. Donato, An Introduction to Homogenization, Oxford University Press, New York, 1999.
[40] W. E, P. Ming, P. Zhang, Analysis of the heterogeneous multi-scale method for elliptic homogenization problems, J. Amer. Math. Soc. 18 (2005) 121–156.
[41] D.P. Bertsekas, Constrained Optimization and Lagrange Multiplier Methods, Athena Scientific, Belmont, 1996.
[42] M. Ohlberger, A posteriori error estimates for the heterogeneous multiscale finite element method for elliptic homogenization problems, Multiscale Model. Simul. 4 (1) (2005) 88–114.
[43] A. Abdulle, A. Nonnenmacher, Adaptive finite element heterogeneous multiscale method for homogenization problems, Comput. Methods Appl. Mech. Engrg. 200 (2011) 2710–2726.
[44] A. Abdulle, Y. Bai, Adaptive reduced basis finite element heterogeneous multiscale method, Comput. Methods Appl. Mech. Engrg. 257 (2013) 203–220.
[45] P.G. Ciarlet, The Finite Elements Method for Elliptic Problems, North Holland, 1978.
[46] O.C. Zienkiewicz, J.Z. Zhu, The superconvergent patch recovery and a posteriori error estimates. Part 1: the recovery technique, Internat. J. Numer. Methods Engrg. 33 (1992) 1331–1364.
[47] O.C. Zienkiewicz, J.Z. Zhu, The superconvergent patch recovery and a posteriori error estimates. Part 2: error estimates and adaptivity, Internat. J. Numer. Methods Engrg. 33 (1992) 1365–1382.
[48] C. Miehe, A. Koch, Computational micro-to-macro transitions of discretized microstructures undergoing small strain, Arch. Appl. Mech. 71 (2002) 300–317.
[49] I. Temizer, P. Wriggers, On the computation of the macroscopic tangent for multiscale volumetric homogenization problems, Comput. Methods Appl. Mech. Engrg. 198 (3) (2008) 495–510.
[50] B. Eidel, A. Fischer, The heterogeneous multiscale finite element method FE-HMM for the homogenization of linear elastic solids, Proc. Appl. Math. Mech. 16 (2016) 521–522.
[51] X.-Y. Yue, W. E, The local microscale problem in the multiscale modelling of strongly heterogeneous media: Effect of boundary conditions and cell size, J. Comput. Phys. 222 (2007) 556–572.
[52] F. Larsson, K. Runesson, S. Saroukhani, R. Vafadari, Computational homogenization based on a weak format of micro-periodicity for RVE-problems, Comput. Methods Appl. Mech. Engrg. 1–4 (2011) 11–26.
[53] A. Abdulle, On a-priori error analysis of fully discrete Heterogeneous Multiscale FEM, SIAM Multiscale Model. Simul. 4 (2) (2005) 447–459.
[54] H. Moulinec, P. Suquet, Fast numerical method for computing the linear and nonlinear properties of composites, C. R. Acad. Sci. II 318 (1994) 1417–1423.
[55] M. Schneider, F. Ospald, M. Kabel, Computational homogenization of elasticity on a staggered grid, Internat. J. Numer. Methods Engrg. 105 (9) (2015) 693–720.
[56] J. Schröder, D. Balzani, D. Brands, Approximation of random microstructures by periodic statistically similar representative volume elements based on lineal-path functions, Arch. Appl. Mech. 81 (7) (2010) 975–997.
[57] M.G.D. Geers, V.G. Kouznetsova, W.A.M. Brekelmans, Multi-scale computational homogenization: trends and challenges, J. Comput. Appl. Math. 234 (2010) 2175–2182.
[58] H.L. Duan, J. Wang, Z.P. Huang, B.L. Karihaloo, Size-dependent effective elastic constants of solids containing nano-inhomogeneities with interface stress, J. Mech. Phys. Solids 53 (7) (2005) 1574–1596.
[59] A. Javili, P. Steinmann, J. Mosler, Micro-to-macro transition accounting for general imperfect interfaces, Comput. Methods Appl. Mech. Engrg. 317 (2017) 274–317.
[60] J. Knap, M. Ortiz, An analysis of the quasicontinuum method, J. Mech. Phys. Solids 49 (2001) 1899–1923.
[61] B. Eidel, A. Stukowski, A variational formulation of the quasicontinuum method based on energy sampling in clusters, J. Mech. Phys. Solids 57 (2009) 87–108.
[62] B. Eidel, Coupling atomistic accuracy with continuum effectivity for predictive simulations in materials research - the Quasicontinuum method, Int. J. Mater. Res. 100 (2009) 1503–1512.
[63] B. Eidel, A. Hartmaier, P. Gumbsch, Atomistic simulation methods and their application on fracture, in: R. Pippan, P. Gumbsch (Eds.), Multiscale Modelling of Plasticity and Fracture by Means of Dislocation Mechanics, in: CISM International Centre for Mechanical Sciences, 2010, pp. 1–57.
[64] J.S. Amelang, G.N. Venturini, D.M. Kochmann, Summation rules for a fully nonlocal energy-based quasicontinuum method, J. Mech. Phys. Solids 82 (2015) 378–413.
[65] D. Lukkassen, L.-E. Persson, P. Wall, Some engineering and mathematical aspects on the homogenization method, Compos. Eng. 5 (1995) 519–531.

View publication stats

8.2 Veröffentlichung: Convergence and error analysis of FE-HMM/FE^2 for energetically consistent micro-coupling conditions in linear elastic solids

Die zweite Veröffentlichung von Andreas Fischer und Prof. Bernhard Eidel mit dem Titel **Convergence and error analysis of FE-HMM/FE^2 for energetically consistent micro-coupling conditions in linear elastic solids** erschien 2019 im *European Journal of Mechanics - A/Solids*.

Auch für diese Veröffentlichungen stammt der verwendete Matlab-Code vollständig von dem Doktoranden. Für diese Veröffentlichung wurden zusätzlich zu den zuvor erfolgten Erweiterungen einige weitere Features implementiert. Für die Untersuchung der Konvergenz in Abhängigkeit unterschiedlicher Mikro-Makro-Kopplungsbedingungen wurden Neumann-Kopplungsbedingungen als dritte Kopplungs-Option implementiert. Zusätzlich wurden erstmalig auch höherwertige Ansatzfunktionen auf Mikro- und Makroebene verwendet, die es in den Matlab-Code zu integrieren galt. Des Weiteren wird in dieser Veröffentlichung eine Fehlerschätzung basierend auf der SPR verwendet, die ebenfalls in Matlab implementiert wurde. Zuletzt wurde der im Anhang der Veröffentlichung beschriebene Semi-Dirichlet-Ansatz für die Neumann-Kopplungsbedingungen in den Code aufgenommen.

Der Doktorand hat sich an mehreren Stellen federführend in die Veröffentlichung eingebracht. Für die Einleitung in Kapitel 1 war erneut Professor Eidel hauptverantwortlich, genauso für die in Kapitel 2 erfolgt kurze Zusammenfassung der FE-HMM und der Vorstellung der a-priori Konvergenzaussagen in Abschnitt 4.1. Die Vorstellung der unterschiedlichen Mikro-Makro-Kopplungsbedingungen lag in der Hand des Doktoranden, ebenso die Beschreibung der Fehlerberechnung, der SPR und der Fehlerschätzung in den Abschnitten 4.2 und 4.3 sowie die Erstellung der zugehörigen Abbildungen.

Der Schwerpunkt des Anteils des Doktoranden lag erneut bei den numerischen Beispielen in Kapitel 5. Neben der Erzeugung der Input-Daten für die Simulationen, lag auch das Durchführen und Auswerten der Konvergenzuntersuchungen genauso in der Hand des Doktoranden wie die grafische Darstellung der Ergebnisse. Auch die Diskussion der Berechnungsergebnisse erfolgte federführend durch den Doktoranden.

Auch in der zweiten Veröffentlichung erfolgte die abschließende Zusammenfassung und das Fazit durch beide Autoren gemeinsam.

European Journal of Mechanics / A Solids 77 (2019) 103735

Contents lists available at ScienceDirect

European Journal of Mechanics / A Solids

journal homepage: www.elsevier.com/locate/ejmsol

Convergence and error analysis of FE-HMM/FE^2 for energetically consistent micro-coupling conditions in linear elastic solids

Andreas Fischer, Bernhard Eidel *

Heisenberg-Group, Institute of Mechanics, Department Mechanical Engineering, University Siegen, 57068 Siegen, Paul-Bonatz-Str. 9–11, Germany

ARTICLE INFO

Keywords:
Computational homogenization
Macro-to-micro modeling
Convergence analysis
Error estimation
Finite element methods

ABSTRACT

A cornerstone of numerical homogenization is the equivalence of the microscopic and the macroscopic energy densities, which is referred to as Hill–Mandel condition. Among these coupling conditions, the cases of periodic, linear displacement and constant traction conditions are most prominent in engineering applications. While the stiffness hierarchy of these coupling conditions is a theoretically established and numerically verified result, very little is known about the numerical errors and convergence properties for each of them in various norms. The present work addresses these aspects both on the macroscale and the microscale for linear as well as quadratic finite element shape functions. The analysis addresses aspects of (i) regularity and how its loss affects the convergence behavior on both scales compared with the a priori estimates, of (ii) error propagation from micro to macro and of (iii) optimal micro–macro mesh refinement strategy. For constant traction conditions two different approaches are compared. The performance of a recovery-type error estimation based on superconvergence is assessed. All results of the present work are valid for both the Finite Element Heterogeneous Multiscale Method FE-HMM and for FE^2.

1. Introduction

The overall aim of computational homogenization is to compute effective properties of microheterogeneous materials. This can be done in an a priori fashion in that effective properties are the result of pre-computations, which enables the identification of parameters in a constitutive law. In strongly nonlinear regimes as for inelastic material behavior, effective properties are rather calculated on the fly in direct micro–macro transitions. The first approach can be seen as a sequential or hierarchical multiscale method, the second variant as a concurrent multiscale method. In either case the methods aim at a trade-off of accuracy with efficiency by capturing the real microstructure along with a sampling of it in volumes of confined size. If the sampling regions are statistically representative, they are referred to as representative volume element (RVE). While an RVE is uncritical to identify for periodic microstructures, the proper choice of the RVE for non-periodic microstructures and random heterogeneous materials is still an item of ongoing research, see e.g. Ostoja-Starzewski (2006), Dŏskár et al. (2018) and references therein.

Among concurrent two-scale methods with direct micro–macro transitions the so-called FE^2 has been advanced in different directions of non-linear solid mechanics and used in a multitude of engineering applications, Michel et al. (1999), Miehe et al. (1999b,a), Fish et al. (1999), Feyel and Chaboche (2000), Kouznetsova et al. (2002a,b), Kanit et al. (2003), Perić et al. (2010), Geers et al. (2010b,a), Larsson et al. (2011), Schröder (2014), Saeb et al. (2016), Javili et al. (2017). More recently, the FE^2 framework has been extended to transient computational homogenization (Pham et al., 2013) and to the elastodynamics of metamaterials and of phononic crystals (Sridhar et al., 2018).

In spite of these advancements, there is a remarkable lack of knowledge about the mathematical properties of FE^2 in a fully or semi-discrete setting as a two-scale finite element method. Here, the so-called Finite Element Heterogeneous Multiscale Method FE-HMM has made substantial contributions providing unified error estimates that comprise the macro error, the total micro error, and the modeling error, Abdulle (2005), Abdulle and Schwab (2005), E et al. (2005), Ohlberger (2005), Abdulle (2009), Abdulle et al. (2012). This advances the understanding and knowledge of FE-HMM, although the obtained results are currently restricted to linear problems; in solid mechanics to the purely linear setting of linear elastic material behavior along with geometrical linearity, Abdulle (2006), Jecker and Abdulle (2016). Beyond the theoretical relevance of a priori error estimates they are of practical relevance, since they prescribe, how a uniform micro–macro refinement strategy shall be carried out in order to achieve optimal convergence for minimal computational efforts.

* Corresponding author.
E-mail address: bernhard.eidel@uni-siegen.de (B. Eidel).

https://doi.org/10.1016/j.euromechsol.2019.02.001
Received 15 April 2018; Received in revised form 25 January 2019; Accepted 3 February 2019
Available online 13 February 2019
0997-7538/© 2019 Elsevier Masson SAS. All rights reserved.

FE^2 and FE-HMM have been developed independently from each other and on almost parallel avenues without joint links or crossroads, FE^2 in mechanics, FE-HMM in mathematics as an off-spring of the very general Heterogeneous Multiscale Method HMM, E and Engquist (2003), E et al. (2003). Quite recently it was shown that despite minor differences in the numerical setup[1] the two methods are equivalent and, as a consequence, the a priori estimates of FE-HMM equally apply for FE^2, Eidel and Fischer (2018).

A theoretical sound and commonly accepted link between the scales is Hill's postulate of energy equivalence between micro and macro energy densities, Hill (1963, 1972). It is applied in both FE^2 and FE-HMM, for the latter method without reference to Hill's work, E and Engquist (2003). Several micro boundary conditions (BC) fulfill the postulate, among them (i) the linear displacement BC also referred to as kinematically uniform BC (KUBC) or Dirichlet BC (DBC), the (ii) constant traction BC (TBC), also called static uniform BC (SUBC) or Neumann BC, and (iii) the periodic BC (PBC). These three micro-coupling conditions, which are frequently called canonical in view of their practical relevance can be ordered according to their stiffness in that PBC has its lower bound by Neumann BC and its upper bound by Dirichlet BC.

The present work aims to advance the understanding of FE^2 and FE-HMM in their numerical characteristics. For that aim we address the following aspects for the particular case of linear elasticity in a geometrical linear frame, since this setting allows for the direct comparison with the a priori estimates of FE-HMM:

1. The numerical error and its convergence is analyzed for the following set of energetically consistent BCs, for (i) KUBC/Dirichlet, for (ii) PBC and for (iii) SUBC/Neumann.
   While the hierarchy of stiffnesses for conditions (i)–(iii) is a theoretically established result that was verified in numerous numerical simulations, Suquet (1987), Miehe (2003), Kanit et al. (2003), Perić et al. (2010), the convergence for the different coupling conditions is largely unexplored; an exception is Yue and E (2007) for the scalar-valued field problem of transport/conductivity. One of the guiding questions is whether there are significant differences in errors and convergence between the micro coupling conditions, and if so, whether they are generally valid similar to the mentioned stiffness hierarchy. Moreover the analysis compares the measured convergence orders against the nominal a priori estimates in different norms. In this context, a discrimination between micro error convergence on the microscale and on the macroscale is relevant, where the latter implies a micro-to-macro error propagation and a somewhat unusual convergence estimate. In either case the regularity of the boundary value problems both on the macro- and the microscale – and its loss due to singularities – is of importance.
   Beyond the analysis of different coupling conditions, we augment the condition for constant tractions in the Lagrange multiplier framework by the condition for proper rotations and compare its computational efficiency with a simple mass-type diagonal perturbation of the stiffness matrix introduced by Miehe and Koch (2002)[2] and with a so-called "Semi-Dirichlet"-approach of Javili et al. (2017).
2. Error estimation based on the Superconvergent Patch Recovery (SPR) and its validation by comparison with the exact error.
   The true numerical error can be calculated quite accurately by comparison of the approximate solution with a reference solution on extremely fine grids. In engineering practice however, suchlike overkill solutions along with error calculation in a post-processing step are not feasible. For that reason error estimation provides an efficient way to analyze accuracy on-the-fly given that the error estimation is validated.
3. For the above analyses of error computation and estimation a set of benchmark problems is considered. They span the range from highly regular boundary value problems (BVP) up to singularity-dominated cases for both the macro as well as the microscale in $n_{dim} = 2$.

[1] While the micro–macro stiffness transfer in FE^2 refers to the homogenized tangent moduli, FE-HMM refers to the microstiffness matrix along with a transfer operator.

[2] Similarly used at finite strains in Miehe (2003).

2. The finite element heterogeneous multiscale method FE-HMM in a nutshell

To put things into perspective and for ready reference this section outlines an FE-HMM formulation for linear elasticity cf. Eidel and Fischer (2016, 2018).

2.1. Model problem of linear elasticity

We consider a body $\mathcal{B}$, a bounded subset of $\mathbb{R}^{n_{dim}}$, $n_{dim} = 2, 3$, with boundary $\partial\mathcal{B} = \partial\mathcal{B}_D \cup \partial\mathcal{B}_N$ where the Dirichlet boundary $\partial\mathcal{B}_D$ and the Neumann boundary $\partial\mathcal{B}_N$ are disjoint sets. The closure of the body $\mathcal{B}$ is denoted by $\bar{\mathcal{B}}$. The body, which exhibits an inhomogeneous microstructure, is subject to body forces $\boldsymbol{f}$ and surface tractions $\bar{\boldsymbol{t}}$ and in static equilibrium.

2.1.1. The microproblem

The displacement $\boldsymbol{u}^\epsilon = (u_1^\epsilon, \dots, u_{n_{dim}}^\epsilon)$ of the body is given by the solution of the system

$$\begin{aligned} -\sigma^\epsilon_{ij,j} &= f_i && \text{in} \quad \mathcal{B} \\ u^\epsilon_i &= \bar{u}_i && \text{on} \quad \partial\mathcal{B}_D \\ \sigma^\epsilon_{ij}\, n_j &= \bar{t}_i && \text{on} \quad \partial\mathcal{B}_N \end{aligned} \tag{1}$$

The constitutive law is assumed to be linear elastic $\sigma^\epsilon_{ij} = \mathbb{A}^\epsilon_{ijlm}\,\varepsilon_{lm}$ where $\mathbb{A}^\epsilon_{ijlm}$ is the fourth order elasticity tensor and ε_{ij} the infinitesimal strain tensor with $\varepsilon_{ij}(\boldsymbol{u}^\epsilon) = 1/2\left(u^\epsilon_{i,j} + u^\epsilon_{j,i}\right)$ or more compact, $\boldsymbol{\varepsilon}(\boldsymbol{u}^\epsilon) = \boldsymbol{L}\,\boldsymbol{u}^\epsilon$ with the linear differential operator $\boldsymbol{L}$. Superscript ϵ throughout indicates the dependency of suchlike marked quantities on the heterogeneity of the elastic material. In $(1)_3$, $\boldsymbol{n} = (n_1, \dots, n_{dim})$ is the unit outward normal to $\partial\mathcal{B}$.

Multiplying the strong form (1) by a test function $\boldsymbol{v} \in \mathcal{V}$ and the application of the Green formula yield the variational form:

Find $\boldsymbol{u}^\epsilon$ such that

$$B_\epsilon(\boldsymbol{u}^\epsilon, \boldsymbol{v}) \overset{\text{def}}{=} \int_{\mathcal{B}} \boldsymbol{\sigma}^\epsilon(\boldsymbol{u}^\epsilon) : \boldsymbol{\varepsilon}(\boldsymbol{v})\, dV = \int_{\mathcal{B}} \boldsymbol{f}\cdot\boldsymbol{v}\, dV + \int_{\partial\mathcal{B}_N} \bar{\boldsymbol{t}}\cdot\boldsymbol{v}\, dA \overset{\text{def}}{=} \boldsymbol{F}(\boldsymbol{v}), \tag{2}$$

which must hold for all $\boldsymbol{v} \in \mathcal{V}$, where $\mathcal{V}$ is the space of admissible (virtual) displacements that fulfill homogeneous Dirichlet BC

$$\mathcal{V} = \{\boldsymbol{v}; \boldsymbol{v} \in H^1(\mathcal{B})^{n_{dim}}, \boldsymbol{v}|_{\partial\mathcal{B}_D} = \boldsymbol{0}\}\,. \tag{3}$$

2.1.2. The macroproblem

The strong form of the macroscopic/homogenized boundary value problem (BVP) reads

$$\begin{aligned} -\sigma^0_{ij,j} &= \langle f_i \rangle && \text{in} \quad \mathcal{B} \\ u^0_i &= \langle \bar{u}_i \rangle_\Gamma && \text{on} \quad \partial\mathcal{B}_D \\ \sigma^0_{ij}\, n_j &= \langle \bar{t}_i \rangle_\Gamma && \text{on} \quad \partial\mathcal{B}_N \end{aligned} \tag{4}$$

for a derivation see Eidel and Fischer (2018). The macroscopic displacement is denoted by u^0_i and $\mathbb{A}^0$ is the homogenized elasticity tensor. In $(4)_{1,3}$ σ^0_{ij} is the macroscopic stress obtained by a volume average over the microdomain.

The values for the Dirichlet as well as Neumann BC in $(4)_{2,3}$ are obtained by surface averages of corresponding BC in $(1)_{2,3}$, for details we refer to Eidel and Fischer (2018). Similarly, $\langle f_i \rangle$ is the volume average of body forces in $(1)_1$.

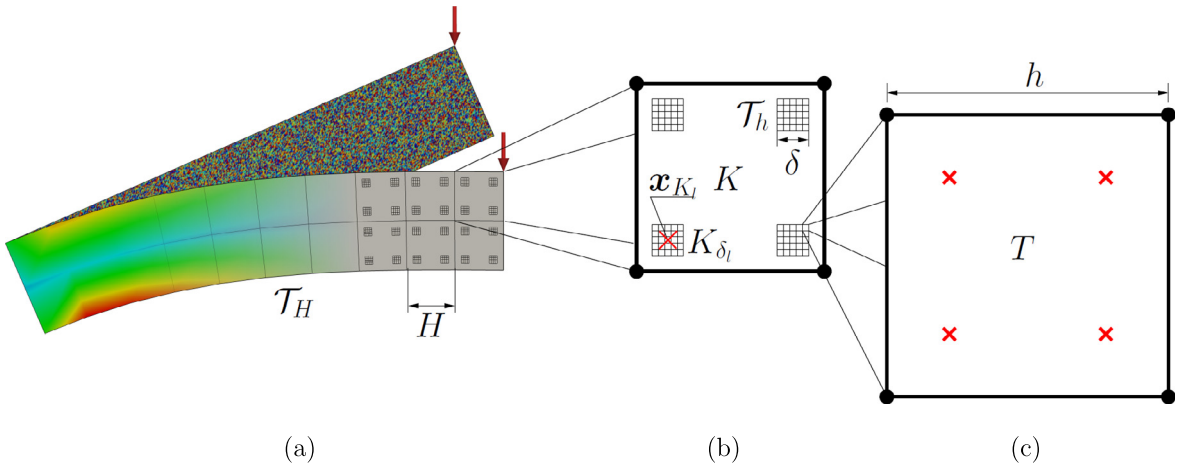


Fig. 1. FE-HMM as a two-scale finite element method: (a) Macroscopic BVP with macrotriangulation $\mathcal{T}_H$, (b) one macro finite element K of size H with microdomains/RVEs K_{δ_l} of triangulation $\mathcal{T}_h$, centered at the macro quadrature points x_{K_l}, (c) micro finite element T of size h with standard quadrature points.

The solution of the homogenized problem is obtained from the variational form

$$B_0(u^0, v) = \int_{\mathcal{B}} \sigma^0(u^0) : \varepsilon(v)\, dV = \int_{\mathcal{B}} f \cdot v\, dV + \int_{\partial\mathcal{B}_N} \bar{t} \cdot v\, dA \qquad \forall\, v \in \mathcal{V}, \tag{5}$$

which follows from multiplying the strong form (4) by test functions v along with the application of Green's formula. For notational convenience we skip in (5) and in the rest of the paper the averaging symbols $\langle\bullet\rangle$, $\langle\bullet\rangle_\Gamma$ for f, $\bar{u}$ and $\bar{t}$ but keep in mind that these quantities follow from volume and surface averages, respectively.

We consider the piecewise linear continuous FEM in macro- and microspace, respectively. We define a macro finite element space as

$$\begin{aligned} &S^p_{\partial\mathcal{B}_D}(\mathcal{B}, \mathcal{T}_H) \\ &= \left\{ u^H \in H^1(\mathcal{B})^d; u^H|_{\partial\mathcal{B}_D} = \bar{u}; u^H|_K \in \mathcal{P}^p(K)^{n_{dim}}, \forall\, K \in \mathcal{T}_H \right\}, \end{aligned} \tag{6}$$

where $\mathcal{P}^p$ is the space of (here: linear, $p = 1$, or quadratic, $p = 2$) polynomials on the element K, $\mathcal{T}_H$ the (quasi-uniform) triangulation of $\mathcal{B} \subset \mathbb{R}^{n_{dim}}$. Superscript H denotes the characteristic element size, with $H \gg \epsilon$ for efficiency. The space $S^p_{\partial\mathcal{B}_D}$ is a subspace of $\mathcal{V}$ defined in (3).

For the solution of (1) in the macrodomain we use the two-scale FEM framework of the FE-HMM as originally proposed in E and Engquist (2003) and analyzed for elliptic PDEs in E et al. (2005), and, with the focus on linear elasticity, in Abdulle (2006).

The macrosolution of the FE-HMM is given by the following variational form:

Find $u^H \in S_{\mathcal{B}_D}(\mathcal{B}, \mathcal{T}_H)$ such that

$$B_H(u^H, v^H) = \int_{\mathcal{B}} f \cdot v^H\, dV + \int_{\partial\mathcal{B}_N} \bar{t} \cdot v^H\, dA \qquad \forall\, v^H \in S_{\partial\mathcal{B}_D}(\mathcal{B}, \mathcal{T}_H), \tag{7}$$

which reads as a standard finite element formulation.

2.2. The modified macro bilinear form of FE-HMM

If the homogenized constitutive tensor $\mathbb{A}^0(x)$ is explicitly known, the bilinear form $B_H(u^H, v^H)$ can be calculated using standard numerical quadrature according to (8), where x_{K_l} and ω_{K_l} are the quadrature points and quadrature weights, respectively

$$B_H(u^H, v^H) = \sum_{K \in \mathcal{T}_H} \sum_{l=1}^{N_{qp}} \omega_{K_l} \left[\sigma^0(u^H(x_{K_l})) : \varepsilon(v^H(x_{K_l})) \right] \tag{8}$$

$$\approx \sum_{K \in \mathcal{T}_H} \sum_{l=1}^{N_{qp}} \omega_{K_l} \left[\frac{1}{|K_l|} \int_{K_l} \sigma^\epsilon(u^h_{K_l}) : \varepsilon(v^h_{K_l})\, dV \right]. \tag{9}$$

Since $\mathbb{A}^0(x)$ is typically not known for heterogeneous materials, the ansatz of FE-HMM is to approximate the virtual work expression at point x_{K_l} in the semidiscrete form (8) by another bilinear form using the known microheterogeneous elasticity tensor $\mathbb{A}^\epsilon$, see (9). According to this approximation, the solution $u^h_{K_l}$ is obtained on microsampling domains $K_{\delta_l} = x_{K_l} + \delta\,[-1/2, +1/2]^{n_{dim}}$, $\delta \geq \epsilon$, which are each centered at the quadrature points x_{K_l} of K, $l = 1, \ldots, N_{qp}$. For a visualization see Fig. 1. These microsampling domains with volume $|K_{\delta_l}|$ provide the additive contribution to the stiffness matrix of the macro finite element. In order to avoid too heavy notation we will replace K_{δ_l} by K_l.

The approximation of (8) by (9) indicates that FE-HMM crucially relies on a modified quadrature rule and fulfills the equality of the macroenergy density with the microenergy density, thus in agreement with Hill's postulate, Hill (1963, 1972).

2.3. Variational formulation of the microproblem

It can be shown that the FE-HMM microproblem resembles the discrete version of the cell problem of asymptotic expansion, if it is formulated for each microdomain K_l in K with $l = 1, \ldots, N_{qp}$, $K \in \mathcal{T}_H$ like this:

Find $u^h_{K_l}$ such that the conditions for macro–micro coupling and for the micro bilinear form (10) are fulfilled:

$$\left.\begin{aligned} \left(u^h_{K_l} - u^H_{lin,K_l}\right) &\in S^q(K_l, \mathcal{T}_h) \\ B_{K_l}(u^h_{K_l}, w^h_{K_l}) &:= \int_{K_l} \sigma^\epsilon(u^h_{K_l}) : \varepsilon(w^h_{K_l})\, dV = 0 \\ &\quad \forall\, w^h_{K_l} \in S^q(K_l, \mathcal{T}_h), \end{aligned}\right\} \tag{10}$$

where the micro finite element space $S^q(K_l, \mathcal{T}_h)$ is defined by

$$S^q(K_l, \mathcal{T}_h) = \{ w^h \in \mathcal{W}(K_l); w^h \in (\mathcal{P}^q(T))^{n_{dim}}, T \in \mathcal{T}_h \}. \tag{11}$$

In (11) $\mathcal{T}_h$ is a quasi-uniform discretization of the sampling domain K_l with mesh size $h \ll \varepsilon$ resolving the finescale and $\mathcal{P}^q$ is the space of polynomials on the element T. In the present work we consider linear and quadratic shape functions, $q = 1, 2$. The particular choice of the Sobolev space $\mathcal{W}(K_l)$ sets the boundary conditions for the micro problems, cf. Abdulle (2009), Section 3.2. Among the coupling conditions that fulfill Hill's postulate we consider (i) periodic BC (PBCs), (ii) kinematically uniform displacement conditions (KUBC), and (iii) constant traction conditions (TBC).

The linearization of u^H in $(10)_1$ is carried out at the quadrature point x_{K_l}

$$u^H_{lin,K_l} = u^H(x_{K_l}) + (x - x_{K_l}) \cdot \nabla u^H(x_{K_l}). \tag{12}$$

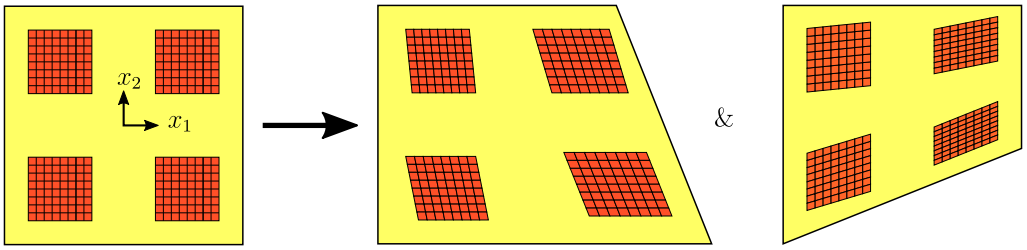


Fig. 2. Unit displacement states in x_i-directions, $i = 1, 2$ applied to the lower right macro element node I and the uniform deformations of the microdomains/RVEs.

It ensures a homogeneous deformation on the microdomain and resembles therein the unit cell problem of asymptotic homogenization (the FE-HMM perspective) and thus is in the frame of strain-driven first order computational homogenization.

For the solution of (10) a basis $\{N_I^H\}_{I=1}^{M_{mac}}$ for the macro finite element space $\mathcal{S}_0^p(\mathcal{B}, \mathcal{T}_H)$ is employed in order to represent the macrosolution $\boldsymbol{u}^H$ of (7). Similarly, a basis $\{N_i^h\}_{i=1}^{M_{mic}}$ of the micro finite element space $\mathcal{S}_0^q(K_l, \mathcal{T}_h)$, (11), is introduced in order to represent the solution $\boldsymbol{u}^h$ of a microproblem. M_{mac} denotes the number of nodes of the macrodomain, and M_{mic} denotes the number of nodes of each microdomain. Hence, the macro- and the microsolution follow the representation

$$\boldsymbol{u}^H = \sum_{I=1}^{M_{mac}} N_I^H \, \boldsymbol{d}_I^H \,, \qquad \boldsymbol{u}^h = \sum_{i=1}^{M_{mic}} N_i^h \, \boldsymbol{d}_i^h \,, \tag{13}$$

where $\boldsymbol{d}_I^H$ is the displacement vector of macronode I, and $\boldsymbol{d}_i^h$ is the displacement vector for micronode i.

2.4. Macrostiffness calculation

The macro bilinear form $B_H^e(\boldsymbol{u}^H, \boldsymbol{v}^H)$ is the virtual internal work for a macro finite element. The corresponding bilinear form in terms of the shape functions $B_H^e(\boldsymbol{N}_I^H, \boldsymbol{N}_J^H)$ results in the macro element stiffness matrix contribution $\boldsymbol{k}_{IJ}^{e,mac}$ for macronodes I, J, a $d \times d$ matrix. It holds

$$\boldsymbol{k}_{IJ}^{e,mac} = B_H^e(\boldsymbol{N}_I^H, \boldsymbol{N}_J^H) = \sum_{l=1}^{N_{qp}} \frac{\omega_{K_l}}{|K_l|} \int_{K_l} (\boldsymbol{L}\boldsymbol{u}_{K_l}^{h(I)})^T \, \mathbb{A}^\epsilon(\boldsymbol{x}) \, \boldsymbol{L}\boldsymbol{u}_{K_l}^{h(J)} \, dV \,. \tag{14}$$

In (14) $\boldsymbol{u}_{K_l}^{h(I)}$ is the counterpart of $\boldsymbol{u}_{K_l}^h$ in (10). It is the dimensionless solution of the microproblem on K_l, which is driven by the shape function N_I^H at macronode I. In the following, we add $x_i, i = 1, \dots, n_{dim}$ to account for the vector-valued field problem of dimension n_{dim}. Consequently, $\boldsymbol{u}_{K_l}^{h(I,x_i)}$ is the microsolution driven by a macroelement unit-displacement state $\boldsymbol{u}_{lin,K_l}^{H(I,x_i)}$ at node I in x_i-direction.

For stiffness calculation, problem (10) is reformulated in that $\boldsymbol{u}_{K_l}^{h(I,x_i)}$ replaces $\boldsymbol{u}_{K_l}^h$.

For the coupling of $\boldsymbol{u}_{lin,K_l}^{H(I,x_i)}$ with $\boldsymbol{u}_{K_l}^{h(I,x_i)}$ the two fields are expanded into the same basis $\{N_i^h\}_{i=1}^{M_{mic}}$ of $\mathcal{S}^q(K_l, \mathcal{T}_h)$,

$$\boldsymbol{u}_{lin,K_l}^{H(I,x_i)} = \sum_{m=1}^{M_{mic}} N_{m,K_l}^h \, \boldsymbol{d}_m^{H(I,x_i)} \,, \qquad \boldsymbol{u}_{K_l}^{h(I,x_i)} = \sum_{m=1}^{M_{mic}} N_{m,K_l}^h \, \boldsymbol{d}_m^{h(I,x_i)} \,. \tag{15}$$

The solution of the microproblems for the minimizers $\boldsymbol{d}^{h(I,x_i)}$ is presented in Section 2.5. The macroelement stiffness matrix according to (14) yields after some algebra

$$\begin{aligned} \boldsymbol{k}_{IJ}^{e,mac} &= B_H^e \left[\boldsymbol{N}_I^H, \boldsymbol{N}_J^H\right] \\ &= \sum_{l=1}^{N_{qp}} \frac{\omega_{K_l}}{|K_l|} \left(\boldsymbol{d}^{h(I)}\right)^T \boldsymbol{K}_{K_l}^{mic} \, \boldsymbol{d}^{h(J)} \,, \end{aligned} \tag{16}$$

where $\boldsymbol{d}^{h(I)} = \left(\boldsymbol{d}^{h(I,x_1)} | \boldsymbol{d}^{h(I,x_2)} | \boldsymbol{d}^{h(I,x_3)}\right)$ for $n_{dim} = 3$. A detailed derivation of (16) is presented in the Appendix.

The assembly of $\boldsymbol{k}_{IJ}^{e,mac}$ results in $\boldsymbol{k}^{e,mac}$ and implies a column-wise assembly of $\boldsymbol{d}^{h(I)}$ for $I = 1, \dots, N_{node}$ that results in the transformation matrix $\boldsymbol{T}_{K_l}$

$$\boldsymbol{k}_K^{e,mac} = \sum_{l=1}^{N_{qp}} \frac{\omega_{K_l}}{|K_l|} \, \boldsymbol{T}_{K_l}^T \, \boldsymbol{K}_{K_l}^{mic} \, \boldsymbol{T}_{K_l} \tag{17}$$

$$\text{with} \quad \boldsymbol{T}_{K_l} = \left[\left[\left[\boldsymbol{d}^{h(I,x_i)}\right]_{i=1,\dots,n_{dim}}\right]_{I=1,\dots,N_{node}}\right]. \tag{18}$$

The matrix dimensions

$$\begin{aligned} &\boldsymbol{T}_{K_l}^T \in \mathbb{R}^{(N_{node} \cdot n_{dim}) \times (M_{mic} \cdot n_{dim})}, \quad \boldsymbol{K}_{K_l}^{mic} \in \mathbb{R}^{(M_{mic} \cdot n_{dim}) \times (M_{mic} \cdot n_{dim})}, \\ &\boldsymbol{T}_{K_l} \in \mathbb{R}^{(M_{mic} \cdot n_{dim}) \times (N_{node} \cdot n_{dim})}, \quad \boldsymbol{k}_K^{e,mac} \in \mathbb{R}^{(N_{node} \cdot n_{dim}) \times (N_{node} \cdot n_{dim})} \end{aligned}$$

underpin that $\boldsymbol{T}_{K_l}$ is not only the agency of a micro-to-macro stiffness transfer but also a compression operator that transforms $\boldsymbol{K}_K^{mic}$ into $\boldsymbol{k}_K^{e,mac}$.

In the context of stiffness computation, a macro element shape function represents a unit displacement state for macro node $I, I = 1, \dots, N_{node}$ in each direction of space $x_i \,|\, i = 1, \dots, n_{dim}$. They drive the microproblem in terms of the corresponding nodal values $\boldsymbol{d}_m^{H(I,x_i)}, m = 1, \dots, M_{mic}$ in each microdomain to evaluate the macroelement stiffness $\boldsymbol{k}_{IJ}^{e,mac}$. Each unit displacement state in x_i-direction induces in $\boldsymbol{d}^{H(I,x_i)}$ nonzero components only in x_i, for example $\boldsymbol{d}^{H(I,x_i)}|_{i=2} = \left[0, d_{1,x_2}^{H(I,x_2)}, 0, \dots, 0, d_{M_{mic},x_2}^{H(I,x_2)}, 0\right]^T$.

Fig. 2 visualizes two unit displacement states applied to the lower right macronode in two directions along with the corresponding uniform RVE-deformations that follow from linearization according to (12).

2.5. Solution of the microproblems

The microstiffness matrix is obtained by Gauss–Legendre numerical quadrature on the element level, the assembly of the element stiffness matrices results in the total stiffness matrix for an RVE.

With the RVE microstiffness matrix in hand, the microproblem can be solved. Here the method of Lagrange multipliers is chosen such that a saddlepoint problem must be solved. The total energy for a macro unit displacement state reads

$$\begin{aligned} \mathcal{L}(\boldsymbol{d}^{h(I,x_i)}, \lambda^{(I,x_i)}) = \; & \frac{1}{2} \left(\boldsymbol{d}^{h(I,x_i)}\right)^T \boldsymbol{K}_{K_l}^{mic} \, \boldsymbol{d}^{h(I,x_i)} \\ & + \lambda^{(I,x_i)T} \boldsymbol{G} \left(\boldsymbol{d}^{h(I,x_i)} - \bar{\boldsymbol{d}}^{H(I,x_i)}\right) \\ & \text{for } I = 1, \dots, N_{node}, \text{ and } x_i \,|\, i = 1, \dots, n_{dim} \,, \end{aligned} \tag{19}$$

where $\boldsymbol{G}$ contains the kinematical coupling constraints. Details of various coupling conditions and their implementation in the frame of Lagrange multipliers are described in Section 3. In either case the Lagrange multipliers represent external forces which enforce the micro coupling condition.

The vector of Lagrange multipliers $\lambda^{(I,x_i)} \in \mathbb{R}^{(1+L) \cdot n_{dim}}$, where L depends on the type of microcoupling, reads for $n_{dim} = 3$ as

$$\lambda^{(I,x_i)} = \{\lambda_{0,x_1}^{(I,x_i)}, \lambda_{0,x_2}^{(I,x_i)}, \lambda_{0,x_3}^{(I,x_i)}, \lambda_{1,x_1}^{(I,x_i)}, \lambda_{1,x_2}^{(I,x_i)}, \lambda_{1,x_3}^{(I,x_i)}, \dots, \lambda_{L,x_1}^{(I,x_i)}, \lambda_{L,x_2}^{(I,x_i)}, \lambda_{L,x_3}^{(I,x_i)}\}^T \,. \tag{20}$$

The first variation of $\mathcal{L}$ with respect to $\boldsymbol{d}^{h(I,x_i)}$ and $\lambda^{(I,x_i)}$ results in the stationarity conditions

$$\begin{bmatrix} \boldsymbol{K}^{mic}_{K_l} & \boldsymbol{G}^T \\ \boldsymbol{G} & \boldsymbol{0} \end{bmatrix} \begin{bmatrix} \boldsymbol{d}^{h(I,x_i)} \\ \lambda^{(I,x_i)} \end{bmatrix} = \begin{bmatrix} \boldsymbol{0} \\ \boldsymbol{G}\,\boldsymbol{d}^{H(I,x_i)} \end{bmatrix}$$
$$\text{for } I = 1,\dots,N_{node},\ i = 1,\dots,n_{dim}\,. \tag{21}$$

The solution of (21) subject to $N_{node}\cdot n_{dim}$ right hand sides can be carried out efficiently since the coefficient matrix in (21) is constant. The solution vectors are augmented to full matrices, hence, $\boldsymbol{d}^{h(I,x_i)} \to \boldsymbol{T}$, $\lambda^{(I,x_i)} \to \boldsymbol{\Lambda}$, $\boldsymbol{d}^{H(I,x_i)} \to \boldsymbol{d}^H$.

The solution of (21) serves the purpose to compute the transformation matrix $\boldsymbol{T}_{K_l}$ according to (18). After the consecutive solution of the global macroproblem for $\boldsymbol{u}^H$, the microproblems have to be solved. Then, (21) is driven by the true macroscopic displacement vector $\boldsymbol{d}^H$, which results in the true microdisplacements $\boldsymbol{d}^h$.

3. The coupling conditions

This section gives a brief account of coupling conditions (Dirichlet, periodic and Neumann) in a Lagrange-Multiplier framework.

3.1. Dirichlet coupling

The simplest coupling condition is the Dirichlet coupling, where linear displacements following from the macro displacement field are applied to the boundaries of a microdomain

$$\boldsymbol{u}^{h(I,x_i)}_{K_l} = \boldsymbol{u}^{H(I,x_i)}_{lin,K_l} \quad \text{on } \partial K_l\,. \tag{22}$$

In this case the constraint matrix $\boldsymbol{G}$ contains $L\cdot n_{dim}$ rows with L the number of boundary nodes and n_{dim} the number of degrees of freedom per node. Each row contains a 1 pointing at a degree of freedom of a boundary node and 0 elsewhere. By doing so (21) directly couples the nodal micro displacements $\boldsymbol{d}^{h(I,x_i)}$ on the RVE boundary to the nodal micro displacements following from the macro displacement field $\boldsymbol{d}^{H(I,x_i)}$.

The expression on the right hand side of the system of equations $\boldsymbol{G}\,\boldsymbol{d}^{H(I,x_i)}$ can be derived by inserting the micro coordinates of the boundary nodes in the reference configuration into the linearized macro shape functions.

3.2. Periodic coupling

Periodic coupling conditions imply periodic displacements and anti-periodic tractions on the boundaries of the microdomain. It holds

$$\left(\boldsymbol{u}^{h,(I,x_i)}_{K_l} - \boldsymbol{u}^{H(I,x_i)}_{lin,K_l}\right)^+ = \left(\boldsymbol{u}^{h,(I,x_i)}_{K_l} - \boldsymbol{u}^{H(I,x_i)}_{lin,K_l}\right)^- \tag{23}$$
$$\boldsymbol{t}^+ = -\boldsymbol{t}^-\,. \tag{24}$$

The boundary of the microdomain is here split up in a part ∂K_l^+ and a part ∂K_l^- such that $\partial K_l^+ \cup \partial K_l^- = \partial K_l$ having opposite outward normal vectors $\boldsymbol{n}^+ = -\boldsymbol{n}^-$.

Details of the constraint matrix $\boldsymbol{G}$ for PBC are described in Eidel and Fischer (2018).

3.3. Neumann coupling

The Neumann coupling condition of constant tractions on the element boundary reads as

$$\boldsymbol{t}(\boldsymbol{x}) \;=\; \boldsymbol{\sigma}_{K_l}(\boldsymbol{u}^{H(I,x_i)})\,\boldsymbol{n}(\boldsymbol{x}) \quad \text{on } \partial K_l\,. \tag{25}$$

Since stress of the macro Gauss point $\boldsymbol{\sigma}_{K_l}(\boldsymbol{u}^{H(I,x_i)})$ for macro unit displacement states is not known, the condition is cast into a weak constraint in terms of a macroscopic strain $\boldsymbol{\varepsilon}_{K_l}(\boldsymbol{u}^{H(I,x_i)})$. In contrast to Miehe and Koch (2002) not only the symmetric part but the full gradient is considered according to

$$\frac{1}{|K_l|}\int_{\partial K_l} [\boldsymbol{u}^{h(I,x_i)}(\boldsymbol{x}) \otimes \boldsymbol{n}]\,dA \;=\; \nabla \boldsymbol{u}^{H(I,x_i)}\,, \tag{26}$$

since then (26) covers both the strain tensor $\boldsymbol{\varepsilon}_{K_l}(\boldsymbol{u}^{H(I,x_i)})$ and – by means of the skew-symmetric part – the infinitesimal rotation tensor $\boldsymbol{\omega}_{K_l}(\boldsymbol{u}^{H(I,x_i)})$.

Introducing a discrete nodal normal vector $\boldsymbol{n}_q := 1/2[\boldsymbol{x}_{q+1} - \boldsymbol{x}_{q-1}]\times \boldsymbol{e}_3$ with $\boldsymbol{x}_{q-1}$ and $\boldsymbol{x}_{q+1}$ being the neighbor nodes of node q on the boundary, the discrete condition is obtained

$$\frac{1}{|K_l|}\sum_{q=1}^{L} \boldsymbol{d}^{h(I,x_i)}_q \otimes \boldsymbol{n}_q \;=\; \nabla \boldsymbol{u}^{H(I,x_i)}_{K_l}\,. \tag{27}$$

In (27), L is the number of nodes on the boundary of the microdomain. The neighboring nodes $\boldsymbol{x}_{q-1}$ and $\boldsymbol{x}_{q+1}$ have to be oriented so that $\boldsymbol{n}_q$ is an outward normal vector. Expression (27) can be cast into a matrix representation

$$\sum_{q=1}^{L} \boldsymbol{G}_q \boldsymbol{d}^{h(I,x_i)}_q \;=\; \nabla \boldsymbol{u}^{H(I,x_i)}_{K_l}\,, \tag{28}$$

where $\boldsymbol{G}_q$ depends on $\boldsymbol{n}_q$ and reads for $n_{dim} = 2$ as

$$\boldsymbol{G}_q \;:=\; \frac{1}{|K_l|}\begin{bmatrix} 2n_1 & 0 \\ 0 & 2n_2 \\ n_2 & n_1 \\ n_2 & -n_1 \end{bmatrix}_q\,. \tag{29}$$

The first three rows in (29) follow from the symmetric part in (26), the fourth row from the skew-symmetric part. While the latter enforces proper rotations of the microdomain, the proper translational embedding of the RVE into the macro continuum can be ensured in various ways, e.g. by coupling the RVE average displacement to the macro displacement, or by coupling a micro node located at (close to) the center of the RVE to the displacements of the corresponding macroscopic quadrature node.

The assembly of the $\boldsymbol{G}_q$ matrices results in the constraint matrix $\boldsymbol{G}$.

4. A priori error estimates and a posteriori error estimation

This Section 4 provides the unified a priori estimates covering the macro error, the micro error and the modeling error. Moreover, the recovery-type error estimator of Zienkiewicz–Zhu based on superconvergent stress and strain is introduced and contrasted to error computation based on reference solutions.

4.1. A priori estimates

FE-HMM as a particular instance of the most general Heterogeneous Multiscale Method HMM E and Engquist (2003), E et al. (2003, 2007), Abdulle et al. (2012) has its foundation in mathematical homogenization by asymptotic expansion, Bensoussan et al. (1976), Sanchez-Palencia (1980), Allaire (1992), Cioranescu and Donato (1999).

A priori estimates for various types of partial differential equations (PDEs) have been derived for FE-HMM by virtue of its foundation in mathematical homogenization; for the elliptic case we refer to E et al. (2005), Ohlberger (2005), for the elliptic case of linear elasticity in a geometrical linear setting to Abdulle (2006, 2009). A posteriori error analysis along with upper and lower bounds of a residual-based error estimator have been presented in Abdulle and Nonnenmacher (2011), for an adaptive strategy governed by quantities of interest we refer to Abdulle and Nonnenmacher (2013).

The total FE-HMM error can be decomposed into three parts

$$\|\boldsymbol{u}^0 - \boldsymbol{u}^H\| \;\le\; \underbrace{\|\boldsymbol{u}^0 - \boldsymbol{u}^{0,H}\|}_{e_{mac}} + \underbrace{\|\boldsymbol{u}^{0,H} - \widetilde{\boldsymbol{u}}^H\|}_{e_{mod}} + \underbrace{\|\widetilde{\boldsymbol{u}}^H - \boldsymbol{u}^H\|}_{e_{mic}}\,, \tag{30}$$

where e_{mac}, e_{mod}, e_{mic} are the macro error, the modeling error, and the micro error.

Here, $\boldsymbol{u}^0$ is the solution of the homogenized problem (4), $\boldsymbol{u}^H$ is the FE-HMM solution, $\boldsymbol{u}^{0,H}$ is the standard (single-scale) FEM solution of problem (5) that is obtained through exact $\mathbb{A}^0$; and $\widetilde{\boldsymbol{u}}^H$ is the FE-HMM solution obtained through exact microfunctions (in $W(K_l)$).

For sufficiently regular problems the following a priori estimates hold in the L^2-norm, the H^1-norm and the energy-norm (definition of these norms in Appendix A.2):

$$\|\boldsymbol{u}^0 - \boldsymbol{u}^H\|_{L^2(\mathcal{B})} \leq C\left(H^{p+1} + \left(\frac{h}{\epsilon}\right)^{2q}\right) + e_{mod}\,, \tag{31}$$

$$\|\boldsymbol{u}^0 - \boldsymbol{u}^H\|_{H^1(\mathcal{B})} \leq C\left(H^{p} + \left(\frac{h}{\epsilon}\right)^{2q}\right) + e_{mod}\,, \tag{32}$$

$$\|\boldsymbol{u}^0 - \boldsymbol{u}^H\|_{A(\mathcal{B})} \leq C\left(H^{p} + \left(\frac{h}{\epsilon}\right)^{2q}\right) + e_{mod}\,. \tag{33}$$

For e_{mod} in (31)–(33) it holds

$$e_{mod} = \begin{cases} 0 & \text{for periodic coupling with } \delta/\epsilon \in \mathbb{N} \\ C\,\dfrac{\epsilon}{\delta} & \text{for Dirichlet coupling with } \delta > \epsilon. \end{cases} \tag{34}$$

given that the hypotheses hold, that the elasticity tensor $\mathbb{A}^\epsilon$ is periodic on the RVE and, that the micro solution is sufficiently smooth, Jecker and Abdulle (2016).

The modeling error for Dirichlet coupling in (31)–(33) is due to boundary layers E et al. (2005) (Thm. 1.2), Abdulle (2009). So even for $H \to 0$ and $h \to 0$ there is a residual error.

Remark 1.

(i) Order $2q$ of the micro error in the L^2-norm according to (31) seems to contradict standard FEM results. Even more, its order each in the H^1- and energy-norm scales with $2q$ in the same order as in the L^2-norm, a phenomenon which is referred to as *superconvergence* in the context of standard (single-scale) finite element methods. For the latter however, superconvergence is not inconditional, since that kind of superconvergence is not only restricted to particular element sites but also to the rectangular shape of them Barlow (1976). Notice that the latter superconvergence can be used for the construction of a recovery-type error estimator based on the so-called Superconvergent Patch Recovery (SPR) introduced by Zienkiewicz and Zhu (1992a,b), a concept which is adopted in Section 4.3 of the present work.

(ii) The alleged inconsistency of the micro convergence error order is resolved by the fact that (31)–(33) describe the micro error as propagated to the macroscale; it is measured by macro quantities, i.e. by $\boldsymbol{u}^H$ in the L^2-norm, and by macroscopic stress and strain in the energy-norm. In contrast to this propagated micro error on the macroscale, the micro error on the microscale, which is measured by micro quantities, scales in the order of $\mathcal{O}((h/\epsilon)^{q+1})$ in the L^2-norm and of $\mathcal{O}((h/\epsilon)^q)$ in the H^1- and energy-norm thus being consistent with estimates of standard finite elements.

(iii) For its composition covering both the macro error as well as the micro error, the estimates (31)–(33) enable strategies to achieve the optimal convergence order for minimal computational costs in uniform micro–macro discretizations; they answer the practical question on how to improve in two-scale finite element frameworks the accuracy by H-/h-refinements on both the macro- and the microscale most efficiently.

Table 1 displays the optimal uniform micro–macro refinement strategies for the error in the L^2-norm and the H^1-/energy-norm. Of course, the strategy's dependency on the polynomial order of macro shape functions p and q on the microscale crucially relies on sufficient regularity of the corresponding BVPs.

(iv) For numerical convergence analyses of the macro error it is enough to compute the total error at various macrodiscretizations H keeping the micro errors constant by employing a constant micro discretization h. Consequently, the reference solution for error computation is $\boldsymbol{u}^{H,\mathrm{ref}}(H \to 0, h = const.)$. Convergence analyses of the micro error are carried out analogously; in this case the reference solution is $\boldsymbol{u}^{H,\mathrm{ref}}(H = const., h \to 0)$.

Table 1
Optimal uniform micro–macro refinement strategies: full order for minimal effort. N_{mic} denotes the number of unknowns on the microscale, N_{mac} on the macroscale.

Macro-,micro-FEM	L^2-norm	H^1-/energy-norm
$P^p,\ P^q$	$N_{mic} = (N_{mac})^{p+1/2q}$	$N_{mic} = (N_{mac})^{p/2q}$

(v) To our knowledge no estimate for the modeling error along with Neumann BC is available in mathematical literature.

4.2. Error computation

For the special case of a micro error convergence analysis on the microscale (as e.g. on a selected microdomain) any macroscopic influence must be switched off. However, since different micro discretizations imply numerical differences in the stiffness approximation, they influence macroscopic displacements, which themselves influence through the postprocessing the microscopic quantities. Consequently, for the micro error analysis on the microscale the macrosolution is kept fixed and only the postprocessing is executed and enters the micro error analysis.

Since the estimates (31)–(33) are carried out on the macroscale and measured in macroscopic quantities, error analyses for their numerical verification equally operate on the macroscale.

The integrals for error calculation in the norms (A.4)–(A.6) are approximated by numerical integration of Gauss–Legendre. The computations are carried out on macro element level of the discretization for the reference solution. For the error in the L^2-norm it follows

$$\|\boldsymbol{u}^{H,\mathrm{ref}} - \boldsymbol{u}^H\|_{L^2(\Omega)} = \left[\sum_{K\in\mathcal{T}_{\mathrm{ref}}}\left(\sum_{i=1}^{ngp}\omega_i\left(\boldsymbol{u}^{H,\mathrm{ref}}(\boldsymbol{x}_i^{\mathrm{ref}}) - \boldsymbol{u}^H(\boldsymbol{x}_i^{\mathrm{ref}})\right)^2 \det\boldsymbol{J}\right)\right]^{1/2}. \tag{35}$$

For evaluating (35) the displacements of both the standard FE-HMM solution $\boldsymbol{u}^H$ and the reference solution $\boldsymbol{u}^{H,\mathrm{ref}}$ have to be known in the quadrature points of the reference solution $\boldsymbol{x}_i^{\mathrm{ref}}$. In the simplest case – when only the micro error convergence is analyzed – both solutions are computed on the same macro discretization $\mathcal{T}_{\mathrm{ref}} = \mathcal{T}_H$ and the elements and their quadrature points therefore coincide, cf. Remark 1(iv).

If the macro error or the total error is investigated, the reference solution has a finer macro triangulation than the single FE-HMM solutions. In this case the results of the FE-HMM solution are projected onto the finer grid of the reference solution.

Fig. 3 schematically displays the projection from a rather coarse macro triangulation $\mathcal{T}_H$ onto the finer reference triangulation $\mathcal{T}_{\mathrm{ref}}$ for one element of the reference mesh. Therein, the quantities of the coarse mesh are projected onto the quadrature points of the reference solution $\boldsymbol{x}_i^{\mathrm{ref}}$ such that the error of the quantities of interest can be calculated, e.g. for the displacement error in the L^2-norm according to (35).

If the absolute figures of the errors are of interest, the total discretization error, its macro and micro parts can be efficiently computed by merely two reference solutions as for example in Table 2.

The computation of reference solutions in (1) and (2) in Table 2 can efficiently be carried out in single-scale finite element simulations on the macroscale using the homogenized elasticity tensor $\mathbb{A}^{0,h}(h \to 0)$ determined in a preprocessing step.

4.3. Error estimation based on the Superconvergent Patch Recovery (SPR)

In (engineering) practice, error computation as described in 4.2 is prohibitive. Instead, the total error is estimated, which is carried out on the particular discretization in use. For that purpose the present work uses the recovery-type error estimation of Zienkiewicz and Zhu,

Table 2
Rationale for the efficient computation of the total error and its macro and micro parts.

Step	Type of error	Reference solution $\boldsymbol{u}^{H,\mathrm{ref}}$
(1)	Total error at H and h: e_{tot}	$\boldsymbol{u}^{H}(H \to 0, h \to 0)$
(2)	Micro error: e_{mic}	$\boldsymbol{u}^{H}(H, h \to 0)$.
(3)	Resultant macro error: $e_{mac} = e_{tot} - e_{mic}$	$\boldsymbol{u}^{H}(H \to 0, h)$

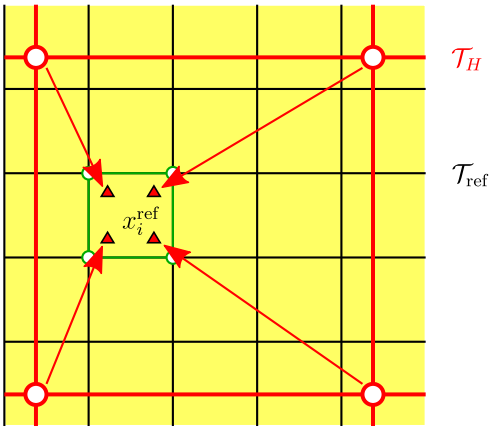


Fig. 3. Projection from a coarse macro mesh (red) onto the quadrature points of an element (green) in the fine mesh of the reference solution (black) for linear shape functions. (For interpretation of the references to color in this figure legend, the reader is referred to the web version of this article.)

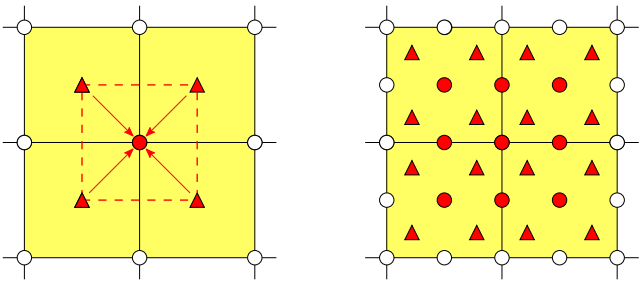


Fig. 4. Recovery of nodal stresses from stresses of surrounding superconvergent points (marked by a ▵) for 4-node elements (left) and 9-node elements (right). The nodal stresses of the red marked nodes can be calculated using the shown patches.

which exploits superconvergence of stress and strain. In Zienkiewicz and Zhu (1992a,b) a procedure for the transfer of the superconvergence property from superconvergent, inner element points to element nodes referred to as "superconvergent patch recovery" (SPR) was proposed. Based on these recovered superconvergent nodal values the same authors constructed an error estimator that guided adaptive mesh refinement.

4.3.1. The SPR on the macroscale

For ready reference, the rationale of the SPR is briefly re-iterated for linear and quadratic shape functions, where we restrict to the $n_{dim} = 2$ case for convenience. Strain and stress are calculated at superconvergent element sites that is for $p = 1$ in the center of a rectangular element, for $p = 2$ in the 2×2 points of Gauss–Legendre quadrature. These values are transferred by a least-square procedure to the finite element node in the direct neighborhood, for a visualization see Fig. 4. Elements having such a node in common are referred to as the patch in the superconvergent recovery procedure.

Stresses on the patch are prescribed component-wise by

$$\boldsymbol{\sigma}_p^{\star} = \boldsymbol{P}\,\boldsymbol{a} \tag{36}$$

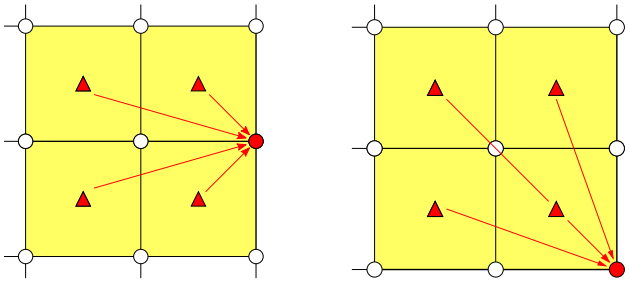


Fig. 5. Recovery of nodal stresses using patch recovery for boundary and corner nodes.

with, for the case of linear shape functions,

$$\boldsymbol{P} = [1,\ x,\ y,\ xy] \quad \text{and} \quad \boldsymbol{a} = \left[a_1,\ a_2,\ a_3,\ a_4\right]. \tag{37}$$

The displayed vector $\boldsymbol{P}$ contains polynomial terms of bilinear shape functions for $n_{dim} = 2$ and a 4-node quadrilateral, for a 9-node quadrilateral quadratic terms are considered additionally. The patch around a finite element node consists of four elements with one (4-node quadrilateral) respectively four (9-node quadrilateral) superconvergent points per element. For the determination of the unknown vector $\boldsymbol{a}$ the function

$$\begin{aligned} F(\boldsymbol{a}) &= \sum_{i=1}^{n} (\boldsymbol{\sigma}_h(x_i,\ y_i) - \boldsymbol{\sigma}_p^{\star}(x_i,\ y_i))^2 \\ &= \sum_{i=1}^{n} (\boldsymbol{\sigma}_h(x_i,\ y_i) - \boldsymbol{P}(x_i,\ y_i)\,\mathbf{a})^2 \end{aligned} \tag{38}$$

has to be minimized. Therein, $(x_i,\ y_i)$ are the coordinates of the superconvergent points, n is the number of superconvergent points of the total patch and $\boldsymbol{\sigma}_h(x_i,\ y_i)$ are the stresses in these superconvergent points. Minimization of $F(\boldsymbol{a})$ implies that $\boldsymbol{a}$ fulfills the condition

$$\sum_{i=1}^{n} \boldsymbol{P}^T(x_i,\ y_i)\,\boldsymbol{P}(x_i,\ y_i)\,\boldsymbol{a} = \sum_{i=1}^{n} \boldsymbol{P}^T(x_i,\ y_i)\,\boldsymbol{\sigma}_h(x_i,\ y_i), \tag{39}$$

which can be solved for $\boldsymbol{a}$

$$\boldsymbol{a} = \boldsymbol{A}^{-1}\,\boldsymbol{b} \tag{40}$$

with

$$\boldsymbol{A} = \sum_{i=1}^{n} \boldsymbol{P}^T(x_i,\ y_i)\,\boldsymbol{P}(x_i,\ y_i) \quad \text{and} \quad \boldsymbol{b} = \sum_{i=1}^{n} \boldsymbol{P}^T(x_i,\ y_i)\,\boldsymbol{\sigma}_h(x_i,\ y_i). \tag{41}$$

Stresses in the central node of the patch can be recovered by inserting its nodal coordinates $(x_N,\ y_N)$ into the $\boldsymbol{P}$-vector in (36).

Fig. 5 shows the patches for boundary nodes lying either on edges or at corners. Corner nodes adjoin only one element which is insufficient for the calculation method described above. A similar situation arises for any node on the boundary which is adjoined to two elements. Here the patches have to be complemented by further elements.

Another peculiarity exists for patches of 9-node elements. For all of the red marked nodes in Fig. 4 –except of the central-one– there are two or even more patches available to compute the nodal stresses. In this case the nodal values are calculated by simply averaging the results from the single patches.

4.3.2. Error estimator and effectivity index

As described above, the error estimator is built on superconvergent stress $\boldsymbol{\sigma}^{\star}$ and strain $\boldsymbol{\varepsilon}^{\star}$. Of course, the procedure is not applicable for an

error estimate in the L^2-norm of displacements, since for the existing continuity of displacements the recovery-type error estimator cannot be constructed. The estimated error in the energy-norm reads as

$$\|\bar{e}\|_{A(\Omega)} = \|\boldsymbol{u}^\star - \boldsymbol{u}^H\|_{A(\Omega)} = \sqrt{\int_\Omega \left(\boldsymbol{\sigma}^\star - \boldsymbol{\sigma}^H\right) : \left(\boldsymbol{\varepsilon}^\star - \boldsymbol{\varepsilon}^H\right) dV}\,, \tag{42}$$

$$\approx \left[\sum_{K\in\mathcal{T}_H}\left(\sum_{i=1}^{ngp}\omega_i \left(\boldsymbol{\sigma}^\star - \boldsymbol{\sigma}^H\right)(\boldsymbol{x}_i^H) : \left(\boldsymbol{\varepsilon}^\star - \boldsymbol{\varepsilon}^H\right)(\boldsymbol{x}_i^H)\,\det\boldsymbol{J}\right)\right]^{1/2}. \tag{43}$$

Compared to the error computation based on a reference solution

$$\|\boldsymbol{e}\|_{A(\Omega)} = \|\boldsymbol{u}^0 - \boldsymbol{u}^H\|_{A(\Omega)} \approx \left[\sum_{K\in\mathcal{T}_{\text{ref}}}\left(\sum_{i=1}^{ngp}\omega_i \left(\boldsymbol{\sigma}^{\text{ref}} - \boldsymbol{\sigma}^H\right)(\boldsymbol{x}_i^{\text{ref}}) : \left(\boldsymbol{\varepsilon}^{\text{ref}} - \boldsymbol{\varepsilon}^H\right)(\boldsymbol{x}_i^{\text{ref}})\,\det\boldsymbol{J}\right)\right]^{1/2} \tag{44}$$

the numerical effort of the error estimation is clearly much smaller, since the integration of the error is carried out on the corresponding macro mesh with triangulation $\mathcal{T}_H$ instead of the reference mesh with triangulation $\mathcal{T}_{\text{ref}}$. More important, error estimation can be carried out on-the-fly, no additional solution on a different mesh is required.

The quality of the error estimator is typically assessed by the so-called effectivity index θ which is defined as the ratio of the estimated error $\bar{e}$ to the true error $\boldsymbol{e}$

$$\theta = \frac{\|\bar{e}\|}{\|\boldsymbol{e}\|}\,. \tag{45}$$

For consistency the effectivity index must tend to unity as the exact error tends to zero which can easily be shown if the error of stress and strain is considered. For the case of stresses entering the error analysis, the effectivity index follows to

$$\theta = \frac{\|\bar{e}_\sigma\|}{\|\boldsymbol{e}_\sigma\|} = \frac{\|\boldsymbol{\sigma}^\star - \boldsymbol{\sigma}^H\|}{\|\boldsymbol{\sigma}^0 - \boldsymbol{\sigma}^H\|} = \frac{\|\boldsymbol{\sigma}^\star - \boldsymbol{\sigma}^0 + \boldsymbol{\sigma}^0 - \boldsymbol{\sigma}^H\|}{\|\boldsymbol{\sigma}^0 - \boldsymbol{\sigma}^H\|}\,. \tag{46}$$

The numerator in (46) contains the error of standard stresses with respect to superconvergent stresses. A distinction of cases provides an upper and a lower bound for θ

$$1 - \frac{\|\boldsymbol{\sigma}^\star - \boldsymbol{\sigma}^0\|}{\|\boldsymbol{\sigma}^0 - \boldsymbol{\sigma}^H\|} \le \theta \le 1 + \frac{\|\boldsymbol{\sigma}^\star - \boldsymbol{\sigma}^0\|}{\|\boldsymbol{\sigma}^0 - \boldsymbol{\sigma}^H\|}\,. \tag{47}$$

Since the error of superconvergent quantities is expected to converge in higher order than the error of standard quantities, both bounds tend to unity as the error tends to zero.

Remark 2. Imagine the case of error estimation on the macroscale for two different (macro-, micro-) discretizations, e.g. (H, h) and $(H, h/2)$; the figures of the error estimates are expected to differ. Does this difference indicate that the error estimator on the macroscale includes the microdiscretization error? If not, why not and what else is indicated by the difference?

Here, the error estimator operates on the macroscale and exclusively estimates the macro discretization error at macro element size H along with an effective macro constitutive law.[3] The macro constitutive law is given in terms of its type and its material parameters, the latter depend on microdiscretization h. For the present case of linear elasticity the approximation $\mathbb{A}^{0,h}$ and its coefficients converge for sufficiently regular problems in the order $\mathcal{O}(h^{2q})$ to $\mathbb{A}^0$ for $h \to 0$ Jecker and Abdulle (2016), Eidel and Fischer (2018). On the microscale the deviation of $\mathbb{A}^{0,h/2}$ to $\mathbb{A}^{0,h}$ indicates a discretization error as the deviation of $\boldsymbol{u}^{h/2}$ to $\boldsymbol{u}^h$ does, which is hence accessible to an error estimator working on the microscale. In the error estimation working on the macroscale however, the deviation of $\mathbb{A}^{0,h/2}$ to $\mathbb{A}^{0,h}$ is not a discretization error but indicates a modeling-type error in terms of different constitutive laws, in the present setting in terms of different model parameters for the same *type* of constitutive law.

[3] Recall, that the reference solution for the computation of the true macro error is $\boldsymbol{u}^H(H \to 0, h)$.

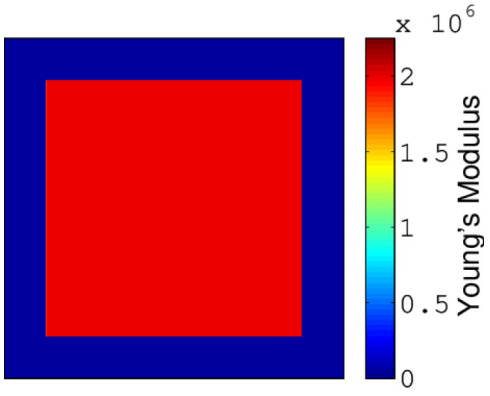


Fig. 6. Matrix-inclusion microstructure. Distribution of Young's modulus on the micro domain.

5. Numerical examples

In this section a thorough convergence and error analysis is carried out for the three coupling conditions employing linear and quadratic shape functions on both the macro- and the microscale.

First, the three micro-coupling conditions are compared in the microscale setting of (i) a matrix-inclusion problem, (ii) a chessboard-type microstructure, and (iii) a sine wave distribution of material stiffness, where the strength and quality of the stiffness contrast between different phases and its impact on the convergence properties is a key aspect of investigation.

The convergence analysis measures the micro error both on the microscale (i.e. on one microdomain) and on the macroscale (as the total micro error that is propagated to the macroscale). Estimates for sufficiently regular problems are provided in Section 4.1. For the microerror on the macroscale the order $2q$ is expected in all three norms, see (31)–(33). For the micro error as measured on the microscale, order $q+1$ is expected in the L^2-norm, and q in the H^1- and energy-norm.

Similarly, the regularity of the macro-BVP is examined through the convergence of the macro error. Here, the results of a clamped, square plate with low regularity due to notch effects at the clamped boundary are contrasted to a tapered cantilever of proven high regularity.

Moreover, the above examples, which have plane strain conditions and loading by volume forces in common, serve the purpose to compare the estimated error with the true error and to verify the optimal uniform micro–macro mesh refinement strategies of Table 1.

5.1. Micro convergence analysis

The macro problem common to all micro problems is a square cantilever subject to a volume forces of $\boldsymbol{f} = [0, -10]^T\ [F/L^2]$. The coupling conditions which will be analyzed are Dirichlet, Neumann and periodic coupling.

5.1.1. Matrix-inclusion problem

In the first numerical example we consider the microstructure of a stiff inclusion in a soft matrix, which is displayed in Fig. 6. The Young's moduli of the inclusion $E_i = 2\,000\,000\ [F/L^2]$ and the matrix phase $E_m = 40\,000\ [F/L^2]$ exhibit a contrast of $E_i/E_m = 50$, for the Poisson's ratio it holds $\nu = 0.2$. The volume ratio of the inclusion phase is $V_i/V_{tot} = 9/16$. The square RVE exhibits side length $\epsilon = 0.005$, which is maintained for all examples in the present work.

The simulation results for linear shape functions are displayed in Fig. 7 (first row). The different coupling conditions show minor deviations from each other in the convergence order. The values of the calculated errors are in good agreement between all coupling conditions, only the error for Neumann coupling in the energy-norm

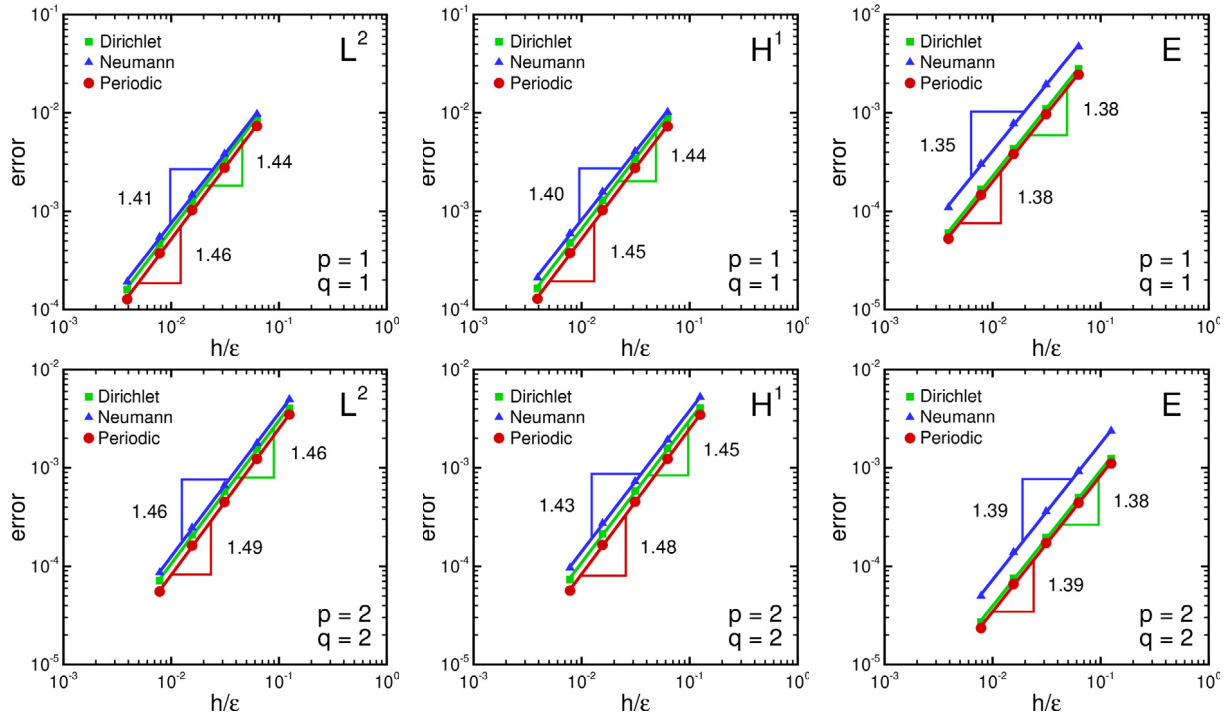


Fig. 7. Micro error convergence on the macroscale for matrix-inclusion problem: (first row) linear shape functions $p = q = 1$, (second row) quadratic shape functions $p = q = 2$, from left to right: L^2-, H^1-, energy-norm.

is slightly larger. Notice that we use here and in the following relative errors, i.e. $\|\boldsymbol{e}\|_{(\Omega)}/\|\boldsymbol{u}\|_{(\Omega)}$.

The observed order reduction from theoretical order $2q = 2$ for $q = 1$ to approximately 1.4 in all three norms is due to the stiffness-jump at the inclusion–matrix interface along with the high contrast of the Young's moduli of the two phases, the corresponding notch effect lowers the regularity of the microproblem.

The diagrams in Fig. 7 (second row) display the simulation results for quadratic shape functions, $p = q = 2$. In all of the above described aspects we observe even quantitatively almost the same behavior as for $p = q = 1$. Hence, it is the singularity of the problem which overrules the theoretical convergence order, i.e. quadratic shape functions do not cure the problem of low regularity.

Micro error convergence on the microscale. The results of an error calculation on one microdomain attached to the macroscopic quadrature point at [0.26, 0.26] is shown in the first row diagrams of Fig. 8 for linear shape functions. The convergence orders for different coupling conditions are in good agreement with each other.

The optimal convergence orders of $q + 1$ in the L^2-norm and q in the H^1- as well as in the energy-norm is not reached due to the above mentioned reduced regularity.

Fig. 8 (second row diagrams) displays the errors on one microdomain for quadratic shape functions. Again the convergence orders of the different coupling conditions are in good agreement with each other except of for Neumann coupling in the L^2-norm. A closer look at these calculated errors reveals that for coarse discretizations the error is too large and for that reason converges faster than expected. If only the two finest discretizations are considered, convergence is in reasonable agreement with the other two coupling conditions.

5.1.2. *Comparison of methods for constant traction BC for efficiency*

The efficiency of the method for constant tractions ("full gradient") outlined in Section 3.3 is compared with the semi-Dirichlet coupling introduced by Javili et al. (2017) (briefly outlined in A.3) and with the perturbation technique of Miehe and Koch (2002). For that aim the already introduced matrix-inclusion problem is considered.

Fig. 9 displays the absolute computational time of each method (left) and the relative computational time related to the computational time (right) on the micro level including the stiffness matrix calculation. The results show the expected difference in the absolute calculation time; the semi-Dirichlet approach requires twice as much time as the other two methods for the required iterations. The relative calculation times indicate that for an increasing number of micro elements the influence of solving the system of equations decreases. Notice that the perturbation technique lacks proper rotations without an extra embedding of the microdomain into the macroscopic rotations, a lack which is overcome by considering the full gradient according to (26) in Section 3.3.

5.1.3. *Chessboard microstructure*

While in the first example of the matrix-inclusion problem the material at the RVE boundary was homogeneous, we choose a chessboard-type microstructure, where the heterogeneity is expanded from the micro domain's interior to its boundaries, see Fig. 10. The aim is to investigate the impact of micro-coupling conditions on the results for that case.

The chessboard pattern of Young's modulus distribution exhibits two phases with $E_1 = 2\,000\,000\ [F/L^2]$ and $E_2 = 40\,000\ [F/L^2]$. The stiffness contrast of the phases is $E_1/E_2 = 50$, for the Poisson's ratio it holds $\nu = 0.2$.

The results for linear shape functions are displayed in Fig. 11 (first row). Again, the different coupling conditions agree well in the convergence order. The relative error however exhibits larger deviations between the coupling conditions. An exception is the energy-norm for PBC which leads to far worse results. Starting with the coarse discretizations on the right side of Fig. 11 (first row, right) the error first increases with finer meshes and finally decreases again. The results of the calculations with rather fine micro meshes fit well into the results for Dirichlet and Neumann coupling, while the calculated errors for coarse meshes seem to be too small.

Again the optimal convergence order cannot be reached in any of the norms due to the reduced regularity of the micro problem which

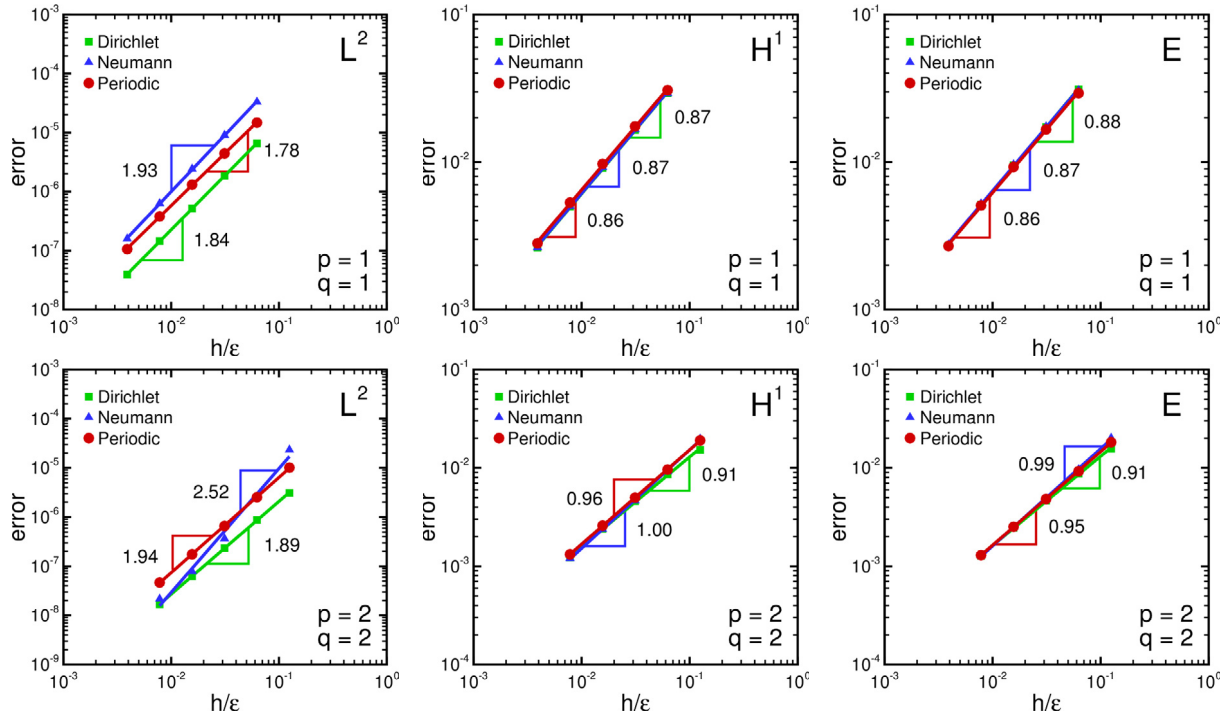


Fig. 8. Micro error convergence on the microscale for matrix-inclusion problem. (first row) linear shape functions, (second row) quadratic shape functions, (from left to right:) L^2-, H^1- and energy-norm.

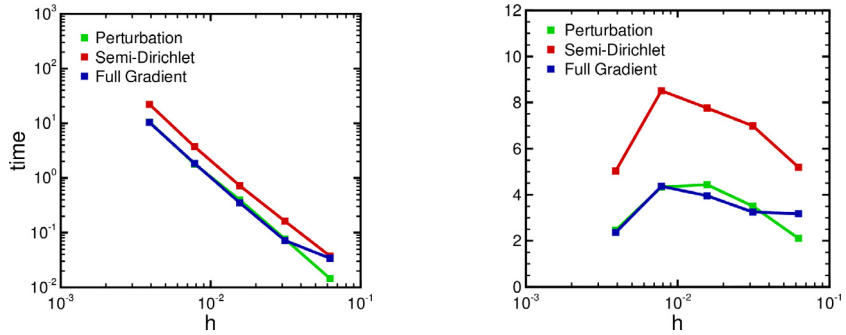


Fig. 9. Computational time of methods for constant traction BC. Absolute computational time (left) and relative computational time related to full computation time on the micro level.

is again based in the stiffness-jump at the interface between the two phases. The deviation from the optimal convergence order is even larger compared to the matrix-inclusion problem.

Remark. The convergence results for PBC in the energy-norm deserve a closer investigation; the analysis reveals that stresses in the macroscopic quadrature points do not exhibit sufficient accuracy. The entries of the homogenized elasticity tensor $\mathbb{A}^0$, which is used to calculate macroscopic stresses, converge with orders in the range from 0.62 ($\mathbb{A}^0_{12}$) to 0.72 ($\mathbb{A}^0_{11}$) which is in the range of the convergence orders of the L^2- and H^1-norm. The investigation of the homogenized elasticity tensor showed that there is a major absolute error in the single entries. The error of the coarsest discretization is about 50% of the numerical values of the reference solution in all entries. For Neumann coupling in contrast, the errors are in the range from 7–12%, and for Dirichlet coupling in the range of 8–21%. These findings suggest that the questionable results for the error in the energy-norm for PBC is caused by the major absolute error of the homogenized tensor.

Fig. 11 (second row) shows the results for quadratic shape functions. The results do not differ significantly from the results for linear shape functions. Again the error in the energy-norm seems to be too small for periodic coupling conditions and rather coarse discretizations.

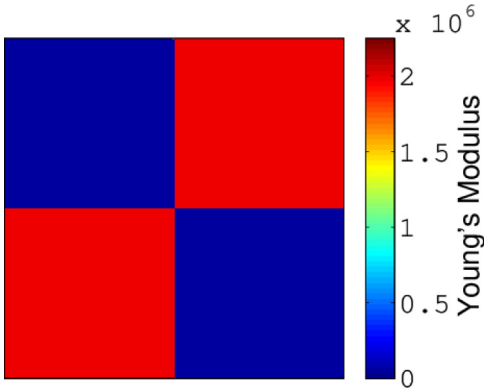


Fig. 10. Chessboard-type microstructure. Distribution of Young's modulus on the micro domain.

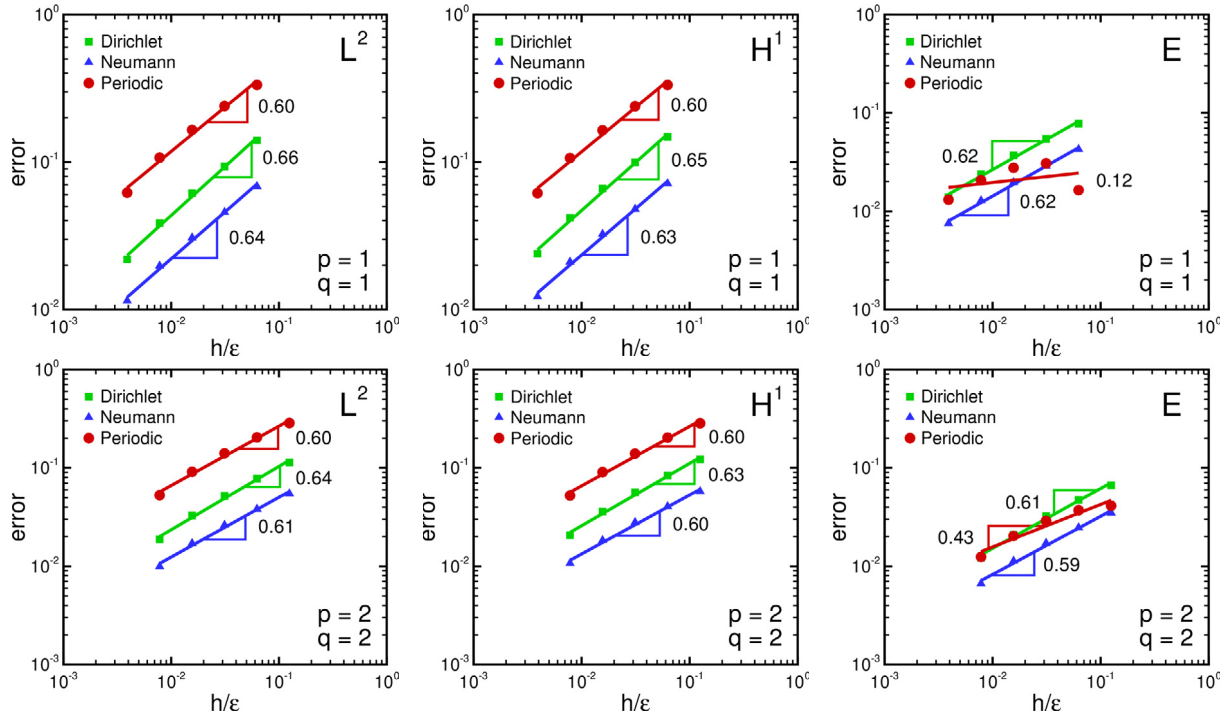


Fig. 11. Micro error convergence on the macroscale for chessboard stiffness pattern. (first row) linear shape functions, $p = q = 1$, (second row) quadratic shape functions, $p = q = 2$, (from left to right:) L^2-, H^1-and energy-norm.

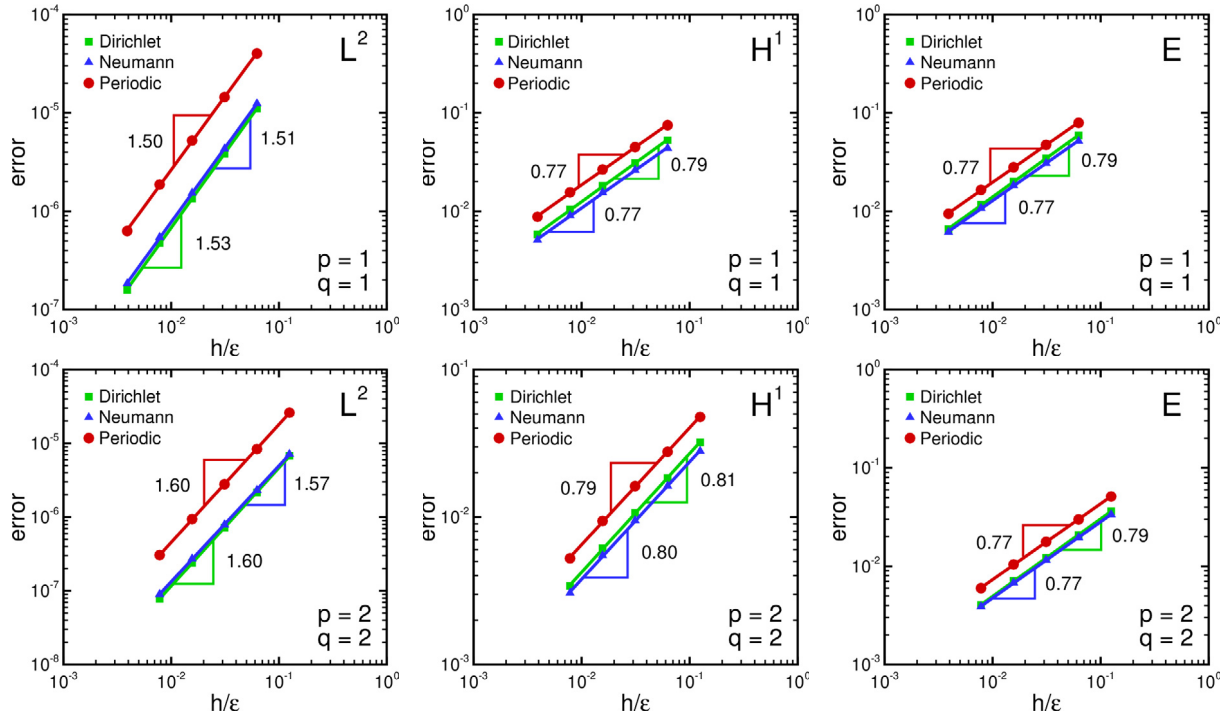


Fig. 12. Micro error convergence on the microscale for chessboard stiffness pattern. (first row) linear shape functions, $p = q = 1$, (second row) quadratic shape functions, $p = q = 2$, (from left to right:) L^2-, H^1-and energy-norm.

The optimal convergence order of $2q = 4$ is clearly missed and the use of quadratic shape functions does not improve the convergence order.

Micro error convergence on the microscale. The results of an error calculation on the microdomain related to the macroscopic quadrature point at [0.26, 0.26] with linear shape functions can be found in Fig. 12 (first row). The convergence orders for different coupling conditions exhibit good agreement.

Fig. 12 (second row) indicates that for quadratic shape functions the convergence orders are in good agreement for the different coupling conditions. The convergence order however is not improved for quadratic shape functions compared to the linear case, which is due to the low regularity.

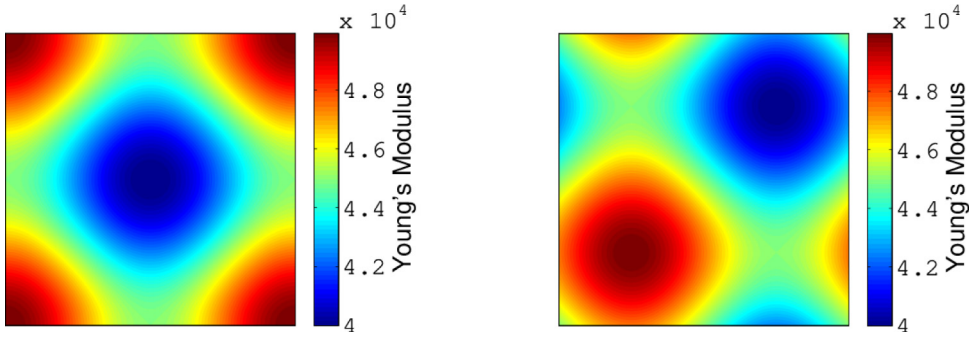


Fig. 13. Sine wave distribution problem. Distribution of Young's modulus on (left) a unit cell with cubic symmetry and (right) an alternative unit cell.

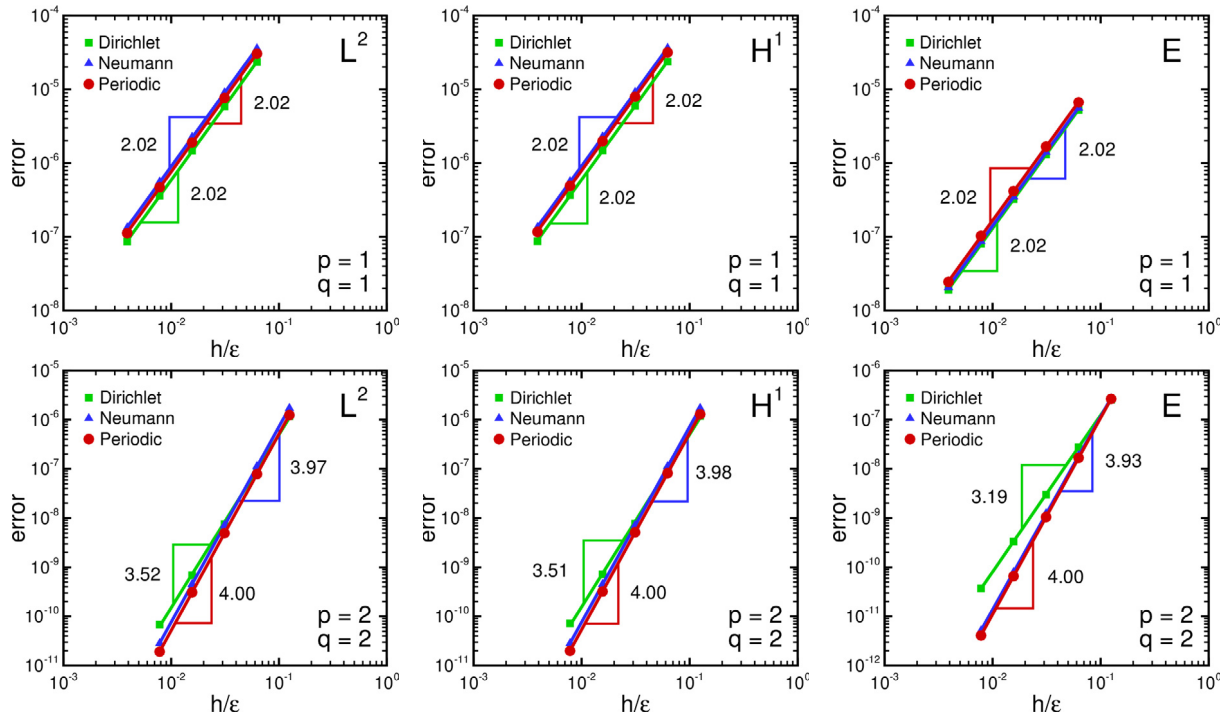


Fig. 14. Micro error convergence on the macroscale for a microstructure with sine wave stiffness distribution. (first row) linear shape functions, $p = q = 1$, (second row) quadratic shape functions, $p = q = 2$, (from left to right:) L^2-, H^1-and energy-norm.

5.1.4. Sine wave distribution

The low regularity of the micro BVP in the first two examples is the reason why convergence for quadratic shape functions shows a strong deviation from the nominal order. Aiming at the full convergence order of $2q$ for the micro error a sine wave-type Young's modulus distribution is chosen, which is expected to exhibit high regularity for its smooth stiffness distribution. Therein, the minimum Young's modulus is $E_{min} = 40\,000\ [F/L^2]$, the maximum is $E_{max} = 50\,000\ [F/L^2]$.

The Young's modulus distribution on the micro domain is depicted in Fig. 13. The unit cell in the left reflects the cubic symmetry of the periodic structure; an alternative definition (among many others) of the unit cell is displayed on the right of Fig. 13. While the stiffness results for Neumann and Dirichlet coupling depend on the choice of the unit cell, for PBC stiffness is invariant with respect to that choice. In the following we use the unit cell in the right of Fig. 13.

Fig. 14 (first row) shows the results for linear shape functions. In all norms and for all coupling conditions the convergence order of the calculated errors is 2.02. The numerical values of the relative errors also show only minor deviations. The sine wave distribution enables full regularity of the solution as indicated by the full theoretical convergence order in all norms.

The results for quadratic micro shape functions are displayed in the second row of Fig. 14. For periodic and Neumann coupling conditions the optimal convergence order of $2q = 4$ is virtually achieved in all norms, while for Dirichlet coupling a reduced order is observed. The numerical values of the relative errors of Neumann and periodic coupling are in good agreement, while the values for Dirichlet coupling exhibit good agreement with the estimates only for coarse discretizations, for finer discretizations they worsen most notably in the energy-norm.

In conclusion, the regularity of the micro BVP enables full convergence order and – opposed to the first two examples – a higher convergence order for quadratic shape functions than for linear shape functions.

Micro error convergence on the microscale. The error calculation on the microdomain related to the macroscopic quadrature point at [0.26, 0.26] for $q = 1$ yields the results that are displayed in Fig. 15 (first row). The convergence orders of $q+1$ in the L^2-norm and q in the H^1- and energy-norm are achieved for Dirichlet and periodic coupling, for Neumann coupling there are some minor deviations in the L^2-norm.

The results of the error calculation on the same microdomain for quadratic shape functions are displayed in Fig. 15 (second row). For periodic coupling the optimal convergence order is achieved in all norms,

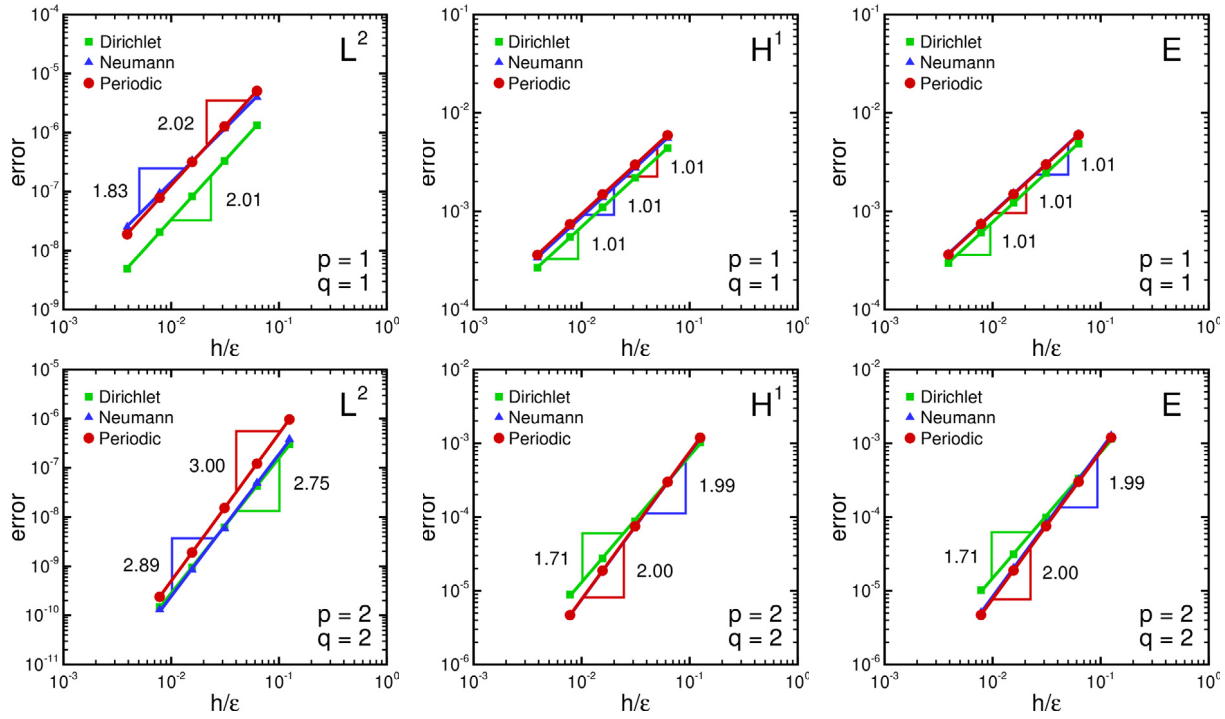


Fig. 15. Micro error convergence on the microscale for a microstructure with sine wave stiffness distribution. (first row) linear shape functions $p = q = 1$, (second row) quadratic shape functions $p = q = 2$, (from left to right:) L^2-, H^1-, and energy-norm.

for Neumann coupling the optimal convergence order is restricted to the H^1- and the energy-norm. Dirichlet coupling however, shows again minor reductions in all three norms, which is consistent with the reduced convergence order of the micro error on the macroscale.

Remark. The measured convergence orders being almost in perfect agreement with the a priori estimates could suggest that the observed regularity is due to the low stiffness contrast (1:1.25). Additional analyses employing an increased stiffness contrast of up to 1:25 yield the same convergence orders and thereby rebut this hypothesis. Instead it is the smoothness of Young's modulus distribution that enables the regularity in terms of full convergence orders.

5.2. Macro convergence analysis

After the assessment of micro errors both on the micro as well as on the macroscale, the macro error convergence is investigated in the following.

5.2.1. Square cantilever

In the first numerical example we consider the square cantilever of Fig. 16, which is subject to volume forces of $\boldsymbol{f} = [0, -10]^T$ $[F/L^2]$. The microstructure is the already introduced sine wave-type distribution of Young's modulus.

The results of the convergence analysis for linear shape functions is shown in the first row of Fig. 17. The optimal convergence orders, of $p+1$ in the L^2-norm and of p in the H^1- and energy-norm are not achieved, but the deviations are small. The micro–macro coupling condition has virtually no influence on the macro error convergence. The results employing quadratic shape functions as displayed in Fig. 17 (second row) exhibit only very minor deviations compared to linear shape functions; first, the results for all coupling conditions coincide in each norm. Second, the convergence orders are 1.64 in the L^2-norm, 0.83 in the H^1-norm and 0.82 in the energy-norm, respectively. In conclusion, the optimal convergence orders are not obtained, the problem of order reduction is not cured at all by increasing the polynomial order of the shape functions.

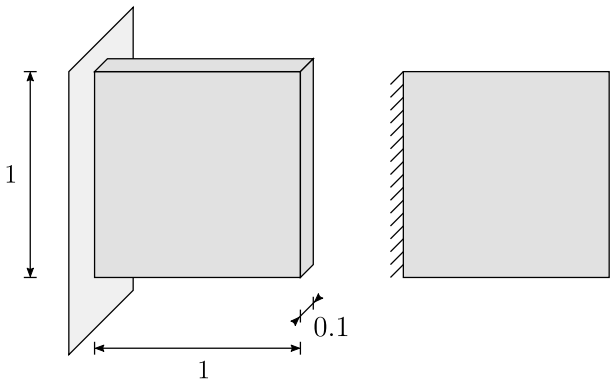


Fig. 16. Model of a square cantilever.

The order reduction is caused by corner singularities at the clamped end of the square cantilever.

The relative elementwise error on the macrodomain is shown in Fig. 18. The error is computed by the ratio of the error in each element and the average energy per element. For the visualization of the error distribution the errors were calculated in the single elements of a coarse macro mesh. For both polynomial orders of shape functions the maximum absolute error is located in the corners of the cantilever's bearing. The high relative error of more than 50% for linear and more than 18% for quadratic shape functions indicates that the total energy in these elements is considerably higher than the average energy per element to which it is related here.

5.2.2. Tapered cantilever

If the angle α is chosen sufficiently large ($\alpha > 28.4°$), then the design of a tapered cantilever as in Fig. 19 avoids the singularities of the square cantilever plate, which was proven by analytical means

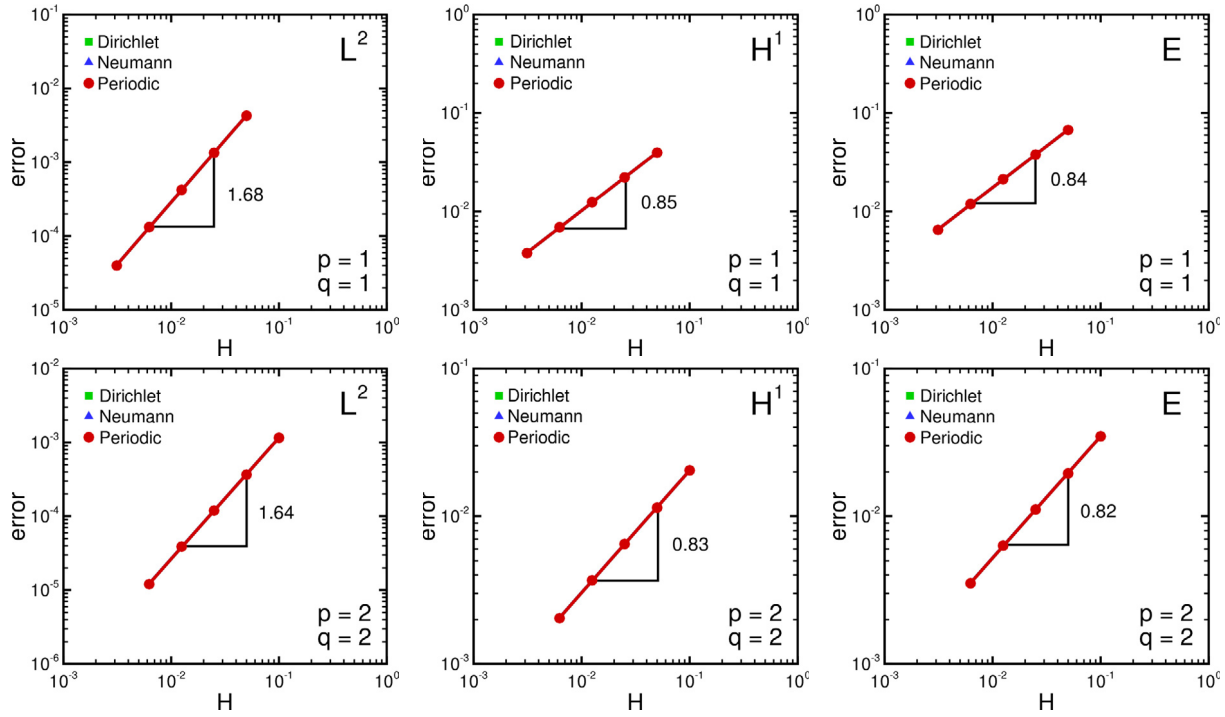


Fig. 17. Macroconvergence for square cantilever under volume force. (first row) linear shape functions $p = q = 1$, (second row) quadratic shape functions $p = q = 2$, (from left to right) L^2-, H^1-, and energy-norm.

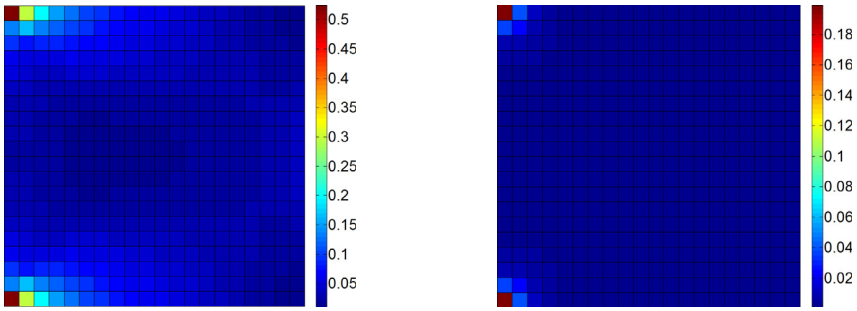


Fig. 18. Square cantilever under volume force. Relative elementwise energy-error distribution on the macrodomain for (left) $p = q = 1$ and (right) $p = q = 2$.

in Rössle (2000). Here we choose $\alpha = 30.4°$. Again, a volume load[4] of $\boldsymbol{f} = [0, -10]^T\ [F/L^2]$ is applied to the cantilever and the sine wave-type microstructure with a Young's modulus contrast of 1.25 is chosen.

The convergence orders for linear shape functions are displayed in the diagrams of the first row in Fig. 20. In all norms the optimal convergence order is achieved. Again, the results of the different coupling conditions coincide.

The results for quadratic shape functions in the second row of Fig. 20 exhibit minor deviations from the full, nominal convergence orders (2.89 instead of 3 in the L^2-norm, and 1.84 instead of 2 in the H^1- and energy-norm). However, compared to the considerable order reduction for the square plate, the present deviations are small.

Fig. 21 displays the relative elementwise error distribution on the macrodomain of the tapered cantilever for linear and for quadratic shape functions. The relative error in the energy-norm is computed as in the previous example. The error distribution reveals that there is no longer a singularity in the lower and upper left corner due to the bearing of the plate. This leads to significantly lower relative errors in these areas.

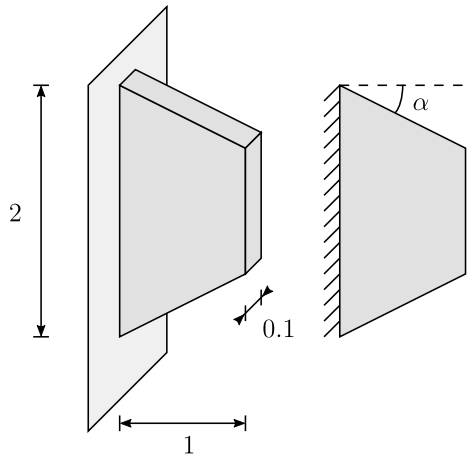


Fig. 19. Model of a tapered cantilever.

[4] According to Rössle (2000) stress-free boundaries on $\partial\mathcal{B}_N$ along with volume loads are an additional condition for the regularity of the BVP.

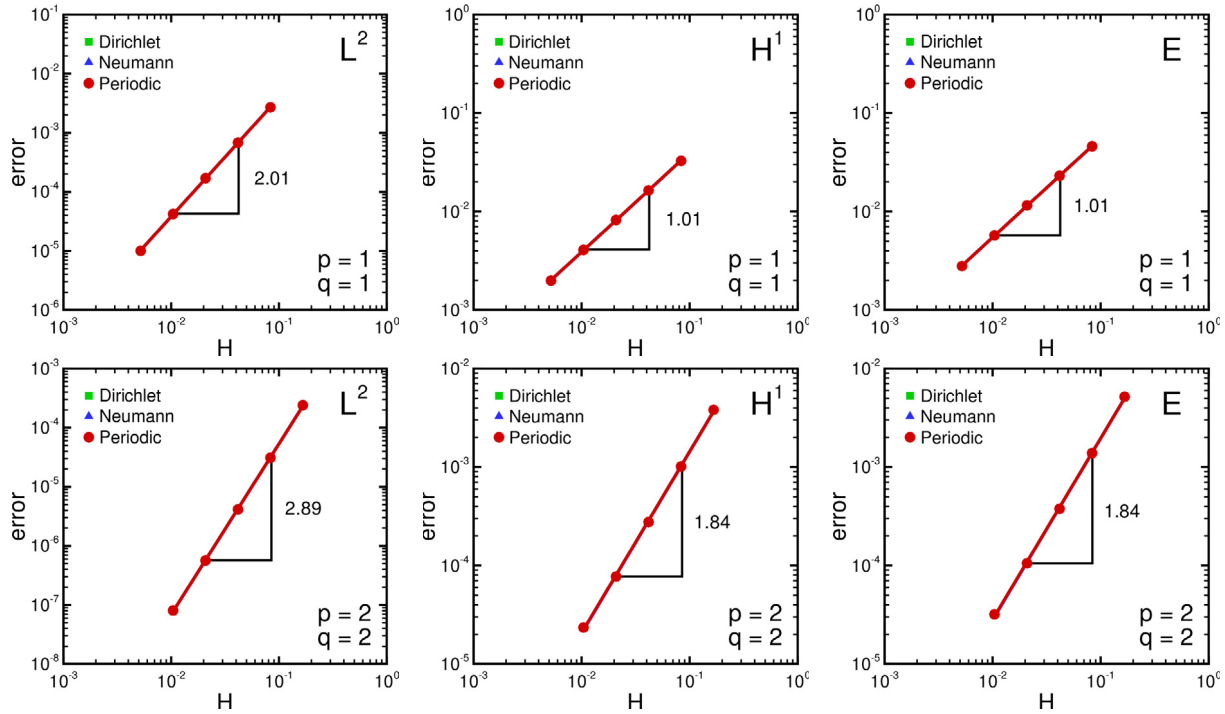


Fig. 20. Tapered cantilever under volume force. Macroconvergence keeping the microdiscretization fixed, (first row) linear shape functions $p = q = 1$, (second row) quadratic shape functions $p = q = 2$, (from left to right) L^2-, H^1-, and energy-norm.

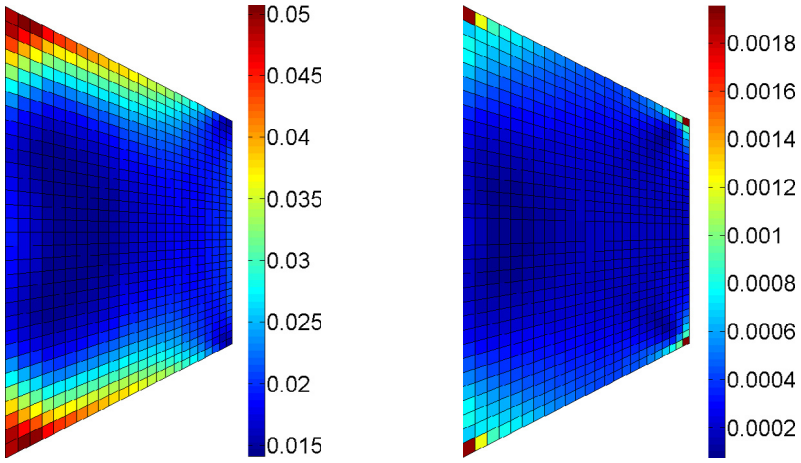


Fig. 21. Tapered cantilever under volume force. Relative elementwise energy-error distribution on the macrodomain for (left) $p = q = 1$ and (right) $p = q = 2$.

5.3. Optimal uniform micro–macro refinement strategy

To investigate the optimal uniform micro–macro refinement strategy for linear and quadratic shape functions, the tapered cantilever is chosen as macro problem and the sine wave distribution is chosen as micro problem for their excellent regularity. The ratio of maximum to minimum Young's modulus is increased to 2.5.

5.3.1. Linear shape functions

For linear shape functions both on the micro and on the macro level the error in the L^2-norm is expected to converge in the order of $p+1 = 2$ on the macro and in the order of $2q = 2$ on the micro level. Since micro and macro error converge in the same order, the micro mesh has to be refined in the same order as the macro mesh in order to achieve the optimal convergence order, $N_{mic} = (N_{mac})^{p+1/2q} = N_{mac}$.

The error in the H^1-/energy-norm converges in the order of $p = 1$ on the macro level and in the order of $2q = 2$ on the micro level. Here the micro error converges in a higher order which means that the micro mesh does not have to be refined "in the same order" as the macro mesh, see Jecker and Abdulle (2016) Tab. 1 on p. 5 and in the present work Table 1, $N_{mic} = (N_{mac})^{p/2q} = (N_{mac})^{1/2}$.

Fig. 22 shows the FE-HMM errors for different micro- and macrodiscretizations. For each line the microdiscretization is kept fixed where N is the number of elements per edge on the micro domain, $N = \epsilon/h$; each marker in the diagrams denotes one macrodiscretization. If the micro mesh is not refined in the same order as the macro mesh, the error of the FE-HMM solution diverges from the line of optimal convergence in the L^2-norm. In the H^1-norm the micro mesh does not need not to be refined in the same order as the macro mesh so that the

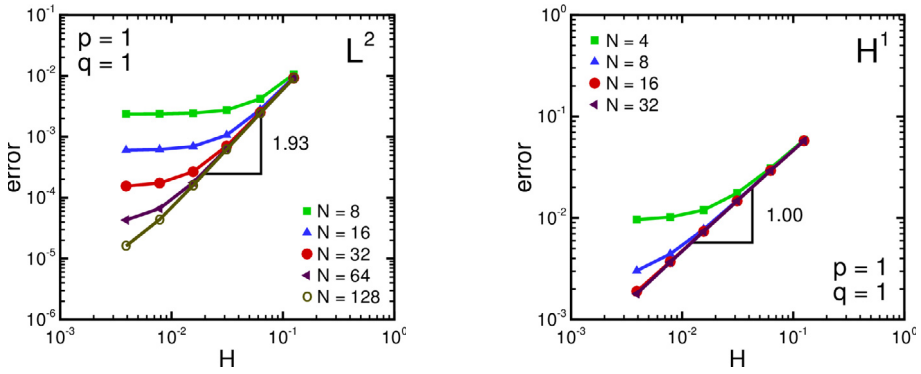


Fig. 22. Optimal uniform micro–macro refinement strategy. (left) Error in the L^2-norm and (right) in the H^1-norm for linear shape functions, $p = q = 1$ with $N = \epsilon/h$.

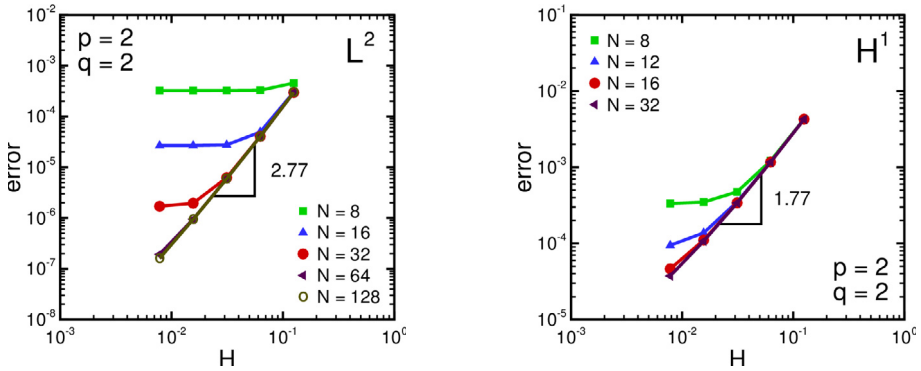


Fig. 23. Optimal micro–macro refinement strategy. Error in L^2-norm (left) and H^1-norm (right) with quadratic shape functions, $p = q = 2$ with $N = \epsilon/h$.

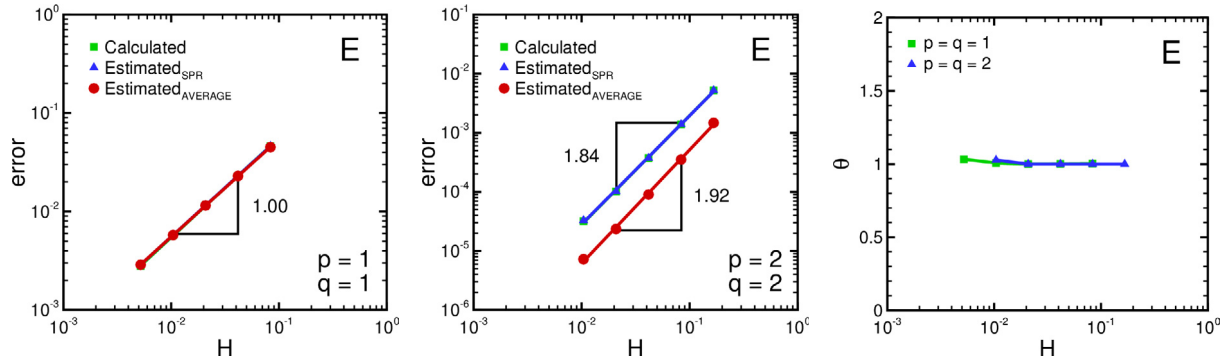


Fig. 24. Accuracy of macro error estimation. Calculated and estimated error in the energy-norm for (left) $p = q = 1$, for (center) $p = q = 2$, and (right) the corresponding effectivity index θ.

point where the single lines of fixed microdiscretizations diverge from the line of optimal convergence is shifted to finer macrodiscretizations.

5.3.2. Quadratic shape functions

The use of quadratic shape functions leads to optimal convergence orders of $p + 1 = 3$ on the macro level and $2q = 4$ on the micro level in the L^2-norm, $N_{mic} = (N_{mac})^{p+1/2q} = (N_{mac})^{3/4}$. In the H^1-norm we have $p = 2$ on the macro level and again $2q = 4$ on the micro level, $N_{mic} = (N_{mac})^{p/2q} = (N_{mac})^{1/2}$.

The results of the optimal refinement strategy analysis is shown in Fig. 23 for quadratic shape functions. Analogue to the linear case the micro mesh has to be refined in a reduced order for optimal convergence in the H^1-norm compared to the L^2-norm.

5.4. Accuracy of error estimation

The accuracy of error estimation is compared with true error computation for the tapered cantilever subject to body forces along with a sine wave type Young's modulus distribution on the microscale and with PBC. Error estimation is based on the superconvergent patch recovery and on a simple averaging of elementwise stresses and strains. The results displayed in the diagrams of Fig. 24 indicate that the estimated errors are in good agreement with the calculated errors for both linear as well as quadratic shape functions.

Notice that if the error estimator is restricted to the macro error part, the computation of the true total error along the lines of an

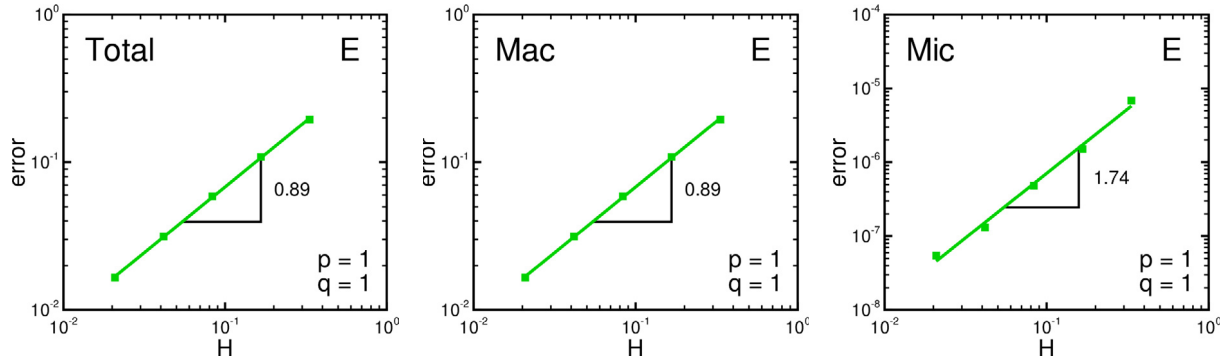


Fig. 25. Tapered cantilever under line load. Total error (left), macroscopic error (center) and microscopic error (right).

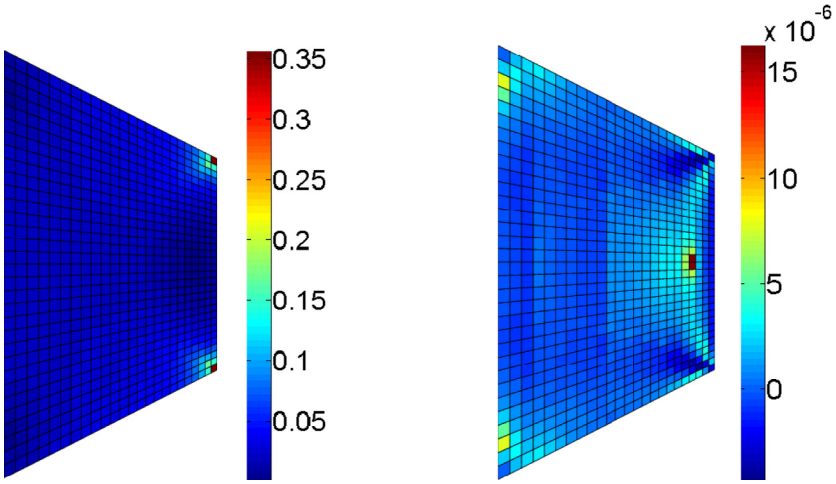


Fig. 26. Tapered cantilever under line load. Relative elementwise energy-error distribution on the macrodomain for $p = q = 1$ with (left) the total discretization error and (right) the micro error.

optimal uniform micro–macro refinement strategy as verified in Section 5.3 cannot be replaced by suchlike error estimation.

We mention in passing that in the present example for the considered discretizations the macro error is orders of magnitude larger than the micro error, a result that will be quantitatively analyzed for the example in the consecutive Section 5.5.

5.5. Efficient decomposition of the true errors

The efficient decomposition of the computed error into its macro and micro parts according to Table 2 in Section 4.2 shall be demonstrated for the tapered beam with the sine wave type Young's modulus distribution along with PBC. Here, in contrast to Section 5.4, a lineload is applied to the free end of structure.

Steps (1) and (2) in Table 2 are carried out along with the corresponding reference solutions ($H \to 0$ by 1536×2048 elements, and $h \to 0$ by 1024×1024 elements). The microscopic error then directly follows as the difference between total error and macroscopic error.

Fig. 25 shows the magnitude and convergence of the three different errors. The considerably larger values of the macro error compared to the micro error indicate the stronger influence of the macro discretization on the accuracy compared with the influence of the micro discretization. As a consequence, the total error and the macroscopic error are close together. The convergence rates are somewhat below the theoretical values which is true for each of the three errors.

Fig. 26 displays the distributions of the total error and the micro error. Recall that suchlike error decomposition clearly cannot be carried out by the error estimator operating on the macroscale, compare Remark 2 in Section 4.3.2.

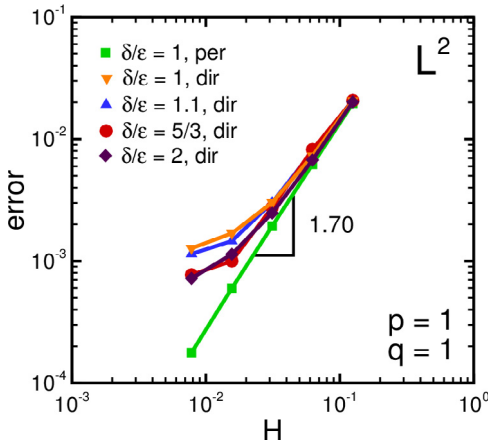


Fig. 27. Error convergence for different ratios of δ/ϵ. Calculated errors for periodic coupling with $\delta/\epsilon = 1$ and for Dirichlet coupling with $\delta/\epsilon \in \{1.0, 1.1, 5/3, 2.0\}$, $\epsilon = 0.005$.

5.6. Modeling error

Next, the modeling error for Dirichlet coupling along with a non-integer ratio δ/ϵ is examined, cf. (31)–(33) along with (34). In the analysis the macro problem of the square plate under volume forces is used, the micro problem is the sine wave stiffness distribution. In order to investigate the convergence and show the modeling error, the macro discretization is continuously refined, while a very fine micro

discretization ensures negligible micro errors. The calculations are run with $\delta/\epsilon = 1$ for PBC to indicate the optimal convergence of the macro problem without any modeling error. For Dirichlet coupling the cases $\delta/\epsilon \in \{1.0, 1.1, 5/3, 2.0\}$ are considered somewhat increasing the range of δ/ϵ in Jecker and Abdulle (2016). The reference solution for error calculation is obtained for PBC and a very fine macro mesh.

Fig. 27 depicts the results of the error calculations. For $\delta/\epsilon = 1$ and PBC the expected constant order is observed; it is the case already reported in Fig. 17 for $p = q$=1 showing a somewhat reduced convergence order of 1.70. In contrast to the constant convergence for the reference case of $\delta/\epsilon = 1$ along with PBC the case of Dirichlet coupling along with various δ/ϵ ratios exhibit an offset between the corresponding curves and the reference solution. This offset indicates the modeling error, which becomes increasingly dominant compared to the macro error for macro mesh refinement. Notice that the modeling error increases for an increasing ratio ϵ/δ for $\delta > \epsilon$ in agreement with (34).

6. Summary and conclusions

The aim of the present work was the numerical analysis of energetically consistent micro-coupling conditions in the homogenization framework of a two-scale finite element method. The obtained results are valid for FE-HMM and FE^2 for the coincidence of the methods, which was shown in Eidel and Fischer (2018). The main results shall be summarized.

1. The **micro error convergence analysis** for different micro problems, micro–macro coupling conditions and polynomial orders of shape functions has led to the following results.
   (a) We have clarified the distinction between the micro-error measured on the microscale with the theoretical convergence order of $q + 1$ and q in the L^2-norm and the H^1-/energy-norm, respectively, and the micro error as propagated to the macroscale with the – somewhat surprising – convergence order of $2q$ in all (L^2-, H^1-, energy-) norms.
   (b) For sufficiently regular micro problems the a priori error estimates of FE-HMM have been confirmed for each of the considered (L^2-, H^1-, energy-) norms. The micro-coupling conditions show no significant deviation from each other in the measured convergence order.
   (c) The regularity of a micro BVP requires a microstructure with smooth distribution of the heterogeneous material parameters (here: Young's modulus). Then the contrast of maximum to minimum material parameters does not influence the convergence order. Vice versa, a stiffness-jump at interfaces in the RVE lowers the convergence order for linear shape functions, and quadratic shape functions do not cure the order reduction.
2. The **constant traction (Neumann) condition**
   (a) The present approach for fulfilling constant traction BC includes the condition for the infinitesimal rotation tensor in the Lagrange multiplier framework. Doing so it avoids the mass-type perturbation of Miehe and Koch (2002) to overcome the singularity of the stiffness matrix due to undetermined rigid body rotations, and it avoids the necessity of getting the proper rotations by an iterative solution characteristic for the recently introduced semi-Dirichlet ansatz by Javili et al. (2017).
   (b) All three procedures fulfill the constant traction condition and thus make no difference in the FE-HMM convergence properties.
3. The **macro error convergence analysis** for two different macro problems applying different micro–macro coupling conditions and linear as well as quadratic shape functions has led to the following results.
   (a) For fully regular macro BVPs the error estimates have been confirmed in all norms. Singularities spoil the convergence such that the order is below the theoretical estimate for linear shape functions, which implies no improvement in the order for quadratic shape functions.
   (b) Two macroproblems underpin the aforementioned statements; a square cantilever which does not achieve the full order due to singularities in the corners of the bearing. At these points and their direct neighborhood the error are maximal. A tapered cantilever plate avoids by its geometry these singularities and enables therefore full order in agreement with the a priori error estimates, which is true for linear shape functions and for quadratic shape functions along with only minor deviations.
   (c) The choice of the coupling conditions on the RVE does not affect the macro convergence order nor the quantitative macro error.
4. **Error estimation and optimal mesh refinements**
   The recovery-type, superconvergent error estimator of Zienkiewicz and Zhu (1992a) was implemented on the macroscale; it exhibits the following properties:
   (a) The error estimator is accurate as indicated by an efficiency index close to unity; the estimated error almost equals the computed discretization error.
   (b) The optimal uniform micro–macro refinement strategies directly following from the a priori error estimates were confirmed for linear and quadratic shape functions. These refinement strategies are of considerable practical value since they enable the optimal convergence of the total error while keeping the numerical effort minimal.
   (c) Although the error estimator on the macroscale exhibits different estimates at (macro-, micro-) discretizations (H, h) and $(H, h/2)$, it merely measures macro discretization errors. The difference in the error estimations for various h is on the macroscale not a discretization error but a modeling error, since indeed the same type of constitutive law is used on the microscale but for different material parameters, which depend on the microdiscretization h.
5. **Analysis of the modeling error.** The modeling error for Dirichlet coupling along with various δ/ϵ ratios was identified and made measurable by uniform macro mesh refinements along with fine micro meshes. The simulation results underpin the a priori estimate in that the modeling error increases for an increasing ϵ/δ ratio with $\delta > \epsilon$. Moreover, for $H \to 0$ and $h \to 0$ the modeling error persists as a discretization-independent residual, again consistent with the estimate.

Declaration of competing interest

None.

Acknowledgments

Bernhard Eidel acknowledges support by the Deutsche Forschungsgemeinschaft (DFG), Germany within the Heisenberg program (grant no. EI 453/2-1). Simulations were performed with computing resources granted by RWTH Aachen University under project ID prep0005.

Appendix

A.1. Derivation of the micro-to-macro stiffness transformation matrix

The derivation of the macro element stiffness matrix part $\boldsymbol{k}_{IJ}^{e,mac}$ in (16) shall be detailed:

$$
\begin{aligned}
\boldsymbol{k}_{IJ}^{e,mac} &= B_H^e \left[\boldsymbol{N}_I^H, \boldsymbol{N}_J^H\right] \\
&= \sum_{l=1}^{N_{qp}} \frac{\omega_{K_l}}{|K_\delta|} \int_{K_\delta} \left(\boldsymbol{L}\boldsymbol{u}_{K_\delta}^{h(I,x_i)}\right)^T \mathbb{A}^\epsilon \boldsymbol{L}\boldsymbol{u}_{K_\delta}^{h(J,x_i)}\, dV \\
&= \sum_{l=1}^{N_{qp}} \frac{\omega_{K_l}}{|K_\delta|} \int_{K_\delta} \left(\boldsymbol{L} \sum_{m=1}^{M_{mic}} \boldsymbol{N}_{m,K_\delta}^h \boldsymbol{d}_m^{h(I,x_i)}\right)^T \\
&\quad \times \mathbb{A}^\epsilon \boldsymbol{L} \sum_{n=1}^{M_{mic}} \boldsymbol{N}_{n,K_\delta}^h \boldsymbol{d}_n^{h(J,x_i)}\, dV \\
&= \sum_{l=1}^{N_{qp}} \frac{\omega_{K_l}}{|K_\delta|} \sum_{T\in\mathcal{T}_h} \int_T \left(\boldsymbol{L} \sum_{m=1}^{n_{node}} \boldsymbol{N}_{m,K_\delta}^h \boldsymbol{d}_m^{h(I,x_i)}\right)^T \\
&\quad \times \mathbb{A}^\epsilon \boldsymbol{L} \sum_{n=1}^{n_{node}} \boldsymbol{N}_{n,K_\delta}^h \boldsymbol{d}_n^{h(J,x_i)}\, dV \\
&= \sum_{l=1}^{N_{qp}} \frac{\omega_{K_l}}{|K_\delta|} \sum_{T\in\mathcal{T}_h} \int_T \left(\boldsymbol{L} \sum_{m=1}^{n_{node}} \boldsymbol{N}_{m,K_\delta}^h \boldsymbol{d}_m^{h(I,x_i)}\right)^T \\
&\quad \times \mathbb{A}^\epsilon \boldsymbol{L} \sum_{n=1}^{n_{node}} \boldsymbol{N}_{n,K_\delta}^h \boldsymbol{d}_n^{h(J,x_i)}\, dV \\
&= \sum_{l=1}^{N_{qp}} \frac{\omega_{K_l}}{|K_\delta|} \sum_{T\in\mathcal{T}_h} \int_T \sum_{m=1}^{n_{node}} \sum_{n=1}^{n_{node}} \left(\boldsymbol{d}_m^{h(I,x_i)}\right)^T \left(\boldsymbol{L}\boldsymbol{N}_{m,K_\delta}^h\right)^T \\
&\quad \times \mathbb{A}^\epsilon \boldsymbol{L}\boldsymbol{N}_{n,K_\delta}^h\, dV\, \boldsymbol{d}_n^{h(J,x_i)} \\
&= \sum_{l=1}^{N_{qp}} \frac{\omega_{K_l}}{|K_\delta|} \\
&\quad \times \sum_{T\in\mathcal{T}_h} \left(\sum_{m=1}^{n_{node}} \sum_{n=1}^{n_{node}} \left(\boldsymbol{d}_m^{h(I,x_i)}\right)^T \int_T \boldsymbol{B}_m^{e,T} \mathbb{A}^\epsilon \boldsymbol{B}_n^e\, dV\, \boldsymbol{d}_n^{h(J,x_i)}\right) \qquad \text{(A.1)} \\
&= \sum_{l=1}^{N_{qp}} \frac{\omega_{K_l}}{|K_\delta|} \sum_{T\in\mathcal{T}_h} \left(\sum_{m=1}^{n_{node}} \sum_{n=1}^{n_{node}} \left(\boldsymbol{d}_m^{h(I,x_i)}\right)^T \boldsymbol{k}_{mn}^{e,mic} \boldsymbol{d}_n^{h(J,x_i)}\right) \\
&= \sum_{l=1}^{N_{qp}} \frac{\omega_{K_l}}{|K_\delta|} \left(\boldsymbol{d}^{h(I)}\right)^T \sum_{T\in\mathcal{T}_h} \boldsymbol{k}_{K_\delta}^{e,mic} \boldsymbol{d}^{h(J)} \\
&= \sum_{l=1}^{N_{qp}} \frac{\omega_{K_l}}{|K_\delta|} \left(\boldsymbol{d}^{h(I)}\right)^T \boldsymbol{K}_{K_\delta}^{mic} \boldsymbol{d}^{h(J)},
\end{aligned}
$$

where $\boldsymbol{d}^{h(I)} = \left(\boldsymbol{d}^{h(I,x_1)} | \boldsymbol{d}^{h(I,x_2)} | \boldsymbol{d}^{h(I,x_3)}\right)$ for $n_{dim} = 3$. The assembly of $\boldsymbol{k}_{IJ}^{e,mac}$ results in

$$
\boldsymbol{k}_K^{e,mac} = \sum_{l=1}^{N_{qp}} \frac{\omega_{K_l}}{|K_l|} \boldsymbol{T}_{K_l}^T \boldsymbol{K}_{K_l}^{mic} \boldsymbol{T}_{K_l} \qquad \text{(A.2)}
$$

$$
\text{with} \quad \boldsymbol{T}_{K_l} = \left[\left[\left[\boldsymbol{d}^{h(I,x_i)}\right]_{i=1,\ldots,n_{dim}}\right]_{I=1,\ldots,N_{node}}\right]. \qquad \text{(A.3)}
$$

A.2. Definition of norms

The norms used in the present work are defined according to

$$
L^2\text{-norm:} \quad \|\boldsymbol{u}\|_{L^2(\Omega)} := \sqrt{\int_\Omega \boldsymbol{u} : \boldsymbol{u}\, dV}, \qquad \text{(A.4)}
$$

$$
H^1\text{-norm:} \quad \|\boldsymbol{u}\|_{H^1(\Omega)} := \sqrt{\left(\sum_{i,j=1}^{n_{dim}} \int_\Omega \left(\frac{\partial u_i}{\partial x_j}\right)^2 dV + \sum_{i=1}^{d} \int_\Omega \left(u_i\right)^2 dV\right)}, \qquad \text{(A.5)}
$$

$$
\text{energy-norm:} \quad \|\boldsymbol{u}\|_{A(\Omega)} := \sqrt{\int_\Omega \mathbb{A}\boldsymbol{\varepsilon}(\boldsymbol{u}) : \boldsymbol{\varepsilon}(\boldsymbol{u})\, dV} = \sqrt{\boldsymbol{d}^T \boldsymbol{K}\, \boldsymbol{d}}. \qquad \text{(A.6)}
$$

A.3. Semi-Dirichlet approach for the constant traction condition

The constant traction BC alone (i.e. considering only the symmetric part in (26)) does not eliminate the rigid body motions of the RVE and the corresponding zero eigenvalues of the stiffness matrix. The rigid body motions must be eliminated by additional kinematical constraints (3 for $n_{dim} = 2$ and 6 for $n_{dim} = 3$), which can be realized e.g. by a so-called semi-Dirichlet coupling introduced in Javili et al. (2017) for finite deformation elasticity. The approach amounts to a nonlinear set of algebraic equations even in the present setting of linear elasticity in a geometrical linear frame, which shall be briefly underpinned.

In Fig. A.28(a) the additional Dirichlet BC in points A and B and their influence on the reaction forces on the boundary are shown. The reaction forces in A and B can be given in terms of the stress $\boldsymbol{\sigma}_{K_l}$ in the corresponding macro quadrature point

$$
\boldsymbol{t}^A = \boldsymbol{\sigma}_{K_l} \cdot \boldsymbol{n}^A + \boldsymbol{\zeta}^A, \qquad \text{(A.7)}
$$

$$
\boldsymbol{t}^B = \boldsymbol{\sigma}_{K_l} \cdot \boldsymbol{n}^B + \boldsymbol{\zeta}^B. \qquad \text{(A.8)}
$$

To enforce the Dirichlet BC in A and B, an additional force is needed which influences the reaction forces in A and B. In order to satisfy (25), the Dirichlet BC have to be chosen such that $\boldsymbol{\zeta}^A = \boldsymbol{\zeta}^B = \boldsymbol{0}$.

To do so the Dirichlet condition in point B, where (here) the node is merely fixed in x_2 direction, is modified by moving point B from its former position about η in x_2 direction. This has to be done until the discrete conditions (28) and $\boldsymbol{\zeta}^A = \boldsymbol{\zeta}^B = \boldsymbol{0}$ are satisfied. Writing down these conditions in a residual vector $\boldsymbol{R}$ leads to

$$
\boldsymbol{R}(\boldsymbol{\sigma}_{K_l}, \eta) = \left[\boldsymbol{G}\boldsymbol{d}^{h(I,x_i)} - \boldsymbol{\varepsilon}_{K_l}^{(I,x_i)}, \boldsymbol{\zeta}^{(B(I,x_i))}\right] \overset{!}{=} \boldsymbol{0}, \qquad \text{(A.9)}
$$

which is solved using the Newton–Raphson scheme. Therefore (A.9) has to be linearized which results in

$$
\boldsymbol{R}(\boldsymbol{\sigma}_{K_{l,i+1}}, \eta_{i+1}) = \boldsymbol{R}(\boldsymbol{\sigma}_{K_{l,i}}, \eta_i) + \left.\frac{\partial \boldsymbol{R}}{\partial \boldsymbol{\sigma}_{K_l}}\right|_i : \Delta\boldsymbol{\sigma}_{K_{l,i}} + \left.\frac{\partial \boldsymbol{R}}{\partial \eta}\right|_i \Delta\eta_i \overset{!}{=} \boldsymbol{0}. \qquad \text{(A.10)}
$$

The Lagrange multipliers which follow from the Neumann coupling condition contain the macroscopic stresses in the corresponding quadrature point. The Lagrange multipliers which follow from the semi-Dirichlet coupling contain the additional forces required to enforce the semi-Dirichlet constraints, which must vanish.

A.4. Direct implementation of Dirichlet and periodic coupling conditions

When Dirichlet or periodic boundary conditions are implemented in a direct manner without using Lagrange multipliers the micro system of equations reads as

$$
\boldsymbol{K}_{K_l}^{mic} \boldsymbol{d}^{h(I,x_i)} = \boldsymbol{0} \qquad \text{(A.11)}
$$

for a macroscopic unit displacement state (I, x_i), a notation that is dropped in the following for notational convenience along with the subscript K_l indicating quadrature point l of macro element K.

For Dirichlet coupling conditions the micro displacements $\boldsymbol{d}^h$ are known since they directly follow from the macroscopic displacement field. For that reason we decompose the microscopic displacement vector

$$
\boldsymbol{d}^h = [\boldsymbol{d}_D^h,\ \boldsymbol{d}_F^h]^T \qquad \text{(A.12)}
$$

into the known displacements $\boldsymbol{d}_D^h$ and an unknown part $\boldsymbol{d}_F^h$. Then the system of equations follows the form

$$
\begin{bmatrix} \boldsymbol{K}_{DD}^{mic} & \boldsymbol{K}_{FD}^{mic} \\ \boldsymbol{K}_{DF}^{mic} & \boldsymbol{K}_{FF}^{mic} \end{bmatrix} \begin{bmatrix} \boldsymbol{d}_D^h \\ \boldsymbol{d}_F^h \end{bmatrix} = \begin{bmatrix} \boldsymbol{0} \\ \boldsymbol{0} \end{bmatrix}. \qquad \text{(A.13)}
$$

It follows that

$$
\boldsymbol{K}_{DF}^{mic} \boldsymbol{d}_D^h + \boldsymbol{K}_{FF}^{mic} \boldsymbol{d}_F^h = \boldsymbol{0} \qquad \text{(A.14)}
$$

which yields the unknown micro displacements according to

$$
\boldsymbol{d}_F^h = -\left(\boldsymbol{K}_{FF}^{mic}\right)^{-1} \left(\boldsymbol{K}_{FD}^{mic} \boldsymbol{d}_D^h\right). \qquad \text{(A.15)}
$$

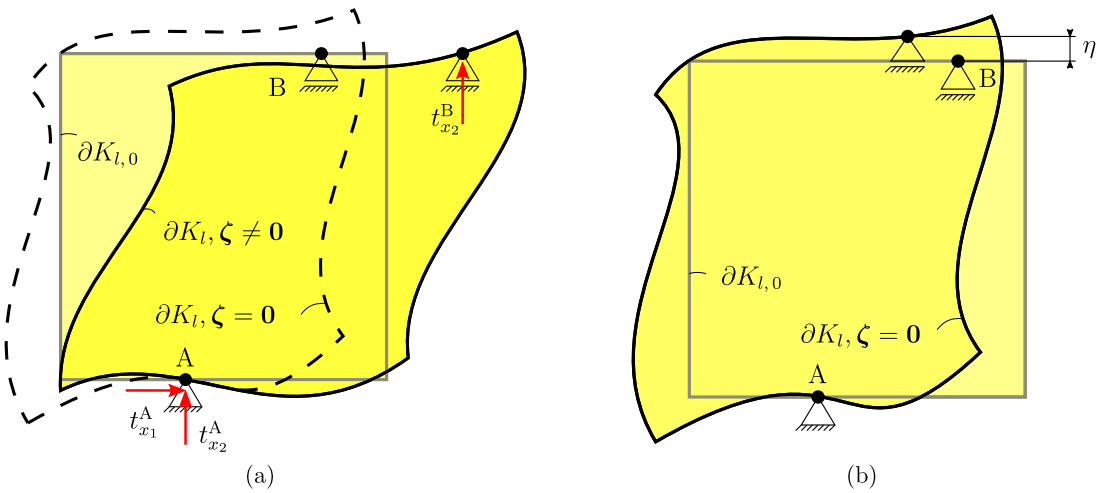


Fig. A.28. Semi-Dirichlet BC for Neumann coupling: (a) Elimination of rigid body motions in $n_{dim} = 2$ by adding three Dirichlet BC at single nodes, which renders the system statically determined. Undeformed microdomain $\partial K_{l,0}$ fixed at node A and node B and deformed microdomain ∂K_l with and without the additional displacement constraints, (b) variation of η to realize the constant traction condition without spurious forces in A and B.

For periodic coupling conditions the direct implementation accounts for the fact that not the micro displacements but the fluctuations between macroscopic and microscopic displacement fields are periodic on opposite boundaries.

First we introduce the fluctuations on the microlevel as the difference between macroscopic and microscopic displacements

$$\tilde{\boldsymbol{d}}^h = \boldsymbol{d}^H - \boldsymbol{d}^h \,. \tag{A.16}$$

Since the system of equations from (A.11) only contains the microscopic displacements, we decompose them into the homogeneous deformation part following from the macroscopic displacements $\boldsymbol{d}^H$ and their fluctuations $\tilde{\boldsymbol{d}}^h$

$$\boldsymbol{d}^h = \boldsymbol{d}^H + \tilde{\boldsymbol{d}}^h \,, \tag{A.17}$$

which is inserted into (A.11) and yields the solution

$$\tilde{\boldsymbol{d}}^h = \left(\boldsymbol{K}^{mic}\right)^{-1} \left(-\boldsymbol{K}^{mic}\boldsymbol{d}^H\right) \,. \tag{A.18}$$

Eq. (A.18) is solved accounting for periodic boundaries. Rigid body motions are removed from the system simply by fixing one arbitrary node in each direction of space. A convenient choice for periodic structures is to set the displacements of a node in the center of an RVE to zero.

References

Abdulle, A., 2005. On a-priori error analysis of fully discrete heterogeneous multiscale FEM. SIAM Multiscale Model. Simul. 4, 2, 447–459.

Abdulle, A., 2006. Analysis of the heterogeneous multiscale FEM for problems in elasticity. Math. Models Methods Appl. Sci. 16 (4), 615–635.

Abdulle, A., 2009. The finite element heterogeneous multiscale method: a computational strategy for multiscale PDEs. Math. Sci. Appl. 31, 31, 133–181.

Abdulle, A., E, W., Engquist, E., Vanden-Eijnden, B., 2012. The heterogeneous multiscale method. Acta Numer. 466, 1–87.

Abdulle, A., Nonnenmacher, A., 2011. Adaptive finite element heterogeneous multiscale method for homogenization problems. Comput. Methods Appl. Mech. Engrg. 200, 2710–2726.

Abdulle, A., Nonnenmacher, A., 2013. A posteriori error estimates in quantities of interest for the finite element heterogeneous multiscale method. Numer. Methods Partial Differential Equations 29 (5), 1629–1656.

Abdulle, A., Schwab, C., 2005. Heterogeneous multiscale FEM for diffusion problems on rough surfaces. Multiscale Model. Simul. 3 (1), 195–220.

Allaire, G., 1992. Homogenization and two-scale convergence. SIAM J. Math. Anal. 23, 1482–1518.

Barlow, J., 1976. Optimal stress locations in finite element models. Internat. J. Numer. Methods Engrg. 10, 243–251.

Bensoussan, A., Lions, J.L., Papanicolau, G., 1976. Asymptotic Analysis for Periodic Structures. North-Holland, Amsterdam.

Cioranescu, D., Donato, P., 1999. An Introduction to Homogenization. Oxford University Press, New York.

Dŏskár, M., Zeman, J., Jarůsková, D., Novák, J., 2018. Wang tiling aided statistical determination of the representative volume element size of random heterogeneous materials. Eur. J. Mech. A Solids 70, 280–295.

E, W., Engquist, B., 2003. The heterogeneous multi-scale methods. Commun. Math. Sci. 1, 87–132.

E, W., Engquist, B., Huang, Z., 2003. Heterogeneous multiscale method: A general methodology for multiscale modeling. Phys. Rev. B 67, 092101.

E, W., Engquist, B., Li, X., Ren, W., Vanden-Eijnden, E., 2007. Heterogeneous multiscale methods: A review. Commun. Comput. Phys. 2, 367–450.

E, W., Ming, P., Zhang, P., 2005. Analysis of the heterogeneous multi-scale method for elliptic homogenization problems. J. Amer. Math. Soc. 18, 121–156.

Eidel, B., Fischer, A., 2016. The heterogeneous multiscale finite element method FE-HMM for the homogenization of linear elastic solids. PAMM 16, 521–522.

Eidel, B., Fischer, A., 2018. The heterogeneous multiscale finite element method FE-HMM for the homogenization of linear elastic solids. Comput. Methods Appl. Mech. Engrg. 329, 332–368.

Feyel, F., Chaboche, J.L., 2000. FE2 Multiscale approach for modelling the elastovis-coplastic behaviour of long fibre SiC/Ti composite materials. Comput. Methods Appl. Mech. Engrg. 183, 309–330.

Fish, J., Yu, Q., Shek, K., 1999. Computational damage mechanics for composite materials based on mathematical homogenization. Internat. J. Numer. Methods Engrg. 45, 1657–1679.

Geers, M.G.D., Kouznetsova, V.G., Brekelmans, W.A.M., 2010a. Computational homogenization. In: Pippan, R., Gumbsch, P. (Eds.), Multiscale Modelling of Plasticity and Fracture By Means of Dislocation Mechanics, CISM International Centre for Mechanical Sciences. pp. 327–394.

Geers, M.G.D., Kouznetsova, V.G., Brekelmans, W.A.M., 2010b. Multi-scale computational homogenization: trends and challenges. J. Comput. Appl. Math. 234, 2175–2182.

Hill, R., 1963. Elastic properties of reinforced solids: some theoretical principles. J. Mech. Phys. Solids 11, 357–372.

Hill, R., 1972. On constitutive macro-variables for heterogeneous solids at finite strain. Proc. R. Soc. Lond. Ser. A Math. Phys. Eng. Sci. 326, 131–147.

Javili, A., Saeb, S., Steinmann, P., 2017. Aspects of implementing constant traction boundary conditions in computational homogenization via semi-Dirichlet boundary conditions. Comput. Mech. 59, 21–35.

Jecker, O., Abdulle, A., 2016. Numerical experiments for multiscale problems in linear elasticity. In: Karasözen, B., Manguoĕglu, M., Tezer-Sezgin, M., Göktepe, S., Uğur, Ö. (Eds.), Numerical Mathematics and Advanced Applications ENUMATH 2015. In: Lecture Notes in Computational Science and Engineering, vol. 112, Springer, Cham, pp. 123–131.

Kanit, T., Forest, S., Galliet, I., Mounoury, V., Jeulin, D., 2003. Determination of the size of the representative volume element for random composites: statistical and numerical approach. Int. J. Solids Struct. 40 (13–14), 3647–3670.

Kouznetsova, V., Brekelmans, W.A.M., Baaijens, F.P.T., 2002a. An approach to micro-macro modeling of heterogeneous materials. Comput. Mech. 27, 37–48.

Kouznetsova, V., Geers, M.G.D., Brekelmans, W.A.M., 2002b. Multi-scale constitutive modelling of heterogeneous materials with a gradient-enhanced computational homogenization scheme. Internat. J. Numer. Methods Engrg. 54, 1235–1260.

Larsson, F., Runesson, K., Saroukhani, S., Vafadari, R., 2011. Computational homogenization based on a weak format of micro-periodicity for RVE-problems. Comput. Methods Appl. Mech. Engrg. 1–4, 11–26.

Michel, J.C., Moulinec, H., Suquet, P., 1999. Effective properties of composite materials with periodic microstructure: a computational approach. Comput. Methods Appl. Mech. Engrg. 172, 109–143.

Miehe, C., 2003. Computational micro-to-macro transitions for discretized micro-structures of heterogeneous materials at finite strains based on the minimization of averaged incremental energy. Comput. Methods Appl. Mech. Engrg. 192, 559–591.

Miehe, C., Koch, A., 2002. Computational micro-to-macro transitions of discretized microstructures undergoing small strain. Arch. Appl. Mech. 71, 300–317.

Miehe, C., Schotte, J., Schröder, J., 1999a. Computational homogenization analysis in finite plasticity simulation of texture development in polycrystalline materials. Comput. Mater. Sci. 16 (1–4), 372–382.

Miehe, C., Schröder, J., Schotte, J., 1999b. Computational homogenization analysis in finite plasticity simulation of texture development in polycrystalline materials. Comput. Methods Appl. Mech. Engrg. 171, 387–418.

Ohlberger, M., 2005. A posteriori error estimates for the heterogeneous multiscale finite element method for elliptic homogenization problems. Multiscale Model. Simul. 4 (1), 88–114.

Ostoja-Starzewski, M., 2006. Material spatial randomness: from statistical to representative volume element. Probab. Eng. Mech. 21 (2), 112–132.

Perić, D., de Souza Neto, E.A., R.A.Feijóo, Partovi, M., Carneiro Molina, A.J., 2010. On micro-to-macro transitions for multi-scale analysis of non-linear heterogeneous materials: unified variational basis and finite element implementation. Internat. J. Numer. Methods Engrg. 87, 149–170.

Pham, K., Kouznetsova, V.G., Geers, M.G.D., 2013. Transient computational homogenization for heterogeneous materials under dynamic excitation. J. Mech. Phys. Solids 61, 2125–2146.

Rössle, A., 2000. Corner singularities and regularity of weak solutions for the two-dimensional Lamé equations on domains with angular corners. J. Elasticity 60, 57–75.

Saeb, S., Steinmann, P., Javili, A., 2016. Aspects of computational homogenization at finite deformations: a unifying review from reuss' to Voigt's bound. Appl. Mech. Rev. 68, 050801.

Sanchez-Palencia, E., 1980. Non-Homogeneous Media and Vibration Theory. In: Lecture Notes in Physics, vol. 127, Springer, Berlin.

Schröder, J., 2014. A numerical two-scale homogenization scheme: the FE^2-method. In: Schröder, J., Hackl, K. (Eds.), Plasticity and beyond. CISM International Centre for Mechanical Sciences, pp. 1–64.

Sridhar, A., Kouznetsova, V.G., Geers, M.G.D., 2018. A general multiscale framework for the emergent effective elastodynamics of metamaterials. J. Mech. Phys. Solids 111, 414–433.

Suquet, P., 1987. Elements of homogenization for inelastic solid mechanics. In: Sanchez-Palencia, E., Zaoui, A. (Eds.), Homogenization Techniques for Composite Media. Springer-Verlag, Berlin, pp. 193–287.

Yue, X.-Y., E, W., 2007. The local microscale problem in the multiscale modelling of strongly heterogeneous media: Effect of boundary conditions and cell size. J. Comput. Phys. 222, 556–572.

Zienkiewicz, O.C., Zhu, J.Z., 1992a. The superconvergent patch recovery and a posteriori error estimates. part 1: the recovery technique. Internat. J. Numer. Methods Engrg. 33, 1331–1364.

Zienkiewicz, O.C., Zhu, J.Z., 1992b. The superconvergent patch recovery and a posteriori error estimates. part 2: error estimates and adaptivity. Internat. J. Numer. Methods Engrg. 33, 1365–1382.

8.3 Veröffentlichung: Error analysis for quadtree-type mesh coarsening algorithms adapted to pixelized heterogeneous microstructures

Die dritte Veröffentlichung von Andreas Fischer und Prof. Bernhard Eidel mit dem Titel **Error analysis for quadtree-type mesh coarsening algorithms adapted to pixelized heterogeneous microstructures** wurde 2020 in *Computational Mechanics* veröffentlicht.

Wie bei den beiden vorherigen Veröffentlichungen war der Doktorand für alle Anpassungen und Erweiterungen in dem zugehörigen Matlab-Code verantwortlich. Maßgeblich waren dies für die dritte Veröffentlichung die Implementierung von den in Abschnitt 2.2 der Veröffentlichung beschriebenen Netzvergröberungsalgorithmen sowie die Einführung von Duplex-Spannungen für Knoten, die sich an Phasengrenzen befinden.

Hauptverantwortlich federführend war der Doktorand im Theorie-Teil der Veröffentlichung. Die Beschreibung der Netzvergröberung und der zugehörigen Algorithmen sowie die grafische Darstellung der Vergröberung in Kapitel 2 erfolgte durch den Doktoranden. Auch die Beschreibung der Fehlerberechnung (Abschnitt 3.1), der Spannungsberechnung für die Fehlerschätzung (Abschnitt 3.2) mit den zugehörigen grafischen Darstellungen lag bei dem Doktoranden.

Analog zu den ersten beiden Veröffentlichungen lag auch die Berechnung der numerischen Beispiele in Kapitel 4 in der Hand des Doktoranden. Auch die Auswertung der Berechnungen, die grafische Darstellung von Ergebnissen und die Diskussion der Ergebnisse erfolgte federführend durch den Doktoranden.

Die Zusammenfassung und das Fazit wurde erneut von beiden Autoren gemeinsam erarbeitet.

Computational Mechanics (2020) 65:1467–1491
https://doi.org/10.1007/s00466-020-01830-4

ORIGINAL PAPER

Error analysis for quadtree-type mesh coarsening algorithms adapted to pixelized heterogeneous microstructures

Andreas Fischer[1] · **Bernhard Eidel**[1]

Received: 11 October 2019 / Accepted: 13 February 2020 / Published online: 3 March 2020
© The Author(s) 2020

Abstract
For pixel-based microstructure representations we propose two different variants of adaptive, quadtree-based mesh coarsening algorithms that serve the purpose of a preprocessor for finite element analyses in the context of numerical homogenization. High resolution is preserved at interfaces for accuracy, coarse-graining in the defect-free interior of phases for efficiency. Error analysis is carried out on the micro scale by error estimation which itself is assessed by true error computation. Modified stress recovery schemes for an error indicator are proposed which overcome the deficits of the standard superconvergent recovery scheme for nodal stress computation in cases of interfaces with stiffness jump. By virtue of error analysis the improved efficiency by the reduction of unknowns is put into relation to the increase of the discretization error and thereby sets a rational basis for decisions on favorable meshes having the best trade-off between accuracy and efficiency as underpinned by various examples.

Keywords Pixelized microstructures · Quadtree · Error analysis · Adaptivity · Homogenization · Finite elements

1 Introduction

Pixel- and voxel-based representation of reconstructed microstructures obtained from tomographic imaging methods (scanning transmission electron microscopy tomography (STEM), focused ion beam tomography (FIB) and X-ray computed tomography (XCT)) finds nowadays an ever more increasing interest not only in research but also in industrial applications [23,25,39]. Reconstructed microstructures can directly be analyzed for characteristic quantities such as volume fractions of phases and pores, size distributions of pores, phases and grains, interface and surface areas, constrictivity, tortuosity, and many more. Furthermore, the pixel/voxel meshes can be used as input for numerical analysis in general, for finite element simulations in particular, in either case for the prediction of effective physical properties in silico. Corresponding voxel to mesh conversions were driven by the representation of bone [22,26], for a general overview see [33].

The corresponding highly resolved, uniform discretizations are well-suited to accurately describe the geometry of interfaces and defects in microstructures and, consequently, to capture the physical processes in these regions of interest. For the defect-free interior of phases and grains with their smooth field properties at slow variations, the high resolution is typically a wasteful luxury and coarse-graining adequate. The present work proposes two different variants of adaptive algorithms for quadtree-based mesh coarsening of the original, uniform, pixel-based meshes that serve the purpose of a preprocessor for consecutive finite element analyses. The criterion for mesh coarsening is enabled for pixels sharing the same phase or grain. We showcase the applicability in various examples and measure the improved efficiency in terms of the reduction of unknowns and a corresponding speed-up in computational homogenization.

Quadtree-/octree-based mesh coarsening of heterogeneous, multiphase materials is frequently used, see e.g. [24,28,29,34,41] for application in homogenization and fracture, in the context of the Scaled Boundary FEM [19,45,46] and many more. In some cases the computational results for the coarse-grained and the uniform discretizations have been checked by visual inspection or by a comparison of global errors, in case of analytical solutions by error computation.

✉ Bernhard Eidel
bernhard.eidel@uni-siegen.de

[1] Heisenberg-Group, Institute of Mechanics, Department Mechanical Engineering, University Siegen, Paul-Bonatz-Str. 9-11, 57068 Siegen, Germany

But what is still missing is a thorough error analysis including spatial distributions of errors.

The present work fills this gap by error estimation which itself is assessed by true error computation, the latter based on overkill solutions. In the context of error estimation we propose two different, modified stress recovery schemes which overcome the deficits of the standard, superconvergent scheme of Zienkiewicz and Zhu for the case of multimaterial-interfaces with stiffness jumps and corresponding stress jumps. We show that the standard scheme spoils error estimation in that case and that the modified recovery leads to a very good agreement of a posteriori estimation with exact error computation.

By virtue of error analysis we can weigh the pres and cons of adaptive mesh coarsening; the improved efficiency by the reduction of unknowns is set into relation to the increased discretization error. Hence, the quantitative error analysis sets a rational basis for deciding on best trade-offs between accuracy and efficiency for the adaptively coarse-grained meshes.

In the present work the pixelized microstructure images are understood as representative area elements (RAE) each of a microheterogeneous multiphase material. They are used in a computational framework for the micro-to-macro scale transition based on mathematical homogenization [5,8,51]. This scale transition is carried out by a two-scale finite element method referred to as Finite Element Heterogeneous Multiscale Method (FE-HMM) introduced as a particular case of the general HMM in [54]. For more comprehensive descriptions of the method see [2,3,53]. A formulation of FE-HMM for linear elastic solid mechanics based on [1] with a conceptual and numerical comparison to the FE^2 method is described in [13], a short precursor in [12]. The numerical analysis for coupling conditions fulfilling the Hill-Mandel postulate of micro-macro energy densities [20,21] is presented in [17]. For an extension to geometrical nonlinearity and hyperelastic materials see [14]. FE-HMM's methodological twin is the FE^2 method, [16,27,31,32,40], with overviews e.g. in [18,42,50].

By the embedding of the pixelized microstructures as RAEs into a macro continuum through homogenization, another relevant aspect of error analysis is how the micro discretization error propagated to the macro scale influences macroscopic properties, here in terms of the effective elasticity tensor and macroscopic deformations.

For the mentioned identity of FE-HMM and FE^2 the achieved results of the present work are equally valid for both methods.

2 Mesh coarsening

The present section introduces two different algorithms for quadtree-based mesh coarsening. Mesh coarsening is applied to pixelized microstructures and works as a preprocessor generating input data for consecutive finite element analyses. Since each pixel exhibits a unique color code, different phases can be distinguished without ambiguity.

2.1 Quadtree-based mesh coarsening

The general procedure of mesh coarsening shall be outlined. As the name "quadtree" already indicates, the origin of all computations is a micro mesh with a uniform triangulation $\mathcal{T}_0$, meaning that each node in the interior of the micro mesh has exactly four neighboring nodes and, consequently, each node is shared by four elements. All elements of the micro mesh initially exhibit the same element side length denoted by h.

Figure 1a shows an example for a quadtree micro mesh with elements of side length h. There are four nodes in the interior of the mesh, each with four neighboring nodes and each adjacent to four elements. In quadtree-based mesh coarsening the set of four elements adjacent to one micro node can be merged to one new element of side length $2h$. One option for suchlike coarsening is shown in Fig. 1b. Here, the elements around the top left of the inner nodes are coarsened to one new element. Similarly, the elements around each of the other internal nodes could have been coarsened.

Mesh coarsening reduces the number of elements and thereby the number of degrees of freedom (ndof). The original uniform mesh contains 32 degrees of freedom (16 nodes, each with 2 degrees of freedom). Mesh coarsening removes three nodes from the uniform mesh (a) which results in the new mesh (b). Furthermore there are two nodes, which do not have four neighboring nodes any more, because they lie on edges of the coarsened element. To preserve continuity at the element edge, these nodes have to be coupled to the coarsened element by a constraint. These nodes are referred to as "hanging nodes", their constraints read as

$$\boldsymbol{x}_{\text{hanging node}} = 1/2\,(\boldsymbol{x}_{\text{master node 1}} + \boldsymbol{x}_{\text{master node 2}}) \tag{1}$$

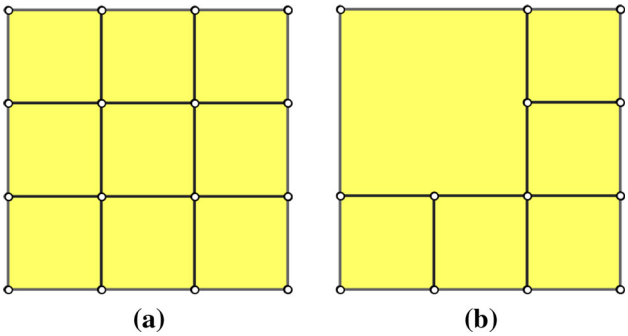


Fig. 1 Quadtree: **a** original, uniform quadtree mesh, **b** quadtree mesh with one coarsened element

with the two master nodes at the end of the edge to which the hanging node is connected. Due to the constraint the hanging nodes do not have any degrees of freedom left. The constraints are realized in analogy to the micro-macro coupling by introducing further Lagrange multipliers. For details about the micro-macro coupling see [17].

This rationale to merge four elements having a node in common into one coarser element shall be used in an efficient preprocessor for finite element analyses. Algorithms are needed to decide, whether an element is target of coarsening or not.

Finite element mesh generation based on quadtrees was introduced by Yerry and Shephard [55], for comprehensive overviews of original works we refer to [43,44].

2.2 Coarsening algorithms

For pixelized microstructures with two or more phases, the elements in the interior of the phases should be marked for coarsening, while the elements at the phase boundaries should preserve their initial, fine discretization. The coarsening criterion is defined as follows.

Algorithm 1 Mesh coarsening criterion

```
for i=1:micro elements do
  if ismember(element node, phase boundary nodes) or
    ismember(element node, constraint nodes) then
     do not mark element for coarsening
  else
     mark element for coarsening
  end if
end for
```

The algorithm contains an **if**-statement, which distinguishes whether an element is marked for coarsening or not. The **if**-statement contains two conditions, which have to be fulfilled to allow the element to be marked for coarsening.

The first condition screens for each micro element, if one of its nodes belongs to a phase boundary. In the case that the element is directly adjacent to a phase boundary, it is not marked for coarsening. Otherwise the element is located inside a phase and target of coarsening.

Typically, a coarsening step is executed more than once to efficiently reduce the number of elements and thereby the number of degrees of freedom. This may lead to $2^n - 1$ hanging nodes on an element edge after n coarsening steps. To prevent multiple hanging nodes on an element edge in additional coarsening steps, the second condition in Algorithm 1 is introduced which scans, if one of the element nodes is already involved in a hanging node constraint. If the element should not be further coarsened, the number of hanging nodes on one edge is limited to one. In the context of quadtree meshing the case of at most one node in a side is referred to as a balanced leaf.

The mesh coarsening following Algorithm 1 might lead to steep gradients in element size at phase boundaries with a densely packed cluster of kinematical constraints, which artificially stiffens these regions.

Algorithm 2 Softer gradient mesh coarsening criterion

```
for i=1:elements do
  if ismember(element node, boundary element nodes) or
    ismember(element node, constraint element nodes) then
     do not mark element for coarsening
  else
     mark element for coarsening
  end if
end for
```

Less restrictions at boundaries imply less steep gradients in element size. For that goal the conditions from Algorithm 1 are slightly modified. Instead of scanning if one of the element's nodes is either a node at the phase boundary or is used for the definition of a hanging node constraint, the modified Algorithm 2 scans, if one of the element's nodes is either adjacent to an element at a phase boundary or is adjacent to an element which is used for the definition of a hanging node constraint.

Figure 2a shows a uniform mesh with elements belonging to two different phases, a yellow and a green phase. All elements marked with a black cross in Fig. 2b are marked for coarsening by both Algorithms 1 and 2. The elements marked with red crosses are only marked for coarsening following Algorithm 1. The once coarsened meshes with crosses marking the elements for the second coarsening step are displayed in Fig. 2c following Algorithm 1 and Fig. 2d following Algorithm 2. In both meshes only few elements are marked for further coarsening, following Algorithm 1 at least the four elements in the upper left corner may be coarsened to one bigger element, displayed in Fig. 2e.

The mesh coarsening following Algorithm 1 leads to a steep gradient of element size at phase boundaries, which results in strong restrictions due to the hanging node constraints. If the red marked element in Fig. 2e is considered, each of its nodes is obviously included in a hanging node constraint.

Algorithm 2 leads to a much smaller gradient in element size than Algorithm 1. It is obvious that less elements vanish by coarsening, such that the number of degrees of freedom will be somewhat larger for the mesh in (d) compared to the mesh in (c), but the reduced number of kinematical constraints leads to better, i.e. less stiff results.

The two coarsening algorithms will be investigated for several examples in Sect. 4, they will be referred to as hard coarsening (following Algorithm 1) and soft coarsening (following Algorithm 2).

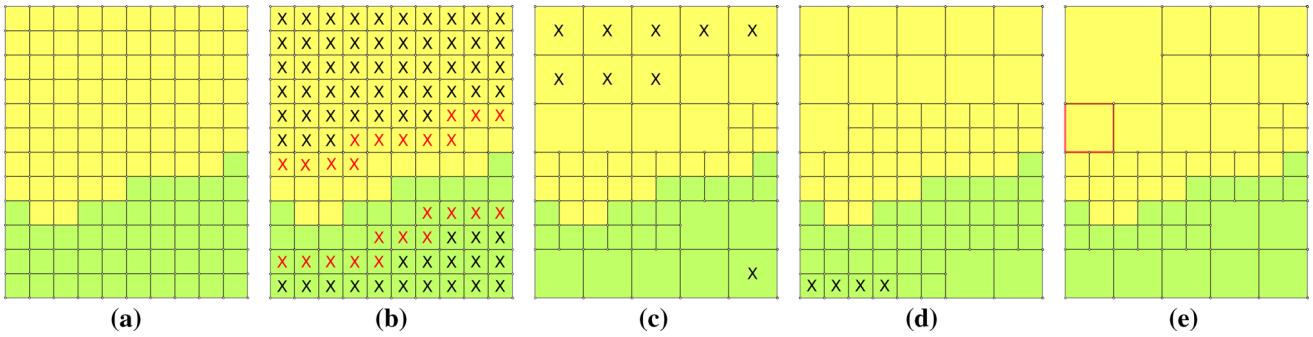


Fig. 2 Quadtree mesh coarsening at material interfaces: **a** original mesh, **b** original mesh with marked elements following Algorithms 1 (black and red crosses) and 2 (black crosses only), **c** once coarsened mesh following Algorithm 1 with elements marked for next coarsening step following Algorithm 1, **d** once coarsened mesh with marked elements for further coarsening following algorithm 2 and **e** resulting twice coarsened mesh following Algorithm 1. (Color figure online)

3 Error computation and error estimation

The aim of the present work is to assess adaptive mesh coarsening as a preprocessor applied to pixelized microstructure images. To compare the results of the coarsened micro meshes to the results of the original, uniform micro mesh, the corresponding micro discretization errors will be investigated. Here, error analysis is based on error computation obtained through a reference solution for a superfine discretization ($h \to 0$) and based on a posteriori error estimation, where the latter will be validated by the former.

For error computation and error estimation we will use the energy norm. The energy norm reads for the solution on the micro domain Ω_ϵ

$$||\boldsymbol{u}||_{A(\Omega_\epsilon)} := \left[\int_{\Omega_\epsilon} \mathbb{A}^\epsilon\, \boldsymbol{\varepsilon}(\boldsymbol{u}^h) : \boldsymbol{\varepsilon}(\boldsymbol{u}^h)\, \mathrm{d}V\right]^{1/2}, \tag{2}$$

where $\mathbb{A}^\epsilon$ is the linear elasticity tensor on the micro scale showing heterogeneity on the micro domain Ω_ϵ for the multiphase characteristics of microstructure in our investigations.

3.1 Error computation

The integrals for error calculation in the energy norm (2) are approximated by numerical integration of Gauss-Legendre. The computations are carried out on micro element level of the discretization for the reference solution. For the error in the energy norm it follows

$$||\boldsymbol{e}||_{A(\Omega_\epsilon)} = \left[\int_{\Omega_\epsilon} \left(\boldsymbol{\sigma}^{\mathrm{ref}} - \boldsymbol{\sigma}^h\right) : \left(\boldsymbol{\varepsilon}^{\mathrm{ref}} - \boldsymbol{\varepsilon}^h\right) \mathrm{d}V\right]^{1/2}, \tag{3}$$

$$\approx \left[\sum_{T\in\mathcal{T}_{\mathrm{ref}}} \left(\sum_{i=1}^{ngp} \omega_i \left(\boldsymbol{\sigma}^{\mathrm{ref}} - \boldsymbol{\sigma}^h\right)(\boldsymbol{x}_i^{\mathrm{ref}}) : \left(\boldsymbol{\varepsilon}^{\mathrm{ref}} - \boldsymbol{\varepsilon}^h\right)(\boldsymbol{x}_i^{\mathrm{ref}})\, \det \boldsymbol{J}\right)\right]^{1/2} \tag{4}$$

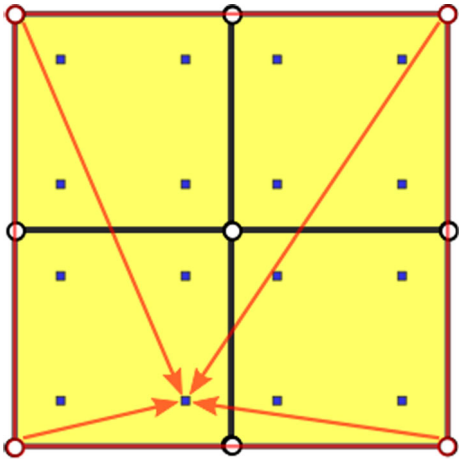


Fig. 3 Error computation: projection from a coarse micro mesh (red boundary) onto a quadrature point of an element (black boundary) in the reference discretization $\mathcal{T}_{\mathrm{ref}}$ for the case of linear shape functions. (Color figure online)

with the quadrature weight ω_i and the Jacobian $\boldsymbol{J}$ of isoparametric finite elements. For evaluating (3), the stresses and strains of both the standard FE-HMM solution $\boldsymbol{u}^h$ and the reference solution $\boldsymbol{u}^{\mathrm{ref}}$ must be available in the quadrature points $\boldsymbol{x}_i^{\mathrm{ref}}$ of the reference discretization. These quadrature points of the reference solution will not coincide with the quadrature points of the meshes with coarser discretizations. In this case the results of the FE-HMM solution on the coarse meshes are projected onto the finer grid of the reference solution.

Figure 3 provides a sketch of the projection from a coarse discretization onto a finer reference discretization for one quadrature point of an element of the reference mesh. Therein, the quantities of the coarse mesh are projected onto the quadrature points of the reference solution such that the error of the quantities of interest can be calculated, e.g. for the error of stress and strain in the energy norm according to (4).

3.2 Stress computation for error estimation

In (engineering) practice, error computation is prohibitive. Instead, an a posteriori error estimation is carried out for the particular discretization in use. The class of reconstruction-based error estimation relies on the computation of improved stresses (and strains for the error in the energy norm) at the nodes of a finite element; the integral deviation of such-like reconstructed stress distribution from the distribution of inner-element stresses at its quadrature points in a suitable norm (typically energy norm or L_2-norm of stress) yields the elemental error estimate called error indicator [56–58]. If bounds cannot be proved, it is referred to as refinement indicator instead of error indicator. The deviation can be understood as a residual (vanishing for a characteristic element size $h \to 0$) that sets the link from reconstruction-based to residual-based error estimation [6]. This relation has been established for particular settings, see for example [56] with the proof of equivalence by Rank in the appendix of that reference; for a comprehensive overview of error estimation in finite element analysis we refer to [4].

The particular aim here is to apply the reconstruction-based error indicator of Zienkiewicz-Zhu in an appropriate format to multiphase microstructures, the material class of interest in the present work.

3.2.1 The standard superconvergent patch recovery (SPR)

The point of departure is the error estimation of Zienkiewicz and Zhu which relies on superconvergence of stress and strain. Superconvergence in the present context refers to the property of strain and stress to converge in the same order as the displacements do $\mathcal{O}(h^{q+1})$ with the polynomial order q of the shape functions. This is an exception to the nominal order q for strain which follows from differentiation for strain calculation. A necessary condition for superconvergence in quadrilaterals is their rectangular shape. In that case along with sufficient regularity, superconvergence can be measured for q=1 in the element center, for q=2 in the 2×2 Gauss points; these points are referred to as Barlow-points [7]. Notice that pixelized images used here as initial, uniform discretization as well as their quadtree coarsened offsprings each exhibit a quadratic shape and therefor fulfill the necessary condition for superconvergence. In [57] a procedure was introduced that transfers the superconvergence property from the Barlow points in the element interior to element nodes; it is referred to as "superconvergent patch recovery" (SPR). These recovered superconvergent nodal values enter the error indicator and thereby largely determine its accuracy; the error distribution is the prerequisite for adaptive mesh refinement [58].

By applying the SPR to calculate nodal stresses, a continuous stress distribution is generated. For finite elements with $\mathcal{C}^0$-continuity the displacement field is continuous, stress and strain is not. Instead, they exhibit jumps at nodes, which is even more pronounced, if a particular node is right at the interface of different materials having a large stiffness mismatch. The original SPR does not account in any form for phase information, so that there are some modifications needed to make it applicable to these structures.

Since the generation of classical patches in the format of SPR is not possible for multiphase structures in any case, a different scheme is introduced for reconstructing nodal stress and strain from their counterparts in the interior of the element.

For ready reference, the rationale of the SPR is briefly reiterated for linear shape functions q=1 in a 2D setting, where strain and stress are calculated each in the center of rectangular elements. These values are transferred by a least-square procedure to the finite element node in the direct neighborhood. Elements having such a node in common are referred to as patch in the recovery procedure.

Stresses on the patch are prescribed component-wise by

$$\sigma_p^\star = \boldsymbol{P}\,\boldsymbol{a} \tag{5}$$

with, for the case of linear shape functions,

$$\boldsymbol{P} = [1,\ x,\ y,\ xy] \quad \text{and} \quad \boldsymbol{a} = [a_1,\ a_2,\ a_3,\ a_4]\,. \tag{6}$$

Vector $\boldsymbol{P}$ contains polynomial terms of bi-linear shape functions for $n_{\text{dim}} = 2$. For the determination of the unknown vector $\boldsymbol{a}$ the function

$$\begin{aligned} F(\boldsymbol{a}) &= \sum_{i=1}^{n} (\sigma^{h*}(x_i,\ y_i) - \sigma_p^\star(x_i,\ y_i))^2 \\ &= \sum_{i=1}^{n} (\sigma^{h*}(x_i,\ y_i) - \boldsymbol{P}(x_i,\ y_i)\mathbf{a})^2 \end{aligned} \tag{7}$$

has to be minimized. Therein, $(x_i,\ y_i)$ are the coordinates of the superconvergent points, n is the number of superconvergent points of the total patch and $\sigma^{h*}(x_i,\ y_i)$ are the stresses in these superconvergent points. Minimization of $F(\boldsymbol{a})$ implies that $\boldsymbol{a}$ fulfills the condition

$$\sum_{i=1}^{n} \boldsymbol{P}^T(x_i,\ y_i)\,\boldsymbol{P}(x_i,\ y_i)\,\boldsymbol{a} = \sum_{i=1}^{n} \boldsymbol{P}^T(x_i,\ y_i)\,\sigma^{h*}(x_i,\ y_i)\,, \tag{8}$$

which can be solved for $\boldsymbol{a}$

$$\boldsymbol{a} = \boldsymbol{A}^{-1}\,\boldsymbol{b} \tag{9}$$

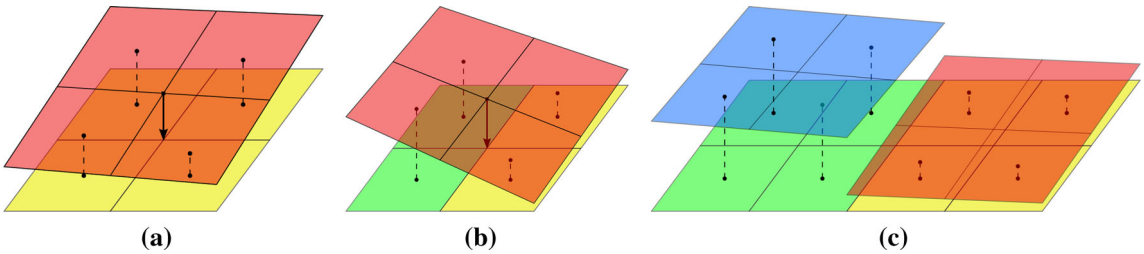


Fig. 4 Recovery of nodal stresses using standard SPR and modified SPR: **a** standard SPR for a patch with only one material phase and **b** standard SPR applied to a two phase material patch ignoring the interface, **c** modified SPR applied to a two-phase material with explicit account of the element phase by introducing two sets of stress at interface nodes

with

$$\boldsymbol{A} = \sum_{i=1}^{n} \boldsymbol{P}^T(x_i,\, y_i)\, \boldsymbol{P}(x_i,\, y_i) \quad \text{and}$$

$$\boldsymbol{b} = \sum_{i=1}^{n} \boldsymbol{P}^T(x_i,\, y_i)\, \sigma^{h*}(x_i,\, y_i)\,. \tag{10}$$

Stresses in the central node of the patch can be recovered by inserting its nodal coordinates $(x_N,\ y_N)$ into the $\boldsymbol{P}$-vector in (5).

3.2.2 The modified superconvergent patch recovery

The standard SPR does not account in any form for different phases and interfaces in patch generation. For all nodes right at phase boundaries the corresponding standard patch is made up of elements belonging to different material phases.

Figure 4a gives a sketch of the standard SPR for a patch with elements from one and the same material phase, Fig. 4b gives the same sketch for a node at the boundary between a stiff (green) and a soft (yellow) phase. The stiffness jump at the phase boundary induces a stress jump, an effect which is the more pronounced, the larger the stiffness mismatch. In the example of Fig. 4b the stiff (green) phase exhibits considerable larger stress values than the softer (yellow) one. Fitting a bi-linear interpolation function through stress and strain at the support of the patch results in a reconstructed stress at the central node which is an average of the values of different magnitudes and thus ignores –i.e. falsifies– the true mechanical phenomenon of a discrete stress jump. In the context of error estimation based on intentionally *improved* nodal stresses in comparison to stress in the element interior, suchlike falsified nodal stresses yield a spoiled support for interpolation, a fact that was already recognized in [35].

A solution to the problem is the assignment of two sets of stress for nodes at interfaces; it accounts for the mechanics and, as it will turn out, improves error estimation.

In order to apply this modified SPR to the central node at the phase boundary from Fig. 4b, two patches have to be generated, one for each phase. Figure 4c displays the patches and the stresses following from each patch. Fitting the bi-linear interpolation function (blue) through the stresses of the supports of the stiffer phase (green) obviously leads to a higher stress value for the central node at the phase boundary than fitting the bi-linear interpolation function (red) through the supports of the weaker phase (yellow). By introducing the duplex stress values, both sets of stress are available for further use.

Expanding the patch into the phase interior is in perfect analogy to the treatment of edge and corner nodes at the mesh boundary for a single-phase material [17].

Nevertheless, there are several cases of element arrangements at interfaces which prevent the generation of standard patches. One case is the scattered element phase distribution which is characterized by a non-straight interface line as illustrated in Fig. 5a. The node marked in blue has only one single adjacent element from the yellow phase. If the patch is expanded to the interior of the phase, there are still only three elements for constructing the node's patch. The yellow element from the upper right of the displayed section of the micro mesh is not a candidate for patch-construction, since there would be three points on a straight line, making matrix $\boldsymbol{A}$ in (9) singular.

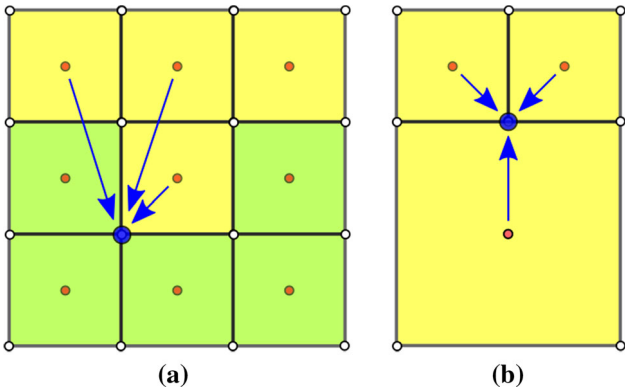


Fig. 5 Examples for irregular patches for SPR: caused by **a** the scattered element phase distribution at the interface, by **b** a hanging node

There are further situations conceivable, where even less than three elements are available for patch generation. Imagine the case of one (or two connected) elements, which are placed in between elements from another phase. In this case the patch has to be build up by one (two) elements. A similar situation arises for hanging nodes, since there are always exactly three elements surrounding them, see Fig. 5b.

To treat patches with less than four elements the number of terms in vector $\boldsymbol{P}$ in Eq. $(6)_1$ may have to be reduced, since otherwise the number of superconvergent points is not sufficient to determine the parameters of vector $\boldsymbol{a}$ in $(6)_2$.

For interface nodes at the corner of two patches belonging to the same phase, nodal stress is computed by averaging the values obtained from the involved patches according to (14).

3.2.3 Averaged stresses and strains based on "intra-element patches"

The main disadvantage of the SPR is the fact, that –especially for adaptively refined meshes and meshes with multiple phases– regular patches based on four surrounding elements can not be properly constructed for all nodes.

To avoid too heavy computational efforts in generating sufficiently regular patches, a different but similar method is proposed and will be investigated. For this method stress and strain from the standard quadrature points are used instead of stress and strain from superconvergent points. Using these stresses and strains and the element shape functions, nodal element stresses ($\boldsymbol{\sigma}_{\text{node,ele}}$) and strains ($\boldsymbol{\varepsilon}_{\text{node,ele}}$) can be calculated.

For each quadrature point with coordinates $\boldsymbol{x}_{qp,i}$ with $i = 1, \ldots, n_{qp}$ it must hold

$$\sigma_{qp} = \sum_{i=1}^{n_{qp}} N_i(\boldsymbol{x}_{qp})\, \sigma_{\text{node,ele},\,i}\,,$$
$$\varepsilon_{qp} = \sum_{i=1}^{n_{qp}} N_i(\boldsymbol{x}_{qp})\, \varepsilon_{\text{node,ele},\,i}\,. \tag{11}$$

Written up in vector-matrix-representation Eq. (11) reads as

$$\boldsymbol{\sigma}_{qp} = \boldsymbol{N}(\boldsymbol{x}_{qp})\boldsymbol{\sigma}_{\text{node,ele}}\,, \quad \boldsymbol{\varepsilon}_{qp} = \boldsymbol{N}(\boldsymbol{x}_{qp})\boldsymbol{\varepsilon}_{\text{node,ele}}\,. \tag{12}$$

Nodal element stresses and strains for each element are obtained by

$$\boldsymbol{\sigma}_{\text{node,ele}} = \boldsymbol{N}(\boldsymbol{x}_{qp})^{-1}\boldsymbol{\sigma}_{qp}\,, \quad \boldsymbol{\varepsilon}_{\text{node,ele}} = \boldsymbol{N}(\boldsymbol{x}_{qp})^{-1}\boldsymbol{\varepsilon}_{qp}\,. \tag{13}$$

The general procedure of using the shape functions to extrapolate stresses and strains from quadrature points to the element nodes–as done in (11)–(13)—is standard. Non-standard is that in the averaging for nodal values according to (14) only those contributions of the same material phase are considered instead of the contribution of all elements

$$\boldsymbol{\sigma}^{\star}_{\text{av}} = \frac{1}{n_{\text{ele,phase}}} \sum_{i=1}^{n_{\text{ele,phase}}} \boldsymbol{\sigma}_{\text{node,ele},i}\,,$$
$$\boldsymbol{\varepsilon}^{\star}_{\text{av}} = \frac{1}{n_{\text{ele,phase}}} \sum_{i=1}^{n_{\text{ele,phase}}} \boldsymbol{\varepsilon}_{\text{node,ele},i} \tag{14}$$

with $n_{\text{ele,phase}}$ the number of adjacent elements from the same material phase.

This procedure is quite similar to the patch recovery method, since it is basically the same as fitting a bi-linear polynomial through the four standard quadrature points thus giving rise to the term "intra-element patch". By doing so each node obtains from the adjacent elements a set of elementwise stress and strain.

Figure 6a shows a patch with two different phases, where for each of its elements the bi-linear shape functions are fitted through the quadrature points (a). The central node exhibits four stress values, one from each of the elements. The duplex stress related to the stiffer (green) phase is averaged from the three nodal stresses following from the bi-linear shape functions (blue) fitted through the quadrature points of the stiffer elements. Analogously, the duplex stress related to the weaker (yellow) phase is directly derived from the bi-linear shape function (red) fitted through the quadrature points of the one element belonging to the weaker phase.

Figure 6b displays the resulting stress, the central node now exhibits exactly two sets of stresses, the duplex stresses following from the two different phases.

By doing so the costs of patch construction vanish, whereas nodal stress and strain are still calculated via bi-linear polynomials.

3.3 Error estimator and effectivity index

As described above, recovery-based error estimation is based on improved nodal stresses and strains, denoted by $\boldsymbol{\sigma}^{\star}$ and $\boldsymbol{\varepsilon}^{\star}$. They are computed by the SPR or by the averaged nodal stresses and strains based on intra-element patches.

The estimated error in the energy norm on the micro domain Ω_ϵ reads as

$$||\bar{\boldsymbol{e}}||_{A(\Omega_\epsilon)} = \left[\int_{\Omega_\epsilon} \left(\boldsymbol{\sigma}^{\star} - \boldsymbol{\sigma}^{h}\right) : \left(\boldsymbol{\varepsilon}^{\star} - \boldsymbol{\varepsilon}^{h}\right) \mathrm{d}V\right]^{1/2}, \tag{15}$$

$$\approx \left[\sum_{T\in\mathcal{T}_h} \left(\sum_{i=1}^{ngp} \omega_i \left(\boldsymbol{\sigma}^{\star} - \boldsymbol{\sigma}^{h}\right)(\boldsymbol{x}_i^h) : \left(\boldsymbol{\varepsilon}^{\star} - \boldsymbol{\varepsilon}^{h}\right)(\boldsymbol{x}_i^h)\, \det \boldsymbol{J}\right)\right]^{1/2}. \tag{16}$$

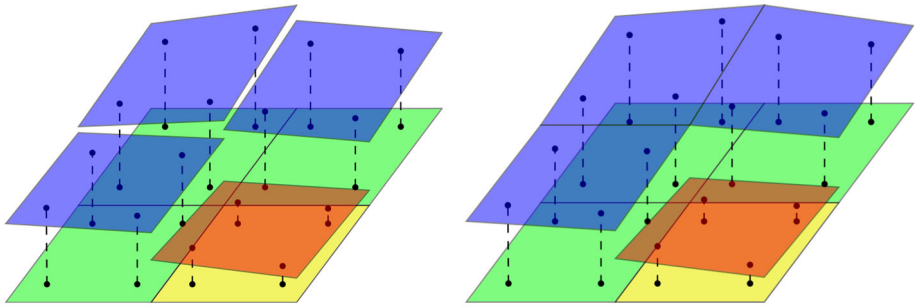


Fig. 6 Averaging method for a node attached to four elements with different phases: **a** the central node obtains from all adjacent elements a set of elementwise stress and strain, **b** the duplex nodal values result from averaging stresses and strains each of the same phase according to (14)

Here the superconvergent nodal stresses and strains have to be evaluated in the quadrature points $\boldsymbol{x}_i^h$. The procedure of calculating quantities in the quadrature points from nodal values is executed using the shape functions, analogous to (11).

Compared to the error computation based on a nominally exact reference solution according to (4), the error estimation is clearly much cheaper, since the integration of the error is carried out on the same mesh with triangulation $\mathcal{T}_h$ instead of on another, reference triangulation $\mathcal{T}_{\text{ref}}$ with $h \to 0$, which needs an extra, expensive computation.

The quality of the error estimator is typically assessed by the so-called effectivity index θ which is defined as the ratio of the estimated error $\|\bar{\boldsymbol{e}}\|$ to the true error $\|\boldsymbol{e}\|$

$$\theta = \frac{\|\bar{\boldsymbol{e}}\|}{\|\boldsymbol{e}\|} \,. \tag{17}$$

For consistency the effectivity index must tend to unity as the exact error tends to zero.

4 Numerical examples

In this section a thorough error analysis is carried out for both the original, uniform discretization of pixelized images and the discretizations following from consecutive mesh coarsening.

Since microstructures are considered representative volume elements (here in the 2D setting: representative area elements RAE) in a two-scale finite element method for computational homogenization such as FE-HMM and FE^2, all quantities in the present numerical analysis refer to the micro scale such that the attribute "micro" can be silently omitted.

In the analysis we will focus on

(i) the accuracy assessment of different recovery schemes for nodal stress computation in error estimation by comparison with true errors, example in Sect. 4.1.
(ii) the errors for mesh coarsening with ("soft") and without ("hard") restrictions on gradient steepness of element size, example in Sect. 4.2.
(iii) the error analysis of adaptive mesh coarsening for different micro coupling conditions applied to the RAE; kinematically uniform boundary conditions (KUBC or "Dirichlet"), periodic boundary conditions (PBC), and constant traction ("Neumann") BC, examples in Sects. 4.3, 4.4.
(iv) on the propagation of micro discretization errors to macro scale properties such as the coefficients of the effective elasticity tensor and macro scale deformation, example in Sect. 4.4.
(v) mesh coarsening for a real microstructure of a Diamond/β-SiC nanocomposite obtained from microscopy pictures, Sect. 4.4.
(vi) mesh coarsening for a microstructure with more than two different material phases, Sect. 4.5.

The macro problem common to all micro problems is chosen to be a bending beam, clamped at x=0 and subject to a volume force of $\boldsymbol{f} = [0, -1]^T$ $[F/L^2]$ as displayed in Fig. 7. It exhibits length l in x-direction, height b in y-direction, and thickness t in z-direction. It holds $l = 5000$ $[L]$, $b = 1000$ $[L]$, $t = 100$ $[L]$. The side length of the square RAE is $\epsilon = 1$ $[L]$. Macroscopic influences on micro error analyses are avoided by keeping the macro discretization fixed with 100×20 macro elements.

All simulations are run for plane strain condition and - unless otherwise stated- for PBC. The results for the micro domain at the macroscopic Gauss point at $x = 4460$ $[L]$, $y = 110$ $[L]$ are shown in the following.

For all microstructures with two phases, one phase exhibits the Young's modulus of silicon carbide SiC with $E_{\text{SiC}} = 250{,}000$ $[F/L^2]$ along with a Poisson's ratio of $\nu = 0.17$; the second one exhibits the elasticity parameters of diamond with $E_{\text{D}} = 775{,}000$ $[F/L^2]$ and $\nu = 0.2$. These values refer to a real material system of a Diamond/β-SiC thin film nanocomposite—therefore with unit (MPa)—which is investigated in Sect. 4.4. For a three-phase microstructure—a tessellation[1] made up of seahorses from the work of M.C.

[1] Tessellations are arrangements of closed shapes that completely cover the plane without overlapping and without leaving gaps.

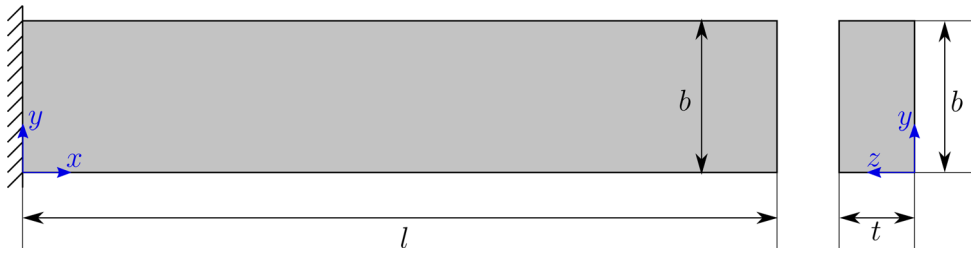
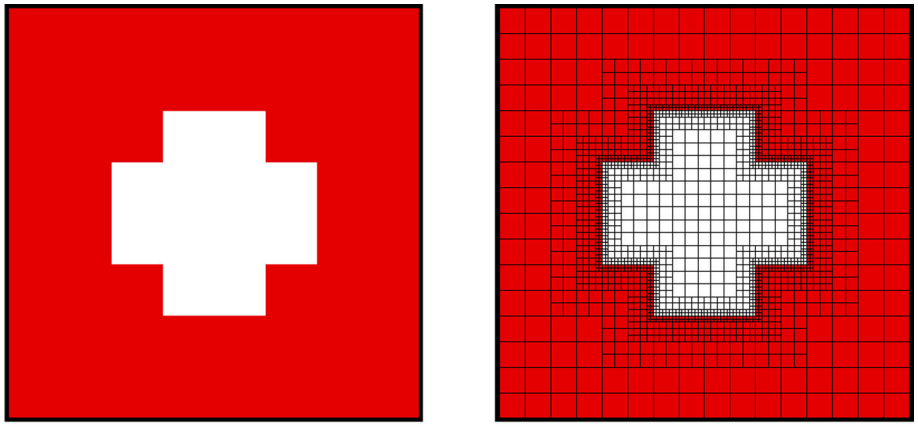


Fig. 7 Macro problem: cantilever beam, geometry and boundary conditions



(a) Cross microstructure **(b)** Coarsened micro mesh

Fig. 8 Cross microstructure: **a** structure with two phases, **b** micro mesh after three coarsening steps with the soft coarsening method

Escher—the phases differ in their Young's moduli, which will be chosen to $E_1 = 40{,}000\ [F/L^2]$, $E_2 = 100{,}000\ [F/L^2]$ and $E_3 = 250{,}000\ [F/L^2]$, the Poisson's ratio is chosen to be $\nu = 0.2$ for all phases.

To investigate the discretization error on one specific RAE the corresponding macroscopic displacement field has to be kept constant for all micro discretizations, otherwise there would be an influence from the macro quantities. Here the macroscopic displacement field obtained from the original, uniform mesh in the RAE will be used and only the postprocessing is executed for all micro meshes.

Remark For linear elasticity it is possible to precompute the effective elasticity tensor for it is constant. Then the macroscopic problem can be solved by a standard, single-scale finite element method. The error analysis on the micro scale however, which is the main topic of the present work, requires a separate consideration of the fully resolved microstructure on the RAE level. Moreover, linear elasticity shall be understood as a simple prototype model for the more general case of hyperelasticity, where the tangent moduli are deformation-dependent and therefore do not allow for calculations beforehand.

4.1 Cross

In the first example a microstructure of a cross-shaped, stiff inclusion in a softer square matrix is considered. For a periodic metamaterial of tetragonal symmetry with similar unit cells, elastic material parameters of a micromorphic material model were identified by nonstandard homogenization [36], which captured the observed band-gap properties fairly well [9].

Table 1 Cross microstructure: number of degrees of freedom (ndof) of the original, uniform and the coarsened micro meshes, the corresponding reduction factor and the number of deactivated degrees of freedom

Coarsening step nos.	0	1	2	3
ndof	33,282	9730	4712	3832
Factor	1.0000	0.2924	0.1416	0.1151
Deactivated ndof	0	512	776	872

The error calculations will be executed on different reference meshes to investigate (i) the convergence of the calculated micro discretization error and (ii) the discretization which is sufficiently fine to serve for a reference solution. Furthermore, (iii) the estimated errors employing different reconstruction schemes are compared with and assessed by the calculated errors which yields their effectivity index as defined in (17).

Figure 8a shows the cross microstructure with its two different phases, silicon carbide SiC (red) and diamond (white), Fig. 8b shows the micro mesh after three coarsening steps employing the soft coarsening method.

4.1.1 Mesh coarsening

Table 1 provides the number of degrees of freedom of the original, uniform mesh (128×128 elements) and the meshes

resulting from the coarsening steps, where coarsening step 0 refers to the original mesh. After three coarsening steps the number of degrees of freedom is reduced to less than 12% compared with the initial mesh. Furthermore the number of constrained degrees of freedom is given. The initial mesh is uniform and thus does not exhibit any deactivated degrees of freedom, after mesh coarsening the ratio of constrained ndof to all ndof increases from 5.0% for the first coarsened mesh to 18.5% for the third coarsened mesh.

Here and in the following the number of degrees of freedom in the tables equals the total number of degrees of freedom of the micro mesh minus the number of deactivated degrees of freedom of the hanging nodes. Since different coupling conditions on the RAE imply additional but different reductions of unknowns, they are not yet subtracted from the tabulated figures to allow for a streamlined comparison.

4.1.2 Computed versus estimated micro discretization error

Table 2 shows the errors in the energy norm for the original, uniform mesh and the meshes from the three coarsening steps based on reference solutions on different discretizations. To achieve reliable results, the discretization of the reference solution should at least be eight times finer per dimension of space than the discretization of the original, uniform mesh.

For future use we validate error estimation by the true error computation and thereby distinguish between different schemes of error estimation/stress computation, (i) the standard SPR blind for phase distributions, (ii) the modified SPR accounting for interfaces, and (iii) the averaging of elementwise quantities belonging to the same material phase.

Table 3 displays the results for the above three different methods (i)–(iii). As expected, the standard SPR, blind for interfaces inside the patch, leads to gross errors, an overestimation of the true error by more than 60% for the uniform mesh.

The estimated errors based on the modified SPR and on the averaging of elementwise quantities exhibit an excellent agreement with the true errors as indicated by effectivity indices θ close to one. The results suggest that error estimation is applicable to multiphase microstructures having interfaces along with a stiffness jump, if the two phases are strictly distinguished in the calculation of nodal stresses and strains.

Table 3 Cross microstructure: estimated error in the energy norm $||\bar{e}||_{A(\Omega_\epsilon)}$ and resulting effectivity index θ for different error estimation schemes

Coarsening step nos.		0	1	2	3
Standard SPR	$\|\|\bar{e}\|\|_{A(\Omega_\epsilon)}$	2.0964	2.4475	2.7880	3.2700
	θ	1.6018	1.3925	1.2915	1.2196
Modified SPR	$\|\|\bar{e}\|\|_{A(\Omega_\epsilon)}$	1.3641	1.8634	2.2928	2.8598
	θ	1.0452	1.0602	1.0620	1.0666
Averaging	$\|\|\bar{e}\|\|_{A(\Omega_\epsilon)}$	1.2429	1.7331	2.1550	2.7044
	θ	0.9497	0.9860	0.9982	1.0086

All error data in $10^{-2}\,[FL]$

4.1.3 Error distribution

For the investigation of error distributions on the micro domain the relative elementwise micro discretization error is analyzed. This relative error is the ratio of the computed or estimated error of an element to the element's energy norm. By doing so the influence of the element size is eliminated which is especially important for the non-uniform meshes.

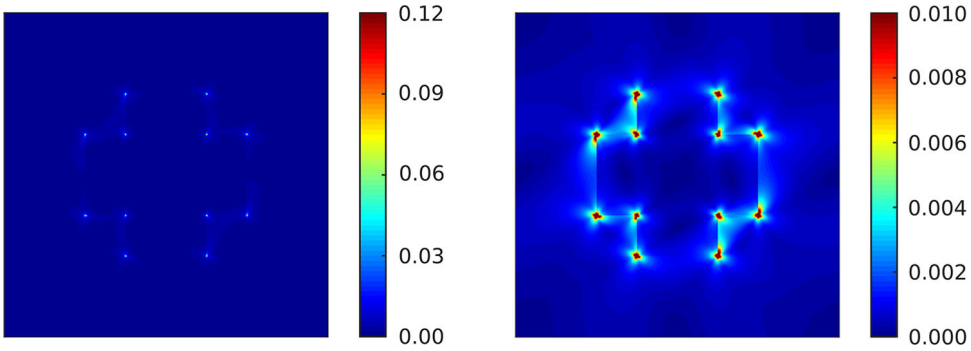
Figure 9 shows the distribution of the estimated error computed with a micro mesh of 1024 × 1024 elements with different color scaling. The original scaling in the left indicates that the maximum relative discretization error of about 12% is located in and confined to the cross' corners. The cross' edges are hardly visible for the errors virtually vanishing–similar to the interior of the two phases. In order to closer investigate the micro discretization errors, the range of the color scaling is changed to [0−1%]. The error distribution with reduced colorbar range underpins that there are only small spots with relative errors of 1% or above at the cross' corners while even the edges exhibit an error of less than 1%.

Remark Since there are only a few, small spots with errors of above 1%, the overall discretization error is small. For efficient mesh coarsening it is preferable to have a contrast in error distribution, major ones all over phase boundaries

Table 2 Cross microstructure: computed errors in the energy norm $||\boldsymbol{e}||_{A(\Omega_\epsilon)}$ for the original, uniform mesh and the coarsened discretizations with reference solutions based on different discretizations

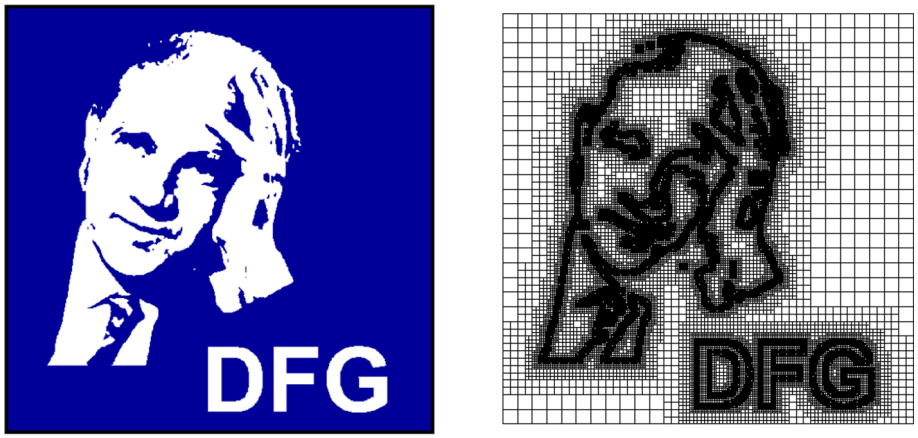
Discretization	No.	Total error $\|\|\boldsymbol{e}\|\|_{A(\Omega_\epsilon)}$			
Original, uniform	0	1.0920	1.2526	1.2987	1.3088
Adaptive coarsening	1	1.6028	1.7163	1.7502	1.7577
	2	2.0348	2.1253	2.1527	2.1588
	3	2.5824	2.6543	2.6764	2.6813
Reference discretization		256 × 256	512 × 512	1024 × 1024	1536 × 1536

Errors in $10^{-2}\,[FL]$



(a) Error distribution **(b)** Error distribution, rescaled

Fig. 9 Cross microstructure: distributions of relative errors $||\bar{e}||_{A(\Omega_e)}/||u||_{A(\Omega_e)}$ with different color scaling on a micro domain for discretization of 1024×1024 elements



(a) DFG-Heisenberg microstructure **(b)** Coarsened micro mesh

Fig. 10 DFG-Heisenberg: **a** microstructure with two different phases, **b** 5th soft coarsened quadtree mesh

and minor ones in the phase interior. In that case, element coarsening in the phase interior leads to an increase of these minor errors, but since the dominant errors at phase boundaries remain unaltered, the overall error does not strongly increase. In this particular example however, the error at the phase boundary is not dominant enough to allow for efficient mesh coarsening. The estimated overall micro discretization error on the micro mesh with 1024×1024 elements is $0.0022\,[FL]$, the estimated micro discretization error of the interface elements is $0.0014\,[FL]$. This is not sufficient for effective mesh coarsening and leads to an already strongly increased error between the original, uniform mesh and the first coarsened mesh, see Tables 2 and 3.

4.1.4 Conclusions

For the excellent accuracy of error estimation in the present example we will discard the expensive, and in engineering practice hardly feasible error computations in the following.

From the computational point of view the averaging technique for nodal stress/strain computation is the simplest one of the three techniques, since no patch generation around each node is required. For its poor results ignoring interfaces with their stress jumps, the standard SPR disqualifies for multiphase error estimation. For that reason we continue our analysis in the following with a focus on the modified SPR and the error estimation based on intra-element patches along with averaging.

4.2 DFG-Heisenberg

The second example is a two-phase microstructure showing a portrait of the physicist Werner Heisenberg[2] as shown in Fig. 10a. The white phase exhibits the elasticity properties of SiC, the blue phase those of diamond. The original, uniform micro mesh exhibits 896×896 elements. In this example the different coarsening algorithms from Sect. 2 are compared, on the one hand the hard mesh coarsening which leads to large gradients in element size at phase boundaries and on the other hand the soft mesh coarsening, where the element size gradient is reduced. The resultant mesh after five soft coarsening steps is displayed in Fig. 10b.

[2] The image refers to the Heisenberg-program logo of the Deutsche Forschungsgemeinschaft (DFG).

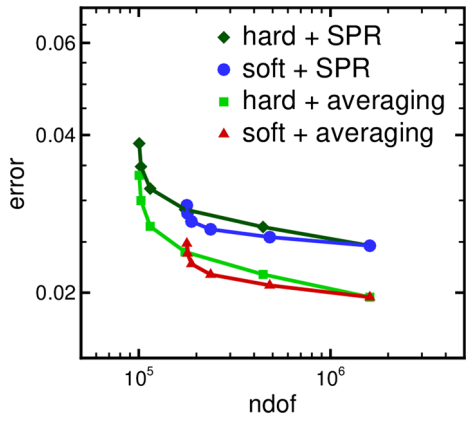


Fig. 11 DFG-Heisenberg: discretization error $||\bar{e}||_{A(\Omega_\epsilon)}$ (in $[FL]$) for soft and hard coarsening along with the averaging method and the modified SPR

4.2.1 Mesh coarsening and discretization error

For its very fine initial discretization compared to the previous example, the DFG-Heisenberg microstructure is subject to more coarsening steps, but restricted to five to avoid too large elements at the RAE boundaries.

Figure 11 shows the error increase for mesh coarsening over the corresponding ndof for the soft and the hard coarsening techniques; the estimated error is obtained by the averaging method and the modified SPR. Both mesh coarsening algorithms yield an almost constant increase of the estimated errors from step to step; since, however, only the first two steps considerably reduce the ndof in contrast to the consecutive ones, the gain in efficiency versus the accuracy loss pays off only in these first two steps.

The diagram indicates that the second mesh obtained by hard coarsening and the fourth mesh obtained by soft coarsening coincide almost quantitatively for the same number of unknowns in their total error. For a comparison of the two coarsening algorithms a focus is on these two micro meshes in the following.

Table 4 shows the number of degrees of freedom of the original, uniform micro mesh and its coarsened counterparts. Especially during the first two coarsening steps the number of degrees of freedom is strongly reduced while the last two coarsening steps reduce them less than 1%. The soft coarsening algorithm reduces the number of degrees of freedom to less than 12%, the hard mesh coarsening even to less than 7%. The ratio of deactivated degrees of freedom is 4.5% (soft) and 5.2% (hard) for the first coarsened mesh and increases to 16.3% (soft) and 28.6% (hard) for the fifth coarsened mesh.

Furthermore, Table 4 shows the estimated errors in the energy norm for both error estimation techniques and both mesh coarsening algorithms. Similar to the first example the estimated errors by the modified SPR are larger than those of the averaging method.

Soft mesh coarsening after its fifth step reduces the number of unknowns by about 88% for an error increase of 27%, when the averaging technique is used, and by 19% for patch recovery. Hence, the considerable efficiency gain need not be paid by a comparable accuracy loss. The hard mesh coarsening leads after five coarsening steps even to a reduction of unknowns of more than 93%, which results however in a major error increase; namely of 56% for the modified SPR and 70% for averaging.

4.2.2 Distributions of error and micro strain

The distribution of relative element errors in the energy norm is the first quantity of interest in the comparison of Fig. 12a–c.

For (a) the major errors are located at the phase boundaries, while they vanish in the phase interior. Only at those interfaces of the letters "DFG", which are aligned with the x- and y-axes, the errors vanish likewise, which is equally true for cases (b) and (c). For (b) there is an increased error in the phases' interior, while the major error is still at phase boundaries. The maximum elementwise error is in quantitative agreement with the one of the initial, uniform discretization. The error distribution for case (c) exhibits minor errors in the phases' interiors compared to case (b) of the fourth soft coarsened micro mesh and resembles therein the original, uniform mesh. In exchange, the errors at the phase boundaries are not as sharp as for both other investigated meshes, resulting in a maximum elementwise error which is slightly decreased.

Complementary to the error plots the high accuracy in the interior of the phases can be visually underpinned by the contour plots of strain, here in terms of component ε_{xx} as displayed in Fig. 12d–f. The results reveal that strain ε_{xx} obtained for the soft coarsened mesh is in good agreement with the uniform mesh in its general distribution and in particular in the maximum, while the hard coarsened mesh shows some minor deviations which are attributed to the increased number of hanging node constraints close to the phase boundaries.

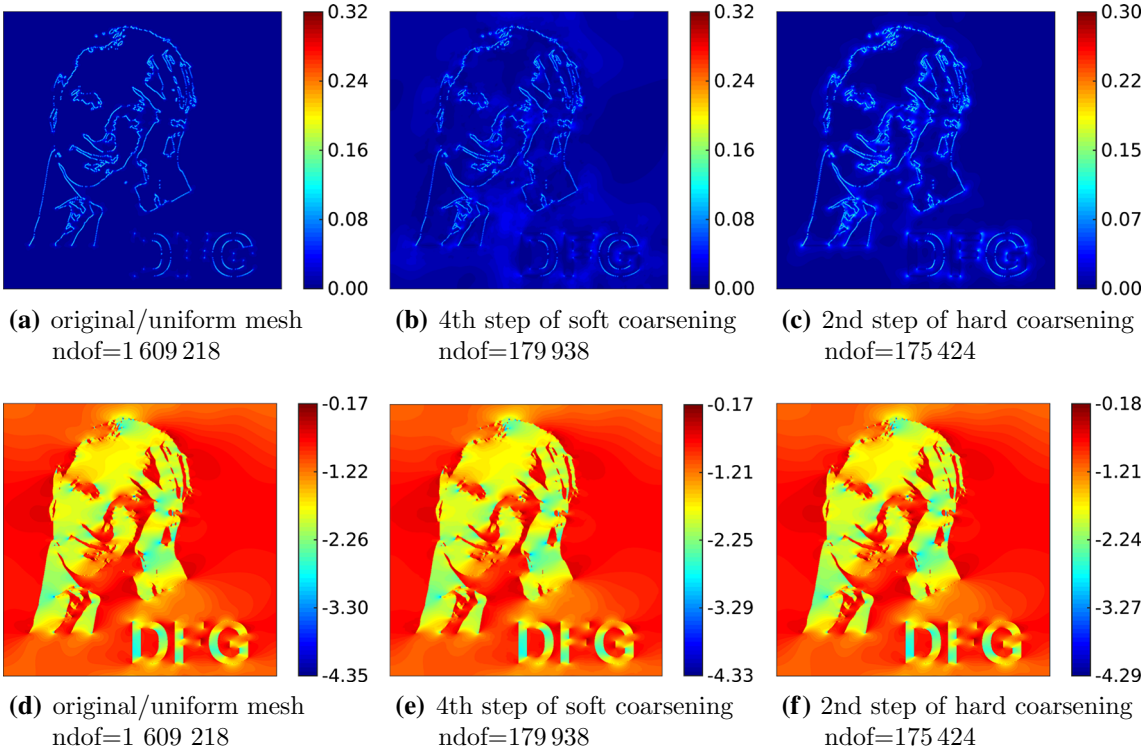
4.2.3 Conclusions

For the DFG-Heisenberg microstructure a strong reduction of unknowns is obtained in the first coarsening steps, while the fourth and fifth coarsening steps do not pay off any more in view of the modest efficiency gain and the rather strong accuracy loss. For the soft coarsened mesh the distributions of discretization error and strain are in quantitative agreement with the uniform mesh almost everywhere, while the hard coarsened micro mesh exhibits some minor deviations.

Table 4 DFG-Heisenberg: for different adaptive mesh coarsening steps (0–5) the number of degrees of freedom (ndof) along with the ndof-factor compared to the uniform mesh, the number of deactivated degrees of freedom, and the estimated errors for different methods with their (increase) factor compared to the uniform/initial discretization are displayed

Coarsening step no.		0	1	2	3	4	5
Soft mesh coarsening							
	ndof	1,609,218	484,146	238,116	188,940	179,938	178,490
	Factor	1.0000	0.3009	0.1480	0.1174	0.1118	0.1109
	Deactivated ndof	0	22,936	31,752	34,096	34,720	34,868
mod SPR	$\|\|\bar{e}\|\|_{A(\Omega_e)}$	2.4589	2.5537	2.6429	2.7351	2.8349	2.9366
	Factor	1.0000	1.0385	1.0748	1.1123	1.1529	1.1942
Averaging	$\|\|\bar{e}\|\|_{A(\Omega_e)}$	1.9607	2.0657	2.1660	2.2693	2.3775	2.4828
	Factor	1.0000	1.0535	1.1047	1.1574	1.2126	1.2663
Hard mesh coarsening							
	ndof	1,609,218	447,122	175,424	115,290	103,032	100,782
	Factor	1.0000	0.2779	0.1090	0.0716	0.0640	0.0626
	Deactivated ndof	0	24,444	34,796	38,860	39,996	40,346
mod SPR	$\|\|\bar{e}\|\|_{A(\Omega_e)}$	2.4589	2.6696	2.8837	3.1602	3.4811	3.8544
	Factor	1.0000	1.0857	1.1727	1.2852	1.4157	1.5675
Averaging	$\|\|\bar{e}\|\|_{A(\Omega_e)}$	1.9607	2.1670	2.3928	2.6772	2.9972	3.3512
	Factor	1.0000	1.1052	1.2204	1.3654	1.5286	1.7092

All error data in 10^{-2} $[FL]$



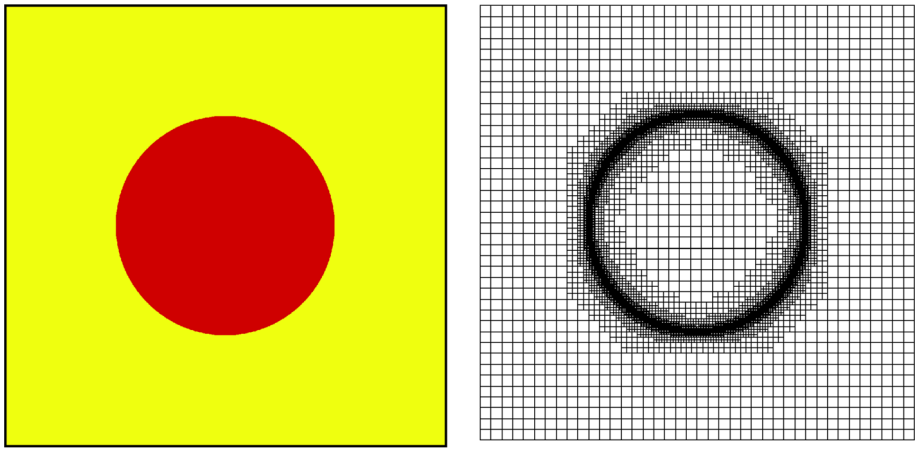
(a) original/uniform mesh ndof=1 609 218 **(b)** 4th step of soft coarsening ndof=179 938 **(c)** 2nd step of hard coarsening ndof=175 424

(d) original/uniform mesh ndof=1 609 218 **(e)** 4th step of soft coarsening ndof=179 938 **(f)** 2nd step of hard coarsening ndof=175 424

Fig. 12 DFG-Heisenberg: distribution of **a**–**c** the relative errors $||\bar{e}||_{A(\Omega_e)}/||\boldsymbol{u}||_{A(\Omega_e)}$ and of **d**–**f** the strain component ε_{xx} (in 10^{-2}) for the initial, uniform mesh and two adaptively coarsened meshes

4.3 Circle

The next example is a stiff circular inclusion in a soft matrix. The microstructure is chosen for its high regularity since it does not contain any sharp corners, where one phase might sting into the other one. While we have used periodic coupling so far, mesh coarsening in the present example shall be analyzed for different coupling conditions on the RAE boundary, for the cases of Dirichlet, Neumann and periodic coupling. A detailed error analysis for different coupling



(a) Circle microstructure **(b)** Coarsened mesh

Fig. 13 Circle microstructure: **a** microstructure with two phases, **b** 5th soft coarsened mesh

Table 5 Circle microstructure: number of degrees of freedom (ndof) along with the ndof-factor compared to the uniform mesh and the number of deactivated degrees of freedom, and the errors for different coupling conditions (Dirichlet, PBC, Neumann) along with their (increase) factor compared to the original, uniform discretization

Coarsening step no.		0	1	2	3	4	5
	ndof	3,281,922	838,210	235,768	89,302	54,670	46,974
	Factor	1.0000	0.2554	0.0718	0.0272	0.0167	0.0143
	Deactivated ndof	0	5120	7684	8960	9592	9904
Dirichlet BC	$\|\|\bar{e}\|\|_{A(\Omega_\epsilon)}$	5.3617	5.4423	5.6755	6.3476	7.8955	10.7014
	Factor	1.0000	1.0150	1.0585	1.1839	1.4726	1.9959
Periodic BC	$\|\|\bar{e}\|\|_{A(\Omega_\epsilon)}$	5.6321	5.7282	6.0117	6.8400	8.7860	12.4618
	Factor	1.0000	1.0170	1.0674	1.2145	1.5600	2.2126
Neumann BC	$\|\|\bar{e}\|\|_{A(\Omega_\epsilon)}$	6.5680	6.7026	7.1169	8.3565	11.3770	17.4521
	Factor	1.0000	1.0205	1.0836	1.2723	1.7322	2.6571

All error data in 10^{-3} $[FL]$

conditions along with (almost) uniform discretizations is presented in [17], for the 3d counterpart with adaptive resolution see [30].

In this example we combine the averaging method for error estimation with the soft mesh coarsening algorithm. For the good agreement of both estimation methods (i.e. averaging with modified SPR) at least in the first coarsening steps of the previous examples, we can focus on one of them. Furthermore, the soft mesh coarsening algorithm is chosen for its smaller errors in its first coarsening steps compared to hard coarsening.

Figure 13 shows the circular inclusion microstructure with its two different phases and the fifth soft coarsened mesh; the red phase is chosen to be SiC, the yellow phase is diamond.

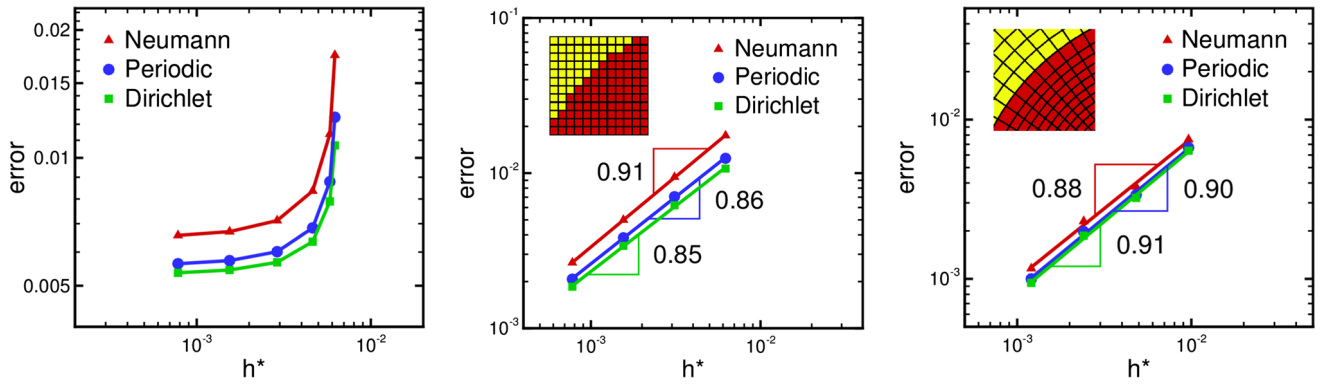
4.3.1 Mesh coarsening and micro discretization error

The original, uniform micro mesh of the circular inclusion problem is discretized by 1280×1280 elements. The number of coarsening steps is again restricted to 5 steps.

Table 5 shows the number of degrees of freedom for the original, uniform microstructure and after the single coarsening steps with their reduction factors. The fact that the inclusion is rather small in both its size and its boundary length enables a very efficient mesh coarsening; in the fifth coarsening step the total number of degrees of freedom is reduced to less than 1.5% of the original number of degrees of freedom. The ratio of deactivated degrees of freedom is 0.6% for the first coarsened mesh and increases to 17.4% for the fifth coarsened mesh.

The estimated micro discretization errors are displayed in Table 5 for different micro-macro coupling conditions. Especially the calculations with the last two coarsened micro meshes show major deviations to the original, uniform mesh, but the number of micro elements is decreased by more than 98% compared to the original, uniform mesh.

The diagram in Fig. 14a reveals the impact of different coupling conditions on the total error for mesh coarsening. The corresponding estimated errors all show the same characteristic trend for mesh coarsening. Dirichlet coupling leads to the smallest error and has the least number of remaining degrees of freedom in the system of equations while Neumann coupling leads to the biggest estimated error and has the highest number of remaining degrees of freedom.



(a) pixel mesh **(b)** pixel mesh **(c)** standard mesh

Fig. 14 Circle microstructure: estimated micro discretization error $||\bar{e}||_{A(\Omega_\epsilon)}$ in $[FL]$ for different coupling conditions versus characteristic element diameter h^* (**a**) for adaptive mesh coarsening, and (**b**), (**c**) for uniform mesh refinement, with $h^* := \sqrt{1/\text{num}_{\text{ele}}}$ and num_{ele} the number of elements in the RAE of side length 1

4.3.2 Convergence analysis

For microstructures in pixelized discretizations the questions arise, whether existing corrugated interfaces are an artefact of a limited pixel resolution or whether they are real; moreover, whether the re-entrant corners are of harm for the regularity of the problem as indicated by a reduced convergence order.

Standard finite element discretizations with their alignment at interfaces tend to make smooth what is possibly non-smooth, pixel-based discretizations tend to introduce corrugated interface representation including singularities due to re-entrant corners.

The first question must be answered separately for each case, the second question is addressed in the following for the matrix-inclusion problem; its interface is defined to be smooth. A pixel-based discretization and a standard finite element discretization are shown in the insets of Fig. 14b, c with a zoom into the interface. A convergence analysis is executed by uniformly refining the initial meshes. The convergence results in Fig. 14b, c are in almost quantitative agreement for the two cases; they fall somewhat behind the nominal order of q=1. In the present setting of a smooth interface the pixelized interface representation with its re-entrant corners does not spoil convergence.

This result can not be generalized. Imagine the limiting case of a coarse pixel resolution where the circular inclusion degenerates into a square. In that case the regularity of the BVP is reduced where the loss of order depends on the relative inclusion size and stiffness mismatch between the phases as shown in [13,17].

Remark *Why do total errors depend on boundary conditions?* All diagrams in Fig. 14 show maximal errors for Neumann coupling, smallest for Dirichlet, PBC is in between. Why is that and why in this order? Notice that for heterogeneous matter the RAE boundaries typically show for constant traction conditions larger small-scale displacement variations than for the "long-wave" PBC kinematics and much more than the straight, linear displacement condition. So the fulfillment of constant tractions is most demanding for a fine spatial resolution among these three. Vice versa, for a given discretization the errors at the boundaries are expected to be largest for Neumann, smallest for Dirichlet, for PBC in between. This rationale is underpinned by the simulation results in Fig. 15.

Although each example in the present work exhibits this order in error size, it can not be generalized as counterexamples indicate [17].

4.3.3 Distributions of error and micro strain

Again, the distribution of the micro discretization error on the micro domain will be investigated. Since the first examples including the present one have cleared that the last coarsening steps do not pay off, we will stick to the third coarsened mesh and compare the results for different coupling conditions to the results of the original, uniform mesh.

The error distributions as well as the normal strain component ε_{xx} in Table 6 show a very good agreement of the coarsened discretization with the uniform one in both the maximum elementwise figures and the distribution.

4.3.4 Conclusions

The high regularity of the circular inclusion and especially the small length of the boundary between the two phases leads to a very efficient mesh coarsening; after three coarsening steps the number of micro elements is reduced by more than 97% along with small discretization errors and good agreement in strain.

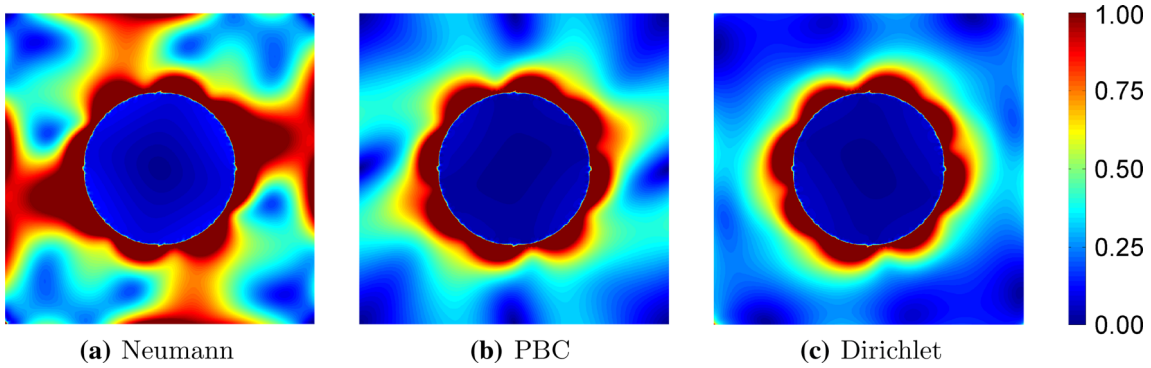
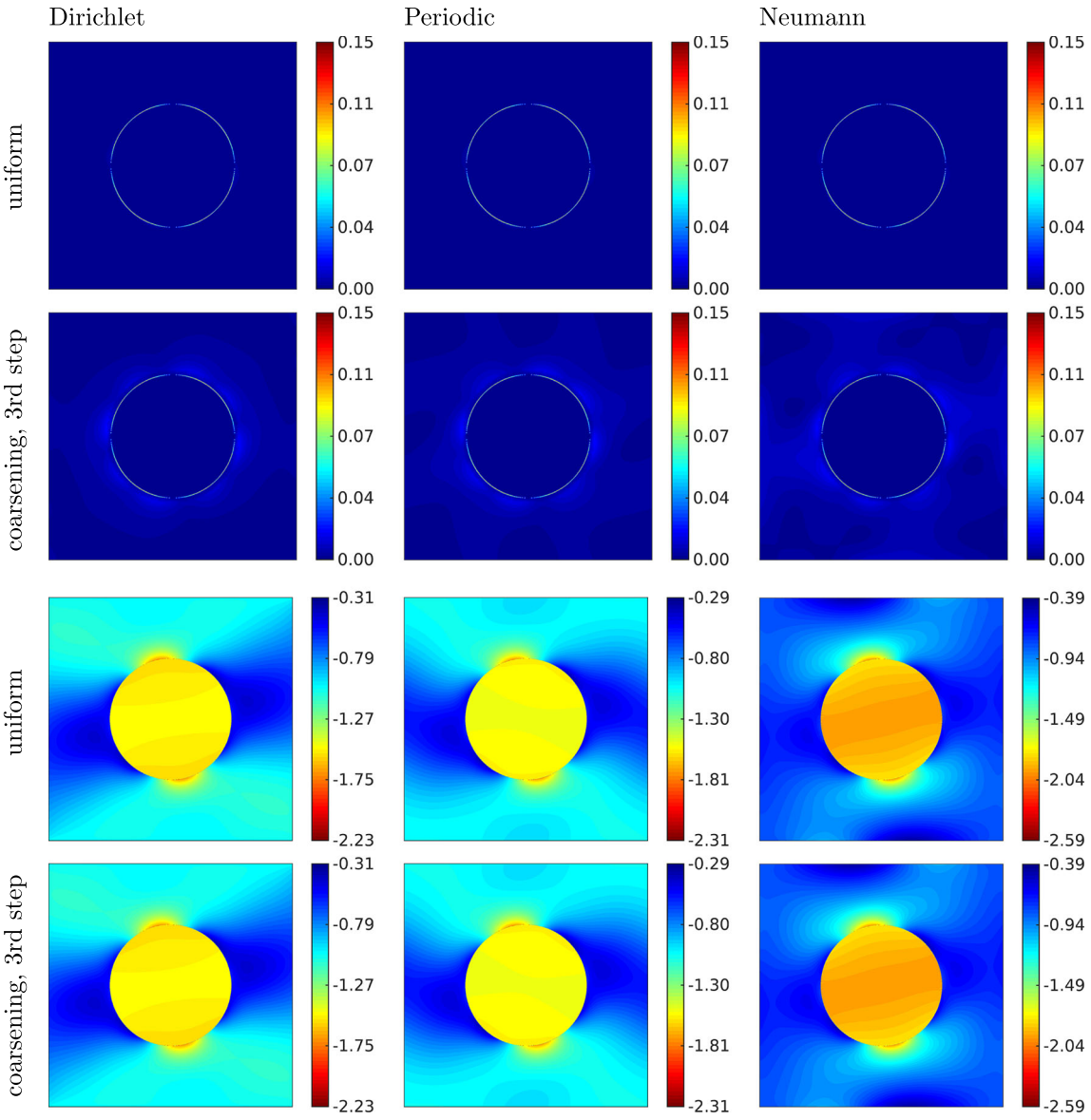
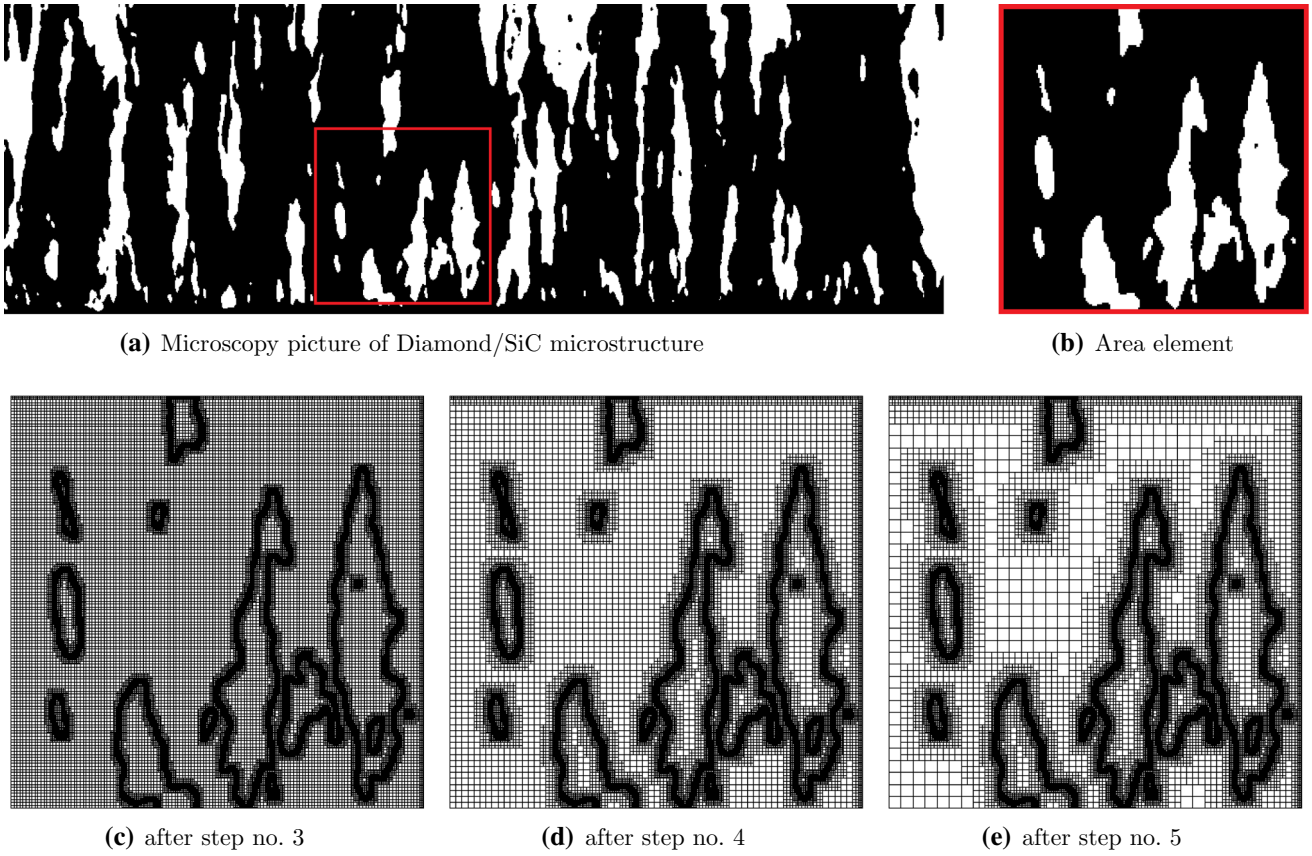


Fig. 15 Circle microstructure: relative errors $||\bar{\boldsymbol{e}}||_{A(\Omega_e)}/||\boldsymbol{u}||_{A(\Omega_e)}$ (in 10^{-3}) for different coupling conditions with contour plots adjusted to the RAE boundaries

Table 6 Circle microstructure: distribution of (first two lines) the relative micro error $||\bar{\boldsymbol{e}}||_{A(\Omega_e)}/||\boldsymbol{u}||_{A(\Omega_e)}$ and of (line 3 and 4) the normal strain component ε_{xx} (in 10^{-3}) for the original, uniform and the 3rd soft coarsened mesh with Dirichlet, periodic and Neumann coupling





(a) Microscopy picture of Diamond/SiC microstructure **(b)** Area element

(c) after step no. 3 **(d)** after step no. 4 **(e)** after step no. 5

Fig. 16 Diamond/SiC microstructure: **a** microstructure with two phases, **b** representative area element chosen for computations, and **c**–**e** adaptively coarsened meshes

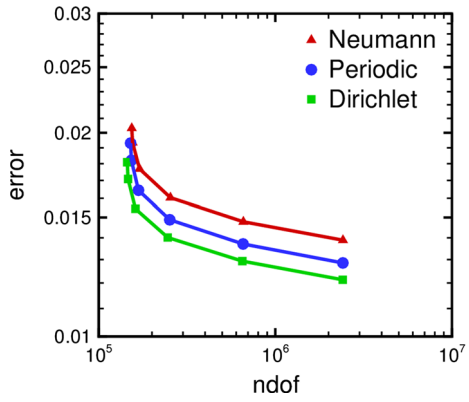


Fig. 17 Diamond/SiC microstructure: estimated micro discretization error $||\tilde{e}||_{A(\Omega_\epsilon)}$ in $[FL]$ for different coupling conditions

Furthermore, different coupling conditions on the micro domain boundary coincide qualitatively in a considerable reduction of unknowns in the first coarsening steps while the discretization error does moderately increase. Again, the last coarsening steps do not pay off for all coupling conditions. The softer the coupling, the larger the error, which is true for the initial, uniform mesh and for the error evolution in coarse-graining.

4.4 Diamond/SiC microstructure

Figure 16 shows microscopy pictures already converted into binaries of a Diamond/SiC thin film microstructure, which was fabricated by chemical vapor deposition (CVD). For the computation of effective elasticity properties through homogenization we refer to [15].

For the computations an area element (marked with red frame in Fig. 16) is chosen which is statistically representative for the basic population of the full image in Fig. 16a with respect to the phase fraction ratio (white phase 22.6% for the full image, 21.1% for the RAE) and the effective elasticity properties (deviations in the coefficients throughout less than 4.5%).

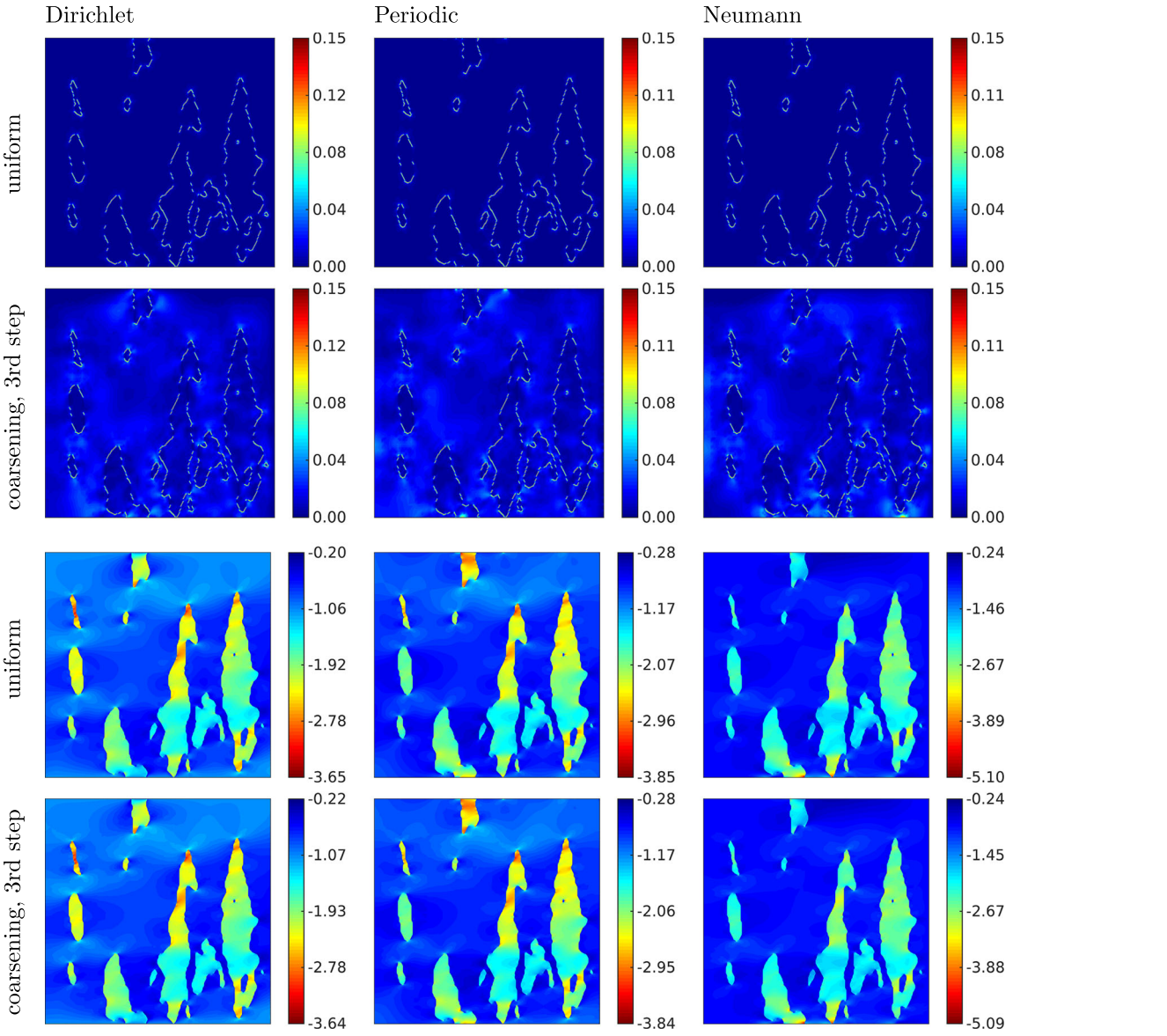
Again we employ averaging in error estimation along with the soft mesh coarsening algorithm. Notice in Fig. 16 that the discretization of the microstructure is relatively fine in the upper and right edge of the RAE compared to its lower and left edges. This is due to the choice–here on purpose–of a sub-optimal initial discretization having 1098 elements per edge where 1098 exhibits 2 in its prime factorization only once.

Table 7 Diamond/SiC microstructure: number of degrees of freedom (ndof), the ndof-factor compared to the uniform mesh, the number of deactivated degrees of freedom and the errors for different coupling conditions (Dirichlet, PBC, Neumann) with their (increase) factor compared to the uniform/initial discretization

Coarsening step no.		0	1	2	3	4	5
	ndof	2,415,602	659,188	254,726	170,200	155,374	153,796
	Factor	1.0000	0.2729	0.1055	0.0705	0.0643	0.0637
	Deactivated ndof	0	19,262	29,556	33,788	35,290	35,664
Dirichlet BC	$\|\|\bar{e}\|\|_{A(\Omega_\epsilon)}$	1.2133	1.2929	1.4010	1.5443	1.7084	1.8087
	Factor	1.0000	1.0656	1.1547	1.2728	1.4080	1.4907
Periodic BC	$\|\|\bar{e}\|\|_{A(\Omega_\epsilon)}$	1.2848	1.3706	1.4883	1.6441	1.8203	1.9302
	Factor	1.0000	1.0667	1.1584	1.2796	1.4168	1.5023
Neumann BC	$\|\|\bar{e}\|\|_{A(\Omega_\epsilon)}$	1.3884	1.4782	1.6034	1.7684	1.9342	2.0308
	Factor	1.0000	1.0646	1.1548	1.2737	1.3931	1.4627

All error data in $10^{-2}\,[FL]$

Table 8 Diamond/SiC microstructure: distribution of (lines 1 and 2) the relative micro error $||\bar{e}||_{A(\Omega_e)}/||\boldsymbol{u}||_{A(\Omega_e)}$ and of (line 3 and 4) the strain component ε_{xx} (in 10^{-2}) for the original, uniform mesh and the 5th soft coarsened mesh with Dirichlet, periodic and Neumann coupling



4.4.1 Mesh coarsening and micro discretization error

The original, uniform micro mesh of the Diamond/SiC microstructure is discretized with 1098 × 1098 elements. The number of coarsening steps is again restricted to 5 steps.

The diagram in Fig. 17 reveals that, similar to the previous examples, the estimated error increases rather moderately during the first coarsening steps, but strongly in the last ones. For an explanation for the dependency of errors on coupling conditions and their order in magnitude see Sect. 4.3.2.

Table 7 underpins the graphical results by explicit figures; again, the mesh coarsening reduces the number of unknowns after five coarsening steps to less than 10% of the original, uniform mesh. The estimated errors exhibit –similar to the previous examples– a modest increase for the first coarsened meshes and a strong increase afterwards.

The ratio of deactivated degrees of freedom is 2.8% for the first coarsened mesh and increases to 18.8% for the fifth coarsened mesh.

The estimated errors in Table 7 underpin that, similar to the previous examples, the errors show modest increase for the first coarsened meshes and a strong increase afterwards.

4.4.2 Distributions of error and micro strain

Since the first examples have shown that the last coarsening steps do not pay off, the focus is on the results for the third coarsened mesh in the comparison with the original, uniform mesh for different coupling conditions. The error distributions of the coarsened meshes in Table 8 exhibit quantitative agreement in the maximal error figures with the uniform, fine discretization. Only in the interior of phases having undergone a considerable mesh coarsening the errors are somewhat increased.

The normal strain component ε_{xx} of the diamond/SiC microstructure on one micro domain is displayed in Table 8 for the different micro-macro coupling conditions for the original, uniform mesh and for the third soft coarsened mesh. For each of the coupling conditions a very good agreement of strain distributions on the micro domain is achieved, although the coarsened micro mesh (line 4) contain less than 8% of the degrees of freedom of its original, uniform counterpart.

4.4.3 How micro discretization errors influence macro scale quantities

Micro discretizations do not only influence the accuracy on the micro level but also have an impact on the macroscopic stiffness through the homogenized elasticity tensor.

In order to investigate and quantify this influence, two different, but related macro scale measures are employed; the maximum nodal displacement $\|\boldsymbol{u}\|_{\max}$ and the coefficients of the homogenized elasticity tensor $\mathbb{A}^0$, for the computation of the latter see [1,13].

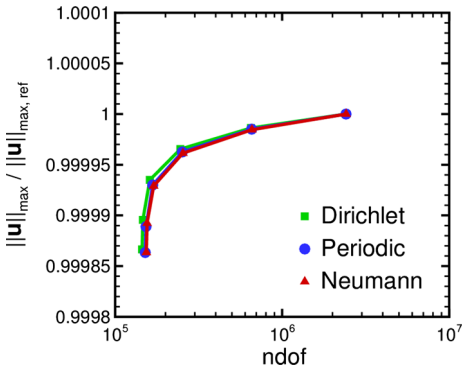


Fig. 18 Diamond/SiC microstructure: maximum nodal displacement $\|\boldsymbol{u}\|_{\max}$ for the initial and all coarsened meshes at various coupling conditions. The displacements are each normed by the corresponding reference value for the uniform mesh.

Figure 18 shows the maximum nodal displacement at the free end of the cantilever beam. The values are each normed by the reference value for the uniform mesh, for Dirichlet by $\|\boldsymbol{u}\|_{\max,\mathrm{ref}} = 1630.7\ [L]$, for PBC by $\|\boldsymbol{u}\|_{\max,\mathrm{ref}} = 1656.1\ [L]$, and for Neumann by $\|\boldsymbol{u}\|_{\max,\mathrm{ref}} = 1708.0\ [L]$. The results indicate that for all coupling conditions the maximum nodal displacement is hardly influenced by mesh coarsening on the micro scale; even for the fifth coarsening step showing large micro errors the macro displacement error is below 0.015%.

The normed entries of the homogenized elasticity tensor displayed in Fig. 19 indicate that mesh coarsening does hardly influence the macroscopic stiffness. Even for the fifth coarsening step the maximal error of the homogenized coefficients is in the range of 0.02%. Notice that the very good agreement of the percentaged errors in $\mathbb{A}^0$ and in $\|\boldsymbol{u}\|_{\max}$ hints at the fact that both the L_2-norm of the macro displacement error and the error in the coefficients of the homogenized elasticity tensor converge in $\mathcal{O}(h^{2q})$ see [2,13,17].

4.4.4 Conclusions

The application of the mesh coarsening to a real world microstructure proves that an efficient mesh coarsening inside of the single phases is possible without significantly falsifying the results. Furthermore, the example has demonstrated that different discretizations on opposite edges of the RAE are not of harm for accuracy. Macro level quantities indicate that the considered mesh coarsening on the micro scale has virtually no impact on the macro level.

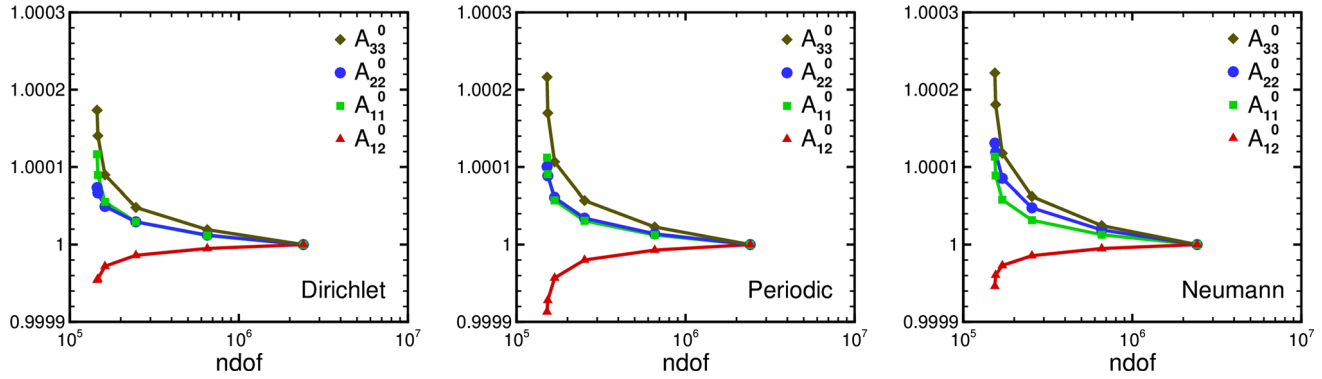
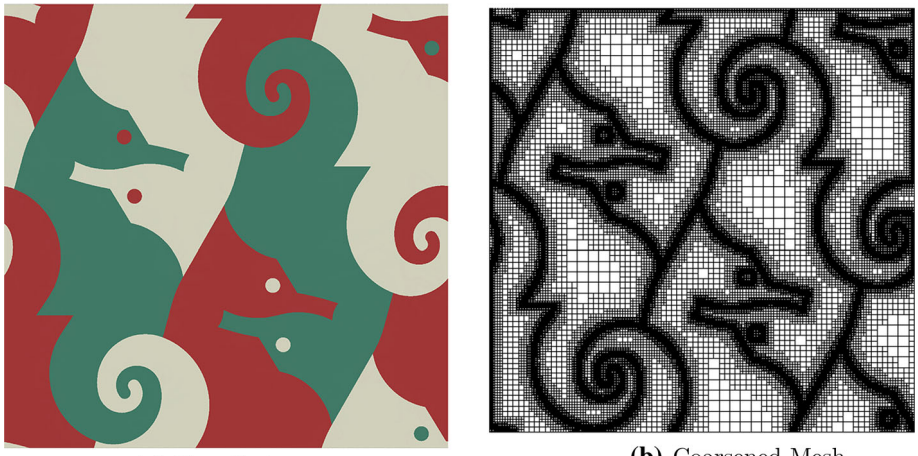


Fig. 19 Diamond/SiC microstructure: coefficients of the homogenized elasticity tensor $\mathbb{A}^0$ for different coupling conditions. The coefficients are each normed by the corresponding value for the original mesh



(a) Tessellation **(b)** Coarsened Mesh

Fig. 20 Seahorse microstructure: **a** tessellation made of three different material phases, **b** mesh after five soft coarsening steps

4.5 Three phases seahorse structure

Figure 20 shows a microstructure with three different phases built up from several seahorses and the fifth soft coarsened micro mesh. It adopts a tessellation of M.C. Escher (Regular Division of the Plane with Seahorses, Nos. 11, 1937-1938).

4.5.1 Mesh coarsening and micro discretization error

Table 9 reveals that the first two coarsening steps already reduce the number of unknowns by 87%, while the last two steps to hardly more than 4%. Results for the fifth coarsened mesh exhibit an error increase of 21% while the number of unknowns is reduced by more than 90%.

Figure 21 displays the estimated micro error for mesh coarsening and the computation time to solve the micro problem. Similar to the previous examples the error shows only minor increase during the first coarsening steps and increases stronger afterwards. As a consequence, the computation time is strongly reduced in the first two coarsening steps to 45% and 18% respectively, while additional coarsening steps render only a minor speedup. The computation time of the fifth coarsened mesh is 11% of the original computation time.

4.5.2 Distributions of error and micro strain

Based on the results of previous examples the analysis of the micro discretization errors has a focus on the third coarsened mesh and and its comparison with the original, uniform mesh for PBC. The error distribution of the coarsened mesh in Fig. 22 agrees very well with that one of the uniform, fine mesh; in the phase interior the larger elements from mesh coarsening induce somewhat larger errors. The same good agreement is observed for the normal strain component ε_{xx} as displayed in Fig. 22. Again, the element size mismatch on opposite RAE edges has no visible influence on accuracy.

4.5.3 Conclusions

The application of the mesh coarsening to a microstructure with more than two different phases leads to similar results as the mesh coarsening for microstructures with only two different phases.

Table 9 Seahorse microstructure: number of degrees of freedom (ndof), the ndof-factor compared to the uniform mesh, the number of deactivated degrees of freedom and the errors for PBC with the (increase) factor compared to the original, uniform discretization (1280 × 1280 elements)

Coarsening step no.	0	1	2	3	4	5
ndof	3,281,922	932,254	405,332	302,104	287,160	286,180
Factor	1.0000	0.2841	0.1235	0.0921	0.0875	0.0872
Deactivated ndof	0	34,590	51,820	59,080	61,432	61,756
$\|\|\bar{e}\|\|_{A(\Omega_\epsilon)}$	6.0804	6.1868	6.3890	6.7304	7.1509	7.3497
Factor	1.0000	1.0175	1.0507	1.1069	1.1760	1.2087

All error data in $10^{-2}\,[FL]$

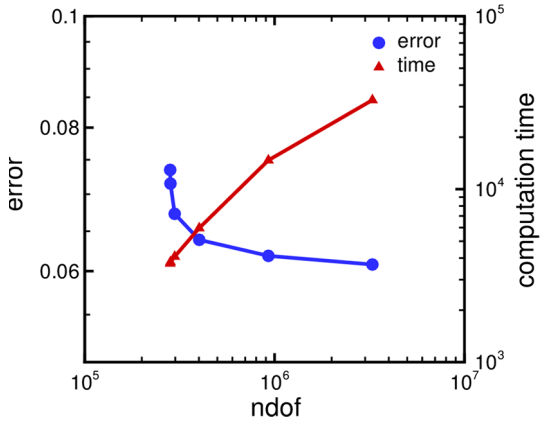


Fig. 21 Seahorse microstructure: estimated discretization error $\|\bar{e}\|_{A(\Omega_\epsilon)}$ in $[FL]$ and computation time (in seconds) over the number of degrees of freedom

5 Summary and conclusions

The aim of the present work was the numerical analysis of quadtree-based adaptive mesh coarsening of pixelized microstructures, which is used as a preprocessor for micro meshes in two-scale finite element frameworks for homogenization such as FE-HMM and FE^2. The basic assumption turned out to be justified in all examples, that interfaces are the mechanical hotspots in multi-material systems (here due to a stiffness mismatch; in a thermomechanical context [52] due to a mismatch in the temperature expansion coefficients, etc.) and therefore shall preserve high spatial resolution, while the phase interior with rather weakly varying field properties can undergo mesh coarsening.

Two different coarsening algorithms were investigated, one with a steep gradient of element size at phase boundaries, a second, modified one with a smaller gradient. To put the improved efficiency by mesh coarsening into relation to the accuracy loss, the corresponding micro discretization error was evaluated.

For that aim the well-known superconvergent patch recovery (SPR) was modified in its stress recovery to fit the requirements of microstructures with multiple material phases. To avoid the numerical effort of the SPR, a scheme based on an intra-element patch for the recovery of nodal stress and strain along with averaging of contributions from elements of the same phase was proposed and compared to the modified SPR.

The simulation results for various examples strongly support the following conclusions.

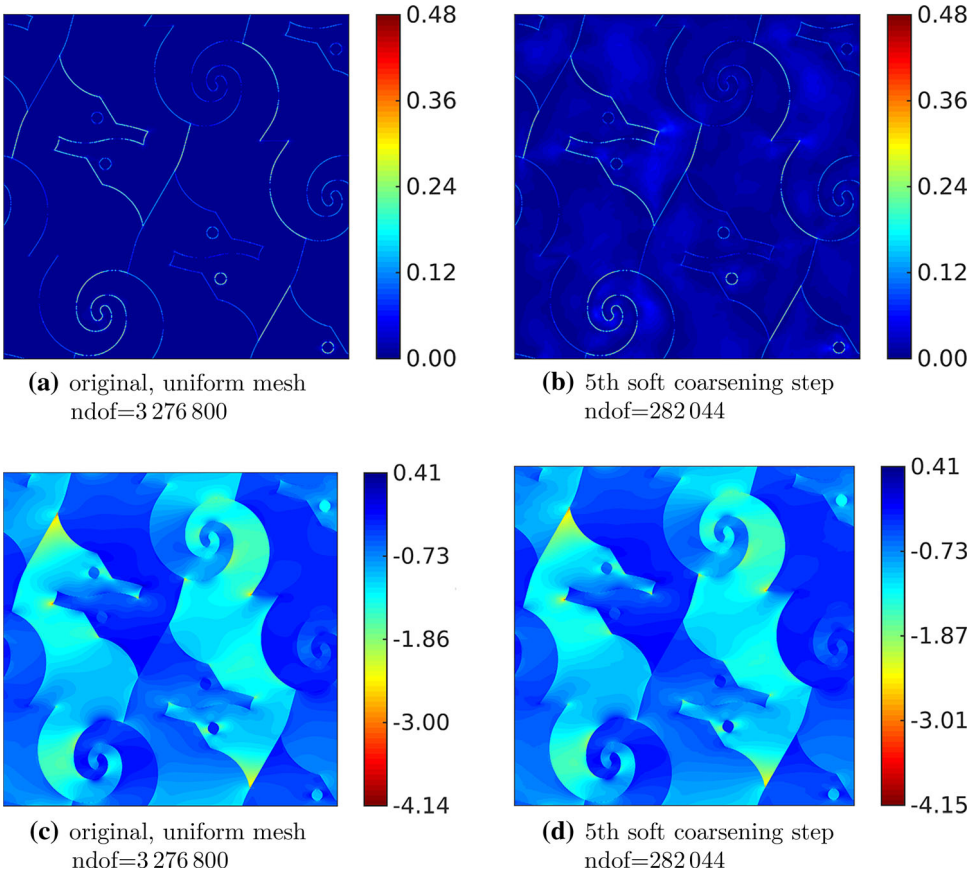
(i) The gradient of element size at a phase boundary should not be chosen too steep. The example in Sect. 4.2 has shown that for a hard and a soft coarsened mesh of virtually the same number of degrees of freedom, the soft coarsened one shows better agreement with the uniform, fine discretization in the distributions of error and strain.

(ii) There is no need to execute expensive calculations of reference solutions on superfine meshes. As the example from Sect. 4.1 has shown, both error estimation schemes –modified SPR and averaging technique–lead to sufficiently accurate estimations of the true micro error.

(iii) It does not pay off to execute as many coarsening steps as possible. All examples from Sect. 4 have shown, that only the first coarsening steps lead to major reductions of the degrees of freedom without a strong increase in the micro discretization error. The number of favorable coarsening steps was two or three for our examples with a number of degrees of freedom in between 1.6 and 3.3 million for the initial, uniform meshes.

(iv) A microstructure with high regularity -meaning no sharp corners- has shown an outstanding relation between reduction of degrees of freedom and increase of micro discretization error. For the circular inclusion from Sect. 4.3 a reduction in the number of degrees of freedom to 8% of the original figure even lead to a micro discretization error which is increased by 8%. To achieve such outstanding results for less regular microstructures, the coarsening algorithms may be further developed, for example by keeping the gradient in element size even smaller at sharp corners.

(v) The pixelized, hence non-smooth representation of smooth interfaces is not necessarily of harm for the regularity of the BVP. For the problem of a circular inclusion in a matrix the comparison with a smooth, standard discretization with elements oriented to the



(a) original, uniform mesh ndof=3 276 800

(b) 5th soft coarsening step ndof=282 044

(c) original, uniform mesh ndof=3 276 800

(d) 5th soft coarsening step ndof=282 044

Fig. 22 Seahorse microstructure: distribution of **a**, **b** the relative elementwise micro error $\|\bar{\boldsymbol{e}}\|_{A(\Omega_e)}/\|\boldsymbol{u}\|_{A(\Omega_e)}$ and of **c**, **d** the strain component ε_{xx} (in 10^{-2}) for (first column) the uniform mesh and for (second column) the 5th soft coarsened micro mesh

interface has shown the same convergence order for both cases. In general, however, re-entrant corners inherent to pixelized meshes can cause order reduction depending on relative pixel size and stiffness mismatch.

(vi) Quadtree-based adaptive remeshing of pixelized microstructures has turned out to be an appropriate preprocessor for efficient finite element analyses. The examples from Sect. 4 have shown that already two coarsening steps are sufficient to reduce the number of degrees of freedom to considerably more than 80%, rather about 90%. The increase of the corresponding discretization error compared to the initial uniform mesh is not more than about 15%.

(vii) While the micro scale exhibits requirements for accuracy and efficiency in its own right, the impact of micro discretization errors on the macro scale in a computational homogenization framework was analyzed as well. Here, the effective macroscopic response in terms of coefficients of the homogenized elasticity tensor and macroscopic displacements has turned out to be virtually insensitive even to considerable micro errors induced by mesh coarsening. The results even foster the considerable efficiency benefits through adaptive mesh coarsening in view of the vanishing accuracy losses.

(viii) All the above results are true for different conditions applied to RAE boundaries, for Dirichlet, periodic and Neumann coupling. For their errors it holds, the softer the condition, the larger the errors.

5.1 Concluding remarks

A comprehensive accuracy analysis must cover all involved aspects, from the image resolution along with possibly blurred interfaces, over segmentation and the assumed, corrugated or sharp characteristics of interface, to the type of discretization and the solution method in use.

In the present work we did not consider the question which initial pixel size is favorable in accuracy while feasible in numerical costs cf. [37,47]. A relatively coarse initial mesh will introduce a modeling error, where ensuing adaptive coarse graining will add a discretization error. The finite cell method shifts to some extent the efforts from meshing to numerical quadrature, but notwithstanding must make an assumption of the interface shape [10,11,38,48,49].

In the present two-scale FEM for homogenization, error-controlled, microstructure-adapted mesh coarsening is the key to enable the usage of highly resolved microstructure representations as a starting point with the benefit of considerably reduced computational costs for minor accu-

racy losses. The extension to 3D mesh coarsening of voxel data is expected not only to intensify the efficiency benefits of the 2D scenario. It is expected that it will enable microstructure analyses in high resolution at all, which are otherwise, for the uniform, voxelized discretization, prevented by memory-limitations, if no parallelized domain-decomposition methods are used.

Acknowledgements Open Access funding provided by Projekt DEAL. Bernhard Eidel acknowledges support by the Deutsche Forschungsgemeinschaft (DFG) within the Heisenberg program (Grant No. EI 453/2-1). Thanks to Dr. Lorenz Holzer for applying FIB-nanotomography analysis to the Diamond/β-SiC nanocomposite sample. Simulations were in parts performed with computing resources granted by RWTH Aachen University under Project ID prep0005.

Compliance with ethical standards

Conflict of interest They authors declare that they have no conflict of interest.

Open Access This article is licensed under a Creative Commons Attribution 4.0 International License, which permits use, sharing, adaptation, distribution and reproduction in any medium or format, as long as you give appropriate credit to the original author(s) and the source, provide a link to the Creative Commons licence, and indicate if changes were made. The images or other third party material in this article are included in the article's Creative Commons licence, unless indicated otherwise in a credit line to the material. If material is not included in the article's Creative Commons licence and your intended use is not permitted by statutory regulation or exceeds the permitted use, you will need to obtain permission directly from the copyright holder. To view a copy of this licence, visit http://creativecommons.org/licenses/by/4.0/.

References

1. Abdulle A (2006) Analysis of the heterogeneous multiscale fem for problems in elasticity. Math Models Methods Appl Sci 16(04):615–635. https://doi.org/10.1142/S0218202506001285
2. Abdulle A (2009) The finite element heterogeneous multiscale method: a computational strategy for multiscale pdes. GAKUTO Int Ser Math Sci Appl 31:133–181
3. Abdulle A, Weinan E, Engquist B, Vanden-Eijnden E (2012) The heterogeneous multiscale method. Acta Numer 21:1–87. https://doi.org/10.1017/S0962492912000025
4. Ainsworth M, Oden J (1997) A posteriori error estimation in finite element analysis. Comput Methods Appl Mech Eng 142(1–2):1–88. https://doi.org/10.1016/S0045-7825(96)01107-3
5. Allaire G (1992) Homogenization and two-scale convergence. SIAM J Math Anal 23(6):1482–1518. https://doi.org/10.1137/0523084
6. Babuška I, Rheinboldt WC (1978) A-posteriori error estimates for the finite element method. Int J Numer Meth Eng 12(10):1597–1615. https://doi.org/10.1002/nme.1620121010
7. Barlow J (1976) Optimal stress locations in finite element models. Int J Numer Meth Eng 10(2):243–251. https://doi.org/10.1002/nme.1620100202
8. Cioranescu D, Donato P (2010) An introduction to homogenization, Oxford lecture series in mathematics and its applications, vol 17. Oxford University Press, Oxford
9. d'Agostino MV, Barbagallo G, Ghiba ID, Eidel B, Neff P, Madeo A (2019) Effective description of anisotropic wave dispersion in mechanical band-gap metamaterials via the relaxed micromorphic model. J Elast 90(10):99. https://doi.org/10.1007/s10659-019-09753-9
10. Düster A, Parvizian J, Yang Z, Rank E (2008) The finite cell method for three-dimensional problems of solid mechanics. Comput Methods Appl Mech Eng 197(45–48):3768–3782. https://doi.org/10.1016/j.cma.2008.02.036
11. Düster A, Sehlhorst HG, Rank E (2012) Numerical homogenization of heterogeneous and cellular materials utilizing the finite cell method. Comput Mech 50(4):413–431. https://doi.org/10.1007/s00466-012-0681-2
12. Eidel B, Fischer A (2016) The heterogeneous multiscale finite element method FE-HMM for the homogenization of linear elastic solids. PAMM 16(1):521–522. https://doi.org/10.1002/pamm.201610249
13. Eidel B, Fischer A (2018) The heterogeneous multiscale finite element method for the homogenization of linear elastic solids and a comparison with the FE^2 method. Comput Methods Appl Mech Eng 329:332–368. https://doi.org/10.1016/j.cma.2017.10.001
14. Eidel B, Fischer A, Gote A (2018) A nonlinear FE-HMM formulation along with a novel algorithmic structure for finite deformation elasticity. PAMM 18(1):e201800457. https://doi.org/10.1002/pamm.201800457
15. Eidel B, Gote A, Ruby M, Holzer L, Keller L, Jiang X (2019) Estimating the effective elasticity properties of a diamond/β-SiC composite thin film by 3d reconstruction and numerical homogenization. Diam Relat Mater 97:107406. https://doi.org/10.1016/j.diamond.2019.04.029
16. Feyel F, Chaboche JL (2000) FE^2 multiscale approach for modelling the elastoviscoplastic behaviour of long fibre SiC–Ti composite materials. Comput Methods Appl Mech Eng 183(3–4):309–330. https://doi.org/10.1016/S0045-7825(99)00224-8
17. Fischer A, Eidel B (2019) Convergence and error analysis of FE-HMM/FE^2 for energetically consistent micro-coupling conditions in linear elastic solids. Eur J Mech A/Solids 77. https://doi.org/10.1016/j.euromechsol.2019.02.001
18. Geers MGD, Kouznetsova VG, Brekelmans WAM (2010) Computational homogenization. In: Maier G, Rammerstorfer FG, Salençon J, Schrefler B, Serafini P, Pippan R, Gumbsch P (eds) Multiscale modelling of plasticity and fracture by means of dislocation mechanics, CISM International Centre for Mechanical Sciences, vol 522, Springer, Vienna, pp 327–394. https://doi.org/10.1007/978-3-7091-0283-1_7
19. Gravenkamp H, Duczek S (2017) Automatic image-based analyses using a coupled quadtree-SBFEM/SCM approach. Comput Mech 60(4):559–584. https://doi.org/10.1007/s00466-017-1424-1
20. Hill R (1963) Elastic properties of reinforced solids: some theoretical principles. J Mech Phys Solids 11(5):357–372. https://doi.org/10.1016/0022-5096(63)90036-X
21. Hill R (1972) On constitutive macro-variables for heterogeneous solids at finite strain. Proc R Soc A Math Phys Eng Sci 326(1565):131–147. https://doi.org/10.1098/rspa.1972.0001
22. Hollister SJ, Kikuchi N (1994) Homogenization theory and digital imaging: a basis for studying the mechanics and design principles of bone tissue. Biotechnol Bioeng 43(7):586–596. https://doi.org/10.1002/bit.260430708
23. Holzer L, Cantoni M (2011) Review of fib-tomography. In: Utke I, Moshkalev S, Russell P (eds) Nanofabrication using focused ion and electron beams, Oxford series on nanomanufacturing, vol 559201222. Oxford University Press, Oxford, pp 410–435

24. Huang Y, Yang Z, Ren W, Liu G, Zhang C (2015) 3d meso-scale fracture modelling and validation of concrete based on in-situ x-ray computed tomography images using damage plasticity model. Int J Solids Struct 67–68:340–352. https://doi.org/10.1016/j.ijsolstr.2015.05.002
25. Ketcham RA, Carlson WD (2001) Acquisition, optimization and interpretation of x-ray computed tomographic imagery: applications to the geosciences. Comput Geosci 27(4):381–400. https://doi.org/10.1016/S0098-3004(00)00116-3
26. Keyak JH, Meagher JM, Skinner HB, Mote CD (1990) Automated three-dimensional finite element modelling of bone: a new method. J Biomed Eng 12(5):389–397. https://doi.org/10.1016/0141-5425(90)90022-F
27. Kouznetsova V, Brekelmans WAM, Baaijens FPT (2001) An approach to micro-macro modeling of heterogeneous materials. Comput Mech 27(1):37–48. https://doi.org/10.1007/s004660000212
28. Legrain G, Cartraud P, Perreard I, Moës N (2011) An x-fem and level set computational approach for image-based modelling: application to homogenization. Int J Numer Meth Eng 86(7):915–934. https://doi.org/10.1002/nme.3085
29. Lian WD, Legrain G, Cartraud P (2013) Image-based computational homogenization and localization: comparison between x-fem/levelset and voxel-based approaches. Comput Mech 51(3):279–293. https://doi.org/10.1007/s00466-012-0723-9
30. Löhnert S, Wriggers P (2013) Homogenisation of microheterogeneous materials considering interfacial delamination at finite strains. Tech Mech 23(1–4):167–177
31. Michel JC, Moulinec H, Suquet P (1999) Effective properties of composite materials with periodic microstructure: a computational approach. Comput Methods Appl Mech Eng 172(1–4):109–143. https://doi.org/10.1016/S0045-7825(98)00227-8
32. Miehe C, Schröder J, Schotte J (1999) Computational homogenization analysis in finite plasticity simulation of texture development in polycrystalline materials. Comput Methods Appl Mech Eng 171(3–4):387–418. https://doi.org/10.1016/S0045-7825(98)00218-7
33. Mishnaevsky LL (2005) Automatic voxel-based generation of 3d microstructural fe models and its application to the damage analysis of composites. Mater Sci Eng A 407(1–2):11–23. https://doi.org/10.1016/j.msea.2005.06.047
34. Miska N, Balzani D (2019) Quantification of uncertain macroscopic material properties resulting from variations of microstructure morphology based on statistically similar volume elements: application to dual-phase steel microstructures. Comput Mech 54(3):1269. https://doi.org/10.1007/s00466-019-01738-8
35. Nambiar RV, Lawrence KL (1992) The Zienkiewicz-Zhu error estimator for multiple material problems. Commun Appl Numer Methods 8(4):273–277. https://doi.org/10.1002/cnm.1630080408
36. Neff P, Eidel B, d'Agostino MV, Madeo A (2019) Identification of scale-independent material parameters in the relaxed micromorphic model through model-adapted first order homogenization. J Elast 16(04):615. https://doi.org/10.1007/s10659-019-09752-w
37. Nguyen T, Ghazlan A, Kashani A, Bordas S, Ngo T (2018) 3d meso-scale modelling of foamed concrete based on x-ray computed tomography. Constr Build Mater 188:583–598. https://doi.org/10.1016/j.conbuildmat.2018.08.085
38. Parvizian J, Düster A, Rank E (2007) Finite cell method. Comput Mech 41(1):121–133. https://doi.org/10.1007/s00466-007-0173-y
39. Pennycook SJ, Nellist PD (2011) Scanning transmission electron microscopy: imaging and analysis. Springer Science+Business Media, LLC, New York, NY
40. Perić D, de Souza Neto EA, Feijóo RA, Partovi M, Molina AJC (2011) On micro-to-macro transitions for multi-scale analysis of non-linear heterogeneous materials: unified variational basis and finite element implementation. Int J Numer Meth Eng 87(1–5):149–170. https://doi.org/10.1002/nme.3014
41. Ren W, Yang Z, Sharma R, Zhang C, Withers PJ (2015) Two-dimensional x-ray ct image based meso-scale fracture modelling of concrete. Eng Fract Mech 133:24–39. https://doi.org/10.1016/j.engfracmech.2014.10.016
42. Saeb S, Steinmann P, Javili A (2016) Aspects of computational homogenization at finite deformations: a unifying review from Reuss' to Voigt's bound. Appl Mech Rev 68(5):050801. https://doi.org/10.1115/1.4034024
43. Samet H (1984) The quadtree and related hierarchical data structures. ACM Comput Surv 16(2):187–260. https://doi.org/10.1145/356924.356930
44. Samet H (1990) Application of spatial data structure. Addison-Wesley, New York
45. Saputra A, Talebi H, Tran D, Birk C, Song C (2017) Automatic image-based stress analysis by the scaled boundary finite element method. Int J Numer Meth Eng 109(5):697–738. https://doi.org/10.1002/nme.5304
46. Saputra AA, Sladek V, Sladek J, Song C (2018) Micromechanics determination of effective material coefficients of cement-based piezoelectric ceramic composites. J Intell Mater Syst Struct 29(5):845–862. https://doi.org/10.1177/1045389X17721047
47. Saxena N, Hofmann R, Alpak FO, Dietderich J, Hunter S, Day-Stirrat RJ (2017) Effect of image segmentation & voxel size on micro-ct computed effective transport & elastic properties. Mar Pet Geol 86:972–990. https://doi.org/10.1016/j.marpetgeo.2017.07.004
48. Schillinger D, Ruess M (2015) The finite cell method: a review in the context of higher-order structural analysis of cad and image-based geometric models. Arch Comput Methods Eng 22(3):391–455. https://doi.org/10.1007/s11831-014-9115-y
49. Schillinger D, Düster A, Rank E (2012) The hp-d-adaptive finite cell method for geometrically nonlinear problems of solid mechanics. Int J Numer Meth Eng 89(9):1171–1202. https://doi.org/10.1002/nme.3289
50. Schröder J (2014) A numerical two-scale homogenization scheme: the FE^2-method. In: Pfeiffer F, Rammerstorfer FG, Guazzelli E, Schrefler B, Serafini P, Schröder J, Hackl K (eds) Plasticity and beyond, CISM international centre for mechanical sciences, vol 550. Springer, Vienna, pp 1–64. https://doi.org/10.1007/978-3-7091-1625-8_1
51. Suquet P (1987) Elements of homogenization for inelastic solid mechanics. In: Sanchez-Palencia E, Zaoui A (eds) Homogenization techniques for composite media. Lecture Notes in Physics, Springer, Berlin, pp 193–287
52. Temizer I, Wriggers P (2011) Homogenization in finite thermoelasticity. J Mech Phys Solids 59(2):344–372. https://doi.org/10.1016/j.jmps.2010.10.004
53. Weinan E, Engquist B, Li X, Ren W, Vanden-Eijnden E (2007) Heterogeneous multiscale methods: a review. Commun Comput Phys 2(3):367–450
54. Weinan E, Engquist B (2003) The heterogeneous multiscale methods. Commun Math Sci 1(1):87–132. https://projecteuclid.org:443/euclid.cms/1118150402
55. Yerry M, Shephard M (1983) A modified quadtree approach to finite element mesh generation. IEEE Comput Gr Appl 3(1):39–46. https://doi.org/10.1109/MCG.1983.262997
56. Zienkiewicz OC, Zhu JZ (1987) A simple error estimator and adaptive procedure for practical engineerng analysis. Int J Numer Meth Eng 24(2):337–357. https://doi.org/10.1002/nme.1620240206

57. Zienkiewicz OC, Zhu JZ (1992) The superconvergent patch recovery and a posteriori error estimates. part 1: the recovery technique. Int J Numer Meth Eng 33(7):1331–1364. https://doi.org/10.1002/nme.1620330702
58. Zienkiewicz OC, Zhu JZ (1992) The superconvergent patch recovery and a posteriori error estimates. part 2: error estimates and adaptivity. Int J Numer Meth Eng 33(7):1365–1382. https://doi.org/10.1002/nme.1620330703

Publisher's Note Springer Nature remains neutral with regard to jurisdictional claims in published maps and institutional affiliations.

8.4 Veröffentlichung: From image data towards microstructure information – Accuracy analysis at the digital core of materials

Die vierte Veröffentlichung von Prof. Bernhard Eidel, Andreas Fischer und Ajinkya Gote mit dem Titel **From image data towards microstructure information – Accuracy analysis at the digital core of materials** wurde 2020 in *ZAMM - Journal of Applied Mathematics and Mechanics* veröffentlicht.

Wie zuvor war der Doktorand für alle Erweiterungen in Zusammenhang mit dem Matlab-Code verantwortlich. Für die vorliegende Veröffentlichung wurden zwei uniforme Netzvergröberungsalgorithmen implementiert. Im Ausblick werden Ergebnisse von Berechnungen mit von-Mises Plastizität präsentiert, auch deren Implementierung lag in der Hand des Doktoranden.

Nach einer Einführung in das Thema, die federführend von Prof. Eidel verfasst wurde, erfolgt in den Kapitel 2 und 3 die Vorstellung der FE-HMM für lineare Elastizität und die Vorstellung der Fehler sowie der a priori Aussagen zur Fehlerkonvergenz. Bei der Vorstellung des Fehlers auf dem Mikrolevel wird hier erstmalig zwischen einem Diskretisierungs- und einem Auflösungsfehler unterschieden.

Die Kapitel 4 und 5 wurden federführend durch den Doktoranden bearbeitet. Die Vorstellung der uniformen Netzvergröberungsalgorithmen und deren grafische Darstellung lag in der Hand des Doktoranden, genauso die Rekapitulation der in der dritten Veröffentlichung behandelten adaptiven Netzvergröberung. Kapitel 5 beginnt mit einer Einführung in die Thematik der Fehlerschätzung und stellt die Notwendigkeit der Einführung von Duplex-Spannungen an diskreten Phasengrenzen heraus. Des Weiteren wird beschrieben inwiefern sich ein ähnliches Vorgehen auf Mikrostrukturen mit gemittelten Phasen anwenden lässt. Auch diese Beschreibungen stammen federführend aus der Hand des Doktoranden.

Kapitel 6 enthält eine ausführliche Berechnung einer zweiphasigen Beispielstruktur. Die Erzeugung der Input-Daten lag hierbei vollständig in der Hand des Doktoranden, die Durchführung der Berechnungen wurde durch Ajinkya Gote unterstützt. Herr Gote war auch verantwortlich für die Erzeugung der Diagramme und Abbildungen in diesem Abschnitt. Die Diskussion der Ergebnisse erfolgte durch die Autoren gemeinsam.

Die Zusammenfassung und der Ausblick entstanden ebenfalls in Kooperation durch die einzelnen Autoren, die Erzeugung der Input-Daten für die Berechnungen mit von-Mises Plastizität im Ausblick erfolgte durch den Doktoranden, die Berechnungen führte Herr Gote durch.

Received: 3 September 2020 | Revised: 8 November 2020 | Accepted: 11 December 2020

DOI: 10.1002/zamm.202000245

ORIGINAL PAPER

From image data towards microstructure information – Accuracy analysis at the digital core of materials

Bernhard Eidel | **Andreas Fischer** | **Ajinkya Gote**

DFG-Heisenberg-Group, Institute of Mechanics, Department Mechanical Engineering, University Siegen, Paul-Bonatz-Str. 9-11, Siegen 57068, Germany

Correspondence
Bernhard Eidel, DFG-Heisenberg-Group, Institute of Mechanics, Department Mechanical Engineering, University Siegen, Paul-Bonatz-Str. 9-11, 57076 Siegen, Germany.
Email: bernhard.eidel@uni-siegen.de

Funding information
Deutsche Forschungsgemeinschaft, Grant/Award Number: EI 453/5-1; RWTH Aachen University, Grant/Award Number: ID BUND0005

A cornerstone of computational solid mechanics in the context of digital transformation are databases for microstructures obtained from advanced tomography techniques. Uniform discretizations of pixelized images in 2D are the raw-data point of departure for simulation analyses. This paper proposes the concept of a unified error analysis for image-based microstructure representations in uniform resolution along with adaptively coarsened discretizations. The analysis distinguishes between a resolution error due to finite, possibly coarsened image resolution and a discretization error, and investigates their quantitative relation, spatial distributions and their impacts on the simulation results both on the microscale and the macroscale in the context of computational homogenization. The assessment of accuracy and efficiency is carried out for an exemplary two-phase material. Beyond the example considered here the concept is a rational tool in the transformation of raw image data into microstructure information adapted to particular simulation needs and endows the digital twin of real microstructures with validated characteristics for reliable, predictive simulations.

KEYWORDS
error analysis, image-based modeling, homogenization, microstructures, multiscale FEM

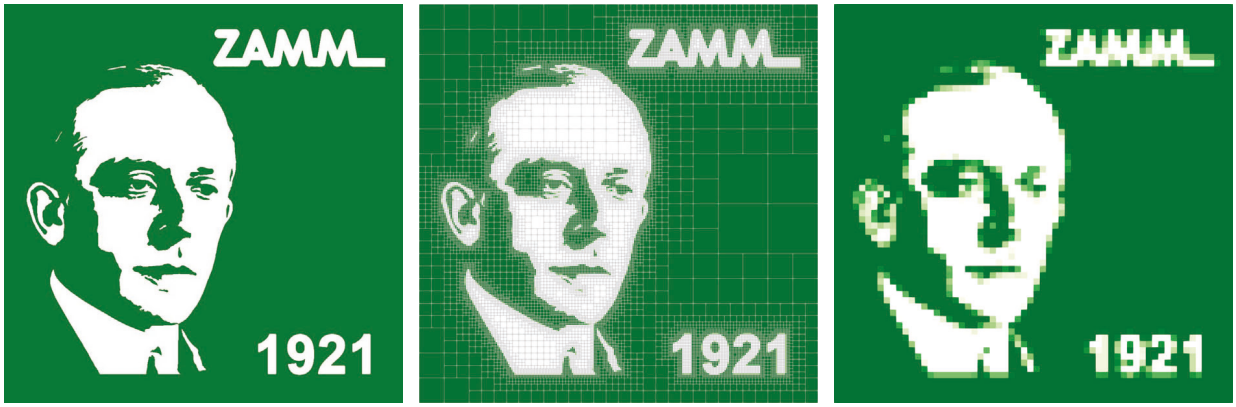
1 | INTRODUCTION

For image-based microstructure representations of heterogeneous solids, in 2D by pixels (px) and by voxels in 3D, the question arises in the numerical analysis, how image resolution influences the simulation results. A finite image resolution introduces an error which comes on top of the standard discretization error. The computation of the resolution and discretization errors, their magnitudes, spatial distributions, their impact on microscale and macroscale results and corresponding simulation costs in computational homogenization is the topic of this paper.

Highlights

- Concept for error analysis of image-based microstructure representation.
- Error-decomposition into finite resolution error and discretization error.
- Embedding into the unified error framework of two-scale FEM for homogenization.
- Concept enables a quantitative accuracy-efficiency balance score.
- Best practice for resolution coarsening along with adaptive mesh coarsening.

This is an open access article under the terms of the Creative Commons Attribution License, which permits use, distribution and reproduction in any medium, provided the original work is properly cited.
© 2020 The Authors. *ZAMM - Journal of Applied Mathematics and Mechanics* published by Wiley-VCH GmbH.



(a) uniform, 1024 px (b) adaptive (c) uniform, 64 px

FIGURE 1 Richard-von-Mises-ZAMM-1921-microstructure: (a) uniform resolution of 1024 px per edge, (b) adaptive mesh of (a), (c) uniform resolution of 64 px per edge

For pixel-/voxel-type microstructure representations the image resolution frequently defines the uniform finite element discretization likewise or it serves as the point of departure for, e.g., quadtree-/octree-type adaptive coarsening. Efficient FFT-based homogenization methods directly use uniform discretizations for the solution of the microscale problem, compare Moulinec-Suquet [39] and others. The alternative of reconstructing smooth phase boundaries as a prerequisite for conforming finite element discretizations is time-consuming and cumbersome. Moreover, a decoupling of discretization from material properties as realized in the finite cell method (FCM) [11, 12, 20, 45, 50, 51] is hardly available by default in commercial and research solvers. The above aspects underpin why pixel- and voxel-based discretizations are of utmost relevance.

Figure 1(a) displays a two-phase microstructure[1] in high, uniform resolution. Figure 1(b) shows for the same resolution as in (a) an adaptively coarsened mesh. In Figure 1(c) the result of a uniform pixel coarsening is displayed, where at the interface new, additional phases are introduced.

The question, which (uniform) image resolution shall be chosen, possibly as the starting point for a consecutive adaptive mesh coarsening, can be answered based on (i) an error analysis which distinguishes between a resolution error and a discretization error and (ii) corresponding computational efforts. The outcome enables the selection of a discretization with a well-balanced accuracy-efficiency score.

Work which considers the impact of image resolution on simulation results is rare and throughout restricted to effective properties. Hutzenlaub et al. [29] investigate for particular cathode catalyst layers how pixel coarsening influences parameters such as diffusivity and conductivity. The work of Nguyen et al. [42] considers for foamed concrete the impact of image resolution to global stress-strain curves, local damage initiation and evolution. For the effect of voxel-resolution on flow in porous media see Shah et al. [53], for applications in digital rock physics see Berg et al. [6].

For the FCM the first mathematical error analysis was provided by Dauge et al. [9]. Error estimation for FCM has very recently been introduced by Di Stolfo et al. [10]. In the FCM context the quadrature error is very similar to the resolution error in the present work.

We assume that in the present concept of coarsening resolution and discretization the selected microstructure sample is representative with respect to phase fractions, morphology, etc., such that resolution coarsening preserves its representative characteristics approximately. Doing so, the present work follows another route than approaches that replace the representative volume element RVE by a simplified microstructure of reduced morphological and therefore reduced computational complexity. Serious attempts have been made to identify suchlike surrogate microstructures which shall qualify as candidates by their degree of statistical similarity [5, 32, 44, 46, 49, 52].

Image segmentation refers to the identification of disjoint phases with sharp boundaries, where the number and properties of phases are assumed to be known, for a full-fledged example see [3, 4], for an overview [44]. The outcome of a standard segmentation looks like the image in Figure 1(a). The present work considers two variants of uniform pixel coarsening; the standard segmentation and an alternative approach which is visualized in Figure 1(c); novel interphases are

[1] Richard von Mises (1883–1953), an Austrian/US-American mathematician, founded the Zeitschrift für Angewandte Mathematik und Mechanik (ZAMM) in 1921.

created at interfaces with a color code, i.e., stiffness reflecting the phase fractions of the contributing pixels being merged in the coarser pixel. As a consequence, this approach, which is the standard of, e.g., images in bitmap format, preserves the overall phase fraction of the microstructure but reduces the stiffness contrast at interfaces. How does that affect stress in terms of extrema and jumps at material interfaces, and corresponding errors? These questions will be answered in Section 6.

Since two-scale finite element methods in homogenization aim at describing processes on the microscale as well as on the macroscale, the accuracy-efficiency balance shall be considered on both scales. On the macroscale the micro error arrives as a propagated error and adds to the macro discretization error. We anticipate that this can result in a microstructure discretization which is rejected at the microscale for its large discretization errors, but still favorable for its excellent accuracy on the macroscale, see for example [23].

The paper is organized as follows; to set the stage Section 2 provides a short outline of the finite element heterogeneous multiscale method (FE-HMM) for linear elasticity and introduces quantities used in the augmented FE-HMM framework of errors and estimates described in Section 3. Section 4 introduces in detail the above-mentioned different concepts of uniform resolution-coarsening along with consecutive adaptive mesh coarsening. Section 5 describes reconstruction-type error estimation for interfaces that have undergone resolution coarsening. Section 6 applies the error analysis to the von-Mises-ZAMM microstructure in Figure 1(a) along with the coarsening features illustrated in (b) and (c).

2 | THE FINITE ELEMENT HETEROGENEOUS MULTISCALE METHOD

2.1 | Model problem of linear elasticity

We consider a body $\mathcal{B}$, a bounded subset of $\mathbb{R}^{n_{\text{dim}}}$, $n_{\text{dim}} = 2, 3$, with boundary $\partial\mathcal{B} = \partial\mathcal{B}_D \cup \partial\mathcal{B}_N$ where the Dirichlet boundary $\partial\mathcal{B}_D$ and the Neumann boundary $\partial\mathcal{B}_N$ are disjoint sets. The closure of the body $\mathcal{B}$ is denoted by $\overline{\mathcal{B}}$. The body shall be in static equilibrium. It shall exhibit an inhomogeneous composition referred to as microstructure and shall be subject to body forces $\boldsymbol{f}$ and surface tractions $\bar{\boldsymbol{t}}$.

2.1.1 | The microproblem

The displacement $\boldsymbol{u}^\epsilon = (u_1^\epsilon, \dots, u_{n_{\text{dim}}}^\epsilon)$ of the body is given by the solution of

$$-\sigma_{ij,j}^\epsilon = f_i \quad \text{in } \mathcal{B}, \quad u_i^\epsilon = \bar{u}_i \quad \text{on } \partial\mathcal{B}_D, \quad \sigma_{ij}^\epsilon n_j = \bar{t}_i \quad \text{on } \partial\mathcal{B}_N. \tag{1}$$

Linear elasticity is assumed to hold $\sigma_{ij}^\epsilon = \mathbb{A}_{ijlm}^\epsilon \varepsilon_{lm}$ with the fourth order elasticity tensor $\mathbb{A}_{ijlm}^\epsilon$ and the infinitesimal strain tensor ε_{ij}; it holds $\varepsilon_{ij}(\boldsymbol{u}^\epsilon) = 1/2(u_{i,j}^\epsilon + u_{j,i}^\epsilon)$ which equally reads $\boldsymbol{\varepsilon} = \boldsymbol{L}\,\boldsymbol{u}^\epsilon$ using the linear differential operator $\boldsymbol{L}$. Superscript ϵ refers to the heterogeneity of the material, in particular to the characteristic length scale of the microstructure. In $(1)_3$, $\boldsymbol{n} = (n_1, \dots, n_{n_{\text{dim}}})^T$ is the unit outward normal to $\partial\mathcal{B}$.

The variational form is obtained by multiplying the strong form (1) by a test function $\boldsymbol{v} \in \mathcal{V}$ and by the application of Green's formula. Find $\boldsymbol{u}^\epsilon$ such that

$$B_\epsilon(\boldsymbol{u}^\epsilon, \boldsymbol{v}) := \int_{\mathcal{B}} \boldsymbol{\sigma}^\epsilon(\boldsymbol{u}^\epsilon) : \boldsymbol{\varepsilon}(\boldsymbol{v})\,\mathrm{d}V = \int_{\mathcal{B}} \boldsymbol{f}\cdot\boldsymbol{v}\,\mathrm{d}V + \int_{\partial\mathcal{B}_N} \bar{\boldsymbol{t}}\cdot\boldsymbol{v}\,\mathrm{d}A =: \boldsymbol{F}(\boldsymbol{v}), \tag{2}$$

which must hold for all $\boldsymbol{v} \in \mathcal{V}$, where $\mathcal{V}$ is the space of virtual displacements fulfilling the homogeneous Dirichlet boundary conditions (BCs) $\mathcal{V} = \{\boldsymbol{v}; \boldsymbol{v} \in H^1(\mathcal{B})^{n_{\text{dim}}}, \boldsymbol{v}|_{\partial\mathcal{B}_D} = \boldsymbol{0}\}$.

2.1.2 | The macroproblem

The strong form of the macroscopic/homogenized boundary value problem (BVP) is given by, cf. [17]

$$-\sigma_{ij,j}^0 = \langle f_i\rangle \text{ in } \mathcal{B}, \quad u_i^0 = \langle\bar{u}_i\rangle_\Gamma \text{ on } \partial\mathcal{B}_D, \quad \sigma_{ij}^0 n_j = \langle\bar{t}_i\rangle_\Gamma \text{ on } \partial\mathcal{B}_N \tag{3}$$

where u_i^0 is the macroscopic displacement and $\mathbb{A}^0$ the homogenized elasticity tensor in the macroscopic linear elasticity law $\sigma_{ij}^0 = \mathbb{A}_{ijlm}^0 \varepsilon_{lm}^0$. In $(3)_{1,3}$ σ_{ij}^0 is the macroscopic stress obtained by the volume average over the microdomain $\mathcal{B}_\epsilon$, generally $\langle \bullet \rangle := \frac{1}{|\mathcal{B}_\epsilon|} \int_{\mathcal{B}_\epsilon} \bullet \, \mathrm{d}V$. Similarly, surface averages are defined by $\langle \bar{u}_i \rangle_\Gamma := \frac{1}{|\Gamma_D|} \int_{\Gamma_D} \bar{u}_i \, \mathrm{d}A$, $\langle \bar{t}_i \rangle_\Gamma := \frac{1}{|\Gamma_N|} \int_{\Gamma_N} \bar{t}_i \, \mathrm{d}A$, where Γ is the surface area ($\Gamma \in \partial\mathcal{B}$) to which the averaging is applied.

The solution of the homogenized problem is obtained from the variational form

$$B_0(\boldsymbol{u}^0, \boldsymbol{v}) = \int_{\mathcal{B}} \boldsymbol{\sigma}^0(\boldsymbol{u}^0) : \boldsymbol{\varepsilon}^0(\boldsymbol{v}) \, \mathrm{d}V = \int_{\mathcal{B}} \boldsymbol{f} \cdot \boldsymbol{v} \, \mathrm{d}V + \int_{\partial\mathcal{B}_N} \bar{\boldsymbol{t}} \cdot \boldsymbol{v} \, \mathrm{d}A \qquad \forall \, \boldsymbol{v} \in \mathcal{V}, \tag{4}$$

which follows from multiplying the strong form (3) by test functions $\boldsymbol{v}$ along with the application of Green's formula. For notational convenience we skip in (4) and in the rest of the paper the averaging symbols $\langle \bullet \rangle$, $\langle \bullet \rangle_\Gamma$ for $\boldsymbol{f}$, $\bar{\boldsymbol{u}}$ and $\bar{\boldsymbol{t}}$ but keep in mind that these quantities follow from volume and surface averages, respectively.

We define a macro finite element space as

$$\mathcal{S}^p_{\partial\mathcal{B}_D}(\mathcal{B}, \mathcal{T}_H) = \left\{ \boldsymbol{u}^H \in H^1(\mathcal{B})^{n_{\mathrm{dim}}}; \boldsymbol{u}^H|_{\partial\mathcal{B}_D} = \boldsymbol{0}; \boldsymbol{u}^H|_K \in \mathcal{P}^p(K)^{n_{\mathrm{dim}}}, \, \forall K \in \mathcal{T}_H \right\}, \tag{5}$$

where $\mathcal{P}^p$ is the space of polynomials on the element K, $\mathcal{T}_H$ the (quasi-uniform) triangulation of $\mathcal{B} \subset \mathbb{R}^{n_{\mathrm{dim}}}$, and H the characteristic macro element size. The space $\mathcal{S}^p_{\partial\mathcal{B}_D}$ is a subspace of $\mathcal{V}$.

For the solution of (1) in the macrodomain the two-scale finite element heterogeneous multiscale method FE-HMM is used. FE-HMM was introduced as an instance of the very general HMM by E and Engquist [14].

The solution of the macro problem in FE-HMM reads, at this stage, as a standard, single-scale finite element method. Find $\boldsymbol{u}^H \in \mathcal{S}^p_{\partial\mathcal{B}_D}(\mathcal{B}, \mathcal{T}_H)$ such that

$$B_H(\boldsymbol{u}^H, \boldsymbol{v}^H) = \int_{\mathcal{B}} \boldsymbol{\sigma}^0(\boldsymbol{u}^H) : \boldsymbol{\varepsilon}^0(\boldsymbol{v}^H) \, \mathrm{d}V = \int_{\mathcal{B}} \boldsymbol{f} \cdot \boldsymbol{v}^H \, \mathrm{d}V + \int_{\partial\mathcal{B}_N} \bar{\boldsymbol{t}} \cdot \boldsymbol{v}^H \, \mathrm{d}A \qquad \forall \boldsymbol{v}^H \in \mathcal{S}^p_{\partial\mathcal{B}_D}(\mathcal{B}, \mathcal{T}_H). \tag{6}$$

2.2 | The modified macro bilinear form of FE-HMM

Standard numerical quadrature[2] is applied to the bilinear form in (6). With $\boldsymbol{x}_{K_l}$, ω_{K_l}, N_{qp} the quadrature points, the quadrature weights, and the number of quadrature points, respectively, $B_H(\boldsymbol{u}^H, \boldsymbol{v}^H)$ is obtained as

$$B_H(\boldsymbol{u}^H, \boldsymbol{v}^H) = \sum_{K \in \mathcal{T}_H} \sum_{l=1}^{N_{qp}} \omega_{K_l} \left[\mathbb{A}^0 \boldsymbol{\varepsilon}^0(\boldsymbol{u}^H(\boldsymbol{x}_{K_l})) : \boldsymbol{\varepsilon}(\boldsymbol{v}^H(\boldsymbol{x}_{K_l})) \right]. \tag{7}$$

Since the homogenized constitutive tensor $\mathbb{A}^0(\boldsymbol{x})$ is typically not known for heterogeneous matter, the bilinear form cannot be calculated according to (7). For that reason FE-HMM approximates the virtual internal work at $\boldsymbol{x}_{K_l}$ in (7) by its micro counterpart in K_l

$$B_H(\boldsymbol{u}^H, \boldsymbol{v}^H) \approx \sum_{K \in \mathcal{T}_H} \sum_{l=1}^{N_{qp}} \omega_{K_l} \left[\frac{1}{|K_l|} \int_{K_l} \mathbb{A}^\epsilon \boldsymbol{\varepsilon}(\boldsymbol{u}^h_{K_l}) : \boldsymbol{\varepsilon}(\boldsymbol{v}^h_{K_l}) \, \mathrm{d}V \right]. \tag{8}$$

According to this approximation, the solution $\boldsymbol{u}^h_{K_l}$ is obtained on microsampling domains $K_l = \boldsymbol{x}_{K_l} + \delta\,[-1/2, +1/2]^{n_{\mathrm{dim}}}$, $\delta \geq \epsilon$, which are each centered at the quadrature points $\boldsymbol{x}_{K_l}$ of K, $l = 1, \ldots, N_{qp}$ as displayed in Figure 2(b).

[2] For quantities that refer to a particular quadrature point l, i.e., microdomain in a macro element K, we use for notational convenience index K_l instead of K_{δ_l}.

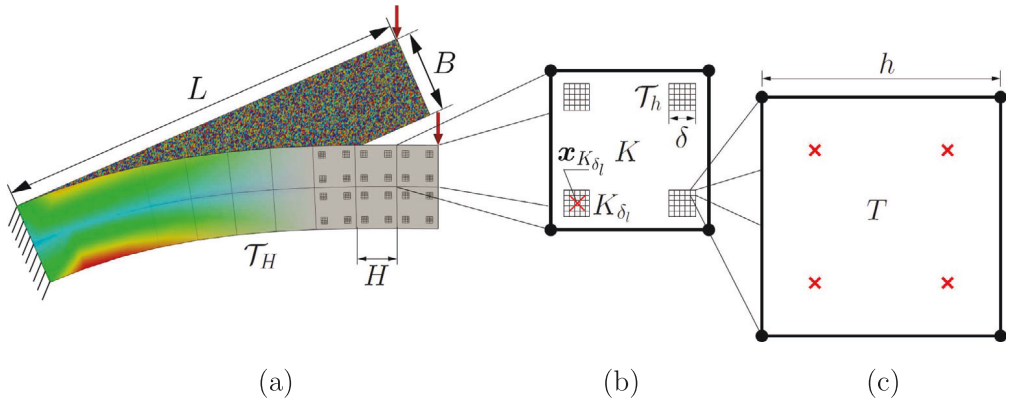


FIGURE 2 Sketch of FE-HMM: (a) Macroscopic BVP with macrotriangulation $\mathcal{T}_H$, (b) one macro finite element K of size H with microdomains/RVEs K_{δ_l} of size δ and of triangulation $\mathcal{T}_h$, centered at the macro quadrature points $\boldsymbol{x}_{K_{\delta_l}}$, (c) micro finite element T of size h, here with Gauss quadrature points for p=q=1 on both scales

The approximation of (7) by (8) is the core of FE-HMM, a modified quadrature rule that fulfills Hill's postulate [27, 28], if energetically consistent boundary conditions are applied to the unit cell.

2.3 | Variational formulation of the microproblem

It can be shown that the FE-HMM microproblem resembles the discrete version of the cell problem of asymptotic expansion, if it is formulated for each microdomain K_l in K with $l = 1, \dots, N_{qp}$, $K \in \mathcal{T}_H$ like this:

Find $\boldsymbol{u}^h_{K_l}$ such that the conditions for both the periodic coupling $(\boldsymbol{u}^h_{K_l} - \boldsymbol{u}^H_{\text{lin},K_l}) \in \mathcal{S}^q_{\text{per}}(K_l, \mathcal{T}_h)$ and for the micro bilinear form are fulfilled

$$B_{K_l}(\boldsymbol{u}^h_{K_l}, \boldsymbol{w}^h_{K_l}) := \int_{K_l} \boldsymbol{\sigma}^\epsilon(\boldsymbol{u}^h_{K_l}) : \boldsymbol{\varepsilon}(\boldsymbol{w}^h_{K_l})\,\mathrm{d}V = 0 \quad \forall\, \boldsymbol{w}^h_{K_l} \in \mathcal{S}^q_{\text{per}}(K_l, \mathcal{T}_h)\,, \tag{9}$$

where the micro finite element space $\mathcal{S}^q_{\text{per}}(K_l, \mathcal{T}_h)$ is defined by

$$\mathcal{S}^q_{\text{per}}(K_l, \mathcal{T}_h) = \{\boldsymbol{w}^h \in \mathcal{W}_{\text{per}}(K_l); \boldsymbol{w}^h \in (\mathcal{P}^q(T))^{n_{\text{dim}}}, T \in \mathcal{T}_h\}\,. \tag{10}$$

In (10) $\mathcal{T}_h$ is a quasi-uniform discretization of the sampling domain K_l with mesh size $h \ll \epsilon$ resolving the finescale, and $\mathcal{P}^q$ is the space of polynomials on the element T. The particular choice of the Sobolev space $\mathcal{W}(K_l)$ sets the boundary conditions for the micro problems, cf. [2], Section 3.2. Here, for periodic boundary conditions (PBCs), it holds by definition $\mathcal{W}_{\text{per}}(Y) = \{\boldsymbol{w}; \boldsymbol{w} \in H^1_{\text{per}}(Y)^{n_{\text{dim}}}\,; \int_Y w_i \mathrm{d}y = 0, i = 1, \dots, n_{\text{dim}}\}$. Beyond PBC, kinematically uniform boundary conditions (KUBC) and constant traction conditions (TBC) fulfill Hill's postulate; for a novel, simple and accurate method to realize TBC see [22].

In the coupling condition, the linearization of $\boldsymbol{u}^H$ at the quadrature point $\boldsymbol{x}_{K_l}$ according to $\boldsymbol{u}^H_{\text{lin},K_l} = \boldsymbol{u}^H(\boldsymbol{x}_{K_l}) + (\boldsymbol{x} - \boldsymbol{x}_{K_l}) \cdot \nabla \boldsymbol{u}^H(\boldsymbol{x}_{K_l})$ realizes a homogeneous deformation on the microdomain and resembles therein the unit cell problem of mathematical homogenization, compare [1, 17]. Such framework is frequently referred to as strain-driven first order computational homogenization.

For the solution of (9), a basis $\{N^H_I\}^{M_{\text{mac}}}_{I=1}$ for the macro finite element space $\mathcal{S}^p_0(\mathcal{B}, \mathcal{T}_H)$ is employed in order to represent the macrosolution $\boldsymbol{u}^H$ of (6). Similarly, a basis $\{N^h_i\}^{M_{\text{mic}}}_{i=1}$ of the micro finite element space $\mathcal{S}^q_0(K_l, \mathcal{T}_h)$, (10), is introduced in order to represent the solution $\boldsymbol{u}^h$ of a microproblem. M_{mac} denotes the number of nodes of the macrodomain, and M_{mic} denotes the number of nodes of each microdomain. Hence, the macro- and the microsolution follow the representation

$$\boldsymbol{u}^H = \sum_{I=1}^{M_{\text{mac}}} N^H_I\, \boldsymbol{d}^H_I\,, \qquad \boldsymbol{u}^h = \sum_{i=1}^{M_{\text{mic}}} N^h_i\, \boldsymbol{d}^h_i\,, \tag{11}$$

where $\boldsymbol{d}^H_I$ is the displacement vector of macronode I, and $\boldsymbol{d}^h_i$ is the displacement vector for micronode i.

2.4 | Macrostiffness calculation

The macro bilinear form $B_H^e(\boldsymbol{u}^H, \boldsymbol{v}^H)$ is the virtual internal work for a macro finite element. The corresponding bilinear form in terms of the shape functions $B_H^e(\boldsymbol{N}_I^H, \boldsymbol{N}_J^H)$ results in the macro element stiffness matrix contribution $\boldsymbol{k}_{IJ}^{e,\mathrm{mac}}$ for macronodes I, J, an $n_{\mathrm{dim}} \times n_{\mathrm{dim}}$ matrix. With the diagonal matrix $\boldsymbol{N}_I^H = \mathrm{diag}(N_I^H, N_I^H, N_I^H)$ (here for 3D) it holds

$$\boldsymbol{k}_{IJ}^{e,\mathrm{mac}} = B_H^e(\boldsymbol{N}_I^H, \boldsymbol{N}_J^H) = \sum_{l=1}^{N_{qp}} \frac{\omega_{K_l}}{|K_l|} \int_{K_l} (\boldsymbol{L}\boldsymbol{u}_{K_l}^{h(I)})^T \mathbb{A}^\epsilon(\boldsymbol{x})\, \boldsymbol{L}\boldsymbol{u}_{K_l}^{h(J)}\, \mathrm{d}V\,. \tag{12}$$

In (12) $\boldsymbol{u}_{K_l}^{h(I)}$ is the counterpart of $\boldsymbol{u}_{K_l}^h$ in (9). It is the dimensionless solution of the microproblem on K_l, which is driven by the shape function N_I^H at macronode I. In the following, we add $x_i, i = 1, \dots, n_{\mathrm{dim}}$ to account for the vector-valued field problem of dimension n_{dim}. Consequently, $\boldsymbol{u}_{K_l}^{h(I,x_i)}$ is the microsolution driven by a macroelement unit-displacement state $\boldsymbol{u}_{\mathrm{lin},K_l}^{H(I,x_i)}$ at node I in x_i-direction.

For stiffness calculation, problem (9) is reformulated in that $\boldsymbol{u}_{K_l}^{h(I,x_i)}$ replaces $\boldsymbol{u}_{K_l}^h$.

For the coupling of $\boldsymbol{u}_{\mathrm{lin},K_l}^{H(I,x_i)}$ with $\boldsymbol{u}_{K_l}^{h(I,x_i)}$ the two fields are expanded into the same basis $\{N_i^h\}_{i=1}^{M_{\mathrm{mic}}}$ of $\mathcal{S}^q(K_l, \mathcal{T}_h)$,

$$\boldsymbol{u}_{\mathrm{lin},K_l}^{H(I,x_i)} = \sum_{m=1}^{M_{\mathrm{mic}}} N_{m,K_l}^h \boldsymbol{d}_m^{H(I,x_i)}\,, \qquad \boldsymbol{u}_{K_l}^{h(I,x_i)} = \sum_{m=1}^{M_{\mathrm{mic}}} N_{m,K_l}^h \boldsymbol{d}_m^{h(I,x_i)}\,. \tag{13}$$

The solution of the microproblems for the minimizers $\boldsymbol{d}^{h(I,x_i)}$ is presented in Sec. 2.5. The macroelement stiffness matrix according to (12) yields after some algebra

$$\boldsymbol{k}_{IJ}^{e,\mathrm{mac}} = \sum_{l=1}^{N_{qp}} \frac{\omega_{K_l}}{|K_l|} \left(\boldsymbol{d}^{h(I)}\right)^T \boldsymbol{K}_{K_l}^{\mathrm{mic}}\, \boldsymbol{d}^{h(J)}\,, \tag{14}$$

where $\boldsymbol{d}^{h(I)} = (\,\boldsymbol{d}^{h(I,x_1)} | \boldsymbol{d}^{h(I,x_2)} | \boldsymbol{d}^{h(I,x_3)}\,)$ for $n_{\mathrm{dim}} = 3$. The assembly of $\boldsymbol{k}_{IJ}^{e,\mathrm{mac}}$ results in $\boldsymbol{k}^{e,\mathrm{mac}}$ and corresponds to an assembly of $\boldsymbol{d}^{h(I)}$ for $I = 1, \dots, N_{node}$ in columns which gives the transformation matrix $\boldsymbol{T}_{K_l}$

$$\boldsymbol{k}_K^{e,\mathrm{mac}} = \sum_{l=1}^{N_{qp}} \frac{\omega_{K_l}}{|K_l|}\, \boldsymbol{T}_{K_l}^T \boldsymbol{K}_{K_l}^{\mathrm{mic}}\, \boldsymbol{T}_{K_l} \tag{15}$$

$$\text{with} \quad \boldsymbol{T}_{K_l} = \left[\left[\left[\boldsymbol{d}^{h(I,x_i)} \right]_{i=1,\dots,n_{\mathrm{dim}}} \right]_{I=1,\dots,N_{\mathrm{node}}} \right]. \tag{16}$$

In the present context of stiffness computation, a macro element shape function represents a unit displacement state for macro node $I, I = 1, \dots, N_{\mathrm{node}}$ in each direction of space $x_i, i = 1, \dots, n_{\mathrm{dim}}$. They drive the microproblem in terms of the corresponding nodal values $\boldsymbol{d}_m^{H(I,x_i)}, m = 1, \dots, M_{\mathrm{mic}}$ in each microdomain to evaluate the macroelement stiffness $\boldsymbol{k}_{IJ}^{e,\mathrm{mac}}$. Each unit displacement state in x_i-direction induces in $\boldsymbol{d}^{H(I,x_i)}$ nonzero components only in x_i, for $n_{\mathrm{dim}} = 3$, e.g., $\boldsymbol{d}^{H(I,x_i)}|_{i=2} = [0, d_{1,x_2}^{H(I,x_2)}, 0, \dots, 0, d_{M_{\mathrm{mic}},x_2}^{H(I,x_2)}, 0]^T$.

2.5 | Solution of the microproblems

The total micro stiffness matrix for an RVE is obtained by standard processes of computing micro stiffness matrices through numerical quadrature and a consecutive assembly.

The solution of the microproblem is obtained by the method of Lagrange multipliers, which renders the total energy for a macro unit displacement state

$$\mathcal{L}(\boldsymbol{d}^{h(I,x_i)}, \boldsymbol{\lambda}^{(I,x_i)}) = \frac{1}{2}\left(\boldsymbol{d}^{h(I,x_i)}\right)^T \boldsymbol{K}^{\text{mic}}_{K_l}\, \boldsymbol{d}^{h(I,x_i)} + \boldsymbol{\lambda}^{(I,x_i)\,T}\, \boldsymbol{G}\left(\boldsymbol{d}^{h(I,x_i)} - \overline{\boldsymbol{d}}^{H(I,x_i)}\right) \tag{17}$$

$$\text{for } I = 1, \dots, N_{\text{node}}, \text{ and } x_i\,|_{i=1,\dots,n_{\text{dim}}},$$

where $\boldsymbol{G}$ contains the coupling constraints of the RVE. The vector of Lagrange multipliers $\boldsymbol{\lambda}^{(I,x_i)} \in \mathbb{R}^{(1+L)\cdot n_{\text{dim}}}$, where L depends on the type of microcoupling, represents forces on the microdomain which enforce the micro coupling condition. The variations of $\mathcal{L}$ with respect to $\boldsymbol{d}^{h(I,x_i)}$ and to $\boldsymbol{\lambda}^{(I,x_i)}$ result in the stationarity conditions

$$\begin{bmatrix} \boldsymbol{K}^{\text{mic}}_{K_l} & \boldsymbol{G}^T \\ \boldsymbol{G} & \boldsymbol{0} \end{bmatrix} \begin{bmatrix} \boldsymbol{d}^{h(I,x_i)} \\ \boldsymbol{\lambda}^{(I,x_i)} \end{bmatrix} = \begin{bmatrix} \boldsymbol{0} \\ \boldsymbol{G}\,\boldsymbol{d}^{H(I,x_i)} \end{bmatrix} \text{ for } I = 1, \dots, N_{\text{node}},\ i = 1, \dots, n_{\text{dim}}, \tag{18}$$

hence, a system of linear equations with $N_{\text{node}} \cdot n_{\text{dim}}$ right hand sides. The solution vectors are augmented to full matrices, hence, $\boldsymbol{d}^{h(I,x_i)} \to \boldsymbol{T}$, $\boldsymbol{\lambda}^{(I,x_i)} \to \boldsymbol{\Lambda}$, $\boldsymbol{d}^{H(I,x_i)} \to \boldsymbol{d}^H$.

The solution of (18) serves the purpose to compute the transformation matrix $\boldsymbol{T}_{K_l}$ according to (16). After the consecutive solution of the global macroproblem for $\boldsymbol{u}^H$, the microproblems have to be solved. Then, (18) is driven by the true macroscopic displacement vector $\boldsymbol{d}^H$, which results in the true microdisplacements $\boldsymbol{d}^h$.

Nonlinear extensions of FE-HMM in solid mechanics have been proposed in [18] and in [41], for applications of FE-HMM in the context of nonstandard homogenization for identifying material parameters in the Relaxed Micromorphic Model see [8] and [40].

3 | ERRORS AND A PRIORI ESTIMATES

3.1 | On the microscale

So far, the microsolution obtained for discretization h was denoted by $\boldsymbol{u}^h$. For the below proposed error analysis on the microscale it is necessary to distinguish between image resolution $h_\square$ and discretization h, which is equally reflected by the solution, hence $\boldsymbol{u}^{h_\square,h}$. Consequently, we denote the exact microsolution, i.e., for $h_\square \to 0, h \to 0$, by $\boldsymbol{u}^{0,0} = \boldsymbol{u}^\epsilon$ and the solution for finite $h_\square$ and $h \to 0$ by $\boldsymbol{u}^{h_\square,0}$.

With these definitions the micro error e^ϵ_{mic} of (19) can be decomposed via (20) into its discretization part $e^{\epsilon\,h}_{\text{mic}}$ and resolution part $e^{\epsilon\,\square}_{\text{mic}}$ according to the (triangle) inequality (21).

$$e^\epsilon_{\text{mic}} = ||\boldsymbol{u}^{h_\square,h} - \boldsymbol{u}^{0,0}||_{(\mathcal{B}_\epsilon)} \tag{19}$$

$$= ||\boldsymbol{u}^{h_\square,h} - \boldsymbol{u}^{h_\square,0} + \boldsymbol{u}^{h_\square,0} - \boldsymbol{u}^{0,0}||_{(\mathcal{B}_\epsilon)} \tag{20}$$

$$\leq \underbrace{||\boldsymbol{u}^{h_\square,h} - \boldsymbol{u}^{h_\square,0}||_{(\mathcal{B}_\epsilon)}}_{e^{\epsilon\,h}_{\text{mic}}} + \underbrace{||\boldsymbol{u}^{h_\square,0} - \boldsymbol{u}^{0,0}||_{(\mathcal{B}_\epsilon)}}_{e^{\epsilon\,\square}_{\text{mic}}} \tag{21}$$

The limit $h_\square \to 0$, a task of image acquisition, is for real microstructures typically to be replaced by a nonzero limit, hence $h_\square \to h^*_\square, h^*_\square > 0$, which is then to be considered in (19)–(21). It generally must hold $h \leq h_\square$.

For the micro error measured on the microscale e^ϵ_{mic} standard a priori estimates of the finite element method hold for sufficient regularity, see [7]. With the extension by $e^{\epsilon\,\square}_{\text{mic}}$ the estimates read in the L^2- and in the energy norm A on a microdomain $\mathcal{B}_\epsilon$

$$||\boldsymbol{u}^\epsilon - \boldsymbol{u}^h||_{L^2(\mathcal{B}_\epsilon)} \leq C\left(\frac{h}{\epsilon}\right)^{q+1} + e^{\epsilon\,\square}_{\text{mic}}, \tag{22}$$

$$||\boldsymbol{u}^\epsilon - \boldsymbol{u}^h||_{A(\mathcal{B}_\epsilon)} \leq C\left(\frac{h}{\epsilon}\right)^{q} + e^{\epsilon\,\square}_{\text{mic}}. \tag{23}$$

Augmenting the result of [2], it holds for the coefficients of the homogenized elasticity tensor

$$||\mathbb{A}^0_{ijkl} - \mathbb{A}^{0,h,\square}_{ijkl}|| \leq C\left(\frac{h}{\epsilon}\right)^{2q} + e^{\epsilon\,\square}_{\text{mic}} \tag{24}$$

with the exact tensor $\mathbb{A}^0_{ijkl}$ and its approximation $\mathbb{A}^{0,h,\square}_{ijkl}$ obtained at micro element size h and resolution $h_\square$. The norm for the elasticity tensors in (24) is the entrywise matrix norm $||\mathbb{A}_{mn}||_{s,s}$ with $s = 2$ and $\mathbb{A}_{mn}$ the elasticity matrix in Voigt notation.

While the estimate for the homogenized elasticities is given according to (24), the corresponding relative error $||\mathbb{A}^0_{ijkl} - \mathbb{A}^{0,h,\square}_{ijkl}||/||\mathbb{A}^0_{ijkl}||$ would be not fully descriptive, since it does not include the stiffness contrast of material phases. For that reason, the relative error for a microstructure consisting of two phases, 1 and 2, at discretization h and resolution $h_\square$ is computed according to

$$e^{\epsilon}_{\text{mic}}(\mathbb{A}^{0,h,\square}_{ijkl}) := \frac{||\mathbb{A}^0_{ijkl} - \mathbb{A}^{0,h,\square}_{ijkl}||}{\min\{||\text{dev}\,\mathbb{A}^{0,r}_{ijkl}||, r = 1,2\}} \tag{25}$$

$$\text{with} \quad \text{dev}\,\mathbb{A}^{0,r}_{ijkl} := \mathbb{A}^0_{ijkl} - \mathbb{A}^{0,r}_{ijkl}, \quad r = 1,2\,. \tag{26}$$

Through the deviation of the exact homogenized elasticities from those of the single phases $\mathbb{A}^{0,r}_{ijkl}$ in (26) the bounds set by the individual phases are included.

Similar to (21) the total error (25) can be decomposed into resolution and discretization parts, the latter by the computation of the reference solution $\mathbb{A}^0_{ijkl}$ at fixed $h_\square$ and $h \to 0$.

3.2 | On the macroscale

The FE-HMM provides unified a priori estimates; for elliptic partial differential equations (PDEs) derived by Ming and Zhang [15], Ohlberger [43], for linear elasticity by Abdulle [1], comprehensively described by Abdulle in [2].

We introduce various macroscopic displacement fields as the solutions to different problems; $\boldsymbol{u}^0$ is the solution of the homogenized problem (3), $\boldsymbol{u}^{0,H}$ is the standard (single-scale) FEM solution of problem (4) that is obtained through exact $\mathbb{A}^0$, $\widetilde{\boldsymbol{u}}^H$ is the FE-HMM solution obtained through exact microfunctions (in $\mathcal{W}(K_l)$, see Section 2.3), $\boldsymbol{u}^{H,\square}$ is the solution for finite $h_\square$ along with $h \to 0$, $\boldsymbol{u}^H$ is the FE-HMM solution obtained for discretizations H, h, and resolution $h_\square$.

With this assignment of variables, the total FE-HMM error can be decomposed into its parts, the macro error e_{mac}, the modeling error e_{mod}, and the propagated micro error e_{mic}, the decomposition of the latter consistent with (21)

$$||\boldsymbol{u}^0 - \boldsymbol{u}^H|| \leq \underbrace{||\boldsymbol{u}^0 - \boldsymbol{u}^{0,H}||}_{e_{\text{mac}}} + \underbrace{||\boldsymbol{u}^{0,H} - \widetilde{\boldsymbol{u}}^H||}_{e_{\text{mod}}} + \underbrace{\underbrace{||\widetilde{\boldsymbol{u}}^H - \boldsymbol{u}^{H,\square}||}_{e^{\square}_{\text{mic}}} + \underbrace{||\boldsymbol{u}^{H,\square} - \boldsymbol{u}^H||}_{e^{h}_{\text{mic}}}}_{\geq e_{\text{mic}}}\,. \tag{27}$$

For sufficient regularity the following a priori estimates hold for the total error (27)

$$||\boldsymbol{u}^0 - \boldsymbol{u}^H||_{L^2(\mathcal{B})} \leq C\left(H^{p+1} + \left(\frac{h}{\epsilon}\right)^{2q}\right) + e_{\text{mod}} + e^{\square}_{\text{mic}}\,, \tag{28}$$

$$||\boldsymbol{u}^0 - \boldsymbol{u}^H||_{A(\mathcal{B})} \leq C\left(H^{p} + \left(\frac{h}{\epsilon}\right)^{2q}\right) + e_{\text{mod}} + e^{\square}_{\text{mic}}\,. \tag{29}$$

For e_{mod} in (28), (29) it holds

$$e_{\text{mod}} = \begin{cases} 0 & \text{for periodic coupling with } \delta/\epsilon \in \mathbb{N} \\ C\,\dfrac{\epsilon}{\delta} & \text{for Dirichlet coupling with } \delta > \epsilon \end{cases} \tag{30}$$

given that the hypotheses hold, that the elasticity tensor $\mathbb{A}^\epsilon$ is periodic on the RVE and, that the micro solution is sufficiently smooth, [30]. The modeling error e_{mod} for Dirichlet coupling is due to boundary layers [15] (Thm. 1.2), [2] and remains as a residual even for $H \to 0$ and $h \to 0$.

Access by intuition to $(30)_2$ shall provide the following example; imagine a 2D square array of edge length δ that consists of $N \times N$ periodic cells of edge length ϵ, hence $\delta = N\epsilon, N \in \mathbb{N}$. The solution for, e.g., linear Dirichlet BCs on the domain will be influenced by these BCs only in a boundary layer of finite width, whereas in the interior of the domain the periodic solution will be recovered for the periodicity of the cells. The larger the array compared to the unit cell, the smaller the corresponding overall influence, hence modeling error, with the limit $e_{\text{mod}} \to 0$ for $N \to \infty$, in agreement with $(30)_2$. In that limit, the stiffness of the full array equals the stiffness of the periodic unit cell. The result $(30)_1$ is immediately clear.

Remarks.

For its composition covering both the macro error as well as the micro error, the estimates (28)–(29) enable strategies to achieve the optimal convergence order for minimal computational costs in uniform micro-macro discretizations, for an assessment see [16, 17, 30].

The above unified error estimates derived for FE-HMM apply for FE^2 for the equality of the methods [17]. FE-HMM and FE^2 were developed independently, the latter in [21, 25, 31, 35, 39, 54].

The computation of the micro errors is carried out by projection of the approximate solution to the Gauss points of a reference mesh ($h \to 0$) with a consecutive numerical quadrature for approximating the integral element error as detailed in [22, 23].

The estimation of the discretization error is described in Section 5 with a focus on peculiarities at interfaces, which have undergone resolution coarsening as detailed in Section 4.

For both error computation and error estimation on the microscale the macro displacement field $\boldsymbol{u}^{0,H}$ is used for consistency.

The resolution part of the micro error is not directly accessible to error estimation and therefore the total micro error neither.

4 | COARSENING OF IMAGE RESOLUTION AND MESH DISCRETIZATION

The present section proposes two types of coarsening, the first is a uniform coarsening of microstructure resolution which implies a coarsening of finite element discretization. Consequently, a resolution error and a discretization error are introduced. The second type is a non-uniform mesh coarsening, which keeps the image resolution constant and therefore the resolution error likewise, but increases the discretization error. These two types of coarsening will be combined in that uniform coarsening of microstructure resolution is followed by adaptive mesh coarsening.

4.1 | Uniform pixel coarsening

In resolution coarsening all pixels of the initial, finely resolved microstructure image undergo uniform coarsening, no matter if they are located on phase boundaries or inside of phases. For phase boundaries rules must be established, how a patch of 2×2 fine pixels having different stiffness (represented by different color codes) merge into one coarser pixel. Since the finite element discretization follows this uniform coarsening, pixels represent finite elements and pass their properties onto them.

In the following two different variants of pixel coarsening are presented.

Variant A follows a rule of mixtures; the newly created pixel exhibits properties of the volume average of the pixels (arithmetic mean for the same pixel size) merging in that coarser pixel, hence a coarsening that creates new interphases at interfaces. If the number of phases is known and their interfaces sharp, the newly created interphases are artifacts, which smoothen discrete interfaces, reduce their stiffness mismatch and consequently reduce corresponding stress jumps. The volume average over the entire microdomain however is preserved.

Variant B aims to overcome the drawbacks of a coarsening that introduces new interphases. For coarsened pixels at interfaces the quantity and properties of the initial phases are preserved following the rule, the majority wins. In case of an equal count the newly created coarser pixel is endowed with those phase properties that shift the overall phase ratio closer to the original one.

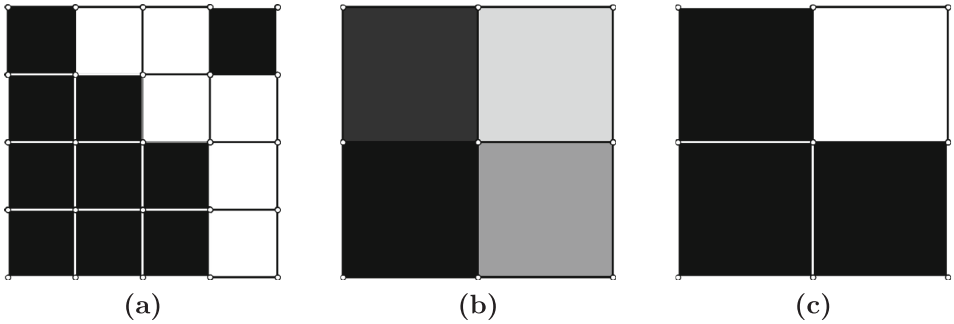


FIGURE 3 Uniform mesh coarsening: (a) Initial, fine discretization, (b) coarsened mesh with intermediate phases and (c) coarsened mesh preserving the initial phases in quantity and properties

FIGURE 4 Adaptive mesh coarsening: (a) Original uniform mesh, (b) quadtree-type adaptively coarsened mesh

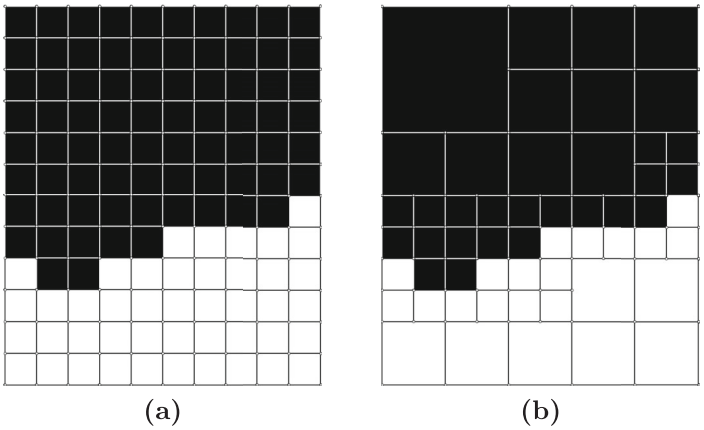


Figure 3 illustrates the two variants of coarsening for a uniform mesh with elements belonging to two different phases, Figure 3(a). Coarsening along with intermediate phases results in the mesh of Figure 3(b). Only for the coarsened element in the lower left no averaging is required. The other three elements obtain their properties from averaging, which is represented in the image by the corresponding color code.

Applying the second approach for uniform mesh coarsening leads to the mesh in Figure 3(c). The majority-wins rule is ambiguous only for the coarsened element in the lower right, the assignment of the black phase leads to a phase ratio closer to the initial one. By that rule for cases of an equal count the outcome of coarsening is not unique; it depends on which path is chosen to go through the pixels. It is assumed that this has a minor influence on the results.

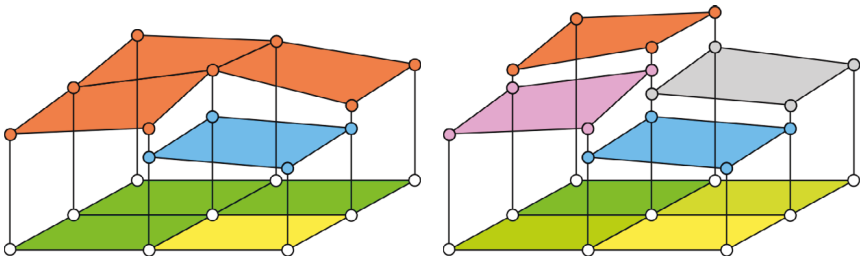
Notice that coarsening variant A generates results of the type how raw image data, e.g., in bitmap format are typically represented. Variant B follows the process of image segmentation applied to microstructures with intermediate phases in terms of intermediate color codes. As a result, using a microstructure representation obtained from coarsening variant A can be interpreted as skipping image segmentation at all.

4.2 | Quadtree-type, adaptive mesh coarsening

The second type is a non-uniform, adaptive mesh coarsening, which keeps the image resolution constant and therefore the resolution error likewise, but increases the discretization error. It starts out from a—possibly already coarsened—uniform mesh.

In this procedure realized by a quadtree-type mesh coarsening algorithm the interface resolution is maintained for accuracy, in the interior of phases mesh coarsening is carried out for efficiency. This type of microstructure-informed adaptivity is frequently used for multiphase materials [33, 34, 37, 38, 47] for application in homogenization and fracture, in the context of the Scaled Boundary FEM [26, 48] and many more. But only very recently a rigorous accuracy analysis based on error estimation was presented in [23].

As an example, Figure 4(a) displays an interface in a two-phase microstructure in its initial uniform pixel resolution coinciding with the micro mesh of element size h. The adaptive, quadtree-type coarsening results in the discretization



(a) duplex stress (b) quadruplex stress

FIGURE 5 Stress distributions at phase boundaries: (a) Duplex stress at the discrete interface between two phases, a stiff one in green and a more compliant one in yellow, (b) quadruplex stress at a boundary with intermediate phases

of Figure 4(b). It preserves the fine resolution at the phase boundary. Inside of the two phases the elements have been coarsened to new elements of side length $2h$ and $4h$.

Uniform pixel coarsening in the present paper is followed by a non-standard adaptive mesh refinement. Here, adaptivity is not directed by the distribution of an a posteriori error estimate. Instead, it is microstructure-informed in that high resolution at interfaces is maintained, whereas mesh coarsening is carried out in the interior of phases. Suchlike preprocessing typically provides a favorable balance of accuracy and efficiency. The obtained, adaptively refined mesh can then be assessed by a posteriori error estimation for various loading conditions [23].

5 | A POSTERIORI ERROR ESTIMATION FOR COARSENED MICROSTRUCTURES

A posteriori error estimation on the microscale using standard techniques is restricted to the discretization error. The resolution error and therefore the total micro error are not directly accessible to estimation.

For reconstruction-type estimation of the discretization error according to Zienkiewicz-Zhu [55–57] the accuracy critically depends on improved nodal stresses $\boldsymbol{\sigma}^\star$ and strains $\boldsymbol{\varepsilon}^\star$. The a posteriori estimate of the micro discretization error in the microdomain $\mathcal{B}_\epsilon$ according to (31) is computed by Gauss quadrature according to (32), with $\boldsymbol{x}_i^h$, ω_i, n_{gp} the quadrature coordinates, the weights and the number of Gauss points, respectively. The determinant of the Jacobian $\det \boldsymbol{J}$ maps the element area from parameter space of isoparametric finite elements into the real physical space.

$$(\bar{e}^{\epsilon\, h}_{\text{mic}})^2 = ||\bar{\boldsymbol{e}}||^2_{A(\mathcal{B}_\epsilon)} = \int_{\mathcal{B}_\epsilon} \left(\boldsymbol{\sigma}^\star - \boldsymbol{\sigma}^h\right) : \left(\boldsymbol{\varepsilon}^\star - \boldsymbol{\varepsilon}^h\right) \mathrm{d}V \tag{31}$$

$$\approx \sum_{T\in\mathcal{T}_h} \left(\sum_{i=1}^{n_{gp}} \omega_i \left(\boldsymbol{\sigma}^\star - \boldsymbol{\sigma}^h\right)(\boldsymbol{x}_i^h) : \left(\boldsymbol{\varepsilon}^\star - \boldsymbol{\varepsilon}^h\right)(\boldsymbol{x}_i^h) \det \boldsymbol{J} \right). \tag{32}$$

In contrast to the true discretization error $e^{\epsilon\, h}_{\text{mic}}$ based on accurate stresses obtained on a discretization $h \to 0$, improved stresses in the estimate $\boldsymbol{\sigma}^\star$ are obtained on the same mesh, the triangulation $T \in \mathcal{T}_h$. Improved stresses for a node in a phase interior are calculated by simple averaging the values extrapolated from quadrature points of adjacent elements to that node or by more sophisticated techniques exploiting superconvergence [56, 57]. Stress averaging for a node at the discrete interface of two different phases ignores the stiffness mismatch and corresponding stress jumps. A phase distinction assigning two different sets of stress to a node (referred to as duplex stress) as displayed in Figure 5(a) does not only overcome these drawbacks but also results in more accurate error estimates compared to a standard stress averaging that ignores interfaces [23]. It is therefore the method of choice for stress computation at interfaces for phase-preserving coarsening, variant B in this work. In the phase interior we use averaging for nodal stress computation, since the corresponding error estimate is similarly accurate as the estimate based on superconvergent stress [23], such that the computational overhead of the latter approach does not pay off in the present context.

If the scheme of phase-distinction in nodal stress computation is consistently applied to interfaces following from coarsening variant A thus creating new interphases, a new situation arises. Figure 5(b) displays the case of a 2×2 element patch each with different phases. Consequently, the central patch node is endowed with a quadruplex stress set.

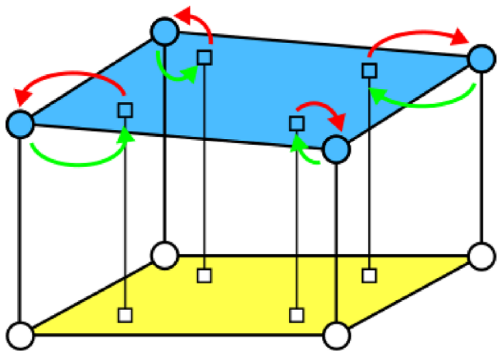
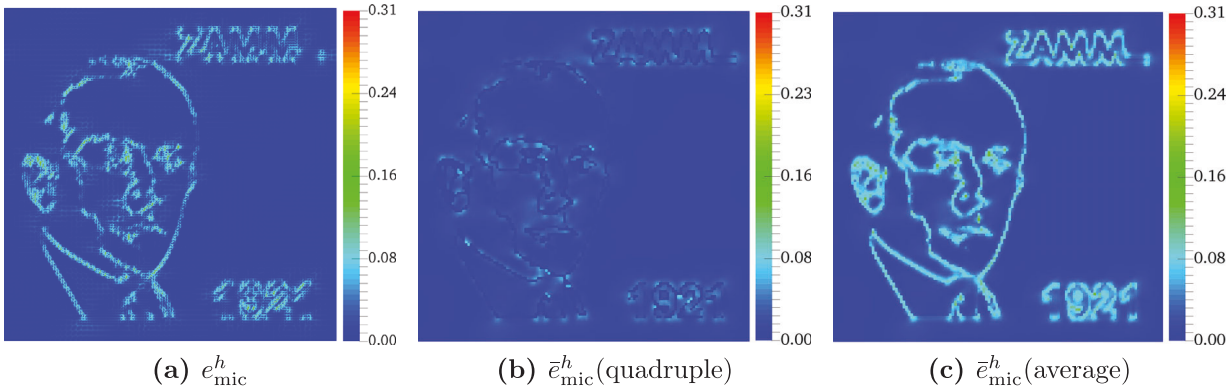


FIGURE 6 Stress-transfer for an element surrounded by elements of different phases: Stresses from quadrature points (squares) are transferred (outward red arrows) to nodes (circles), for error estimation they are transferred back (inward green arrows) into the quadrature points and compared with the original values. Identical values result in a zero value for the estimated error



(a) e^h_{mic} (b) $\bar{e}^h_{\text{mic}}(\text{quadruple})$ (c) $\bar{e}^h_{\text{mic}}(\text{average})$

FIGURE 7 Discretization errors for coarsening with intermediate phases: (a) Calculated error e^h_{mic}, max.: 0.31 (b) estimated error based on quadruplex stresses $\bar{e}^h_{\text{mic}}(\text{quadruplex})$, max.: 0.08 (c) estimated error based on averaged stress $\bar{e}^h_{\text{mic}}(\text{average})$, max.: 0.17. All relative errors per element are obtained by division by the energy of the element $||\boldsymbol{u}||_A$. Unified color table is adjusted to the true error distribution in (a)

5.1 | Coarsening with new interphases in error estimation

A new, related issue shall be illustrated in Figure 6 for nodes of an isolated element having throughout different phases in direct neighborhood. Notice that stresses are computed in the first place in the quadrature points, for $q = 1$ in the 2×2 quadrature points marked with squares. Next, these stress values are extrapolated to the element nodes by the shape functions, a transfer marked by red arrows. For error estimation according to (31) the improved nodal stresses $\boldsymbol{\sigma}^\star$ have to be transferred back to the quadrature points as marked by green arrows. When no averaging is carried out at all nodes due to phase-distinction, the nominally improved stresses transferred back into the quadrature points coincide with the original stress values therein, which results in a vanishing error in the stresses. This is clearly an artefact that spoils error estimation.

Notice that for a microstructure starting from two different phases in the initial resolution, n coarsening steps could lead to $2^{2n} + 1$ newly created phases at maximum, where an interface node is typically part of four different adjacent phases. Hence, the setup in Figures 5(b) and 6 is rather the rule than an exception for coarsening variant A.

As a consequence, the underestimation of the true error is expected locally at interfaces where it is typically largest and as an overall error of the total microdomain as well. This behavior shall be underpinned by an example. We compare at interface nodes the quadruplex stress computation with the standard concept where nodal stresses are obtained by averaging the elementwise nodal stresses of all adjacent elements independent from their phase.

Figure 7 displays the relative discretization error for an example discussed in detail in Section 6. The discretization used here follows from three consecutive steps of uniform coarsening according to variant A thus creating intermediate phases.

The true discretization error is displayed in 7(a). Estimated errors for nodal quadruplex stresses are shown in Subfig. 7(b), for nodal stress averaging without phase distinction in Subfig. 7(c). Notice that the latter version qualitatively

TABLE 1 Comparison of discretization errors: Calculated and estimated errors with their effectivity index $\Theta := \bar{e}^{\epsilon\,h}_{\text{mic}} / e^{\epsilon\,h}_{\text{mic}}$. All error data in 10^{-4} (MPa)

	quadruplex		average	
$e^{\epsilon\,h}_{\text{mic}}$	$\bar{e}^{\epsilon\,h}_{\text{mic}}$	Θ	$\bar{e}^{\epsilon\,h}_{\text{mic}}$	Θ
15.8114	8.2921	0.5244	22.1951	1.3865

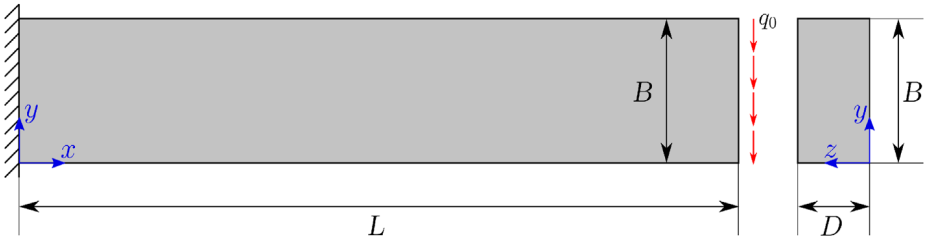


FIGURE 8 Macroproblem: cantilever subject to a line load q_0 at $x = L$

captures the true distribution of discretization errors showing maxima at interfaces. The error distribution based on quadruplex stresses however exhibits the artefact of vanishing errors at the phase boundary (dark blue stripes), in agreement with our elementary reasoning.

Table 1 shows the numbers of the calculated and estimated discretization errors for the full microdomain along with the effectivity indices, the ratios of the estimated to the actual error. While the estimated error based on quadruplex stresses $\bar{e}^{\epsilon\,h}_{\text{mic}}$ underestimates the calculated discretization error $e^{\epsilon\,h}_{\text{mic}}$ due to the vanishing error on the phase boundary, the estimation based on averaged stresses overestimates the error. Qualitatively, at least the estimation based on averaged nodal stresses renders acceptable distributions. Quantitatively however, none of both methods achieves accurate results as indicated by effectivity indices considerably deviating from unity, again consistent with the above reasoning.

Notice that here, the 'crime' of resolution coarsening that creates new, additional interphases with its inherent artifacts, must be alleviated by another 'crime', the required stress averaging in order to avoid further artifacts in error estimation.

6 | NUMERICAL EXAMPLE

6.1 | Two-phase microstructure

This section provides an error analysis of an image-based microstructure representation which undergoes coarsening in resolution and in discretization.

We consider the two-phase microstructure of Figure 1(a) subject to PBC; the isotropic, linear elasticity of the inclusion phase (white) is characterized by $E_i = 192.1$ MPa, $\nu_i = 0.2$, the matrix phase by $E_m = 100.0$ MPa, $\nu_m = 0.2$. The square unit cell of edge length $\epsilon = 1$ mm exhibits an initial uniform pixel resolution of 1024^2, hence $h_\square = 1/1024$ mm; the reference finite element discretization is 2048^2 elements, hence $h = 1/2048$ mm. The plane-strain macro problem is a cantilever beam of length $L = 5000$ mm, height $B = 1000$ mm and width $D = 100$ mm, see Figure 8. It is loaded at its free end by a line-load of $q_0 = 0.02$ N/mm. Postprocessing is carried out on a microdomain at $x = y = 2.1132$ mm.

Remark. A Young's modulus contrast of similar magnitude exists for example for diamond/β-SiC microcomposites—analyzed for effective properties in [19, 24]—making the present setting representative for real materials.

6.2 | Uniform pixel coarsening

The outcome of uniform pixel coarsening is shown in Figure 9, for the case of introducing new interphases in (a)–(f), for the phase-preserving case in (g)–(l). Since in the first case the color code of the coarsened pixel is the volume average of the contributing four pixels, it preserves the volume average of the Young's moduli. In the limiting case of one single pixel



(a) 1024^2px (b) 64^2px (c) 32^2px

(d) 16^2px (e) 8^2px (f) 1^2px

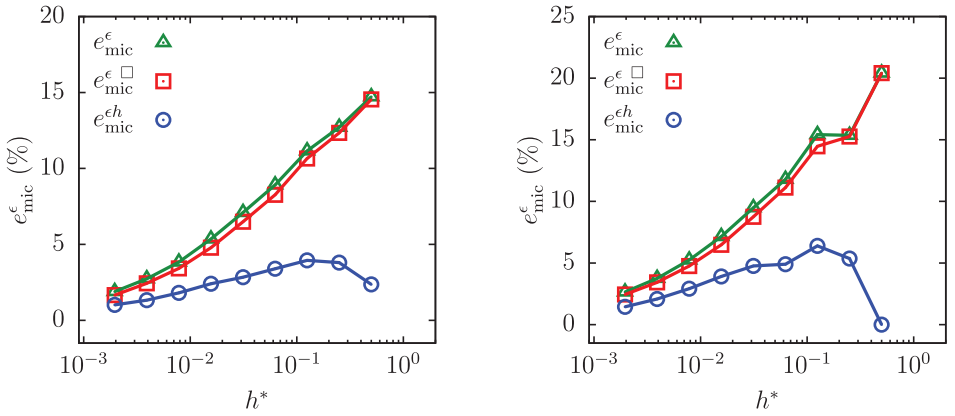
(g) 256^2px (h) 64^2px (i) 32^2px

(j) 16^2px (k) 8^2px (l) 1^2px

FIGURE 9 Pixel coarsening in two variants: (a)–(f) variant A with additional interphases and (g)–(l) variant B preserving the two-phase composition

TABLE 2 Pixel coarsening, both variants: for various resolutions the number of degrees of freedom (ndof), ndof reduction factors, estimated versus true errors along with their effectivity index Θ based on different stress computations at interface nodes. Error data in the energy norm in 10^{-4} (MPa)

uniform mesh coarsening						
step no.	**0**	**1**	**2**	**3**	**4**	**5**
px	1024^2	512^2	256^2	128^2	64^2	32^2
ndof	2 097 152	524 288	131 072	32 768	8 192	2 048
factor	1.0000	0.2500	0.0625	0.0156	0.0039	0.0010
phase-preserving						
$e^{\epsilon}_{\text{mic}}$	7.8277	23.1379	32.8531	45.8962	62.5401	83.1333
$\bar{e}^{\epsilon h}_{\text{mic}}$	7.5989	10.7376	15.1268	21.1626	28.8471	36.7235
$e^{\epsilon h}_{\text{mic}}$	7.8277	12.6256	18.1766	25.4883	34.2359	41.7658
Θ(duplex)	0.9708	0.8505	0.8322	0.8303	0.8426	0.8793
$e^{\epsilon\square}_{\text{mic}}$	0.00	21.4106	30.0302	41.5990	56.6115	76.6315
additional interphases						
$e^{\epsilon}_{\text{mic}}$	7.8277	16.5271	23.9076	33.5541	46.8402	62.2162
$\bar{e}^{\epsilon h}_{\text{mic}}$(quadruplex)	7.5989	6.2388	6.6837	8.2921	9.3745	11.2591
$\bar{e}^{\epsilon h}_{\text{mic}}$(average)	10.7730	11.9762	15.8392	21.9222	30.0643	37.1357
$e^{\epsilon h}_{\text{mic}}$	7.8277	8.8569	11.5926	15.8114	21.0864	24.9076
Θ(quadruplex)	0.9708	0.7044	0.5766	0.5244	0.4446	0.4520
Θ(average)	1.3763	1.3522	1.3663	1.3865	1.4258	1.4909
$e^{\epsilon\square}_{\text{mic}}$	0.00	14.4814	21.3185	29.9109	41.8428	56.8764



(a) additional interphases (b) phase-preserving

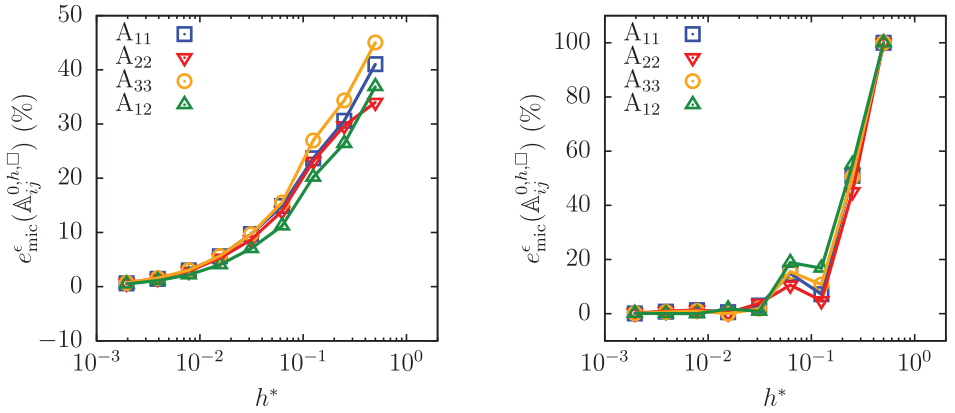
FIGURE 10 Pixel coarsening: relative percental micro errors, total $e^{\epsilon}_{\text{mic}}/||\boldsymbol{u}||_{A(\mathcal{B}_\epsilon)}$, resolution $e^{\epsilon\square}_{\text{mic}}/||\boldsymbol{u}||_{A(\mathcal{B}_\epsilon)}$, and discretization $e^{\epsilon h}_{\text{mic}}/||\boldsymbol{u}||_{A(\mathcal{B}_\epsilon)}$ versus characteristic element length h^*, resolution from 512^2 px to 2^2 px

the homogenized Young's modulus equals this volume average. For the present phase fraction ratio of matrix to inclusion of 75.81% to 24.19% the obtained Young's modulus is 122.28 MPa in that limiting case.

For the phase-preserving coarsening variant B the "majority-wins" strategy violates the initial phase ratio. Here, in the limiting case of one single pixel the homogenized elasticity coincides with that of the matrix phase.

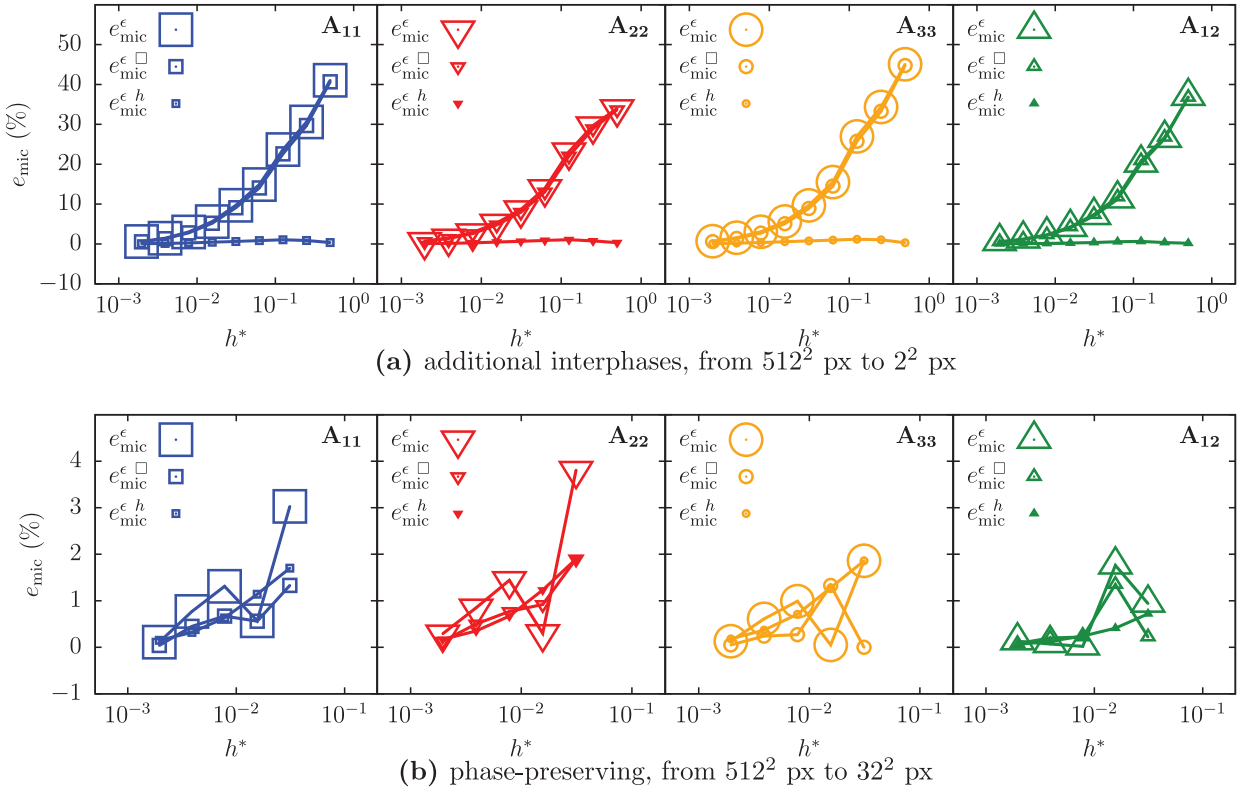
The reference solution is obtained on a grid with $h_\square = h = 1/2048$ mm. The phase distribution coincides for $h_\square = 1/2048$ mm and $h_\square = 1/1024$ mm which implies that there is no resolution error for the case of 1024^2 pixels.

Results are displayed in Table 2 and in Figure 10. We use $h^* := \sqrt{1/num_{\text{elem}}}$ with num_{elem} the number of elements in a unit cell for the inclusion of results for nonuniform meshes. For square microdomains with uniform meshes it holds $h^* = h$. The micro error and its parts monotonously increase for both coarsening variants with the exception of the discretization error in the last two steps of extremely coarse resolutions, which are in either case not competitive. The resolution error



(a) additional interphases (b) phase-preserving

FIGURE 11 Pixel coarsening: relative total micro error $e^{\epsilon}_{\mathrm{mic}}(\mathbb{A}^{0,h,\square}_{ij})$ versus characteristic element length h^*, resolution from 512^2 px to 2^2 px



(a) additional interphases, from 512^2 px to 2^2 px

(b) phase-preserving, from 512^2 px to 32^2 px

FIGURE 12 Pixel coarsening: relative micro errors for $\mathbb{A}_{ij}$, total $e^{\epsilon}_{\mathrm{mic}}$, resolution $e^{\epsilon\square}_{\mathrm{mic}}$, and discretization $e^{\epsilon\,h}_{\mathrm{mic}}$ versus characteristic element length h^*

is larger than the discretization error, having a ratio of approximately 2:1. Inequality (21) is fulfilled. Error estimation for coarsening with new interphases is less accurate than for phase-preserving coarsening; for phase-distinction in stress computation at interfaces it considerably overestimates the error, see Θ(quadruplex) in Table 2, for stress averaging it considerably underestimates it, Θ(average). For the phase-preserving coarsening case however error estimation (based on duplex stress) is quite accurate, Θ(duplex).

A second measure of the total micro error is the error in the coefficients of the homogenized elasticity tensor displayed in Figure 11. In Figure 12 the decomposition into resolution and discretization error is provided. The errors are computed

TABLE 3 Elastic coefficients: for the two phases and the two-phase composite in (MPa) based on a 2048^2 element discretization for a 1024^2 px resolution

	vol.%	$\mathbb{A}_{11}$	$\mathbb{A}_{22}$	$\mathbb{A}_{33}$	$\mathbb{A}_{12}$
inclusion phase	24.2	213.44	213.44	80.04	53.36
homogenized		127.99	129.54	47.82	32.13
matrix phase	75.8	111.11	111.11	41.67	27.78

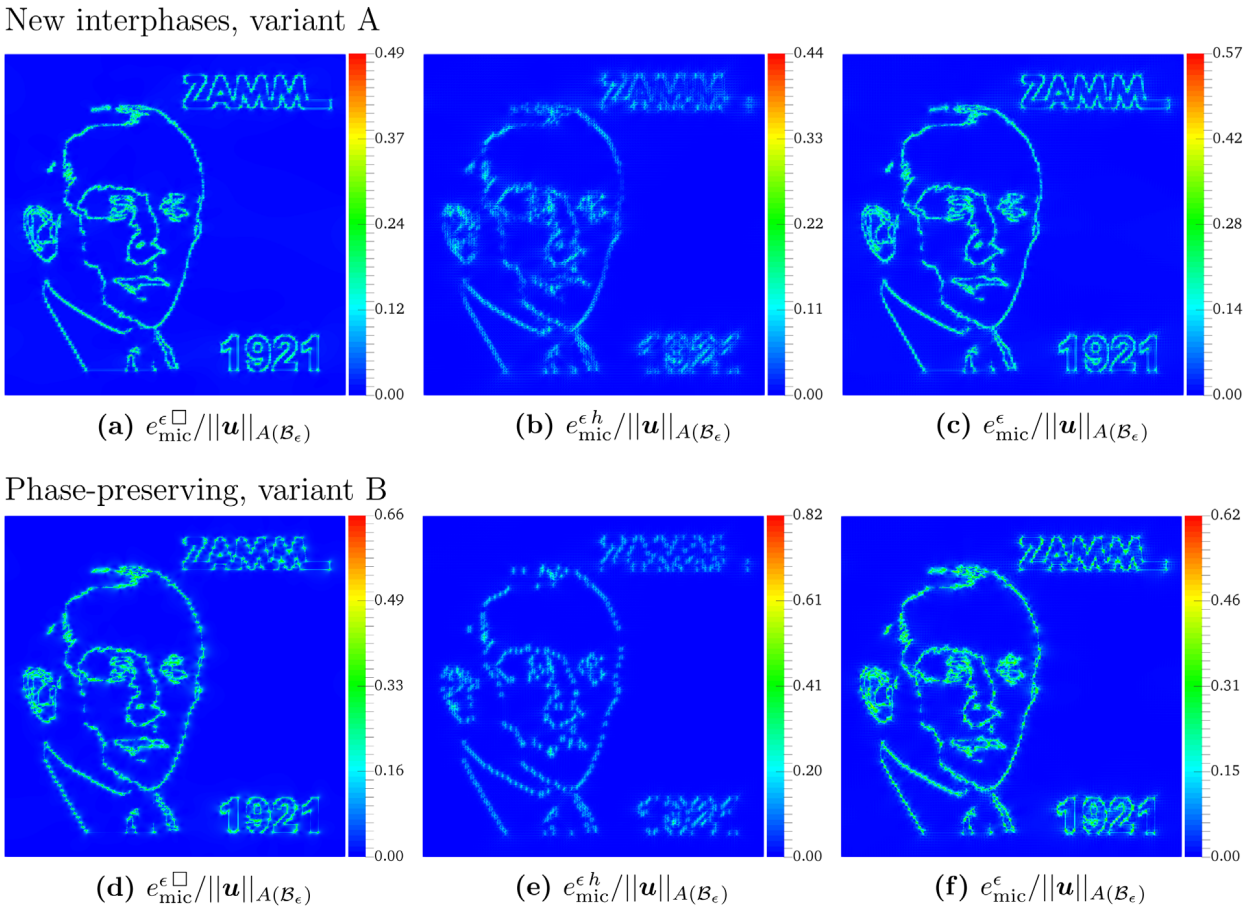


FIGURE 13 Error distributions for 128^2 px resolution: (from left to right) resolution error, discretization error, total error

according to (21) in the adaption to the case of the elasticity coefficients (24). Exact values of the homogenized elasticities for a 2048^2 discretization along with a 1024^2 px resolution are listed in Table 3.

For the coarsening with additional interphases the micro error is continuously increasing in all components of the homogenized elasticity tensor, thereby overestimating the true stiffness, see Figure 11(a). The resolution error is predominant in comparison to the discretization error, the latter is bounded to less than 2% in the first 5 stages of coarsening Figure 12(a).

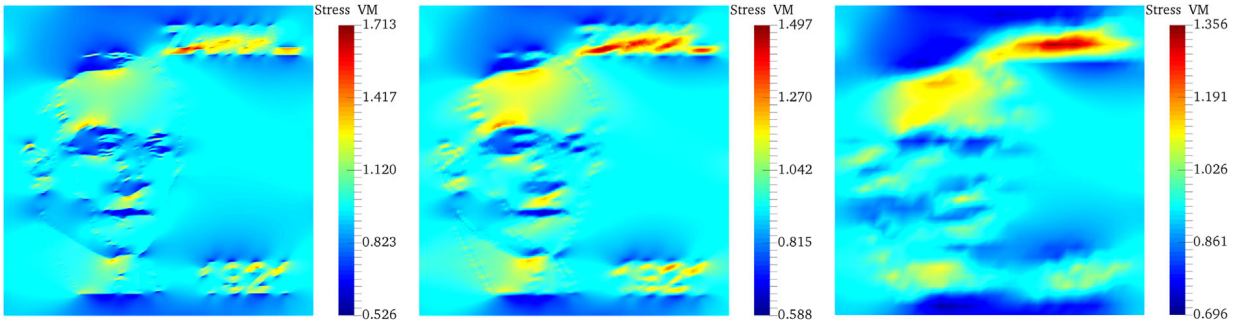
For the phase-preserving coarsening variant the micro error is throughout smaller in the first five coarsening steps (down to 32^2 px) than for the coarsening with new interphases Figure 11(b). The error continuously increases, coarsening step no. 4 is an outlier. The resolution and discretization error are roughly of the same magnitude Figure 12(b).

Figure 13 shows the distribution of micro errors and their constituents for the two coarsening variants A and B. Errors are confined to phase boundaries.

Table 4 lists with the maximal deflection of the macrostructure a macro accuracy measure and with the maximal von Mises stress on the chosen microdomain a local micro accuracy measure. The latter becomes relevant if inelastic material behavior comes into play.

TABLE 4 Pixel coarsening: maximum deflection u_{max} in (mm) of cantilever beam and maximum value of von Mises stress in (N/mm^2) for macro GP at $x = y = 2.1132$ mm

uniform pixel coarsening										
px	**2048^2**	**512^2**	**256^2**	**128^2**	**64^2**	**32^2**	**16^2**	**8^2**	**4^2**	**2^2**
additional interphases										
u_{max}	86.57	86.50	86.40	86.22	85.92	85.45	84.86	83.90	83.15	82.11
$\max\{\sigma_{\text{von Mises}}\}$	1.930	1.652	1.553	1.473	1.377	1.285	1.112	1.034	1.011	0.987
phase-preserving										
u_{max}	86.57	86.56	86.48	86.40	86.48	86.17	88.22	87.25	92.68	99.74
$\max\{\sigma_{\text{von Mises}}\}$	1.930	1.713	1.595	1.497	1.38	1.356	1.067	1.04	0.908	0.791



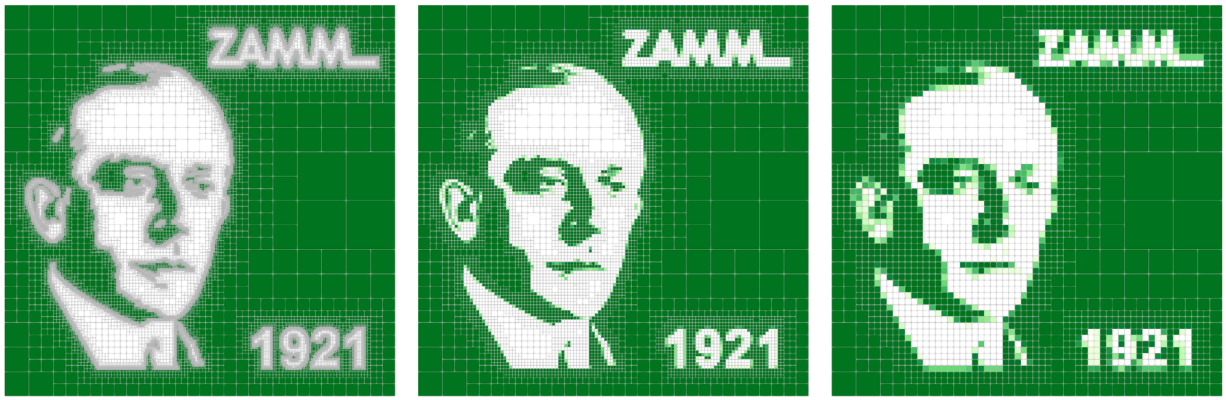
(a) 512^2px (b) 128^2px (c) 32^2px

FIGURE 14 Von Mises stress for uniform discretizations from phase-preserving coarsening

6.3 | Adaptive mesh coarsening

The first step of coarsening was a uniform pixel coarsening changing the image resolution. The second step carries out a consecutive, adaptive, microstructure-guided mesh coarsening based on the uniformly coarsened pixel resolutions. In this second step the discretization at interfaces is maintained for accuracy, but in the phase interior mesh coarsening is carried for efficiency. Consequently, this step introduces an additional discretization error but preserves exactly the existing phase distributions including their boundaries. Three different versions of adaptively coarsened meshes are shown in Figure 15, which are each based on different uniform pixel resolutions. As a consequence, the maximal number of quadtree-type adaptive coarsening steps differs between these versions.

Table 5 indicates the considerable computational savings of adaptive mesh coarsening at moderate accuracy losses. Error estimation for phase-preserving coarsening turns out to be much more accurate than coarsening with new interphases as

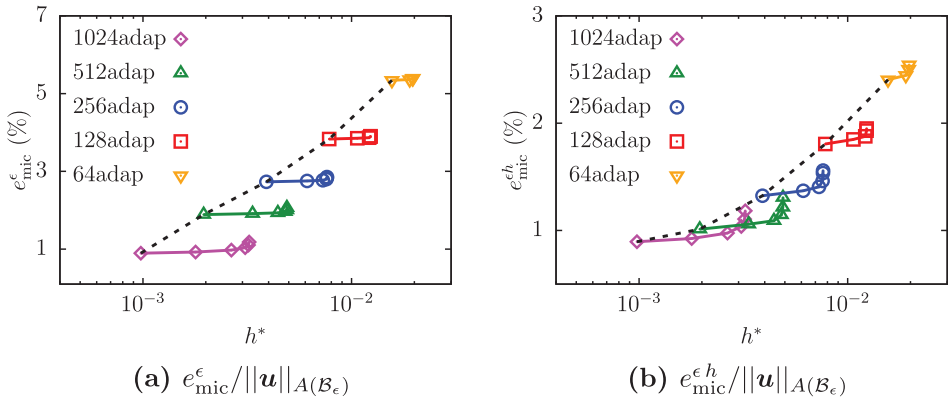


(a) 1024^2 px, adap7 (b) 128^2px, adap4 (c) 64^2px, adap3

FIGURE 15 Adaptive mesh coarsening after uniform pixel coarsening along with new interphases in (b) and (c). The first entry in the subcaptions refers to the resolution, the second to the number of steps carried out in adaptive mesh coarsening

TABLE 5 Adaptive mesh coarsening: for different adaptive mesh coarsening steps (1 to 5, 0 refers to the discretization with 512^2 px) the number of degrees of freedom (ndof) along with the ndof-factor compared to the uniform mesh, and the estimated errors for different methods are displayed. All error data in 10^{-4} (MPa)

adaptive mesh coarsening						
step no.	**0**	**1**	**2**	**3**	**4**	**5**
additional interphases						
ndof	524 288	177 298	106 272	91 398	88 668	88 264
factor	1.0000	0.3382	0.2027	0.1743	0.1691	0.1684
$e^{\epsilon}_{\mathrm{mic}}$	16.5271	16.7479	16.9109	17.1809	17.5462	18.0478
$\bar{e}^{\epsilon h}_{\mathrm{mic}}$(quadruplex)	6.2388	6.8115	7.2112	7.8506	8.6029	9.4534
$\bar{e}^{\epsilon h}_{\mathrm{mic}}$(average)	11.9762	12.2845	12.5108	12.8904	13.3627	13.9266
$e^{\epsilon h}_{\mathrm{mic}}$	8.8569	9.2594	9.5493	10.0171	10.6284	11.4299
Θ(quadruplex)	0.7044	0.7356	0.7552	0.7837	0.8094	0.8271
Θ(average)	1.3522	1.3267	1.3101	1.2868	1.2573	1.2184
$e^{\epsilon\square}_{\mathrm{mic}}$	14.4814					
phase-preserving						
ndof	524 288	172 422	100 642	85 644	82 868	82 452
factor	1.0000	0.3289	0.1920	0.1634	0.1581	0.1573
$e^{\epsilon}_{\mathrm{mic}}$	23.1379	23.3216	23.4440	23.6409	23.9109	24.2939
$\bar{e}^{\epsilon h}_{\mathrm{mic}}$	10.7376	11.1378	11.3956	11.8141	12.3389	12.9726
$e^{\epsilon h}_{\mathrm{mic}}$	12.6256	12.9611	13.1778	13.5233	13.9912	14.6310
Θ (duplex)	0.8505	0.8593	0.8648	0.8736	0.8819	0.8867
$e^{\epsilon\square}_{\mathrm{mic}}$	21.4106					
Reference solution for 2048^2 px, ndof= 8 445 856.						



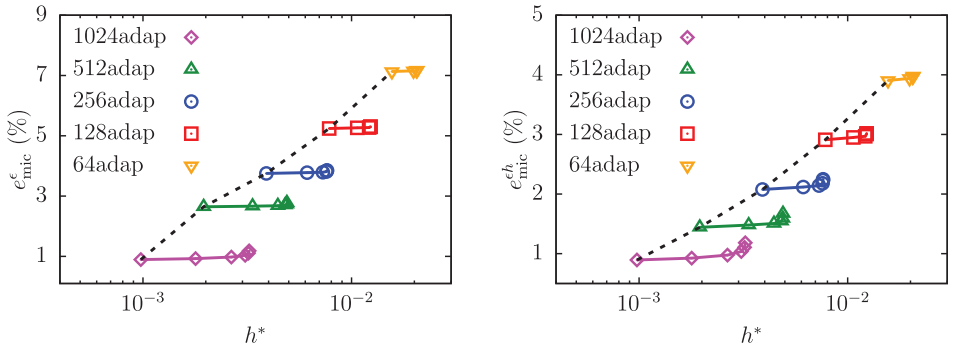
(a) $e^{\epsilon}_{\mathrm{mic}}/||\boldsymbol{u}||_{A(\mathcal{B}_\epsilon)}$ (b) $e^{\epsilon h}_{\mathrm{mic}}/||\boldsymbol{u}||_{A(\mathcal{B}_\epsilon)}$

FIGURE 16 Adaptive mesh coarsening, additional interphases: relative micro errors: (a) total error and (b) discretization error versus characteristic element length h^*. The dashed line marks the path of uniform pixel/mesh coarsening

indicated by effectivity indices much closer to one. Notice that the effectivity indices for the different stress computations in error estimation confirm the preliminary results of Section 5.

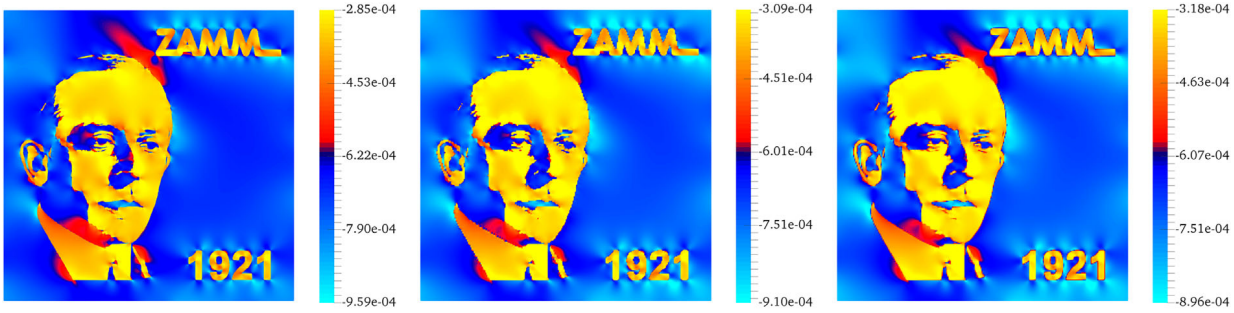
The diagrams in Figures 16 and 17 underpin that uniform resolution coarsening along with the same uniform discretization implies a discrete error jump, which is considerably larger than the error accumulating in several adaptive mesh coarsening steps at a fixed resolution. More precisely, adaptive mesh coarsening at discretization $h_\square$ is in general the better choice than resolution and discretization $2\,h_\square$, since the corresponding reduction of unknowns is at least as strong as the ndof-reduction of the pixel coarsening step, the error increase throughout much smaller.

Notice that in Figures 16 and 17 a relative error is chosen defined as the absolute micro error over the total energy of the microdomain. In this representation the error is put into the perspective of the energy which is more descriptive than e.g. the percental error increase which was used in [23].



(a) $e^{\epsilon}_{\mathrm{mic}}/||\boldsymbol{u}||_{A(\mathcal{B}_\epsilon)}$ (b) $e^{\epsilon\, h}_{\mathrm{mic}}/||\boldsymbol{u}||_{A(\mathcal{B}_\epsilon)}$

FIGURE 17 Adaptive mesh coarsening, phase-preserving: relative micro errors: (a) total error and (b) discretization error versus characteristic element length h^*. The dashed line marks the path of uniform pixel/mesh coarsening



(a) ndof=2 097 152 uni (b) ndof=131 072 uni, preserv2 (c) ndof=131 072 uni, interph2

(d) ndof=209 250 adap3 (e) ndof=36 886 preserv2 & adap2 (f) ndof=40 322 interph2 & adap2

FIGURE 18 Shear strain distributions: on microdomain at $x = 2\,752.1$ mm, $y = 552.1$ mm for (a) uniform mesh and its (d) three times adaptively coarsened counterpart, (b) phase-preserving, twicely uniform resolution coarsening and its (e) twicely adaptively coarsened counterpart, (c) twicely uniform resolution coarsening with interphases and its (f) twicely adaptively coarsened counterpart

6.4 | Comparison of strain

Figure 18 shows the distribution of shear strain at an exemplary microdomain for the initial uniform micro mesh and several coarsened meshes having a reduction of unknowns of at least 90%. The best agreement—both qualitative and quantitative—with the reference solution in Figure 18(a) is observed for the three times adaptively coarsened mesh in Figure 18(d) having the same pixel resolution as the reference. Compared to the other coarsened meshes this one exhibits the largest ndof due to the finely resolved interfaces, where coarsening is confined to the phase interior.

Nevertheless, the solutions with uniformly coarsened meshes (phase-preserving in Figure 18(b) and with interphases in Figure 18(c)) also show a very good agreement with the initial uniform discretization. There are only minor deviations in the maximum and minimum values of the shear strain, the qualitative strain distribution is quite accurate.

A further adaptive mesh coarsening on top of the already uniformly coarsened resolution/meshes (Figure 18(e) and (f)) renders an additional ndof reduction for very minor deviations in the resulting strain distributions.

6.5 | Results and discussion

The results can be summarized as follows:

1. Pixel coarsening along with new, artificial interphases, variant A and standard in bitmap image representation, introduces physical artifacts. They manifest in reduced interfacial stiffness mismatch and therefore in reduced maxima of stress and of their interfacial jumps. Error estimation along with the sound phase-distinction in stress computation introduces vanishing errors at interfaces, where they are truly largest. It is of all things the falsifying stress computation based on stress averaging, which reduces this effect. Hence the 'crime' in resolution coarsening can only be alleviated by an additional 'crime' in stress-computation. Although errors in the approximation of true micro errors are of the same magnitude as for variant B, errors in the effective elasticities are considerably larger.
2. Phase-preserving coarsening, variant B and the very standard in image segmentation, primarily relies on the knowledge of number and properties of individual phases. It maintains the phase contrast and therefore interfacial stress maxima and jumps, at least approximately, if the physically sound phase-distinction in stress computation for interface nodes is applied. Another plus compared to variant A of coarsening is its accuracy in estimating the discretization error. The phase fraction ratio is not preserved, deviations typically increase the more, the coarser the resolution.
3. Adaptive mesh coarsening—fine resolution at interfaces, mesh coarsening in the phases—is a most effective means to achieve computational savings at very moderate error increases. The best strategy for achieving a target accuracy at minimal costs is to carry out resolution coarsening, which defines the accuracy level, and consecutive adaptive mesh coarsening steps, which preserves this accuracy level.
4. The almost constant error in effective properties for micro resolutions 1024^2 px down to 64^2 px for the phase-preserving case indicates the trustworthiness in image acquisition of this microstructure. It is however restricted to macroscale results.
5. Microscale quantities are clearly much more sensitive to microscale resolution than macroscale, effective properties. A microstructure, coarse in resolution and discretization, which is likely rejected on the microscale for its large errors, can show accurate macroscale properties as, e.g., effective stiffness or maximal deflection of the macrostructure.
6. The augmented micro error analysis enables a detailed accuracy-efficiency balance. It quantifies the potential of resolution coarsening and adaptive mesh coarsening for a considerable efficiency gain at target accuracy. For the present microstructure in its initial, uniform 1024^2 px resolution, a reduction of unknowns to 0.6% (from 2.1 mio. to 12k) can be achieved by a 128^2 px resolution along with adaptive mesh coarsening with the total micro error hardly above 5%.

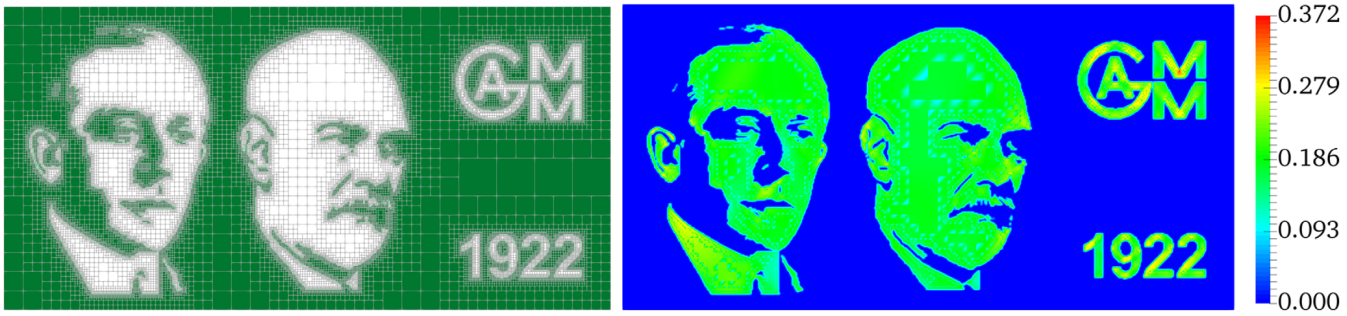
With its newly introduced error analysis on the microscale the present work goes beyond the few existing investigations on the impact of image resolution on effective properties. They refer to diffusivity and conductivity of cathode catalyst layers [29], to the impact on global stress-strain curves, local damage initiation of foamed concrete [42] and on flow in porous media [53] and some applications in digital rock physics [6].

Feasibility in practice. Error computation is not feasible in practice in view of the need for very fine resolutions and discretizations. A posteriori error estimation however is—by standard means—restricted to the discretization error, and even for that error part the accuracy hence reliability is not granted. In practice, already a subvolume of the full RVE preserving stiffness contrast of the phases and key characteristics of interface topology can inform about the quality of error estimation, since a reference solution on a fine mesh is then within reach. When the point of departure is a microstructure in intermediate resolution, the deviations in the homogenized elasticities for further resolution coarsening provides a pragmatic hint on accuracy, but it should not be mistaken for a verified error measure.

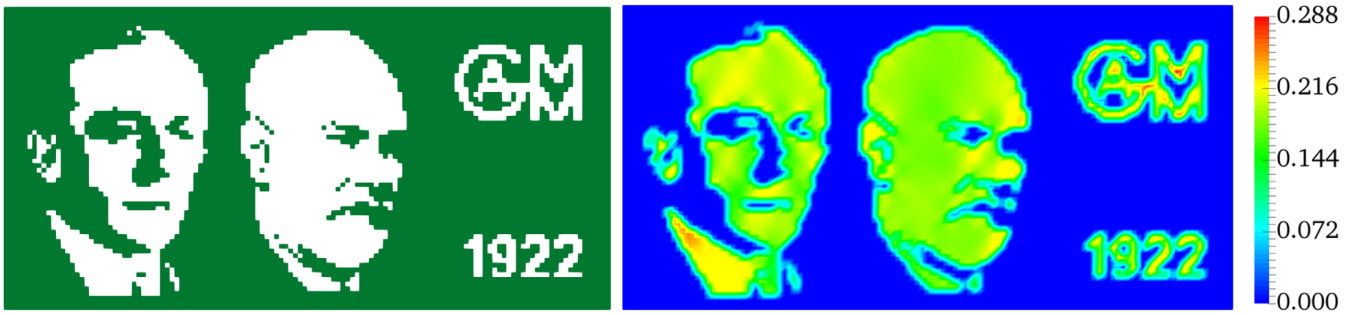
For the first steps of uniform, phase-preserving pixel coarsening, the resolution error is approximately twice the value of the discretization error in this example. If such a—problem-specific—ratio was available, then the estimate of the discretization error could approximate the resolution error and thereby (an upper bound of) the total micro error by (21). It provides an interesting link to the FCM where the quadrature error (which corresponds to the resolution error in the



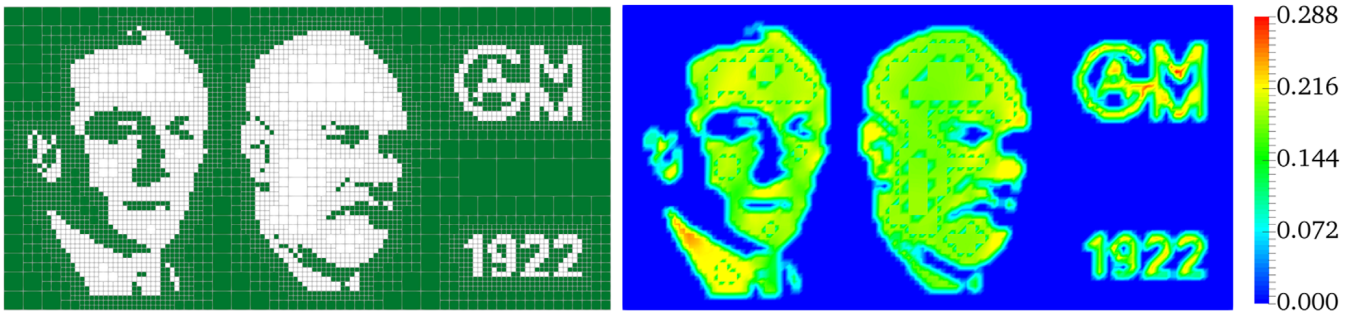
(a) 512×256 resolution, uniform mesh, ndof=1 191 192 : equiv. pl. strain α.



(b) 512×256 resolution, 5 adaptive coarsening steps, ndof=365 400 : equiv. pl. strain α.



(c) 128×64 resolution, uniform mesh, ndof=76 632 : equiv. pl. strain α.



(d) 128×64 resolution, 3 adaptive coarsening steps, ndof=49 206 : equiv. pl. strain α.

FIGURE 19 GAMM-founders microstructure with von Mises elasto-plasticity: (a,c) different uniform, two-phase resolutions along with their (b,d) adaptively coarsened meshes result in (a–d, right column) different distributions of equivalent plastic strain

present work) shall be bound to the magnitude of the discretization error. Only very recently error estimation for FCM has been introduced [10].

For the prototype model of linear elasticity considered here, the method of choice would be of course the pre-computation of an accurate homogenized elasticity tensor for the microstructure in high resolution on a fine micromesh, which is then employed in all consecutive, single-scale finite element simulations. This is the setting of a serial or hierarchical multiscale method in contrast to the concurrent framework of a two-scale FEM.

7 | CONCLUSION AND OUTLOOK

In this work we have introduced a rationale to assess microstructure images of finite resolution for use in computational solid mechanics. The analysis of multiphase solids distinguishes between a finite resolution error and a discretization error. It is consistently embedded in the unified framework of errors in two-scale finite element methods for numerical homogenization, FE-HMM and FE^2.

For the considered example the best choice is a combination of phase-preserving resolution coarsening with a consecutive adaptive mesh coarsening; it results in considerable computational savings at controlled errors. We consider that combination as advantageous for other examples likewise, but the range of resolution and discretization at a target accuracy is case-dependent, its identification therefore left to an explicit error analysis.

Since the resolution error is not directly accessible to error estimation and for that reason the total micro error neither, this aspect deserves further investigation. Worth for additional investigations is the influence of pixel size with respect to a characteristic microstructural length scale and the impact of phase contrast on errors. The gradual deviation from the true RVE characteristics by means of continuous resolution coarsening could be measured by statistical similarity measures thus making a link to the computed resolution errors.

The analysis of resolution and discretization errors in image data is similarly applicable to 3D problems following from reconstructed voxel-microstructures. Moreover, the concept of error-controlled, phase-preserving coarsening opens the door to other applications, in the mechanics of solids to nonlinear models and methods such as hyperelasticity or inelastic constitutive laws in nonlinear computational homogenization.

As an example, we consider a two-phase von-Mises-Prandtl-microstructure[3] subject to PBC. The 3D unit cell of edge lengths $\epsilon_x = 2$ mm, $\epsilon_y = 1$ mm, and thickness $\epsilon_z = 0.1$ mm exhibits an initial uniform pixel resolution of 2048×1024×2. The elastic properties coincide with the previous example. The matrix phase is purely elastic, the inclusion phase follows von-Mises elasto-plasticity [36], a model not only frequently used for metal plasticity but also a source of inspiration for further original work till today [13]. The initial yield stress is $y_0 = 0.1$ MPa, the constant modulus of isotropic hardening is $H = 5$ MPa. For a uniaxial stretch in x-direction of $\varepsilon_{xx} = 0.088$ using 22 uniform load steps, Figure 19 displays for two different resolutions along with their adaptively coarsened discretizations the results in terms of equivalent plastic strain as the quantity of interest. Image resolution has a strong effect on maximal values, adaptive coarsening maintaining the resolution however only a very minor one. This suggests that elasto-plastic analyses are more demanding in resolution for results of high fidelity than merely elastic analyses are. Results in depth are discussed elsewhere.

ACKNOWLEDGEMENTS

Bernhard Eidel acknowledges support by the Deutsche Forschungsgemeinschaft (DFG) within the Heisenberg program (grant no. EI 453/5-1). Simulations were performed with computing resources granted by RWTH Aachen University under project ID BUND0005.

Open access funding enabled and organized by Projekt DEAL.

REFERENCES

[1] Abdulle, A.: Analysis of the heterogeneous multiscale FEM for problems in elasticity. Math. Models Methods Appl. Sci. 16(04), 615–635 (2006)

[2] Abdulle, A.: The finite element heterogeneous multiscale method: a computational strategy for multiscale PDEs. GAKUTO Int. Ser. Math. Sci. Appl. 31, 133–181 (2009)

[3] Andrä, H., Combaret, N., Dvorkin, J., Glatt, E., Han, J., Kabel, M., Keehm, Y., Krzikalla, F., Lee, M., Madonna, C., Marsh, M., Mukerji, T., Saenger, E.H., Sain, R., Saxena, N., Ricker, S., Wiegmann, A., Zhan, X.: Digital rock physics benchmarks—Part I: imaging and segmentation. Comput. Geosci. 50, 25–32 (2013)

[4] Andrä, H., Combaret, N., Dvorkin, J., Glatt, E., Han, J., Kabel, M., Keehm, Y., Krzikalla, F., Lee, M., Madonna, C., Marsh, M., Mukerji, T., Saenger, E.H., Sain, R., Saxena, N., Ricker, S., Wiegmann, A., Zhan, X.: Digital rock physics benchmarks—Part II: computing effective properties. Comput. Geosci. 50, 33–43 (2013)

[5] Balzani, D., Scheunemann, L., Brands, D., Schröder, J.: Construction of two- and three-dimensional statistically similar RVEs for coupled micro-macro simulations. Comput. Mech. 54(5), 1269–1284 (2014)

[6] Berg, C.F., Lopez, O., Berland, H.: Industrial applications of digital rock technology. J. Petroleum Sci. Eng. 157, 131–147 (2017)

[7] Ciarlet, P. G.: The Finite Element Method for Elliptic Problems. Volume V.4 of *Studies in Mathematics and Its Applications*. North-Holland, Elsevier North-Holland, Amsterdam and New York (1978)

[3] Richard von Mises (1883–1953) and Ludwig Prandtl (1875–1953) founded the Gesellschaft für Angewandte Mathematik und Mechanik (GAMM) in 1922.

[8] d'Agostino, M. V., Barbagallo, G., Ghiba, I.-D., Eidel, B., Neff, P., Madeo, A.: Effective description of anisotropic wave dispersion in mechanical band-gap metamaterials via the relaxed micromorphic model. J. Elast. 90(10), 99 (2019)

[9] Dauge, M., Düster, A., Rank, E.: Theoretical and numerical investigation of the finite cell method. J. Sci. Comput. 65(3), 1039–1064 (2015)

[10] Di Stolfo, P., Rademacher, A., Schröder, A.: Dual weighted residual error estimation for the finite cell method. J. Numerical Math. 27(2), 101–122 (2019)

[11] Düster, A., Parvizian, J., Yang, Z., Rank, E.: The Finite Cell Method for three-dimensional problems of solid mechanics. Comput. Methods Appl. Mechan. Eng. 197(45-48), 3768–3782 (2008)

[12] Düster, A., Sehlhorst, H.-G., Rank, E.: Numerical homogenization of heterogeneous and cellular materials utilizing the finite cell method. Comput. Mech. 50(4), 413–431 (2012)

[13] Dyck, A., Böhlke, T.: A micro–mechanically motivated phenomenological yield function for cubic crystal aggregates. ZAMM 100(4), 582 (2020)

[14] E, W., Engquist, B.: The heterogeneous multiscale methods. Commun. Math. Sci. 1(1), 87–132 (2003)

[15] E, W., Ming, P., Zhang, P.: Analysis of the heterogeneous multiscale method for elliptic homogenization problems. J. Am. Mathe. Soc. 18(01), 121–157 (2005)

[16] Eidel, B., Fischer, A.: The heterogeneous multiscale finite element method FE-HMM for the homogenization of linear elastic solids. PAMM 16(1), 521–522 (2016)

[17] Eidel, B., Fischer, A.: The heterogeneous multiscale finite element method for the homogenization of linear elastic solids and a comparison with the FE^2 method. Comput. Methods Appl. Mechanics Eng. 329, 332–368 (2018)

[18] Eidel, B., Fischer, A., Gote, A.: A nonlinear FE-HMM formulation along with a novel algorithmic structure for finite deformation elasticity. PAMM 18(1), e201800457 (2018)

[19] Eidel, B., Gote, A., Ruby, M., Holzer, L., Keller, L., Jiang, X.: Estimating the effective elasticity properties of a diamond/β-SiC composite thin film by 3D reconstruction and numerical homogenization. Diam. Relat. Mater. 97, 107406 (2019)

[20] Fangye, Y.F., Miska, N., Balzani, D.: Automated simulation of voxel-based microstructures based on enhanced finite cell approach. Arch. Appl. Mech. 90(10), 2255–2273 (2020)

[21] Feyel, F., Chaboche, J.-L.: FE^2 multiscale approach for modelling the elastoviscoplastic behaviour of long fibre SiC/Ti composite materials. Comput. Methods Appl. Mechanics Eng. 183(3-4), 309–330 (2000)

[22] Fischer, A., Eidel, B.: Convergence and error analysis of FE-HMM/FE^2 for energetically consistent micro-coupling conditions in linear elastic solids. Eur. J. Mechan. - A/Solids 77 (2019)

[23] Fischer, A., Eidel, B.: Error analysis for quadtree-type mesh coarsening algorithms adapted to pixelized heterogeneous microstructures. Comput. Mech. 16(04), 615 (2020)

[24] Glüge, R., Altenbach, H., Mahmood, N., Beiner, M.: On the difference between the tensile stiffness of bulk and slice samples of microstructured materials. Appl. Compos. Mater. (2020)

[25] Golanski, D., Terada, K., Kikuchi, N.: Macro and micro scale modeling of thermal residual stresses in metal matrix composite surface layers by the homogenization method. Comput. Mech. 19(3), 188–202 (1997)

[26] Gravenkamp, H., Duczek, S.: Automatic image-based analyses using a coupled quadtree-SBFEM/SCM approach. Comput. Mech. 60(4), 559–584 (2017)

[27] Hill, R.: Elastic properties of reinforced solids: some theoretical principles. J. Mech. Phys. Solids 11(5), 357–372 (1963)

[28] Hill, R.: On constitutive macro-variables for heterogeneous solids at finite strain. Proc. R. Soc. A: Math. Phys. Eng. Sci. 326(1565), 131–147 (1972)

[29] Hutzenlaub, T., Becker, J., Zengerle, R., Thiele, S.: How coarsening the 3d reconstruction of a porous material influences diffusivity and conductivity values. ECS Electrochem. Lett. 2(2), F14–F17 (2013)

[30] Jecker, O., Abdulle, A.: Numerical experiments for multiscale problems in linear elasticity. In: Karasözen, B., Manguoğlu, M., Tezer-Sezgin, M., Göktepe, S., Uğur, Ö., (eds.), Numerical Mathematics and Advanced Applications ENUMATH 2015, volume 112 of *Lecture Notes in Computational Science and Engineering*, pp. 123–131. Springer International Publishing, Cham (2016)

[31] Kouznetsova, V., Brekelmans, W.A.M., Baaijens, F.P.T.: An approach to micro-macro modeling of heterogeneous materials. Comput. Mech. 27(1), 37–48 (2001)

[32] Kumar, H., Briant, C.L., Curtin, W.A.: Using microstructure reconstruction to model mechanical behavior in complex microstructures. Mech. Mater. 38(8-10), 818–832 (2006)

[33] Legrain, G., Cartraud, P., Perreard, I., Moës, N.: An X-FEM and level set computational approach for image-based modelling: application to homogenization. Int. J. Numer. Methods Eng. 86(7), 915–934 (2011)

[34] Lian, W.D., Legrain, G., Cartraud, P.: Image-based computational homogenization and localization: comparison between X-FEM /levelset and voxel-based approaches. Comput. Mech. 51(3), 279–293 (2013)

[35] Miehe, C., Schröder, J., Schotte, J.: Computational homogenization analysis in finite plasticity simulation of texture development in polycrystalline materials. Comput. Methods Appl. Mechan. Eng. 171(3-4), 387–418 (1999)

[36] Mises, R.v.: Mechanik der plastischen Formänderung von Kristallen. ZAMM 8(3), 161–185 (1928)

[37] Mishnaevsky, L.L.: Automatic voxel-based generation of 3D microstructural FE models and its application to the damage analysis of composites. Mater. Sci. Eng.: A 407(1-2), 11–23 (2005)

[38] Miska, N., Balzani, D.: Quantification of uncertain macroscopic material properties resulting from variations of microstructure morphology based on statistically similar volume elements: application to dual-phase steel microstructures. Comput. Mech. 54(3), 1269 (2019)

[39] Moulinec, H., Suquet, P.: A numerical method for computing the overall response of nonlinear composites with complex microstructure. Comput. Methods Appl. Mechan. Eng. 157(1-2), 69–94 (1998)
[40] Neff, P., Eidel, B., d'Agostino, M.V., Madeo, A.: Identification of scale-independent material parameters in the relaxed micromorphic model through model-adapted first order homogenization. J. Elast. 16(04), 615 (2019)
[41] Nejad, R.S., Wieners, C.: Parallel inelastic heterogeneous multi-scale simulations. In: Diebels, S., Rjasanow, S. (eds.), Multi-scale Simulation of Composite Materials, volume 23 of *Mathematical Engineering*, pp. 57–96. Springer, Berlin, Heidelberg, (2019)
[42] Nguyen, T.T., Yvonnet, J., Zhu, Q.-Z., Bornert, M., Chateau, C.: A phase field method to simulate crack nucleation and propagation in strongly heterogeneous materials from direct imaging of their microstructure. Eng. Fract. Mech. 139:18–39 (2015)
[43] Ohlberger, M.: A posteriori error estimates for the heterogeneous multiscale finite element method for elliptic homogenization problems. Multiscale Modeling Simulation 4(1), 88–114 (2005)
[44] Ohser, J., Schladitz, K.: 3D Images of Materials Structures: Processing and Analysis. Wiley, Weinheim (2006)
[45] Parvizian, J., Düster, A., Rank, E.: Finite cell method. Comput. Mech. 41(1), 121–133 (2007)
[46] Povirk, G.L.: Incorporation of microstructural information into models of two-phase materials. Acta Metall. Mater. 43(8), 3199–3206 (1995)
[47] Ren, W., Yang, Z., Sharma, R., Zhang, C., Withers, P.J.: Two-dimensional X-ray CT image based meso-scale fracture modelling of concrete. Eng. Fract. Mech. 133, 24–39 (2015)
[48] Saputra, A., Talebi, H., Tran, D., Birk, C., Song, C.: Automatic image-based stress analysis by the scaled boundary finite element method. Int. J. Numer. Methods Eng. 109(5), 697–738 (2017)
[49] Scheunemann, L., Balzani, D., Brands, D., Schröder, J.: Design of 3D statistically similar representative volume elements based on Minkowski functionals. Mech. Mater. 90, 185–201 (2015)
[50] Schillinger, D., Düster, A., Rank, E.: The hp-d-adaptive Finite Cell Method for geometrically nonlinear problems of solid mechanics. Int. J. Numer. Methods Eng. 89(9), 1171–1202 (2012)
[51] Schillinger, D., Ruess, M.: The Finite Cell Method : A review in the context of higher-order structural analysis of CAD and image-based geometric models. Arch. Comput. Methods Eng. 22(3), 391–455 (2015)
[52] Schröder, J., Balzani, D., Brands, D.: Approximation of random microstructures by periodic statistically similar representative volume elements based on lineal-path functions. Arch. Appl. Mech. 81(7), 975–997 (2011)
[53] Shah, S.M., Gray, F., Crawshaw, J.P., Boek, E.S.: Micro-computed tomography pore-scale study of flow in porous media: effect of voxel resolution. Adv. Water Resour. 95, 276–287 (2016)
[54] Smit, R., Brekelmans, W., Meijer, H.: Prediction of the mechanical behavior of nonlinear heterogeneous systems by multi-level finite element modeling. Comput. Methods Appl. Mechan. Eng. 155(1-2), 181–192 (1998)
[55] Zienkiewicz, O.C., Zhu, J.Z.: A simple error estimator and adaptive procedure for practical engineering analysis. Int. J. Numer. Methods Eng. 24(2), 337–357 (1987)
[56] Zienkiewicz, O.C., Zhu, J.Z.: The superconvergent patch recovery and a posteriori error estimates. Part 1: The recovery technique. Int. J. Numer. Methods Eng. 33(7), 1331–1364 (1992)
[57] Zienkiewicz, O.C., Zhu, J.Z.: The superconvergent patch recovery and a posteriori error estimates. Part 2: error estimates and adaptivity. Int. J. Numer. Methods Eng. 33(7), 1365–1382 (1992)

How to cite this article: Eidel B, Fischer A, Gote A. From image data towards microstructure information – Accuracy analysis at the digital core of materials. *Z Angew Math Mech*. 2020;e202000245.
https://doi.org/10.1002/zamm.202000245

8.5 Veröffentlichung: Computational homogenization of concrete in the cyber Size-Resolution-Discretization (SRD) parameter space

Die fünfte Veröffentlichung von Ajinkya Gote, Prof. Bernhard Eidel, Prof. Chuanzeng Zhang und Andreas Fischer mit dem Titel **Computational homogenization of concrete in the cyber Size-Resolution-Discretization (SRD) parameter space** wurde 2022 in *Finite Elements in Analysis & Design* veröffentlicht.

Der Anteil des Doktoranden an dieser Veröffentlichung beschränkte sich auf die Unterstützung bei Handhabung der Tools, die im Rahmen der vorherigen Arbeiten entstanden sind. Neben dem FE-HMM-Code lag der Schwerpunkt hierbei auf der Unterstützung bei der Generierung der verwendeten Netze.

Finite Elements in Analysis and Design 198 (2022) 103653

Contents lists available at ScienceDirect

Finite Elements in Analysis & Design

journal homepage: www.elsevier.com/locate/finel

Computational homogenization of concrete in the cyber Size-Resolution-Discretization (SRD) parameter space

Ajinkya Gote [a], Andreas Fischer [a], Chuanzeng Zhang [b], Bernhard Eidel [a,*]

[a] DFG-Heisenberg-Group, Institute of Mechanics, Department of Mechanical Engineering, Germany
[b] Chair of Structural Mechanics, Department of Civil Engineering, University Siegen, 57068 Siegen, Paul-Bonatz-Str. 9-11, Germany

ARTICLE INFO

Keywords:
Homogenization
Elasticity
Concrete
Error analysis
Adaptivity
Finite elements

ABSTRACT

Micro- and mesostructures of multiphase materials obtained from tomography and image acquisition are an ever more important database for simulation analyses. Huge data sets for reconstructed 3d volumes typically as voxel grids call for criteria and measures to find an affordable balance of accuracy and efficiency. The present work shows for a 3d mesostructure of concrete in the elastic deformation range, how the computational complexity in analyses of numerical homogenization can be reduced at controlled errors. Reduction is systematically applied to specimen size S, resolution R, and discretization D, which span the newly introduced SRD parameter space. Key indicators for accuracy are (i) the phase fractions, (ii) the homogenized elasticity tensor, (iii) its invariance with respect to the applied boundary conditions and (iv) the total error as well as spatial error distributions, which are computed and estimated. Pre-analyses in the 2d SRD parameter sub-space explore the transferability to the 3d case. Beyond the concrete specimen undergoing elastic deformations in the present work, the proposed concept enables accuracy-efficiency balances for various classes of heterogeneous materials in different deformation regimes and thus contributes to build comprehensive digital twins of materials with validated attributes.

1. Introduction

Concrete is a multiphase material consisting of a mortar phase and an aggregate phase, frequently accompanied by distributed pores. When laboratory experiments such as the Brazilian-type compression test as in [1] are carried out for precisely prescribed specimen sizes and boundary conditions, there is little ambiguity about model dimensions and boundary conditions (BC) for the modeling and simulation; the simulation model must coincide with the experiment. For simulations on larger length scales in the context of computational homogenization, the appropriate size is closely related to the definition of a representative volume element (RVE) and to effective properties [2–8].

According to Hill [2] the microstructural features of the RVE must be statistical representative for the heterogeneous material and large enough to be insensitive to the applied boundary conditions. The reference to the statistical properties of interest instead of all material properties was suggested by Drugan and Willis [3] for the definition of the RVE and has led to smaller volumes matching this requirement. A turn to the statistics of apparent properties of multiple samples for the definition of effective properties was introduced by Kanit et al. [4] based on the precursor work of Jeulin [9].

Statistical analyses for the definition of the RVE are typically executed for randomly generated, synthetic samples, since real 3d microstructures from tomography are expensive and therefore available typically in small numbers only. For suchlike "solitary" snapshot samples as in the present case of one concrete specimen, the criterion for the RVE and effective properties is based on simulation results for periodic (PBC), kinematical uniform (KUBC) or stress uniform (SUBC) boundary conditions (BC). Deviations among them in the stiffness response render the properties as "apparent" according to Huet [10], which turn into "effective" ones, when the size is sufficiently large to render the stiffness invariant to the applied BCs and the sample can be considered an RVE. For effective properties the stiffness inequalities for different BCs $\mathbb{C}(\text{SUBC}) \leq \mathbb{C}(\text{PBC}) \leq \mathbb{C}(\text{KUBC})$ turn into equalities, where the relations between positive fourth-order tensors are understood in terms of quadratic forms.

The vast majority of concrete homogenization analyses so far was carried out rather for apparent properties without testing the required size to achieve invariance with respect to the applied BCs in the above mentioned sense; for elastic properties in Das et al. [11], Wimmer et al. [12], Youssef et al. [13] and Luo et al. [14]; for mechanical, diffusive, and chemo-expansive properties in Bosco et al. [15]; and

* Corresponding author.
E-mail address: bernhard.eidel@uni-siegen.de (B. Eidel).

https://doi.org/10.1016/j.finel.2021.103653
Received 26 May 2021; Received in revised form 16 August 2021; Accepted 17 September 2021
Available online 8 October 2021
0168-874X/© 2021 Elsevier B.V. All rights reserved.

similarly, in homogenization investigations for effective thermal conductivity in El Moumen et al. [16] and in Wei et al. [17], as well as in homogenization with a hydro-thermo-chemo-mechanical coupling in Wu et al. [18].

Highly resolved Focused Ion Beam (FIB)-Tomography and X-ray Computed Tomography Technique (XCT) in Pennycoock and Nellist [19], Holzer and Cantoni [20], and in Ketcham and Carlson [21] have become standard in the characterization of multiphase composites not only for concrete but also for a great variety of materials.

The obtained ordered stack of pixelized images is used for the reconstruction of 3d micro- and mesostructures. Resultant voxel-grids can directly be used as 3d finite element discretizations as shown in Keyak et al. [22], Hollister et al. [23], Mishnaevsky [24], Young et al. [25], with applications to an open-cell foam in Michailidis et al. [26], to reinforced composites in Sencu et al. [27], to concrete and asphalt construction materials in the review of Du Plessis and Boshoff [28] and to cement-based materials in the overview work of Chung et al. [29] to name but a few. For an overview of various techniques for the (re)construction of microstructures and RVEs see Bargmann et al. [30].

The impact of pixel and voxel resolution on simulation results was studied in Nguyen et al. [31] for foamed concrete, in Bernachy-Barbe and Bary [32] in a study on the creep behavior of concrete, in Sha et al. [33] for conductivity in porous media and for applications in digital rock physics see Berg et al. [34]. Huang et al. [1] carried out a resolution compression by factor 4 in each direction of space and monitored the phase fraction ratios, which were virtually constant.

Adaptive mesh coarsening of an initially uniform pixel- or voxel-grid employing quadtree- and octree-type coarsening is instrumental to reduce the computational complexity, interfaces preserve their high resolution for accuracy and phase interiors are subject to coarsening for efficiency, Legrain et al. [35], Huang et al. [1], Ren et al. [36], Saputra et al. [37], Gravenkamp and Duczek [38], Saputra et al. [39]. Only very recently the adaptive coarsening was carried out along with an accompanying error control [40,41].

The present work is based on data for a concrete specimen obtained by Huang et al. in [1]. The cubic specimen exhibits 371^3 voxels which implies more than 150 million unknown degrees of freedom (ndof). The number of unknowns is prohibitive for two-scale simulations using FE^2/FE-HMM, where to each quadrature point of the macroscopic finite element an RVE of that problem size is attached. Even more important, high resolution and full specimen size can turn out to be wasteful in view of sub-volumes and/or reduced resolutions which are enough to serve as an RVE.

In either case, and beyond the particular example of concrete, there is a strong need for methods to tame an excess of data and thereby reduce the computational complexity while preserving sufficient accuracy and overall reliability of simulations. The geometrical properties of a sample in terms of its size S, resolution R and discretization D are key parameters that influence the accuracy and costs of simulations. These three span the newly-introduced "SRD parameter space", which is visualized in Fig. 1.

In the workflow of Fig. 2, only size S exists in physical space, whereas resolution R is added by image acquisition in tomography, and discretization D is added in the cyber space[1] of simulation which completes the SRD parameter space. Data transfer exhibits a hierarchy in that the cyber space of tomography and imaging generates data in the physical space of the specimen and transfers them to the cyber agency of simulation and data analysis where it is processed. As a consequence, losses in data generation and transfer with respect to size and resolution can hardly be compensated by the recipient. This circumstance inherently favors image acquisition in size and resolution tending to the edges of feasibility which may turn out luxuriant

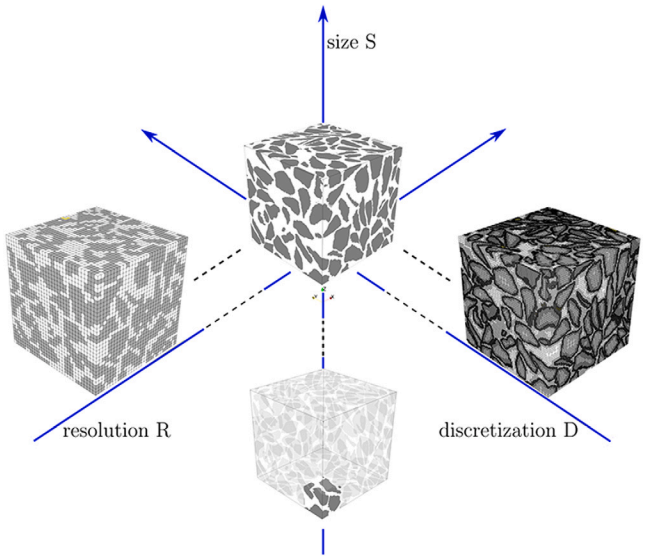


Fig. 1. The SRD parameter space of the digital twin of a concrete specimen. The computational complexity can be reduced by the reduction of size S, by coarse-graining of resolution R or of discretization D, or a combination thereof. But how about the corresponding losses in accuracy?

for particular simulation purposes and, therefore, calls for adequate reductions.

For the exploration of the SRD space as illustrated in Fig. 1 several questions arise, which are exemplarily analyzed and answered for a particular specimen of concrete:

1. **Size S:** Which specimen size is sufficiently large to serve as an RVE?
2. **Resolution R:** Which image-, hence pixel- and voxel-resolution provides the best balance between accuracy and efficiency?
3. **Discretization D:** What can adaptive mesh coarsening contribute to reduce the computational efforts of a discretization which coincides with full resolution? How do resolution errors compare to discretization errors?
4. **Accuracy:** The complexity reduction in the SRD parameter space must be accompanied by error control. How accurate is error estimation as validated by the computation of actual errors in terms of global errors as well as error-distributions?
5. **Transfer from 2d to 3d:** To which extent is a transfer from the 2d SRD parameter subspace to the 3d space possible? How can 3d simulations profit from 2d pre-analyses?

As the above introduction outlines, considerable progress already has been achieved with respect to the points 1.-3., but separately, whereas a panoramic view combining all three dimensions of the SRD parameter space, most notably with a rigorous error control, is lacking and therefore the topic of this work.

Conclusions from 2d to 3d addressed in point 4. are of general interest, for elastic properties this was considered in Saxena and Mavko [44]; moreover it has revealed a dimensional effect in stiffness, see Glüge et al. [45] and references therein. Here, we test the transferability of specimen size for the concrete specimen by monitoring "convergence" of homogenized elastic properties in the 2d and 3d SRD parameter space and the transferability of the quality of error estimation. Transferability in this respect would enable cheap 2d pre-analyses and thus have positive consequences for all of the above mentioned aspects 1.–4. As an example, the accuracy of error estimation had not to be validated by expensive "overkill" solutions in 3d, which is for large specimen sizes hardly accessible.

Limitations. The present work has its focus on the above methodological questions related to geometrical features; to size, resolution

[1] This scheme can be understood as part of the established, broad concepts of *cyber–physical systems* (CPS) [42] and of the *digital twin* (DT) [43].



Fig. 2. Workflow. Processing and data transfer from physical to and within cyber space.

Table 1
Phases. Phase fractions and elastic properties of the constituents.

	Aggregate	Mortar	Pore
3d phase fractions	0.5580	0.4312	0.0109
2d phase fractions	0.5629	0.4357	0.0014
E (GPa)	50	20	–
ν	0.3	0.3	–

and discretization. Aspects related to the constitutive behavior are excluded on purpose; such as the scatter of the elastic properties of the constituents, the inelastic behavior of concrete in general and in particular the role of defects such as voids or the interfacial transition zones ITZ between aggregate and filler [46–48] for crack nucleation and failure. Spatial variations in the microstructure of composites may have a minor influence on the elastic properties but a strong impact on the overall inelastic behavior [7].

Notation. The starting point in this work is the case of full specimen size S in full resolution, where voxel size $h_\square$ coincides with finite element size h. Within certain bounds however (e.g. $h \leq h_\square$) almost arbitrary combinations in the SRD parameter space are possible. To give an example, the abbreviation S256-RD128adap2 denotes a specimen size S256 of edge length 256×0.1 mm $= 25.6$ mm, which indicates that the length unit is 0.1 mm. Moreover it exhibits a resolution R128, which refers to the voxels per edge, hence after one step of resolution coarsening. Third, the discretization D128 denotes the elements per edge, and the appendix adap2 indicates that two consecutive adaptive mesh coarsening steps are applied to the discretization D128. Notice that the pixel/voxel size immediately follows from the S-value divided by the R-value times 0.1 mm.

2. Microstructure

The starting point of the present analysis is a cubic specimen of concrete with a side length of 37.1 mm. The mesoscale multiphase composition referred to as microstructure in the following is displayed in Fig. 3(a). It exhibits a resolution of 371^3 voxels and is the outcome of reconstruction from in-situ X-ray Computed Tomography (XCT) images provided in Huang et al. [1]. The specimen consists of three phases; beyond the aggregate and the mortar of a relatively small pore phase. The solid phases each exhibit isotropic, linear elastic material behavior described by $\sigma_{ij} = \mathbb{C}^\epsilon_{ijkl}\,\varepsilon_{kl}$, with the Cauchy-stress tensor σ_{ij}, the fourth order elasticity tensor $\mathbb{C}^\epsilon_{ijkl}$, and the infinitesimal strain tensor ε_{kl}. For convenience, we use Voigt notation in the following. The volume fractions of the phases and the isotropic elasticity parameters of the solid phases are given in Table 1. The aggregate-mortar stiffness contrast is 2.5. The chosen area element in Fig. 3(b) is a slice in the XZ-plane. It is considered as representative for its good match of the phase fractions with the 3d specimen.

3. Computational homogenization with adaptivity

The methods used in the present work are briefly described with links to further references.

3.1. Numerical homogenization

The mechanical analysis of the concrete specimen is conducted in the framework of a two-scale finite element method for computational homogenization, the Finite Element Heterogeneous Multiscale Method FE-HMM or FE^2 (for their comparison and their development on different tracks we refer to [49]) based on the equivalence of macro and micro energy densities $\overline{\boldsymbol{\sigma} : \boldsymbol{\epsilon}} = \overline{\boldsymbol{\sigma}} : \overline{\boldsymbol{\epsilon}}$ with volume averages over the microdomain $\mathcal{B}_\epsilon$ defined as $\bar{\bullet} := \frac{1}{|\mathcal{B}_\epsilon|}\int_{\mathcal{B}_\epsilon} \bullet \, \mathrm{d}V$. The application of energetically consistent boundary conditions of KUBC, PBC and SUBC to the microproblem is realized by the method of Lagrange multipliers [40]. The computation of the homogenized elasticity tensor $\mathbb{C}$ (frequently referred to as $\overline{\mathbb{C}}$) based on the given elasticity tensors for the single phases $\mathbb{C}^\epsilon$ follows the result of asymptotic homogenization [50] along with a modification for efficient computation [49]. Details of FE-HMM for linear elastic solids along with error and convergence analyses can be found in [49,51], and extensions to geometrical and material nonlinearity in [52,53].

3.2. Resolution coarsening

In resolution coarsening all voxels of the initial, finely resolved microstructure image undergo a uniform coarsening, in the phases and at interfaces. At interfaces rules must be introduced which define on how a cube of 2^3 fine voxels having different Young's moduli (represented by different color codes of images) merge into one coarser voxel. Since the finite element discretization follows this uniform coarsening, voxels represent hexahedral finite elements with shape functions of polynomial order $q = 1$ and pass their properties onto them. The same applies to pixel-coarsening in 2d.

In the following, two different methods of pixel and voxel coarsening are applied to microstructures, which exist in the field of digital image processing in similar variants, see e.g. [54]. The first version obeys a rule of mixtures as already used in homogenization in [55]; the newly created voxel exhibits properties of the volume average of the voxels merging in that coarser voxel, which amounts to taking the arithmetic mean for the same voxel size. For a sketch see the transformation of (a) into (b) in Fig. 5. The newly introduced phases with mixed properties at interfaces are an artifact for the case of distinguished phases with sharp boundaries. As a result, the sharp contrast in stiffness at interfaces is flattened, which similarly reduces the corresponding stress jumps as the material response. The volume average of Young's moduli over the entire microdomain is preserved by the very definition of the mixture rule. This coarsening rule creates microstructures which resemble or even coincide with the outcome of tomography image acquisition in that they are typically rastergraphics showing mixed colors for pixels at interfaces. In a novel approach of characterizing digital microstructures by the Minkowski-based quadratic normal tensor proposed by Ernesti et al. [56], blurred interfaces are a feature inherent in the method.

The second variant overcomes the above mentioned drawbacks of the coarsening type which falsifies the real, discrete stiffness and stress jumps at interfaces. For coarsened voxels at interfaces the quantity and properties of the initial phases are preserved following the rule, "the-majority-wins". In case of an equal count, the newly created coarser voxel is endowed with those phase properties that shift the global phase ratio closer to the original one, compare the turn from (a) to (c) in Fig. 5. This version corresponds to image segmentation which restores the number of real phases along with their sharp boundaries. Both variants are compared in a detailed error analysis in [41].

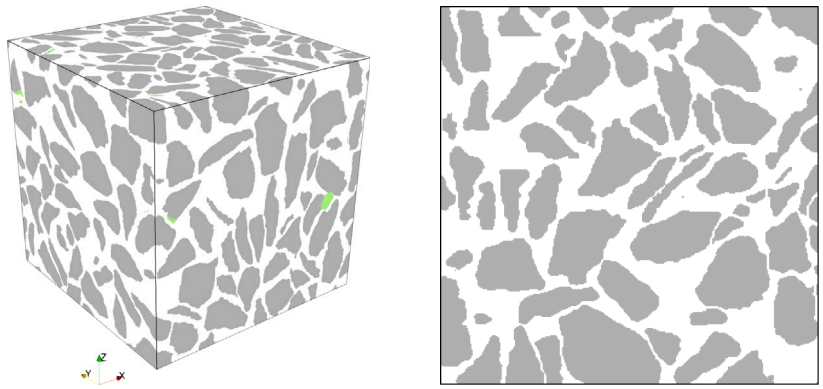


Fig. 3. Concrete microstructure. (a) Original 3d specimen of Ref. [1], (b) exemplary 2d slice. Three phases, gray for aggregate, white for mortar, and green for pore.

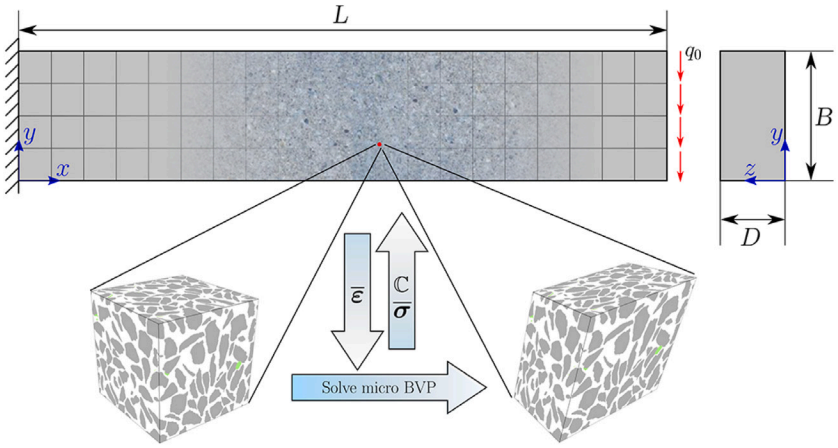


Fig. 4. Micro–macro-transition in computational homogenization. Macro–micro transfer (localization): macro-strain $\bar{\varepsilon}$, micro–macro transfer (homogenization): averaged stress $\bar{\sigma}$ and homogenized elasticity tensor $\mathbb{C}$ from the solution of the micro boundary value problem (BVP).

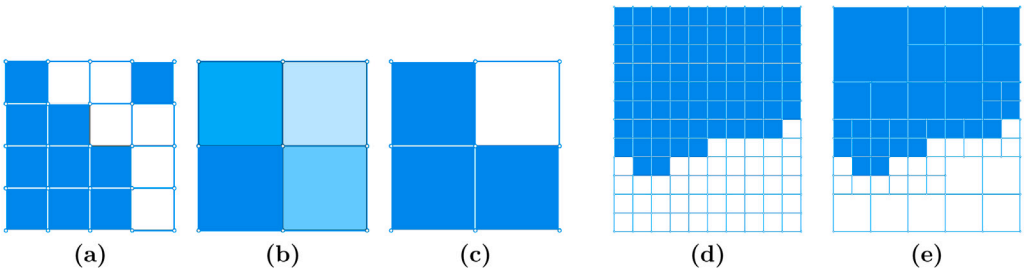


Fig. 5. Coarsening methods. Resolution coarsening of a two-phase patch from (a) initial, high resolution into a coarsened grid (b) with new phases (mixture rule) and (c) with preserving the number of phases (”the-majority-wins” rule). Adaptive mesh coarsening of (d) a uniform mesh into (e) a quadtree-type, 1-irregular mesh. In a 1-irregular mesh on each edge not more than one hanging node may exist.

3.3. Adaptive mesh coarsening

Adaptive mesh coarsening of the initially high resolution serves the purpose to reduce computational costs of discretizations following the highly resolved pixel/voxel grid. Therein, fine discretizations are preserved at interfaces for accuracy, and mesh coarsening is performed in the phase interiors for efficiency as visualized in Fig. 5, from (d) to (e) for the 2d case. In the transition from fine to coarse the gradient of element size should not be too steep in order to avoid a stiffening of the transition region due to the multitude of kinematical constraints applied to the hanging nodes on the transition elements [40]. This requirement is accomplished by 1-irregular meshes as displayed in Fig. 5(e). The corresponding constraints are introduced via Lagrange multipliers. For an alternative using transition elements we refer to [57–59].

The attribute adaptive applies since the mesh coarsening in a preprocessing step anticipates the qualitative outcome of the simulation instead of following an a posteriori error distribution by mesh adaption. A thorough error analysis of quadtree-based mesh coarsening in the context of homogenization can be found in [40] and [41]. Quadtree-/octree-based finite element mesh generation was introduced in [60] by Yerry and Shephard and an early overview can be found in Samet [61].

3.4. Error estimation and error computation

Error computation based on reference solutions for very fine discretizations controls the discretization error, but can become prohibitive. For this reason error estimation is required, which must be validated by comparison with actual errors. In this work, a modified version of the reconstruction-based error indicator of Zienkiewicz and Zhu [62–64] is employed and measured by the energy norm. The energy norm of the solution $\boldsymbol{u}^h$ for a micro domain $\mathcal{B}_\epsilon$ is given by (1).

$$\| \boldsymbol{u}^h \|^2_{A(\mathcal{B}_\epsilon)} = \int_{\mathcal{B}_\epsilon} \mathbb{C}^\epsilon : \boldsymbol{\varepsilon}(\boldsymbol{u}^h) : \boldsymbol{\varepsilon}(\boldsymbol{u}^h) \, \mathrm{d}V \tag{1}$$

$$e^2_{\mathrm{mic}} := \|\boldsymbol{e}\|^2_{A(\mathcal{B}_\epsilon)} = \int_{\mathcal{B}_\epsilon} \left(\boldsymbol{\sigma}^{\mathrm{ref}} - \boldsymbol{\sigma}^h\right) : \left(\boldsymbol{\varepsilon}^{\mathrm{ref}} - \boldsymbol{\varepsilon}^h\right) \mathrm{d}V \tag{2}$$

$$\bar{e}^2_{\mathrm{mic}} := \|\bar{\boldsymbol{e}}\|^2_{A(\mathcal{B}_\epsilon)} = \int_{\mathcal{B}_\epsilon} \left(\boldsymbol{\sigma}^\star - \boldsymbol{\sigma}^h\right) : \left(\boldsymbol{\varepsilon}^\star - \boldsymbol{\varepsilon}^h\right) \mathrm{d}V \tag{3}$$

$$\Theta = \|\bar{\boldsymbol{e}}\|_{A(\mathcal{B}_\epsilon)} / \|\boldsymbol{e}\|_{A(\mathcal{B}_\epsilon)} \tag{4}$$

The actual discretization error $\|\boldsymbol{e}\|_{A(\mathcal{B}_\epsilon)}$ in terms of actual stresses $\boldsymbol{\sigma}^{\mathrm{ref}}$ and strains $\boldsymbol{\varepsilon}^{\mathrm{ref}}$ according to (2) is obtained for a reference discretization, nominally with $h \to 0$, in practice for considerably finer discretizations than the mesh in use. Since the errors refer to the micro domain $\mathcal{B}_\epsilon$, they are called micro errors in the following.

Since the computation of the true error can become very expensive for large 3d problems, the estimation of errors obtained for the discretization in use is the method of choice. In the reconstruction-type error estimation of Zienkiewicz and Zhu according to (3) the accuracy critically depends on the improved nodal stresses $\boldsymbol{\sigma}^\star$ and strains $\boldsymbol{\varepsilon}^\star$. The method for their computation is described in Section 3.5 with a particular account of interfaces.

The effectivity index Θ in (4) as the ratio of the estimated error to the actual error is a measure for the accuracy of error estimation. For $h \to 0$ it must hold $\Theta \to 1$ for consistency.

3.5. Calculation of accurate/improved stresses

Stress computation is of cardinal importance in the context of multiphase materials, in particular for error estimation. In the reconstruction-based error estimation, improved stresses $\boldsymbol{\sigma}^\star$ have direct impact on the quality of the error estimate as described in Section 3.4. For nodes in the phase interior they are calculated simply by averaging the values extrapolated from quadrature points of adjacent elements to that node. More sophisticated techniques exploiting superconvergence as proposed in Zienkiewicz and Zhu [63,64] have not shown a superior error estimate such that their computational overhead does not pay off in the present context. Stress averaging for a node at the discrete interface of different phases would ignore the stiffness mismatch and the corresponding stress jumps. For this reason, a phase distinction assigning multiple sets of stresses to a node avoids the falsifying effects of averaging. Moreover, the phase distinction in stress computation results in more accurate error estimates compared to a standard stress averaging that ignores interfaces [40,41].

4. Preliminary analysis for 2D

The overall aim of this section is to explore, to which extent the 2d simulation results are transferable to the 3d case with respect to size, resolution, and discretization, but also with regard to the quality of error estimation.

The corresponding macro problem is chosen to be a square plate of edge length l=1000 mm, with a discretization of 20 × 20 quadrilateral elements with linear shape functions $p = 1$. Dirichlet boundary conditions are applied to the left side of the cantilever plate, Neumann boundary conditions with a load $\boldsymbol{g} = [0, -100]^T$ N/mm^2 are applied to the opposite edge. The square micro domain is a slice of the 3d specimen with side length S (in 0.1 mm) and subjected to plane strain conditions in the simulations and, if not otherwise stated, to PBC. The microdomain is located at $[960.57, 960, 57]$ (mm) in the upper right corner of the plate. Fig. 3(b) shows the 2d slice taken from the original 3d concrete specimen.

Table 2
Specimen slice SRD320. Number of degrees of freedom (ndof) of the original, uniform mesh (0) and the adaptively coarsened meshes (1–3), the corresponding ndof-reduction factor and the constrained ndof for hanging nodes.

SRD320	Adaptive mesh coarsening			
	0	1	2	3
ndof	205 852	108 228	95 628	94 938
Factor	1.0000	0.5258	0.4645	0.4612
Constrained ndof	0	6 581	8 208	8 367

Table 3
Specimen slice SRD320. Actual errors e_{mic} and estimated errors $\bar{e}_{\mathrm{mic}}$ along with the increase factors for the uniform mesh (0) and the adaptively coarsened discretizations (1–3). Actual errors for various reference discretizations, SR320 D ∈ {640, 1280, 1920, 2560}. Effectivity index Θ for D2560. Errors e_{mic} and $\bar{e}_{\mathrm{mic}}$ in 10^{-4} (Nmm).

SRD320	Adaptive mesh coarsening			
Reference D	0	1	2	3
e_{mic}(D640)	6.2297	6.5747	6.8850	7.0670
Factor	1.000	1.0554	1.1052	1.1344
e_{mic}(D1280)	7.2830	7.5803	7.8509	8.0109
Factor	1.0000	1.0408	1.0780	1.0999
e_{mic}(D1920)	7.5137	7.8021	8.0652	8.2211
Factor	1.000	1.0384	1.0734	1.0942
e_{mic}(D2560)	7.6051	7.8902	8.1505	8.3048
Factor	1.000	1.0374	1.0717	1.0920
$\bar{e}_{\mathrm{mic}}$(D320)	5.8034	6.1197	6.3782	6.4913
Factor	1.0000	1.0545	1.0991	1.1185
θ(D2560)	0.7631	0.7756	0.7826	0.7816

4.1. Quadtree-based adaptive mesh coarsening

Adaptive mesh coarsening is applied to the initially uniform discretization. It is based on a quadtree-type discretization as described in [40]; the rule is that at interfaces the fine resolution is maintained for accuracy, while in the interior of phases the mesh-coarsening is carried out for efficiency (see Fig. 6).

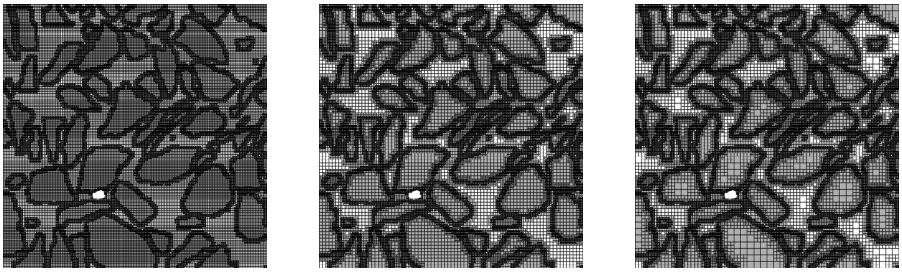
Table 2 provides the number of unknowns of the original mesh and the meshes resulting from the coarsening steps. After three coarsening steps the ndof is reduced to 46% compared with the initial mesh.

Here and in the following the ndof in the tables equals the ndof of the micro mesh minus the constrained ndof of the hanging nodes.

4.2. Validation of error estimation by comparison with actual errors

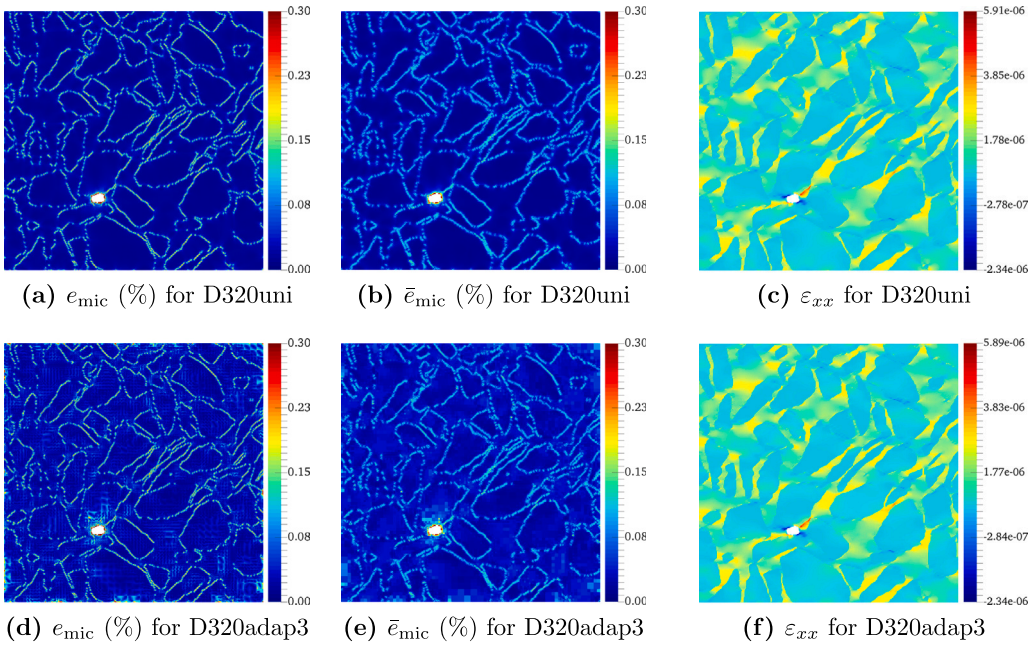
Table 3 shows the errors in the energy norm for the original, uniform mesh and the meshes from the three coarsening steps based on reference solutions for different discretizations. Even though the ndof is decreased by up to 54%, the increase of the actual error remains below 10%. The estimated errors are smaller than the calculated errors. The values of the effectivity index are close to 0.8 and indicate a good agreement of the estimated and the true errors for both uniform and adaptively coarsened meshes. A reference solution obtained by $h^{\mathrm{ref}} = h/4$ (here at D1280) with h being the current element size is enough to obtain a sufficiently accurate solution for the computation of the actual error.

For the investigation of the error distributions on the micro domain the relative elementwise micro discretization error is analyzed. This relative error is the ratio of the computed or estimated error of an element to the element's energy norm. By doing so the influence of



(a) SRD320adap1 (b) SRD320adap2 (c) SRD320adap3

Fig. 6. Specimen slice SRD320. Adaptively coarsened meshes.



(a) e_{mic} (%) for D320uni (b) $\bar{e}_{\text{mic}}$ (%) for D320uni (c) ε_{xx} for D320uni

(d) e_{mic} (%) for D320adap3 (e) $\bar{e}_{\text{mic}}$ (%) for D320adap3 (f) ε_{xx} for D320adap3

Fig. 7. Specimen slice SR320. For uniform and adaptively coarsened meshes, the distributions of the actual relative errors $\|\boldsymbol{e}\|_{A(\mathcal{B}_\varepsilon)}/\|\boldsymbol{u}\|_{A(\mathcal{B}_\varepsilon)}$ in (a) and (d), and estimated relative errors $\|\bar{\boldsymbol{e}}\|_{A(\mathcal{B}_\varepsilon)}/\|\boldsymbol{u}\|_{A(\mathcal{B}_\varepsilon)}$ in (b) and (e), and of the strain component ε_{xx} in (c) and (f).

the element size is eliminated which is especially important for the non-uniform meshes.

The results in Fig. 7 indicate that (i) the error is largest at the aggregate-mortar interfaces, (ii) it is comparatively small in the interior of the two solid phases, which (iii) justifies the adaptive mesh-coarsening preserving fine resolution at interfaces and coarsening in the phase interior. Moreover, it can be seen that (iv) the estimated errors are qualitatively and quantitatively in good agreement with the true errors, see the distributions and their maxima in Fig. 7.

4.3. Dependence of the 2d homogenized elastic constants on various parameters

4.3.1. Dependence on slice size

Fig. 8 displays the coefficients of the homogenized elasticity tensor for different slice sizes, each with PBC. In the right of Fig. 8 some of them are shown. As a result, the magnitude of the coefficients directly depends on the phase fraction of the aggregate as the stiffest phase having discrete peaks at S64 and S240. Since the finite element size coincides with the pixel size, the results for smaller samples exhibit larger discretization errors.

Fig. 9 displays the percentage deviation in $\mathbb{C}_{ij}$ for KUBC, SUBC and PBC, where PBC(S371) is taken as the reference. The convergence characteristics, for SUBC from below, for KUBC from above, for PBC in between, indicate the transition from apparent to effective properties for sufficiently large S following the terminology used since the work of Huet [10]. The well-known order[2] $\mathbb{C}(\text{KUBC}) \geq \mathbb{C}(\text{PBC}) \geq \mathbb{C}(\text{SUBC})$ is observed for all sizes in all components. The characteristics are not monotonic and the deviations do not decrease in a monotonic way, but show rapid convergence, with an outlier for S240; for size S200 and above the deviations stay below 2%.

A setup, where a sample size automatically implies a size-dependent resolution and finite element discretization with corresponding errors, is not satisfactory and not necessary. In contrast, the finite element discretization h can be chosen smaller than the pixel size $h_\square$ in either case, which reduces the discretization error as discussed in [41]. For this reason Section 4.3.2 separately analyzes the influence of resolution, and Section 4.3.3 the influence of discretization.

4.3.2. Dependence on resolution

Fig. 10 shows the sample size S320 in different resolutions, where two types of resolution coarsening according to Section 3.2 are carried out. The first type applies a mixture rule as shown in Fig. 10(b). The second type follows the rule the-majority-wins, for the outcome see Fig. 10(c).

[2] Inequalities between positive fourth-order tensors are understood in terms of quadratic forms, here in terms of energy densities, i.e. ${}^1\mathbb{C} \geq {}^2\mathbb{C} \iff \boldsymbol{\varepsilon} : {}^1\mathbb{C}\,\boldsymbol{\varepsilon} \geq \boldsymbol{\varepsilon} : {}^2\mathbb{C}\,\boldsymbol{\varepsilon}\ \forall \boldsymbol{\varepsilon}$.

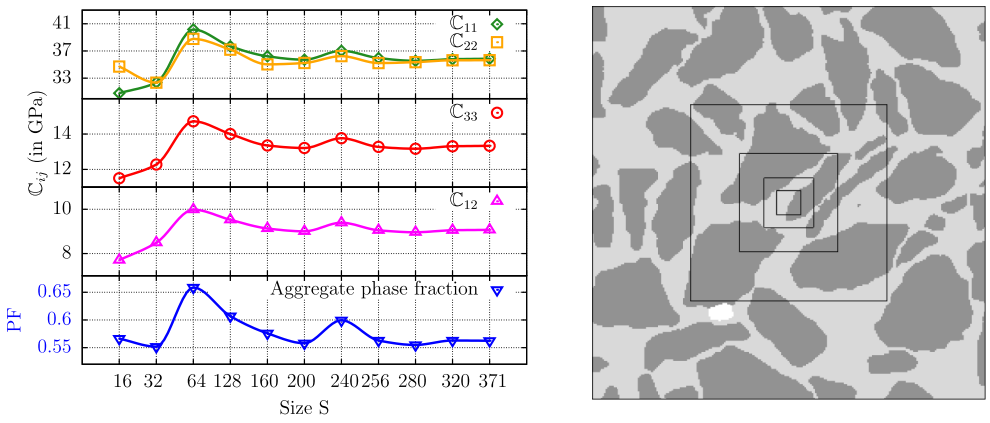


Fig. 8. Homogenized 2d elasticity tensor for PBC. $\mathbb{C}_{ij}$ for different slice sizes. Explicit numbers are given in the Supplement. Selected specimen sizes are $S2^n, n = 4, 5, 6, 7, 8$.

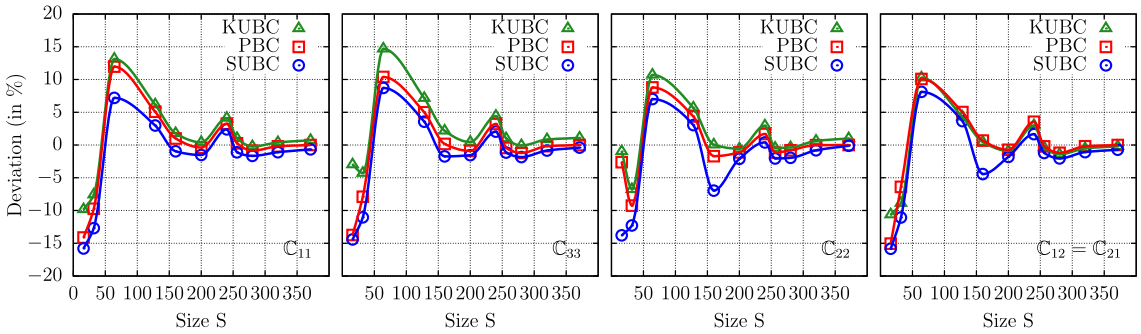
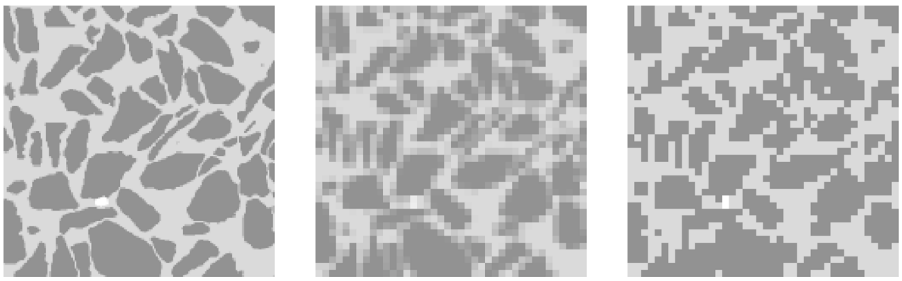


Fig. 9. From apparent to effective properties in 2d. Percentage deviations of $\mathbb{C}_{ij}$ for KUBC, PBC and SUBC with different slice sizes from $\mathbb{C}_{ij}$(PBC, S371).



(a) S320-RD160 (0.2mm) **(b)** S320-RD40 (0.8mm) **(c)** S320-RD40 (0.8mm)

Fig. 10. Slice of S320 in different resolutions. For specimen SR320 three coarsening steps of resolution R (pixels per edge) are done, in (b) for phase averaging, in (c) for phase preserving coarsening. Pixel size in brackets.

Image coarsening introduces a resolution error and, if the finite element discretization follows the pixel grid, additionally an increase in the discretization error will be induced. For a novel concept that decomposes micro errors into a resolution part and the standard discretization part of (2) we refer to [41]. Here, however, the discretization D320 is kept constant during the coarsening procedure which has the advantage of keeping the discretization error constant and thereby isolates the effect of resolution coarsening.

Fig. 11 displays the corresponding results for the homogenized elasticity tensor. In Fig. 11(a) for the case of averaging phase properties, it is obvious that although the volume average of the Young's modulus $< E >$ remains constant (here in terms of the aggregate phase fraction "on average") in coarsening, the homogenized elastic constants show larger changes compared to the phase-preserving case of Fig. 11(b). In the latter case, the components of the homogenized elasticity tensor follow quantitatively the stiffest phase fraction. Helpful in the preservation of the phase fractions is that in case of an equal count of pixels of different properties being merged, the attributed property to the novel voxel shifts the global phase fraction closer to the original one.

4.3.3. Dependence on discretization

Fig. 12 displays for the same sample size the influence of discretization by subdividing each pixel into 2^2, 4^2, 6^2 square sub-elements. Explicit numbers for that case are listed in the Supplement. The influence is rather minor, most notably in comparison with the influence of the image resolution shown in Fig. 11.

4.4. Check of isotropy-2d

The specimen size S320 is selected to measure the deviation from isotropy. The isotropic elasticity law in terms of the compliance matrix

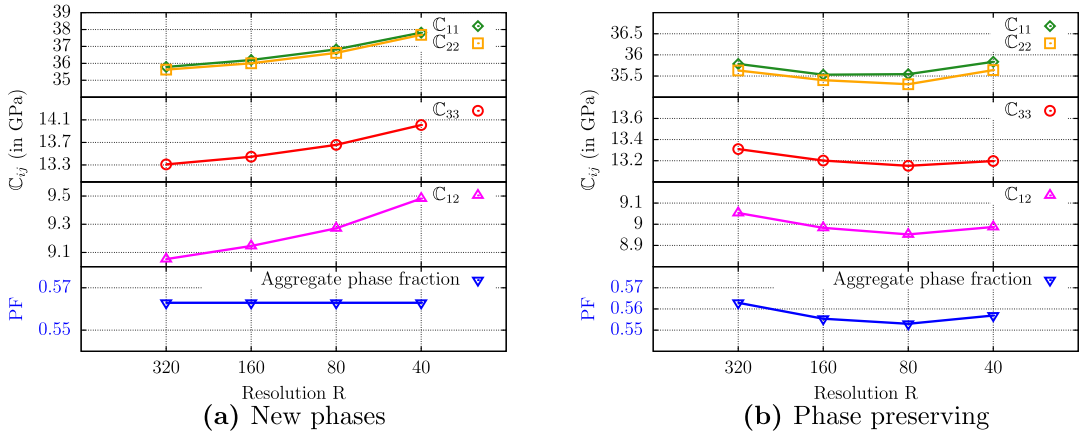


Fig. 11. Resolution-dependent 2d homogenized elasticity tensor. Components $\mathbb{C}_{ij}$ and phase fraction (PF) of the stiff aggregate phase for size S320 at different resolutions R but each with the same discretization D320, hence S320-R i-D320, (a) with new phases at interfaces, (b) for the case preserving the number of phases. Numbers are given in the Supplement.

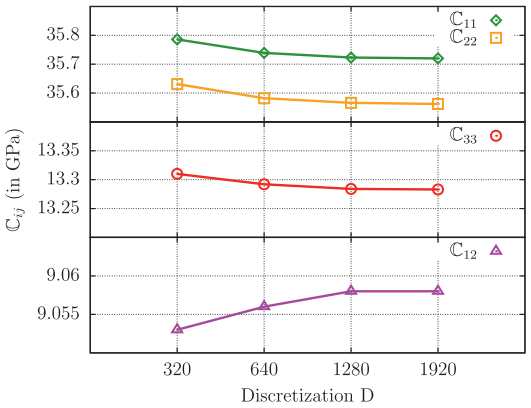


Fig. 12. Discretization-dependent 2d homogenized elasticity tensor. Components $\mathbb{C}_{ij}$ of the size and resolution SR320 but each which different discretizations D.

Table 4
Identification. Elastic constants for S320 assuming isotropy and deviation [%] of the remaining coefficients from isotropy.

Identification		Check of isotropy			
E (MPa)	ν	$\frac{\mathbb{C}_{11}-\mathbb{C}_{22}}{\mathbb{C}_{11}}$	$\frac{\lvert\mathbb{C}_{33}-G\rvert}{G}$	$\frac{\lvert\mathbb{C}_{13}\rvert}{\mathbb{C}_{11}}$	$\frac{\lvert\mathbb{C}_{23}\rvert}{\mathbb{C}_{11}}$
32111.77	0.203	0.43%	0.30%	0.02%	0.11%

for plane strain conditions reads

$$\begin{bmatrix}\varepsilon_{11}\\ \varepsilon_{22}\\ 2\varepsilon_{12}\end{bmatrix} = \underbrace{\begin{pmatrix}\frac{1-\nu^2}{E} & -\frac{\nu(1+\nu)}{E} & 0\\ & \frac{1-\nu^2}{E} & 0\\ \text{sym.} & & \frac{2(1+\nu)}{E}\end{pmatrix}}_{\text{Elastic compliance matrix } \mathbb{S}} \begin{bmatrix}\sigma_{11}\\ \sigma_{22}\\ \sigma_{12}\end{bmatrix}. \tag{5}$$

The parameters E and ν –and therefore the shear modulus $G = E/(2(1+\nu))$– are identified by the homogenized elastic coefficients $\mathbb{S}_{11}$ and $\mathbb{S}_{12}$. The remaining coefficients are used to validate the hypothesis of isotropy. Eq. (5) implies (i) $\mathbb{S}_{11} = \mathbb{S}_{22}$, (ii) $\mathbb{S}_{33} = 1/G$, (iii) $\mathbb{S}_{13} = 0$, (iv) $\mathbb{S}_{23} = 0$ or in terms of the stiffness matrix (i) $\mathbb{C}_{11} = \mathbb{C}_{22}$, (ii) $\mathbb{C}_{33} = G$, (iii) $\mathbb{C}_{13} = 0$, (iv) $\mathbb{C}_{23} = 0$. Conditions (i)–(iv) are used to check the homogenized elasticity tensor with respect to isotropy, [65] (see Table 4).

Since the maximal deviation of the elastic coefficients from the isotropic ones is less than 0.5% and $\mathbb{C}_{13}$ and $\mathbb{C}_{23}$ virtually vanish, the elasticity law of the specimen S320 can be reasonably regarded as isotropic.

5. Analysis for 3D

For the 3d simulations with up to 371^3 voxels (more than 150 million unknowns) iterative solvers along with preconditioners of the PETSc library are used based on MPI-parallelization employing up to 200 compute nodes, each with 256 GB RAM and 64 cores.

The macro problem is a 3d cantilever beam of length $L = 5000$ mm, height $B = 1000$ mm and width $D = 100$ mm, see Fig. 4. It is loaded at $x = L$ by a line-load of $q_{0y} = -40.0$ N/mm. The considered volume of the microstructure is centered at the point with $x = y = z = 2.1$ mm, where stress, strain, and discretization errors are calculated. For the 3d concrete specimen various subvolumes of cubic shape are considered for different resolutions R and discretizations D.

5.1. Specimen size and adaptive mesh-coarsening

Table 5 shows the outcome of the octree-based adaptive mesh-coarsening applied to the slightly reduced specimen size S368. The number of unknowns of initially more than 150 millions is considerably reduced in three steps to less than 55% which is the end in the adaptive D-dimension of the SRD space. The remaining problem size however is still quite large and shall be lowered by reductions in size S in the following.

The diagrams in Fig. 13 indicate a direct dependence of $\mathbb{C}_{ij}$ on the phase fraction of the stiffest phase. Their larger values for small sample sizes is of course accidental since they depend on the selection in the domain of S371. Apart from that, the phase fraction ratio is almost "converged" at S64.

Fig. 14 displays the percentage deviation of different coefficients $\mathbb{C}_{ij}$ for KUBC, SUBC and PBC, where the case of PBC(S371) serves as the reference. The type of convergence, for SUBC from below, for KUBC from above, indicate the transition from apparent to effective properties. The order $\mathbb{C}$(KUBC) $\geq$ $\mathbb{C}$(PBC) $\geq$ $\mathbb{C}$(SUBC) is observed for all sizes. The characteristics show rapid convergence and are monotonic for small S, where S200 is an outlier already visible in Fig. 13.

Since the concrete specimen is not periodic, its true deformation in the bulk of a structural element is unknown. For this reason the invariance of the calculated elasticity tensor to different BCs is of practical relevance in building materials and beyond, and similar transitions are observed in coupled problems, for e.g., in magneto-mechanics see Zabihyan et al. [66].

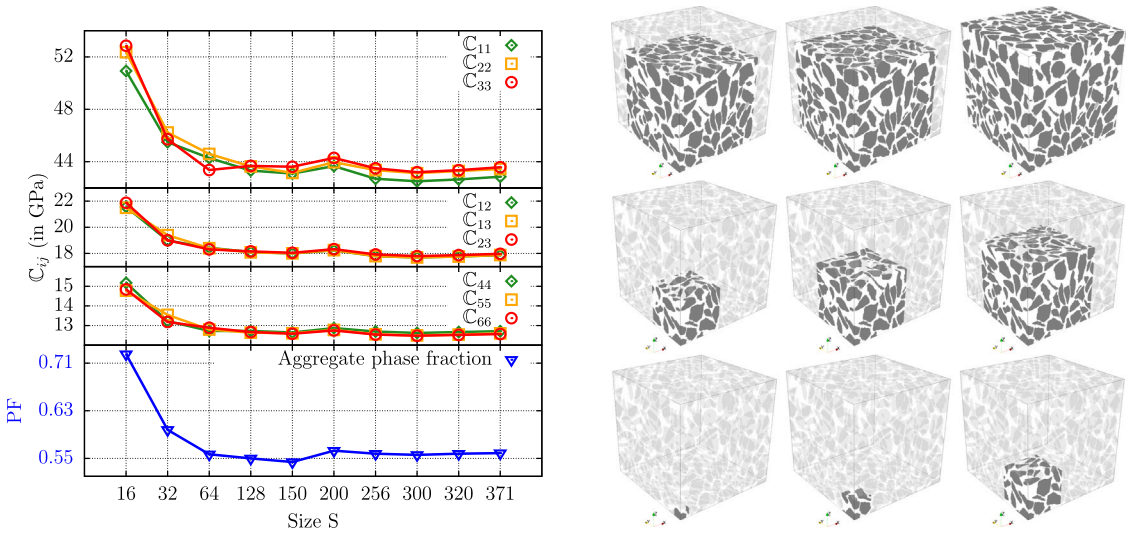


Fig. 13. Size-dependent homogenized 3d elasticity tensor. $\mathbb{C}_{ij}$ versus the specimen size and aggregate phase fraction, the corresponding numbers are given in the Supplement. In the right, a bottom-up series of specimens from S32 to S371 is presented.

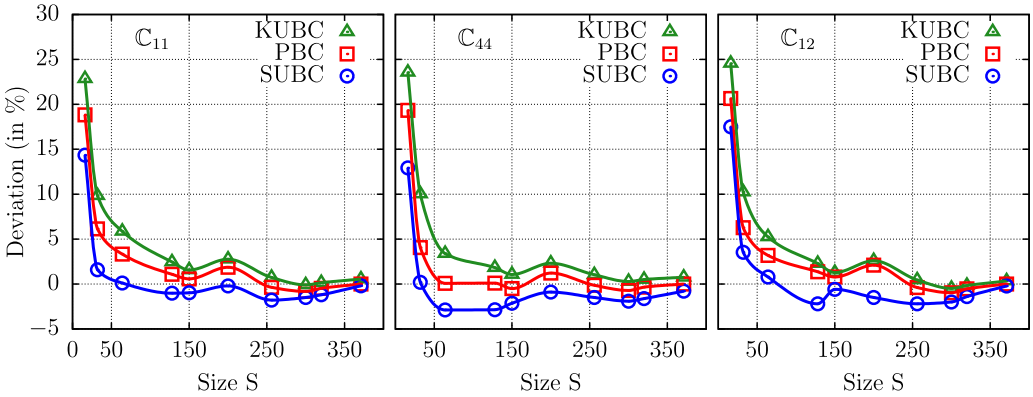


Fig. 14. From apparent to effective properties in 3d. Percentage deviation of the coefficients $\mathbb{C}_{11}$, $\mathbb{C}_{44}$ and $\mathbb{C}_{12}$ from the reference $\mathbb{C}_{ij}$(PBC,SRD371) for different microdomain sizes SRDi subject to KUBC, PBC and SUBC.

Table 5
Specimen SRD368. Values of ndof of the uniform mesh and the coarsened meshes, the corresponding ndof-reduction factor and the constrained ndof for hanging nodes.

SRD368	Adaptive mesh coarsening			
	0	1	2	3
ndof	150 730 227	84 301 767	82 651 488	82 649 319
Factor	1.0000	0.5593	0.5484	0.5483
Constrained ndof	0	24 357 456	26 241 495	26 250 483

5.2. Validation of error estimation

Two key questions are investigated in the following. Firstly, how does the estimated error match the actual one? Secondly, can the error estimation be validated by using smaller sample sizes where a reference solution is readily available?

The results shown in Fig. 15 and listed in Table 6 indicate the following error characteristics.

- **Errors for the total microdomain**: The error estimation for the full microdomain according to (3) is close to the actual error as indicated by effectivity indices Θ close to 0.8 at uniform meshes of sizes S32 and S64, for adaptively coarsened meshes it is throughout above 0.65. The fact that Θ is almost invariant for the two different samples, most notably at uniform discretization, suggests that the accuracy of error estimation can be transferred to larger sample sizes. In that case, the expensive computation of actual errors becomes dispensable.
- **Local micro error distributions**: The error distributions in the contour plots of Fig. 15 indicate the following characteristics.
  - (i) Larger errors are confined to interfaces, whereas the errors in the phase interiors are comparatively small.
  - (ii) The behavior (i) justifies the adaptive mesh-coarsening which preserves high resolution at interfaces but carries out coarsening in the phase interior.
  - (iii) Both the error estimation and the error computation agree well in the observed properties of (i).
  - (iv) The true errors are more confined to interfaces, less blurred and exhibit higher values. The reason is simply that the true errors are obtained with a much finer discretization, which localizes the errors to the interfaces.

5.3. Uniform coarsening of resolution

The diagrams in Fig. 16 display the changes in the homogenized elasticity tensor for both variants of the uniform resolution coarsening. For phase-preserving coarsening as shown in Fig. 16(b) the homogenized elastic constants follow the fraction of the stiffest phase during coarsening, which increase following the drop from RD256 to RD128.

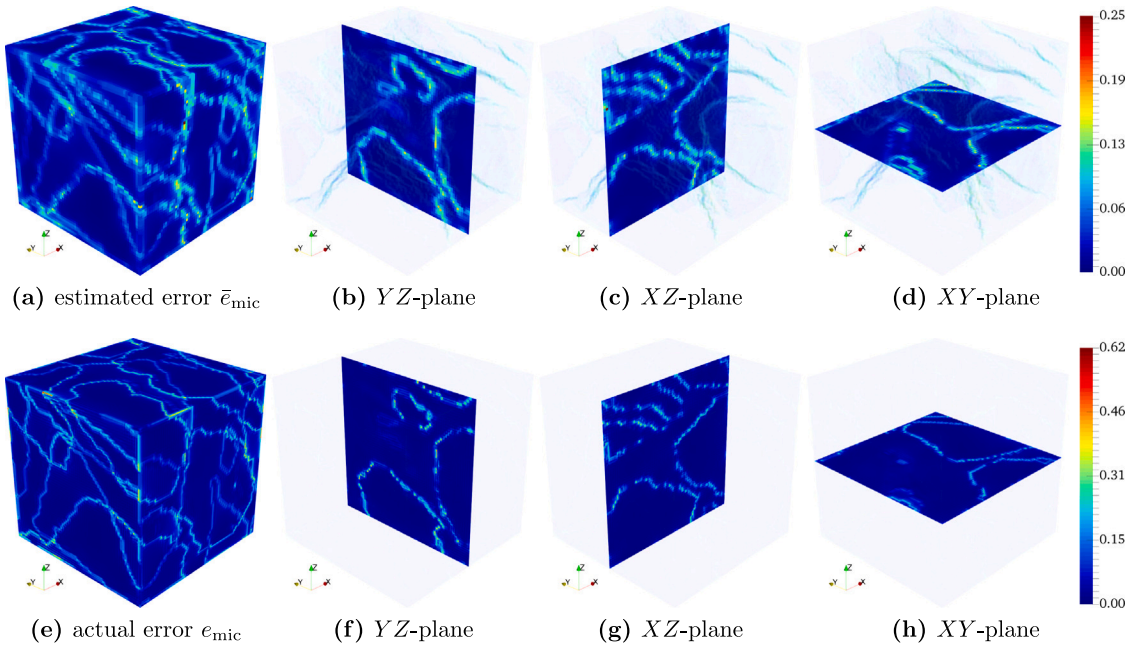


Fig. 15. Error distributions for SRD64. Estimated (a)–(d) versus actual (e)–(h) relative errors. Reference solutions for actual errors on SR64-D256.

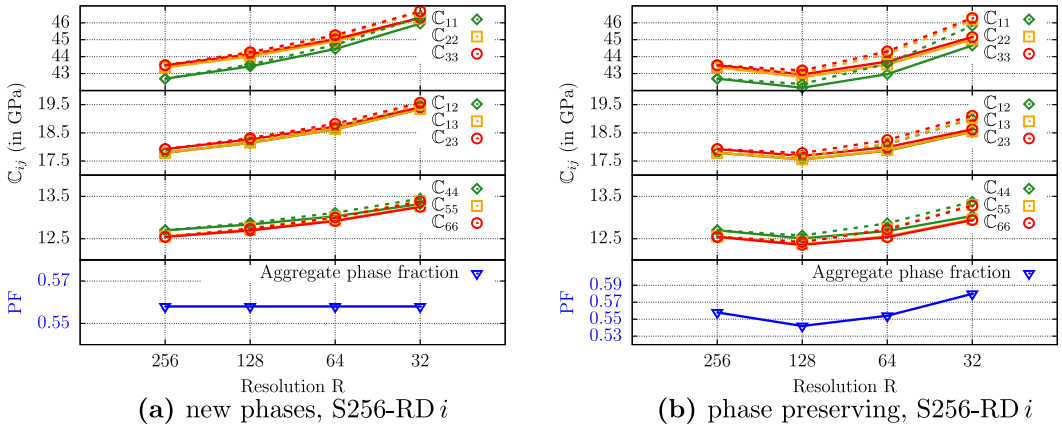


Fig. 16. Resolution-dependent 3d elasticity. Components $\mathbb{C}_{ij}$ of size S256 at different resolutions R. Dashed lines for the case that R and D coincide, hence S256-RD i, solid lines for the case of throughout constant D256. Corresponding numbers in the Supplement.

Table 6
Specimen sizes SRD32, 64. Number of unknowns (ndof), the corresponding ndof-reduction factors, actual errors e_{mic}, estimated errors $\bar{e}_{\text{mic}}$, effectivity index Θ for the uniform mesh (referred to as 0) and the adaptively coarsened discretizations (1–3). The discretization for the reference solution in the error computation is $h^{\text{ref}} = h/4$.

Size		Adaptive coarsening			
		0	1	2	3
S32	ndof	107 811	62 715	61 200	61 179
	Factor	1.000	0.5817	0.5677	0.5675
	e_{mic}(D128)	4.6283	5.3454	6.2689	6.6116
	$\bar{e}_{\text{mic}}$(D32)	3.6734	4.0361	4.2783	4.3090
	Θ	0.7936	0.7551	0.6825	0.6517
S64	ndof	823 875	436 728	424 221	424 110
	Factor	1.000	0.5301	0.5149	0.5148
	e_{mic}(D256)	11.2579	12.2820	12.9257	13.0031
	$\bar{e}_{\text{mic}}$(D64)	8.6605	9.3428	9.6798	9.7025
	Θ	0.7693	0.7607	0.7489	0.7462

For the resolution coarsening taking the arithmetic mean of the elastic constants as shown in Fig. 16(a) the homogenized elastic constants continuously increase with the coarsening step.[3] In this behavior both variants are in good agreement with the 2d case.

The dashed lines in Fig. 16 refer to the case where resolution and discretization coincide, hence R=D, while the solid lines stand for the case where the discretization is kept constantly fine at D256. The comparison quantifies the influence of the discretization, which turns out to be relatively small compared to the impact of the resolution, for the phase preserving case somewhat stronger (see Fig. 16(b)) than for the case with new phases (see Fig. 16(a)).

The data for the ndof and the absolute and relative energy errors in Table 7 complement the information in Fig. 16. By resolution coarsening the ndof can be drastically reduced, while the relative energy errors remain small, even for S32 they are hardly above 11%. Here and for error calculation in the components of the homogenized elasticity tensor, SRD256 is chosen as the reference. As an alternative route to consecutive resolution coarsening, two adaptive mesh coarsening steps are carried out for the resolution RD128, hence S256-RD128adap1/2 which further realizes an ndof reduction at very small error increase,

[3] The volume average of the Young's modulus $< E >$ remains constant.

Table 7
Resolution and mesh coarsening of SRD256. Numbers of ndof, the corresponding ndof-reduction factor, the estimated absolute error $\bar{e}_{\text{mic}}$ and relative error $\bar{e}_{\text{mic}}/||\boldsymbol{u}||_{A(\mathcal{B}_c)}$, and the errors in the elasticity coefficients err$[\mathbb{C}_{ij}]$. For adaptive mesh refinements, adap1 and adap2 the ndof and ndof-reduction factor compared with the initial, uniform mesh, and corresponding (relative) estimated errors. The quantities refer to SRD256 and its derived variants for phase-preserving resolution coarsening and adaptive mesh coarsening. Energies in (Nmm). SRD256 is the reference for $||\boldsymbol{u}||_{A(\mathcal{B}_c)}$ and for err$[\mathbb{C}_{ij}]$.

		⟶ Uniform resolution coarsening ⟶			
	RD	256	128	64	32
S256	ndof	50 923 779	6 440 067	823 875	107 811
	Factor	1.000	0.1265	0.0162	0.0021
	$\bar{e}_{\text{mic}}$	80.935	110.536	151.250	191.304
	$\bar{e}_{\text{mic}}/\|\|\boldsymbol{u}\|\|_{A(\mathcal{B}_c)}$	4.67%	6.38%	8.73%	11.04%
	err$[\mathbb{C}_{11}]$	0%	0.72%	2.06%	7.33%
	err$[\mathbb{C}_{12}]$	0%	0.82%	1.71%	6.78%
	err$[\mathbb{C}_{44}]$	0%	0.96%	1.29%	5.32%
	adap 1	ndof	5 261 679	803 556	107 778
		Factor	0.1033	0.0158	0.0021
		$\bar{e}_{\text{mic}}$	113.835	152.063	191.308
		$\bar{e}_{\text{mic}}/\|\|\boldsymbol{u}\|\|_{A(\mathcal{B}_c)}$	6.57%	8.78%	11.04%
	adap 2	ndof	5 259 459	–	–
		Factor	0.1032	–	–
		$\bar{e}_{\text{mic}}$	113.922	–	–
		$\bar{e}_{\text{mic}}/\|\|\boldsymbol{u}\|\|_{A(\mathcal{B}_c)}$	6.58%	–	–

for corresponding numbers see the second and third block of Table 7. In the same table the results for S256RD64/32 are displayed; in these two cases only one adaptive mesh coarsening step can be carried out. Generally, the ndof-reduction by adaptive mesh-coarsening is very limited for resolutions R128 and below.

Figs. 17(a)–(d) show the outcome of the consecutive RD coarsening, the images (e) and (f) display the adaptive discretizations based on S256-RD128.

5.4. Check of isotropy

The lack of pronounced material directions in the two-phase composite suggests isotropic material behavior. The specimen size S256 is chosen to measure its deviation from elastic isotropy, since it is sufficiently large and exhibits "converged" elastic properties. In the 3d case, the linear elastic constitutive law is given by

$$\begin{bmatrix} \varepsilon_{11} \\ \varepsilon_{22} \\ \varepsilon_{33} \\ 2\varepsilon_{12} \\ 2\varepsilon_{23} \\ 2\varepsilon_{13} \end{bmatrix} = \underbrace{\begin{pmatrix} \frac{1}{E} & -\frac{\nu}{E} & -\frac{\nu}{E} & 0 & 0 & 0 \\ -\frac{\nu}{E} & \frac{1}{E} & -\frac{\nu}{E} & 0 & 0 & 0 \\ -\frac{\nu}{E} & -\frac{\nu}{E} & \frac{1}{E} & 0 & 0 & 0 \\ & & & \frac{2(1+\nu)}{E} & 0 & 0 \\ & & & & \frac{2(1+\nu)}{E} & 0 \\ sym. & & & & & \frac{2(1+\nu)}{E} \end{pmatrix}}_{\text{Elastic compliance matrix } \mathbb{S} \text{ for isotropy}} \begin{bmatrix} \sigma_{11} \\ \sigma_{22} \\ \sigma_{33} \\ \sigma_{12} \\ \sigma_{23} \\ \sigma_{13} \end{bmatrix} \tag{6}$$

Isotropic elasticity is characterized by two independent material parameters E and ν which are identified by the homogenized coefficients $\mathbb{S}_{11}$ and $\mathbb{S}_{12}$, the shear modulus follows through $G = E/(2(1+\nu))$. The remaining coefficients are used to validate the hypothesis of isotropy, which turns out to be justified by the slight deviations throughout below 2% in Table 8.

6. Results and discussion

On the search for an error-controlled reduction of the computational costs of the microstructure of a concrete sample having 371^3 voxels, the present analysis has exemplarily explored the newly introduced SRD parameter space. Without any claim of generality for concrete or even of transferability to other multiphase systems the following results have been obtained:

1. **Size S.** For the identification of a necessary specimen size for an RVE we have used three criteria, (i) phase fraction ratio, (ii) homogenized components of the elasticity tensor, (iii) invariance of the elastic response with respect to the applied BCs. The results for the homogenized components of the elasticity tensor in Fig. 13 indicate that the homogenized elastic constants correlate approximately with the phase fraction of the stiffest phase, the aggregate phase. From the sample size S64 the phase fractions and therefore, the elasticities remain almost unaltered up to the size S371. This suggests that already the considered S64 can provide a representative volume size for characterizing the homogenized elastic behavior. The same is true with respect to criterion (iii) where we see in 3d that at the size S128 (with an outlier for S200) and above the maximal deviations between the different BCs are lower than 3%. For deviations below 1% it requires a S256 specimen. For the case of S256 in 3d and S320 in 2d, we can show that the effective elasticity law is virtually isotropic.
2. **Resolution coarsening R.** It enables a considerable efficiency gain at controlled accuracy. The reduction of SRD256 to S256RD32 reduces the ndof from almost 51 millions to less than 0.11 million, while the relative error in the energy norm increases from 4.7% to 11.1% as shown in Table 7, and in the main components of the homogenized elasticity tensor less than 7.5% throughout, compare data in Fig. 16.
3. **Discretization adapted to microstructure D.** For adaptive mesh coarsening of the samples S64 to S256, it is mainly the first step which realizes the best efficiency-accuracy trade-off, since it results in the strongest ndof-reduction of 53%–57% at rather moderate error increases.
   The comparison of the corresponding error distributions in Fig. 15 reveals that the discretization errors are confined to aggregate-mortar interfaces but remain small in the interior of the phases, which justifies the microstructure-guided coarsening strategy. In the error distributions, the estimation is in its qualitative picture similar to actual errors, although local maximal values are underestimated. Combinations of the RD coarsening fully unfolds the potential of the ndof reduction.
4. **Quality of error estimation? Best practice of assessment?** The accuracy of error estimation is assessed for the sample sizes of 32 and 64 voxels per edge. The reference solutions are obtained on the corresponding meshes with $h^{\text{ref}} = h/4$. The effectivity index in the range of 0.7 to 0.8 indicates a sufficient and almost size-independent accuracy of the reconstruction-based error estimate as shown in Table 6. The results suggest that the validation of error estimation at smaller subvolumes is transferable to larger sample sizes, if the phase fractions and interface structure are approximately representative for the smaller sample sizes.
5. **Transfers from 2d analyses to 3d valid?** Since a single 2d slice cannot be statistically representative for the full 3d specimen, conclusions from 2d to 3d with respect to the sample size, the required resolution and discretization are generally questionable. A new finding and very useful for applications is that the accuracy of error estimation for 2d samples is very close to that for the 3d case, and the corresponding effectivity indices are in the range of 0.7 to 0.8. Hence, the transferability from 2d error analysis to 3d is possible, which implies a drastic reduction of the computational costs in 3d, since the true error computation based on very fine discretizations can be replaced.
6. **Relevance in practice.** Real concrete volumes in the bulk of structural elements are hardly periodic and therefore, do hardly deform according to PBC which is equally the case for direct numerical simulations (DNS). Hence, the particular BCs (KUBC, PBC, SUBC) replace in homogenization analyses, what is truly unknown by an idealized, artificial setup. For this reason the

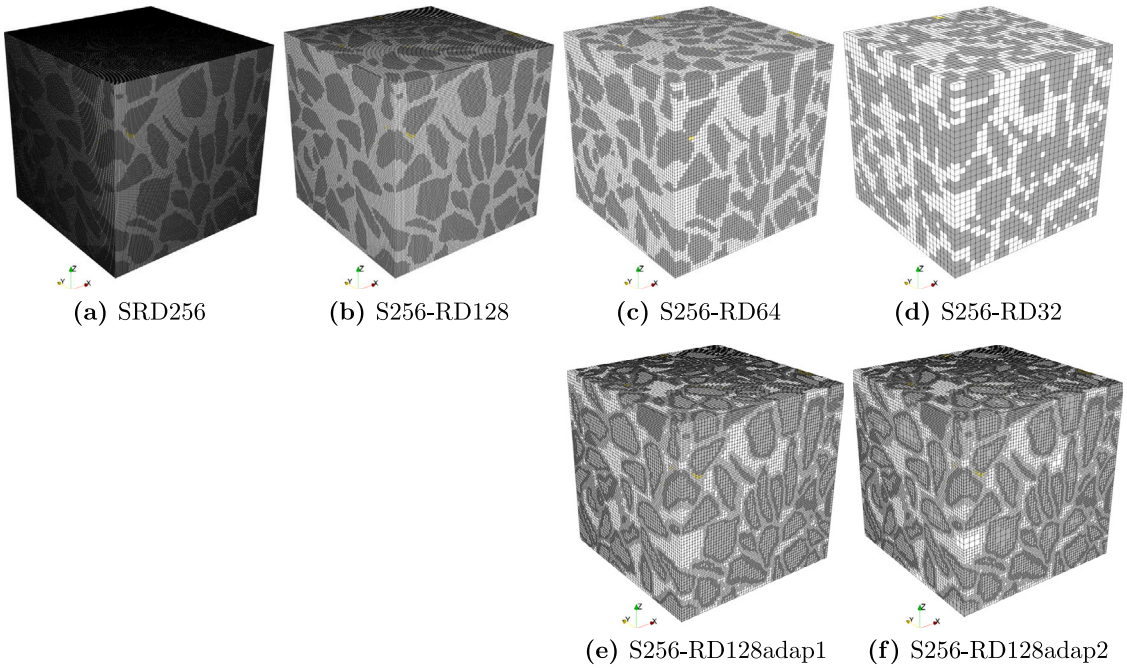


Fig. 17. Coarsening 3d. Resolution and discretization coarsening with coinciding RD for the phase-preserving case in (a)–(d). Notice that the cases in (e) and (f) with two consecutive adaptive mesh coarsening steps start from the phase-preserving, uniform case S256-RD128 in (b) and thus represent the second, alternative branch to uniform mesh and resolution coarsening shown in (c) and (d).

Table 8
Specimen SRD256. Identified isotropic material parameters and the deviation [%] of the remaining elastic coefficients from those of isotropy.

Identification		Check of isotropy							
E (MPa)	ν	$\frac{\mathbb{C}_{11}-\mathbb{C}_{22}}{\mathbb{C}_{11}}$	$\frac{\mathbb{C}_{11}-\mathbb{C}_{33}}{\mathbb{C}_{11}}$	$\frac{\mathbb{C}_{44}-G}{G}$	$\frac{\mathbb{C}_{55}-G}{G}$	$\frac{\mathbb{C}_{66}-G}{G}$	$\frac{\mathbb{C}_{14}}{\mathbb{C}_{11}}$	$\frac{\mathbb{C}_{24}}{\mathbb{C}_{11}}$	$\frac{\mathbb{C}_{34}}{\mathbb{C}_{11}}$
32374.7	0.29	1.56%	1.86%	1.26%	0.11%	0.02%	0.00%	0.03%	0.02%

demonstrated invariance of the effective elastic response of an RVE to the applied BCs is of considerable relevance in practice; it brings the results back from the cyber into the physical world.

7. **Alternative methods.** Alternatives to the present approach shall be briefly discussed. Homogenization simulations for voxel grids with periodic boundary conditions can be efficiently carried out by solvers using the fast Fourier transform (FFT), which were introduced by Moulinec and Suquet [67,68]. These methods, which can be used for finite element problems [69,70], stand out for their speed and the handling of large problems at small memory consumption, for a comprehensive overview we refer to [71]. The latter reference illustrates for a matrix-inclusion problem a major issue of FFT-based methods; they all exhibit stress-artifacts at interfaces such as ringing, checkerboarding or oscillations. Inaccurate stresses at interfaces may falsify the true deformation and failure scenario, although the averaged stress might be sufficiently accurate. Efforts are undertaken to improve the accuracy of stress and strain at interfaces by furnishing the interface voxel with the corresponding laminate stiffness [72], for overcoming a related issue due to diffuse interfaces inherent in the phase-field method see [73].

7. Conclusions and outlook

The present work proposes a concept for error-controlled reduction of the computational complexity for the numerical homogenization analysis of image-based multiphase composite microstructures. Reduction is achieved in the so-called SRD parameter space of size, resolution and discretization, and combinations thereof. This concept is applied to the highly resolved voxel-representation of a concrete specimen. Key criteria for reductions in the elastic analysis of homogenization are the (i) phase fraction ratio, (ii) homogenized elasticity tensor components, (iii) invariance of the elastic response with respect to the applied BCs, and (iv) total errors as well as error distributions in the energy norm.

For the elastic analyses of the concrete sample the best practice turns out to be a combination of coarsening the voxel resolution along with an additional adaptive coarsening of the finite element mesh. For the latter, adaptivity preserves the high resolution at mortar-aggregate interfaces and carries out mesh coarsening only in the interior of both phases. The achieved computational savings are considerable and monitored by validated error estimation.

The present work considers the elastic properties of the analyzed microstructure not only at a few spots but rather for a broad range in the SRD parameter space. For elastic properties it is a comprehensive step towards a digital twin of a representative concrete specimen in homogenization analysis.

In databases currently under construction or rapidly increasing in numbers and volume, digital twins obtain their properties typically from both physical and cyber worlds. Which properties are relevant and reliable? Largest errors and deviations among different choices of R and D are observed not in the homogenized quantities, but locally in the energy errors at interfaces. Energy/stress concentrations are typically the sources of inelastic mechanisms up to failure. Hence R and D are important for discretization methods and therefore, shall be incorporated as object properties of a material's digital twin in databases. Corresponding ontologies,[4] which bring a structure in databases and enable a fast finding, should equally account for that.

[4] e.g. the European Materials Modelling Ontology EMMO (https://emmc.info/emmo-info/).

Future work shall analyze how the coarsening in voxel resolution and finite element discretization does influence the material response taking into account the inelastic behavior. Then it will become clear, whether and to which extent the presented elastic pre-analyses are guiding for the inelastic case. Since for concrete the weakest link occurs at the mortar-aggregate interfaces, the nucleation and propagation of cracks is expected in these regions. For this case the high resolution preserved at interfaces through the present adaptive mesh-coarsening is a valuable feature for the sake of accuracy.

Notwithstanding, and it is also a limitation of the present work, that the spatial variations in the microstructure of composites may have a minor influence on the elastic properties but a strong impact on the overall inelastic behavior [7]. Modeling the inelastic behavior of concrete must account for effects of combined damage-plasticity, cracking, phase separation and decohesion, and uncertainty in properties, see e.g. Unger and Eckardt [74], Snozzi et al. [75], Nguyen et al. [76], Grassl et al. [77], Huang et al. [1], Wang et al. [78], Oliver et al. [79], Liu et al. [80], Ma et al. [81], Thilakarathna et al. [82], Aldakheel [83] to name but a few of many previous relevant works.

Beyond the particular material system of concrete considered here, the present work describes a generally applicable concept for the systematic and error-controlled reduction of the computational complexity of numerical homogenization analysis of image-based, multiphase composite microstructures.

CRediT authorship contribution statement

Ajinkya Gote: Investigation, Visualization, Software, Data curation. **Andreas Fischer:** Investigation, Software. **Chuanzeng Zhang:** Resources, Writing – review & editing. **Bernhard Eidel:** Conceptualization, Methodology, Supervision, Resources, Writing – original draft, Reviewing and editing.

Declaration of competing interest

The authors declare that they have no known competing financial interests or personal relationships that could have appeared to influence the work reported in this paper.

Acknowledgments

Bernhard Eidel acknowledges support by the Deutsche Forschungsgemeinschaft (DFG) within the Heisenberg program (grant no. EI 453/5-1). Simulations were in parts performed with computing resources granted by RWTH Aachen University under project ID BUND0005, in parts with resources at the University of Siegen. The authors are very grateful to Professor Zhenjun Yang (Wuhan University, China) for providing the XCT image data used in [1].

Appendix A. Supplementary data

Supplementary material related to this article can be found online at https://doi.org/10.1016/j.finel.2021.103653.

References

[1] Y. Huang, Z. Yang, W. Ren, G. Liu, C. Zhang, 3D meso-scale fracture modelling and validation of concrete based on in-situ X-ray computed tomography images using damage plasticity model, Int. J. Solids Struct. 67–68 (2015) 340–352.
[2] R. Hill, Elastic properties of reinforced solids: Some theoretical principles, J. Mech. Phys. Solids 11 (5) (1963) 357–372.
[3] W.J. Drugan, J.R. Willis, A micromechanics-based nonlocal constitutive equation and estimates of representative volume element size for elastic composites, J. Mech. Phys. Solids 44 (4) (1996) 497–524.
[4] T. Kanit, S. Forest, I. Galliet, V. Mounoury, D. Jeulin, Determination of the size of the representative volume element for random composites: statistical and numerical approach, Int. J. Solids Struct. 40 (13–14) (2003) 3647–3679.
[5] M. Ostoja-Starzewski, Material spatial randomness: From statistical to representative volume element, Probab. Eng. Mech. 21 (2) (2006) 112–132.
[6] I.M. Gitman, H. Askes, L.J. Sluys, Representative volume: Existence and size determination, Eng. Fract. Mech. 74 (16) (2007) 2518–2534.
[7] M. Geers, V.G. Kouznetsova, W. Brekelmans, Multi-scale computational homogenization: Trends and challenges, J. Comput. Appl. Math. 234 (7) (2010) 2175–2182.
[8] J. Schröder, A numerical two-scale homogenization scheme: the FE^2-method, in: F. Pfeiffer, F.G. Rammerstorfer, E. Guazzelli, B. Schrefler, P. Serafini, J. Schröder, K. Hackl (Eds.), Plasticity and beyond, vol. 550, CISM International Centre for Mechanical Sciences, Vienna, 2014, pp. 1–64.
[9] D. Jeulin, Random texture models for material structures, Stat. Comput. 10 (2) (2000) 121–132.
[10] C. Huet, Application of variational concepts to size effects in elastic heterogeneous bodies, J. Mech. Phys. Solids 38 (6) (1990) 813–841.
[11] S. Das, P. Yang, S.S. Singh, J.C. Mertens, X. Xiao, N. Chawla, N. Neithalath, Effective properties of a fly ash geopolymer: Synergistic application of X-ray synchrotron tomography, nanoindentation, and homogenization models, Cem. Concr. Res. 78 (2015) 252–262.
[12] J. Wimmer, B. Stier, J.-W. Simon, S. Reese, Computational homogenisation from a 3D finite element model of asphalt concrete—linear elastic computations, Finite Elem. Anal. Des. 110 (2016) 43–57.
[13] M.B. Youssef, F. Lavergne, K. Sab, K. Miled, J. Neji, Upscaling the elastic stiffness of foam concrete as a three-phase composite material, Cem. Concr. Res. 110 (2018) 13–23.
[14] Q. Luo, D. Liu, P. Qiao, Z. Zhou, Y. Zhao, L. Sun, Micro-CT-based micromechanics and numerical homogenization for effective elastic property of ultra-high performance concrete, Int. J. Damage Mech. 29 (1) (2020) 45–66.
[15] E. Bosco, R. Claessens, A. Suiker, Multi-scale prediction of chemo-mechanical properties of concrete materials through asymptotic homogenization, Cem. Concr. Res. 128 (2020) 105929.
[16] A. El Moumen, T. Kanit, A. Imad, H. El Minor, Computational thermal conductivity in porous materials using homogenization techniques: Numerical and statistical approaches, Comput. Mater. Sci. 97 (2015) 148–158.
[17] S. Wei, C. Yiqiang, Z. Yunsheng, M.R. Jones, Characterization and simulation of microstructure and thermal properties of foamed concrete, Constr. Build. Mater. 47 (2013) 1278–1291.
[18] T. Wu, İ. Temizer, P. Wriggers, Computational thermal homogenization of concrete, Cem. Concr. Compos. 35 (1) (2013) 59–70.
[19] S.J. Pennycook, P.D. Nellist, Scanning Transmission Electron Microscopy: Imaging and Analysis, New York, NY, 2011.
[20] L. Holzer, M. Cantoni, Review of FIB-tomograph, in: I. Utke, S. Moshkalev, P. Russell (Eds.), Nanofabrication using Focused Ion and Electron Beams, in: Oxford series on nanomanufacturing, vol. 559201222, Oxford University Press, Oxford, 2011, pp. 410–435.
[21] R.A. Ketcham, W.D. Carlson, Acquisition, optimization and interpretation of X-ray computed tomographic imagery: applications to the geosciences, Comput. Geosci. 27 (4) (2001) 381–400.
[22] J.H. Keyak, J.M. Meagher, H.B. Skinner, C.D. Mote, Automated three-dimensional finite element modelling of bone: a new method, J. Biomed. Eng. 12 (5) (1990) 389–397.
[23] S.J. Hollister, J.M. Brennan, N. Kikuchi, A homogenization sampling procedure for calculating trabecular bone effective stiffness and tissue level stress, J. Biomech. 27 (4) (1994) 433–444.
[24] L.L. Mishnaevsky, Automatic voxel-based generation of 3D microstructural FE models and its application to the damage analysis of composites, Mater. Sci. Eng. A 407 (1–2) (2005) 11–23.
[25] P.G. Young, T.B.H. Beresford-West, S.R.L. Coward, B. Notarberardino, B. Walker, A. Abdul-Aziz, An efficient approach to converting three-dimensional image data into highly accurate computational models, Phil. Trans. Ser. A 366 (1878) (2008) 3155–3173.
[26] N. Michailidis, F. Stergioudi, H. Omar, D.N. Tsipas, An image-based reconstruction of the 3D geometry of an al open-cell foam and FEM modeling of the material response, Mech. Mater. 42 (2) (2010) 142–147.
[27] R.M. Sencu, Z. Yang, Y.C. Wang, P.J. Withers, C. Rau, A. Parson, C. Soutis, Generation of micro-scale finite element models from synchrotron X-ray CT images for multidirectional carbon fibre reinforced composites, Composites A 91 (2016) 85–95.
[28] A. Du Plessis, W.P. Boshoff, A review of X-ray computed tomography of concrete and asphalt construction materials, Constr. Build. Mater. 199 (2019) 637–651.
[29] S.-Y. Chung, J.-S. Kim, D. Stephan, T.-S. Han, Overview of the use of micro-computed tomography (micro-CT) to investigate the relation between the material characteristics and properties of cement-based materials, Constr. Build. Mater. 229 (2019) 116843.
[30] S. Bargmann, B. Klusemann, J. Markmann, J.E. Schnabel, K. Schneider, C. Soyarslan, J. Wilmers, Generation of 3D representative volume elements for heterogeneous materials: A review, Prog. Mater. Sci. 96 (2018) 322–384.
[31] T.T. Nguyen, J. Yvonnet, Q.-Z. Zhu, M. Bornert, C. Chateau, A phase field method to simulate crack nucleation and propagation in strongly heterogeneous materials from direct imaging of their microstructure, Eng. Fract. Mech. 139 (2015) 18–39.

[32] F. Bernachy-Barbe, B. Bary, Effect of aggregate shapes on local fields in 3D mesoscale simulations of the concrete creep behavior, Finite Elem. Anal. Des. 156 (2019) 13–23.

[33] S.M. Shah, F. Gray, J.P. Crawshaw, E.S. Boek, Micro-computed tomography pore-scale study of flow in porous media: Effect of voxel resolution, Adv. Water Resour. 95 (2016) 276–287.

[34] C.F. Berg, O. Lopez, H. Berland, Industrial applications of digital rock technology, J. Pet. Sci. Eng. 157 (2017) 131–147.

[35] G. Legrain, P. Cartraud, I. Perreard, N. Moës, An X-FEM and level set computational approach for image-based modelling: Application to homogenization, Internat. J. Numer. Methods Engrg. 86 (7) (2011) 915–934.

[36] W. Ren, Z. Yang, R. Sharma, C. Zhang, P.J. Withers, Two-dimensional X-ray CT image based meso-scale fracture modelling of concrete, Eng. Fract. Mech. 133 (2015) 24–39.

[37] A. Saputra, H. Talebi, D. Tran, C. Birk, C. Song, Automatic image-based stress analysis by the Scaled Boundary Finite Element Method, Internat. J. Numer. Methods Engrg. 109 (5) (2017) 697–738.

[38] H. Gravenkamp, S. Duczek, Automatic image-based analyses using a coupled quadtree-SBFEM/SCM approach, Comput. Mech. 60 (4) (2017) 559–584.

[39] A.A. Saputra, V. Sladek, J. Sladek, C. Song, Micromechanics determination of effective material coefficients of cement-based piezoelectric ceramic composites, J. Intell. Mater. Syst. Struct. 29 (5) (2018) 845–862.

[40] A. Fischer, B. Eidel, Error analysis for quadtree-type mesh coarsening algorithms adapted to pixelized heterogeneous microstructures, Comput. Mech. 16 (04) (2020) 615.

[41] B. Eidel, A. Fischer, A. Gote, From image data towards microstructure information – accuracy analysis at the digital core of materials, ZAMM Z. Angew. Math. Mech. 101 (6) (2021).

[42] R. Baheti, H. Gill, Cyber-physical systems, in: T. Samad, A. Annaswamy (Eds.), Impact Control Technol, vol 12, IEEE Control Systems Society, 2011, pp. 161–166.

[43] W. Kritzinger, M. Karner, G. Traar, J. Henjes, W. Sihn, Digital twin in manufacturing: A categorical literature review and classification, IFAC-PapersOnLine 51 (11) (2018) 1016–1022.

[44] N. Saxena, G. Mavko, Estimating elastic moduli of rocks from thin sections: Digital rock study of 3D properties from 2D images, Comput. Geosci. 88 (2016) 9–21.

[45] R. Glüge, H. Altenbach, N. Mahmood, M. Beiner, On the difference between the tensile stiffness of bulk and slice samples of microstructured materials, Appl. Compos. Mater. 27 (6) (2020) 969–988.

[46] J. Xiao, W. Li, Z. Sun, D.A. Lange, S.P. Shah, Properties of interfacial transition zones in recycled aggregate concrete tested by nanoindentation, Cem. Concr. Compos. 37 (2013) 276–292.

[47] J. Xiao, W. Li, D.J. Corr, S.P. Shah, Effects of interfacial transition zones on the stress–strain behavior of modeled recycled aggregate concrete, Cem. Concr. Res. 52 (2013) 82–99.

[48] J. Xiao, Recycled Aggregate Concrete Structures, Springer Berlin Heidelberg, Berlin, Heidelberg, 2018.

[49] B. Eidel, A. Fischer, The heterogeneous multiscale finite element method for the homogenization of linear elastic solids and a comparison with the FE^2 method, Comput. Methods Appl. Mech. Engrg. 329 (2018) 332–368.

[50] A. Abdulle, Analysis of the Heterogeneous Multiscale FEM for problems in elasticity, Math. Models Methods Appl. Sci. 16 (04) (2006) 615–635.

[51] B. Eidel, A. Fischer, The heterogeneous multiscale finite element method FE-HMM for the homogenization of linear elastic solids, PAMM 16 (1) (2016) 521–522.

[52] B. Eidel, A. Fischer, A. Gote, A nonlinear FE-HMM formulation along with a novel algorithmic structure for finite deformation elasticity, PAMM 18 (1) (2018) e201800457.

[53] B. Eidel, A. Fischer, A. Gote, A nonlinear finite element heterogeneous multiscale method for the homogenization of hyperelastic solids and a novel staggered two-scale solution algorithm, arXiv-ID arXiv:1908.08292v2, 22.08.2019.

[54] R.C. Gonzalez, R.E. Woods, Digital Image Processing, Pearson, New York NY, 2018.

[55] C. Toulemonde, R. Masson, J. El Gharib, Modeling the effective elastic behavior of composites: a mixed finite element and homogenisation approach, C. R. Mec. 336 (3) (2008) 275–282.

[56] F. Ernesti, M. Schneider, S. Winter, D. Hug, G. Last, T. Böhlke, Characterizing digital microstructures by the Minkowski-based quadratic normal tensor: arXiv-ID arXiv:2007.15490v1, 30.07.2020.

[57] A.K. Gupta, A finite element for transition from a fine to a coarse grid, Internat. J. Numer. Methods Engrg. 12 (1) (1978) 35–45.

[58] C.G. Provatidis, Three-dimensional coons macroelements: application to eigenvalue and scalar wave propagation problems, Internat. J. Numer. Methods Engrg. 65 (1) (2006) 111–134.

[59] S. Duczek, A.A. Saputra, H. Gravenkamp, High order transition elements: The xy-element concept—Part I: Statics, Comput. Methods Appl. Mech. Engrg. 362 (2020) 112833.

[60] M. Yerry, M. Shephard, A modified quadtree approach to finite element mesh generation, IEEE Comput. Graph. Appl. 3 (1) (1983) 39–46.

[61] H. Samet, Application of Spatial Data Structure, Addison-Wesley, New York, 1990.

[62] O.C. Zienkiewicz, J.Z. Zhu, A simple error estimator and adaptive procedure for practical engineering analysis, Internat. J. Numer. Methods Engrg. 24 (2) (1987) 337–357.

[63] O.C. Zienkiewicz, J.Z. Zhu, The Superconvergent Patch Recovery and a posteriori error estimates. Part 1: The recovery technique, Internat. J. Numer. Methods Engrg. 33 (7) (1992) 1331–1364.

[64] O.C. Zienkiewicz, J.Z. Zhu, The Superconvergent Patch Recovery and a posteriori error estimates. Part 2: Error estimates and adaptivity, Internat. J. Numer. Methods Engrg. 33 (7) (1992) 1365–1382.

[65] B. Eidel, A. Gote, M. Ruby, L. Holzer, L. Keller, X. Jiang, Estimating the effective elasticity properties of a diamond/ β-SiC composite thin film by 3D reconstruction and numerical homogenization, Diam. Relat. Mater. 97 (2019) 107406.

[66] R. Zabihyan, J. Mergheim, A. Javili, P. Steinmann, Aspects of computational homogenization in magneto-mechanics: Boundary conditions, RVE size and microstructure composition, Int. J. Solids Struct. 130–131 (2018) 105–121.

[67] H. Moulinec, P. Suquet, A fast numerical method for computing the linear and nonlinear mechanical properties of composites, C. R. Acad. Sci. 318 (11) (1994) 1417–1423.

[68] H. Moulinec, P. Suquet, A numerical method for computing the overall response of nonlinear composites with complex microstructure, Comput. Methods Appl. Mech. Engrg. 157 (1–2) (1998) 69–94.

[69] M. Schneider, D. Merkert, M. Kabel, FFT-Based homogenization for microstructures discretized by linear hexahedral elements, Internat. J. Numer. Methods Engrg. 109 (10) (2017) 1461–1489.

[70] M. Leuschner, F. Fritzen, Fourier-Accelerated nodal solvers (FANS) for homogenization problems, Comput. Mech. 62 (3) (2018) 359–392.

[71] M. Schneider, A review of nonlinear FFT-based computational homogenization methods, Acta Mech. 232 (6) (2021) 2051–2100.

[72] M. Kabel, D. Merkert, M. Schneider, Use of composite voxels in FFT-based homogenization, Comput. Methods Appl. Mech. Engrg. 294 (2015) 168–188.

[73] D. Schneider, O. Tschukin, A. Choudhury, M. Selzer, T. Böhlke, B. Nestler, Phase-field elasticity model based on mechanical jump conditions, Comput. Mech. 55 (5) (2015) 887–901.

[74] J.F. Unger, S. Eckardt, Multiscale modeling of concrete, Arch. Comput. Methods Eng. 18 (3) (2011) 341–393.

[75] L. Snozzi, A. Caballero, J.F. Molinari, Influence of the meso-structure in dynamic fracture simulation of concrete under tensile loading, Cem. Concr. Res. 41 (11) (2011) 1130–1142.

[76] V.P. Nguyen, M. Stroeven, L.J. Sluys, Multiscale failure modeling of concrete: Micromechanical modeling, discontinuous homogenization and parallel computations, Comput. Methods Appl. Mech. Engrg. 201–204 (2012) 139–156.

[77] P. Grassl, D. Grégoire, L. Rojas Solano, G. Pijaudier-Cabot, Meso-scale modelling of the size effect on the fracture process zone of concrete, Int. J. Solids Struct. 49 (13) (2012) 1818–1827.

[78] X.F. Wang, Z.J. Yang, J.R. Yates, A.P. Jivkov, C. Zhang, Monte Carlo simulations of mesoscale fracture modelling of concrete with random aggregates and pores, Constr. Build. Mater. 75 (2015) 35–45.

[79] J. Oliver, M. Caicedo, A.E. Huespe, J.A. Hernández, E. Roubin, Reduced order modeling strategies for computational multiscale fracture, Comput. Methods Appl. Mech. Engrg. 313 (2017) 560–595.

[80] T. Liu, S. Qin, D. Zou, W. Song, J. Teng, Mesoscopic modeling method of concrete based on statistical analysis of CT images, Constr. Build. Mater. 192 (2018) 429–441.

[81] J. Ma, W. Du, W. Gao, P. Wriggers, X. Xue, Multiscale finite element analysis of uncertain-but-bounded heterogeneous materials at finite deformation, Finite Elem. Anal. Des. 149 (2018) 15–31.

[82] P. Thilakarathna, K.S. Kristombu Baduge, P. Mendis, V. Vimonsatit, H. Lee, Mesoscale modelling of concrete – A review of geometry generation, placing algorithms, constitutive relations and applications, Eng. Fract. Mech. 231 (2020) 106974.

[83] F. Aldakheel, A microscale model for concrete failure in poro-elasto-plastic media, Theor. Appl. Fract. Mech. 107 (2020) 102517.

8.6 Veröffentlichung: A nonlinear finite element heterogeneous multiscale method for the homogenization of hyperelastic solids and a novel staggered two-scale solution algorithm

Zusätzlich zu den fünf bereits veröffentlichten Artikeln, entstand ein weiteres Paper mit dem Titel **A nonlinear finite element heterogeneous multiscale method for the homogenization of hyperelastic solids and a novel staggered two-scale solution algorithm**, das bisher allerdings nur als Preprint veröffentlicht wurde und sich mit der Lösung von nichtlinearen Problemen beschäftigt.

Schwerpunkt der Arbeit des Doktoranden war die aufwändige Erweiterung des Matlab-Codes, der zuvor nur für lineare Randwertprobleme anwendbar war. In der Veröffentlichung werden zwei unterschiedliche Lösungs-Algorithmen für nichtlineare Zwei-Skalen FE-Verfahren vorgestellt, die beide durch den Doktoranden in dem Matlab-Code umgesetzt wurden.

Daneben wurde der Doktorand in diesem Preprint an diversen Stellen auch federführend tätig. Der Aufschrieb der Theorie in den Kapiteln 2, 3 & 4 erfolgte im Zusammenspiel durch Prof. Eidel und den Doktoranden. Die Beschreibung der beiden Lösungs-Algorithmen in Kapitel 5 erfolgte durch Prof. Eidel, die Durchführung der Berechnungen in Kapitel 6 oblag Herrn Gote. Hierfür wurde ein C++-Code verwendet, der auf dem durch den Doktoranden (weiter)entwickelten Matlab-Code basiert und durch eine MPI-Parallelisierung deutliche Performance-Vorteile gegenüber dem Matlab-Code besitzt.

Die Auswertung der Berechnungen in Kapitel 6 und die Auswertung in Kapitel 7 erfolgte schlussendlich als Gemeinschaftsaufgabe durch die drei Autoren.

arXiv:1908.08292v2 [math.NA] 20 Dec 2019

A Nonlinear Finite Element Heterogeneous Multiscale Method for the Homogenization of Hyperelastic Solids and a Novel Staggered Two-Scale Solution Algorithm

Bernhard Eidel, Andreas Fischer, Ajinkya Gote

Heisenberg Group, Institute of Mechanics, Department Mechanical Engineering
Universität Siegen, 57068 Siegen, Paul-Bonatz-Str. 9-11, Germany
e-mail: bernhard.eidel@uni-siegen.de, phone: +49 271 740 2224, fax: +49 271 740 2436

Abstract

In this paper we address three aspects of nonlinear computational homogenization of elastic solids by two-scale finite element methods. First, we present a nonlinear formulation of the finite element heterogeneous multiscale method FE-HMM in a Lagrangean formulation that covers geometrical nonlinearity and, more general, hyperelasticity. Second, a-priori estimates of FE-HMM, which exist so far only for the fully linear elastic case in solid mechanics, are assessed in the regime of nonlinear elasticity. The measured convergence rates agree fairly well with those of the fully linear regime. Third, we revise the standard solution algorithm of FE^2 which is a staggered scheme in terms of a nested loop embedding the full solution of the micro problem into one macro solution iteration step. We demonstrate that suchlike staggered scheme, which is typically realized by a nested two-level Newton algorithm, can safely and efficiently be replaced by direct alternations between micro and macro iterations. The novel algorithmic structure is exemplarily detailed for the proposed nonlinear FE-HMM, its efficiency is substantiated by a considerable speedup in numerical tests.

Keywords: Heterogeneous multiscale method; Finite element method; Macro-to-micro modeling; Homogenization

1 Introduction

For the solution of homogenization problems, two-scale finite element methods like the FE^2 method and the Finite Element Heterogeneous Multiscale Method FE-HMM combine in a favorable manner the needs for both accuracy and efficiency in that they sample the real microstructure in representative volume elements RVEs of confined size. By virtue of the equivalence of the coarse scale energy density with the fine-scale energy density these methods stand on sound ground in physics, by virtue of the a priori estimates developed for FE-HMM, they are equipped with necessary ingredients in mathematics.

In spite of considerable achievements in the field, there is space for improvements; the present work addresses three of them.

1. **Nonlinear FE-HMM**. A nonlinear version of the Finite Element Heterogeneous Multiscale Method FE-HMM is developed for the homogenization of solids.
2. **A priori estimates**. An assessment of the a priori estimates of linear FE-HMM is carried out in the nonlinear regime of hyperelasticity.

3. **Solution algorithm**. The revision and improvement of the standard algorithmic structure of nonlinear two-scale finite element methods for homogenization like the FE² method and the present nonlinear FE-HMM.

These aims shall be motivated and put into perspective by a brief account of the state of the art.

1.1 Development of a nonlinear FE-HMM

FE-HMM formulations for problems in solid mechanics are so far restricted to linear problems, i.e. to linear elasticity in a geometrical linear setting; [1] presents a fully discrete convergence analysis taking into account the discretization errors at both micro and macro levels.

FE² and FE-HMM are equivalent methods, for a comparison see [2]; they are siblings (if not twins) having different parents. FE², an engineering mechanics off-spring, is quite outgoing since its infancy and, unburdened from the necessity of delivering mathematical results on existence and uniqueness of solutions, has appreciated direct contact with nonlinear problems since its first appearance [3], [4], [5], [6], [7]. FE-HMM as a method of mathematicians has grown up subject to the restriction, first prove, then apply; consequently its playground of applications was mostly in linear problems, comprehensive overviews are given in [8], [9], [10]. For the mathematical analysis of FE-HMM in the nonlinear regime of elliptic PDEs, results are sparse. [11] consider nonlinear monotone elliptic problems. For the same case [12] derive a posteriori error estimates for the L^2-error between the HMM approximation and the solution of the macroscopic limit equation. [13] present an FE-HMM formulation for inelasticity that draws on the tangent moduli for stiffness-transfer and therein very much resembles the FE² method.

The present work proposes a nonlinear FE-HMM formulation for solid mechanics, which implies geometrical nonlinearity, either along with linear elasticity or nonlinear hyperelasticity. The extension to inelastic constitutive laws is a minor step following the perspective that inelasticity –in finite element numerics– can be understood as a type of nonlinear elasticity along with evolution equations for the inelastic deformation part treated as internal variables.

1.2 Test of the a priori estimates of linear FE-HMM for hyperelasticity

Error estimates are a necessary equipment of numerical methods to serve as reliable tools in science and engineering. By virtue of its foundation in mathematical homogenization by asymptotic expansion a priori estimates are available for FE-HMM; the elliptic case is considered in [14], [15], the elliptic case of linear elasticity in a geometrical linear setting in [1], [9]. An assessment of the a priori estimates for various energetically consistent boundary conditions applied to the micro domain is presented in [16].

In the present work we assess the convergence of FE-HMM solutions in the nonlinear regime of hyperelastic material behavior, although the estimates are derived for the setting of linear elasticity (generally, for linear elliptic PDEs). This will be carried out by a comparison with the linear case, which clarifies, whether the deviation from the estimates

are caused by a lowered regularity of the boundary value problem or whether the deviation follows from the nonlinearities of the considered setting.

1.3 Speedup through modified algorithmic structure of two-scale FEM

In view of the considerable computational costs of two-scale FEM in homogenization there is a need for methodic advancements aiming at improved performance. For that aim several new and modified methods have been developed beyond parallelization.

Homogenization techniques based on Fast Fourier Transforms (FFT) were introduced in [17], [18], which are built on a Lippmann-Schwinger formulation [19], [20]; applicability and efficiency was demonstrated in [21], [22], and many more. Reduced basis methods and model order reduction exhibit considerable potential to speed up simulations; [23] introduced a general (Galerkin) projection based reduced order model referred to as R3M where the reduced basis is obtained via snapshot proper orthogonal decomposition. Applications to nonlinear elasticity in [24], to homogenization problems in [25]. The derived reduced problems are low-dimensional and nonlinear. In an effort to reduce the computational complexity by a modified modeling [26] consider in FE^2 statistically similar representative volume elements (SSRVE) in order to replace the true microstructure in its full geometrical complexity by a simplified surrogate that resembles the original one by geometrical features as analyzed by different geometrical similarity measures. Domain-decomposition based on a FETI (finite element tearing and interconnect) have been proposed and successfully applied [27], [28].

Pixel- and voxel-based representations of reconstructed microstructures obtained from tomographic imaging methods is frequently used in various fields [29], [30], [31]. Suchlike spatially uniform discretizations are typically the point of departure for quadtree- and octree-based mesh coarsening which can strongly reduce computational efforts in homogenization [32], [33]. While the gain in efficiency was quantified earlier, the error introduced by adaptive mesh coarsening was for the first time assessed in [34].

The present work aims at speeding up computations through an improvement of the standard algorithmic concept of FE^2. The discretized variational form of the balance of linear momentum both on the macro level and the micro level amount to systems of nonlinear algebraic equations, which are each typically but not necessarily solved by Newton's method. More important, the algorithmic solution framework is not monolitic, but exhibits a staggered structure, which provides a mutual exchange of coupling quantities (micro-to-macro: current micro stiffness and stress, macro-to-micro: current macro deformation) between the macro problem and the micro problems.

The very standard of suchlike staggered scheme is realized by a nested loop embedding the full solution of the micro problems into one macro solution iteration step as sketched in the pseudocode of "Algorithm 1".

The attribute *standard* is set by a multitude of contributions to the field, [6] p. 313, [7] pp. 41,42, [35] pp. 302,303, [36] p. 574, [37] p. 3236, [38] p. 5532, for thermo-mechanical problems [39] p. 606, [40] p. 499, [41] p. 8, for different coupling conditions at finite deformations [42] p. 20, for nonlinear monotone elliptic problems in FE-HMM [11] p. 966, [43] p. 7, to name but a few.

Algorithm 1: nested (standard)

```
while macro residual < macro tolerance do
    macro iteration;
    while micro residual < micro tolerance do
        micro iteration;
    end
end
```

In the present work a revision of this established scheme is carried out along with the proposal to replace it by an algorithm of direct alternations between micro and macro iterations as sketched in the pseudocode box "Algorithm 2".

Algorithm 2: alternating (novel)

```
while macro residual < macro tolerance do
    macro iteration;
    micro iteration;
end
```

The novel scheme, which was introduced in [44], is described in more detail in Sec. 5.2. Its properties and benefits in terms of accuracy, efficiency and stability with respect to large load step sizes are assessed in the example section 6.

The paper is organized along the route of the above aims.

2 Strong and variational forms

We consider a body $\mathcal{B}_0$, a bounded subset of $\mathbb{R}^{n_{\text{dim}}}$, $n_{\text{dim}} = 2, 3$, with boundary $\partial\mathcal{B}_0 = \partial\mathcal{B}_{0D} \cup \partial\mathcal{B}_{0N}$ where $\partial\mathcal{B}_{0D}$ and $\partial\mathcal{B}_{0N}$ are disjoint sets. The closure of the body $\mathcal{B}$ is denoted by $\overline{\mathcal{B}}$. The body undergoes deformation $\boldsymbol{\varphi} : \Omega \to \mathbb{R}^{n_{\text{dim}}}$ with deformation gradient $\boldsymbol{F} = \partial_{\boldsymbol{X}}\boldsymbol{\varphi}(\boldsymbol{X})$ and the Jacobian $J = \det\boldsymbol{F} > 0$, where $\boldsymbol{X}$ is a material point in the reference configuration. The body is subject to body forces $\boldsymbol{b}$ and surface tractions $\boldsymbol{g}$ and in static equilibrium

$$\text{Div}[\boldsymbol{P}] + \rho\,\boldsymbol{b} = \boldsymbol{0} \tag{1}$$

in terms of the first Piola-Kirchhoff stress tensor $\boldsymbol{P}$, density ρ in the reference configuration, and body forces $\boldsymbol{b}$ neglecting inertia terms.

Dirichlet and Neumann boundary conditions are prescribed by

$$\boldsymbol{u} = \hat{\boldsymbol{u}} \quad \text{on} \quad \partial\mathcal{B}_{0D} \qquad \text{and} \quad \boldsymbol{P}\cdot\boldsymbol{N} = \boldsymbol{t} \quad \text{on} \quad \partial\mathcal{B}_{0N}\,. \tag{2}$$

The corresponding variational form of the Boundary Value Problem (BVP) (1), (2) reads

$$G := \int_{\mathcal{B}_0} (\text{Div}[\boldsymbol{P}] + \rho\,\boldsymbol{b}) \cdot \delta\boldsymbol{u}\,\mathrm{d}V = 0\,, \tag{3}$$

with virtual displacements/test functions $\delta\boldsymbol{u}$ which can be transformed by $\mathrm{Div}[\boldsymbol{P}^T\cdot\delta\boldsymbol{u}]-\boldsymbol{P}:\mathrm{Grad}[\boldsymbol{P}^T\cdot\delta\boldsymbol{u}]$ into

$$G:=\underbrace{\int\limits_{\mathcal{B}_0}\boldsymbol{P}:\mathrm{Grad}[\delta\boldsymbol{u}]\,\mathrm{d}V}_{=G^{\mathrm{ext}}}\underbrace{-\int\limits_{\partial\mathcal{B}_{0N}}\boldsymbol{t}\cdot\delta\boldsymbol{u}\,\mathrm{d}A-\int\limits_{\mathcal{B}_0}\rho\,\boldsymbol{b}\cdot\delta\boldsymbol{u}\,\mathrm{d}V}_{=G^{\mathrm{int}}}=0\,, \tag{4}$$

which has to hold for all $\delta\boldsymbol{u}\in\mathcal{V}$, where $\mathcal{V}$ is the space of admissible displacements, i.e. virtual displacements that fulfill homogeneous Dirichlet boundary conditions

$$\mathcal{V}=\{\delta\boldsymbol{u};\boldsymbol{u}\in H^1(\mathcal{B}_0)^{n_{\mathrm{dim}}},\boldsymbol{u}|_{\partial\mathcal{B}_{0D}}=\boldsymbol{0}\}\,. \tag{5}$$

With

$$\boldsymbol{P}:\mathrm{Grad}[\delta\boldsymbol{u}]=\boldsymbol{S}:\boldsymbol{F}^T\cdot\mathrm{Grad}[\delta\boldsymbol{u}]=\boldsymbol{S}:\frac{1}{2}(\boldsymbol{F}^T\cdot\delta\boldsymbol{F}+\delta\boldsymbol{F}^T\cdot\boldsymbol{F})=\boldsymbol{S}:\delta\boldsymbol{E} \tag{6}$$

the virtual work can be equally expressed by the second Piola-Kirchhoff stress tensor $\boldsymbol{S}$ and the Green-Lagrange strain tensor $\boldsymbol{E}$

$$G:=\int\limits_{\mathcal{B}_0}\frac{1}{2}\boldsymbol{S}:\delta\boldsymbol{E}\,\mathrm{d}V-\int\limits_{\partial\mathcal{B}_{0N}}\boldsymbol{t}\cdot\delta\boldsymbol{u}\,\mathrm{d}A-\int\limits_{\mathcal{B}_0}\rho\,\boldsymbol{b}\cdot\delta\boldsymbol{u}\,\mathrm{d}V=0\,. \tag{7}$$

2.1 Characteristics and conditions for computational homogenization

For the solution of the BVP in its variational form, a constitutive law must be defined in the domain $\mathcal{B}_0$ for which we assume matter to be heterogeneous in its properties, such that the solution to the BVP shall be found through homogenization. For the application of homogenization in terms of computational micro-macro transitions several conditions must be fulfilled, which partly refer to the characteristics of the physical problem, partly to mathematical homogenization, and partly to the properties of the solution method. Consequently, the following assumptions are made:

- **Scale separation**. A prerequisite of homogenization is that the characteristic length of microstructural features must be *considerably* smaller than the characteristic length on the macro scale[1] $L_{\mathrm{mac}}\gg L_{\mathrm{mic}}$. The deeper root of this requirement is the separation of variables in mathematical homogenization which requires a separation of length scales with the implicit, tacit or explicit assumption that the micro solution and macro solution equally reflect this scale separation [45], [46], [47], [48], [49].
- **Sampling domains**. For the microstructure on the fine scale a statistically representative volume element RVE is available, [50], [51], [52], [53].
- **Constitutive equations**. The type of constitutive law and its parameters are available for matter in the RVE, for its constituents (grains, phases, etc.) and interfaces, but not on the macro scale in terms of effective laws and their parameters.

[1] We use macro/coarse scale and micro/fine scale each as synonyms.

- **Coupling conditions**. The coupling conditions cover a kinematical and an energetic aspect. The equivalence of energy densities of the coarse scale with the fine scale is a cornerstone of homogenization, from which different boundary conditions on the RVE are derived each fulfilling this equivalence [50], [54], [55], [56]. The kinematical embedding of the RVE into the macro domain is part of the modeling assumptions; if the deformation applied to the RVE is homogeneous, it is referred to as first order computational homogenization.

- **Scale interaction and data transfer**. The conditions for these two items follow from the above items of constitutive equations and coupling conditions. The macro BVP is the driver of the micro BVP through deformation in the coupling conditions, the top-down direction of data transfer. Since constitutive equations with parameters are a priori exclusively available on the micro scale, the numerical solution of the macro BVP requires stiffness and stress from the fine scale, the bottom-up direction of data transfer.

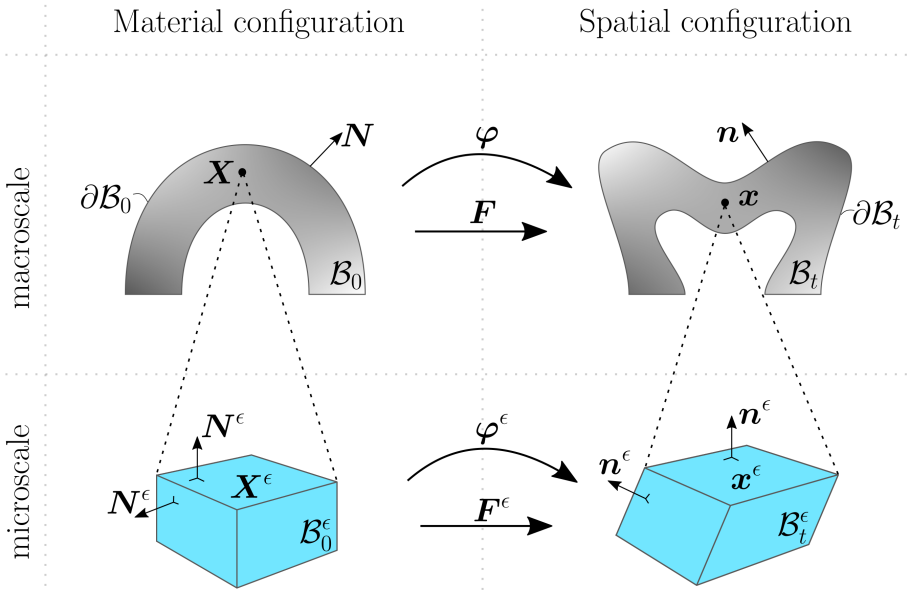


Figure 1: Homogenization: The general setting of micro-macro transition in material and spatial configurations. Sketch adapted from [42].

While balance laws are scale invariant and therefore are known and apply for the macro as well as the micro scale, the effective constitutive law along with its parameters is not known for the macro scale but exclusively for the micro scale, here in terms of the hyperelasticity relations

$$\boldsymbol{P}^\epsilon = \frac{\partial \psi^\epsilon}{\partial \boldsymbol{F}^\epsilon}, \quad \mathbb{A}^\epsilon = \frac{\partial^2 \psi^\epsilon}{\partial \boldsymbol{F}^\epsilon \partial \boldsymbol{F}^\epsilon}, \quad \boldsymbol{S}^\epsilon = \boldsymbol{F}^{\epsilon\,-1}\,\boldsymbol{P}^\epsilon, \tag{8}$$

where we indicate micro scale quantities by ϵ as borrowed from mathematical homogenization, where it refers to the (periodic) cell size.

The Hill-Mandel energy equivalence principle is formulated as an equivalence of stress power in terms of the first Piola-Kirchhoff stress tensor and the material time derivative

of the work-conjugate deformation gradient $\boldsymbol{F}$

$$\boldsymbol{P} : \dot{\boldsymbol{F}} = \frac{1}{|\mathcal{B}_0|} \int_{\mathcal{B}_0} \boldsymbol{P}^\epsilon : \dot{\boldsymbol{F}}^\epsilon \, \mathrm{d}V \,, \tag{9}$$

where their averages are defined according to

$$\boldsymbol{P} \;=\; \langle \boldsymbol{P}^\epsilon \rangle_0 \,, \qquad \boldsymbol{F} \;=\; \langle \boldsymbol{F}^\epsilon \rangle_0 \,, \quad \text{with} \quad \langle \{\bullet\} \rangle_0 = \frac{1}{|\mathcal{B}_0|} \int_{\mathcal{B}_0} \{\bullet\} \, \mathrm{d}V \,, \tag{10}$$

with $|\mathcal{B}_0|$ the measure of $\mathcal{B}_0$. The volume average for the deformation gradient according to $(10)_2$ is only valid for microstructures without hollow spaces; for materials with voids, cracks, or for cellular materials it holds

$$\boldsymbol{F} := \frac{1}{|\mathcal{B}_0|} \int_{\partial\mathcal{B}_0} \boldsymbol{x} \otimes \boldsymbol{N} \, \mathrm{d}A = \frac{1}{|\mathcal{B}_0|} \left[\int_{\mathcal{B}_0} \boldsymbol{F} \, \mathrm{d}V - \int_{|\circ|} \boldsymbol{x} \otimes \boldsymbol{N} \, \mathrm{d}A \right] \,, \tag{11}$$

where $\boldsymbol{x}$ is the position vector of a point in $\mathcal{B}_0$, $\boldsymbol{N}$ is the normal on $\partial\mathcal{B}_0$, and where $|\circ|$ represents the boundaries of hollow space.

Since the present FE-HMM framework is formulated in the reference configuration with the work conjugate pair of the second Piola-Kirchhoff stress and the Green-Lagrange strain tensor, the macro average stress must be consistent with (10) in (9), it holds

$$\boldsymbol{S} \;=\; \langle \boldsymbol{F}^\epsilon \rangle_0^{-1} \langle \boldsymbol{P}^\epsilon \rangle_0 \,. \tag{12}$$

An averaged macro stress according to $\boldsymbol{S}^* := \langle \boldsymbol{S}^\epsilon \rangle_0$ is not consistent with (10) since $\boldsymbol{S} \neq \boldsymbol{S}^*$.

A framework for equivalence relationships for finite strain multi-scale solid constitutive models based on the volume averaging of the microscopic stress and deformation gradient fields over a representative volume element (RVE) is presented in [57]. Based on a purely kinematically-based variational framework they derive sufficient conditions under which the volume average of the microscopic first Piola-Kirchhoff stress over the material configuration of the RVE is mechanically equivalent to the average of the microscopic Cauchy stress field over the spatial configuration.

Similar to the present work, the weak form in $\boldsymbol{S}$ and $\boldsymbol{E}$ in the context of FE^2 is chosen in [58] and [59].

3 The Heterogeneous Multiscale Finite Element Method

A nonlinear version of FE-HMM is derived for the application to geometrical nonlinear problems in solid mechanics based on linear elastic or (nonlinear) hyperelastic constitutive laws. In the example section 6 we will consider Neo-Hookean-type hyperelasticity. While the majority of homogenization schemes is formulated in reference configuration in terms of $\boldsymbol{P}$ and $\boldsymbol{F}$, we employ the work-conjugate pair $\boldsymbol{S}$ and $\boldsymbol{E}$.

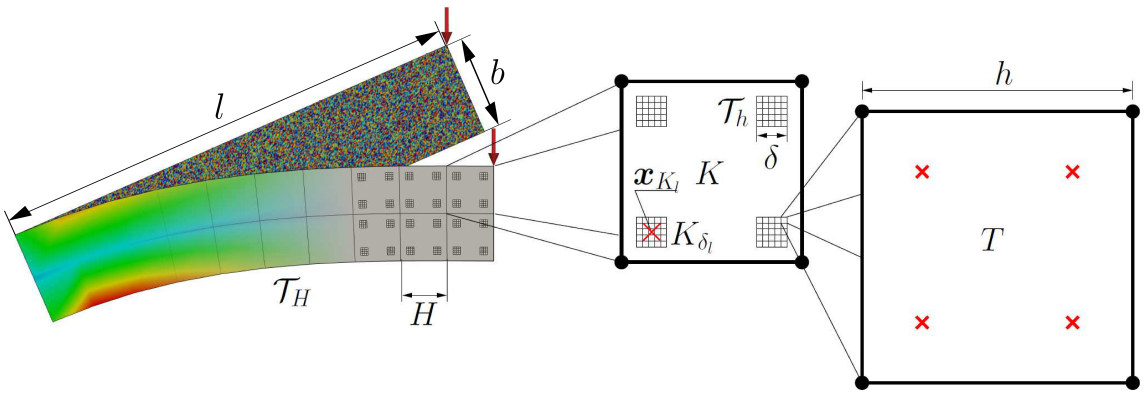


Figure 2: Micro-macro transition of FE-HMM: The triangulation of the macro problem $\mathcal{T}_H$ results in finite elements K of size H. Micro sampling domains of characteristic length δ in triangulation $\mathcal{T}_h$ into elements T of size h are attached to the macro quadrature points $\boldsymbol{x}_{K_{\delta_l}}$ of K, hence spanning the sampling domain $K_{\delta_l} = \boldsymbol{x}_{K_{\delta_l}} + \delta\,[-1/2, +1/2]^{n_{\text{dim}}}$, $\delta \geq \epsilon$, centered at quadrature points (qp), $l = 1, \ldots, N_{qp}$. The separation of length scales imposes the condition $\{l, b\} \gg \epsilon$.

3.1 Discretization and linearization of the variational form

Here we consider the piecewise linear continuous FEM in macro and micro space, respectively.

We define a macro finite element space as

$$\mathcal{S}^p_{\partial\mathcal{B}_{0D}}(\mathcal{B}_0, \mathcal{T}_H) = \left\{ \boldsymbol{u}^H \in H^1(\mathcal{B}_0)^{n_{\text{dim}}}; \boldsymbol{u}^H|_{\partial\mathcal{B}_{0D}} = \boldsymbol{0}; \boldsymbol{u}^H|_K \in \mathcal{P}^p(K)^{n_{\text{dim}}}, \forall\, K \in \mathcal{T}_H \right\} \quad (13)$$

where $\mathcal{P}^p$ is the space of (in the present work: linear, $p = 1$) polynomials on the element K, $\mathcal{T}_H$ the (quasi-uniform) triangulation of $\mathcal{B}_0 \subset \mathbb{R}^{n_{\text{dim}}}$. The space $\mathcal{S}^p_{\partial\mathcal{B}_{0D}}$ is a subspace of $\mathcal{V}$ defined in (5). The characteristic element size on the macro scale H (Fig. 2) refers in index or superscript to macro scale quantities in the discretized setting, the characteristic micro element size h analogously marks micro scale quantities of the discrete case.

For the solution of the macro scale BVP we use the two-scale FEM framework of the FE-HMM, as originally proposed in [56] and analyzed for elliptic PDEs in [14].

The macro solution of the FE-HMM is given by the following variational form:

Find $\boldsymbol{u}^H \in \mathcal{S}_{\mathcal{B}_{0D}}(\mathcal{B}_0, \mathcal{T}_H)$ such that

$$G^H(\boldsymbol{u}^H, \delta\boldsymbol{u}^H) = \int_{\mathcal{B}_0} \frac{1}{2}\boldsymbol{S}^H : \delta\boldsymbol{E}^H \,\mathrm{d}V - \int_{\partial\mathcal{B}_{0N}} \boldsymbol{t} \cdot \delta\boldsymbol{u}^H \,\mathrm{d}A - \int_{\mathcal{B}_0} \boldsymbol{b} \cdot \delta\boldsymbol{u}^H \,\mathrm{d}V \quad \forall\, \delta\boldsymbol{u}^H \in \mathcal{S}_{\partial\mathcal{B}_{0D}}(\mathcal{B}_0, \mathcal{T}_H)\,. \quad (14)$$

Standard finite element shape functions N_I are used for the interpolation

$$\boldsymbol{u}^H = \sum_{I=1}^{N_{\text{node}}} N_I \boldsymbol{d}^H_I\,, \quad \boldsymbol{u}^h = \sum_{I=1}^{n_{\text{node}}} N_I \boldsymbol{d}^h_I\,, \quad (15)$$

of nodal displacement vectors $\boldsymbol{d}^H_I$, $\boldsymbol{d}^h_I$, where N/n_{node} is the number of nodes per element on the macro/micro scale. Virtual displacements $\delta\boldsymbol{u}^H$ and $\delta\boldsymbol{u}^h$ are equally obtained through interpolation of nodal values $\delta\boldsymbol{d}^H_I$ and $\delta\boldsymbol{d}^h_I$, respectively. Consequently, we obtain for G^H

in (14)

$$G^H(\boldsymbol{u}^H, \delta\boldsymbol{u}^H) \;=\; \sum_{I=1}^{N_{\text{node}}} \left(\delta \boldsymbol{d}_I^H\right)^T \boldsymbol{f}_I^H \quad \text{with} \quad \boldsymbol{f}_I^H = \boldsymbol{f}_I^{\text{int},H} - \boldsymbol{f}_I^{\text{ext},H} \tag{16}$$

and for the analogously defined G^h on the micro domain

$$G^h(\boldsymbol{u}^h, \delta\boldsymbol{u}^h) \;=\; \sum_{I=1}^{n_{\text{node}}} \left(\delta \boldsymbol{d}_I^h\right)^T \boldsymbol{f}_I^h \quad \text{with} \quad \boldsymbol{f}_I^h = \boldsymbol{f}_I^{\text{int},h} - \boldsymbol{f}_I^{\text{ext},h}\,. \tag{17}$$

The internal and external nodal force vectors are defined for node I of macro element K with volume $|K|$ and surface ∂K and for node I of micro element T with volume $|T|$ and surface ∂T

$$\boldsymbol{f}_I^{\text{int},H} \;=\int\limits_{|K|} \boldsymbol{B}_I^T \boldsymbol{S}^H \,\mathrm{d}V\;, \quad \boldsymbol{f}_I^{\text{int},h} \;=\int\limits_{|T|} \boldsymbol{B}_I^T \boldsymbol{S}^h \,\mathrm{d}V \tag{18}$$

$$\boldsymbol{f}_I^{\text{ext},H} \;=\int\limits_{\partial K} N_I \bar{\boldsymbol{t}} \,\mathrm{d}A\;, \quad \boldsymbol{f}_I^{\text{ext},h} \;=\int\limits_{\partial T} N_I \boldsymbol{t} \,\mathrm{d}A\,. \tag{19}$$

For the computation of $\boldsymbol{f}_I^{\text{int},H}$ on the macro domain the second Piola-Kirchhoff stress $\boldsymbol{S}^H$ is obtained according to (12), hence, along with our notation for the discretized case, by

$$\boldsymbol{S}^H \;=\; \langle \boldsymbol{F}^h \rangle_0^{-1} \langle \boldsymbol{P}^h \rangle_0\,. \tag{20}$$

3.2 The micro-to-macro stiffness transfer and assembly

Since G^H is nonlinear in $\boldsymbol{u}^H$, it is linearized at the current macro displacement state $\boldsymbol{u}^H$

$$\mathrm{Lin}\left[G^H(\boldsymbol{u}^H, \delta\boldsymbol{u}^H)\right] \;=\; G^H(\boldsymbol{u}^H, \delta\boldsymbol{u}^H) + \mathrm{D}G^H(\boldsymbol{u}^H, \delta\boldsymbol{u}^H)\cdot\Delta\boldsymbol{u}^H \;=\; 0\,. \tag{21}$$

The first term $G^H(\boldsymbol{u}^H, \delta\boldsymbol{u}^H)$ is the evaluation of G^H for the current macro displacement field, the second term is the linearization of G^H in the direction of the incremental macro displacements $\Delta\boldsymbol{u}^H$ (a Directional- or Gateaux-derivative).
In analogy to the linear case, the key step of nonlinear FE-HMM is to approximate in the numerical quadrature of (22) the macro values at the quadrature points by the volume-averaged integral of micro scale quantities according to (23)

$$\mathrm{D}G^H(\boldsymbol{u}^H, \delta\boldsymbol{u}^H)\cdot\Delta\boldsymbol{u}^H \;=\; \sum_{K\in\mathcal{T}_H} \sum_{l=1}^{N_{qp}} \omega_{K_{\delta_l}} \left[\delta\boldsymbol{E}^H : \mathbb{C}_T^{0,h} : \Delta\boldsymbol{E}^H + \boldsymbol{S}^H : \Delta\delta\boldsymbol{E}^H\right] \mathrm{d}V \tag{22}$$

$$\approx \sum_{K\in\mathcal{T}_H} \sum_{l=1}^{N_{qp}} \omega_{K_{\delta_l}} \left[\frac{1}{|K_{\delta_l}|} \int\limits_{K_{\delta_l}} \left[\delta\boldsymbol{E}^h : \mathbb{C}_T^{\epsilon} : \Delta\boldsymbol{E}^h + \boldsymbol{S}^h : \Delta\delta\boldsymbol{E}^h\right]\right] \mathrm{d}V. \tag{23}$$

The approximation reflects that the constitutive law in terms of the free energy function $\psi^0(\boldsymbol{x})$, and the derived quantities of stress $\boldsymbol{S}^H$ and the tangent $\mathbb{C}_T^{0,h}$ are not known.

The micro solution $\boldsymbol{u}^h$ and derived quantities $\boldsymbol{E}^h$, $\boldsymbol{S}^h$ are obtained

- on micro sampling domains $K_{\delta_l} = \boldsymbol{x}_{K_{\delta_l}} + \delta\,[-1/2, +1/2]^{n_{\text{dim}}}$, $\delta \geq \epsilon$, volume $|K_{\delta_l}|$
- centered at quadrature points $\boldsymbol{x}_{K_{\delta_l}}$ of K, $l = 1, \ldots, N_{qp}$ with weights $\omega_{K_{\delta_l}}$,

for a visualization see Fig. 2. The micro sampling domains render the additive contribution to the tangential stiffness matrix of the macro finite element.

The approximation in numerical quadrature is consistent with the Hill-Mandel postulate of energy equivalence. It is, however, not sufficient. Since the pointwise macroscopic energy density is replaced by microscopic energy density in a volume, boundary conditions consistent to the postulate must be chosen.

The macro element tangential stiffness matrix contribution $\boldsymbol{k}^H_{T,IJ}$ for nodes I and J of element K are obtained –in analogy to the linear case– by inserting finite element shape functions into (22), hence $\delta\boldsymbol{u}^H(\boldsymbol{N}_I)$ and $\Delta\boldsymbol{u}^h(\boldsymbol{N}_J)$, which results in[2]

$$\boldsymbol{k}^H_{T,IJ,K} = \mathrm{D}G^H(\boldsymbol{u}^H, \delta\boldsymbol{u}^H(\boldsymbol{N}_J)) \cdot \Delta\boldsymbol{u}^H(\boldsymbol{N}_I) \tag{24}$$

$$= \sum_{l=1}^{N_{qp}} \frac{\omega_{K_{\delta_l}}}{|K_{\delta_l}|} \left(\boldsymbol{D}^{h(I)}\right)^T \boldsymbol{K}^h_{T,K_{\delta_l}} \boldsymbol{D}^{h(J)}\,, \tag{25}$$

$$\text{where} \quad \boldsymbol{D}^{h(I)} = \left(\, \boldsymbol{D}^{h(I,x_1)} | \boldsymbol{D}^{h(I,x_2)} | \boldsymbol{D}^{h(I,x_3)} \,\right) \quad \text{for } n_{\text{dim}} = 3\,, \tag{26}$$

$$\boldsymbol{k}^H_{T,K} = \sum_{l=1}^{N_{qp}} \frac{\omega_{K_{\delta_l}}}{|K_{\delta_l}|} \boldsymbol{T}^T_{K_{\delta_l}} \boldsymbol{K}^h_{T,K_{\delta_l}} \boldsymbol{T}_{K_{\delta_l}}\,, \tag{27}$$

$$\text{where} \quad \boldsymbol{T}_{K_{\delta_l}} = \left[\left[\left[\boldsymbol{D}^{h(I,x_i)} \right]_{i=1,\ldots,n_{\text{dim}}} \right]_{I=1,\ldots,N_{\text{node}}} \right]. \tag{28}$$

The assembly of the global micro stiffness matrix implies the arrangement of $\boldsymbol{D}^{h(I)}$ in different columns for $I = 1, \ldots, N_{\text{node}}$, which results in the transformation matrix $\boldsymbol{T}_{K_{\delta_l}}$.

With M_{mic} for the number of nodes in the micro domain, and N_{node} for the number of elements on a macro element, it can be easily verified that the matrix dimensions of $\boldsymbol{T}_{K_{\delta_l}} \in \mathbb{R}^{(M_{\text{mic}}\cdot n_{\text{dim}})\times(N_{\text{node}}\cdot n_{\text{dim}})}$, $\boldsymbol{K}^h_{T,K_{\delta_l}} \in \mathbb{R}^{(M_{\text{mic}}\cdot n_{\text{dim}})\times(M_{\text{mic}}\cdot n_{\text{dim}})}$, and of $\boldsymbol{k}^H_{T,K} \in \mathbb{R}^{(N_{\text{node}}\cdot n_{\text{dim}})\times(N_{\text{node}}\cdot n_{\text{dim}})}$ are consistently used in (27), and that $\boldsymbol{T}_{K_{\delta_l}}$ is an operator of micro-to-macro stiffness transfer and dimensional compression.

The single columns of this transformation matrix contain dimensionless displacements of the micro nodes following from macro unit displacement states in terms of shape functions. The superscript (I, x_i) encodes the unit displacement state at macro node $I, I = 1, \ldots, N_{\text{node}}$ in the direction of $x_i, i = 1, \ldots, n_{\text{dim}}$.

The transformation matrix and its derivation provide the information on how to carry out the computations for its entries; first, on the driver of the micro problem in terms of shape functions as described, second, on the corresponding solutions $\boldsymbol{d}^{h(I,x_i)}$, which build up $\boldsymbol{T}_{K_l}$. These two characteristics are not sufficient to properly solve the micro problem. The missing links are the coupling conditions, cf. Sec. 2.1.

- **Energetically consistent BCs**. They must be applied to the micro domain to comply (the Hill-Mandel postulate of) the micro-macro energy equivalence. The

[2]Here and in the following small letters (for stiffness matrices $\boldsymbol{k}$, force vectors $\boldsymbol{f}$, displacements $\boldsymbol{d}$) refer to the element level, capital letters to global, assembled quantities, which is applied for micro scale (h) and macro scale quantities (H).

most frequently used BCs are periodic (PBC), linear displacement or kinematically uniform BCs (KUBC/Dirichlet), and constant traction (Neumann) BCs.

- **Order of computational homogenization**. If the macro deformation imparted on the micro domain is homogeneous, the micro problem resembles the unit cell problem of (asymptotic) mathematical homogenization, which is the foundation of FE-HMM. In computational mechanics this setting is frequently referred to as first order computational homogenization. For that aim the macro displacements $\boldsymbol{u}^H$ are linearized at quadrature points $\boldsymbol{x}_{K_{\delta_l}}$ according to

$$\boldsymbol{u}^H_{\mathrm{lin},K_{\delta_l}} = \boldsymbol{u}^H(\boldsymbol{x}_{K_{\delta_l}}) + (\boldsymbol{x} - \boldsymbol{x}_{K_{\delta_l}}) \cdot \nabla \boldsymbol{u}^H(\boldsymbol{x}_{K_{\delta_l}})\,. \tag{29}$$

With these coupling conditions the embedding of the micro problem into the macro continuum is defined and the micro problem can be solved. The task is cast into a saddle-point problem with the corresponding Lagrange-functional to be minimized.

For the micro problem driven by the linearized macroscopic unit displacement states (I, x_i) and thereby subject to energetically consistent BC, solve

$$\mathcal{L}(\boldsymbol{D}^{h(I,x_i)}, \boldsymbol{\Lambda}^{(I,x_i)}) = \frac{1}{2}\boldsymbol{D}^{h(I,x_i)T}\boldsymbol{K}^h_T\boldsymbol{D}^{h(I,x_i)} + \boldsymbol{\Lambda}^{(I,x_i)\,T}\boldsymbol{G}\left(\boldsymbol{D}^{h(I,x_i)} - \overline{\boldsymbol{d}}^{H(I,x_i)}\right) \;\rightarrow\; \min. \tag{30}$$

where[3] $\overline{\boldsymbol{d}}^{H(I,x_i)}$ is the prescribed nodal displacement vector that follows from linearization in (29), and where the nodal constraints are encoded in matrix $\boldsymbol{G}$. For convenience we have dropped the index of $\boldsymbol{K}^h_T$ but keep in mind that it refers to a micro problem at macro quadrature point K_{δ_l}. The first variation of $\mathcal{L}$ with respect to both $\boldsymbol{D}^{h(I,x_i)}$ and $\boldsymbol{\Lambda}^{(I,x_i)}$ results in the set of linear equations to be solved for $I = 1, ..., N_{\mathrm{node}}$, $i = 1, ..., n_{\mathrm{dim}}$:

$$\begin{bmatrix} \boldsymbol{K}^h_T & \boldsymbol{G}^T \\ \boldsymbol{G} & \boldsymbol{0} \end{bmatrix} \begin{bmatrix} \boldsymbol{D}^{h(I,x_i)} \\ \boldsymbol{\Lambda}^{(I,x_i)} \end{bmatrix} = \begin{bmatrix} \boldsymbol{0} \\ \boldsymbol{G}\,\overline{\boldsymbol{d}}^{H(I,x_i)} \end{bmatrix}, \tag{31}$$

where for PBC condition $\boldsymbol{G}^T\boldsymbol{\Lambda}^{(I,x_i)} = \boldsymbol{0}$ is fulfilled by the periodic displacements and antiperiodic tractions.

The solution vector contains the dimensionless micro displacements $\boldsymbol{D}^{h(I,x_i)}$, and the Lagrange multipliers $\boldsymbol{\Lambda}^{(I,x_i)}$ enforce the coupling condition. With $\boldsymbol{D}^{h(I,x_i)}$ the transformation matrix $\boldsymbol{T}_{K_{\delta_l}}$ and thereby the macro element stiffness matrix can be built as described by (27) and (28). Assembling the macro scale element contributions results in the global system of equations

$$\mathop{\mathsf{A}}_{\mathrm{e}=1}^{num_{ele}} \sum_{I=1}^{N_{\mathrm{node}}} \sum_{J=1}^{N_{\mathrm{node}}} \left(\delta\boldsymbol{d}^H_I\right)^T \left(\boldsymbol{k}^H_{T,IJ}\Delta\boldsymbol{d}^H_J + \boldsymbol{f}^H_I\right) = 0\,. \tag{32}$$

For PBC it holds for node p and its counterpart q at opposite edges (for $n_{\mathrm{dim}} = 2$) and at opposite faces (for $n_{\mathrm{dim}} = 3$) of a micro domain K_{δ_l} the constraint condition with $\boldsymbol{u}^H_{\mathrm{lin},K_{\delta_l}}$ according to (29)

$$\left(\boldsymbol{u}^h_{K_{\delta_l}} - \boldsymbol{u}^H_{\mathrm{lin},K_{\delta_l}}\right)(p) = \left(\boldsymbol{u}^h_{K_{\delta_l}} - \boldsymbol{u}^H_{\mathrm{lin},K_{\delta_l}}\right)(q) \tag{33}$$

$$\boldsymbol{G}\left(\boldsymbol{D}^h_{K_{\delta_l}} - \overline{\boldsymbol{d}}^H_{K_{\delta_l}}\right) = \boldsymbol{0}\,, \tag{34}$$

[3]The basis of the macro element quantity $\overline{\boldsymbol{d}}^H$ is that one of the micro space; therefore and to avoid notational confusion with assembled macro displacements, we employ small letter $\boldsymbol{d}$.

where (34) is the Lagrange multiplier counterpart, in which matrix $\boldsymbol{G}$ encodes both the macro-micro coupling condition of homogeneous deformation mediated by $\overline{\boldsymbol{d}}^H_{K_{\delta_l}}$ and the non-redundant periodic coupling conditions for partner nodes p, q on the micro domain boundary.

Notice that the micro problem and its solution in Sec. 3.2 merely serves the purpose of building the stiffness carrier $\boldsymbol{T}_K$. For the solution of the macro problem (i) macro stress $\boldsymbol{S}^H$ from averaged micro stresses and (ii) macro stiffness $\boldsymbol{k}^H_T$ from $\boldsymbol{K}^h_T$ must be available, namely for the micro state fulfilling the weak form of balance of linear momentum. For that purpose the micro problem is to be solved which is described in the following Sec. 3.3.

3.3 The microproblem and its solution

The micro problem is solved on the RVE of each macro quadrature point K_{δ_l}, $l = 1, ..., n_{qp}$ in all finite elements K of the macro triangulation $\mathcal{T}^H$.

The solution of the nonlinear system of equations on the micro domain from (17) requires the linearization at the current micro displacement state $\boldsymbol{u}^h$

$$\mathrm{Lin}\left[G^h(\boldsymbol{u}^h, \delta\boldsymbol{u}^h)\right] \;=\; G^h(\boldsymbol{u}^h, \delta\boldsymbol{u}^h) + \mathrm{D}G^h(\boldsymbol{u}^h, \delta\boldsymbol{u}^h) \cdot \Delta\boldsymbol{u}^h \;=\; 0\,, \tag{35}$$

with the definitions already introduced in the context of the linearization of G^H.

The approximation of $\mathrm{D}G \cdot \Delta\boldsymbol{u}$ is given by

$$\mathrm{D}G^h(\boldsymbol{u}^h, \delta\boldsymbol{u}^h) \cdot \Delta\boldsymbol{u}^h \;=\; \int_T \left(\delta\boldsymbol{E}^h \colon \mathbb{C}^\varepsilon_T \colon \Delta\boldsymbol{E}^h + \boldsymbol{S}^h \colon \Delta\delta\boldsymbol{E}^h\right) \mathrm{d}V\,. \tag{36}$$

Inserting the approximations into the framework of the finite element method leads to

$$\mathrm{D}G^h(\boldsymbol{u}^h, \delta\boldsymbol{u}^h) \cdot \Delta\boldsymbol{u}^h \;=\; \sum_{I=1}^{n_{\mathrm{node}}} \sum_{K=1}^{n_{\mathrm{node}}} \left(\delta\boldsymbol{d}^h_I\right)^T \underbrace{\int_T \left(\boldsymbol{B}^T_I \mathbb{C}^\varepsilon_T \boldsymbol{B}_K + \hat{\boldsymbol{G}}_{IK}\right) \mathrm{d}V}_{=:\, \boldsymbol{k}^h_{T,IK}} \Delta\boldsymbol{d}^h_K\,, \tag{37}$$

with the tangential element stiffness matrix contribution of nodes I and K and the initial stress matrix $\hat{\boldsymbol{G}}_{IK}$ reflecting the contribution of the current stress state to the stiffness of a deformed structure

$$\hat{\boldsymbol{G}}_{IK} \;=\; \hat{S}^h_{IK}\mathbf{1} \qquad \text{with} \tag{38}$$

$$\begin{aligned}\hat{S}^h_{IK} \;=\; & S^h_{11}N_{I,1}N_{K,1} + S^h_{22}N_{I,2}N_{K,2} + S^h_{33}N_{I,3}N_{K,3} + S^h_{12}(N_{I,1}N_{K,2} + N_{I,2}N_{K,1}) + \\ & S^h_{13}(N_{I,1}N_{K,3} + N_{I,3}N_{K,1}) + S^h_{23}(N_{I,2}N_{K,3} + N_{I,3}N_{K,2})\,.\end{aligned} \tag{39}$$

The corresponding global finite element approximation on the micro scale is obtained by assembling the contributions of all micro finite elements (number: num_{ele})

$$\mathop{\mathbf{A}}_{e=1}^{num_{ele}} \sum_{I=1}^{n_{\mathrm{node}}} \sum_{K=1}^{n_{\mathrm{node}}} \left(\delta\boldsymbol{d}^h_I\right)^T \left(\boldsymbol{k}^h_{T,IK}\Delta\boldsymbol{d}^h_K + \boldsymbol{f}^h_I\right) \;=\; 0\,. \tag{40}$$

The assembled system of equations (40) is subject to the coupling conditions, hence

$$\boldsymbol{K}_T^h \, \Delta \boldsymbol{D}^h + \boldsymbol{F}^h \;=\; \boldsymbol{0} \qquad \text{subject to} \qquad \boldsymbol{G} \left(\Delta \boldsymbol{D}^h - \overline{\boldsymbol{d}}^H \right) = \boldsymbol{0} \,. \tag{41}$$

In the incremental setting of linearized equations along with the constraint matrix $\boldsymbol{G}$, the constraint for energetically consistent BCs is written in terms of the yet unknown micro displacement increment $\Delta \boldsymbol{D}^h$ and the macroscopic displacements $\overline{\boldsymbol{d}}^H$ imposed on the RVE boundary nodes to realize the required homogeneous deformation.

For the solution of (41) a Lagrange-functional is constructed which is to be minimized.

$$\mathcal{L}(\Delta \boldsymbol{D}^h, \Delta \boldsymbol{\Lambda}^h) = \frac{1}{2} \Delta \boldsymbol{D}^{h\,T} \boldsymbol{K}_T^h \Delta \boldsymbol{D}^h + \boldsymbol{F}^{h\,T} \, \Delta \boldsymbol{D}^h + \Delta \boldsymbol{\Lambda}^{h\,T} \boldsymbol{G} \left(\Delta \boldsymbol{D}^h - \overline{\boldsymbol{d}}^H \right) \longrightarrow \text{min.} \tag{42}$$

The partial derivative of $\mathcal{L}$ with respect to $\Delta \boldsymbol{D}^h$ and with respect to $\Delta \boldsymbol{\Lambda}^h$ yield the stationarity conditions

$$\begin{bmatrix} \boldsymbol{K}_T^h & \boldsymbol{G}^T \\ \boldsymbol{G} & \boldsymbol{0} \end{bmatrix} \begin{bmatrix} \Delta \boldsymbol{D}^h \\ \Delta \boldsymbol{\Lambda}^h \end{bmatrix} \;=\; \begin{bmatrix} -\boldsymbol{F}^h \\ \boldsymbol{G}\, \overline{\boldsymbol{d}}^H \end{bmatrix} . \tag{43}$$

Therein, the first set of equations

$$\boldsymbol{K}_T^h \Delta \boldsymbol{D}^h = \underbrace{-\boldsymbol{F}^h - \boldsymbol{G}^T \Delta \boldsymbol{\Lambda}^h}_{=:\, -\boldsymbol{R}^h} \tag{44}$$

corresponds to (41), the term $\boldsymbol{G}^T \Delta \boldsymbol{\Lambda}^h$ describes the change of the external node forces (Lagrange multipliers enforcing the coupling), which, together with the internal force vector $\boldsymbol{F}^h$, render the residual $\boldsymbol{R}^h$. In the case of PBC the change of these external node forces is not considered in the linearization, since $\boldsymbol{G}^T \Delta \boldsymbol{\Lambda}^h = \boldsymbol{0}$ is fulfilled by periodic displacements and antiperiodic tractions.

The solution of (43) yields the updates

$$\boldsymbol{D}^h \;\longleftarrow\; \boldsymbol{D}^h + \Delta \boldsymbol{D}^h \,, \tag{45}$$

$$\boldsymbol{\Lambda}^h \;\longleftarrow\; \boldsymbol{\Lambda}^h + \Delta \boldsymbol{\Lambda}^h \,. \tag{46}$$

Iterations along with updates stop for sufficiently small residuals. Then the computation of the micro-to-macro stiffness transfer by means of the current tangential stiffness matrix and by means of the current stress transfer is carried out.

The application of energetically consistent BCs fulfilling the Hill-Mandel condition in the FE-HMM framework are analyzed in [16] for linear elasticity along with convergence and error analysis, for finite deformations see [42].

Remarks

The differences in the Lagrange functionals of (30) in comparison to (42) reflects their different purpose; (42) is constructed for the continuation of a Newton iteration by linearized equations in (43), whereas (30) is constructed from truely linear equations; for a state fulfilling the balance equations after having solved the nonlinear set of algebraic equations, it is now purely the task of the micro-to-macro stiffness transfer. The stiffness

transfer coincides with that one in linear homogenization. For the linear case the tangential stiffness matrix boils down to the deformation- and stress-independent stiffness matrix, [60], [2].

The FE^2 method realizes the micro-macro stiffness transfer in terms of the homogenized elasticity tensor/tangent moduli, which are obtained by means of the micro stiffness matrix. FE-HMM in contrast directly draws on the micro stiffness matrices as described.

4 A priori error estimates

By virtue of its roots in mathematical homogenization, the FE-HMM exhibits a priori estimates; for the elliptic case in [14], [15], for the elliptic case of linear elasticity in a geometrical linear setting to [1], [9].

The total FE-HMM error can be decomposed into three parts

$$||\boldsymbol{u}^0 - \boldsymbol{u}^H|| \leq \underbrace{||\boldsymbol{u}^0 - \boldsymbol{u}^{0,H}||}_{e_{\text{mac}}} + \underbrace{||\boldsymbol{u}^{0,H} - \widetilde{\boldsymbol{u}}^H||}_{e_{\text{mod}}} + \underbrace{||\widetilde{\boldsymbol{u}}^H - \boldsymbol{u}^H||}_{e_{\text{mic}}}, \tag{47}$$

where e_{mac}, e_{mod}, e_{mic} are the macro error, the modeling error, and the micro error.

Here, $\boldsymbol{u}^0$ is the solution of the homogenized problem, $\boldsymbol{u}^H$ is the FE-HMM solution, $\boldsymbol{u}^{0,H}$ is the standard (single-scale) FEM solution that is obtained through exact $\mathbb{C}^0$ (in linear elasticity); and $\widetilde{\boldsymbol{u}}^H$ is the FE-HMM solution obtained through exact micro solutions.

For sufficiently regular problems the following a priori estimates hold in the L^2-norm, the H^1-norm and the energy-norm:

$$||\boldsymbol{u}^0 - \boldsymbol{u}^H||_{L^2(\mathcal{B}_0)} \leq C\left(H^{p+1} + \left(\frac{h}{\epsilon}\right)^{2q}\right) + e_{\text{mod}}\,, \tag{48}$$

$$||\boldsymbol{u}^0 - \boldsymbol{u}^H||_{H^1(\mathcal{B}_0)} \leq C\left(H^{p} + \left(\frac{h}{\epsilon}\right)^{2q}\right) + e_{\text{mod}}\,, \tag{49}$$

$$||\boldsymbol{u}^0 - \boldsymbol{u}^H||_{A(\mathcal{B}_0)} \leq C\left(H^{p} + \left(\frac{h}{\epsilon}\right)^{2q}\right) + e_{\text{mod}}\,. \tag{50}$$

For e_{mod} in (48)–(50) it holds

$$e_{\text{mod}} = \begin{cases} 0 & \text{for periodic coupling with } \delta/\epsilon \in \mathbb{N} \\ C\,\dfrac{\epsilon}{\delta} & \text{for Dirichlet coupling with } \delta > \epsilon \end{cases} \tag{51}$$

given that the hypotheses hold, that the elasticity tensor $\mathbb{C}^\epsilon$ is periodic on the RVE and, that the micro solution is sufficiently smooth, [61].

The modeling error for Dirichlet coupling in (48)–(50) is due to boundary layers [14] (Thm. 1.2), [9]. So even for $H \to 0$ and $h \to 0$ there is a residual error.

The second terms in the estimates (48)–(50) each represent the micro error which is propagated to the macro scale. The deviations from the convergence order of the micro error on the micro scale is threefold; first, in that the error in the L^2-norm is of order

$2q$ instead of $q+1$, second, in that errors in the H^1- and energy-norm are of the order of $2q$ instead of q and therefore and third, in that it coincides for the L^2-norm with the H^1-/energy-norm.

For the particular case of linear elasticity it holds

$$||\mathbb{C}^0_{ijkl} - \mathbb{C}^{0,h}_{ijkl}|| \leq C \left(\frac{h}{\epsilon}\right)^{2q} \tag{52}$$

with the exact homogenized elasticity tensor $\mathbb{C}^0_{ijkl}$ and its approximation $\mathbb{C}^{0,h}_{ijkl}$ obtained on a grid with element size h.

The unified estimates covering both the macro error as well as the micro error enable uniform micro-macro (h-/H-) mesh refinements for optimal convergence order but for minimal computational costs.

macro, micro FEM	L^2-norm	H^1-/energy-norm
P^p, P^q	$N_{\text{mic}} = (N_{\text{mac}})^{(p+1)/2q}$	$N_{\text{mic}} = (N_{\text{mac}})^{p/2q}$

Table 1: Optimal uniform micro-macro refinement strategies: full order for minimal effort. N_{mic} denotes the number of unknowns on the micro scale, N_{mac} on the macro scale.

Table 1 displays the optimal uniform micro-macro refinement strategies for the error in the L^2-norm and the H^1-/energy-norm. Of course, the strategies' dependency on the polynomial orders of the macro and micro shape functions p and q rely on full regularity of the corresponding BVPs. In the present context of nonlinear homogenization, the additional question arises, whether the estimates apply at all. For that aim we measure the convergence and compare it with the fully linear case in order to properly identify the source of possible order reductions.

For linear problems in elasticity the estimates (48)–(51), (52) as well as the optimal refinement strategies according to Tab. 1 were assessed and for sufficient regularity confirmed in [60], [61], [2], [16].

5 Novel Algorithmic Solution Concept

5.1 The standard: nested loops

The algorithmic standard of nonlinear FE^2 is a staggered solution scheme in terms of a nested loop[4] embedding the complete solution of the micro problem into one macro solution iteration step as displayed in pseudocode "Algorithm 1" in Sec. 1. The scheme is typically realized by a nested two-level Newton method.

This approach is depicted for a Lagrangean formulation in Fig. 3 and goes like this; a loading increment –here in terms of an external force increment $\Delta \boldsymbol{F}^{\text{ext}}$– shifts both the macro scale as well as the micro scale out of balance of linear momentum, the lights go from green to red. For the solution of the macro problem, the current states of macro stiffness $\boldsymbol{k}^H_T$ and stress $\boldsymbol{S}^H$ are computed on the micro scale and transferred from micro to

[4] In [6], p.313, referred to as "interleaved finite element algorithms"

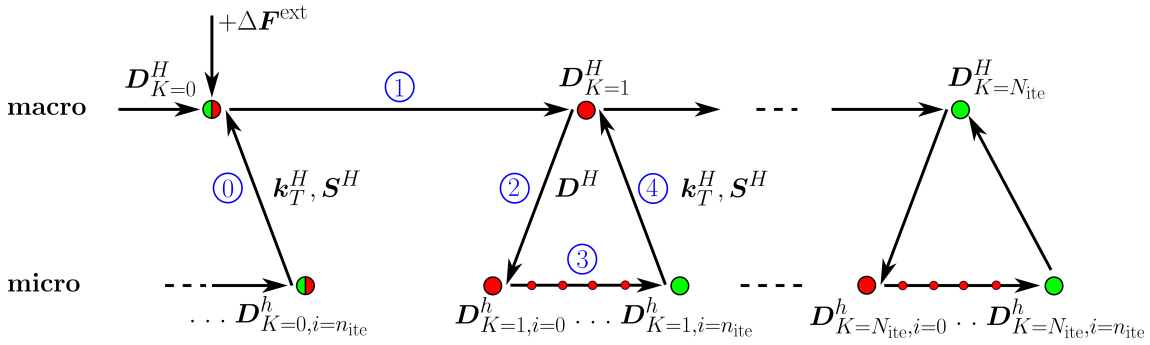


Figure 3: The conventional staggered scheme based on nested, macro-micro solution loops for the nonlinear homogenization by a two-level FEM. Green (red) circles indicate stages (not) in equilibrium.

macro; it is an initialization for the start of a simulation, or an update for the continuation of a simulation, in either case denoted by (0) in Fig. 3. The updated macro stiffness and residual –stress enters the internal force vector being part of the residual– enable the first iteration of the macro Newton, indicated by step (1) in Fig. 3 and its resultant macro displacement vector $\boldsymbol{D}^H_{K=1}$.

In parallel, the fluctuations (for periodic BCs on the RVE) of the converged micro solution $\boldsymbol{D}^h_{K=0,i=n_{\text{ite}}}$ from the finished previous loading step are maintained. They are superimposed to the updated displacement field –step (2) in Fig. 3– to provide favorable start values for solving the micro problems by Newton's method in the current loading step. The iterations in the solution of the micro problem are indicated by the counter $i = 0, \ldots, n_{\text{ite}}$, step (3) in Fig. 3. Despite its finally vanished micro residuals, the obtained micro solutions each represent a pseudo-equilibrium state[5] for the macro residual still being non-zero.

Based on the obtained micro solution, macro (element) stiffness $\boldsymbol{k}^H_T$ and stress $\boldsymbol{S}^H$ are passed over to the macro level, step (4) in Fig. 3, which completes the cycle of one macro Newton iteration. These cycles are repeated until the macro Newton is converged, which is indicated by $K = n_{\text{ite}}$. An accuracy polish by a final iteration on the micro scale completes the loading step on both scales.

The inherent hierarchy in the standard staggered scheme in that the outer loop for the macro Newton can only proceed with an update of micro scale quantities follows from the very multiscale setup with its scale-dependencies; the continuation of the macro solution process after one iteration requires the update of stiffness and stress from the micro scale. It is, however, not clear, whether the macro Newton requires fully converged micro solutions for continuation.

5.2 The novel: direct alternations

The present work analyzes, whether the nested solution algorithm as described is necessary or at least favorable for the homogenization of hyperelastic solids. The criterion is of purely numerical nature, related to convergence in a qualitative and a quantitative manner. The only physical requirement is that balance laws must be fulfilled both on the micro scale and the macro scale at the end of each load step, here the balance of linear momentum.

[5]They are notwithstanding in green color in Fig. 3 even if the macro Newton is not yet converged.

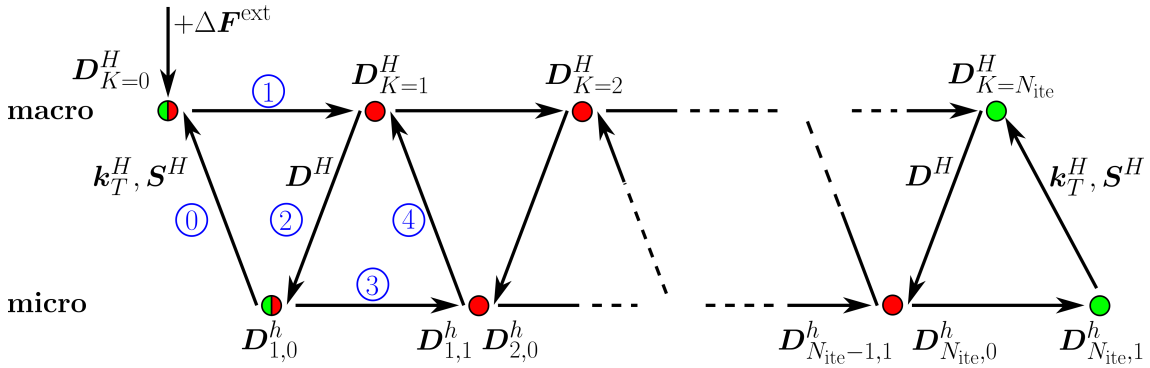


Figure 4: The novel staggered scheme with direct macro-micro alternations in the two-level Newton iterations for the nonlinear homogenization by a two-level FEM. Green (red) circles indicate stages (not) fully converged.

We hypothesize that the continuation of the macro Newton does neither require nor take profit in its overall performance from micro solutions that are fully converged. In that case the standard is an expensive luxury.

In line with this hypothesis we advocate an alternative route for a novel staggered scheme as depicted in pseudocode "Algorithm 2" in Sec. 1 and –applied to the mechanical problem– in Fig. 4, which promises considerable computational savings.

The idea is to replace the embedded-loop solution scheme by a loop of direct micro-macro alternations; after each micro Newton iteration the current stiffness $\boldsymbol{k}^H_T$ and stress $\boldsymbol{S}^H$ are passed over to the macro scale which is followed –as in the standard– by a macro iteration along with a displacement update for the micro scale.

In the novel version the number of consecutive iterations on the micro level is reduced to one, e.g. the step from $\boldsymbol{D}^h_{1,0}$ to $\boldsymbol{D}^h_{1,1}$ (first index K, second index i) denoted by (3) in Fig. 4, the rest $i = 2, \ldots, n_{\text{ite}}$ of the standard scheme is discarded. After the consecutive macro iteration an updated displacement field yields micro displacements $\boldsymbol{D}^h_{2,0}$ which contain for PBC the fluctuations stored from the state $\boldsymbol{D}^h_{1,1}$. Consequently, the last micro iteration carries out a step from $\boldsymbol{D}^h_{N_{\text{ite}},0}$ to $\boldsymbol{D}^h_{N_{\text{ite}},1}$. For an already converged macro solution, an additional accuracy polish of macro stress is realized by this final micro iteration, which is equally carried out in the standard solution algorithm.

6 Numerical Examples

In this section the nonlinear FE-HMM formulation is assessed with a focus on two aspects.

(A) For the two-level Newton algorithm we compare the performance of the standard version with the novel version using direct micro-macro alternations.

(B) Assessment of the a priori error estimates (48)–(50) for the case of geometrical nonlinearity along with either linear elasticity or (nonlinear) hyperelasticity. Doing so we keep in mind that the estimates are proved for linear elasticity in a geometrical linear frame. A comparison with the convergence of the fully linear case is necessary to identify, whether a deviation from the theoretical order is due to the nonlinearity

of the considered problem or due to the reduced regularity of the micro problem setting itself. Errors are calculated by means of an accurate reference solution obtained on very fine meshes.

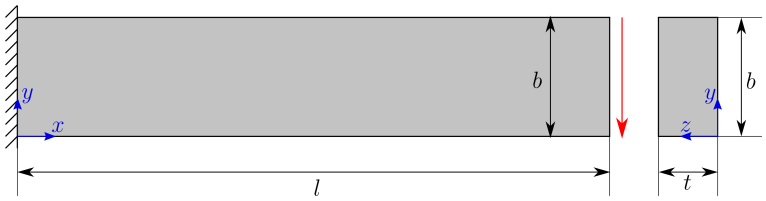


Figure 5: Macro problem: Cantilever beam, geometry and boundary conditions. For notational convenience we use the Cartesian coordinates (x, y, z) replacing the previous (x_1, x_2, x_3) coordinate system.

The macro problem common to all micro problems is a bending-dominated cantilever beam. It exhibits length l in x-direction, height b in y-direction, and thickness t in z-direction. It is clamped at x=0 and subject to force control by an external line load $\boldsymbol{f}$ or to displacement control at x=l. If not otherwise stated, it holds $l = 5000$ mm, $b = 1000$ mm, $t = 100$ mm. The RVE side length ϵ as well as the type and magnitude of loading is defined in each example separately.

For hyperelasticity we consider an isotropic neo-Hookean constitutive law frequently used for rubber-like materials. The free energy function exhibits the form

$$\psi = \frac{\lambda}{4}\left(J^2-1\right) - \left(\frac{\lambda}{2}+\mu\right)\ln J + \frac{\mu}{2}\left(\operatorname{tr}\boldsymbol{C}-3\right), \tag{53}$$

where λ and μ are the Lamé parameters, $J = \det \boldsymbol{F}$ is the Jacobian and $\boldsymbol{C}$ is the right Cauchy-Green deformation tensor. From ψ and the hyperelasticity relations for stress and the tangent, $\boldsymbol{S} = 2\partial_{\boldsymbol{C}}\psi$, $\mathbb{C} = 4\partial^2_{\boldsymbol{C}\boldsymbol{C}}\psi$, we obtain

$$\boldsymbol{S} = \frac{\lambda}{2}\left(J^2-1\right)\boldsymbol{C}^{-1} + \mu\left(\boldsymbol{I}-\boldsymbol{C}^{-1}\right), \tag{54}$$

$$\mathbb{C}_{ijkl} = \left[\lambda\left(J^2-1\right)-2\mu\right]\mathbb{A}_{ijkl} + \lambda J^2 C^{-1}_{ij}C^{-1}_{kl}, \tag{55}$$

$$\text{with}\quad \mathbb{A}_{ijkl} = \frac{\partial \boldsymbol{C}^{-1}}{\partial \boldsymbol{C}} = -\frac{1}{2}\left(C^{-1}_{ik}C^{-1}_{jl} + C^{-1}_{jk}C^{-1}_{il}\right). \tag{56}$$

Notice that the constitutive law is defined on the micro scale; for notational convenience we discard in (53)–(56) the explicit micro scale label of ϵ.

The considered microstructures consist of two different elastic phases. In view of their considerable differences in morphology, the elasticities of the phases are comprehensively chosen to be same for all examples; the material parameters are given in Tab. 2 for linear elasticity and neo-Hookean hyperelasticity.

The simulations are carried out by a C++ code using MPI-parallelization.

6.1 Escher's Pegasus

The first example considers on the macro scale a cantilever beam as displayed in Fig. 5, which is subject at $x = l$ to a lineload of magnitude 200 N/mm in negative y-direction.

	Linear Elasticity		Neo-Hookean	
phase	E (N/mm^2)	ν	λ (N/mm^2)	μ (N/mm^2)
1	100 000	0.2	27 777.78	41 666.67
2	40 000	0.2	11 111.11	16 666.67

Table 2: Material parameters for two-phase microstructures.

The material is a periodic, two-phase microstructure as displayed in Fig. 6 similar to the tessellation "Pegasus N°105" of the Dutch graphic artist M.C. Escher. The material's elastic parameters are given in Tab. 2.

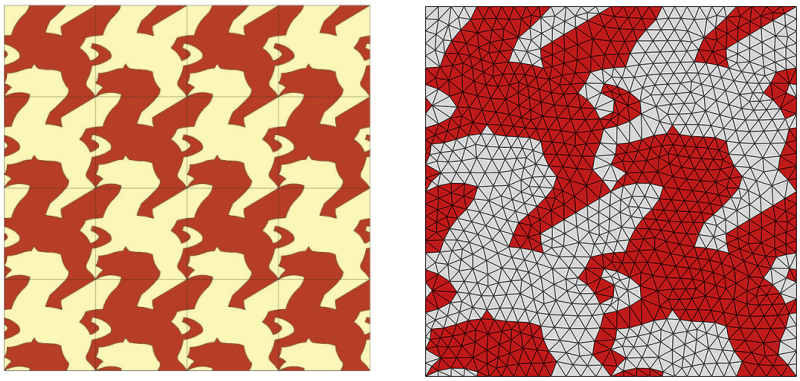


Figure 6: Escher's Pegasus: (left) Periodic tessellation with 2×2 unit cells and (right) a triangulation of a unit cell.

6.1.1 Micro convergence for linear elasticity and Neo-Hookean hyperelasticity The reference solution for micro convergence analysis is calculated with ndof=24 on the macro scale domain (5×1 macro elements) and ndof=2 262 584 on the micro scale with $\epsilon = 110$ mm.

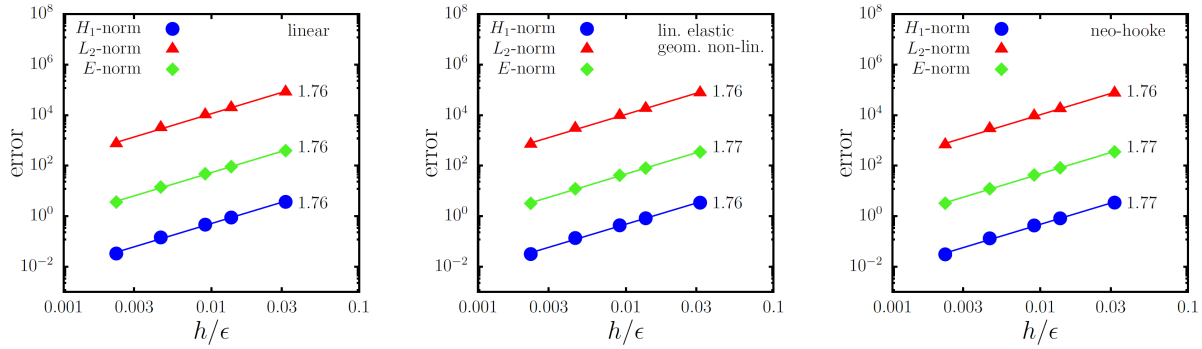


Figure 7: Escher's Pegasus: Micro convergence for (left:) fully linear setting, (center:) linear elasticity along with geometrical nonlinearity, (right:) Neo-Hookean hyperelasticity.

The convergence diagrams in Fig. 7 indicate that the convergence order in all considered norms is virtually insensitive to the nonlinearities introduced by the kinematics and the hyperelastic constitutive law. The measured convergence orders are below the full theoretical order of $2q = 2$ which is caused by the reduced regularity of the micro problem already visible in the results for the fully linear case.

6.1.2 Standard Newton versus Alternating Newton In order to calculate the speedup factor of the alternating Newton method related to the standard Newton method, the solution for $\text{ndof}_{\text{mac}} = 24$ along with $\text{ndof}_{\text{mic}} = 2\,262\,584$ is calculated by both methods employing 4 loading steps. The corresponding overall performance and computation times are compared in Table 3.

method	load step	$N_{\text{ite}}^{\text{mac}}$	$t_{\text{ite}}^{\text{mac}}$	$u_{\max}$	t_{LS}
standard Newton	1	4	00:07:27	276.8	00:27:09
	2	5	00:08:45	550.7	00:42:31
	3	5	00:08:47	818.1	00:43:53
	4	5	00:08:45	1076.5	00:43:52
alternating Newton	1	5	00:05:08	276.8	00:25:27
	2	5	00:05:09	550.7	00:25:45
	3	5	00:05:10	818.1	00:25:48
	4	5	00:05:09	1076.5	00:25:52
					total speedup factor = 1.53

Table 3: Escher's Pegasus: Standard Newton versus alternating Newton with $N_{\text{ite}}^{\text{mac}}$ the number of macro iterations, $t_{\text{ite}}^{\text{mac}}$ the compute time for the first macro Newton iteration including micro Newton iteration(s), $u_{\max}$ the maximum of the normed nodal displacement vectors and t_{LS} the compute time for a complete load step. Compute time has the format (HH:mm:ss) for hours, minutes, and seconds.

Table 3 indicates that the alternating Newton converges to the correct solution in terms of the maximum nodal displacement. Remarkably, in only one out of four loading steps the alternating Newton requires one additional macro Newton iteration for convergence. The overall speedup of 1.53 indicates the improved efficiency of the alternating Newton.

load step number	macro ite	macro residual	
		standard Newton	alternating Newton
4 (out of 4)	1	1.0000e+00	9.9999e-01
	2	1.4152e+01	1.4114e+01
	3	6.3705e-02	4.7410e-02
	4	4.5369e-04	5.8777e-04
	5	1.8262e-08	6.1250e-06
1 (out of 1)	1	1.0000e+00	1.0000e+00
	2	6.6287e+01	6.6301e+01
	3	4.0499e+00	3.1304e+00
	4	2.3008e-02	1.1509e-02
	5	7.5719e-05	1.4101e-04
	6	5.0931e-09	1.5738e-06

Table 4: Escher's Pegasus: Comparison of the macro residuals for standard Newton versus alternating Newton in load step 4 (out of 4) and load step 1 (out of 1).

Table 4 compares the convergence of the macro Newton for the two different solution strategies in terms of their macro residuals. For that aim, two cases are considered; in

the first case the total load is decomposed in four increments of equal magnitude, in the second case in one single step. Independent of the magnitude of the load step the number of required iterations is the same for both methods, although the alternating Newton exhibits a minor deviation from quadratic convergence in its last iteration.

macro ndof	micro ndof	speedup factor linear elastic		speedup factor neo-Hookean	
		$N_{\mathrm{LS}}=4$	$N_{\mathrm{LS}}=1$	$N_{\mathrm{LS}}=4$	$N_{\mathrm{LS}}=1$
24	1 946	1.50	1.38	1.50	1.27
	11 942	1.40	1.56	1.31	1.28
	25 820	1.44	1.48	1.39	1.29
	101 918	1.44	1.47	1.38	1.31
	384 930	1.48	1.48	1.39	1.30
	2 262 584	1.53	1.56	1.45	1.40
1 122	1946	1.64	1.63	1.35	2.57
4 242		1.66	1.58	1.31	1.80
16 482		1.59	1.59	1.31	1.83
64 962		1.56	1.40	1.33	1.76
257 922		1.57	1.44	1.33	1.70
4 103 682		1.55	1.49	1.31	1.63

Table 5: Escher's Pegasus: speedup factors of alternating Newton compared to standard Newton depending on discretizations and the type of the employed elastic constitutive law, where N_{LS} is the total number of load steps.

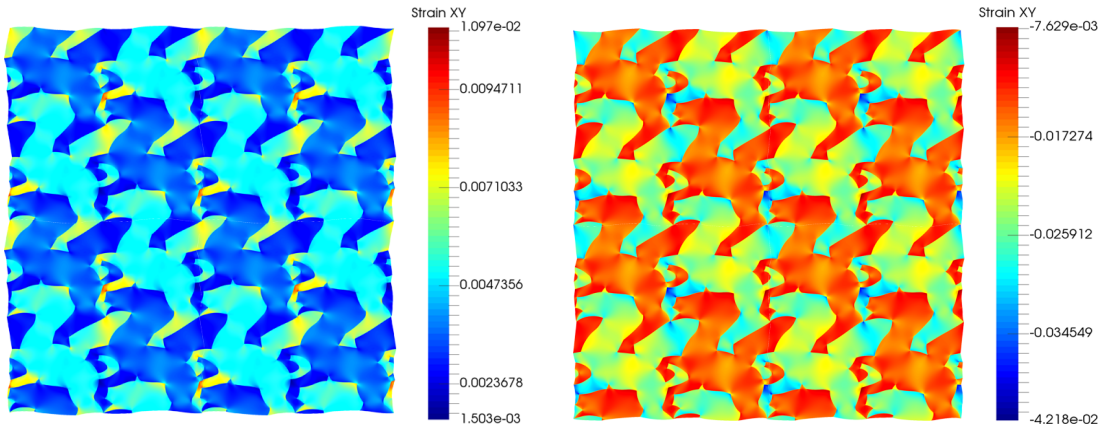


Figure 8: Escher's Pegasus: contour plot of shear strain component E_{xy} (left) at $x = 3943.37$mm, $y = 211.32$ mm and (right) at $x = 1056.62$ mm, $y = 788.67$ mm.

Table 5 lists the speedup factors of the novel solution strategy for different discretizations; they vary from 1.27 to almost 2.6. Increasing the micro discretization while keeping the macro discretization fixed results in a modest increase of the speedup factor. Vice versa, increasing the macro discretization while keeping the micro discretization fixed results in a modest decrease of the speedup factors. The two trends hold –apart from some outliers– for linear elasticity as well as for neo-Hookean hyperelasticity and they are insensitive to the load step size likewise. The speedup factor for linear elasticity is generally higher than

for the neo-Hookean case, the exception is the case where ndof_{mac} is in the order of or larger than ndof_{mic}; here the speedup factor for the hyperelastic case is higher, if the load is applied in one single step instead of four steps.

Figure 8 shows the distribution of shear strain $2E_{xy}$ for a 2×2 RVE-array of the Pegasus microstructure with periodic fluctuations at two selected points in the beam.

6.2 Escher's Swan

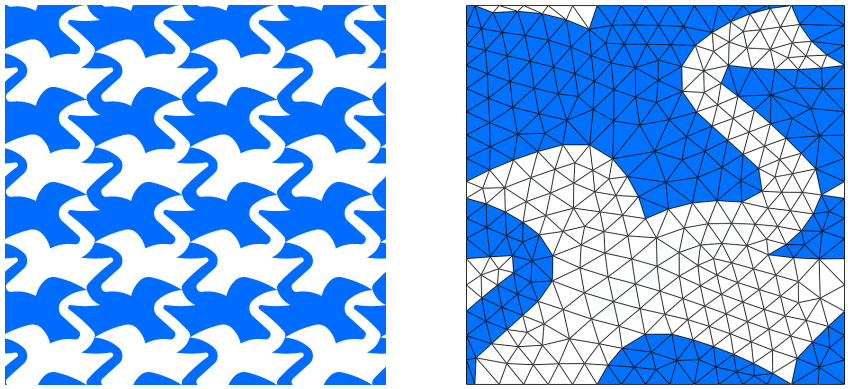


Figure 9: Escher's Swan: (left) Periodic tessellation, (right) discretization of a unit cell.

In this example a two-phase microstructure is used that follows Escher's "Swan N°96" tessellation as displayed in the left of Fig. 9; each phase follows from each other by reflection and translation. Figure 9 (right) shows a unit cell along with a discretization using linear triangles, hence $q = 1$. In this example phase 1 is assigned to the swan to the left in blue color, phase 2 is assigned to the swan to the right in white color. The material parameters for linear elastic and neo-Hookean material laws are given in Tab. 2 of Sec. 6.1.

The macro scale BVP is again the cantilever beam with unaltered dimensions l, b, t which is subject at $x = l$ to a displacement control where the total displacement of 1100 mm is applied in four loading steps.

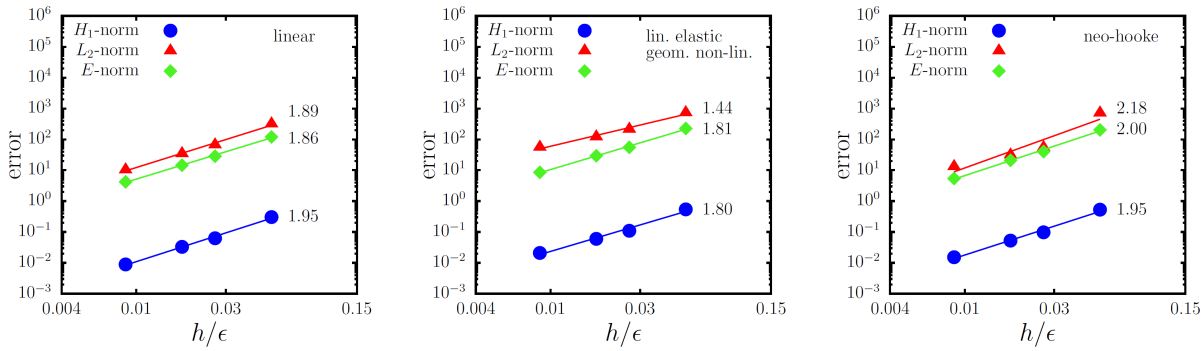


Figure 10: Escher's Swan: Micro convergence for (left:) the fully linear case, (center:) for linear elasticity with geometrical nonlinearity, and (right:) for Neo-Hookean hyperelasticity.

6.2.1 Micro convergence for linear elasticity and neo-Hookean hyperelasticity

The reference solution for the micro convergence analysis is obtained for ndof=24 on

the macro domain (5×1 macro elements) and ndof=574 922 on micro domains with $\epsilon =$ 11.4 mm.

The convergence diagrams for linear elasticity and neo-Hookean material laws are displayed in Fig. 10. Here, the fully linear case achieves almost the full theoretical order in all norms, $2q = 2$. For the combination of linear elasticity and geometrical nonlinearity, the convergence order is throughout reduced compared to the linear case, most pronounced in the L_2-norm. Remarkably, the convergence order for the fully nonlinear case of neo-Hookean hyperelasticity exhibits excellent convergence rates, in the L_2-norm even above the nominal order 2.0.

method	load step	$N_{\text{ite}}^{\text{mac}}$	$t_{\text{ite}}^{\text{mac}}$	$u_{\max}$	t_{LS}
standard Newton	1	4	00:01:54	279.3	00:07:03
	2	4	00:02:12	561.7	00:08:32
	3	4	00:02:12	847.3	00:08:49
	4	4	00:02:16	1136.6	00:08:59
alternating Newton	1	4	00:01:22	279.3	00:05:27
	2	5	00:01:23	561.7	00:06:54
	3	5	00:01:23	847.3	00:06:54
	4	5	00:01:22	1136.6	00:06:53
				total speedup factor = 1.28	

Table 6: Escher's Swan: Standard Newton versus alternating Newton where $N_{\text{ite}}^{\text{mac}}$ is the number of macro iterations, $t_{\text{ite}}^{\text{mac}}$ the compute time for the first macro Newton iteration including micro Newton iteration(s), $u_{\max}$ is the maximum of the normed nodal displacement vectors and t_{LS} is the compute time for a load step.

macro ndof	micro ndof	speedup factor linear elastic	speedup factor neo-Hookean
24	674	1.25	1.20
	3 248	1.68	1.05
	7 222	1.26	1.11
	27 444	1.25	1.20
	74 486	1.21	1.18
	574 922	1.28	1.23
1 122	674	2.13	1.50
4 242		1.53	1.44
16 482		1.56	1.26
64 962		1.56	1.37
257 922		1.76	1.44
4 103 682		1.63	1.49

Table 7: Escher's Swan: speedup factors of alternating Newton compared to standard Newton for different discretizations and types of elastic constitutive laws.

6.2.2 Standard Newton versus alternating Newton The overall performance and computational time of the reference solution calculated by standard and alternating Newton method is compared in Tab. 6. Maximum nodal displacements are in agreement for both methods, the speedup factor is 1.28. In the present example the alternating Newton method requires in 3 out of 4 loading steps 5 macro Newton iterations and therefore one more than for the standard, nested Newton.

A richer picture on the speedup factors of the alternating Newton method for different discretizations is given in Tab. 7. Among the four cases considered therein the case of linear elasticity along with geometrical nonlinearity results for $\text{ndof}_{\text{mac}} \gg \text{ndof}_{\text{mic}}$ in the highest speedup factors, throughout above 1.5.

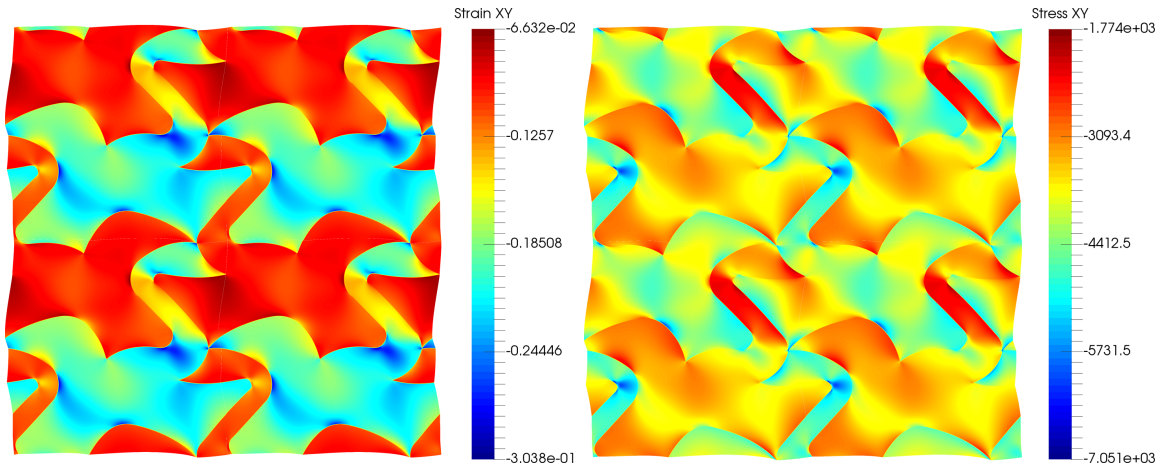


Figure 11: Escher's Swan: at $x = 1056.62$ mm, $y = 788.67$ mm the contour plot (left) of shear strain $2E_{xy}$ and (right) of von-Mises stress S_{xy}.

Figure 11 (left) underpins that phase 1 (swan to the left) is the stiffer one due to its smaller shear strains, the contour plot in the right displays the corresponding shear stress distribution.

6.3 DFG-Heisenberg

As an example of pixel-based microstructure representation we consider the two-phase portrait of the physicist Werner Heisenberg[6] as shown in the left of Fig. 12.

The discretization of this image is carried out using pixel to mesh conversion, phases are defined by conversion into binaries according to the pixels' rgb color code. The blue matrix is the softer phase 1, the white inclusions are the stiffer phase 2 as indicated by the reduced strain in the right of Fig. 12. The elasticity parameters of each phase are listed in Tab. 2.

The macro scale BVP is a cantilever beam with length $l = 1000$ mm, $b = 1000$ mm, $t = 100$ mm, which is loaded at $x = l$ by a line load of magnitude 100 N/mm in negative y-direction. PBCs are applied to the micro domains of length $\epsilon = 1$ mm.

6.3.1 Micro convergence for linear elasticity and neo-Hookean hyperelasticity The reference solution for the convergence analysis is obtained by a discretization of

[6] in the format that serves as the program logo of the German Research Foundation (DFG).

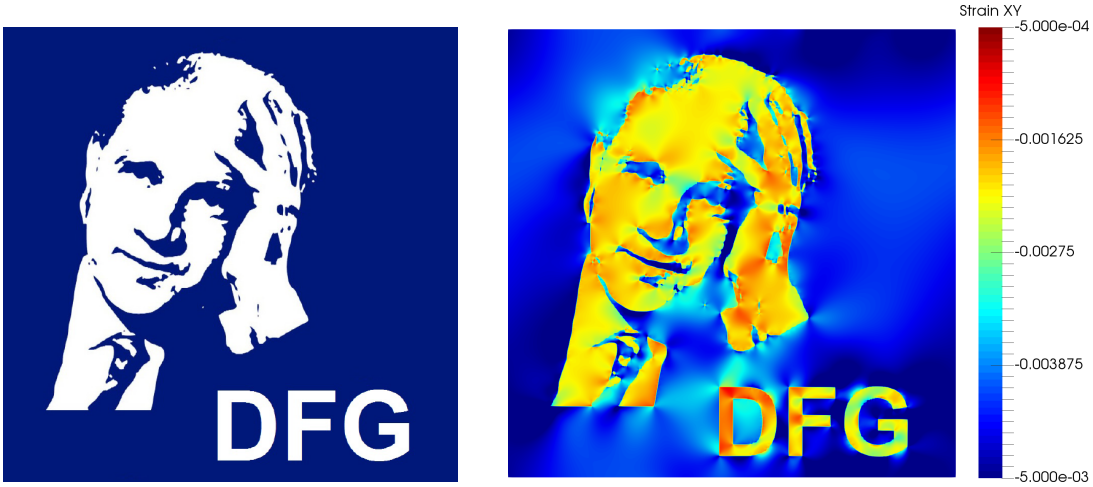


Figure 12: DFG-Heisenberg: (Left) two-phase distribution, (right) contour plot of shear strain $2E_{xy}$ at position $x = 666.67$ mm, $y = 333.34$ mm.

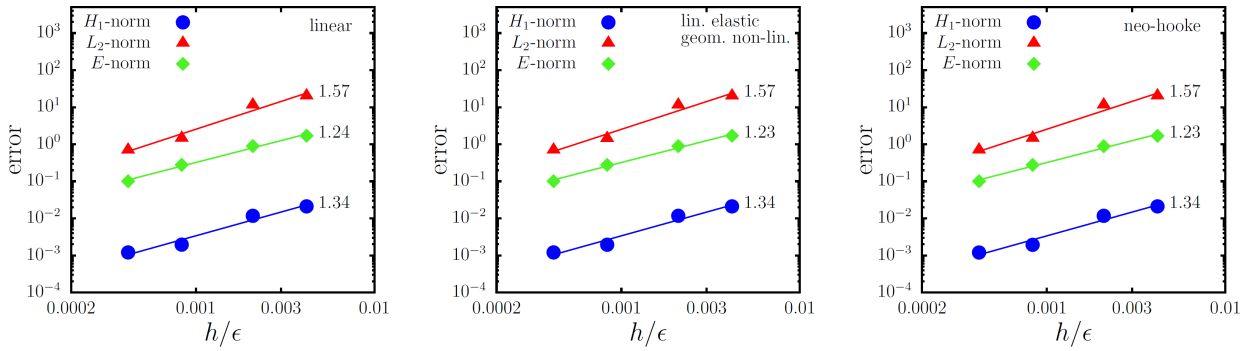


Figure 13: DFG-Heisenberg: Micro convergence for (left:) the fully linear case, (center:) for linear elasticity with geometrical nonlinearity, and (right:) for neo-Hookean hyperelasticity.

ndof= 46 099 202 on the micro domain employing a characteristic element width of $h = 1/4800$ mm with $q = 1$. The discretization directly follows from the pixels of the original image. Since we are mostly interested in the micro convergence and differences between the cases having different levels of nonlinearity, a simple driver on the macro scale in terms of one triangular macro element with $p = 1$ is enough.

The measured convergence orders in the diagrams of Fig. 13 are considerably reduced compared to the theoretical order of $2q = 2$; it is most pronounced in the energy-norm and least pronounced in the L_2-norm. The reduced order is caused by the stiff inclusion phase pinching into the softer matrix phase, compare the shear strain distribution in Fig. 12. Due to almost identical results for the fully linear case with the nonlinear cases it can be concluded that the nonlinearities by geometry and material have no impact on convergence.

6.3.2 Standard Newton versus alternating Newton The speedup factors of the novel scheme compared to the standard solution procedure are given in Tab. 8.

macro ndof	micro ndof	speedup factor linear elastic	speedup factor neo-Hookean
8	116162	1.41	1.41
	462 722	1.37	1.32
	1 847 042	1.51	1.41
	2 884 802	1.58	1.49
	11 529 602	1.82	1.58
	46 099 202	1.73	1.73
882	116 162	1.21	1.38
3 362		1.22	1.41
13 122		1.22	1.41
51 842		1.28	1.41
206 082		1.27	1.25

Table 8: DFG-Heisenberg: speedup factors of alternating Newton compared to standard Newton depending on discretizations and type of elastic constitutive law.

The speedup is throughout in between 1.2 and 1.8, such that the novel solution strategy pays off in either case. For a fixed macro discretization the speedup factor is the larger, the finer the micro discretization, which is independent of the elasticity law and true apart from some outliers. For the case of a fixed micro discretization the speedup-factor is relatively insensitive to the macro discretization. These trends are consistent with the previous example of Escher's Pegasus.

6.4 Nanoporous gold

Nanoporous gold exhibits extraordinary properties such as high catalytic activity [62], surface-stress induced macroscopic bending of cantilevers [63], and it is a promising component for gold-polymer nanocomposites [64].

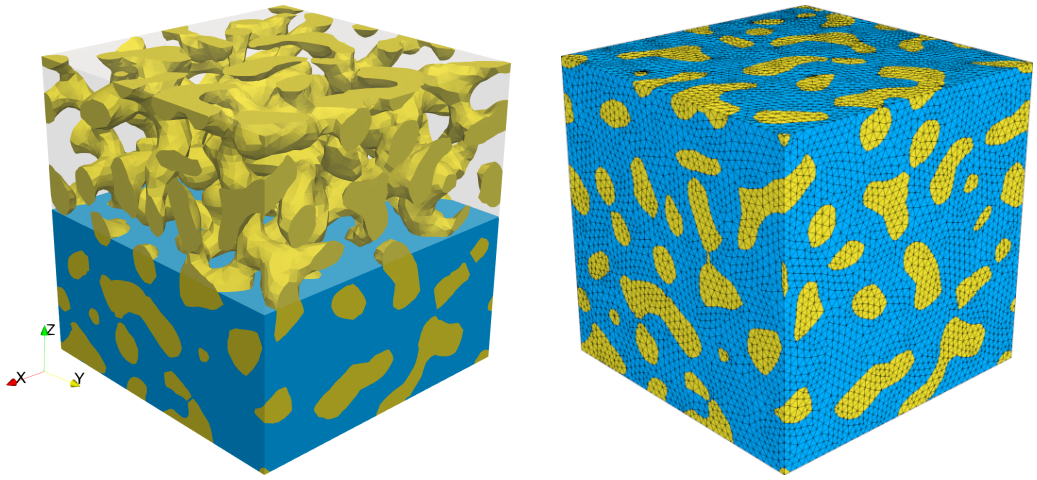


Figure 14: Nanoporous gold composite: (Left) gold phase distribution, (right) discretization with ndof=1 807 389.

Here we consider a gold-polymer nanocomposites with the nanoporous gold phase embedded in a softer second phase. Linear Dirichlet boundary conditions are applied on the RVE. Instead of using true material parameters for the phases, we stick to the unified material parameters valid throughout this work. The Young's moduli of the gold phase are set to $E_i = 100\,000$ N/mm^2 and the matrix phase $E_m = 40\,000$ N/mm^2, $\nu = 0.2$ for both phases, see Tab. 2. The volume ratio of the gold phase is $V_i/V_{\text{tot}} = 0.36$.

The macro BVP is a cantilever beam with length $l = 5000$ mm, height $b = 1000$ mm, and thickness $t = 1000$ mm. At its free end the cantilever beam is subject to displacement control with a total displacement of 200 mm applied to all nodes at $x = l$ in four loading steps.

6.4.1 Micro convergence for linear elasticity and neo-Hookean hyperelasticity

The reference solution for the convergence study is obtained by ndof=72 on the macro domain (5×1×1 hexahedral macro elements) and ndof=5 484 291 on the micro domain with $\epsilon = 4.03$ mm.

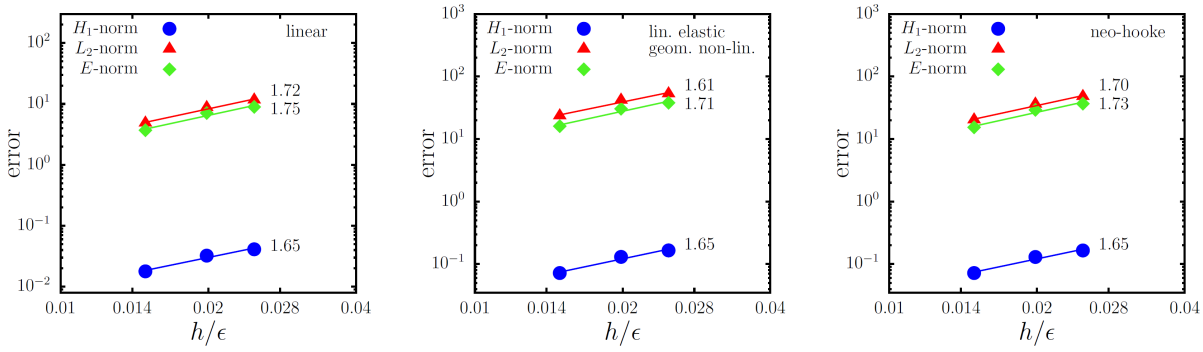


Figure 15: Nanoporous gold composite: Micro convergence for (left:) the fully linear case, (center:) linear elasticity with geometrical nonlinearity, and (right:) the case of Neo-Hookean hyperelasticity.

The convergence diagrams are displayed in Fig. 15. The convergence order for the case of geometrical nonlinearity as well as for additional material nonlinearity is virtually the

same as for the fully linear case, an exception is the case of geometrical nonlinearity along with linear elasticity in the L_2-norm.

macro ndof	micro ndof	speedup factor linear elastic	neo-Hookean
72	262 308	1.75	1.69
	353 904	1.77	1.71
	690 162	1.98	1.82
	1 518 654	1.88	1.86
	1 807 389	1.86	1.86
297	262 308	1.85	1.85
1575		1.90	1.89
4557		1.78	1.81

Table 9: Nanoporous gold composite: speedup factors of the alternating Newton compared to the standard Newton depending on discretizations and the type of elasticity law.

6.4.2 Standard Newton versus alternating Newton The speedup factors in Tab. 9 range from 1.7 to almost 2 and are higher than in the previously considered homogenization problems in 2d. There is no clear trend in the speedup factors for finer meshes except of for the case of neo-Hookean hyperelasticity, where the speedup is the larger, the finer the micro mesh. For the other cases of various discretizations (combinations of micro to macro) the speedup is around 1.8 with relatively minor variance.

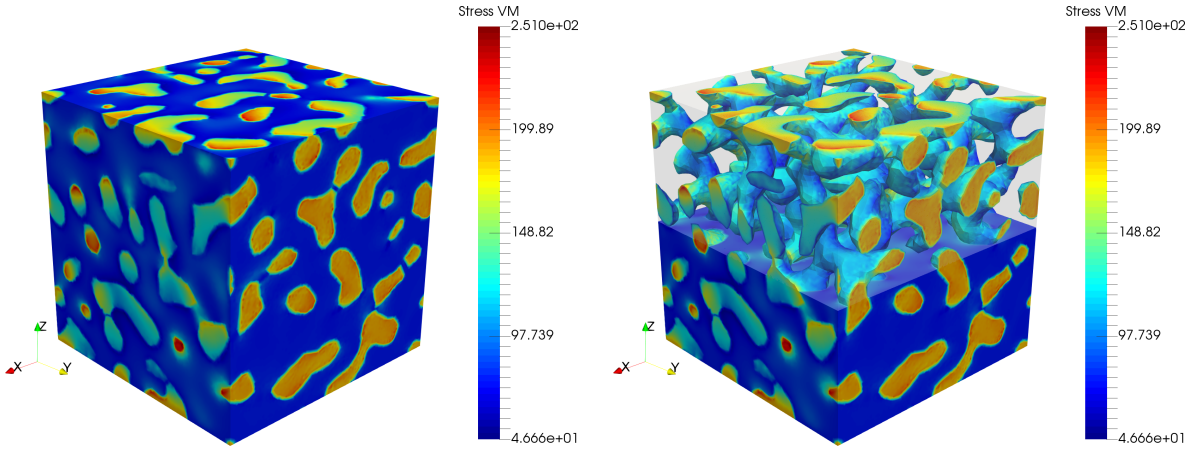


Figure 16: Nanoporous gold composite: von-Mises stress distribution in (N/mm²) at $x = y = z = 605.6624$ mm.

7 Summary

The main results of the present paper shall be summarized.

1. A Finite Element Heterogeneous Multiscale Method FE-HMM was developed for geometrical nonlinearity and hyperelastic solids in a Lagrangean setting.

2. Existing a priori estimates for the fully linear case (linear elasticity in a geometrical linear frame) were assessed for the present nonlinear case in numerical tests and confirmed for sufficient regularity of the BVPs. In either case the convergence results in the nonlinear elastic regime are close to those of the fully linear case for the investigated examples.

3. The staggered, micro-macro solution concept in terms of a two-level Newton algorithm was revised along with the proposal of an alternative scheme.

   - The standard approach in terms of nested loops can safely and efficiently be replaced by direct alternations between micro and macro solution iterations. The fully converged solution of micro problems for each macro iteration is neither necessary for achieving convergence nor favorable for the efficiency.
   - For the considered problems the novel concept (i) is robust with respect to large loading steps, (ii) exhibits speedup factors in the range of 1.05 up to 2.6 in 2D, and in the range from 1.7 to 2.0 in 3D, where the speedup is on average higher in 3D than in 2D.
   - The observed minimal speedup is above 1.0, such that the novel concept does not slow down simulations. Since the speedup of 1.0 is clearly not a granted lower bound, monitoring the macro convergence on-the-fly in terms of the required iterations can avoid deficits in efficiency.
   - A particular appeal of the proposed concept is its simplicity and ease of implementation.

4. The advantages of the novel concept was demonstrated for FE-HMM simulations. It equally applies for FE^2 for the equality of the methods despite a minor difference in micro-macro stiffness transfer.

It is expected that the novel speedup concept can be used in different applications as e.g. in coupled problems such as electro-/magneto-/mechanical-coupling, or generally, in any other nonlinear problem set for which a staggered, two-level algorithmic solution concept in terms of an embedded loop is standard.

Inelastic problems in homogenization require a separate analysis in order to arrive at valid conclusions on the applicability of the proposed speedup concept, which will be presented elsewhere.

Acknowledgments. Bernhard Eidel acknowledges support by the Deutsche Forschungsgemeinschaft (DFG) within the Heisenberg program (grant no. EI 453/2-1). Simulations were performed with computing resources granted by RWTH Aachen University under project ID prep0005. This has enabled the present work.

References

[1] Assyr Abdulle. Analysis of the heterogeneous multiscale FEM for problems in elasticity. *Mathematical Models and Methods in Applied Sciences*, 16(04):615–635, 2006.

[2] Bernhard Eidel and Andreas Fischer. The heterogeneous multiscale finite element method for the homogenization of linear elastic solids and a comparison with the FE2 method. *Computer Methods in Applied Mechanics and Engineering*, 329:332–368, 2018.

[3] J. C. Michel, H. Moulinec, and P. Suquet. Effective properties of composite materials with periodic microstructure: a computational approach. *Computer Methods in Applied Mechanics and Engineering*, 172(1-4):109–143, 1999.

[4] Christian Miehe, Jörg Schröder, and Jan Schotte. Computational homogenization analysis in finite plasticity simulation of texture development in polycrystalline materials. *Computer Methods in Applied Mechanics and Engineering*, 171(3-4):387–418, 1999.

[5] Christian Miehe, Jan Schotte, and Jörg Schröder. Computational micro–macro transitions and overall moduli in the analysis of polycrystals at large strains. *Computational Materials Science*, 16(1-4):372–382, 1999.

[6] Frédéric Feyel and Jean-Louis Chaboche. FE2 multiscale approach for modelling the elastoviscoplastic behaviour of long fibre sic/ti composite materials. *Computer Methods in Applied Mechanics and Engineering*, 183(3-4):309–330, 2000.

[7] V. Kouznetsova, W. A. M. Brekelmans, and F. P. T. Baaijens. An approach to micro-macro modeling of heterogeneous materials. *Computational Mechanics*, 27(1):37–48, 2001.

[8] Weinan E, Björn Engquist, Xiantao Li, Weiqing Ren, and Eric Vanden-Eijnden. Heterogeneous multiscale methods : A review. *Communications in Computational Physics*, 2(3):367–450, 2007.

[9] Assyr Abdulle. The finite element heterogeneous multiscale method: A computational strategy for multiscale PDEs. *GAKUTO International Series Mathematical Sciences and Applications*, 31:133–181, 2009.

[10] Assyr Abdulle, Weinan E, Björn Engquist, and Eric Vanden-Eijnden. The heterogeneous multiscale method. *Acta Numerica*, 21:1–87, 2012.

[11] Assyr Abdulle and Martin E. Huber. Error estimates for finite element approximations of nonlinear monotone elliptic problems with application to numerical homogenization. *Numerical Methods for Partial Differential Equations*, 32(3):955–969, 2016.

[12] Patrick Henning and Mario Ohlberger. Error control and adaptivity for heterogeneous multiscale approximations of nonlinear monotone problems. *Discrete and Continuous Dynamical Systems - Series S*, 8(1):119–150, 2015.

[13] Ramin Shirazi Nejad and Christian Wieners. Parallel inelastic heterogeneous multiscale simulations. In Stefan Diebels and Sergej Rjasanow, editors, *Multi-scale Simulation of Composite Materials*, volume 23 of *Mathematical Engineering*, pages 57–96. Springer Berlin Heidelberg, Berlin, Heidelberg, 2019.

[14] Weinan E, Pingbing Ming, and Pingwen Zhang. Analysis of the heterogeneous multiscale method for elliptic homogenization problems. *Journal of the American Mathematical Society*, 18(01):121–157, 2005.

[15] Mario Ohlberger. A posteriori error estimates for the heterogeneous multiscale finite element method for elliptic homogenization problems. *Multiscale Modeling & Simulation*, 4(1):88–114, 2005.

[16] Andreas Fischer and Bernhard Eidel. Convergence and error analysis of FE-HMM/FE2 for energetically consistent micro-coupling conditions in linear elastic solids. *European Journal of Mechanics - A/Solids*, 77, 2019.

[17] H. Moulinec and P. Suquet. A fast numerical method for computing the linear and nonlinear mechanical properties of composites. *Comptes rendus de l'Académie des Sciences Paris II*, 318:1417–14230, 1994.

[18] H. Moulinec and P. Suquet. A numerical method for computing the overall response of nonlinear composites with complex microstructure. *Computer Methods in Applied Mechanics and Engineering*, 157(1-2):69–94, 1998.

[19] R. Zeller and P. H. Dederichs. Elastic constants of polycrystals. *Physica Status Solidi (b)*, 55(2):831–842, 1973.

[20] Ekkehart Kröner. *Statistical continuum mechanics: Course held ... October 1971*, volume no. 92 of *Courses and lectures / International Centre for Mechanical Sciences*. Springer, Wien, 1972.

[21] Matti Schneider, Felix Ospald, and Matthias Kabel. Computational homogenization of elasticity on a staggered grid. *International Journal for Numerical Methods in Engineering*, 105(9):693–720, 2016.

[22] Matti Schneider, Dennis Merkert, and Matthias Kabel. FFT-based homogenization for microstructures discretized by linear hexahedral elements. *International Journal for Numerical Methods in Engineering*, 109(10):1461–1489, 2017.

[23] J. Yvonnet and Q.-C. He. The reduced model multiscale method (R3M) for the non-linear homogenization of hyperelastic media at finite strains. *Journal of Computational Physics*, 223(1):341–368, 2007.

[24] Annika Radermacher and Stefanie Reese. POD-based model reduction with empirical interpolation applied to nonlinear elasticity. *International Journal for Numerical Methods in Engineering*, 107(6):477–495, 2016.

[25] Dominic Soldner, Benjamin Brands, Reza Zabihyan, Paul Steinmann, and Julia Mergheim. A numerical study of different projection-based model reduction techniques applied to computational homogenisation. *Computational Mechanics*, 60(4):613–625, 2017.

[26] Jörg Schröder, Daniel Balzani, and Dominik Brands. Approximation of random microstructures by periodic statistically similar representative volume elements based on lineal-path functions. *Archive of Applied Mechanics*, 81(7):975–997, 2011.

[27] Axel Klawonn and Oliver Rheinbach. Robust feti-dp methods for heterogeneous three dimensional elasticity problems. *Computer Methods in Applied Mechanics and Engineering*, 196(8):1400–1414, 2007.

[28] A. Klawonn and O. Rheinbach. Highly scalable parallel domain decomposition methods with an application to biomechanics. *Journal of Applied Mathematics and Mechanics*, 90(1):5–32, 2010.

[29] Lorenz Holzer and Marco Cantoni. Review of FIB-tomography. In Ivo Utke, Stanislav Moshkalev, and Phillip Russell, editors, *Nanofabrication Using Focused Ion and Electron Beams*, volume 559201222 of *Oxford series on nanomanufacturing*, pages 410–435. Oxford University Press, Oxford, 2011.

[30] Erik H. Saenger, Frieder Enzmann, Youngseuk Keehm, and Holger Steeb. Digital rock physics: Effect of fluid viscosity on effective elastic properties. *Journal of Applied Geophysics*, 74(4):236–241, 2011.

[31] Heiko Andrä, Nicolas Combaret, Jack Dvorkin, Erik Glatt, Junehee Han, Matthias Kabel, Youngseuk Keehm, Fabian Krzikalla, Minhui Lee, Claudio Madonna, Mike Marsh, Tapan Mukerji, Erik H. Saenger, Ratnanabha Sain, Nishank Saxena, Sarah Ricker, Andreas Wiegmann, and Xin Zhan. Digital rock physics benchmarks—Part I: Imaging and segmentation. *Computers & Geosciences*, 50:25–32, 2013.

[32] G. Legrain, P. Cartraud, I. Perreard, and N. Moës. An X-FEM and level set computational approach for image-based modelling: Application to homogenization. *International Journal for Numerical Methods in Engineering*, 86(7):915–934, 2011.

[33] W. D. Lian, G. Legrain, and P. Cartraud. Image-based computational homogenization and localization: comparison between X-FEM/levelset and voxel-based approaches. *Computational Mechanics*, 51(3):279–293, 2013.

[34] Andreas Fischer and Bernhard Eidel. Error analysis for quadtree-type mesh-coarsening algorithms adapted to pixelized heterogeneous microstructures, 2019.

[35] C. Miehe and A. Koch. Computational micro-to-macro transitions of discretized microstructures undergoing small strains. *Archive of Applied Mechanics (Ingenieur Archiv)*, 72(4-5):300–317, 2002.

[36] Christian Miehe. Computational micro-to-macro transitions for discretized microstructures of heterogeneous materials at finite strains based on the minimization of averaged incremental energy. *Computer Methods in Applied Mechanics and Engineering*, 192(5-6):559–591, 2003.

[37] Frédéric Feyel. A multilevel finite element method (FE2) to describe the response of highly non-linear structures using generalized continua. *Computer Methods in Applied Mechanics and Engineering*, 192(28-30):3233–3244, 2003.

[38] V. G. Kouznetsova, M.G.D. Geers, and W.A.M. Brekelmans. Multi-scale second-order computational homogenization of multi-phase materials: a nested finite element solution strategy. *Computer Methods in Applied Mechanics and Engineering*, 193(48-51):5525–5550, 2004.

[39] I. Özdemir, W.A.M. Brekelmans, and M.G.D. Geers. FE^2 computational homogenization for the thermo-mechanical analysis of heterogeneous solids. *Computer Methods in Applied Mechanics and Engineering*, 198(3-4):602–613, 2008.

[40] İ. Temizer and P. Wriggers. On the computation of the macroscopic tangent for multiscale volumetric homogenization problems. *Computer Methods in Applied Mechanics and Engineering*, 198(3-4):495–510, 2008.

[41] Jörg Schröder. A numerical two-scale homogenization scheme: the FE2-method. In Friedrich Pfeiffer, Franz G. Rammerstorfer, Elisabeth Guazzelli, Bernhard Schrefler, Paolo Serafini, Jörg Schröder, and Klaus Hackl, editors, *Plasticity and Beyond*, volume 550 of *CISM International Centre for Mechanical Sciences*, pages 1–64. Springer Vienna, Vienna, 2014.

[42] Saba Saeb, Paul Steinmann, and Ali Javili. Aspects of computational homogenization at finite deformations: A unifying review from Reuss' to Voigt's bound. *Applied Mechanics Reviews*, 68(5):050801, 2016.

[43] Axel Klawonn, Stephan Köhler, Martin Lanser, and Oliver Rheinbach. Computational homogenization with million-way parallelism using domain decomposition methods. *Computational Mechanics*, 21(1):1, 2019.

[44] Bernhard Eidel, Andreas Fischer, and Ajinkya Gote. A nonlinear FE-HMM formulation along with a novel algorithmic structure for finite deformation elasticity. *PAMM*, 18(1):e201800457, 2018.

[45] G. Papanicolau, A. Bensoussan, and J. L. Lions. *Asymptotic Analysis for Periodic Structures*. Elsevier, Burlington, 1978.

[46] Enrique Sanchez-Palencia. *Non-homogenous media and vibration theory*. Springer-Verlag, Berlin, 1980.

[47] JoséMiranda Guedes and Noboru Kikuchi. Preprocessing and postprocessing for materials based on the homogenization method with adaptive finite element methods. *Computer Methods in Applied Mechanics and Engineering*, 83(2):143–198, 1990.

[48] Grégoire Allaire. Homogenization and two-scale convergence. *SIAM Journal on Mathematical Analysis*, 23(6):1482–1518, 1992.

[49] D. Cioranescu and Patrizia Donato. *An introduction to homogenization*, volume 17 of *Oxford lecture series in mathematics and its applications*. Oxford University Press, Oxford and New York, 1999.

[50] R. Hill. Elastic properties of reinforced solids: Some theoretical principles. *Journal of the Mechanics and Physics of Solids*, 11(5):357–372, 1963.

[51] Martin Ostoja-Starzewski. Material spatial randomness: From statistical to representative volume element. *Probabilistic Engineering Mechanics*, 21(2):112–132, 2006.

[52] K. Sab. On the homogenization and the simulation of random materials. *European Journal of Mechanics A-Solids*, 11(5):585–607, 1992.

[53] W. J. Drugan and J. R. Willis. A micromechanics-based nonlocal constitutive equation and estimates of representative volume element size for elastic composites. *Journal of the Mechanics and Physics of Solids*, 44(4):497–524, 1996.

[54] Jean Mandel. *Plasticité classique et viscoplasticité*, volume No 97 of *Courses and Lectures, International centre for mechanical sciences*. Springer, Vienna, 1972.

[55] R. Hill. On constitutive macro-variables for heterogeneous solids at finite strain. *Proceedings of the Royal Society A: Mathematical, Physical and Engineering Sciences*, 326(1565):131–147, 1972.

[56] Weinan E and Bjorn Engquist. The heterogeneous multiscale methods. *Communications in Mathematical Sciences*, 1(1):87–132, 2003.

[57] E. A. de Souza Neto and R. A. Feijóo. On the equivalence between spatial and material volume averaging of stress in large strain multi-scale solid constitutive models. *Mechanics of Materials*, 40(10):803–811, 2008.

[58] R. Grytz and G. Meschke. Consistent micro-macro transitions at large objective strains in curvilinear convective coordinates. *International Journal for Numerical Methods in Engineering*, 73(6):805–824, 2008.

[59] N. P. van Dijk. Formulation and implementation of stress-driven and/or strain-driven computational homogenization for finite strain. *International Journal for Numerical Methods in Engineering*, 107(12):1009–1028, 2016.

[60] Bernhard Eidel and Andreas Fischer. The heterogeneous multiscale finite element method FE-HMM for the homogenization of linear elastic solids. *PAMM*, 16(1):521–522, 2016.

[61] Orane Jecker and Assyr Abdulle. Numerical experiments for multiscale problems in linear elasticity. In Bülent Karasözen, Murat Manguoğlu, Münevver Tezer-Sezgin, Serdar Göktepe, and Ömür Uğur, editors, *Numerical Mathematics and Advanced Applications ENUMATH 2015*, volume 112 of *Lecture Notes in Computational Science and Engineering*, pages 123–131. Springer International Publishing, Cham, 2016.

[62] Takeshi Fujita, Pengfei Guan, Keith McKenna, Xingyou Lang, Akihiko Hirata, Ling Zhang, Tomoharu Tokunaga, Shigeo Arai, Yuta Yamamoto, Nobuo Tanaka, Yoshifumi Ishikawa, Naoki Asao, Yoshinori Yamamoto, Jonah Erlebacher, and Mingwei Chen. Atomic origins of the high catalytic activity of nanoporous gold. *Nature materials*, 11(9):775–780, 2012.

[63] Dominik Kramer, Raghavan Nadar Viswanath, and Jörg Weissmüller. Surface-stress induced macroscopic bending of nanoporous gold cantilevers. *Nano Letters*, 4(5):793–796, 2004.

[64] Emma Griffiths, Swantje Bargmann, and B. D. Reddy. Elastic behaviour at the nanoscale of innovative composites of nanoporous gold and polymer. *Extreme Mechanics Letters*, 17:16–23, 2017.